# ELECTROCHEMICAL CHARACTERIZATION AND TIME-VARIANT STRUCTURAL RELIABILITY ASSESSMENT OF POST-TENSIONED, SEGMENTAL CONCRETE BRIDGES

A Dissertation

by

RADHAKRISHNA PILLAI GOPALAKRISHNAN

Submitted to the Office of Graduate Studies of
Texas A&M University
in partial fulfillment of the requirements for the degree of

DOCTOR OF PHILOSOPHY

May 2009

Major Subject: Civil Engineering

# ELECTROCHEMICAL CHARACTERIZATION AND TIME-VARIANT STRUCTURAL RELIABILITY ASSESSMENT OF POST-TENSIONED, SEGMENTAL CONCRETE BRIDGES

A Dissertation

by

RADHAKRISHNA PILLAI GOPALAKRISHNAN

Submitted to the Office of Graduate Studies of
Texas A&M University
in partial fulfillment of the requirements for the degree of

DOCTOR OF PHILOSOPHY

Approved by:

| | |
|---|---|
| Co-Chairs of Committee, | David Trejo |
| | Mary Beth D. Hueste |
| Committee Members, | Paolo Gardoni |
| | Kenneth F. Reinschmidt |
| | Daren B.H. Cline |
| Head of Department, | David V. Rosowsky |

May 2009

Major Subject: Civil Engineering

# ABSTRACT

Electrochemical Characterization and Time-Variant Structural Reliability Assessment of Post-Tensioned, Segmental Concrete Bridges. (May 2009)

Radhakrishna Pillai Gopalakrishnan, B.E., University of Allahabad, India;
M.S., Texas A&M University

Co-Chairs of Committee, Dr. David Trejo
Dr. Mary Beth D. Hueste

In post-tensioned (PT) bridges, prestressing steel tendons are the major load carrying components. These tendons consist of strands, ducts, and cementitious grout that fill the interstitial space between the strands and ducts. However, inspections on PT bridges have reported the presence of voids, moisture, and chlorides inside grouted ducts as the major cause of accelerated corrosion of strands. Corrosion of the strands has resulted in PT bridge failures in Europe and tendon failures in the United States. As most of the PT bridges have high importance measures and the consequences of failure are significant, it is important to maintain high levels of safety and serviceability for these bridges. To meet this goal, bridge management authorities are in dire need of tools to quantify the long-term performance of these bridges. Time-variant structural reliability models can be useful tools to quantify the long-term performance of PT bridges.

This doctoral dissertation presents the following results obtained from a comprehensive experimental and analytical program on the performance of PT bridges.

- Electrochemical characteristics of PT systems
- Probabilistic models for tension capacity of PT strands and wires exposed to various void and environmental conditions
- Time-variant structural reliability models (based on bending moment and stress limit states) for PT bridges

- Time-variant strength and service reliabilities of a typical PT bridge experiencing HS20 and HL93 loading conditions and different exposure conditions for a period of 75 years

The experimental program included exposure of strand specimens to wet-dry and continuous-atmospheric conditions. These strand specimens were fabricated to mimic void and/or grout-air-strand (GAS) conditions inside the tendons. It was found that the GAS interface plays a major role in strand corrosion. The GAS interfaces that are typically located in the anchorage zones of harped PT girders or vertical PT columns can cause aggressive strand corrosion. At these locations, if voids are present and the environment is relatively dry, then limited corrosion of the strands occurs. However, if the presence of high relative humidity or uncontaminated and chloride-contaminated water exists at these interfaces, then corrosion activity can be high. The strands were exposed for a period of 12, 16, and 21 months, after which the remaining tension capacity was determined.

The analytical program included the development of probabilistic strand capacity models (based on the experimental data) and the structural reliability models. The time-variant tension capacity predicted using the developed probabilistic models were reasonably consistent with the tendon failures observed in PT bridges in Florida and Virginia. The strength reliability model was developed based on the moment capacity and demand at midspan. Service reliability model was developed based on the allowable and applied stresses at midspan. Using these models, the time-variant strength and service reliabilities of a typical PT bridge were determined based on a set of pre-defined constant and random parameters representing void, material, exposure, prestress, structural loading, and other conditions. The strength and service reliabilities of PT bridges exposed to aggressive environmental conditions can drop below the recommended values at relatively young ages. In addition, under similar conditions the service reliability drops at a faster rate than the strength reliability.

# DEDICATION

To my wife and parents

## ACKNOWLEDGMENTS

The author takes this opportunity to acknowledge the excellent academic guidance and financial assistance offered by Dr. David Trejo during my entire graduate studies at Texas A&M University (TAMU). Without his guidance on electrochemical and materials testing, and other aspects of my research, this dissertation would not have become a reality. Working with Dr. Trejo was a wonderful experience in many ways and I will never forget him in my life. I sincerely appreciate the excellent guidance provided by Dr. Mary Beth Hueste and Dr. Paolo Gardoni on the structural behavior and structural reliability aspects of my doctoral research. I am also grateful to Dr. Kenneth Reinschmidt for his guidance and advices on the importance of developing practical and feasible solutions. The timely guidance offered by Dr. Daren B.H. Cline is also appreciated. In general, I am very fortunate to have an extraordinary advisory committee with a wide range of expertise that helped me view the engineering challenges from multiple persective and shape this dissertation in its current form.

I sincerely acknowledge the Texas Department of Transportation for funding the research project through Texas Transportation Institute (TTI). I thank Jeff Perry and Matt Potter of the High Bay Structural Materials Laboratory; Scott Crauneur of the Zachry Depart of Civil Engineering; Duane Wagner, Cheryl Burt, Scott Dobrovolny, Robert Kocman, and Gary Gerke of TTI for their assistance at various stages of my research. I appreciate the assistance from Dr. Ceki Halmen, Dr. Young Hoon Kim, Suresh Kataria, Srikanth Bondugula, Seok Been Im, Sean Eglinton, Jayashankar, Brian Wiggins, Rhett Dotson, Laura Bolduc, Michael Gamble, Thanh Ngo, and other student members of our research group. I thank Ramesh Kumar and Byoung Chan for extending their expertise in Matlab programming and helping me resolve some techincal challenges in structural reliability analysis.

I am grateful to have a good friend like Anand (Abang), who was there to help me in various capacities during my doctoral studies. I thank him for reviewing sections 7, 8, and 9 of this dissertation and assisting me in facing many technical and professional challenges during my doctoral studies. Abang, you will be remembered throughout my life for the discussions we had on life and civil engineering. Mugdha, I thank you for spending some of your weekends with us.

I appreciate the constant encouragement from my good old Monorecan Mallu friends, Vipin, Hari, Nebu, KK, Manu, Unni, Titto, and others. I also extend my sincere thanks to Dutta and Subrata for their encouragement. Vipul, I am highly grateful to you for your support and the financial statement, which helped me in keeping my I-20 valid during the last semester of my studies.

I offer special thanks to Achan and Amma for their continous support, which helped me achieve my "Ph.D. dream." I appreciate the support from my sister, Sandhya, brother-in-law, Rajesh, and niece, Devooty. I am highly grateful to my foster parents for encouraging me in this endeavour. Continuous support from Mummy, Pappa, and Varun is also highly appreciated. Support from other family members is also appreciated.

Finally, my very special thanks go to my wife, Thushi, for her encouragement, patience, and support in achieving this dream.

# TABLE OF CONTENTS

Page

ABSTRACT ..... iii

DEDICATION ..... v

ACKNOWLEDGMENTS ..... vi

TABLE OF CONTENTS ..... viii

LIST OF FIGURES ..... xv

LIST OF TABLES ..... xxiii

1. INTRODUCTION ..... 1

    1.1. Prestressed Concrete Technology ..... 1
    1.2. Definitions ..... 2
    1.3. Classification of Post-Tensioned Systems ..... 2
        1.3.1. Internal post-tensioned systems ..... 3
        1.3.2. External post-tensioned systems ..... 4
    1.4. Research Motivation ..... 5
    1.5. Research Objectives ..... 7
    1.6. Research Assumptions ..... 7
    1.7. Research Methodology ..... 9
    1.8. Organization of Dissertation ..... 10

2. LITERATURE REVIEW ..... 13

    2.1. Introduction ..... 13
    2.2. Deterioration of Post-Tensioned Bridges ..... 13
        2.2.1. Failures of internal, grouted, post-tensioned systems ..... 13
        2.2.2. Failures of external, grouted post-tensioned systems ..... 15
    2.3. Parameters Influencing Corrosion of Post-Tensioned Systems ..... 22
        2.3.1. Dissimilar metallic materials in post-tensioned systems ..... 22
        2.3.2. Grout class ..... 24
        2.3.3. Voids ..... 25

Page

2.3.4. Oxygen concentration ....27
2.3.5. Cementitious pore-solution and pH....27
2.3.6. Carbon dioxide concentration ....29
2.3.7. Moisture conditions and precipitation....30
2.3.8. Time of wetness ....32
2.3.9. Relative humidity ....32
2.3.10. Chloride concentration ....34
2.3.11. Temperature ....35
2.3.12. Axial stress ....35
2.3.13. Other factors....36
2.4. Corrosion Evaluation Using Visual Inspection Tools....37
2.5. Modeling Corrosion of Steel (Immersion Conditions) ....38
2.6. Modeling Corrosion of Steel (Continuous-Atmospheric Conditions) ....40
2.6.1. Atmospheric corrosion models based on environmental parameters, time functions, or both....40
2.6.2. Atmospheric corrosion models based on time functions only ....42
2.6.3. Developing and updating the power corrosion model ....46
2.7. Structural Capacity of Post-Tensioned, Segmental Bridges ....48
2.7.1. Parameters directly influencing structural behavior of PT girders....48
2.7.2. A history of design codes/practices for concrete bridges....52
2.7.3. Differences in the behavior of monolithic and segmental post-tensioned beams ....53
2.7.4. Stress-strain relationship for unbonded tendons ....53
2.7.5. Stress-strain relationship for concrete cross sections....54
2.7.6. In-service and allowable stresses in a cross section....56
2.7.7. Existing approaches to determine flexural capacity of prestressed girders....58
2.8. Structural Demand on Post-Tensioned Bridges ....59
2.8.1. Dead load....59
2.8.2. Live and impact loads ....60
2.9. Structural Reliability of Post-Tensioned Bridges....62
2.9.1. Modeling and assessment of structural reliability....62
2.9.2. Structural reliability of bridges with uncorroded strands....65
2.9.3. Target reliability index ....66
2.10. Typical Characteristics of Segmental Concrete Bridges in Texas ....69
2.10.1. Segmental concrete bridges in Texas ....69
2.10.2. San Antonio “Y” bridge ....70
2.10.3. Span and girder inventory in San Antonio “Y” bridge ....73
2.10.4. Tendon inventory on San Antonio “Y” bridge....77
2.10.5. Cross-sectional properties of girders in San Antonio “Y” bridge....77
2.11. Summary ....79

Page

3. CURRENT NEEDS AND RESEARCH SIGNIFICANCE ..... 80

4. ENVIRONMENTAL CHARACTERIZATION MAPS OF TEXAS ..... 83

4.1. Introduction ..... 83
4.2. Freeze-Day, Temperature, Relative Humidity, and Rain-Day maps ..... 84
4.3. Chloride Maps ..... 86
4.4. Total Corrosion Risk Maps ..... 88
4.5. Summary ..... 91

5. ELECTROCHEMICAL AND TENSION CAPACITY BEHAVIOR OF WIRES AND STRANDS - EXPERIMENTAL PROGRAM ..... 92

5.1. Introduction ..... 92
5.2. Materials Used in the Experimental Program ..... 93
5.2.1. Metallic reinforcement ..... 93
5.2.2. Mineral aggregates used in concrete ..... 96
5.2.3. Cementitious materials ..... 98
5.2.4. Water ..... 101
5.2.5. Chloride concentration in the exposure solutions and grouts ..... 102
5.3. Cyclic Polarization Tests ..... 103
5.3.1. Introduction and objectives ..... 103
5.3.2. Experimental design and specimen layout ..... 104
5.3.3. Sample preparation and test procedures ..... 106
5.4. Galvanic Corrosion Tests ..... 108
5.4.1. Introduction and objectives ..... 108
5.4.2. Experimental design and specimen layout - Modified ASTM G109 tests ..... 108
5.4.3. Casting, curing, and exposure procedures - Modified ASTM G109 tests ..... 111
5.4.4. Experimental design and specimen layout - Bearing plate tests ..... 112
5.4.5. Casting, curing, and exposure procedures – Bearing plate tests ..... 114
5.4.6. Corrosion evaluation procedures ..... 116
5.5. Strand and Wire Corrosion Tests ..... 116
5.5.1. Introduction and objectives ..... 116
5.5.2. Experimental design and specimen layout ..... 117
5.5.3. Concrete reaction frames and stressing operations for stressed strand specimens ..... 128
5.5.4. Casting, curing, and exposure procedures ..... 136
5.5.5. Corrosion evaluation procedures ..... 142
5.5.6. Tension capacity determination or estimation procedures ..... 142
5.6. Summary ..... 147

Page

6. ELECTROCHEMICAL AND TENSION CAPACITY BEHAVIOR OF WIRES AND STRANDS - RESULTS ..... 148

6.1. Introduction ..... 148
6.2. Cyclic Polarization Test Results ..... 148
6.3. Galvanic Corrosion Test Results ..... 152
6.3.1. Modified ASTM G109 test results ..... 152
6.3.2. Bearing plate test results ..... 155
6.4. Strand and Wire Corrosion Test Results ..... 157
6.4.1. General visual observations ..... 157
6.4.2. Estimating tension capacity from strand photographs ..... 158
6.4.3. Tension capacities of strand and wire specimens ..... 160
6.5. Critical Parameters Influencing Tension Capacity of PT Strands ..... 168
6.5.1. Statistical hypothesis tests ..... 168
6.5.2. Effect of grout class ..... 169
6.5.3. Effect of moisture and chloride conditions ..... 169
6.5.4. Effect of stress conditions ..... 173
6.5.5. Effect of void conditions ..... 174
6.6. Summary ..... 175

7. MODELING TENSION CAPACITY OF STRANDS EXPOSED TO WET-DRY (WD) CONDITIONS ..... 177

7.1. Introduction ..... 177
7.2. Statistical Procedures to Develop Probabilistic Models ..... 177
7.2.1. Statistical diagnosis of experimental data ..... 177
7.2.2. Formulation of probabilistic capacity models ..... 178
7.2.3. Assessment or calibration of probabilistic capacity models ..... 179
7.3. Probabilistic Models for Tension Capacity of "As-Received" Strands ..... 184
7.4. Tension Capacity Models for Strands Under WD Exposure conditions - Analytical Program ..... 184
7.4.1. Parameters used in the models for wet-dry conditions ..... 185
7.4.2. Analytical steps to develop capacity models for strands under wet-dry (WD) conditions (Steps WD-1 through WD-5) ..... 186
7.4.3. Assumptions for predicting strand capacity under wet-dry conditions ..... 192
7.5. Tension Capacity Models for Strands Under WD Exposure conditions: Results ..... 193
7.5.1. Step WD-1: Identifying groups of void types with statistically dissimilar effects on tension capacity ..... 193
7.5.2. Step WD-2: Models for unstressed strands under WD exposure conditions (using unstressed strand data only) ..... 194

Page

7.5.3. STEP WD-3: Models for stressed strands under WD exposure conditions (using stressed strand data only).....208
7.5.4. STEP WD-4: Models for stressed strands under WD exposure conditions (using unstressed strand model and stressed strand data).....221
7.5.5. STEP WD-5: Selection of the most appropriate set of models for WD conditions .....230
7.5.6. Summary of strand capacity models for wet-dry conditions.....232

8. RELATIONSHIPS BETWEEN THE TENSION CAPACITIES OF UNSTRESSED WIRES AND STRESSED STRANDS.....234

8.1. Introduction .....234
8.2. Relationships Between Tension Capacities of Stressed Strands and Unstressed Wires – Analytical Program .....234
8.2.1. Introduction and objectives .....234
8.2.2. Parameters used in the probabilistic models for tension capacity.....235
8.2.3. Analytical steps to develop "unstressed wire-stressed strand" capacity model (Steps WS-1 through WS-4) .....236
8.3. Relationships Between Tension Capacities of Stressed Strands and Unstressed Wires - Results.....242
8.3.1. STEP WS-1: Develop models for wires exposed to solutions with $\%sCl^-$ levels below and above critical chloride threshold .....242
8.3.2. STEP WS-2: Develop UW-US-$SS_{WD,\ BIOV}$ model .....246
8.3.3. STEP WS-3: Develop UW-$SS_{WD,\ BIOV}$ Model .....251
8.3.4. Step WS-4: Select the more suitable "wire-strand" relationship for both WD and CA exposure conditions.....254
8.3.5. Summary of wire-strand relationships .....255

9. MODELING TENSION CAPACITY OF STRANDS EXPOSED TO CONTINUOUS-ATMOSPHERIC (CA) CONDITIONS.....256

9.1. Introduction .....256
9.2. Disclaimer .....256
9.3. Probabilistic Models for Tension Capacity of Strands – Analytical Program .....257
9.3.1. Introduction and objectives .....257
9.3.2. Parameters used in the probabilistic models for tension capacity.....258
9.3.3. Steps to develop tension capacity models for strands under CA conditions (Steps CA-1 through CA-4).....259
9.3.4. Assumptions for predicting strand capacity under CA conditions.....262

Page

9.4. Tension Capacity Models for Strands Under CA Exposure Conditions-Results ....263
9.4.1. Step CA-1: Develop probabilistic model for tension capacity of strands under CA and NV conditions ....263
9.4.2. Step CA-2: Develop probabilistic models for unstressed wires under CA and BIOV conditions ....263
9.4.3. Step CA-3: Predict the capacity of stressed strands at 9 months ....268
9.4.4. Step CA-4: Develop the model for stressed strands under CA and BIOV exposure conditions ....270
9.4.5. Prediction of tension capacity of stressed strands under CA and BIOV conditions ....270
9.5. Summary ....272

10. MODELING AND ASSESSMENT OF STRUCTURAL RELIABILITY OF SEGMENTAL BRIDGES ....273

10.1. Introduction and Objective ....273
10.2. Framework to Determine Structural Reliability ....273
10.3. Modeling Strength Reliability ....275
10.3.1. Strength limit state function, probability of strength failure, and strength reliability index ....275
10.3.2. Probabilistic modeling of moment capacity of the girder at midspan ....276
10.3.3. Probabilistic modeling of moment demand on the girder at midspan ....290
10.4. Modeling Service Reliability ....291
10.4.1. Service limit state function, probability of service failure, and service reliability index ....291
10.4.2. Probabilistic modeling of stress capacity of extreme fibers at midspan ....292
10.4.3. Probabilistic modeling of stress demand on extreme fibers at midspan ....293
10.5. Random Parameters in the Probabilistic Models ....296
10.5.1. Void and damage/opening conditions on post-tensioning systems ....296
10.5.2. Tension capacity of strands ....297
10.5.3. Prestress loss of strands ....300
10.5.4. Compressive strength of concrete ....301
10.5.5. Dead and live load parameters ....301
10.6. Time-Variant Structural Reliability Assessment of Typical Post-Tensioned Bridge ....302
10.6.1. Geometrical and structural characteristics of typical post-tensioned bridge ....302
10.6.2. Definitions of parameters for the reliability assessment ....304

Page

10.6.3. Time-variant strength reliability index....307
10.6.4. Time-variant service reliability index....312
10.7. Summary....317

11. CONCLUSIONS AND RECOMMENDATIONS....318

11.1. Introduction....318
11.2. Limitations and Assumptions....318
11.3. Conclusions....319
11.3.1. Corrosion risks at different geographic locations in Texas....319
11.3.2. Cyclic polarization curves of prestressing steel....320
11.3.3. Galvanic corrosion testing of post-tensioned systems....320
11.3.4. Probabilistic tension capacity of strands and wires....321
11.3.5. Structural reliability of post-tensioned bridges....323
11.4. Recommendations for Future Research....325
11.5. Recommendations for Field Implementations....327

REFERENCES....328

APPENDIX A ALL TENSION CAPACITY DATA....340

APPENDIX B STRUCTURAL DETAILING OF CONCRETE REACTION FRAMES....360

APPENDIX C TRIAL MODELS FOR THE TENSION CAPACITY OF WIRES UNDER CONTINUOUS-ATMOSPHERIC CONDITIONS....364

APPENDIX D STRENGTH AND SERVICE RELIABILITY INDICES....372

VITA…….....374

## LIST OF FIGURES

Page

Figure 1-1. Cross Section of a PT Box Girder With Internal and External Tendons.....3

Figure 1-2. Typical Cross-sectional Views of Tendons With and Without Voids. .....6

Figure 1-3. Schematic Showing the Elements of Experimental-Analytical Program. .....10

Figure 2-1. Collapsed Ynys-y-Gwas Bridge (YouTube 2009). .....14

Figure 2-2. Niles Channel Bridge, Florida Keys, Florida (Structurae 2009). .....16

Figure 2-3. Mid-Bay Bridge, Choctawhatchee Bay, Florida (Worldbreak 2009).....17

Figure 2-4. (a) Tendon Corrosion Near Anchorage Zone (b) Tendon Corrosion at Anchorage (c) An Exposed Strand Along a Bleed Water Trail, and (d) Cracked PT Ducts in the Mid-Bay Bridge, Florida (FDOT 2001a). .....17

Figure 2-5. Bob Graham Sunshine Skyway Bridge, Tampa Bay, Florida (Wikipedia 2009). .....19

Figure 2-6. Severely Corroded Strands at Anchorage Zones of PT Columns in the Bob Graham Sunshine Skyway Bridge, Tampa Bay, Florida (FDOT 2001b). .....19

Figure 2-7. Varina-Enon Bridge, Over the James River, Virginia (Roadstothefuture 2009). .....21

Figure 2-8. Tendon Corrosion in Varina-Enon Bridge, Virginia (Hansen 2007). .....21

Figure 2-9. Pitting Corrosion on ASTM A 53 Pipe and ASTM A 416/A 416M-99 Strand Due to Coupled Galvanic- and Chloride-induced Corrosion (FDOT 2002). .....23

Figure 2-10. Elevations Showing Typical Void Locations in Grouted Tendon Systems. .....26

Figure 2-11. Variation of Pore Solution Composition With Time of Hydration (Diamond 1981).....28

Figure 2-12. Carbonated GAS Interfaces in Anchorage Zones. .....29

Figure 2-13. Daily Precipitation in San Antonio, Texas. (NCDC, 2009) .....31

Page

Figure 2-14. Thickness Loss of Steel Surfaces on Ships Exposed to Seawater (Predicted Using Existing Corrosion Models). ..... 39

Figure 2-15. Thickness Loss of Carbon Steel Due to Atmospheric Corrosion (Predicted Using Existing Power Models). [Note: 1 inch = 25.4 mm] ..... 45

Figure 2-16. Stress-Strain Curve (using Todeschini (1964) model) for a Concrete With a Specified Compressive Strength, $f'_c$, of 6000 psi. ..... 56

Figure 2-17. HL93 Loading Specified by AASHTO (1998, 2007): (a) Truck and Uniform Lane Load and (b) Tandem and Uniform Lane Load. ..... 61

Figure 2-18. Locations of Post-tensioned, Segmental, Concrete Bridges in Texas. ..... 70

Figure 2-19 Layout and Phases of San Antonio "Y" Bridge (Wollmann et al., 2001). ..... 71

Figure 2-20. Estimated Trucks Carrying U.S.-Mexico Trade on U.S. Highway Corridors To and From the Lower Rio-Grande Valley Region (McGray 1998). ..... 72

Figure 2-21. Estimated Trucks Carrying U.S.-Mexico Trade on U.S. Highway Corridors To and From the Laredo Region (McGray 1998). ..... 72

Figure 2-22 Typical Cross Sections of Girder Types in San Antonio "Y" Bridge. ..... 75

Figure 2-23. Symbolic Notations for a Cross Sections of Segmental Box Girders. ..... 78

Figure 4-1. Average Number of Freeze-Days in Texas (Data Collected from 1995-2000). ..... 84

Figure 4-2. Annual Average Temperature in Texas (Data Collected from 1961-1990). ..... 85

Figure 4-3. Annual Average Relative Humidity in Texas (Data Collected from 1961-1990). ..... 85

Figure 4-4. Average Number of Rain-Days in Texas (Data Collected from 1961-1990) ..... 86

Figure 4-5. Total Chloride Factor for Texas. ..... 88

Figure 4-6. Quantitative Assessment of Total Corrosion Risk. ..... 90

Figure 4-7. Qualitative Corrosion Risk Level. ..... 90

Page

Figure 5-1. Experimental Program (Electrochemical and Tension Capacity Behavior of Wires and Strands). ....92

Figure 5-2. Observed Tension Capacities of "As-Received" Strands and Wires. ....96

Figure 5-3. Particle Size Distribution Curves for Fine and Coarse Aggregates. ....97

Figure 5-4. Schematic of the Cyclic Polarization Test Setup (Note: Not drawn to scale). ....105

Figure 5-5. Cyclic Polarization Test Setup (Left: Corrosion Cell (Perkin Elmer, Inc.,); Right: Potentiostat (Solartron Model 1287) and a Laptop Computer)....106

Figure 5-6. Photograph and Schematic of a Modified ASTM G109 Test Specimen.....110

Figure 5-7. Photographs and Schematics of a Bearing Plate Test Specimen.....114

Figure 5-8 Experimental Designs for All the Strand and Wire Corrosion Tests. ....118

Figure 5-9. Schematics of Strand Corrosion Test Specimens. ....123

Figure 5-10. Schematic and Photograph of Wire Corrosion Test Specimen. ....127

Figure 5-11. Schematic and Photograph of Vertical Concrete Reaction Frame with Stressed Strand Specimens. ....129

Figure 5-12. Schematic and Photograph of Horizontal Concrete Reaction Frames With Stressed Strand Specimens. ....130

Figure 5-13. Schematics and Photographs of (a) Live and (b) Dead End of the Stressed Strand on a Concrete Reaction Frame. ....132

Figure 5-14. LVDT Setup to Measure the Strand Shortening During Stressing Operation. ....133

Figure 5-15. Schematic and Photograph of Strand Stressing Setup.....135

Figure 5-16. Exposure of Wire Specimens to WD Conditions. ....138

Figure 5-17. Exposure of Wire Specimens to CA Conditions with 100% *RH*. ....139

Figure 5-18. Exposure of Wire Specimens to CA Conditions with 45 and 70% *RH*.....141

Figure 5-19. Cross-sectional Area Measurement Using Surface Replicating Media and Profilometer. ....144

Page

Figure 5-20. A Graphical Representation of the Analytical Determination of Tension Capacity of Wire Specimens Under 9-month CA Exposure. .....145

Figure 6-1. Cyclic Polarization Curves for ASTM A416 Steel. .....150

Figure 6-2. Total Corrosion on the Modified ASTM G109 Samples With Wet-dry Exposure to 0 %$sCl^-$ Solution.....153

Figure 6-3. Total Corrosion on the Modified ASTM G109 Samples With Wet-dry Exposure to 9 %$sCl^-$ Solution.....154

Figure 6-4. Total Corrosion on the Bearing Plate Samples (0 %$sCl^-$ solution). .....156

Figure 6-5. Total Corrosion on the Bearing Plate Samples (9 %$sCl^-$ solution). .....156

Figure 6-6. Micrographs Showing (a) Localized Corrosion Near Grout-air-strand (GAS) Interface; (b) Linear and Pitting Patterns of Corrosion. .....158

Figure 6-7. Cleaned Strand Surface, Corrosion Characteristics, and Residual Tension Capacity. .....159

Figure 6-8. Tension Capacities of Unstressed Strands Exposed to NV and PV Conditions. .....161

Figure 6-9. Tension Capacities of Unstressed Strands Exposed to OV, IV, BV, and BIOV Conditions. .....162

Figure 6-10. Tension Capacities of Stressed Strands Exposed to NV, PV, and BIOV Conditions. .....163

Figure 6-11. Tension Capacities of Unstressed Wires Exposed to WD and OV Conditions. .....165

Figure 6-12. Tension Capacities of Unstressed Wires Exposed to CA and OV Conditions. .....167

Figure 6-13. Tension Capacity of Unstressed and Stressed Strand Specimens at the End of 12-months of WD Exposure. .....171

Figure 7-1. Flowchart for Developing the Tension Capacity Models for Strands in WD Conditions. .....188

Figure 7-2. Graphical Representations of Analytical Steps WD-2, WD-3, and WD-4. .....191

Page

Figure 7-3. Annual Wet-time for Tendons (Based on Assumed Values of Time Required to Dry the Tendons). .....192

Figure 7-4. Effect of Wet-dry Exposure Time on Capacity of Unstressed Strands (with $\phi_{wet} = 0.5$).....195

Figure 7-5. Effect of $\%sCl^-$ on Capacity of Unstressed Strands (with $\phi_{wet} = 0.5$). .....197

Figure 7-6. Effect of $\ln[\%sCl^-]$ on Capacity of Unstressed Strands (with $\phi_{wet} = 0.5$).....198

Figure 7-7. Validation Plot for the Model $US_{WD, NV}$. .....202

Figure 7-8. Validation Plot for the Model $US_{WD, PV}$.....204

Figure 7-9. Validation Plot for the Model $US_{WD, BIOV}$. .....206

Figure 7-10. Capacity of Unstressed Strands under WD Exposure to Various Chloride Solutions (Predicted Using $US_{WD}$ Models). .....207

Figure 7-11. Effect of Wet-dry Exposure Time on Capacity of Stressed Strands (with $\phi_{wet} = 0.5$).....209

Figure 7-12. Effect of $\%sCl^-$ on Capacity of Stressed Strands (with $\phi_{wet} = 0.5$). .....211

Figure 7-13. Effect of $\ln[\%sCl^-]$ on Capacity of Stressed Strands (with $\phi_{wet} = 0.5$). ....212

Figure 7-14. Validation Plot for the Model $SS_{WD, NV}$.....215

Figure 7-15. Validation Plot for the Model $SS_{WD, PV}$. .....217

Figure 7-16. Validation Plot for the Model $SS_{WD, BIOV}$. .....219

Figure 7-17. Capacity of Stressed Strands under WD Exposure ($\phi_{wet} = 0.17$) to Various Chloride Solutions (Predicted Using $SS_{WD}$ Models). .....220

Figure 7-18. Scatter Plots between the Capacities of Unstressed and Stressed Strands. .....222

Figure 7-19. Validation Plot for US-$SS_{WD, NV}$ Model. .....224

Figure 7-20. Validation Plot for US-$SS_{WD, PV}$ Model.....226

Figure 7-21. Validation Plots for US-$SS_{WD, BIOV}$ Model. .....228

Page

Figure 7-22. Capacity of Stressed Strands under WD Exposure ($\phi_{wet}$ = 0.17) to Various Chloride Solutions (Predicted Using US-$SS_{WD}$ Models). .....229

Figure 8-1. Flowchart for Developing the "Wire-strand" Capacity Relationships. .....239

Figure 8-2. Graphical Representation of Step WS-1.....240

Figure 8-3. Graphical Representations of Steps WS-2a and WS-3.....241

Figure 8-4. Scatter Plot between Capacity of Unstressed Wires, $C_{T,UW}$, and Wet-dry Exposure Time, $t_{WD}$. .....243

Figure 8-5. Validation Plot for the $UW_{WD,\ below}$ Model. .....245

Figure 8-6. Validation Plot for the $UW_{WD,\ above}$ Model. .....246

Figure 8-7. Scatter Plot between Predicted Capacity of Unstressed Wires, $C_{T,UW}$, and Observed Capacity of Unstressed Strands, $C_{T,US}$. .....247

Figure 8-8. Validation Plots for UW-$US_{WD}$ Model.....249

Figure 8-9. Validation Plot for UW-US-$SS_{WD,\ BIOV}$ Model.....251

Figure 8-10. Scatter Plot between Predicted Capacity of Unstressed Wires, $C_{T,UW}$, and Observed Capocity of Stressed Strands, $C_{T,SS}$. .....252

Figure 8-11. Validation Plot for the UW-$SS_{WD,\ BIOV}$ Model. .....254

Figure 9-1. Flowchart for Developing the Tension Capacity Models for Strands Under CA and BIOV Exposure Conditions.....261

Figure 9-2. Graphical Representations of Steps CA-2, CA-3, and CA-4. .....262

Figure 9-3. Scatter Plot between $\%gCl^-$ and Wire Capacity at 9-month CA Exposure. .....264

Figure 9-4. Scatter Plot between $\%RH$ and Wire Capacity at 9-month CA Exposure. .....264

Figure 9-5. Scatter Plot between $T$ and Wire Capacity at 9-month CA Exposure. .....265

Figure 9-6. Scatter Plot between the 3-way Interaction Term and Wire Capacity at 9-month CA Exposure. .....266

Figure 9-7. Validation Plot for the $UW_{CA,\ BIOV}$ Model.....268

Page

Figure 9-8. Capacity of Stressed Strands under CA Conditions with $n_{CA} = -0.005$. .....271

Figure 10-1. Framework to Determine the Generalized Reliability Index, $\beta$.....274

Figure 10-2. Sectional Analysis of a Typical T-girder at Nominal Conditions. .....278

Figure 10-3. Simplified Flowchart of the Main Function to Determine Moment Capacity of a PT Girder. .....281

Figure 10-4. Schematic Showing the Movement of Curvature, $\phi$.....282

Figure 10-5. Simplified Flowchart of the Subfunction to Determine the Bending Moment Corresponding to a Curvature. .....284

Figure 10-6. Simplified Flowchart of the Subfucntion to Determine the Total Tensile Force, $F_T$.....287

Figure 10-7. Simplified Flowchart of the Subfunction to Determine the Total Compressive Force, $F_C$. .....289

Figure 10-8. Schematic Showing the Movement of Curvature, $\phi$.....296

Figure 10-9. Strategy to Select the Strand Capacity Models Based on Exposure Conditions. .....300

Figure 10-10. Cross Section at Midspan of the Typical PT Girder Used in This Study. .....303

Figure 10-11. Parameter Combinations for the Reliability Assessment Program. .....305

Figure 10-12. Strength Reliability of the Typical PT Bridge with Tendons Exposed to Wet-dry Cycles (0.006 %$sCl^-$). .....309

Figure 10-13. Strength Reliability of the Typical PT Bridge with Tendons Exposed to Wet-dry Cycles (0.018 %$sCl^-$). .....310

Figure 10-14. Strength Reliability of the Typical PT Bridge with Tendons Exposed to Wet-dry Cycles (1.8 %$sCl^-$). .....311

Figure 10-15. Service Reliability of the Typical PT Bridge with Tendons Exposed to Wet-dry Cycles (0.006 %$sCl^-$). .....314

Figure 10-16. Service Reliability of the typical PT Bridge with Tendons Exposed to Wet-dry Cycles (0.018 %$sCl^-$). .....315

Page

Figure 10-17. Service Reliability of the Typical PT Bridge with Tendons Exposed to Wet-dry Cycles (1.8 %$sCl^-$). .....316

## LIST OF TABLES

Page

Table 2-1. Percentage of Voided Tendons among the External Tendons on San Antonio "Y" Bridge (Adapted from TxDOT (2004)).....27

Table 2-2. Existing Models for Thickness Loss of Steel Surfaces on Ships Exposed to Seawater.....38

Table 2-3. Existing Atmospheric Corrosion Models (as a Function of Environmental Parameters and Exposure Time) for Steel.....41

Table 2-4. Power Law Models for Atmospheric Corrosion of Carbon Steel.....44

Table 2-5. Statistics of Concrete Compressive Strength (Nowak and Collins 2000).....52

Table 2-6. Compressive and Tensile Stress Limits for Fully Prestressed Components in Segmental Concrete at Service Limit State after Losses (AASHTO LRFD Specifications 2007).....57

Table 2-7. Dead Load Parameters from TxDOT Bridge Drawings.....60

Table 2-8. Governing Limit States for Pre-tensioned Girders with Short and Long Spans.....66

Table 2-9. Summary of $\beta_{target}$ and $P_f$ (Adapted from ISO 13822).....68

Table 2-10. Span and Girder Inventory of San Antonio "Y" Bridge.....74

Table 2-11. Quantity and Location of Longitudinal Tendons at Midspan on San Antonio "Y" Bridge.....76

Table 2-12 Typical Geometrical Parameters of Box Girders in San Antonio "Y" Bridge.....78

Table 4-1. Chloride Usage Factor.....87

Table 4-2. Chloride Frequency Factor.....87

Table 4-3. Total Corrosion Risk Factors.....89

Table 5-1. Different Steel Reinforcement Types Used in this Research Program.....93

Page

Table 5-2. Representative Chemical Compositions of Steel Reinforcement Types Used. ....95

Table 5-3 Material Characteristics of Fine and Coarse Aggregates....98

Table 5-4. Representative Chemical Compositions of Cementitious Materials Used. ....99

Table 5-5. Representative Mixture Proportions of Concrete and Grout Used. ....100

Table 5-6. Concentrations of Impurities in the Water Used in this Research Program....102

Table 5-7. Chemical Compositions of Exposure Solutions Used in this Research....103

Table 5-8. Experimental Design for Modified ASTM G109 Test Program. ....109

Table 5-9. Experimental Design for Bearing Plate Test Program....113

Table 5-10. Experimental Design Showing the Number of Test Specimens in the Unstressed Strand Corrosion Test under WD Exposure Conditions*....120

Table 5-11. Experimental Design Showing the Number of Test Specimens in the Stressed Strand Corrosion Test under WD Exposure Conditions*. ....121

Table 5-12. Experimental Design Showing the Number of Test Specimens in the Unstressed Wire Corrosion Test under WD Exposure Conditions*....125

Table 5-13. Experimental Design Showing the Number of Test Specimens in the Unstressed Wire Corrosion Test under CA Exposure Conditions*....126

Table 6-1. Approximate Active, Passive, and Transpassive Potential Regions for the ASTM A416 Steel....151

Table 6-2. Mean‡, Coefficient of Variation (COV), and Mean Capacity Loss ($C_{T,\ loss}$)* of Tension Capacities Observed at the End of 12-month WD Exposure. ....172

Table 6-3. Groups of Void Conditions with Similar Effects on Tension Capacity. ....175

Table 7-1. List of Tension Capacity Models for Strands under WD Exposure Conditions. ....187

Table 7-2. MAPE and Posterior Statistics of the $US_{WD,\ NV}$ Model. ....200

Page

Table 7-3. MAPE and Posterior Statistics of the $US_{WD, PV}$ Model. ..... 202

Table 7-4. MAPE and Posterior Statistics of the $US_{WD, BIOV}$ Model. ..... 205

Table 7-5. MAPE and Posterior Statistics of the $SS_{WD, NV}$ Model. ..... 214

Table 7-6. MAPE and Posterior Statistics of the $SS_{WD, PV}$ Model. ..... 216

Table 7-7. MAPE and Posterior Statistics of the $SS_{WD, BIOV}$ Model. ..... 218

Table 7-8. MAPE and Posterior Statistics of the US-$SS_{WD, NV}$ Model. ..... 224

Table 7-9. MAPE and Posterior Statistics of the US-$SS_{WD, PV}$ Model. ..... 225

Table 7-10. MAPE and Posterior Statistics of the US-$SS_{WD, BIOV}$ Model. ..... 227

Table 7-11. MAPEs of $US_{WD}$, $SS_{WD}$, and US-$SS_{WD}$ Models. ..... 231

Table 7-12. Model Error Coefficients ($\sigma$) of $US_{WD}$, $SS_{WD}$, and US-$SS_{WD}$ Models. ..... 231

Table 8-1. List of Wire and "Wire-strand" Capacity Models for BIOV Conditions. .... 236

Table 8-2. MAPE and Posterior Statistics of $UW_{WD}$ Models. ..... 244

Table 8-3. MAPE and Posterior Statistics of UW-$US_{WD, BIOV}$ Full Model. ..... 248

Table 8-4. MAPE and Posterior Statistics of Full UW-$SS_{WD, BIOV}$ Model. ..... 253

Table 9-1. MAPE and Posterior Statistics of $UW_{CA, BIOV}$ Model. ..... 267

Table 10-1. Definitions of the Terms in the Strand Capacity Models. ..... 298

Table 10-2. Mean estimates of Model Parameters in the Strand Capacity Models. ..... 299

Table 10-3. Effective Flange Widths for Each Side of the Web. ..... 303

Table 10-4. Average Annual Temperature and Relative Humidity Conditions in Some Major Cities in the US (Source: www.cityrating.com). ..... 306

Table 10-5. Random Parameters for Reliability Assessment. ..... 307

# 1. INTRODUCTION

## 1.1. PRESTRESSED CONCRETE TECHNOLOGY

In the late 1920s, Eugene Freyssinet, a French civil engineer, pioneered the *prestressed concrete technology*. He patented *prestressed concrete technology* in 1928 and is considered as the *father of prestressed concrete* (Emmanuel 1980). Although Freyssinet pioneered prestressed concrete, Doehring patented prestressing methods as early as 1888. Freyssinet recognized that only high-strength prestressing wire could counteract the effects of creep, develop anchorage, and improve other load-carrying attributes, which helped in the widespread use of prestressed concrete technology in many structural systems including long-span segmental bridges. Two types of stressing technologies are commonly used. These include: 1) pre-tensioning, where the stress is applied before the concrete hardens and 2) post-tensioning, where the stress is applied after the concrete hardens. This document focuses on the electrochemical characterization and probabilistic capacity modeling of post-tensioning strands and structural reliability of grouted, post-tensioned (PT), segmental concrete bridges (denoted as "PT bridges" herein).

In the 1950s, Europeans started the construction of long-span PT bridges. About a decade later, the United States (US) also began constructing similar PT bridges. Later, grouted post-tensioned systems became economically viable and popular for long-span PT bridge construction (NCHRP 1998). The definitions of some important terminologies used in this document are provided next.

---

This dissertation follows the format of the *ASCE Journal of Engineering Mechanics*.

## 1.2. DEFINITIONS

Various components of grouted PT systems include wires, strands, ducts, and tendons. In this document, they are defined as follows:

- Wire (or PT Wires) – Single wire with 0.2 inch (5 mm) diameter and made of high strength steel meeting ASTM A416 specifications.
- Strand (or PT Strands) – Seven helically coiled wires (six outer wires helically coiled around one center wire) with a nominal diameter of 0.6 inches (15.24 mm).
- Ducts (or PT Ducts) – Metallic or high-density polyethylene (HDPE) pipe in which several strands are placed and then the interstitial spaces are filled with cementitious grouts.
- Tendons (or PT Tendons) – The system containing a group of several strands (structural load-carrying elements) and the cementitious grout and ducts (non-structural, corrosion-protection elements).
- Grout – The cementitious grout placed around the strands and inside the ducts in a tendon system.
- Void – The air space inside a PT duct system formed due to the absence of grout.

## 1.3. CLASSIFICATION OF POST-TENSIONED SYSTEMS

Based on the location of the tendons, grouted PT systems are classified into two types, namely internal and external PT systems. A tendon that is placed outside the concrete is defined as an external tendon. A tendon that is placed inside the concrete is defined as an internal tendon. In general, PT bridges may have either or both of these tendon systems. Figure 1-1 shows a schematic of a cross section at midspan of a typical PT bridge girder. In this figure the T1 through T3 tendons are external and the T4 through T9 tendons are internal.

Tendons are also classified as bonded and unbonded tendons. A tendon that is in direct contact or bonded to the adjacent concrete is defined as a bonded tendon. A

tendon that is not in direct contact with concrete or cannot transfer the stress through the surface bonding is defined as an unbonded tendon. In general, external tendons are considered unbonded tendons and internal tendons are considered bonded tendons when they are completely filled with grout and have no voids. Voids, if present, can cause discontinuity in stress transfer to the adjacent concrete along the tendon length. Hence, in this document, internal tendons are considered unbonded tendons. Following is a discussion on internal and external PT systems.

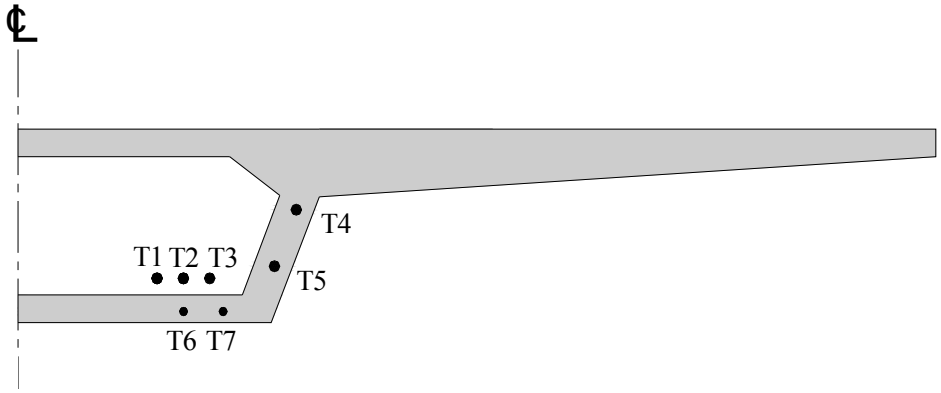


**Figure 1-1. Cross Section of a PT Box Girder With Internal and External Tendons.**

### 1.3.1. Internal post-tensioned systems

In an internal PT system the tendons are located or embedded inside the reinforced concrete box section. In other words, the steel strands are placed inside metallic or HDPE ducts that are embedded inside the hardened concrete. Also, the interstitial spaces between the strands and ducts are supposed to be filled with cementitious grout. Although the grout, duct, and concrete components assist in protecting the strands from external corrosive environments, corrosion of the internal PT system resulted in the sudden collapse of the Bickton Meadows footbridge in 1967 and the Ynys-y-Gwas Bridge in 1985 (NCHRP 1998). These sudden bridge collapses played a major role in eliciting a moratorium in 1992 that banned the construction of new, bonded, grouted PT bridges in the United Kingdom (UK). In 1996, the moratorium on grouted PT,

cast-in-place bridge construction in the UK was removed. However, because of concerns with the corrosion protection of internal tendons at the joints between the precast segments, the moratorium on grouted PT, precast, segmental bridge construction in the UK remains in place even today.

In the recently constructed bridges in the US, this potential problem of internal tendon corrosion at box-girder or segment joints has been minimized by replacing the older practice of constructing with dry-joints with epoxy resin-joints. Contrary to the experience in the UK, the internal PT systems in US bridges have been reported as performing '*good*' (NCHRP 1998). Based on the tendon failure cases in US bridges, the internal PT system seems to be less vulnerable to corrosion than the external PT strands.

### 1.3.2. External post-tensioned systems

In an external PT system, the tendons are located inside the interior void space (typically rectangular or trapezoidal in cross section) of the concrete box girder and not embedded in the hardened concrete. The external tendons are connected to the concrete box at anchorage zones and deviator blocks. The deviator blocks are used only to control tendon profile. The steel strands are placed inside HDPE ducts and the interstitial space between the strands and the HDPE ducts is filled with cementitious grout. Because the tendons are not embedded inside the hardened concrete section, the monitoring, repair, and maintenance of external PT systems are not as complex as those for internal PT systems. However, because of the absence of concrete cover protection and the possible presence of unwanted air-voids, external tendons can be more vulnerable to corrosion than internal tendons within the same bridge segment. Tendon failures have been reported on the Mid-Bay, Niles Channel, Sunshine Skyway, and 17 other PT bridges in Florida (FDOT 1999, FDOT 2001a, FDOT 2001b, NCHRP 1998) and the Varina–Enon PT bridge in Virginia (Hansen 2007). The literature cites the presence of voids and exposure to corrosive environments as major causes for these tendon failures. It should

be noted that these external PT system failures were observed in bridges at relatively young ages (i.e., between 8 and 17 years after construction).

### 1.4. RESEARCH MOTIVATION

Although grouted PT systems gained acceptance and popularity due to good economy, better aesthetics, faster construction and other positive aspects, the PT segmental bridge industry witnessed corrosion related failures of grouted PT systems at relatively young ages. This raises questions on the long-term performance of these infrastructure systems. According to NCHRP (1998), "…there is a pressing need for US bridge engineers to gain an understanding of durability issues associated with segmental construction and to be able to judge on a technical and rational basis the veracity of the on-going moratorium in the UK pertaining to segmental construction…". Moreover, various studies on the tendon failure cases and recent inspections conducted by various federal and state transportation agencies reported the presence of air-voids (voids herein) in the grouted tendons as one of the causes for strand corrosion (ASBI 2000, FDOT 1999, FDOT 2001a, FDOT 2001b, Hansen 2007, NCHRP 1998).

Figure 1-2 shows cross-sectional views of tendons with and without voids. Bleed-water evaporation, poor grouting, poor construction practices, or a combination of these are possible reasons for this unwanted void formation inside the tendons (FDOT 1999, FDOT 2001a, FDOT 2001b, NCHRP 1998, Schupack 2004). The strands in the voids with corrosive conditions, such as rainwater, seawater, salt-fog, de-icing /anti-icing salts, or a combination of these, can result in a higher probability of corrosion, especially localized corrosion, resulting in a reduction in tension capacity ($C_T$). The reduction in $C_T$ of these strands can adversely affect the structural capacity and reliability of PT bridges. According to Poston et al. (2003), "…depending upon the initial prestress in the tendon, a reduction in strength to 75 percent of the original minimum specified reduces the live-load capacity by 50 percent or more…." These studies and field observations indicate that there is a dire need to assess the long-term

corrosion and structural reliability of PT bridges with voided tendons. These assessments will assist engineers in strategizing and developing better repair and maintenance programs to mitigate the risks and to ensure safe, reliable, and long-lasting PT bridges.

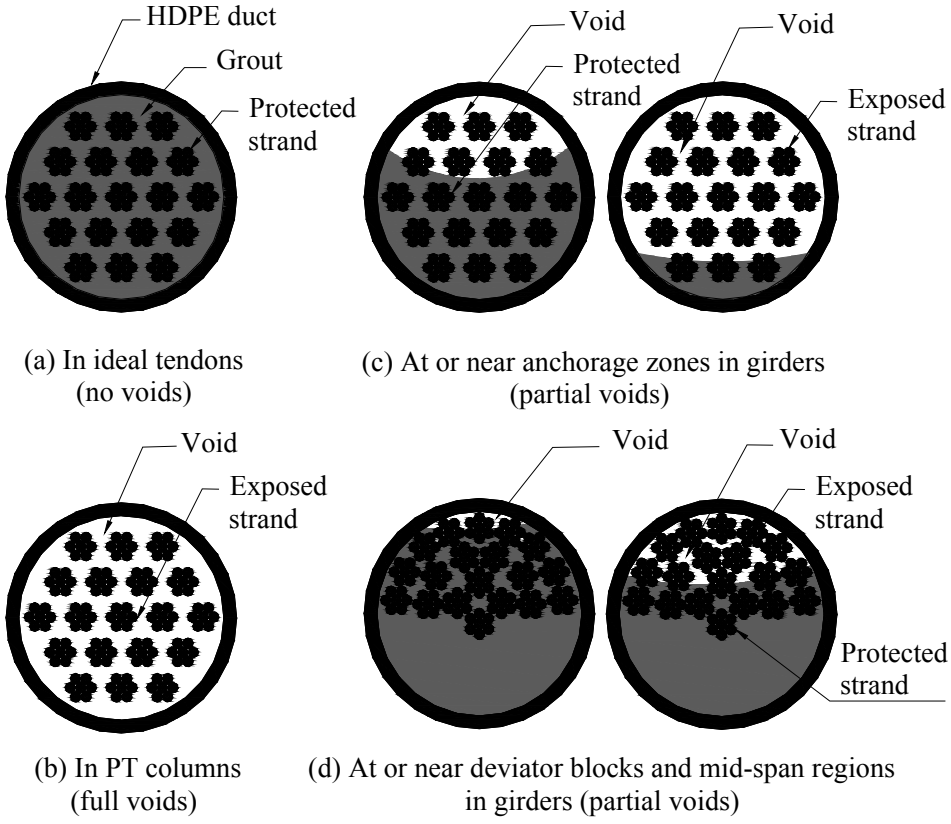


**Figure 1-2. Typical Cross-sectional Views of Tendons With and Without Voids.**

## 1.5. RESEARCH OBJECTIVES

The major objectives of this research are:

1. to develop environmental characterization maps of Texas to assist in assessing the corrosion risk level of a PT bridge based on its geographic location [results presented in Section 4].

2. to investigate the electrochemical corrosion characteristics of the steel meeting the ASTM A416 specifications when exposed to cementitious material environments with and without chloride contamination [results are presented in Section 6].

3. to test whether galvanic corrosion occurs between the conventional reinforcement and strands and bearing plates at the anchorage zones; and if so, to assess the increased level of corrosion activity [results are presented in Section 6].

4. to identify critical material, environmental, void, and stress parameters that influence corrosion and $C_T$ of strands in PT bridges [results are presented in Section 6].

5. to develop probabilistic models for $C_T$ of strands exposed to various material, environmental, void, and stress conditions [results are presented in Section 7, 8, and 9].

6. to develop a time-variant structural reliability model for typical PT bridges and then assess the structural reliability of a typical PT bridge [results are presented in Section 10].

## 1.6. RESEARCH ASSUMPTIONS

To attain the research objectives, the following research hypotheses and assumptions have been made:

- The $C_T$ of PT wires and strands is reduced when exposed to high moisture, temperature, and chloride conditions. The $C_T$ is further reduced as a function of time.

- Environmental conditions at the strand interface can be determined.

- The reduced $C_T$ of corroding PT wires and strands can be probabilistically modeled with reasonable levels of accuracy.

- No theoretical model could be developed or found in the literature for the time-dependent corrosion of strands exposed to wet-dry (WD), continuous-atmospheric (CA), or both these conditions. Hence, all the models developed in this document are empirical in nature.

- There exists a relationship between wire and strand corrosion processes, when exposed to similar WD or CA conditions.

- The long-term corrosion of strands under field conditions can be modeled using the experimental data from shorter-term wire corrosion tests under controlled laboratory conditions.

- The stressed strands (i.e., strands experiencing in-service stress conditions) may exhibit more reduction in $C_T$ than the unstressed strands.

- Because most tendons in the field were found to have voids, all the internal and external tendons are assumed to be unbonded tendons while determining moment capacity ($C_M$) of the girder.

- Only external tendons are assumed to exhibit corrosion-induced loss in $C_T$. Internal tendons are relatively well-protected from the external environment and free of active corrosion.

- Among the external tendons, the rate of corrosion of strands exposed to No Void (NV) and CA conditions is negligible. In addition, it is highly unlikely that there will be a Parallel Void (PV) and not a Bleedwater, Inclined, or Orthogonal Void (BIOV) condition (see detail definitions and schematics in Subsection 5.5.2.1) inside a tendon.

- The $C_M$ and stresses at extreme fibers at midspan of a PT bridge girder can be modeled using probabilistic models for $C_T$ of strands, statistical expressions for compressive strength of concrete, prestress losses in strands, void and damage conditions of PT systems, and principles of structural mechanics.

- Moment demand at midspan can be modeled using statistical expressions for the dead loads and live and impact loads due to HS20 and HL93 loading conditions.

- Time-variant structural reliability can be assessed based on strength and service limit states.

- Time-variant strength reliability (i.e., based on ultimate bending moment) can be modeled and assessed using $C_M$ and moment demand ($D_M$) models of PT bridge girders.

- Time-variant service reliability (i.e., based on in-service stresses on extreme fibers) can be modeled and assessed using the allowable and applied in-service stresses (i.e., stress capacity and demand, respectively) of PT bridge girders.

## 1.7. RESEARCH METHODOLOGY

A coupled experimental-analytical research methodology has been developed to attain the research objectives listed in Section 1.5. A schematic showing experimental and analytical programs of this research is provided in Figure 1-3.

The experimental program includes electrochemical characterization of PT strands and systems. This is performed using the results from electrochemical testing: cyclic polarization tests, galvanic corrosion tests, strand corrosion tests, and wire corrosion tests. These electrochemical tests are shown in the shaded-box in Figure 1-3.

The analytical program include: 1) the development of probabilistic models for time-variant $C_T$ of PT strands and 2) the modeling and assessment of time-variant structural reliability of PT bridges. The results from the strand and wire corrosion tests will be used to perform this analytical program, as indicated by the dashed-box in Figure 1-3.

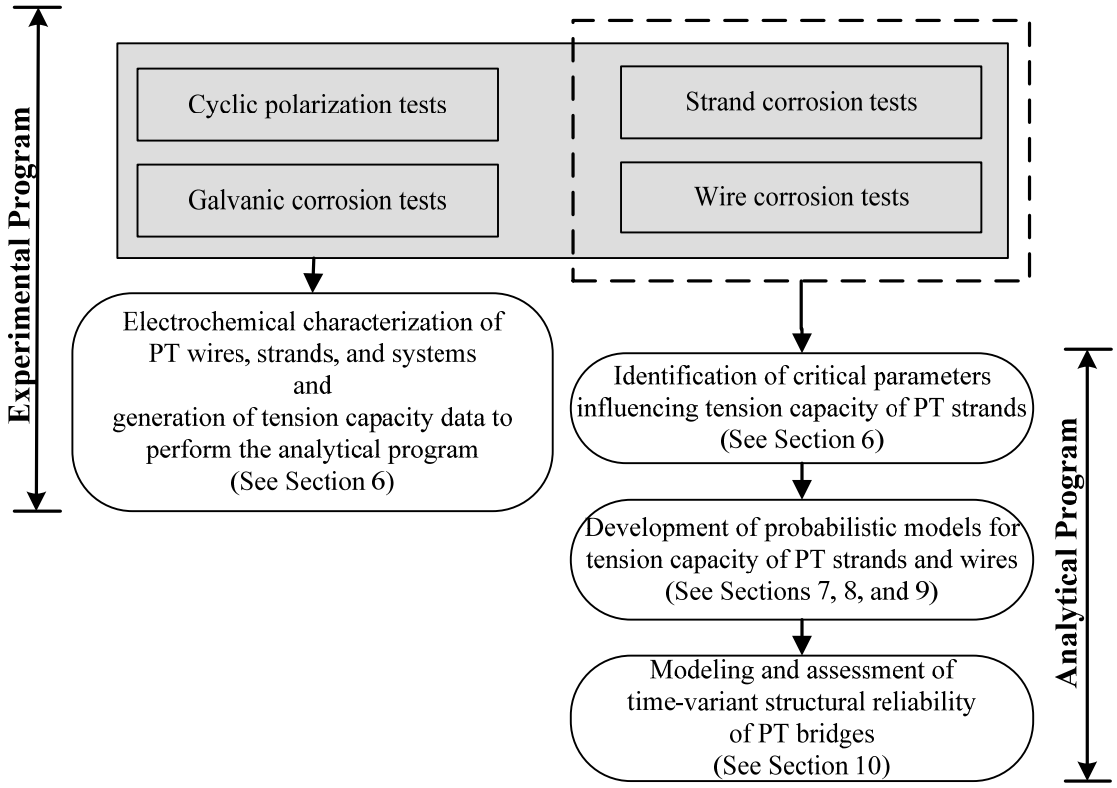


**Figure 1-3. Schematic Showing the Elements of Experimental-Analytical Program.**

## 1.8. ORGANIZATION OF DISSERTATION

This dissertation is organized using a section-subsection format. There are eleven sections and several subsections within each section. The word "section" corresponds to the first heading level and "subsection" corresponds to the second, third, and fourth heading levels. Following is a brief explanation of the various sections in this dissertation.

- Section 1 (the current section) started with a brief discussion on prestressed concrete technology and its development. This was followed by discussions on key definitions used in this research. The

research motivation and objectives were then presented. Following this, the assumptions and methodology of this research were provided.

- Section 2 provides a comprehensive review of literature. This section starts with a review of some case histories of failure of PT systems. A review of parameters influencing and modeling of electrochemical process is then provided. Following this, modeling the $C_M$, in-service stresses, and load demands on bridge is reviewed. Then modeling and assessment of structural reliability is reviewed. Towards the end of the section 2, typical characteristics of segmental bridges in Texas are discussed.

- Section 3 presents the current research needs and the significance of this research.

- Section 4 presents the environmental characterization maps and corrosion risks of various geographic locations in Texas.

- Section 5 provides details of the experimental program. Details of all the materials used in the experimental program are provided first. The experimental design and test layout and other details of cyclic polarization, galvanic corrosion, and strand and wire corrosion test programs are then provided.

- Section 6 presents the experimental results from the cyclic polarization test, galvanic corrosion tests, and strand and wire corrosion tests. Also, critical parameters influencing $C_T$ of strands are identified in this section.

- Section 7 presents the probabilistic models for the $C_T$ of strands under WD exposure conditions. This section also presents the statistical procedures used to develop probabilistic models for $C_T$ of strands.

- Section 8 presents the probabilistic models relating the $C_T$ of the strands and wires under WD exposure conditions.

- Section 9 presents the probabilistic models for the $C_T$ of strands under WD and CA exposure conditions.

- Section 10 presents the development of strength and service reliability models of PT bridges. As an application of these models, this section also presents the time-variant structural reliability of a typical PT bridge at various exposure conditions.

- Section 11 presents conclusions from this research. Recommendations for future research initiatives and field implementation are also presented in this section.

# 2. LITERATURE REVIEW

## 2.1. INTRODUCTION

This section starts with the review of existing literature on various deterioration and failure cases of PT bridges. Parameters affecting strand corrosion mechanisms are then reviewed. Following this is a review of procedures and principles to determine the moment capacity ($C_M$) and moment demand ($D_M$) of PT bridges. This is followed by a review of structural reliability assessment methods. Typical material, geometrical, and design characteristics of PT bridges in Texas are then reviewed.

## 2.2. DETERIORATION OF POST-TENSIONED BRIDGES

Most PT bridges are structurally healthy. However, due to poor construction and design practices, cases have occurred with the failure of one or more tendons, collapse of the entire PT bridge superstructure, or both. A review of failures of bridges with internal and external PT systems is provided next.

### 2.2.1. Failures of internal, grouted, post-tensioned systems

#### *2.2.1.1. Bickton Meadows Footbridge, UK*

The collapse of Bickton Meadows footbridge (located in Hampshire, UK) in 1967 was the first significant corrosion-related failure case of bonded PT bridges (NCHRP 1998). The precast segments in this bridge were jointed with mortar. These mortar joints were thin and highly permeable and hence allowed moisture, chlorides, and oxygen to be easily transported towards the steel tendons that cross the joints. This resulted in

accelerated corrosion of steel tendons. The bridge was 15 years old at the time of collapse.

#### *2.2.1.2. Ynys-y-Gwas Bridge, West Glamorgan, UK*

The Ynys-Y-Gwas Bridge, West Glamorgan, UK, was a segmental, PT, I-beam bridge spanning across the Afan river (Figure 2-1). This bridge had a clear span of 60 ft (18.3 m) and was constructed in 1952. The construction was based on a proprietary design with nine longitudinal beams supporting the deck. These beams were made of segmental I-sections and box sections and were held together using five longitudinal prestressing cables. Each cable consisted of twelve 0.2 inch (5 mm) diameter high tensile steel wires. In 1985 (i.e., after 33 years of service), this bridge collapsed (Figure 2-1) under self load and without warning.

**Figure 2-1. Collapsed Ynys-y-Gwas Bridge (YouTube 2009).**

A post-disaster study conducted by Transport and Road Research Laboratory (TRRL), UK, reported the following findings (TRRL 1987):

- Corrosion of the longitudinal tendons near the joints between the segments was the main cause for the bridge failure;
- The chlorides and moist environment under the bridge seem to be the major causes for corrosion of wires;

- The 1-inch (25-mm) wide transverse joints between the segments were filled with in-situ dry mortar caulking, through which moisture and chlorides easily infiltrated;
- Chlorides, possibly from de-icing salt, were present in the grout collected from joints between the segments (but not in the grout collected from the regions within the segments) and in the corrosion products;
- Large voids were found in ducts, but wires were covered with a layer of cement paste,
- Exposed wires in partially grouted ducts were severely corroded, and
- No corrosion was found in fully grouted tendons.

### 2.2.2. Failures of external, grouted post-tensioned systems

Although rare, some early-age tendon failures on external, grouted PT bridges in Florida, a state with 72 PT bridges, and Virginia raise concerns about the durability of such bridges, especially when exposed to moist and saline environments. This section provides a review of the tendon failures on the Niles Channel, Mid-Bay, Bob Graham Sunshine Skyway, and Varina-Enon bridges.

#### *2.2.2.1. Niles Channel Bridge, Florida, US*

The Niles Channel Bridge (Figure 2-2) is part of the Overseas Highway in the Florida Keys and is a 7-mile long low-level precast segmental bridge with 234 external, grouted tendons. The bridge was constructed in 1983 and after 16 years of exposure to salt-water, one of the tendons near an expansion joint failed (FIB 2001). This failure was due to severe corrosion caused by the infiltration of chloride-contaminated water into the tendon anchorage that contained voids (FIB 2001, FDOT 1999). This failed anchorage was located at a expansion joint. A FDOT (1999) study recommended the inspection and *intense scrutiny* of all the tendons adjacent to open expansion joints. Also, recommendations were made for the visual inspection and chloride analysis of

pourback material at anchorages (cementitious material covering the face of the tendon anchorage) to assess the corrosion vulnerability of the tendon systems.

**Figure 2-2. Niles Channel Bridge, Florida Keys, Florida (Structurae 2009).**

*2.2.2.2. Mid-Bay Bridge, Florida, US*

The Mid-Bay Bridge in Choctawhatchee Bay, Florida (Figure 2-3) is another low-level precast segmental bridge with each span typically consisting of five 18-ft (5.5-m) segments. A routine inspection in 2000 detected corrosion-induced failure of one external tendon and part of a second external tendon. Figure 2-4 shows typical images of this strand corrosion, exposed strand along a bleed water trail, and cracked PT ducts in this bridge. The degree of corrosion was so severe that a total of 11 out of 846 tendons had to be replaced on this bridge (FDOT 2001a).

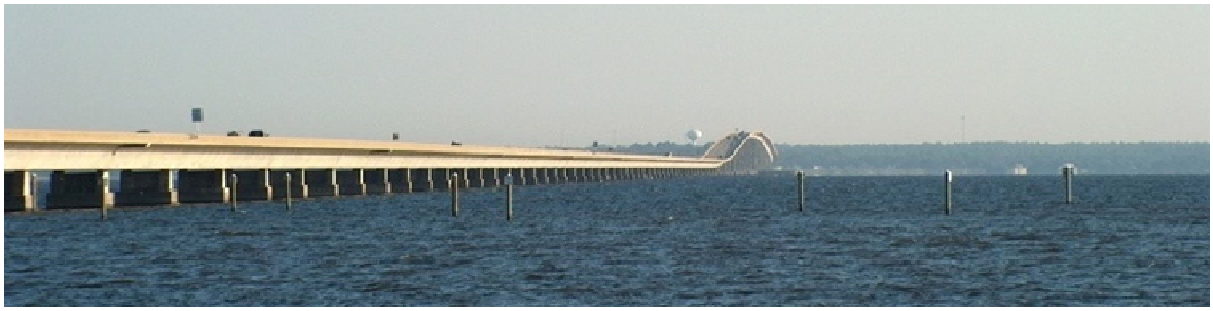

**Figure 2-3. Mid-Bay Bridge, Choctawhatchee Bay, Florida (Worldbreak 2009).**


**(a)**

**(b)**

**(c)**

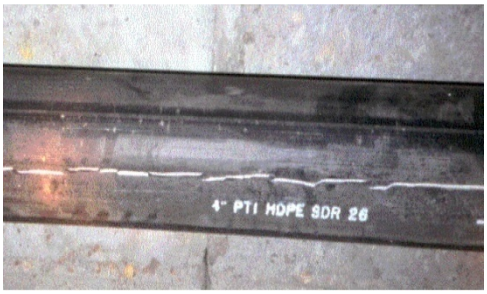


**(d)**

**Figure 2-4. (a) Tendon Corrosion Near Anchorage Zone (b) Tendon Corrosion at Anchorage (c) An Exposed Strand Along a Bleed Water Trail, and (d) Cracked PT Ducts in the Mid-Bay Bridge, Florida (FDOT 2001a).**

FDOT (2001a) reported the following major findings regarding the damages on this bridge:

- Severe tendon corrosion was found at and near anchorage zones;
- A large amount of voids (formed due to the formation and evaporation of bleed water) were found in the ducts at or near the anchorage zones and the midspan regions;
- The grout cover around the strands inside the ducts varied from 0 to 1.5 inches (38 mm);
- Because of the carbonation of the grout to a depth of approximately ¼ inches (6 mm), the pH of the grout near the void regions was between 8 and 9 and the pH of the bulk grout inside was approximately 12. The color of the grout surface adjacent to the voids and the bulk grout varied from chalky white to dark grey. Also, a white powdery deposit, possibly the aluminum powder from an expansive agent, was observed on the grout surfaces near voids, and;
- Some HDPE ducts surrounding the tendon were cracked, possibly because the duct could not meet the construction specifications and/or resist the bending stresses. This excessive bending stress may have been the combined effect of the stresses developed due to the setting of grout at low temperature, expansion of grout with expansive agent, and the presence of voids.

#### *2.2.2.3. Bob Graham Sunshine Skyway Bridge, Florida, US*

On May 9, 1980, *Summit Venture*, a large freight ship, collided and damaged the piers of the old Sunshine Skyway Bridge, which was located in Tampa Bay, Florida. The bridge was demolished and a new bridge, the Bob Graham Sunshine Skyway Bridge (Figure 2-5), was later constructed and commissioned in 1987. The cost of the structure was $244 million. Later, this 4-mile long segmental, cable-stayed, PT bridge won many awards for its design and construction. However, within eight years after construction, the top and bottom anchorage zones of the vertical tendons in the new bridge piers experienced severe corrosion damage, as shown in Figure 2-6.

**Figure 2-5. Bob Graham Sunshine Skyway Bridge, Tampa Bay, Florida (Wikipedia 2009).**

**(a)**

**(b)**

**Figure 2-6. Severely Corroded Strands at Anchorage Zones of PT Columns in the Bob Graham Sunshine Skyway Bridge, Tampa Bay, Florida (FDOT 2001b).**

FDOT (2001b) reported that the major direct and indirect causes for the tendon failure were:

- poor grout quality and grouting practices;
- presence of voids, formed due to bleed water evaporation, inside PT ducts, especially near anchorage zones;
- cracked HDPE ducts;
- infiltration of saltwater or surface drainage water into the PT ducts through the poorly sealed joints between the segments, openings at anchorages, cracks on ducts, etc., and;
- moist and chloride contaminated environment near the exposed strands.

#### *2.2.2.4. Varina-Enon Bridge, Virginia, US*

The Varina-Enon cable-stayed, post-tensioned, segmental concrete bridge over the James River near Richmond, Virginia (Figure 2-7) was opened to traffic in 1990. One of the external tendons in this bridge failed in 2007 (after 17 years of service). Figure 2-8 shows the failed tendon. This tendon failure draws special attention because of the fact that the failure occurred at approximately 3 to 4 years after the voids in the tendon/duct was grouted or repaired. This repair work included filling voids inside the ducts using a high performance grout. Hansen (2007) reported that the location of tendon failure was at the interface between the existing Class A grout and newer Class C repair grout. This failure indicates a critical need for research into the influence of new repair grouts on tendon corrosion, especially at the interface between existing and repair grouts. This interface could possibly generate a galvanic corrosion cell. However, the validity of this argument needs to be investigated. It was also observed that many tendons were not completely sealed during the original construction. This likely enabled moist air from the environment to enter the voided ducts and accelerate corrosion of the exposed tendons.

**Figure 2-7. Varina-Enon Bridge, Over the James River, Virginia (Roadstothefuture 2009).**

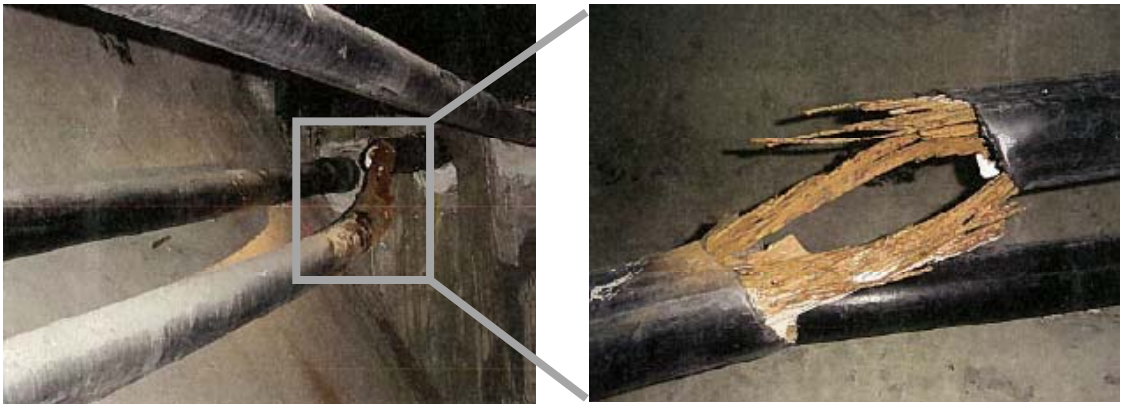

**Figure 2-8. Tendon Corrosion in Varina-Enon Bridge, Virginia (Hansen 2007).**

## 2.3. PARAMETERS INFLUENCING CORROSION OF POST-TENSIONED SYSTEMS

This section discusses the mechanisms of and parameters influencing corrosion of strands in PT bridges.

### 2.3.1. Dissimilar metallic materials in post-tensioned systems

In general, PT systems can consist of a variety of dissimilar metals. These metals can include ASTM A 416 (prestressing strands), ASTM A 615 (spiral bursting reinforcement), ASTM A 536 (cast iron bearing plate or trumpet), ductile iron trumpet, ASTM A 53 (mild steel pipe), and others. The corrosion of any of these metallic materials can cause significant issues in load transfer mechanisms of PT systems. These dissimilar metallic materials are sometimes in close vicinity of each other. Such a situation, with or without the presence of other corrosive conditions, can initiate galvanic corrosion. According to Jones (1996) cast iron in seawater is more noble than steel in seawater. FDOT (2002) investigated galvanic corrosion activity (under moist and chloride environments) between ASTM A 513 mild steel pipe (metallurgically comparable to the ASTM A 53 mild steel pipe used in column foundations of the Bob Graham Sunshine Skyway Bridge), ASTM A416 strands, and ductile iron bearing plates. Figure 2-9 shows pitting corrosion on the ASTM A 53 Grade 5 pipe and ASTM A 416 strand due to coupled galvanic- and chloride-induced corrosion.

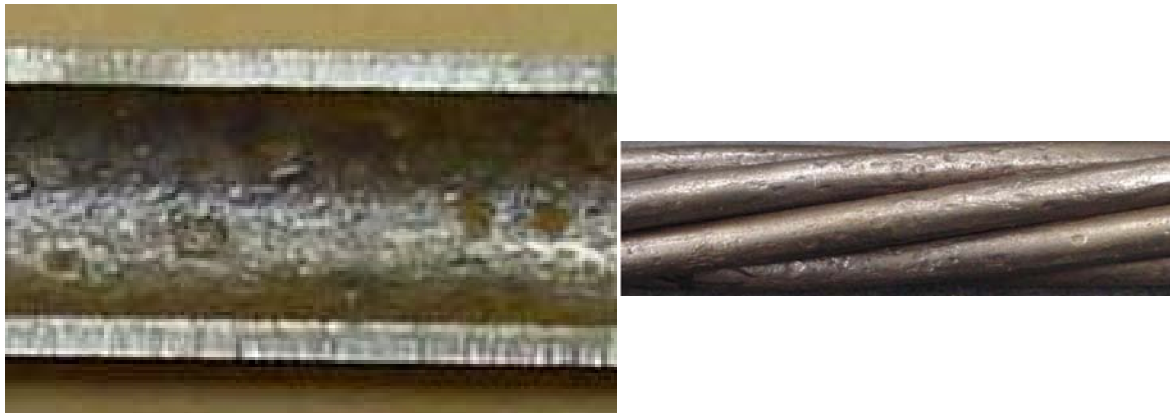

**Figure 2-9. Pitting Corrosion on ASTM A 53 Pipe and ASTM A 416/A 416M-99 Strand Due to Coupled Galvanic- and Chloride-induced Corrosion (FDOT 2002).**

The major findings of the FDOT (2002) study are summarized as follows:

- The electrochemical potentials of both mild steel pipe and strands were approximately –575 millivolts versus a $Cu/CuSO_4$ electrode. However, visual observations and electrical measurements on the pipes and strands indicated that the pipe is more anodic to the strands;
- The electrochemical potential of the strand was approximately 100 mV more negative (i.e., more anodic) than that of bearing plate;
- The rate of the chloride- and moisture-induced corrosion of the strands was higher than the rate of galvanic-corrosion, and
- If the dissimilar metals and their surroundings remain dry, it is less likely for galvanic corrosion to occur.

Although the FDOT (2002) study found that galvanic corrosion is not a concern if the PT systems are kept dry, it is practically impossible to ensure that the moisture and chlorides do not contaminate the PT systems. Hence, Sanchez et al. (2003) recommended that additional studies be performed on galvanic corrosion of PT concrete systems exposed to moisture and chloride environments. This recommendation was

based on the corrosion stains observed on conventional reinforcement at or near anchorages on PT bridges in Texas.

### 2.3.2. Grout class

The Post-Tensioning Institute (PTI) classifies grout materials into four classes based on material specifications and field requirements (PTI 2003). Class A grout consists of cement and water only. Class B grout consists of portland cement, water, and mineral/chemical admixtures. Class C grout consists of pre-packaged, engineered grout material and water only. Class D grout is defined as any *special* grout designed by the engineer.

In general, Class A grout was used for most PT bridges constructed before the year 2000. Many research reports (ASBI 2000, FDOT 2001a, FDOT 2001b) indicate that Class A (non-thixotropic) grout results in more bleed water and therefore a greater number of voids and cracks than Class C (thixotropic and low-bleed) grouts. Hence, given that other conditions remain the same, the tendons with Class A grout will likely have more voids or crack locations with accelerated corrosion than tendons with Class C grout. This may result in a higher joint probability of failure of tendons with Class A grout than those with Class C grout. For these reasons, Class C grout is being used in most new PT bridge construction that started after 2000 (Hansen 2007). In short, Class A and Class C grouts have been used in most PT bridges in the US.

Many Class C grouts with good flow characteristics are commercially available and being used in PT bridges. Three major commercially available Class C grouts are Sikagrout 300PT®, Masterflow® 816, and Euco Cable grout PTX. As mentioned before in Section 2.2.2.4, although not within the scope of this research, the corrosiveness of these and other emerging new grout products needs to be investigated, especially when used as a repair material.

### 2.3.3. Voids

Many research reports (FDOT 1999, FDOT 2001a, FDOT 2001b, NCHRP 1998) cite voids as one of the major causes for corrosion of strands in PT systems. Review of these documents indicates that the corrosion is more severe at inclined and vertical anchorage zones than at horizontal locations on tendon systems. Figure 2-10 shows elevation views with typical void conditions at the anchorages in a PT column and at the anchorage, deviator block, and midspan regions in PT girders. Earlier, Figure 1-2 showed typical cross-sectional views of these tendons with no, partial, and full voids.

In addition to the increased degree of corrosive exposure conditions at anchorage zones with voids, the geometry of the interface between grout, air, and strands (GAS interface) at these voids may also influence the rate of corrosion. This is based on the well-known fact that, the rate of electrochemical corrosion at an interface between a metallic and non-metallic material can be different from that at non-interface on the same metallic material. In the case of the GAS interfaces in tendons, the changes in corrosion rates can be due to the differential pH and other interfacial characteristics. These corrosion rates also depend on the cathode-to-anode ratios at these interfaces.

The size, number, and distribution of voids in a PT duct can be different at different locations and depend on global tendon profiles, local strand profiles, material characteristics, grouting techniques, design considerations, and other factors. Due to limited accessibility, the difficulty in determining the continuity of voids, and other issues, it is difficult to measure the number and size of voids in tendons. However, it can be presumed that the size of critical voids can ranges from small to large volumes.

Woodward (1981) reported that more than 50 percent of ducts in 12 bridges constructed between 1958 and 1977 contained voids with sufficient size to expose the tendon and accelerate corrosion. An inspection, performed in the early 1970s, of a segmental PT bridge constructed in 1961 reported that 62 percent of the internal ducts contained voids that were continuous along the whole length of tendons. The same

inspection found that two ducts contained no grout (Woodward et al. 2001). Later more and more voids and void-induced corrosion were detected in approximately a dozen PT bridges worldwide. TxDOT (2004) provides information on the percentage of voids present in the anchorage and along the tendons in the San Antonio "Y" bridge. A summary of this information is provided in Table 2-1.

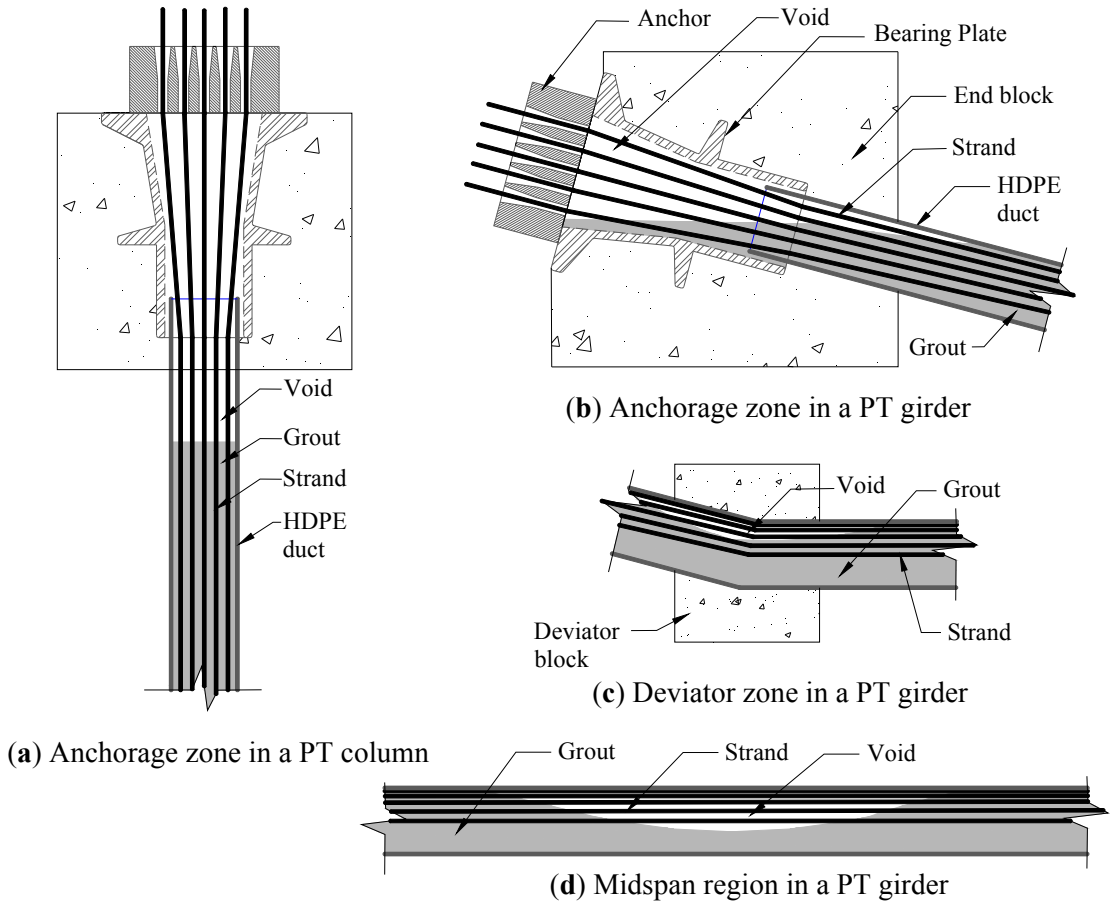


**Figure 2-10. Elevations Showing Typical Void Locations in Grouted Tendon Systems.**

**Table 2-1. Percentage of Voided Tendons among the External Tendons on San Antonio "Y" Bridge (Adapted from TxDOT (2004)).**

| Test location | Number of tests performed | No. of voids detected | Percentage of voids detected |
|---|---|---|---|
| At or near anchorage zones | 601 | 462 | 78.6 |
| Near midspan regions | 2963 | 86 | 6.6 |

### 2.3.4. Oxygen concentration

The presence of oxygen ($O_2$) is necessary for the occurrence of electrochemical corrosion of steel embedded in cementitious materials (ACI 2003). In general, the normal atmospheric oxygen level is 21 percent. However, because box girders can be considered as confined spaces and if the steel tendons are covered by cementitious grout and encased by high density polyethylene (HDPE) ducts with low air permeability, the level of oxygen to which the strands are exposed can be lower than 21 percent. However, the presence of many cracks on the HDPE ducts and other openings in the tendon and anchorage systems have been reported (FDOT 1999, FDOT 2001a, FDOT 2001b). In these cases, a sufficient amount of oxygen can infiltrate the ducts to facilitate the electrochemical process. Less oxygen availability may be one reason why there is less corrosion near the midspan regions than at the anchorage regions of a PT duct with no cracks.

### 2.3.5. Cementitious pore-solution and pH

In bridge structures, the metallic reinforcing materials are embedded in cementitious materials. For example, the immediate environment of the steel embedded in concrete and grout is the pore solution (liquid phase). Diamond (1981) discovered that the grout pore solution contains $Na^+$, $K^+$, $Ca^+$ ions and the concentration varies during the initial curing period but stabilizes with the time of hydration (Figure 2-11).

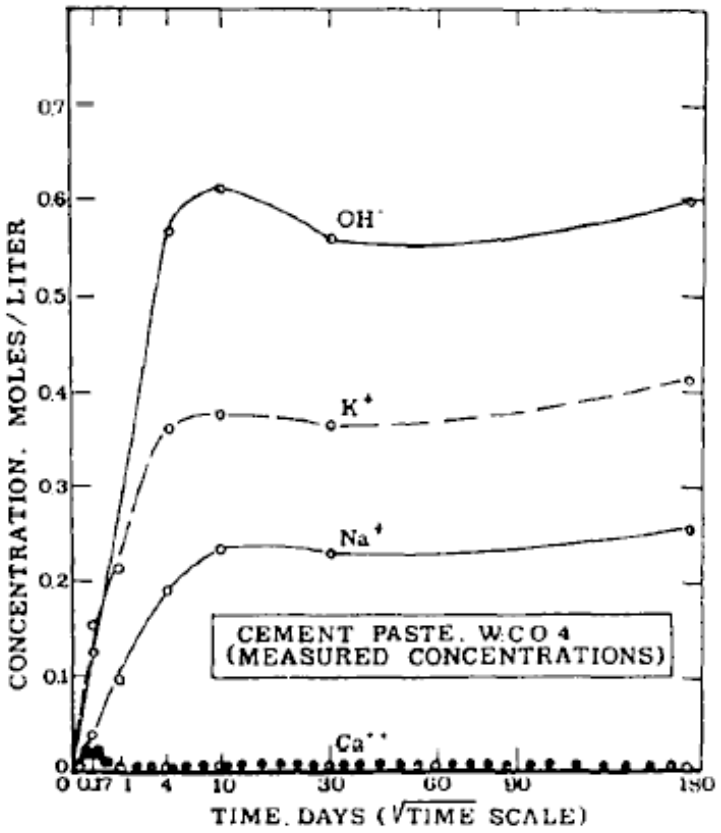


**Figure 2-11. Variation of Pore Solution Composition With Time of Hydration (Diamond 1981)**

Several researchers have studied the pore solution chemistry. Diamond (1981) and Cui and Sagues (2003) provide the chemical composition for the laboratory test solutions to simulate the actual grout pore solution for electrochemical tests. As in the case of uncontaminated grouts, the pH of these simulated pore solutions is very high (say, approximately 13.5); indicating high alkalinity. Neville (1998) and others indicate that steel is resistant to corrosion when exposed to a highly alkaline pore solution and as the pH drops (say, due to carbonation or other mechanisms) the steel becomes more vulnerable to corrosion.

### 2.3.6. Carbon dioxide concentration

The presence of carbon dioxide ($CO_2$) in the atmosphere also poses a challenge for corrosion of steel reinforcement embedded in cementitious materials. When carbonated, the pH of the cementitious material can drop from between 12.6 to 13.5 to as low as 9 (Neville 1998). Because of this drop in the pH pore solution, the embedded steel reinforcement actively corrodes (ACI 2003). Hence, the corrosion rate of strands, when exposed to carbonated grout, could be useful in predicting the time-variant structural reliability.

According to ACI (2003), the $CO_2$ level under normal atmospheric conditions is 0.03 percent. However, the $CO_2$ level to which the PT box girders are exposed may vary due to the exhaust gases from vehicles, industrial chimneys, or both. This indicates that a PT bridge in an urban or industrial area can have higher rate of carbonation than one in a rural area. Sagues (2003) reported the carbonation of surface grout as a possible reason for localized corrosion at the GAS interface (Figure 2-12). According to a FDOT (2001a) report, the grout in a PT tendon on the Mid-Bay Bridge was carbonated to a depth of approximately ¼ inches (6 mm) resulting in a drop in the pH of grout near the void regions from approximately 12 to a value between 8 and 9.

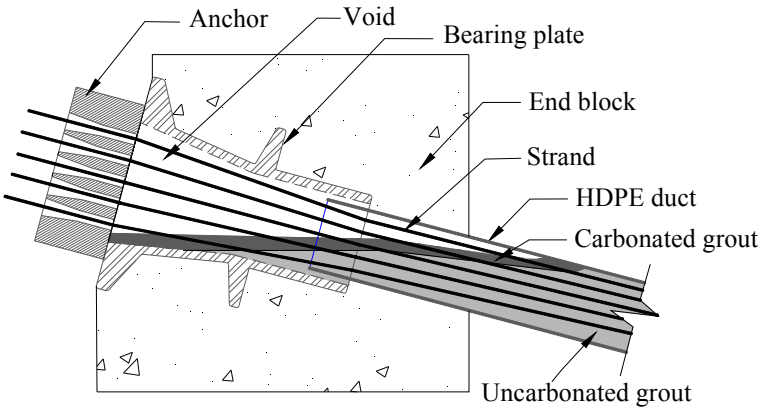


**Figure 2-12. Carbonated GAS Interfaces in Anchorage Zones.**

### 2.3.7. Moisture conditions and precipitation

It is well known that moisture conditions (*MC*) at the metal surface are an essential component for electrochemical processes of steel embedded in cementitious materials ACI (2003). Woodward et al. (2001) reported the presence of water in internal tendons of a segmental bridge constructed in 1961. According to FDOT (2001a) and Hansen (2007), the infiltration of moisture into the PT ducts can occur through cracks or openings on HDPE ducts and at anchorage zones, especially at or near construction joints. Once water collects inside the ducts, it may never evaporate or escape from the duct system, unless the moisture is dried due to self-desiccation of the cementitious grout or artificial drying methods (e.g., passing dry air or inert gases through PT ducts). Perret et al. (2002) reported that the self-desiccation characteristic is commonly found in highly impermeable cementitious grouts and Sagues (2003) identified this as the case with grouted tendons in PT bridges. There may also be cases with winter-summer (rainy-sunny) seasons that may induce an annual WD condition inside the PT ducts. However, the literature typically does not provide information on the history of moisture conditions inside PT ducts.

Direct exposure to WD conditions can create very severe corrosive conditions. Fortunately, such conditions are not predominant in many of the PT bridges that are located away from large bodies of water and protected from rainwater infiltration. However, FDOT (2001b) reported that cyclic charging (i.e., a WD condition) occurred on a bottom portion of a vertical tendon system and seawater leaked through joints between the segments and other openings. This caused failure of the tendons in the Bob Graham Sunshine Skyway Bridge.

A history of daily precipitation can provide an indication or assist in making an engineering judgment about the possible WD conditions that might exist inside a PT duct. The history of daily precipitation in San Antonio, Texas in the years 2001 through 2005 is presented in Figure 2-13.

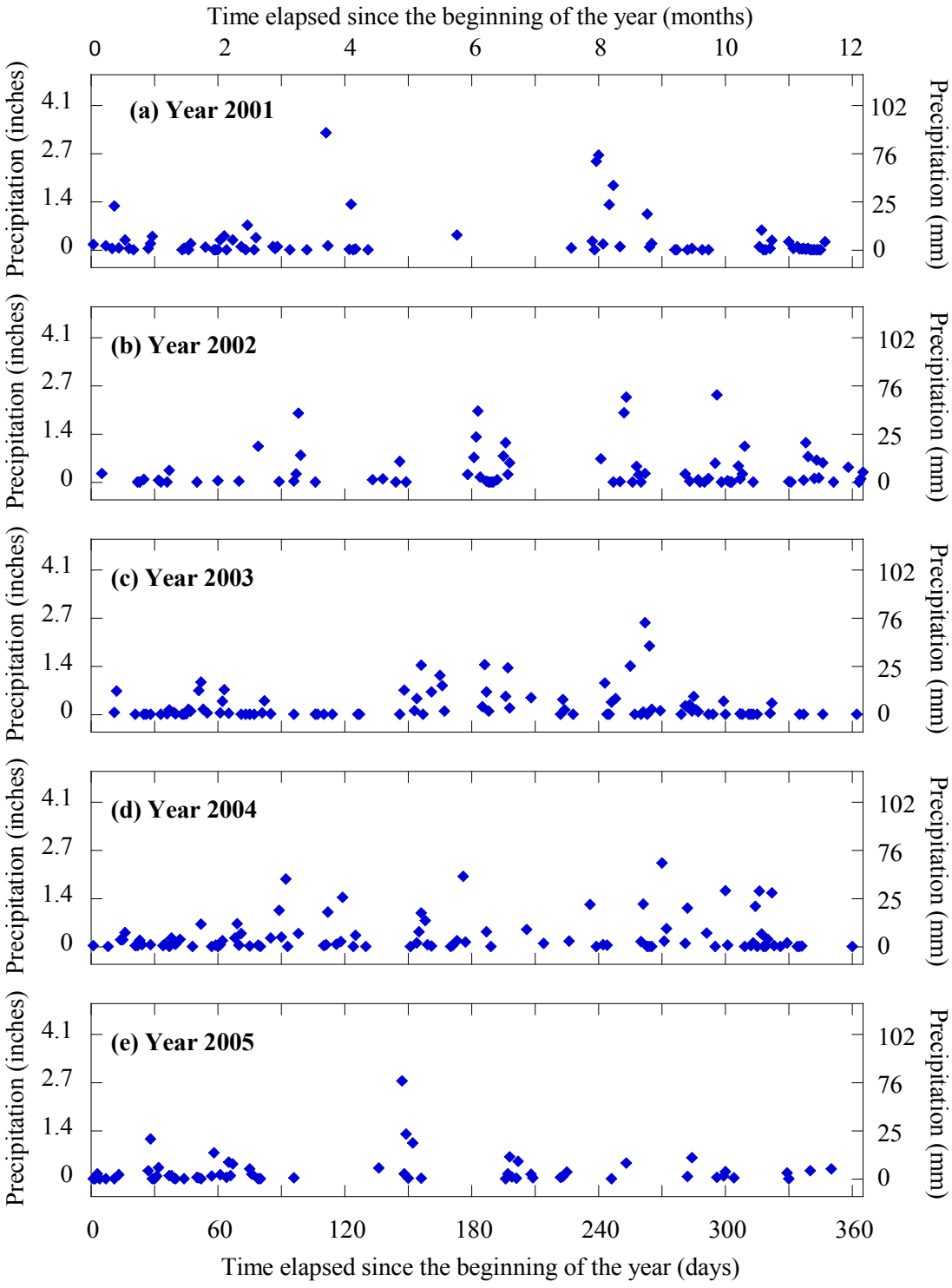


**Figure 2-13. Daily Precipitation in San Antonio, Texas. (NCDC, 2009)**

Li et al. (2004) determined a threshold precipitation (defined as minimum rainfall required to produce runoff) for concrete surface to be 0.06 inches (1.5 mm). Note that this indicates a near zero precipitation for practical engineering purposes.

### 2.3.8. Time of wetness

For atmospheric corrosion of steel specimens, many researchers (Guttman and Serada 1968, Barton 1980, Hakkarainen and Ylasaari 1982, Knotkova et al. 1984, and Klinesmith et al. 2007) used Time of Wetness (*TOW*) as a parameter to model atmospheric corrosion of steel specimens. In these studies and per ISO 9223 designation, the *TOW* is defined as the time when the relative humidity (*RH*) is greater than 80 percent and temperature is greater than $0^{o}$C ($32^{o}$F). Corvo et al. (2008) found that *TOW* is dependent on the presence of atmospheric pollutants, metal surface cleanliness, rain, dew, and water adsorption on metal surfaces. They do not recommend the use of *TOW* for predicting atmospheric corrosion under indoor and contaminated environments. Moreover, if *TOW* is used in corrosion modeling, the influence of contaminants and their interaction with *TOW* has to be established. Kucera and Mattsson (1987) reported that no clear relationship exists between *TOW* and these influencing factors. Per ISO 9223 designation, Dean and Reiser (2002) assumed or approximated *TOW* as the time when *RH* was greater than 80 percent and the temperature (*T*) was greater than $32^{o}$F ($0^{o}$C). Because of the model errors associated with such approximations and the *TOW*'s dependence on other exposure conditions, it would be more useful for practicing engineers to use *RH*, instead of *TOW*, to predict metal loss due to corrosion.

### 2.3.9. Relative humidity

A necessary requirement for atmospheric corrosion is the formation of a thin film electrolyte. In general, the higher the *RH* level, the greater the chances of formation of

this thin film. Chung et al. (2000) reported that as the thickness of this film increases, the more difficult it will be for the oxygen to diffuse to the metal surface, resulting in a reduction in corrosion rate. According to Roberge (1999), there exists a critical *RH* level, defined as the minimum *RH* level needed to form this thin film. This critical *RH* level depends on the corrosion characteristics of the metallic surface, the tendency of corrosion products and surface deposits to absorb moisture, and the presence and type of atmospheric pollutants. Duncan and Ballance (1988) found that the presence of hygroscopic salts in the environment can lower the critical *RH* level. They reported that the critical *RH* level for a metallic surface contaminated by $MgCl_2.6H_2O$ is 34 percent and NaCl is 77 percent. Many PT bridges are exposed to these salts in the form of air-borne chlorides, seawater, or de-icing/anti-icing salt deposition.

In short, *RH* is a parameter that influences the rate of corrosion of steel surfaces exposed to atmospheric conditions. Haynie and Upham (1974) and Mansfeld (1979) indicated that as *RH* increases, especially when greater than 60 percent, the corrosion loss increases exponentially. The corrosion rate of an exposed tendon or strand at a void location could be related to the *RH* conditions inside the PT duct. Hansen (2007) cited moist air that infiltrated into the ducts through the cracks and openings in the tendon system as a cause for strand corrosion. Given that ducts can be cracked and openings can exist at anchorages, the *RH* at a void region inside PT ducts might be correlated to seasonal climatic conditions or proximity of the bridge to a water body. However, no mathematical relationship has been developed. Research addressing this issue could help to predict the long-term performance of the majority of PT bridges (i.e., those that are not exposed to aggressive corrosive conditions) and develop an appropriate repair and maintenance strategy. However, development of such a relationship is not within the scope of this research.

### 2.3.10. Chloride concentration

Corrosion can be significantly accelerated in the presence of water and chlorides. When available in sufficient quantities at the steel surface, chlorides act as a catalyst for the electrochemical corrosion of steel embedded in cementitious material. Trejo and Pillai (2003) determined the critical chloride threshold, defined as the minimum amount of chlorides required to initiate corrosion, for ASTM A615 steel embedded in a plain cement mortar to be 0.9 $lb/yd^3$ (0.5 $kg/m^3$, 0.09 weight % cement). However, there exists a large scatter in reported values for mild steels. A review of critical chloride threshold values of mild steel is provided in Pillai (2003).

This literature review could not find any significant information on the critical chloride threshold of prestressing steel strands. Krauss and Nmai (1997) reported that this high chloride threshold could be because of the effects of lubricants used during the manufacturing processes and the smooth drawn surface of prestressing wires. Mammoliti et al. (1996) and Pillai and Trejo (2005) reported that, in general, the smoother the metallic surface the higher the critical chloride threshold. However, FHWA's report that the critical chloride threshold of prestressing strands is approximately six times higher than that of mild steel provided limited data to justify this finding and further experimental work is needed.

NCHRP (1998) and FDOT (1999, 2001a and b) reported the presence of a high amount of chlorides in the tendons on the Bob Graham Sunshine Skyway Bridge. In general, the water-borne or air-borne chlorides can infiltrate into the ducts and reach the strand surfaces, especially when the bridge is located above seawater and/or exposed to de-icing/anti-icing salts. If the bridge is located away from the salt water, the air salinity, a measure of atmospheric chloride concentration, will be low compared to that near seawater (Albrecht and Naeemi 1984). Knotkava et al. (1984) used air salinity to empirically predict the atmospheric corrosion process.

### 2.3.11. Temperature

Electrochemical reactions are influenced by the temperature of the metal surface. The higher the temperature, the greater will be the molecular energy levels and collision rates and, hence, higher rates of electrochemical reactions. The Arrhenius equation can be used to represent the main effect of temperature on the corrosion rate constant, $k$, as follows:

$$k = A \cdot \exp\left(-\frac{E_a}{RT}\right) \tag{2.1}$$

where, $A$ is a pre-exponential factor, $E_a$ is the activation energy of the reaction process, $R$ is the Universal Gas Constant (8.314472 $JK^{-1}mol^{-1}$ (6.132440 $lbf{\cdot}ft{\cdot}K^{-1}{\cdot}g{\cdot}mol^{-1}$)), and $T$ is the absolute temperature (in $^{o}K$). Zor et al. (2005) determined the activation energy of the corrosion of iron in 0.1 M NaCl to be 24500 J $mol^{-1}$. Tang et al. (2006) determined that activation energy and the pre-exponential factor for the corrosion of cold rolled steel in a solution with 0.1 M NaCl, 0.001 M 8-hydroxyquinoline, and 0.5 M $H_2SO_4$ is 81000 J $mol^{-1}$ and $2.375\times10^{20}$ μg $cm^{-2}$ $s^{-1}$ ($6.597\times10^{14}$ g $m^{-2}$ $h^{-1}$), respectively.

The main effect of temperature on strand corrosion may be minimal or neglible during normal atmospheric temperature conditions. However, even in this temperature range, an interaction between the temperature, relative humidity/moisture, and chloride conditions could possibly result in a significant corrosion rate.

### 2.3.12. Axial stress

According to ACI (2003), the stress level does not play a major role in the corrosion susceptibility of conventional steel reinforcement (meeting ASTM A615 specifications) embedded in cementitious materials. PT strands (meeting ASTM A416 specifications) experience very high axial stresses ($f_{axial}$). The $f_{axial}$ on PT strands could be

approximately four times more than that experienced by ASTM A615 steel in bridges and the influence of $f_{axial}$ on corrosion could be significant. It should also be noted that conventional reinforcement is hot-rolled and PT strands are cold-rolled. The very high axial stress levels and the cold-rolled surface could influence the corrosion rate and susceptibility. Naaman (2004) reported that the average in-situ stress of a PT strand can be assumed to be equal to $0.545 f_{pu}$ or 147 ksi (1014 MPa). Proverbio and Longo (2003), Kovač et al. (2007), and Sanchez et al. (2007) reported that the synergistic effect of high stress levels and corrosive mediums can influence corrosion susceptibility, especially stress corrosion cracking of prestressing strands. Also, Kovač et al. (2007) reported that cold-rolled, prestressing steel has a non-uniform microstructure with no cracks when $f_{axial}$ is zero and transgranular cracks (with typical crack length equal to approximately 100 μm) when $f_{axial}$ is approximately $0.6 f_{pu}$. These have not been observed in conventional steel reinforcement. Smaller transgranular cracks could be formed at stress levels lower than $0.6 f_{pu}$. However, sufficient information on these surface cracks in PT strands and their effects on corrosion is not available in the literature. The difference in processing and finishing of conventional reinforcement and PT strands can have a significant effect on their corrosion performance.

### 2.3.13. Other factors

Fatigue loading could cause serious durability issues for bridge systems. However, Ryals et al. (1993) reported that fatigue is not a significant problem in external tendons if the variation in $f_{axial}$ is within 70 Mpa (10 ksi). Wollmann et al. (2001) performed live load tests (using AASHTO HS20 trucks) on several spans of the San Antonio "Y" bridge and found that the $f_{axial}$ varies less than 7 Mpa (1 ksi). Because this is much less than the 70 Mpa (10 ksi) criteria set by Ryall et al. (1993), it can be concluded that fatigue may not be a significant durability issue of typical PT bridges in Texas. However, a synergistic effect of fatigue and aggressive corrosive conditions might cause durability issues. Other concrete deterioration mechanisms such as alkali-aggregate reaction

(AAR), delayed-ettringite formation (DEF), freeze-thaw cycles, and other mechanisms affecting the integrity of hardened concrete can also create durability issues for PT bridges.

## 2.4. CORROSION EVALUATION USING VISUAL INSPECTION TOOLS

Visual observation of uncleaned, corroded strands by the unaided eye cannot generate reliable information on the degree, form, or pattern of corrosion, especially when the corrosion attack is not significant, does not vary significantly from one sample to another, or both. Sason (1992) recommended a strand cleaning method to help field engineers in "accepting" or "rejecting" new PT strands before placing inside the ducts. In this method, strands are hand-rubbed with a synthetic cleaning pad until the loose corrosion products or rust are removed. Because no mechanical pressure is applied and the pad is non-metallic, it will not remove the base metallic material from the strands. Sason (1992) also reported, *"In many cases, heavily rusted strands with relatively large pits will still test to an ultimate strength greater than specification requirements. However, it will not meet the fatigue test requirements."* No definition was provided for *"relatively large pits"* and hence, corrosion evaluation would heavily depend on the inspector's experience, judgment, or both. Also, effective visual inspection of strands or tendons inside box girders could be very difficult and time consuming because of the large number of strands, insufficient lighting, opaque HDPE duct covering and other factors. Although difficulties exist, direct inspection (using naked eyes) and indirect inspection (using photographs or micrographs) of cleaned strands can assist in identifying the presence of surface corrosion, pitting corrosion, corrosion at or near GAS interfaces, or other unique patterns that could influence the capacity of PT strands.

## 2.5. MODELING CORROSION OF STEEL (IMMERSION CONDITIONS)

Strands in PT bridges may experience WD conditions. Probabilistic models that predict the corrosion and/or capacity loss of strands exposed to WD conditions would be helpful to develop time-variant structural reliability models. Such models were not identified in this literature review. However, corrosion models for unprotected steel (i.e., bare steel) exposed to immersion conditions have been developed by Southwell and colleagues in 1979 (Southwell 1979) and later by Melchers (1998, 1999). These models were based on data collected from actual steel structures (e.g., ship hulls exposed to sea water) and are not necessarily suitable for the WD conditions inside a PT duct or tendon. Table 2-2 shows mathematical expressions and Figure 2-14 shows graphical expressions of these linear, bi-linear, tri-linear, and power models.

**Table 2-2. Existing Models for Thickness Loss of Steel Surfaces on Ships Exposed to Seawater.**

| Model type | Existing wet-dry corrosion models | Reference |
|---|---|---|
| Linear | $K = 0.076 + 0.038t$ | Southwell et al. (1979) |
| Bi-linear | $K = \begin{cases} 0.09t, & 0 < t < 1.46 \text{ years} \\ 0.076 + 0.038t, & 1.46 < t < 16 \text{ years} \end{cases}$ | Southwell et al. (1979) |
| Tri-linear | $K = \begin{cases} 0.170t, & 0 \le t < 1 \text{ year} \\ 0.152 + 0.0186t, & 1 \le t < 8 \text{ years} \\ -0.364 + 0.083t, & 8 \le t < 16 \text{ years} \end{cases}$ | Melchers (1998) |
| Power | $K = 0.1207t^{0.6257}$ | Melchers (1998) |
| Power | $K = 0.084t^{0.823}$ | Melchers (1999) |

$K$ = corrosion loss (in mm); 1 inch = 25.4 mm

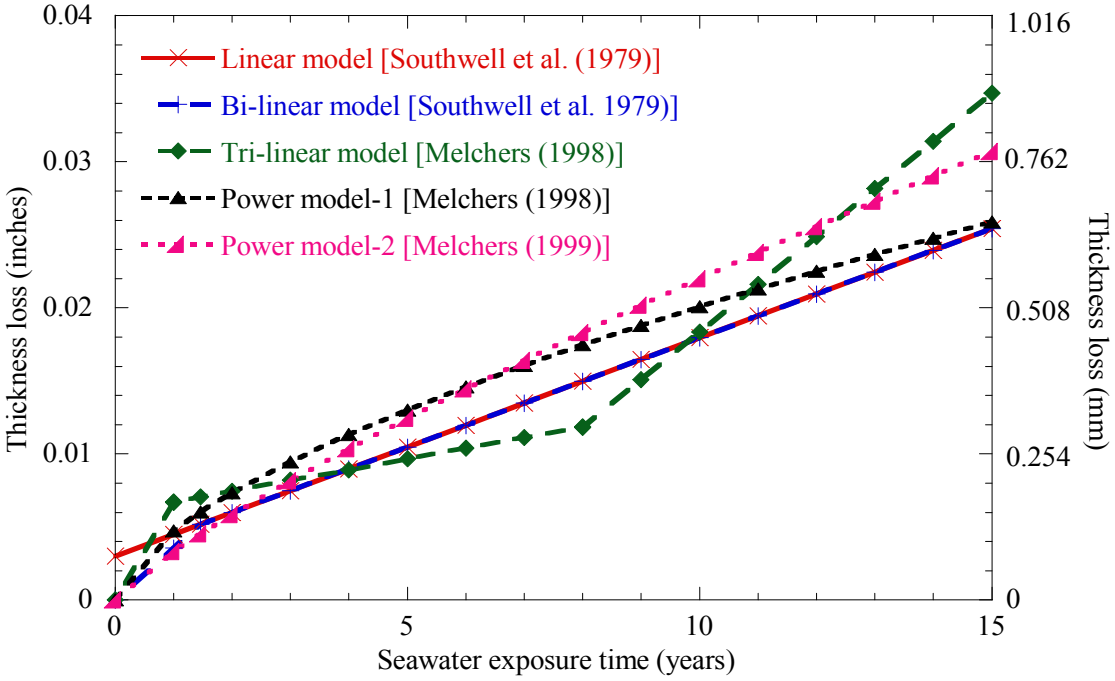


**Figure 2-14. Thickness Loss of Steel Surfaces on Ships Exposed to Seawater (Predicted Using Existing Corrosion Models).**

In Table 2-2, note that the linear model and the second part of the bi-linear model are identical. In Figure 2-14, the tri-linear model, with diamond data markers, underpredicts the thickness loss when time is between approximately 5 and 10 years and overpredicts the thickness loss after 10 years; when compared to those predicted by linear, bi-linear, and power models. Moreover, for practical engineering purposes, all these models tend to provide similar results up to 5 years, beyond which there are only slight variations. However, these models that are made for seawater exposure of ship structures cannot be used for predicting capacity loss of PT strands exposed to WD environments. This is mainly because of the different material, void, oxygen, moisture, and stress conditions of the PT systems.

## 2.6. MODELING CORROSION OF STEEL (CONTINUOUS-ATMOSPHERIC CONDITIONS)

This subsection begins with a review of various atmospheric corrosion models as a function of environmental parameters and time. The model forms that are used to predict long-term corrosion are then discussed. Following this, the procedures to determine and modify the power corrosion model based on recent field data are provided. Various long-term corrosion models are then presented.

### 2.6.1. Atmospheric corrosion models based on environmental parameters, time functions, or both

In 1946, Brooks proposed a general deterioration model for materials as a function of atmospheric impurities and other environmental parameters as follows:

$$Rate\ of\ \ deterioration = a\alpha^{T} + b\frac{RH-k}{100}1.054^{T}(1+cI)(1+0.067WV) \tag{2.2}$$

where, $T$ is temperature, $RH$ is relative humidity, $I$ is the concentration of effective impurities, $WV$ = wind velocity, and $a, \alpha, b, k, c$ are empirical constants. Later, based on experimental and field observations, many researchers developed empirical models to predict the corrosion of steel under atmospheric conditions with various impurities such as $SO_2$ and $Cl^-$. A collection of atmospheric models that use environmental parameters, exposure time function, or both is provided in Table 2-3. The symbols in Table 2-3 are as defined by the corresponding authors and may or may not be representative of symbols used in the remainder of this document.

**Table 2-3. Existing Atmospheric Corrosion Models (as a Function of Environmental Parameters and Exposure Time) for Steel.**

| Atmospheric corrosion models | Reference |
|---|---|
| $K = 0.16\,TOW^{0.7}(SO_2 + 1.78)$<br>where, $K$ = grams; $TOW$ = days; $SO_2$ = ppm | Guttman and Serada (1968) |
| $K = 32.55 \cdot \sqrt{t} \cdot \mathrm{e}^{\left(0.00275\,SO_2 - \frac{163.2}{RH}\right)}$<br>where, $K$ = mm; $t$ = years; $SO_2 = \mathrm{mg/m^3}$; $RH$ = % | Haynie and Upham (1974) |
| $K = 0.0152 \cdot TOW^{0.428} \cdot SO_2{}^{0.57}$<br>where, $K$ = g/ $\mathrm{m^2}$/day; $TOW$ = hours/year; $SO_2$ = $\mathrm{mg/m^2/day}$ | Barton (1980) |
| $K = 1.17 \cdot TOW^{0.66} \cdot (SO_2 + 0.048)$<br>where, $K$ = mm; $TOW$ = hour/year; $SO_2$ = $\mathrm{mg/m^2/day}$ | Hakkarainen and Ylasaari (1982) |
| $K = 1.327 + 0.4313\,SO_2 + 0.0057\,TOW + 0.1384\,Cl^-$<br>where, $K$ = mm; $TOW$ = days; $SO_2 = \mathrm{mg/m^3}$; $Cl^-$ = $\mathrm{mg/m^2/day}$ | Knotkova et al. (1984) |
| $K = 132.4Cl^-(1 + 0.038T - 1.96TOW - 0.53SO_2) + 74.6TOW(1 + 1.07SO_2) - 6.3$<br>$K = 33.0 + 57.4Cl^- + 26.6SO_2$<br>where, $K$ = μm; $TOW$=annual fraction; $T$ =° C; $SO_2$ = $\mathrm{mg/m^2/day}$ | Feliu et al. (1993) |
| $K = 18.851\,t^{1.0947}(Cl^-)^{0.4313}(RF/D)^{-0.2447}$<br>where, $K = \mathrm{g/m^2}$; $t$ = months; $Cl^- = \mathrm{mg/m^2/day}$; $RF$ = mm; $D$ = days | Corvo et al. (2005) |
| $K = 0.0157\left(\frac{TOW}{3800}\right)^{0.15}\left(1 + \frac{Cl^-}{50}\right)^{0.22}(RH)^{2.3}\,\mathrm{e}^{(-0.0019(T+20))}$<br>where, $K$ = mm; $TOW$ = hours/year; $Cl^- = \mathrm{mg/m^2/day}$; $RH$ = %; $T$ = °C | Klinesmith et al. (2007) |

$Cl^-$ = Chloride concentration; D = Number of rainfall days; $K$ = Corrosion loss; $RF$ = Rainfall; $RH$ = Relative humidity; $SO_2$ = Sulfur dioxide concentration; $T$ = Temperature; $TOW$ = Time of wetness;

In the models provided in Table 2-3, the time function is represented by either *TOW* or an exponent of time in years. As shown in Subsection 2.3.8, the accurate estimation of *TOW* is very complex (Corvo et al. 2008). Moreover, sometimes it is not possible to obtain a good estimate of the environmental parameters over a long duration.

Therefore, the use of models in Table 2-3 for long-term prediction of corrosion is limited.

### 2.6.2. Atmospheric corrosion models based on time functions only

To predict long-term corrosion loss, researchers have developed simple corrosion models that have only exposure time as a parameter. These models are developed based on long-term exposure data collected from corrosion test sites/stations.

The International Standard Organization (ISO) designation 9224, *Corrosion of Metals and Alloys – Corrosivity of Atmospheres*, provides guidelines for atmospheric corrosion rates of metallic materials. This standard assumes the following equation:

$$\begin{aligned} K &= tr_{av} && ;0 \le t \le 10 \text{ years} \\ K &= 10r_{av} + (t-10)r_{lin} && ;t > 10 \text{ years} \end{aligned} \tag{2.3}$$

where, $t$ is the time of exposure (in years) and $r_{av}$ is the average corrosion rate (in mm/year) during the first 10 years, and $r_{lin}$ is the steady-state corrosion rate (in mm/year). However, this steady-state corrosion rate assumption does not represent the decaying corrosion rate as observed in most atmospheric corrosion processes.

To represent the decaying corrosion rates, a power model form has been used by many researchers including Haynie and Upham (1974), McCuen et al. (1992), Kobus (2000), Laco et al. (2004), Corvo et al. (2005), Natesan et al. (2006), and Klinesmith et al. (2007). The ASTM G101, *Standard Guide for Estimating the Atmospheric Corrosion Resistance of Low-Allow Steels*, also suggests a power model form for predicting thickness loss due to corrosion. This model form is mathematically expressed as follows:

$$\text{Total corrosion loss} = At^{n} \tag{2.4}$$

where, $A$ equals the corrosion loss in the first year of exposure, $t$ equals the exposure time, and $n$ is a constant. In 1989, Drazic and Vascic proposed another corrosion model based on a natural logarithmic approximation as follows:

$$\text{Total corrosion loss} = a + b\ln[t] \tag{2.5}$$

where, $a$ and $b$ are constants and $t$ is the exposure time in years. This model also conforms to the decaying corrosion rate. However, the power model form seems to be more appropriate and, hence, widely used by researchers for modeling atmospheric corrosion processes. A collection of existing power corrosion models, following the model form in Equation (2.4) for carbon steel under marine, industrial, and rural exposure conditions is provided in Table 2-4. Figure 2-15 (a), (b), and (c) show the predicted thickness loss (using these power models) for carbon steel under marine, industrial/urban, and rural exposure, respectively. Note that the highest thickness loss is predicted by a model for industrial/urban exposure condition in Figure 2-15 (b). However, a general comparison between the prediction curves in Figure 2-15 (a) and (b) indicates that marine and industrial/urban atmospheric exposure conditions may, in general, result in approximately similar thickness losses. Also, note that the lowest thickness loss is observed or predicted for the rural exposure condition, as shown in Figure 2-15 (c). It should be understood that all these models were developed based on the data from widely varying geographical, environmental, and other corrosive conditions. However, a general conclusion that the atmospheric corrosion of steel follows a power model is reasonable.

**Table 2-4. Power Law Models for Atmospheric Corrosion of Carbon Steel.**

| No. | *A* | n | Exposure condition | Location | Exposure times | Reference |
|---|---|---|---|---|---|---|
| 1 | 50.44 | 0.5413 | Marine | Kure Beach, NC, US (250 m from sea coast) | Last test at 7.5 years | McCuen et al. (1992) |
| 2 | 46.74 | 0.45 | | Barcelona, Spain (close to sea coast) | 0-, 3-, 6-, 9-, and 12-month tests | Laco et al. (2004) |
| 3 | 58.57 | 0.65 | | Cudallore, India (50 m from sea coast) | Based on a 5-year test | Natesan et al. (2006) |
| 4 | 32.43 | 0.35 | | Nagapattinam, India (50 m from sea coast) | | |
| 5 | 115.04 | 0.50 | | Mangalore, India (130 m from sea coast) | | |
| 6 | 30.58 | 0.62 | | Goa, India (50 m from sea coast) | | |
| 7 | 107.74 | 0.49 | Industrial -marine | Manali, India ($SO_2$, $Cl^-$, $NO_3$, sea coast) | Based on a 5-year test | Natesan et al. (2006) |
| 8 | 59.69 | 0.7356 | Industrial/ Urban | Rankin, PA, US | Last test at 10 years | McCuen et al. (1992) |
| 9 | 72.11 | 0.4501 | | Bethlehem, PA, US | | |
| 10 | 53.82 | 0.5242 | | Columbus, OH, US | | |
| 11 | 51.24 | 0.3297 | | Newark, NJ, US | Last test at 16 years | |
| 12 | 75.27 | 0.3105 | | Bethlehem, PA, US | | |
| 13 | 50.51 | 0.3586 | | Newark, NJ, US | Last test at 15.5 years | |
| 14 | 58.00 | 0.3445 | | Kearny, NJ, US | Last test at 20 years | |
| 15 | 73.50 | 0.21 | | Katowice, Poland | 0-, 1-, 2-, 4-, and 6-year tests | Kobus (2000) |
| 16 | 37.50 | 0.35 | | Warsaw, Poland | | |
| 17 | 22.37 | 0.635 | | Barcelona, Spain | 0-, 3-, 6-, 9-, and 12-month tests | Laco et al. (2004) |
| 18 | 44.31 | 0.29 | | Mumbai, India | Based on a 5-year test | Natesan et al. (2006) |
| 19 | 29.65 | 0.46 | | Surat, India | | |
| 20 | 36.14 | 0.5984 | Rural | Saylorsburg, PA, US | Last test at 16 years | McCuen et al. (1992) |
| 21 | 27.50 | 0.44 | | Boreka Forest, Poland | 0-, 1-, 2-, 4-, and 6-year tests | Kobus (2000) |
| 22 | 14.52 | 0.35 | | Mahendragiri, India | Based on a 5-year test | Natesan et al. (2006) |

$\Delta T$ = Thickness loss in $\mu m$; $A$ and $n$ empirical constants.

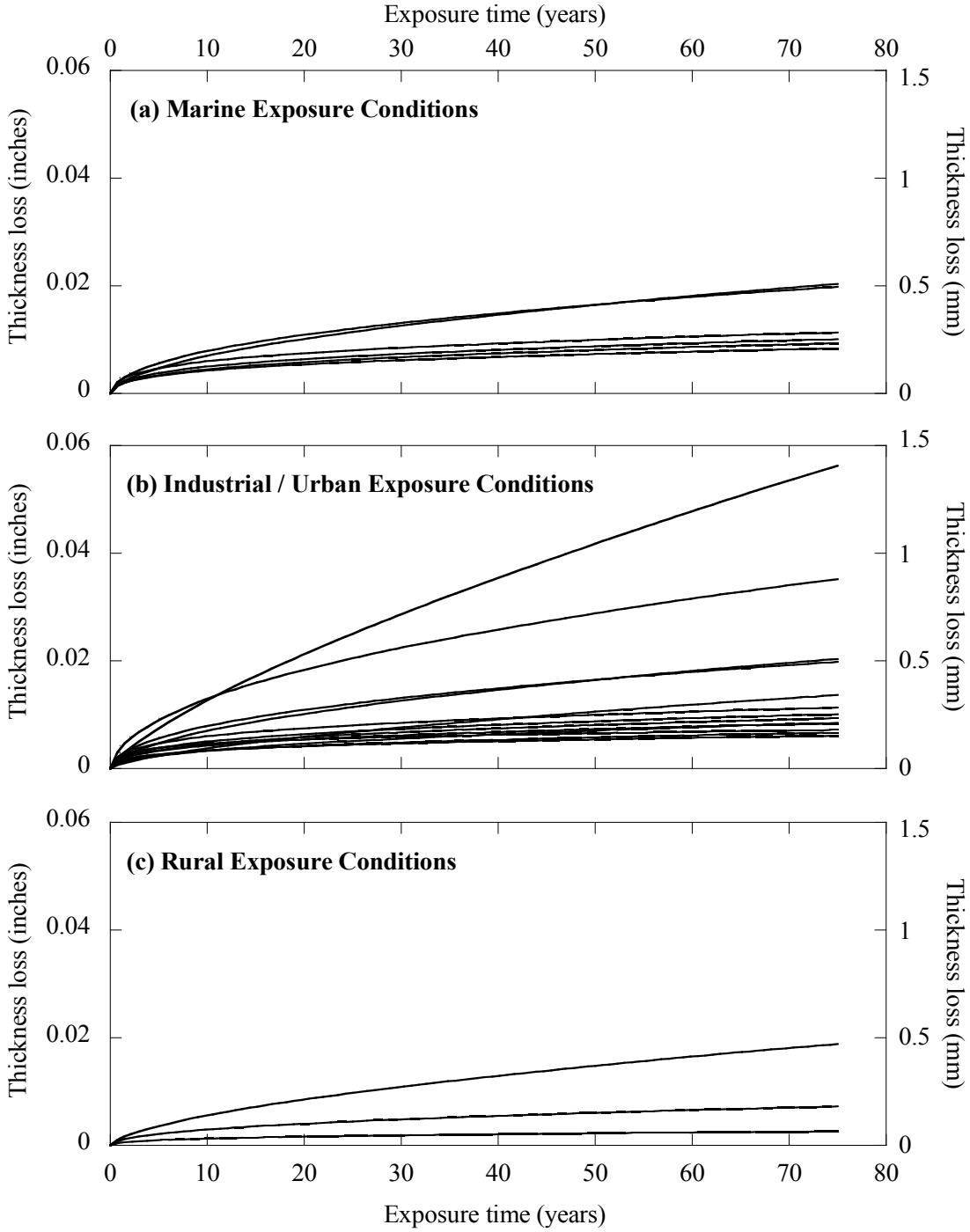


**Figure 2-15. Thickness Loss of Carbon Steel Due to Atmospheric Corrosion (Predicted Using Existing Power Models). [Note: 1 inch = 25.4 mm]**

In addition to predicting atmospheric corrosion, the power models have been used in underground corrosion modeling. For example, Decker et al. (2008) proposed the following equation for corrosion losses in steel piles embedded in soil:

$$\Delta T = 59\, t^{0.67} \tag{2.6}$$

where, $\Delta T$ is the average thickness loss (in μm) in $t$ years of exposure. Romanoff (1962) proposed an exponent of 0.55 for predicting metallic corrosion in soils. Schlosser and Bastick (1991) suggested an exponent 0.65 for galvanized steel in soils. In general, it can be concluded that the power model is very helpful in predicting long-term corrosion of various metal-electrolyte systems. In addition, the power corrosion model can be updated or modified based on new data available, possibly from field inspections. Following is a discussion on procedures for developing and then modifying/updating power corrosion models.

### 2.6.3. Developing and updating the power corrosion model

For the power corrosion model form in Equation (2.4), the initial estimate of $A$ can be determined using the data from a short-term (say, 1 year) corrosion test. The initial estimate of $n$ can be determined using the data from multiple times, if available. As evident from Table 2-4, the value of $A$ and $n$ can vary as the atmospheric exposure conditions change. Table 2-4 also indicates that the exponent term ranges between 0.21 and 0.79 as the exposure condition changes. The value of the exponent may also depend on the duration or time of exposure when the data was collected and the number of data. As more long-term corrosion loss data become available, the existing power models can be modified using numerical optimization (i.e., curve fitting) procedures to provide a better prediction for the future.

McCuen et al. (1992) provided a numerical optimization procedure to modify the coefficients in the power corrosion model and it is provided here. Consider the power corrosion model in Equation (2.4). Using a Taylor series expansion, the sum of squares of errors for this model can be approximated as follows:

$$\sum e^2 = \sum \left[\hat{p} - p\right]^2 = \sum \left[ h_0 \left( \frac{\hat{p}_0 - \hat{p}}{\Delta A} \right) + h_1 \left( \frac{\hat{p}_1 - \hat{p}}{\Delta n} \right) \right]^2 \tag{2.7}$$

where, $h_0$ and $h_1$ are step sizes for coefficients $A$ and $n$, respectively; $\hat{p}_0$ and $\hat{p}_1$ are the predicted values of $p$ when $A$ and $n$ are incremented by $\Delta A$ and $\Delta n$, respectively, with the other coefficient held constant; and $\hat{p}$ is the predicted value of $p$ for the estimates of $A$ and $n$. The iterative procedure can be continued until a minimum value for the *sum of squares of errors* is obtained.

This numerical optimization might result in model coefficients with the best overall goodness-of-fit for the power corrosion model. However, due to the possibly large number of data points at earlier years, the local goodness-of-fit at the earlier years may be better than that at the later years. For an accurate prediction of service life, it is more important to have a model that has better local goodness-of-fit at the later years than at the earlier years. McCuen et al. (1992) suggests a stepwise deletion of earlier data to improve the goodness-of-fit of the power model, especially at the exposure times corresponding to the latest observed value of corrosion loss. Hence, the power corrosion model form can be updated based on the latest field data available.

This literature review could not find any corrosion models that can predict the $C_T$ of strands as a function of material, environmental, stress, and void conditions. However, such models are needed to predict the long-term structural capacity of a PT girder, and are developed in Section 7. The next subsection provides a review of procedures to determine structural capacity of PT segmental girders.

## 2.7. STRUCTURAL CAPACITY OF POST-TENSIONED, SEGMENTAL BRIDGES

### 2.7.1. Parameters directly influencing structural behavior of PT girders

In Subsection 0, a review of material, void, environmental, and stress parameters that directly affect the corrosion and remaining tension capacity of tendons or strands was provided. In this subsection, a review of parameters that directly influence the flexural capacity of PT girders is provided. These parameters include:

- tension capacity of PT strands, $C_T$;
- axial stresses and their losses on strands;
- compressive strength of concrete, $f_c$, and;
- typical geometrical, structural design, and other parameters of box girders

#### *2.7.1.1. Tension capacity of prestressing strands*

In this document, the strands and wires with negligible corrosion are referred to as "as-received" strand and "as-received" wire, respectively. While used in symbols, these terms are abbreviated as "ARS" and "ARW", respectively. Tension capacities of ARS and ARW are denoted as $C_{T,\,ARS}$ and $C_{T,\,ARW}$, respectively.

According to PTI (1998), the minimum ultimate tensile strength (*MUTS*) of a strand is defined as the force equal to the nominal cross-sectional area of a strand, or bar, times its nominal ultimate tensile stress. *MUTS* of a 270 ksi (1860 MPa) grade, 0.6 inch (15.2 mm) diameter, seven-wire "as-received" strand meeting the ASTM A 416 specifications is 58.6 kips (261 kN). This is denoted as $MUTS_{ARS}$, herein. Because of liability concerns, the $C_{T,\,ARS}$ is generally higher than the $MUTS_{ARS}$. However, this literature review could not find any statistical expressions for $C_{T,\,ARS}$. Such statistical expressions for "as-received" strands are developed in Subsection 7.3.

As discussed in Subsection 0, the $C_T$ can be reduced as a result of corrosion due to the exposure to material, void, environmental, and stress conditions over time. Poston et al. (2003) reported that a 75 percent reduction in strand capacity can result in a 50 percent or more reduction in the live load carrying capacity of the bridge. Moreover, structural failures have been reported due to reduced capacity of strands in voided tendons that are exposed to corrosive environments (NCHRP 1998, ASBI 2000, FDOT 2001a, b, and Hansen 2007). These studies and field observations indicate a critical need to develop time-variant structural reliability models for these bridge structures. This literature review could not find probabilistic expressions for time-variant $C_T$ of strands exposed to these conditions. However, such expressions are necessary for time-variant reliability assessment of PT bridges and will be developed in this research (refer to Section 7).

#### *2.7.1.2. Axial stresses and their losses on strands*

Subsection 2.3.12 discusses the possible effects of axial stresses in the strands, $f_{axial}$, on corrosion and capacity loss. Two expressions for the effective prestress, $f_{pe}$, can be expressed as follows:

$$f_{pe} = \begin{cases} f_{pJ} - \Delta f_{pT} \\ or \\ f_{pi} - \Delta f_{pLT} \end{cases} \tag{2.8}$$

where $f_{pJ}$ is the jacking stress; $\Delta f_{pT}$ is the total prestress losses; $f_{pi}$ is the initial prestress after anchoring; and $\Delta f_{pLT}$ is the prestress loss at a given time due to long-term effects. Depending on long-term creep, shrinkage, and other mechanisms, the value of $\Delta f_{pLT}$ can change as a function of time. The $\Delta f_{pT}$ can be calculated as follows:

$$\Delta f_{pT} = \Delta f_{pF} + \Delta f_{pA} + \Delta f_{pES} + \Delta f_{pLT} \tag{2.9}$$

where $\Delta f_{pF}$, $\Delta f_{pA}$, and $\Delta f_{pES}$ are instantaneous prestress losses due to friction, anchorage seating, and elastic shortening, respectively. The $f_{pi}$ can be calculated as follows:

$$f_{pi} = f_{pJ} - \left(\Delta f_{pF} + \Delta f_{pA} + \Delta f_{pES}\right) \tag{2.10}$$

Depending on the available data, an appropriate expression from Equation (2.8) can be chosen to calculate $f_{pe}$. The value of $f_{pe}$, on individual strands is a key parameter influencing $f_{axial}$. Because of the variability in the $f_{pJ}$ and $\Delta f_{pT}$, different strands may experience different levels of $f_{pe}$. Hence, ideally, $f_{pe}$ should be statistically expressed for performing structural reliability analysis. One way to obtain a statistical expression for $f_{pe}$ is to use statistical expressions for the terms in Equation (2.8).

According to TxDOT (2004), the recommended maximum $f_{pJ}$ and average $f_{pi}$ are 77 and 70 percent of $MUTS_{ARS}$. These are calculated to be 208 and 189 ksi (1433 and 1304 MPa), respectively. Due to various technical, equipment, measurement, and human error factors, the actual applied $f_{pJ}$ could vary. However, this literature review could not find any statistical expressions for $f_{pJ}$.

The instantaneous prestress losses (i.e., $\Delta f_{pF}$, $\Delta f_{pA}$, and $\Delta f_{pES}$) in the case of PT segmental bridges can be minimal because of long tendon lengths and advanced stressing operations and equipment. This literature review could not find sufficient information to develop statistical expressions for $\Delta f_{pF}$, $\Delta f_{pA}$, and $\Delta f_{pES}$. In addition, the variations in $\Delta f_{pLT}$ also can contribute to variations in the value of $f_{pe}$ for each strand in a segmental girder. It should be noted that for design purposes, $f_{pe}$ is assumed to be the same for all strands. According to the Article C5.9.5.1 in AASHTO LRFD

Specifications (2007), for segmental construction, "*...calculations for loss of prestress should be made in accordance with a time-step method supported by proven research data...*" According to Table 5.9.5.3-1 in AASHTO (2007), the lump sum estimate of $\Delta f_{pLT}$ in 270-ksi (1861-kMPa) strands in PT box girders is:

$$\Delta f_{pLT} = (19.0 + 4.0PPR) \text{ ksi}; \quad PPR = \text{partial prestress ratio} = \left( \frac{A_s f_y}{A_{ps} f_{py} + A_s f_y} \right) \qquad (2.11)$$

where, $A_s$ and $A_{ps}$ are cross-sectional areas of conventional and prestressing steels and $f_y$ and $f_{py}$ are yield strengths of conventional and prestressing steels. For PT segmental bridges, the *PPR* can be assumed to be zero. However, according to Article C5.9.5.3 in AASHTO (2007), "*…For segmental concrete bridges, lump sum losses may be used only for preliminary design purposes...*". In addition, this literature review could not find statistical expressions for $\Delta f_{pLT}$, especially for PT segmental bridges.

### *2.7.1.3. Compressive strength of concrete*

The actual and specified compressive strengths of concrete are defined as $f_c$ and $f_c'$, respectively. Nowak and Collins (2000) compiled information from various research programs and reported key statistical information for $f_c$ (see Table 2-5). From Table 2-5, it seems that the COV decreases as the specified compressive strength, $f_c'$, increases. Based on this information a suitable statistical expression for $f_c$ of concrete used in PT bridges in Texas is developed in Subsection 10.5.4.

**Table 2-5. Statistics of Concrete Compressive Strength (Nowak and Collins 2000).**

| Specified compressive strength, $f_c'$ (ksi) | Coefficient of Variation (COV) | Standard deviation (ksi) |
|---|---|---|
| 3 | 0.18 | 0.497 |
| 4 | 0.18 | 0.610 |
| 5 | 0.15 | 0.604 |

1 ksi = 6.89 MPa.

### 2.7.2. A history of design codes/practices for concrete bridges

AASHTO began publishing the bridge design specifications in the 1930s. The initial documents were based on the Allowable Stress Design (ASD) method that uses only one factor of safety (representing an overall safety factor). In the 1970s, AASHTO made the transition from ASD to the Load Factor Design (LFD) method for bridge design through interim revisions to the existing design documents. Unlike ASD that considers one safety factor, LFD considers different safety factors for each of the load parameters. Bridge designers are making another transition from LFD to Load and Resistance Factor Design (LRFD). The first five editions of *The AASHTO Specifications for Design of Highway Bridges* (AASHTO 1994, 1998, 2004, 2006, 2007) incorporate limit state design philosophies that are based on structural reliability methods to achieve a more uniform or standardized safety level in new bridge designs. Also, in 2000, AASHTO and FHWA set October 1, 2007 as the transition date for all the government initiated bridges to be designed following the AASHTO LRFD Specifications. It should be noted that the AASHTO LRFD Specifications are general design documents for all types of bridges.

Due to special construction sequences and other reasons, segmental concrete bridges need special design considerations. To meet this requirement, AASHTO published *AASHTO Guide Specifications for Design and Construction of Segmental Concrete Bridges* (AASHTO 1999), which is widely used in the segmental bridge

industry. Until now, no modifications have been made to AASHTO (1999) and many sections in AASHTO (1999) refer to AASHTO (1998).

### 2.7.3. Differences in the behavior of monolithic and segmental post-tensioned beams

Section 4.12.5.4 in Nawy (2003) provides a scientific explanation supporting the suitability of using the flexural formulations for sections with bonded tendons for analyzing the sections with unbonded tendons. However, this explanation seems to be provided for unbonded tendons in monolithic beams and not for segmental beams with external tendons. The key idea behind this explanation is because the non-prestressed reinforcement strains more than its yield strain when near failure situations (i.e., post-elastic range) and control the flexural crack development and width. In a segmental bridge span with several segments, the nonprestressed reinforcement is generally not extended across the transverse joints between the segments. Hence the above-mentioned explanation for monolithic beams does not suit the case of segmental beams.

### 2.7.4. Stress-strain relationship for unbonded tendons

According to Naaman and Alkhairi (1992), AASHTO (1996), and Tabsh (1995), for PT beams with unbonded, external tendons, the average axial stress at nominal or ultimate conditions, $f_{ps}$, on tendons is influenced by the load configuration and span, in addition to the material and longitudinal- and cross-sectional properties. They also found that $f_{ps}$ of the unbonded tendon is always less than its yield strength, $f_{py}$, which is the limiting value of $f_{ps}$ in AASHTO (1996). Sections 5.7.3.1.1 and 5.7.3.1.2 in AASHTO LRFD Specifications (2007) simplified these equations and provide separate formulations to determine the average stress, $f_{ps}$, in bonded and unbonded tendons, respectively. The formulation in 5.7.3.1.2 of AASHTO LRFD Specifications (2007) can be used to

determine the $f_{ps}$ in tendons in order to assess the flexural capacity of segmental bridges with unbonded tendons (both internal and external).

In the case of PT bridges with external tendons, the flexural capacity assessment is further complicated when the strands have different distances from the extreme top fiber, different effective prestress levels, and different cross-sectional areas due to different corrosion rates and resulting changes in tension capacity. These corrosion rates can be different because of varying material, environmental, void, and stress factors. A procedure to determine the probabilistic $C_M$ of PT girders with external, unbonded tendons is needed and is developed in Section 10. The next subsection provides a review of parameters that directly affect the structural capacity of PT girders.

### 2.7.5. Stress-strain relationship for concrete cross sections

To assess the structural behavior under normal service loading conditions, the stress-strain relationship in concrete can be assumed to be linear. This will provide a sufficient level of accuracy, if deformations are minimal. However, as the loading conditions become severe, especially at ultimate behavior, the stress-strain relationship in concrete becomes nonlinear. Design documents such as AASHTO LRFD Specifications (2007) use the Whitney stress block, which is a close approximation of this nonlinear behavior. More accurate nonlinear stress-strain relationships have been developed by Hognestad (1951), Todeschini et al. (1964), and Mander et al. (1988a, b), and are more appropriate for assessing behavior at ultimate conditions. The models by Hognestad (1951) and Mander et al. (1988a, b) divide the concrete cross section into several layers and then determine stresses in each layer. On the other hand, Todeschini et al. (1964) provides a closed form solution for determining stress in concrete. Considering the time required to perform numerous simulations required in structural reliability analysis, the model developed by Todeschini et al. (1964) provide computational efficiency. A description of the Todeschini et al. (1964 model is as follows.

Todeschini's model provides a continuous function (or closed-form solution) for determining stress in concrete. The maximum compressive stress, $f''_c$, is taken to be $0.9f'_c$. The strain, $\varepsilon_0$, corresponding to $f''_c$ is assumed to be equal to $1.71(f'_c/E_c)$, where $E_c$ is the elastic modulus of concrete. According to Todeschini (1964), the compressive stress, $f_c$, corresponding to any strain, $\varepsilon$, is as follows:

$$f_c = \frac{2f_c'' x}{1+x^2} \tag{2.12}$$

where $x$ is the ratio between $\varepsilon$ and $\varepsilon_0$ ($x$ is in radians). As a demostration, Figure 2-16 shows the stress-strain curve (developed using Todeschini's model) for a concrete with a specified compressive strength, $f'_c$, of 6000 psi.

The average stress, $f_{c,\,average}$, under the stress block from $\varepsilon = 0$ to $\varepsilon$ is as follows:

$$f_{c,\,average} = \lambda_1 f_c''; \;\; \lambda_1 = \frac{\ln(1+x^2)}{x} \tag{2.13}$$

The center of gravity of the area of the stress-strain distribution between $\varepsilon = 0$ to $\varepsilon$ can be calculated as follows:

$$\mathrm{CG}(A_{\text{stress-strain}}) = \left(1 - \frac{2(x - \tan^{-1} x)}{x^2 \lambda_1}\right) c \tag{2.14}$$

These formulations will be used to determine the total compressive force, $F_C$, and its center of gravity, CG($F_C$) in Section 10 on structural reliability analysis.

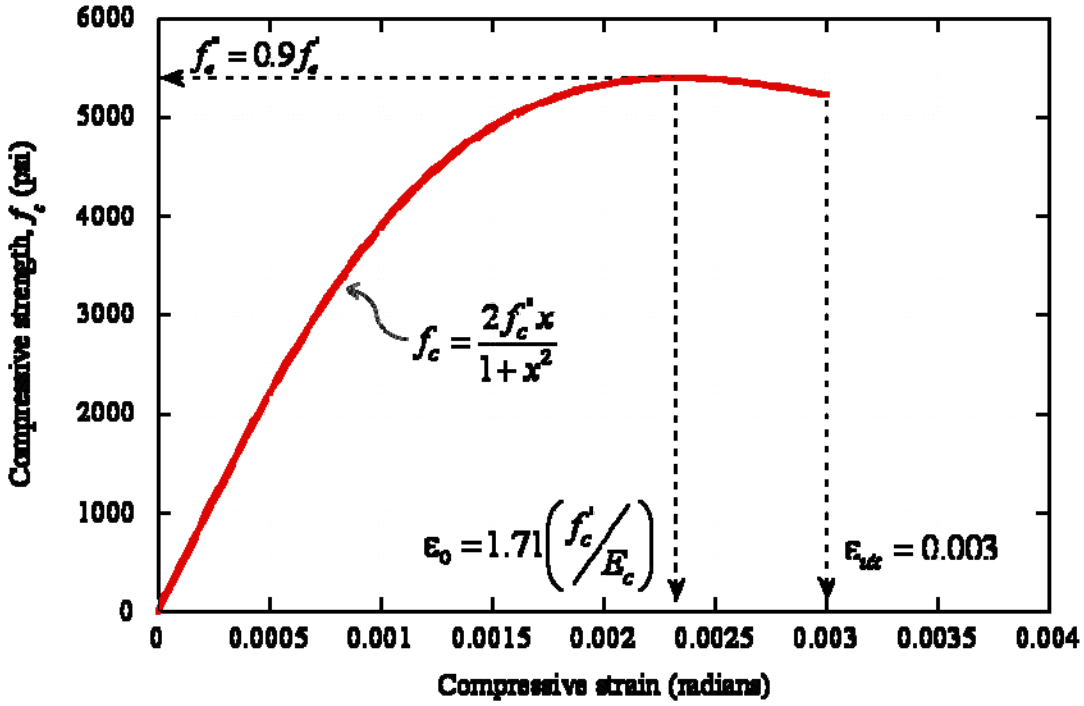


**Figure 2-16. Stress-Strain Curve (using Todeschini (1964) model) for a Concrete With a Specified Compressive Strength, $f'_c$, of 6000 psi.**

### 2.7.6. In-service and allowable stresses in a cross section

The applied compressive and tensile stresses at service at extreme fibers can be calculated using the following expressions provided in the PCI (1999) handbook, and other text books including Nawy (2003) and Naaman (2004):

$$\text{Compressive stress at extreme top fiber, } f^t = \left[-\frac{P_e}{A_c}\left(1-\frac{ec_t}{r^2}\right)-\frac{M_T}{S^t}\right]$$

$$\text{Tensile stress at extreme bottom fiber, } f_b = \left[-\frac{P_e}{A_c}\left(1+\frac{ec_b}{r^2}\right)+\frac{M_T}{S_b}\right] \qquad (2.15)$$

where, $M_T$ is the total applied moment; $P_e$ is the effective prestress force after losses; $e$ is the eccentricity of each strand from the center of gravity of the concrete cross section; $r$ is the radius of gyration; $A_c$ is the area of the concrete cross section; $S^t$ and $S_b$ are section modulii of the concrete section about the extreme top and bottom fibers, respectively; and $c_t$ and $c_b$ are the distance of the extreme top and bottom fibers, respectively, from the centroid of the concrete cross section. The values of $f^t$ and $f_b$ are positive and negative when tensile and compressive stresses, respectively, exists.

Table 5.9.4.2.1-1 and Table 5.9.4.2.2-1in AASHTO LRFD Specifications (2007) recommend the compressive and tensile stress limits, respectively, in fully prestressed components in segmental concrete at the service limit state after prestress losses. These are reproduced in Table 2-6.

**Table 2-6. Compressive and Tensile Stress Limits for Fully Prestressed Components in Segmental Concrete at Service Limit State after Losses (AASHTO LRFD Specifications 2007).**

| Stress type | | Stress limit |
|---|---|---|
| Longitudinal compressive stresses in extreme concrete fibers | Due to the sum of effective prestress and permanent loads | $0.45 f_c'$ |
| | Due to the sum of effective prestress, permanent loads, and transient loads and during shipping and handling | $0.60 \phi_w f_c'$ |
| Longitudinal tensile stresses through joints in the precompressed tensile zone | At joints with minimum bonded auxiliary reinforcement through the joints sufficient to carry the calculated longitudinal tensile force at a stress of $0.5 f_y$; internal or external tendons | $0.0948\sqrt{f_c'}$ (in ksi) or $3\sqrt{f_c'}$ (in psi) |
| | At joints without the minimum bonded auxiliary reinforcement through joints | No tension |

In Table 2-6, one of the compressive stress limits uses the stress limit reduction factor, $\phi_w$. Per Article 5.9.4.2 in AASHTO LRFD Specifications (2007), the use of $\phi_w$ to reduce the stress limit in the walls of box girders at the service limit state is not

theoretically correct, but is a rational approach. The procedures to calculate $\phi_w$ are provided in Article 5.7.4.7.1 in AASHTO LRFD Specifications (2007).

### 2.7.7. Existing approaches to determine flexural capacity of prestressed girders

Section 5.7 of AASHTO LRFD Specifications (2007) provides empirical and analytical formulations for flexural *design* of conventionally reinforced and prestressed concrete beams. However, difficulties exist in directly using these formulations for flexural analysis of a girder with corroding strands. Computer programs need to be developed to accommodate the effect of changes in effective prestress, prestress losses, and tension capacity of individual strands on flexural capacity of the girder. Ting and Nowak (1991) reported that, unlike the case of a reinforced concrete beam, the formulation of an analytical model for flexural behavior of a prestressed beam is complex because of the presence of prestressing strands instead of conventional reinforcement.

Ting and Nowak (1991) provided an iterative algorithm to determine the curvature and depth of the neutral axis for a particular bending moment in a rectangular pre-tensioned beam with a composite reinforced concrete slab. This algorithm is based on the strain compatibility approach and is applicable for pre-tensioned beams with internal, bonded tendons; but not for PT beams with external, unbonded tendons. This is because, according to AASHTO (1999), the strain compatibility approach can be used for unbonded tendon systems only if "... *the analysis correctly recognizes the differences between the tendons and the concrete section, and the effect of deflection geometry changes on the effective stress in the tendons*...". In addition, the model developed by Ting and Nowak (1991) needs modifications to account for the varying capacity of strands located at the same depth (say, different strands within a tendon, especially when strand corrosion occurs).

Cavell and Waldron (2001) developed a nonlinear flexural capacity model for PT beams with internal, grouted, and bonded tendons. This model was based on the strain

compatibility approach with modifications to account for the effect of locally unbonded tendon regions at void locations and the flexural capacity loss due to failed tendons. However, this model cannot be used for beams with external tendons because of the difference in the average stress on external, unbonded tendons when compared to that in internal, bonded tendons. These analytical approaches with necessary modifications can be used to determine the flexural capacity of segmental bridges with external, unbonded tendons.

## 2.8. STRUCTURAL DEMAND ON POST-TENSIONED BRIDGES

The estimation of structural reliability may be performed on the basis of the unfactored, unbiased demand loads. These demand loads may be obtained using basic structural analysis principles (such as the influence line theorem), suitable statistical expressions, and recommendations from AASHTO LRFD Specifications (2007) for dead, live, and impact loads.

### 2.8.1. Dead load

In general, the dead load, *DL*, can be obtained by adding the weight of the steel, concrete, and overlay materials on the girder elements. Table 2-7 provides information that can be used to determine the average dead load on a bridge. It is usual to consider *DL* as a constant parameter for bridges throughout their service life. However, to account for designers' tendency to underestimate the dead load, Table 6.1 in Nowak and Collins (2001) suggests expressing dead load parameters in terms of a normal distribution with bias factors (mean-to-nominal ratio) and COVs of 1.05 and 0.10, respectively. However, because the dead load cannot usually be negative a lognormal distribution is assumed for dead load parameters in Section 10.

**Table 2-7. Dead Load Parameters from TxDOT Bridge Drawings.**

| Factors contributing towards the dead load | Unit weight |
|---|---|
| Reinforced concrete | 155 pcf (0.025 N/m$^3$) |
| Wearing surface (concrete overlay) | 25 psf (0.0012 MPa) |
| Future wearing surface (concrete overlay) | 25 psf (0.0012 MPa) |
| Concrete barrier rails (on each side of the roadway) | 326 plf (4757 N/m) per rail |

### 2.8.2. Live and impact loads

Live and impact loads are induced by moving vehicles and their vertical dynamic actions. Live loads can be estimated by considering various factors including the clear span, total vehicular weight, axle loads and configurations, transverse and longitudinal position of vehicles, and structural stiffness. The HS20 live load model was used to design highway bridges until AASHTO (1996) document was used for design purposes. According to TxDOT (2004), PT bridges in Texas were designed following the AASHTO (1982) Standard Specification to carry the dead load and live load with three lanes of AASHTO HS20-44 loading with allowance for impact and alternate military loading.

The AASHTO (1998) document suggests a heavier live load model, which originated from the work by Nowak and Hong (1991) and Nowak (1993). This model considered the factors noted and was based on load measurements (Moses et al. 1985) from seven major bridges in the greater Detroit area and statistical parameters provided by Ghosn and Moses (1985). This live load model is known as HL93 loading (Figure 2-17) and is also recommended in Section 3.6 of AASHTO LRFD Specifications (2007). Figure 2-17 is an approximately scaled drawing.

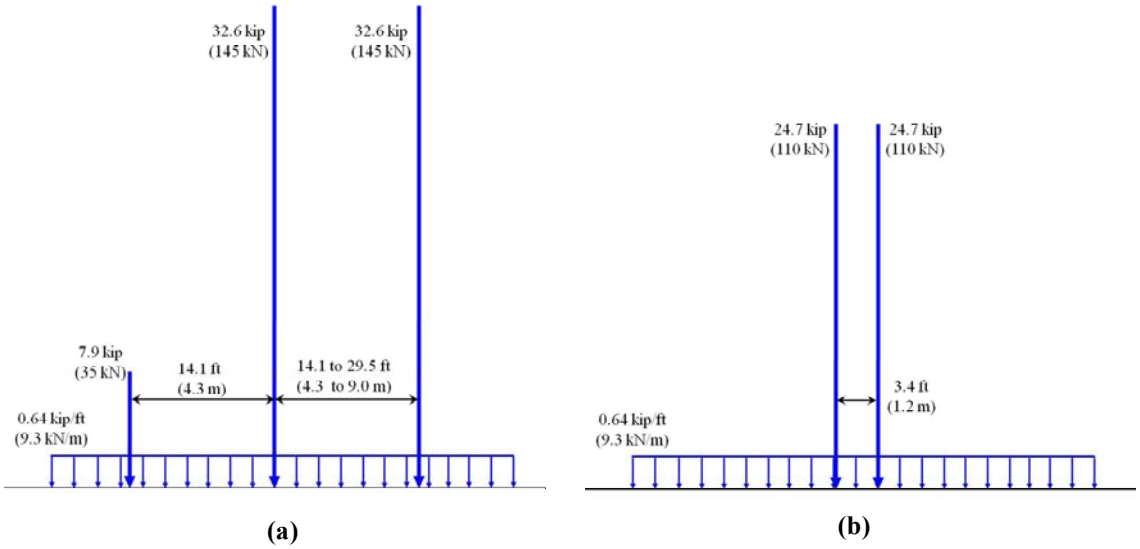


**Figure 2-17. HL93 Loading Specified by AASHTO (1998, 2007): (a) Truck and Uniform Lane Load and (b) Tandem and Uniform Lane Load.**

The HL93 loading is a combination of a design truck or design tandem and a design lane load. Nowak and Collins (2000) reported a bias factor of 1.25 for live load. In addition, the impact loading is considered equivalent to 33 percent of the live load (AASHTO 2007). According to Nowak and Collins (2000), the COV of the joint effect of live and impact loading is 0.18. A normal distribution based on this information can be assumed for live load distribution. AASHTO LRFD Specifications (2007) also provides a multiple lane factor to calculate the total live load. The multiple lane factors are 1.20, 1.00, 0.85, and 0.65 for one, two, three, and greater than three lanes, respectively. Further details on the procedures to determine total demand loads are provided in the AASHTO LRFD Specifications (2007) document and are not reproduced here. Based on the random realization of the load parameters and their configuration, the moment demand, $D_M$, can be computed using standard structural analysis methods.

## 2.9. STRUCTURAL RELIABILITY OF POST-TENSIONED BRIDGES

This literature review could not find significant information on the structural reliability of PT bridges, especially those with voided tendons. This section reviews mathematical expressions and some of the existing work on structural reliability of bridges and existing methodologies that could be useful for developing a structural reliability model for PT bridges. A review of available techniques to model and assess structural reliability is provided next.

### 2.9.1. Modeling and assessment of structural reliability

#### *2.9.1.1. Limit state functions*

The definition and determination of an appropriate limit state function (or a performance function) is essential in modeling structural reliability. Following the conventional notation in structural reliability theory (Ditlevsen and Madsen 1996), the limit state function, *g,* can be formulated as:

$$g(C, D) = C - D \tag{2.16}$$

where $C$ and $D$ represent capacity and demand, respectively, such that the events with $g \leq 0$ represent failure. In general, the limit state functions for strength and service criteria are used to assess structural reliability. Modeling and evaluating appropriate limit state functions for complex structural systems such as PT segmental bridges pose challenges and these could not be found in this literature review. The current research addresses these challenges through modeling strength and service limit states for segmental bridges (see Section 10).

*2.9.1.2. Generalized structural reliability index and probability of failure*

The structural reliability can be expressed in terms of the generalized reliability index, $\beta$, defined as follows (Ditlevsen and Madsen 1996):

$$\beta = -\Phi^{-1}\left(\mathrm{P}_f\right) = -\Phi^{-1}\left(\mathrm{P}\left(g \le 0\right)\right) \tag{2.17}$$

where $\Phi$ is the cumulative distribution function of the standard normal distribution and $\mathrm{P}_f$ is the probability of failure (estimated as the probability of $\mathrm{g} \le 0$). Standard procedures such as the closed-form solution, first order reliability method (FORM), and second order reliability method (SORM) can be used to determine $\beta$, when $g$ is simple and differentiable. However, these methods are not suitable when $g$ is complex and non-differentiable, as in the case of PT bridges. In such cases, Monte Carlo simulation techniques can be used to determine $\beta$. In Monte Carlo simulation techniques, the probability of failure, $\mathrm{P}_f$, is determined as follows:

$$\mathrm{P}_f = \frac{N_f}{N_{sim}} \tag{2.18}$$

where $N_f$ indicates number of failure instances and $N_{sim}$ indicates the number of simulations of $g$. The estimated $\mathrm{P}_f$ can be used to determine $\beta$ using Equation (2.17). Accuracy of $\mathrm{P}_f$ is reflected in the accuracy of $\beta$. A sufficient level of accuracy in the estimation of $\mathrm{P}_f$ can be attained by setting an upper limit on the coefficient of variation of $\mathrm{P}_f$, COV($\mathrm{P}_f$). COV($\mathrm{P}_f$) can be determined as follows (Ditlevsen and Madsen 1996):

$$\mathrm{COV}\left(\mathrm{P}_f\right) \approx \frac{1}{\mathrm{P}_f} \cdot \sqrt{\frac{\left(1\text{-}\mathrm{P}_f\right)\mathrm{P}_f}{N_{sim}}} \tag{2.19}$$

Various computer programs are available to use as a platform to perform these calculations and then to estimate $\beta$. These computer programs are discussed next.

### *2.9.1.3. Assessing structural reliability using existing computer programs*

Der Kiureghan et al. (2006) provided discussions on three reliability related software programs developed at the Pacific Earthquake Engineering Research Center (PEER) at the University of California, Berkeley. The three major software programs developed by researchers at PEER were CalREL, *Open System for Earthquake Engineering Simulation* (OpenSEES), and *Finite Element Reliability Using MATLAB* (FERUM).

CalREL was initially developed by Liu et al. (1989) and was modified later by researchers at PEER. CalREL is a general purpose structural reliability analysis program written in FORTRAN®. CalREL incorporates FORM, SORM, importance sampling, and Monte Carlo simulation techniques for reliability analysis. CalREL provided the technical basis for the development of FERUM and OpenSEES (Der Kiureghan et al. 2006).

OpenSEES, initially developed by McKenna et al. (2000) and later modified with significant contributions from researchers at PEER, is an object-oriented general purpose program written in $C^{++}$ language and was developed for earthquake engineering applications. OpenSEES is a platform that can combine the static and dynamic nonlinear finite element analysis and reliability methods. The capabilities of OpenSEES include reliability analysis by FORM, SORM, importance sampling, and Monte Carlo simulation.

FERUM is a MATLAB® toolbox consisting of a set of MATLAB® functions. FERUM can be used to perform reliability analysis of limit state functions that are defined using either finite element or other analytical methods. Version 3.1 of FERUM can perform reliability analyses using approaches such as FORM, SORM, importance sampling simulation, system reliability, and inverse FORM. According to Der

Kiureghan et al. (2006), the most attractive features of FERUM are: 1) the ease in modifying the limit state function(s), 2) user-friendly debugging and error handling utilities, and 3) the ability to use numerous mathematical functions available with MATLAB®.

Traditionally these programs have been mainly used in the reliability assessment of structural systems exposed to various earthquake scenarios. However, these computer programs can also be used for assessing time-variant reliability of deteriorating structural systems, provided $g$ is probabilistically formulated. In the case of this research on the structural reliability of segmental bridges, FERUM was determined to be a useful tool to incorporate $g$ and then assess $\beta$.

### 2.9.2. Structural reliability of bridges with uncorroded strands

In the past, the strength and service reliabilities have been generally assessed based on flexural capacity of and allowable stresses on the structural element, respectively. Tabsh (1995) studied flexural reliability of cast-in-place PT slab bridges with unbonded tendons. This study found that the AASHTO *Standard Specifications for Highway Bridges* (AASHTO 1992) underestimate the stresses in unbonded tendons at ultimate, especially if the reinforcement index (defined as the ratio of the area of steel reinforcement to total area of cross section) is low. The amount of reinforcement influences the statistics of the axial stress experienced by unbonded tendons and the bending stress experienced by the beam. These observations indicate the importance of the amount of steel reinforcement, which could decrease due to time-dependent corrosion, on structural capacity. However, Tabsh (1995) did not consider the possible capacity loss of strands and found that, based on the "as-received" strand condition, the $\beta$ for typical AASHTO slab bridges can vary between 2.75 and 5.0. The values of $\beta$ can decrease as the available cross-sectional area (or tension capacity) of strands decrease. Hence, this emphasizes the need for probabilistic models for $C_T$ of corroding strands in order to estimate structural capacity and reliability with better accuracy and precision.

Du and Au (2005) performed a comparative study on the structural reliability of a pre-tensioned T-girder assessed based on AASHTO (1998), Chinese code (CDCHB 1991), and Hong Kong code (SDMHR 1997). Du and Au (2005) determined the governing limit states for prestressed concrete girders with long and short spans designed using these codes and these are shown in Table 2-8.

**Table 2-8. Governing Limit States for Pre-tensioned Girders with Short and Long Spans.**

| Design Code | Short span (i.e., 25 to 30m [82 to 98 ft]) | Long span (i.e., 35 to 40m [115 to 131 ft]) |
|---|---|---|
| AASHTO LRFD | Service limit state | Service limit state |
| Chinese | Service limit state | Service limit state |
| Hong Kong | Strength limit state | Service limit state |

Based on the fact that the service limit state governs most cases, Du and Au (2005) recommended that the bridge design codes be calibrated based not only on the strength limit state but also on the service limit state.

Because the structural reliability varies as a function of time, methodologies are needed to assess time-variant structural reliability based on strength and service limit state conditions. Then the available reliability can be compared with the required level of reliability.

### 2.9.3. Target reliability index

Various parameters such as $\beta$ and condition rating factor exist to assess structural safety. According to Akgul and Frangopol (2004), $\beta$ is a measure of the structural reliability with respect to the limit state functions whereas the condition rating factor is a measure of the reserve structural capacity with respect to the applied load. The latter can be a

qualitative or deterministic assessment parameter while the former is a fully- or semi-probabilistic assessment parameter. Because, in reality, the structural behavior and loading conditions can be truly probabilistic in nature, $\beta$ is preferred over the condition rating factor. Structural design is now being performed using standardized design codes that are calibrated such that a minimum required $\beta$ is achieved during the design/construction phase. This $\beta$ during the design/construction stage can be defined here as the initial reliability index, $\beta_0$. For structures with no deteriorated structural elements, the desired value of $\beta$ (based on $C_M$) is generally higher than 3.5 (indicating a corresponding $P_f$ less than $2.33 \times 10^{-4}$). Tabsh (1995) found that the value of $\beta$ for typical AASHTO cast-in-place PT slab bridges with uncorroded strands can vary between 2.75 and 5.0 (corresponding values of $P_f$ are $3.0 \times 10^{-3}$ and $2.87 \times 10^{-7}$, respectively) However, the $\beta$ of a structure can decrease over time as materials deteriorate (say, strand corrosion in the case of PT bridges) over time.

To ensure sufficient levels of safety during service, $\beta$ of existing structures must be greater than a minimum required value. This minimum required value of $\beta$ is defined as the target reliability index, $\beta_{target}$. Normally, the design specifications such as AASHTO LRFD Specifications (2007) are calibrated based on a $\beta_{target}$ equal to 3.5 for flexural analysis of structural systems (Nowak and Collins (2000)). According to Stewart (1996), $\beta_{target}$ can be defined as a weighted average of $\beta$ values obtained using various existing design/assessment practices. The reasons behind this difference are attributed to the differences in various considerations during the design/construction phase and assessment/maintenance/repair phases of the structure. According to ISO 13822, the fundamental differences in various considerations during design/construction and assessment/maintenance/repair procedures for a structure can be categorized into three distinct groups as follows:

- *Economic considerations* – issues related to the cost to increase the safety of an existing structure. This cost can be higher than that

required to increase the safety level of a structure during the design phase.

- *Social considerations* – issues related to the disruption and displacement of current users and their activities as an effect of post-assessment repair works. This is generally not an issue during the design/construction phase.

- *Sustainability considerations* – issues related to the disposal, recycling, or both of structural components during or after the repairs. This is generally not an issue during the design/construction phase.

Values of $\beta_{target}$ used for different $g$ functions in structural reliability assessment procedures, as provided in ISO 13822, are summarized in Table 2-9. The corresponding $P_f$ values are also shown in Table 2-9.

**Table 2-9. Summary of $\beta_{target}$ and $P_f$ (Adapted from ISO 13822).**

| Reference Period | Limit States | | $\beta_{target}$ | $P_f = \Phi(-\beta_{target})$ |
|---|---|---|---|---|
| Remaining service life | Serviceability | CoF – Reversible | 0.0 | $5.0 \times 10^{-1}$ |
| | | CoF – Irreversible | 1.5 | $6.7 \times 10^{-2}$ |
| | Fatigue | Inspection is possible | 2.3 | $1.1 \times 10^{-2}$ |
| | | Inspection is not possible | 3.1 | $9.7 \times 10^{-4}$ |
| Design life | Ultimate strength (e.g., flexural) | CoF – Very Low | 2.3 | $1.1 \times 10^{-2}$ |
| | | CoF – Low | 3.1 | $9.7 \times 10^{-4}$ |
| | | CoF – Medium | 3.8 | $7.2 \times 10^{-5}$ |
| | | CoF – High | 4.3 | $8.5 \times 10^{-6}$ |

CoF indicates "Consequences of Failure".

In Table 2-9, note that for each type of limit state, the higher the consequences of failure (CoF), the higher the value of $\beta_{target}$ will be. For example, a nuclear reactor may have a larger CoF than an urban highway bridge, which in turn might have a larger CoF than a rural highway bridge. Accordingly, $\beta_{target}$ for a nuclear reactor will be higher than that for an urban highway bridge; and $\beta_{target}$ for an urban highway bridge will be higher than that for a rural highway bridge. Also, note that $\beta_{target}$ for the ultimate strength

(e.g., flexural capacity) limit state is greater than that for the service (i.e., allowable stress) limit state. To assess the structural reliability based on strength and service limit states, typical parameters of segmental bridges need to be characterized. These characteristics are presented next.

## 2.10. TYPICAL CHARACTERISTICS OF SEGMENTAL CONCRETE BRIDGES IN TEXAS

### 2.10.1. Segmental concrete bridges in Texas

Depending on structural, aesthetic, and other requirements, the geometrical and structural design parameters of segmental box girders vary from one bridge to another and even within the same bridge. There are 10 major segmental bridges in Texas. They are located in San Antonio, Austin, Corpus Christi, Port Arthur, Matagorda Island, Dallas, and at the Interstate Highway-10 (I-10) crossings over the Trinity and Niches rivers (see Figure 2-18). The intra-coastal bridge in Corpus Christi was constructed in the 1970s and was the first segmental bridge in the US. This bridge has only internal tendons grouted with Class A grout. The segmental bridges in Austin, Port Arthur, and San Antonio were constructed in the 1980s and have both internal and external tendons grouted with Class A grout. Other bridges shown in Figure 2-18 were constructed in the 2000s or are under construction and have both internal and external tendons with high performance Class C grout.

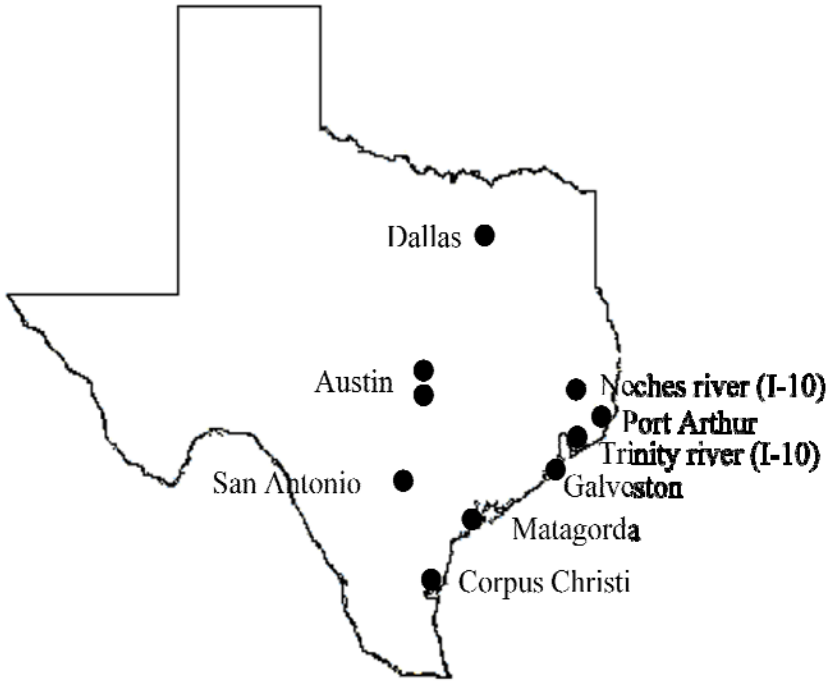


**Figure 2-18. Locations of Post-tensioned, Segmental, Concrete Bridges in Texas.**

### 2.10.2. San Antonio "Y" bridge

In the late 1980s and early 1990s, the San Antonio "Y" bridge, an urban viaduct, was designed using AASHTO (1982) and constructed using span-by-span techniques. Usually, in this technique, multiple segments within a span are first positioned in-place and externally supported using rigid steel frames. The longitudinal tendons travelling between the outer ends of the exterior segments (placed on the piers) are then post-tensioned. The rigid supports are released after post-tensioning all the tendons. The bridges constructed this way behave like a simply supported beam. In most spans in the San Antonio "Y" bridge some tendons are post-tensioned before and some tendons are post-tensioned after releasing the rigid steel supports. Because of this special post-tensioning sequence, most spans in the San Antonio "Y" bridge do not behave like

simply-supported beams. In addition, some tendons travel across multiple spans indicating a structural behavior similar to that of a continuous-support beam. However, this is also not true because some tendons are post-tensioned before and some tendons are post-tensioned after releasing the rigid steel supports. In summary, the San Antonio "Y" bridge behaves neither like a simply-supported nor like a continuous-support beam. Figure 2-19 shows a layout of the San Antonio "Y" bridge and its different phases. The San Antonio "Y" bridge is located at the intersection of I-10 and I-35 highways around downtown San Antonio, Texas.

.

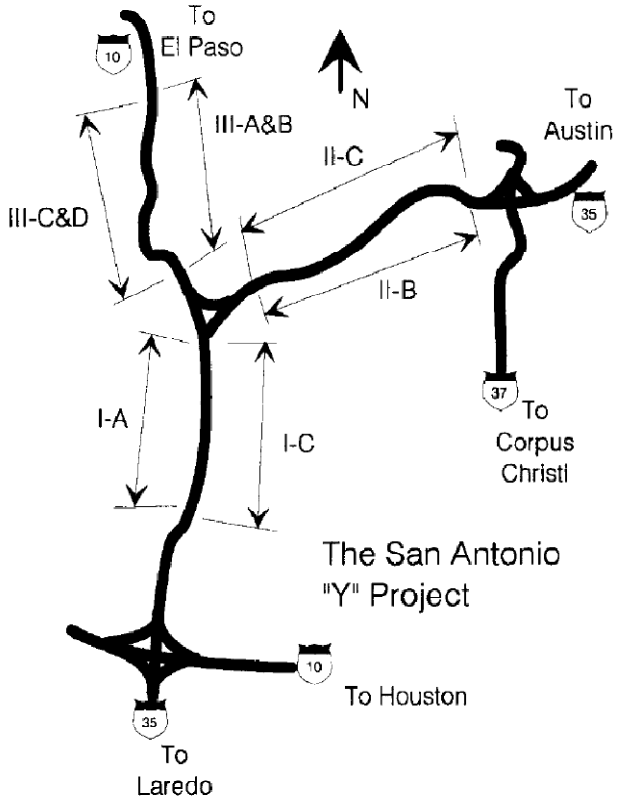


**Figure 2-19 Layout and Phases of San Antonio "Y" Bridge (Wollmann et al., 2001).**

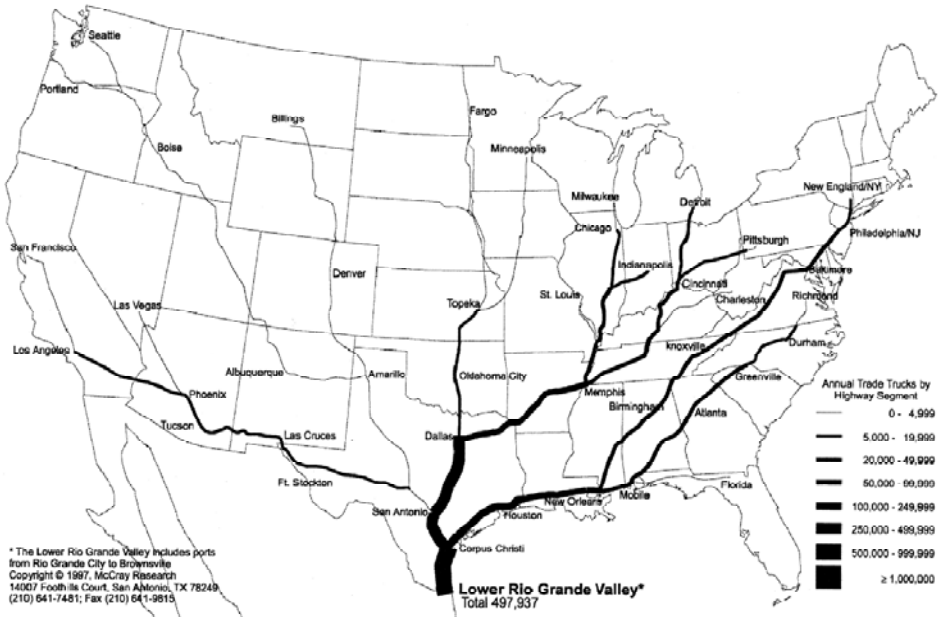


**Figure 2-20. Estimated Trucks Carrying U.S.-Mexico Trade on U.S. Highway Corridors To and From the Lower Rio-Grande Valley Region (McGray 1998).**


**Figure 2-21. Estimated Trucks Carrying U.S.-Mexico Trade on U.S. Highway Corridors To and From the Laredo Region (McGray 1998).**

McGray (1998) determined the traffic density, especially due to the US-Mexico trade, on US highways. Graphical representations of these data are provided by McGray (1998) and are re-produced in Figure 2-20 and Figure 2-21. It is clear that the San Antonio "Y" bridge has a high importance measure compared to most other segmental bridges in Texas and other states.

### 2.10.3. Span and girder inventory in San Antonio "Y" bridge

This bridge system is divided into various spines and ramps. These spines and ramps are constructed using precast concrete segments with different basic cross-sectional properties (Figure 2-22). Table 2-10 provides span and girder inventory on the bridge.

The cumulative overall length of Type I, II, III, and IV girders are 58,512, 55,847, 65,248, and 35,414 ft (17,834, 17,022, 19,888, and 10,794 m), respectively. This indicates widespread use of Type I, II, and III girders. It was also observed that Type I girder with relatively narrow flange widths are mainly used for ramps (with 26,866 ft (8,189 m) of these on Ramp E). Also, Type II, III, and IV girders with relatively wide flanges are used mainly on spines. It is assumed here that the spines, which constitute main traffic lanes, have higher significance or importance factors than ramps. Due to these reasons, Type II and III girders can be pre-selected for structural performance and reliability studies.

**Table 2-10. Span and Girder Inventory of San Antonio "Y" Bridge.**

| Bridge Name | Type of girder | No. of traffic lanes | Flange width (ft) | Number of spans | Span (ft) | Overall length (ft) | Overall traffic lane length (ft) |
|---|---|---|---|---|---|---|---|
| IH-10 | II | 3 | 58 | 79 | 100 | 8030 | 24,090 |
| | I | 1 | 26 | 50 | 100 | 5129 | 5129 |
| | I | 3 | 58 | 89 | 100 | 8955 | 26,866 |
| | II | 1 | 26 | 9 | 100 | 913 | 914 |
| | II | 1 | 26 | 11 | 100 | 1157 | 1157 |
| | I | 3 | 58 | 11 | 100 | 1111 | 3335 |
| | I | 1 | 26 | 8 | 100 | 810 | 810 |
| IH-35 SouthBound | I / III | 2 | 42/48 | 78 | 100 | 7448 | 14,896 |
| | I | 2 | 42 | 51 | 100 | 5000 | 10,000 |
| | I | 2 | 42 | 51 | 100 | 5028 | 10,056 |
| | I / III | 2 | 42/56 | 76 | 100 | 7468 | 14,937 |
| | I | 2 | 42 | 4 | 100 | 401 | 802 |
| | II | 1 | 26 | 2 | 100 | 190 | 190 |
| | II | 1 | 26 | 5 | 100 | 481 | 481 |
| | I | 1 | 42 | 7 | 100 | 720 | 720 |
| | II | 1 | 26 | 8 | 90 | 740 | 740 |
| | I / II | 2 | 42/26 | 12 | 90 | 1079 | 2158 |
| | II | 1 | 26 | 3 | 100 | 284 | 284 |
| | II | 1 | 26 | 6 | 100 | 578 | 578 |
| IH-35 NorthBound | III / IV | 3 | 58/58 | 60 | 100 | 6103 | 18,310 |
| | II/III/IV | 3 | 26/58/67 | 63 | 90 | 5701 | 17,104 |
| | I | 1 | 26 | 7 | 100 | 794 | 794 |
| | II | 1 | 26 | 15 | 90 | 1384 | 1384 |
| | II | 2 | 38 | 18 | 100 | 1712 | 3423 |
| | II | 2 | 38 | 18 | 100 | 1672 | 3344 |

Note: 1 ft = 0.3048 m

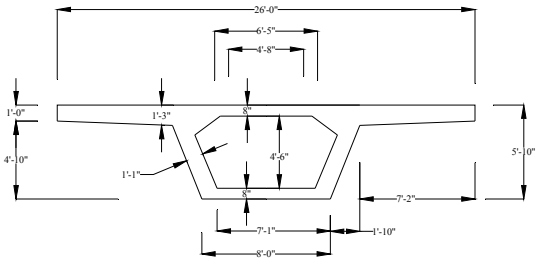


Type I Superstructure Segment (San Antonio "Y"; TxDOT Bridge Drawings, Page 1225)

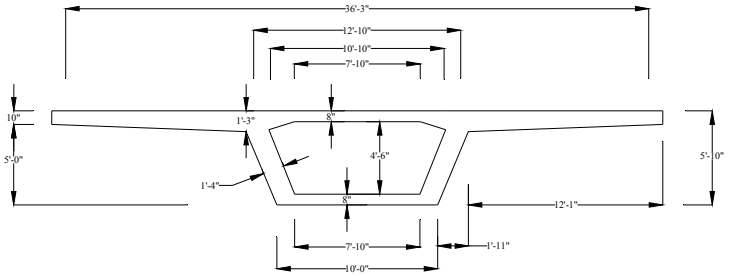


Type II Superstructure Segment (San Antonio "Y"; TxDOT Bridge Drawings, Page 1227)

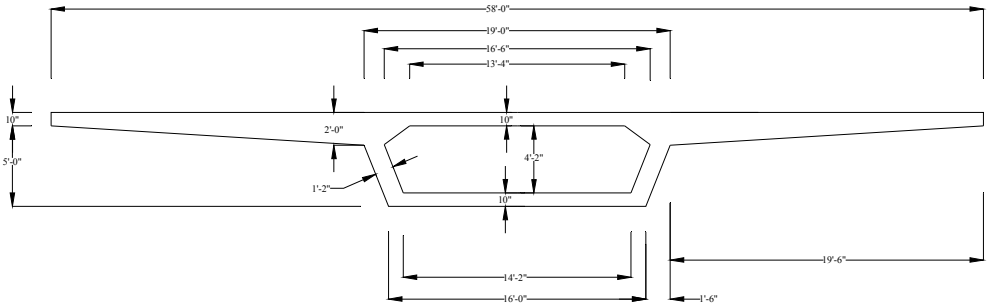


Type III Superstructure segment (San Antonio "Y"; TxDOT Bridge Drawings, Page 1229)

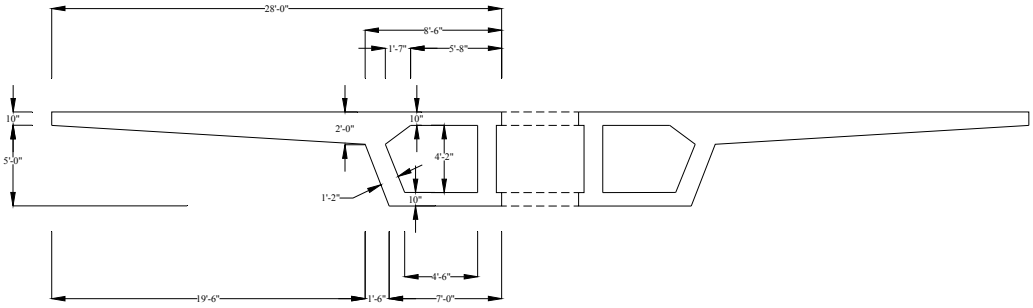


Type IV Superstructure segment (San Antonio "Y"; TxDOT Bridge Drawings, Page 1231)

**Figure 2-22 Typical Cross Sections of Girder Types in San Antonio "Y" Bridge.**

**Table 2-11. Quantity and Location of Longitudinal Tendons at Midspan on San Antonio "Y" Bridge.**

| Girder type | No. of spans | Total number of strands in tendons | | | |
|---|---|---|---|---|---|
| | | External tendons | | Internal tendons | |
| | | Depth of centroid from extreme top fiber (inches (mm)) | | | |
| | | 54 (1372) | 54 (1372) | 40 (1016) | 66 (1676) |
| Type I | 3 | 2 x 7 | - | 6 x 12 | - |
| | 1 | 4 x 12 | - | 6 x 12 | - |
| | 3 | 2 x 12 | - | 6 x 12 | - |
| | 2 | 4 x 19 | - | 6 x 12 | - |
| | 3 | 2 x 19 | - | 6 x 12 | - |
| | 2 | - | - | 6 x 12 | - |
| Type II | 3 | 1 x 7 | - | 6 x 12 | - |
| | 1 | 1 x 12 | - | 6 x 12 | - |
| | 6 | 2 x 7 | - | 6 x 12 | - |
| | 1 | 4 x 12 | - | 6 x 12 | - |
| | 9 | 2 x 12 | - | 6 x 12 | - |
| | 12 | 3 x 19 | - | 6 x 12 | - |
| | 3 | 2 x 19 | - | 6 x 12 | - |
| | 1 | 1 x 7 | - | 6 x 12 | - |
| Type III | 5 | 4 x 12 | - | 4 x 19 | 4 x 12 |
| | 4 | 4 x 12 | - | 4 x 19 | 4 x 12 |
| | 4 | 2 x 12 | - | 4 x 19 | 4 x 12 |
| | 17 | 6 x 19 | - | 4 x 19 | 4 x 12 |
| | 17 | 4 x 19 | - | 4 x 19 | 4 x 12 |
| | 3 | 2 x 19 | - | 4 x 19 | 4 x 12 |
| Type IV | 1 | 2 x 7 | - | 4 x 19 | 4 x 12 |
| | 4 | 2 x 12 | - | 4 x 19 | 4 x 12 |
| | 2 | 2 x 19 | 4 x 12 | 4 x 19 | 4 x 12 |
| | 3 | 2 x 19 | 2 x 12 | 4 x 19 | 4 x 12 |
| | 1 | 2 x 19 | - | 4 x 19 | 4 x 12 |
| | 1 | 2 x 19 | - | 4 x 19 | 4 x 12 |

The number before and after the 'x' sign indicates number of tendons and number of strands in each tendon

1 inch = 25.4 mm

### 2.10.4. Tendon inventory on San Antonio "Y" bridge

The San Antonio "Y" bridge consists of both internal and external PT systems. Table 2-11 provides the total number of internal and external longitudinal strands in the different girder types used in Phase II-C of the bridge system, as shown in Figure 2-19. Also, Table 2-11 shows that these girders have different longitudinal tendon layout and different numbers of span inventory. It also provides information on the depth of the centroid of the tendon from the extreme concrete compression fiber. Among the Type II and III girders, Type III girders are more widely used and hence will be assumed to be a typical girder cross section for the reliability studies.

### 2.10.5. Cross-sectional properties of girders in San Antonio "Y" bridge

A schematic with symbols for different geometrical parameters of the cross section of segmental box girders is shown in Figure 2-23. Table 2-12 provides typical values for these geometrical parameters. Earlier, in Figure 2-22 the cross-sectional views of four typical box sections in the San Antonio "Y" bridge was provided. It could be easily identified that Type I has less flange width in comparison to the other three girder types. This is consistent with general bridge dimensions where ramps have smaller dimensions compared to main lanes or spines.

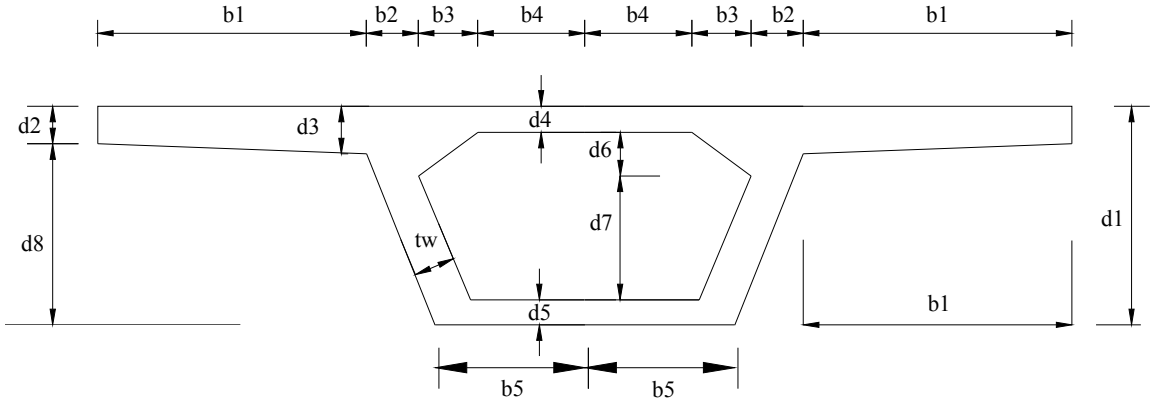


**Figure 2-23. Symbolic Notations for a Cross Sections of Segmental Box Girders.**

**Table 2-12 Typical Geometrical Parameters of Box Girders in San Antonio "Y" Bridge.**

| Parameter (Symbol) | Type I | Type II | Type III | Type IV |
|---|---|---|---|---|
| b1 | 74 | 136 | 222 | - |
| b2 | 16 | 14 | 15 | - |
| b3 | 19 | 19 | 19 | - |
| b4 | 35 | 47 | 80 | - |
| b5 | 48 | 60 | 96 | - |
| $t_w$ | 12 | 12 | 14 | 14 |
| d1 | 70 | 70 | 70 | 70 |
| d2 | 10 | 10 | 10 | 10 |
| d3 | 15 | 19 | 25 | 25 |
| d4 | 8 | 8 | 10 | 10 |
| d5 | 8 | 8 | 10 | 10 |
| d6 | 14 | 14 | 14 | 14 |
| d7 | 40 | 40 | 36 | 36 |
| d8 | 55 | 51 | 45 | 45 |

Note: 1 inch = 25.4 mm

It should be noted that the structural reliability studies presented in Section 10 use a cross section similar to that of the Type III girder used in the San Antonio "Y" bridge, but may not be exact. Also, other assumptions used for the reliability analysis may not represent the structural and exposure conditions experienced by the San Antonio "Y" bridge, as the objective of this research is only to develop models for typical PT bridges. Hence, the structural reliability analysis presented in Section 10 of this document does not intend to represent that of the San Antonio "Y" bridge. In addition, unlike structural capacity, stress, and deflection models, which can be validated using field measurements, the structural reliability models cannot be validated in the field.

## 2.11. SUMMARY

A comprehensive review of literature on failure cases of PT bridges, mechanisms and parameters influencing corrosion and tension capacity of strands/tendons, existing corrosion models for immersion and atmospheric exposure conditions, parameters influencing structural capacity of PT girders, and procedures for determining structural capacity and reliability of PT girders were performed. Then a review of typical characteristics of PT bridge girders in Texas was reviewed. This information will be used to meet the goals and objectives of this research program. However, note that the combination of PT bridge characteristics and support and exposure conditions used in the structural reliability studies and the results from this study presented in Section 10 do not represent any specific bridge in Texas. The following section provides a brief discussion on current research needs and significance of this research.

# 3. CURRENT NEEDS AND RESEARCH SIGNIFICANCE

Bridge inspections have reported the presence of voids, moisture, and chlorides inside grouted PT ducts as being the major cause of accelerated corrosion of strands. This corrosion results in the reduction of tension capacity and can eventually lead to tensile failure of PT strands (NCHRP 1998, ASBI 2000, FDOT 2001a and b, and Hansen 2007). The reduction in tension capacity or tensile failure of PT strands can in turn significantly and adversely affect the safety and serviceability of PT bridges. As these bridges have high importance measures and the consequences of failures are significant, it is important to maintain high levels of safety and serviceability for these PT bridges. According to NCHRP (1998), *"*…there is a pressing need for US bridge engineers to gain an understanding of durability issues associated with segmental construction and to be able to judge on a technical and rational basis the veracity of the on-going moratorium in the UK pertaining to segmental construction…" To meet this pressing need and to ensure high levels of safety and serviceability, bridge management authorities are in dire need of tools to quantify the long-term performance of these bridges.

The presence of voids, damages, and openings on PT ducts and anchorages in combination with exposure to severe environmental conditions can result in corrosion of PT strands. This time-variant process can in turn cause reduction in the strength and service reliability indices over time. Therefore, strength and service reliability indices can be considered as quantified measures or indicators for the safety and serviceability, respectively, of PT bridges. The time-variant strength reliability index can be modeled and estimated by using structural reliability techniques and moment capacity and demand models for PT bridges. The time-variant strength reliability index can be modeled and estimated by using structural reliability techniques and in-service stress capacity and demand models for PT bridges. The estimated reliability indices at future

times can be then compared with corresponding target reliability indices. This comparison will help in making decisions on the degree of inspection, repair, and maintenance required. In summary, time-variant structural reliability models can be useful tools to quantify the long-term performance of PT bridges. Probabilistic models for tension capacity of PT strands are necessary to develop time-variant structural reliability models. Experimental data on electrochemical and tension capacity behavior of PT strands are necessary to develop these probabilistic models for tension capacity of PT strands. Unfortunately, the current literature does not provide sufficient information on the electrochemical and tension capacity behavior of PT strands. Furthermore, knowledge of the electrochemical characteristics of ASTM A416 steel when immersed in various cementitious pore solutions and the potential for galvanic corrosion in these systems could assist engineers in developing non-destructive tools for the inspection of corrosion in PT bridges. However, such information is not sufficiently addressed in the literature.

A coupled experimental and analytical program was developed and conducted to fill these knowledge gaps and answer the following questions:

- Can environmental characterization maps be generated to assess corrosion risks in Texas?
- Can information be generated to non-destructively inspect or detect electrochemical corrosion of strands in PT systems?
- What are the critical void, material, environmental, and other factors that can significantly influence the corrosion activity of embedded strands?
- Does this corrosion significantly influence the tension capacity of strands over time? If so, how can the probabilistic tension capacity of strands be modeled and assessed?
- Does the corrosion-induced loss in tension capacity of strands affect the strength and serviceability of PT bridges? If so, how can the strength and service reliabilities of PT bridges be modeled and assessed?

This research will attempt to answer these questions to assist bridge owners in ensuring safe and reliable PT bridges for long durations. The experimental part of this research includes electrochemical and tension capacity testing of PT strands exposed to various exposure conditions. The analytical part of this research includes modeling and assessing the probabilistic tension capacity of PT strands and modeling and assessing the structural reliability of PT bridges. Both strength and service reliability are modeled as a function of time and other influencing parameters for a typical PT bridge. These reliability models are then used to assess time-variant strength and service reliability of a PT bridge subjected to HS20 and HL93 loading conditions. It is important to note that these models can assess the structural reliability based on climatic conditions and the data on void and damage conditions of bridges while minimizing expensive and non-routine bridge inspections. It should also be noted that the objective of this research is to develop general reliability models for PT bridges. Further development of the model will be needed for assessing the reliability of specific PT bridges in Texas. Based on long-term structural reliability assessments, inspection, repair, and maintenance programs can be optimized and funds can be appropriately allocated to meet public needs, while ensuring safe PT bridges.

# 4. ENVIRONMENTAL CHARACTERIZATION MAPS OF TEXAS

## 4.1. INTRODUCTION

The information provided in this section was collected by Rhett Dotson, as part of the TxDOT 0-4588 research project (Trejo et al 2009). However, this section is included in this dissertation because the author believes that this material is essential for conveying a more complete picture of the potential corrosion risk experienced by PT bridges in Texas. However, the remaining sections in this dissertation are relevant to all PT bridges worldwide.

This section provides environmental characterization maps of Texas. These maps can assist engineers in preliminary assessments of the corrosion risk of a PT bridge based on its geographic location. In general, a detailed map could lead engineers to believe that a particular geographic location poses a low-level corrosion risk to PT bridges, while a much higher corrosion risk might actually be present. Therefore, it is important that this map be relied upon only as a guide and not as a map providing specific information regarding corrosion activity in tendon systems. It should be noted that these maps do not take into account the corrosion risks due to local exposure conditions (e.g., the presence of moisture, chlorides, voids, and damage in PT systems). The effects of these and other factors are presented in Sections 5, 6, 7, and 8.

The ArcView® (version 8.2) software program was used to analyze TxDOT organizational districts in order to assess a corrosion risk level for PT bridge systems. Maps showing environmental factors and their distributions across the US were divided into equal portions and assigned a corrosion risk factor. Arcview 8.2 was then used to trim each of these maps to the TxDOT districts. A questionnaire was sent to each TxDOT district office. Responses obtained from the district engineers were then used to determine the chloride factors for each of the districts. ArcView® program was used to

summarize the chloride and corrosion risk factors for each district. Finally, a qualitative analysis was performed to determine the corrosion risk posed to PT bridges in each district in Texas.

## 4.2. FREEZE-DAY, TEMPERATURE, RELATIVE HUMIDITY, AND RAIN-DAY MAPS

Four environmental factors (i.e., freeze period, temperature, relative humidity, and rainfall) were developed for the Texas. The maps showing freeze-days, temperature, relative humidity, and rain-days are shown in Figure 4-1, Figure 4-2, Figure 4-3, and Figure 4-4, respectively.

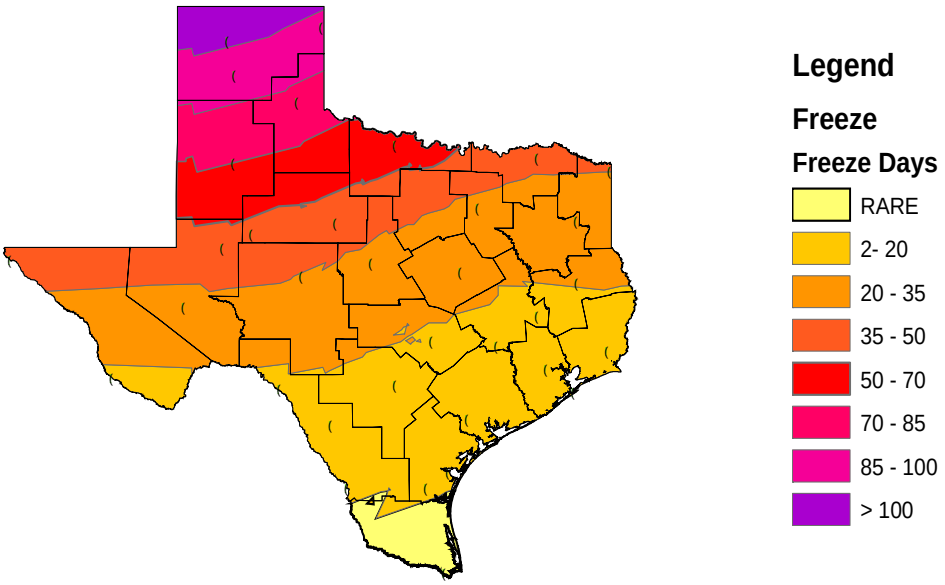


**Figure 4-1. Average Number of Freeze-Days in Texas (Data Collected from 1995-2000).**

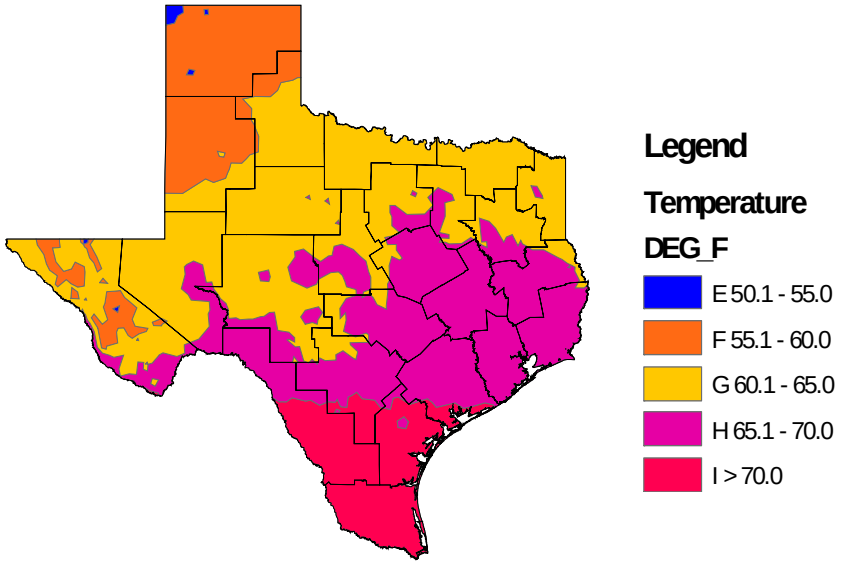


**Figure 4-2. Annual Average Temperature in Texas (Data Collected from 1961-1990).**

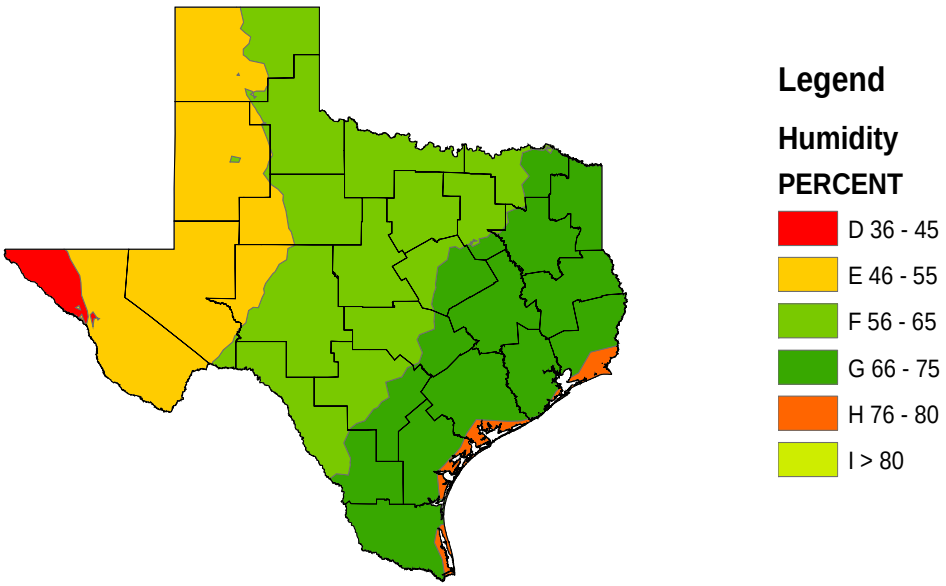


**Figure 4-3. Annual Average Relative Humidity in Texas (Data Collected from 1961-1990).**

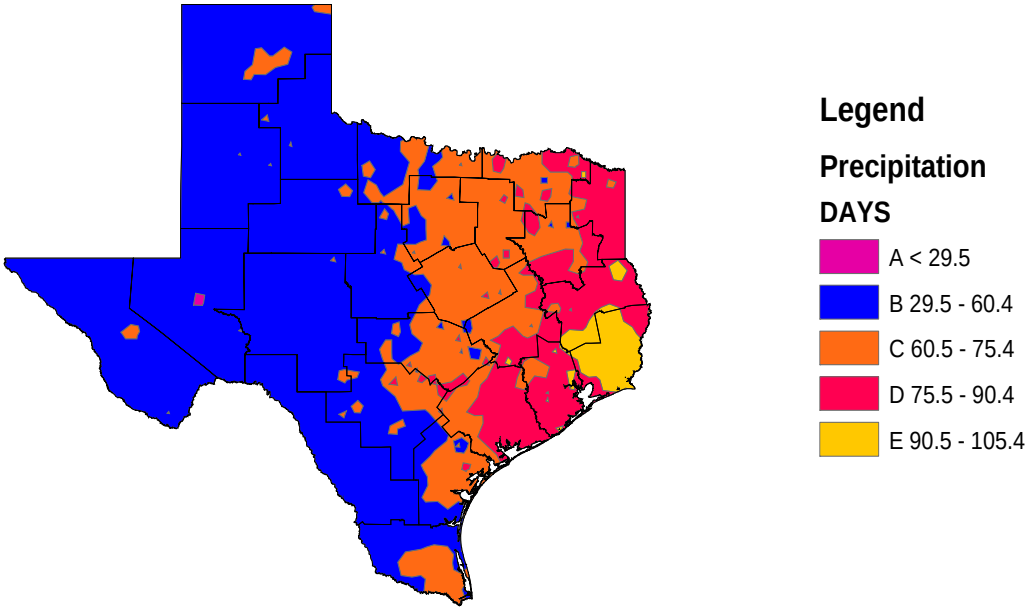


**Figure 4-4. Average Number of Rain-Days in Texas (Data Collected from 1961-1990)**

## 4.3. CHLORIDE MAPS

The information for the chloride factors for the state of Texas was gathered. For each of the 25 TxDOT districts, the district maintenance engineer was contacted via telephone and given the questionnaire. The information gathered from this survey was used to define a chloride usage factor and a chloride frequency factor with both factors ranging from 1-5. The chloride usage factor is a measure of the presence of chlorides for a particular district based on the de-icing measures used by that district or the proximity to the coastline. The chloride frequency factor is a measure of a district's exposure to chlorides. The two factors must be measured independently and then combined because it is possible for a district to use sodium chloride for de-icing, which is a severe corrosion agent, but to only use this once a year on average. Several distinctions were made concerning the chloride usage factor and the chloride frequency factor, with the divisions being derived from answers to the survey (see Table 4-1 and Table 4-2).

**Table 4-1. Chloride Usage Factor.**

| Usage Factor | Description |
|---|---|
| 1 | Previous use of chlorides |
| 2 | Mixed use of aggregate and chlorides |
| 3 | Limited use of MgCl or NaCl |
| 4 | Consistent use of only chlorides |
| 5 | Coastline |

**Table 4-2. Chloride Frequency Factor.**

| Frequency Factor | Description |
|---|---|
| 1 | Rare usage |
| 2 | 1-5 times per year |
| 3 | 6-15 times per year |
| 4 | 15-30 times per year |
| 5 | More than 30 times per year |
| | Constant exposure (Coastline) |

Based on the results from the survey, each district was assigned a chloride usage factor and a chloride frequency factor. These factors were then multiplied to determine a total chloride factor. This total chloride factor was then divided by five in order to scale the chloride factor down to the levels of the environmental factors. For example, if a particular district had limited use of MgCl and applied this approximately ten times per year, they would be assigned a chloride usage factor of three and a chloride frequency factor of three. Multiplying these factors together and dividing by five gives a total chloride factor of 1.8, which would be rounded up to 2. The total chloride factor distribution for the state of Texas can be seen in Figure 4-5.

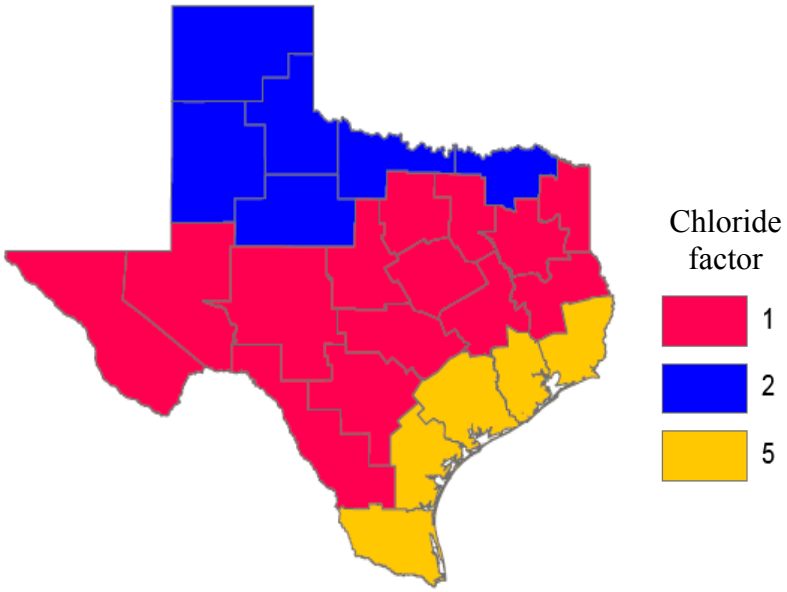


**Figure 4-5. Total Chloride Factor for Texas.**

## 4.4. TOTAL CORROSION RISK MAPS

All of the individual environmental and chloride factors for each of the districts were summed to find a total risk factor for each district. Each of the risk factors was weighted equally rather than assigning a weight to each one. The completed maps showing the total corrosion risk factor for each of the TxDOT districts can be seen in Figure 4-6. After finding the total chloride factor for each district, a scale was then developed to compare Texas's district to the rest of the nation. The scale illustrated in Table 4-3 was used as it provided a solid, qualitative analysis for the districts. It is interesting to note that the highest corrosion risk factor can be arrived at with 20 points. This is due to the fact that it is unlikely for any place in the US to have extreme corrosion risk factors in every category; furthermore, it is not necessary for a district to experience high corrosion risks in every category for a substantial threat to be posed to a PT bridge.

After developing this quantitative risk scale, the districts in Texas were then reassigned to a particular division, and a final qualitative map was created displaying all of the Texas districts and their respective corrosion risk assessments (Figure 4-7). As expected, the coastal regions pose the greatest threat to PT bridges due to the constant exposure to chlorides. It is also interesting to note that the remainder of the Texas districts fell within a moderate corrosion risk category. This indicates that even with a large state such as Texas, environmental and corrosion factors affecting PT bridges are fairly homogenous. This indicates that an analysis could be applied across the United States considering the states as individual entities rather than the smaller transportation districts. The only problem in such an analysis would be the mountain regions where climate patterns can vary significantly across a state.

**Table 4-3. Total Corrosion Risk Factors.**

| Corrosion Risk Factor | Corrosion Risk Assessment |
|---|---|
| Less than 10 | Mid risk |
| 15-11 | Moderate risk |
| 16-20 | High risk |
| More than 20 | Extreme risk |

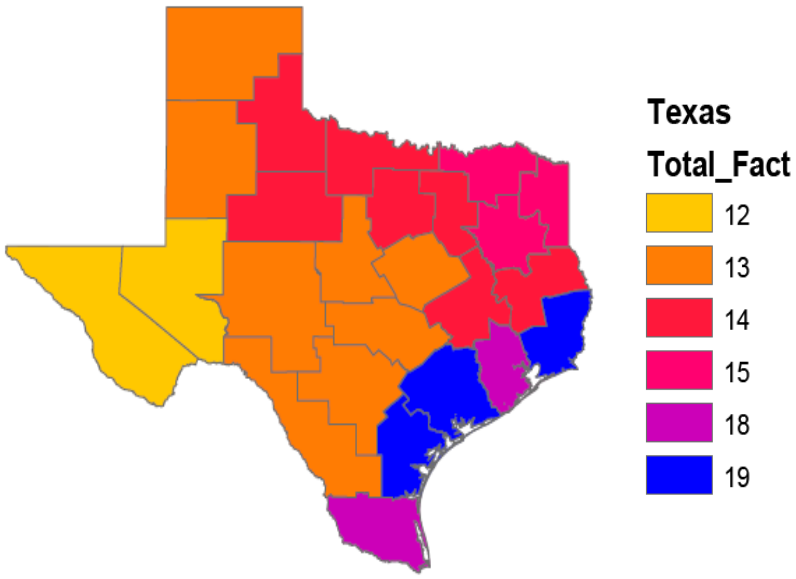


**Figure 4-6. Quantitative Assessment of Total Corrosion Risk.**

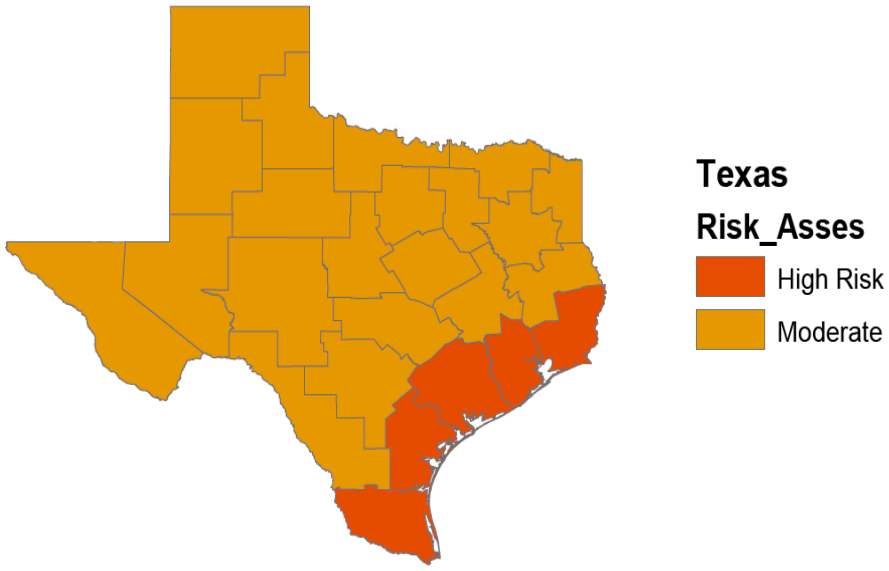


**Figure 4-7. Qualitative Corrosion Risk Level.**

## 4.5. SUMMARY

The locations of PT bridges in Texas are provided in subsection Figure 2-18. The majority of PT bridges inTexas lies in a moderate to high corrosion risk region. Coastal regions present the highest threat due to consistent exposure to chlorides. The developed environmental characterization map provides valuable insight into the corrosion risk levels across the state of Texas. Additional research could provide valuable insight into how the individual factors could be weighted providing for a more detailed map. In addition, a better model for combining the chloride exposure and usage factors also needs to be developed, but the procedure for doing this is beyond the scope of this project.

# 5. ELECTROCHEMICAL AND TENSION CAPACITY BEHAVIOR OF WIRES AND STRANDS - EXPERIMENTAL PROGRAM

## 5.1. INTRODUCTION

The major objectives of this research were outlined in Subsection 1.5. To attain these research objectives, a comprehensive experimental and analytical program was developed. Figure 5-1 shows various elements of the experimental program. This section presents the details of the experimental program. Results from the cyclic polarization and galvanic corrosion tests are provided in Subsections 6.2 and 6.3, respectively. The tension capacity results from the strand and wire corrosion tests are presented in 6.4 and 6.5. Prior to discussing the objectives, design, layout, and procedures of the experimental program, a discussion on the characteristics of various materials used in the experimental program is provided.

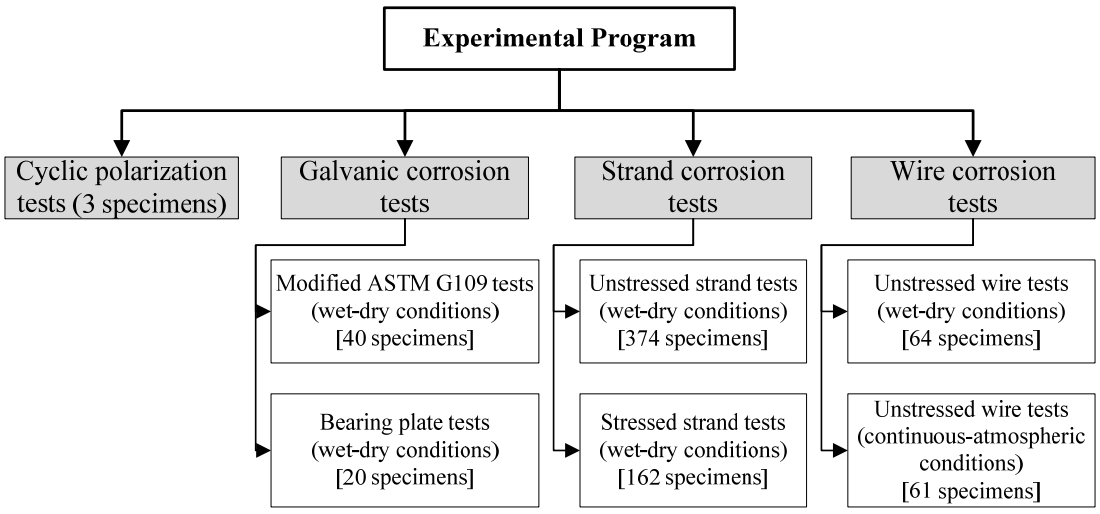


**Figure 5-1. Experimental Program (Electrochemical and Tension Capacity Behavior of Wires and Strands).**

## 5.2. MATERIALS USED IN THE EXPERIMENTAL PROGRAM

This subsection presents the characteristics of metallic reinforcement, mineral aggregates, cementitious materials, water, exposure solutions, and other materials used to prepare test specimens and perform the corrosion exposure and tension tests.

### 5.2.1. Metallic reinforcement

Three steel reinforcing material types were used in this research program. Table 5-1 provides the ASTM designations and titles which these reinforcing materials meet and the corresponding notation used in this document. The specific details of each of these specimens and the test in which they have been used are provided in the notes below Table 5-1. Further details on how these materials are used are provided in the Subsections 5.3 through 5.5. The strands and wires received from the producer/supplier had a negligible amount of corrosion and are referred to as "as-received strands" and "as-received wires", respectively, herein. It should be noted that all the strands and wires used in this test program are from one roll or strand coil.

**Table 5-1. Different Steel Reinforcement Types Used in this Research Program.**

| ASTM designation and title | Notation used in this document |
|---|---|
| ASTM A416 / A416M - 99/A416M-99 "Standard Specification for Steel Strand, Uncoated Seven-Wire for Prestressed Concrete" | ASTM A416[1] |
| ASTM A536 - 84 (2004) "Standard Specification for Ductile Iron Castings" | ASTM A536[2] |
| ASTM A615 / A615M - 99 "Standard Specification for Deformed and Plain Carbon-Steel Bars for Concrete Reinforcement" | ASTM A615[3] |

1. The 0.6 inch (15 mm) diameter, seven-wire, low-relaxation prestressing strand and the 0.2 inch (5.08 mm) king-wire from this strand used in all the tests.
2. The cast iron bearing plates used in galvanic corrosion tests.
3. The 0.625 inch (16 mm) diameter, deformed, conventional reinforcement (straight and/or spiral) used in galvanic corrosion tests.

Table 5-2 provides the chemical compositions of these metallic reinforcing materials. The chemical compositions were obtained using Wavelength Dispersive X-ray Spectroscopy following ASTM E 1621-94, *Standard Guide for X-Ray Emission Spectrometric Analysis*, at 15 kV using a calibrated JEOL Superprobe 733. The carbon contents were determined by combustion methods per ASTM E 350-90e1, *Standard Test Methods for Chemical Analysis of Carbon Steel, Low-Alloy Steel, Silicon Electrical Steel, Ingot Iron, and Wrought Iron*, using a LECO C-200 analyzer. The notes below Table 5-2 indicate the test program in which these materials are used.

Because the nominal cross-sectional area and ultimate tensile strength of "as-received" strands were 0.217 inch$^2$ (140 mm$^2$) and 270 ksi (1862 MPa), respectively, the *MUTS* of the "as-received" ASTM A416 strand is 58.6 kips (261 kN). Because of liability concerns, architects, engineers, and designers use $MUTS_{ARS}$ for design purposes. The first column (solid-diamond markers) in Figure 5-2 shows the dot plot with observed tension capacities of "as-received" strands (denoted as $C_{T,\,ARS}$). The second column (solid-square markers) in Figure 5-2 shows the dot plot with tension capacity of "as-received" wires (denoted as $C_{T,\,ARW}$). In Figure 5-2, the solid-horizontal lines in each column (passing through the data points) indicate the mean values of $C_{T,\,ARS}$ and $C_{T,\,ARW}$. The dashed-horizontal line at 58.6 kips (261 kN) indicates $MUTS_{ARS}$. As expected, the actual tension capacities are generally found to be higher than $MUTS_{ARS}$. Among the 24 datapoints, one was found to be 0.1 kip (0.445 kN) less than $MUTS_{ARS}$. Considering the 24 data points, the mean and standard deviation of the $C_{T,\,ARS}$ was found to be 59.27 kips (263.7 kN) and 0.29 kips (1.3 kN), respectively. The corresponding COV is 0.0049 and it indicates a very small variation.

**Table 5-2. Representative Chemical Compositions of Steel Reinforcement Types Used.**

| Element | ASTM A416[1] | | | ASTM A536[2] | ASTM A615[3a] | ASTM A615[3b] |
|---|---|---|---|---|---|---|
| | Sample 1 | Sample 2 | Sample 3 | | | |
| C | 0.812 | 0.841 | 0.842 | 3.62 | 0.40 | 0.38 |
| Mn | 0.70 | 0.811 | 0.819 | 0.276 | 1.03 | 1.13 |
| P | 0.010 | < 0.01 | 0.0001 | 0.016 | 0.015 | 0.012 |
| S | 0.010 | 0.010 | 0.010 | 0.009 | 0.045 | 0.031 |
| Si | 0.25 | 0.241 | 0.230 | 2.61 | 0.20 | 0.21 |
| Cu | 0.12 | 0.120 | 0.115 | 0.553 | 0.54 | 0.46 |
| Ni | 0.06 | 0.050 | 0.071 | 0.026 | 0.22 | 0.16 |
| Nb | - | 0.039 | 0.022 | - | - | - |
| Mg | - | 0.018 | 0.007 | 0.046 | - | - |
| Cr | 0.03 | 0.029 | 0.032 | - | 0.12 | 0.14 |
| Mo | 0.015 | 0.0007 | 0.0008 | - | 0.073 | 0.040 |
| Ti | - | 0.001 | 0.003 | - | - | - |
| V | 0.069 | 0.081 | 0.082 | - | 0.000 | 0.002 |
| Sn | 0.005 | < 0.01 | < 0.01 | - | 0.000 | 0.014 |
| Al | 0.002 | 0.0003 | <0.01 | - | - | - |
| Cb | 0.000 | - | - | - | 0.000 | 0.004 |
| $N_2$ | 0.007 | 0.0436 | 0.0079 | - | - | - |
| Fe | Remaining | Remaining | Remaining | Remaining | Remaining | Remaining |

1. The strands and/or wires used in all the tests; Sample 1 indicates the data from mill report and Samples 2 and 3 indicates the data from laboratory testing.
2. The bearing plates used in the galvanic corrosion tests.
3a. The straight reinforcement used in the galvanic corrosion tests.
3b. The spiral reinforcement used in the galvanic corrosion tests.

Six "as-received" wire samples (i.e., the king-wires collected from the "as-received" strands) were tested for tension capacity and the obtained $C_{T,\,ARW}$ are shown in the second column in Figure 5-2. Considering all 10 data points, the mean and standard deviation of the $C_{T,\,ARW}$ was determined to be 9.15 kips (40.7 kN) and 0.05 kips (0.22 kN), respectively. This indicates a very small COV of 0.005 for "as-received" wires and is almost equal to the corresponding COV observed for "as-received" strands. Also, note that ASTM A416 steel exhibited a Rockwell C hardness of 45.

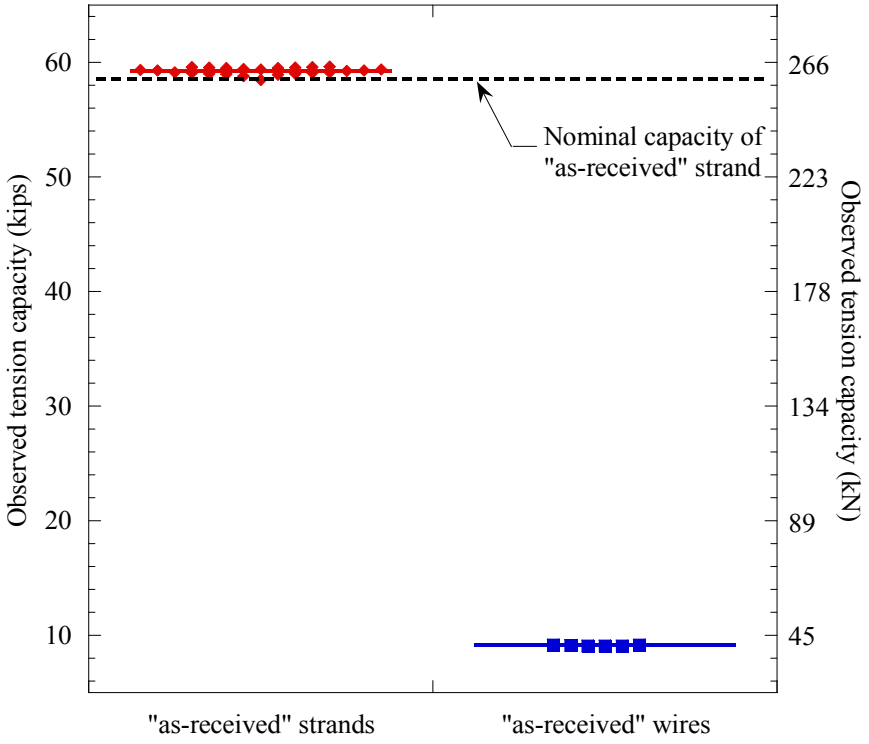


**Figure 5-2. Observed Tension Capacities of "As-Received" Strands and Wires.**

### 5.2.2. Mineral aggregates used in concrete

Mineral aggregates were used in the concrete used to make the galvanic corrosion test specimens. Various characteristics of both fine and coarse aggregates were determined using various ASTM standard test procedures, as mentioned later. The particle size distribution curves for the fine and coarse aggregates are shown in Figure 5-3. In Figure 5-3, the three thinner lines (left most) represent fine aggregate and the three thicker lines (right most) represent coarse aggregate. Also, the solid lines indicate measured values and the dashed lines indicate the upper and lower limits, prescribed by ASTM C136, *Standard Test Method for Sieve Analysis of Fine and Coarse Aggregates*. Figure 5-3 shows that the particle size distributions of fine and coarse aggregates were within the

prescribed upper and lower limits. The fineness modulus of fine aggregate was calculated to be 3.12.

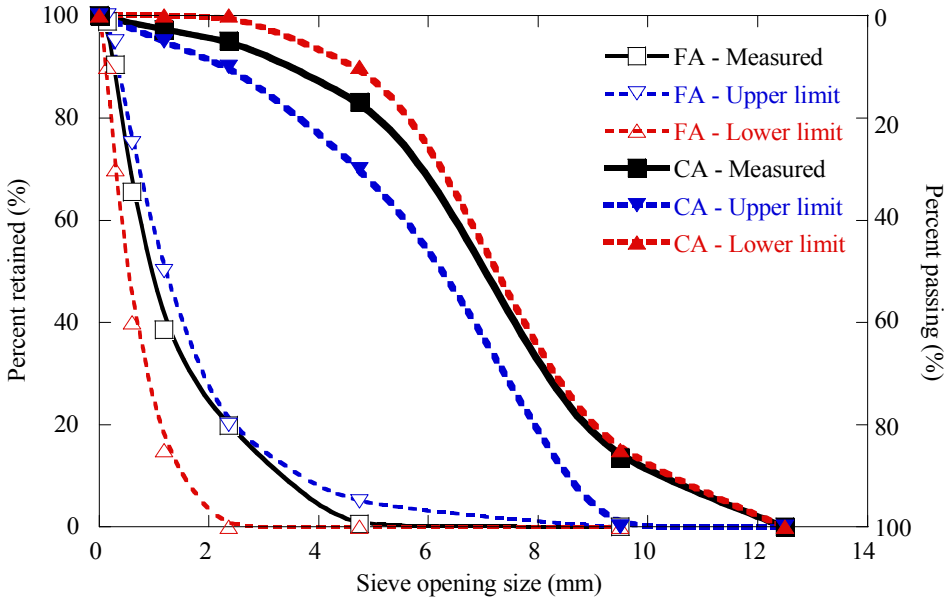


**Figure 5-3. Particle Size Distribution Curves for Fine and Coarse Aggregates.**

The saturated surface dry (SSD) bulk specific gravity, absorption capacity, and bulk density of the fine and coarse aggregates were determined using ASTM standard test procedures. In addition, the total evaporable moisture content, fineness modulus, and organic impurities content of fine aggregates was also determined using ASTM standard test procedures. Table 5-3 summarizes these test results and the standard test procedures used. These data were used to proportion the concrete mixtures.

**Table 5-3 Material Characteristics of Fine and Coarse Aggregates.**

| Aggregate type | Characteristic property | Quantity | Standard test procedure used |
|---|---|---|---|
| Fine | Bulk specific gravity | 2.61 | ASTM C128-97, Standard Test Method for Specific Gravity and Absorption of Fine Aggregate |
| | Absorption capacity | 1.50% | |
| | Fineness modulus | 3.12 | |
| | Moisture content | 1.8% | ASTM C566-97, Standard Test Method for Total Evaporable Moisture Content of Aggregate by Drying |
| Coarse | Bulk specific gravity | 2.63 | ASTM C127-97, Standard Test Method for Specific Gravity and Absorption of Coarse Aggregate |
| | Absorption capacity | 1.07% | |
| | Bulk density | 2718 lb/yd$^3$ (1613 kg/m$^3$) | ASTM C29-97, Standard Test Method for Bulk Density ("Unit Weight") and Voids in Aggregate |
| | Moisture content | 2.0% | ASTM C566-97, Standard Test Method for Total Evaporable Moisture Content of Aggregate by Drying |

### 5.2.3. Cementitious materials

Subsection 2.3.2 reviewed different classes of grouts. It was found that Class A and Class C grouts have been used in most PT bridges in the US. In this test program, Class A grout with a 0.44 water-cement ratio (w/cm) and a commercially available Class C grout (Sikagrout® 300PT) with a 0.27 w/cm were used to prepare the galvanic, strand, and wire corrosion test specimens. It should be noted that the objective of this research was to assess the potential galvanic coupling between different metallic systems in adjacent and different cementitious materials; not that formed by embedding similar metals in adjacent and different cementitious materials. In addition, Type III cement concrete was also used in preparing the galvanic corrosion test specimens. Table 5-4 shows the chemical compositions of the Type I and III cements used in this test program. Because the Class C grout is proprietary, no chemical analysis was performed on this

material. Table 5-5 shows the mixture proportions of the Type III cement concrete and the Class A and C grouts used in this test program.

**Table 5-4. Representative Chemical Compositions of Cementitious Materials Used.**

| Element | Type I cement (used to prepare Class A grout ) | Type III Cement (used to prepare concrete) |
|---|---|---|
| $SO_3$ | 3.16 | 4.30 |
| $SiO_2$ | 20.74 | 20.20 |
| $Fe_2O_3$ | 1.76 | 1.60 |
| MgO | 1.18 | 1.70 |
| $Al_2O_3$ | 5.12 | 5.10 |
| as $Na_2O$ | 0.49 | 0.12 |
| CaO | 64.97 | 64.00 |
| $C_3S$ | 61.00 | 59.00 |
| $C_2S$ | - | 14.00 |
| $C_3A$ | 11.00 | 11.00 |
| $C_4AF$ | - | 5.00 |
| LOI | 1.42 | 1.80 |
| IR | 0.24 | 0.20 |

LOI: loss on ignition; IR: insoluble residue.

**Table 5-5. Representative Mixture Proportions of Concrete and Grout Used.**

| Ingredient | Type III cement concrete | Class A grout | Class C grout |
|---|---|---|---|
| | w/cm = 0.40 | w/cm or w/p = 0.44 | w/p = 0.27 |
| | Batch volume | | |
| | 3 $ft^3$ (0.085 $m^3$) | 2.1 $ft^3$ (0.059 $m^3$) | 2.1 $ft^3$ (0.059 $m^3$) |
| Water, lb (kg) | 38.8 (17.6) | 76.1 (34.6) | 60.2 (27.4) |
| Cement or grout powder, lb (kg) | 96.9 (44.0) | 173.0 (78.6) | 223.1 (101.4) |
| Coarse aggregate*, lb (kg) | 151.0 (68.6) | - | - |
| Fine aggregate, lb (kg) | 142.7 (64.9) | - | - |

"w/cm" indicates water-cementitious ratio (used only for Type III cement concrete)
"w/p" indicates water-powder ratio (used for Class A and C cementitious grout powder)
* Maximum size aggregate (MSA) = 0.375 inch (9.5 mm)

A total of 10 batches of Type III concrete with a water-cementitious material ratio (w/cm) of 0.40 were prepared to cast the galvanic corrosion test specimens. These concrete batches showed an average slump, measured per ASTM C143, *Standard test method for slump of hydraulic cement concrete*, of 8 inches (20 mm). The average air content, measured per ASTM C231, *Standard Test Method for Air Content of Freshly Mixed Concrete by the Pressure Method*, was 1.7 percent. Following ASTM C192, *Standard Practice for Making and Curing Concrete Test Specimens in the Laboratory*, three 4 × 8 inch (10 × 20 mm) size concrete cylinders were prepared from each concrete batch. The average and standard deviation of the 28-day compressive strength of these cylinders were 7.9 ksi (54.4 MPa) and 0.5 ksi (3.4 MPa).

A total of 26 grout batches (13 batches each of Class A and Class C grouts) were prepared and used to cast the strand and wire corrosion test specimens. The water-powder ratios (w/p) of the Class A and C grouts were 0.44 and 0.27, respectively. From the flow cone tests (per ASTM C939-02, *Standard Test Method for Flow of Grout for Preplaced-Aggregate Concrete* (*Flow Cone Method*)), the average efflux times within 1 minute of mixing for the Class A and C grouts were 19 and 23 seconds,

respectively. These values fall within the PTI (2003) recommended efflux time limits of 11 to 30 seconds and 5 to 30 seconds for Class A and C grouts, respectively. The average volume of bleed water collected, per ASTM C940-98a, *Standard Test Method for Expansion and Bleeding of Freshly Mixed Grouts for Preplaced-Aggregate Concrete in the Laboratory*, from the Class A and C grout samples were 0.23 and 0 ounces (6.7 and 0 ml), respectively. The average 28-day compressive strengths of 2 × 2 inch cubes of the Class A and C grouts were 6.4 and 7.2 ksi (44.1 and 49.6 MPa), respectively.

### 5.2.4. Water

The ionic impurities in the water used to prepare the Type III cement concrete, Class A and C grouts, and exposure solutions were determined using an ion-chromatometer (Dionex Model DX-80) and are provided in Table 5-6. Note that the chloride ion concentration (%$Cl^-$) in the water used to prepare the concrete and grout (first, second, and fifth rows in Table 5-6) was as high as 62 ppm (0.006 %wt. or 62 mg/l) whereas the %$Cl^-$ in the water used for other solutions (row #3 and 4 in Table 5-6) was negligible. No ionic impurities were found in the de-ionized water used for cyclic polarization tests.

**Table 5-6. Concentrations of Impurities in the Water Used in this Research Program.**

| Row No. | Type of usage | Usage | Concentration in ppm or mg/l | | | | | | |
|---|---|---|---|---|---|---|---|---|---|
| | | | F | Cl | $NO_2$ | Br | $NO_3$ | $HPO_4$ | $SO_4$ |
| 1 | Mixing water | To prepare concrete and grout for galvanic corrosion, unstressed strand and wire corrosion specimens (i.e., standard tap water) | 0.188 | 58.542 | - | 0.035 | 0.799 | 0.469 | 11.203 |
| 2 | | To prepare grout for stressed strand corrosion specimens (i.e., standard tap water) | 0.027 | 61.777 | - | 0.086 | 0.465 | - | 13.867 |
| 3 | Exposure solution | For cyclic polarization tests (i.e., de-ionized water) | - | - | - | - | - | - | - |
| 4 | | For galvanic corrosion and wire corrosion specimens (i.e., distilled water) | 0.253 | 0.711 | - | - | - | 0.036 | - |
| 5 | | For unstressed and stressed strand corrosion specimens (i.e., standard tap water) | 0.027 | 61.777 | - | 0.086 | 0.465 | - | 13.867 |

### 5.2.5. Chloride concentration in the exposure solutions and grouts

In this experimental study, exposure solutions and cementitious grouts with different concentrations of chloride ions are used. The percent chloride concentration in the exposure solutions is denoted as $\%sCl^-$. The percent chloride concentration in the cementitious grout at or near the GAS interface is denoted as $\%gCl^-$.

The exposure solutions with different $\%sCl^-$ were prepared to simulate possible WD exposure conditions in PT bridge elements. Table 5-7 provides the chemical compositions of the exposure solutions used in the cyclic polarization, galvanic corrosion, and strand and wire corrosion tests. In Table 5-7, the first three simulated pore solutions were used as exposure/immersion solutions for cyclic polarization tests. These simulated pore solutions were prepared using the de-ionized water shown in Table 5-6. The 0.0001 and 9 $\%sCl^-$ solutions were used to perform the WD exposure for the galvanic corrosion tests. The 0.0001, 0.006, 0.018, 0.18, and 1.8 $\%sCl^-$ solutions were used to perform WD exposure in strand and wire corrosion test programs.

**Table 5-7. Chemical Compositions of Exposure Solutions Used in this Research.**

| Name of exposure solution | Chemical composition (mg/l) | | | | |
|---|---|---|---|---|---|
| | $H_2O$ | NaCl | $Ca(OH)_2$ | NaOH | KOH |
| Simulated pore solution (0 %$sCl^-$) | 966.08 | 0.00 | 300 | 10400 | 23230 |
| Simulated pore solution (0.06 %$sCl^-$) | 965.08 | 1000.00 | 300 | 10400 | 23230 |
| Simulated pore solution (1.8 %$sCl^-$) | 936.08 | 30000.00 | 300 | 10400 | 23230 |
| 0 %s$Cl^-$ | 1000.00 | 0.00 | 0 | 0 | 0 |
| 0.006 %$sCl^-$ | 990.00 | 0.10 | 0 | 0 | 0 |
| 0.018 %$sCl^-$ | 999.70 | 0.30 | 0 | 0 | 0 |
| 0.18 %$sCl^-$ | 997.00 | 3.00 | 0 | 0 | 0 |
| 1.8 %$sCl^-$ | 970.00 | 30.00 | 0 | 0 | 0 |
| 9 %s$Cl^-$ | 850.00 | 150.00 | 0 | 0 | 0 |

The grouts with different %$gCl^-$ are attained by immersing the test specimens in exposure solutions with different %$sCl^-$ and used in the wire corrosion testing under continuous-atmospheric (CA) exposure conditions. Further information on %$gCl^-$ is provided in Subsection 5.5.4.2.

## 5.3. CYCLIC POLARIZATION TESTS

### 5.3.1. Introduction and objectives

Cyclic polarization testing is used to determine electrochemical characteristics, especially the pitting susceptibility, of ASTM A416 steel when immersed in an electrolyte. Results from this test program are provided in Subsection 6.2.

In cyclic polarization testing, a steel specimen is immersed in an electrolyte and kept at a predefined initial potential. This predefined initial potential is more negative to its open circuit potential (OCP), which is defined as the potential at which there is no

current (i.e., rest potential or equilibrium potential). This is followed by a scan in the positive direction (i.e., forward scan) through the OCP to a more positive potential. As the potential reaches a predefined maximum value, the direction of the scan is reversed (i.e., reverse scan), swept through the OCP until the potential reaches the initial potential. The resulting plot between the applied potential and logarithm of the measured current density is known as the cyclic polarization curve. Key electrochemical characteristics that are determined from the cyclic polarization curves and the qualities of the cyclic polarization curves are defined as follows:

- Breakdown potential, $E_b$: the potential after which the current increases with increasing potential;
- Primary passivation potential, $E_{pp}$: the potential after which the current either decreases, or becomes essentially constant over a finite range of potential;
- Repassivation potential, $E_{rp}$: the potential corresponding to the lowest current density on the reverse scan of the cyclic polarization curve;
- Passive region: the portion of the forward scan between $E_{pp}$ and $E_b$;
- Active region: the portion of the forward scan where the potentials are less (more negative) than $E_{pp}$;
- Transpassive region: the portion of the forward scan where the potentials are larger (more positive) than $E_b$;
- Positive hysteresis: occurs when the current corresponding to a particular potential is more in the forward scan than in the reverse scan, and;
- Negative hysteresis: occurs when the current corresponding to a particular potential is less in the forward scan than in the reverse scan;

### 5.3.2. Experimental design and specimen layout

The schematic of the test setup is shown in Figure 5-4. The three major components of the test setup are a corrosion cell, a potentiostat, and a laptop computer. The corrosion

cell consists of a steel sample being evaluated known as working electrode (WE), two graphite counter electrodes (CE), one saturated calomel reference electrode (RE), and electrolytic exposure/immersion solution. The cyclic polarization tests in this research were performed using a potentiostat (Model 1287) manufactured by Solartron Inc., and the data acquisition and analysis was performed using CorrWare Version 2.80 software developed by Scribner Associates, Inc. The experimental design included cyclic polarization tests of ASTM A416 wire specimens immersed in chloride solutions (i.e., 0, 0.06, and 1.8 %s$Cl^-$ solutions) simulating concrete pore solution.

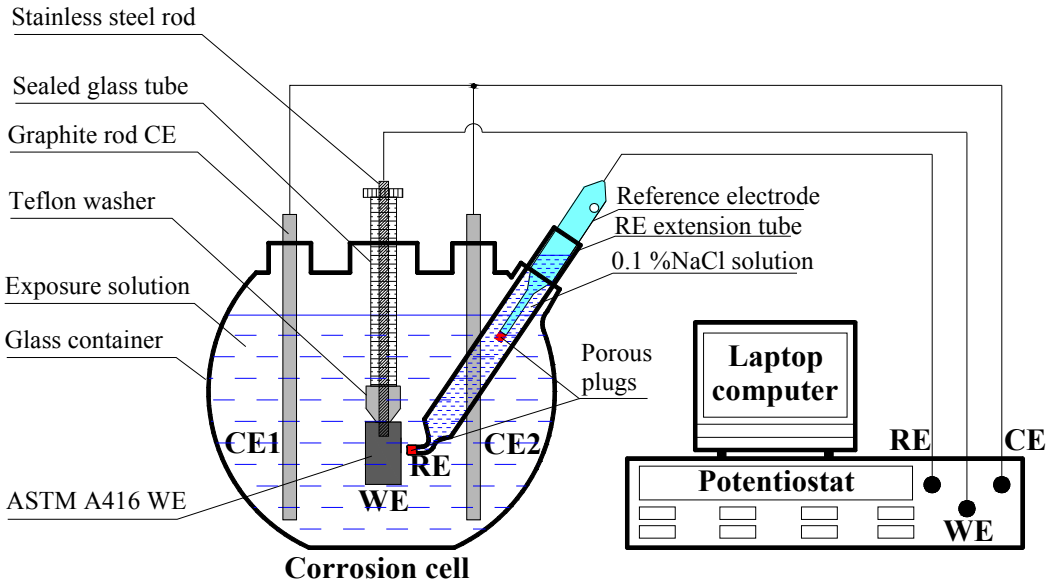


Notes
CE - Counter electrode (Graphite rod)
RE - Reference electrode (Saturated Calomel electrode with 0.241 V vs SHE)
WE - Working electrode (ASTM A416 steel wire)

**Figure 5-4. Schematic of the Cyclic Polarization Test Setup (Note: Not drawn to scale).**

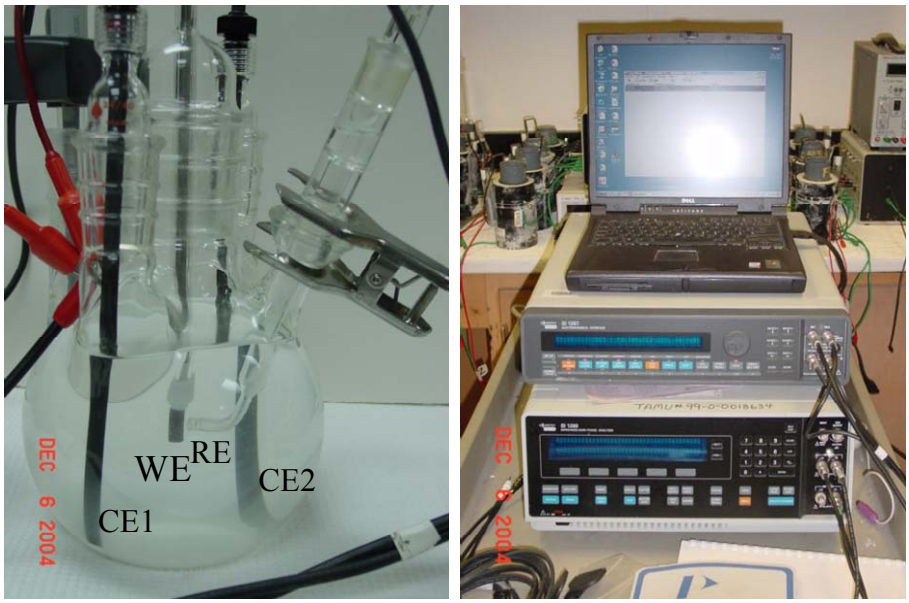


**Figure 5-5. Cyclic Polarization Test Setup (Left: Corrosion Cell (Perkin Elmer, Inc.,); Right: Potentiostat (Solartron Model 1287) and a Laptop Computer)**

### 5.3.3. Sample preparation and test procedures

The center king-wire from ASTM A416 seven-wire strand was used as the WE. Each cylindrical WE was 0.6 inches (15 mm) in length and 0.2 inches (5.1 mm) in diameter. To minimize the change in surface characteristics due to possible heat generation during the cutting process, the wire specimens were cut using an abrasive cutter with continuous supply of coolant. A 0.08-inch (2-mm) deep hole was then drilled into the specimen and a 3-42 size thread was tapped into one of the end faces. The wire specimens were then immersed in ethyl alcohol and cleaned using an ultrasonic cleaner. The stainless steel threaded rod-Teflon washer system (a part of the corrosion cell kit) was then fastened to the drilled hole on the wire specimen. To ensure uniform current flow at the exposed area and minimize excess current near the edges during the cyclic polarization testing, the end faces and edges of the wire specimens were coated with a thin layer of low-viscosity epoxy (Sikadur 35 Hi-Mod LV). Hence, only the

curved surface area (0.325 inch$^2$ (210 mm$^2$)) was directly exposed to the simulated pore solution.

A set of three electrochemical tests were performed as follows:

- Open circuit potential (OCP) measurement
- Potentiostatic experiment, and
- Cyclic polarization (or potentiodynamic scanning).

As soon as the fabricated WE was immersed in the electrolyte the OCP was measured using the potentiostat for a period of 60 minutes. After WE has attained a stable OCP, the potentiostatic experiment was initiated. The WE was held at an overpotential of –0.100 V versus OCP. The third test in the series was the cyclic polarization. This test was performed at a scan rate of 0.0001 V. The forward scanning potentials ranged from –0.100 V versus OCP to +1 V versus OCP. Following the forward scan, a backward scan was initiated – the final potential being –0.100 V versus OCP. One forward and one backward (or reverse) scan took approximately 10 hours to complete.

As shown in Figure 5-4, the RE was placed inside an inclined RE extension tube filled with 0.1% NaCl solution. In Figure 5-4, there are two porous plugs (Vicor® frits); one at the tip of RE and the other at the tip of RE extension tube. The porous plug at the end of RE extension tube is kept at approximately 0.38 to 0.79 inches (1 to 2 mm) from the curved exposed surface of the WE. During the 10-hour cyclic polarization testing, the alkaline exposure solution can partially disintegrate and dissolve the porous plug at the tip of the extension tube. This can cause exchange of solutions on either side of the porous plug. To avoid complete disintegration during the 10-hour long test, a new frit was used for each test. This prevented the leakage of the electrode solution into the exposure solution. Subsection 6.2 presents the results from this test program.

## 5.4. GALVANIC CORROSION TESTS

### 5.4.1. Introduction and objectives

In Subsection 2.3.1, a review of the literature on possible galvanic corrosion was provided. To further improve the knowledge on galvanic corrosion in PT systems, the following two galvanic corrosion test programs were developed and conducted:

- Modified ASTM G109 tests and
- Bearing plate tests

The objective of the Modified ASTM G109 test program is to test if galvanic corrosion occurs between the ASTM A615 (conventional) and A416 (prestressing) reinforcement located at the anchorage zones in PT systems and if so, to assess the increased level of corrosion activity. The objective of the bearing plate test program is to test if galvanic corrosion occurs between the ASTM A615 and A536 steels located at the anchorage zones in PT systems and if so, to assess the increased level of corrosion activity. The results from this test program are provided in Subsection 6.3.

### 5.4.2. Experimental design and specimen layout - Modified ASTM G109 tests

In PT systems, the ASTM A615 and A416 reinforcing steels are embedded inside Type III cement concrete and grout, respectively. When exposed to moisture and chloride conditions and sufficient conductivity exists between these reinforcing steels, galvanic corrosion could occur. To study galvanic corrosion under these conditions, a modified ASTM G109 test specimen was designed. The experimental design (see Table 5-8) is such that the galvanic corrosion between ASTM A416 and A615 steel reinforcements in PT systems that are under negligible ($\approx 0\ \% sCl^-$) and very high ($\approx 9\ \% sCl^-$) chloride exposure conditions can be assessed. A total of 40 test specimens

(with five specimens for each variable combination) were tested for an exposure period of 10 months.

**Table 5-8. Experimental Design for Modified ASTM G109 Test Program.**

| Concrete type | Grout class | Chloride concentration in the exposure solution (%$sCl^-$) | Anode | Cathode | Number of samples tested |
|---|---|---|---|---|---|
| Type III cement concrete (0.40 w/cm) | A (0.44 w/p) | ≈ 0 | A615 | A615 | 5* |
| | | | A615 | A416 (Strand) | 5 |
| | | ≈ 9 | A615 | A615 | 5* |
| | | | A615 | A416 (Strand) | 5 |
| | C (0.27 w/p) | ≈ 0 | A615 | A615 | 5* |
| | | | A615 | A416 (Strand) | 5 |
| | | ≈ 9 | A615 | A615 | 5* |
| | | | A615 | A416 (Strand) | 5 |

* indicates control specimens with identical anodic and cathodic material.

Figure 5-6 shows a picture and schematic of the modified ASTM G109 test specimen. Each test specimen consists of an anodic top reinforcement (ASTM A615) embedded in a layer of concrete and two cathodic bottom reinforcement pieces (ASTM A416 or A615) embedded in grout. This provides a cathode-anode ratio of two. When the cementitious material between the anodic (top) and cathodic (bottom) reinforcement is sufficiently conductive, the 100 Ω electrical resistor connected across the anode and cathode completes the electrical circuit and this facilitates corrosion measurements. Also, the concrete-grout interface in the test specimens can have an effect on the

resulting corrosion activity. To appropriately recognize the effect, if any, of this concrete-grout interface on galvanic corrosion, control specimens with ASTM A615 reinforcements embedded in grout were also tested. Note that no ASTM A615 reinforcement is embedded in grout in PT bridges. In Table 5-8, these control specimens are marked with an asterisk (*). This will facilitate identical effects of concrete-grout interface on corrosion in all the test specimens and enable an appropriate comparative study.

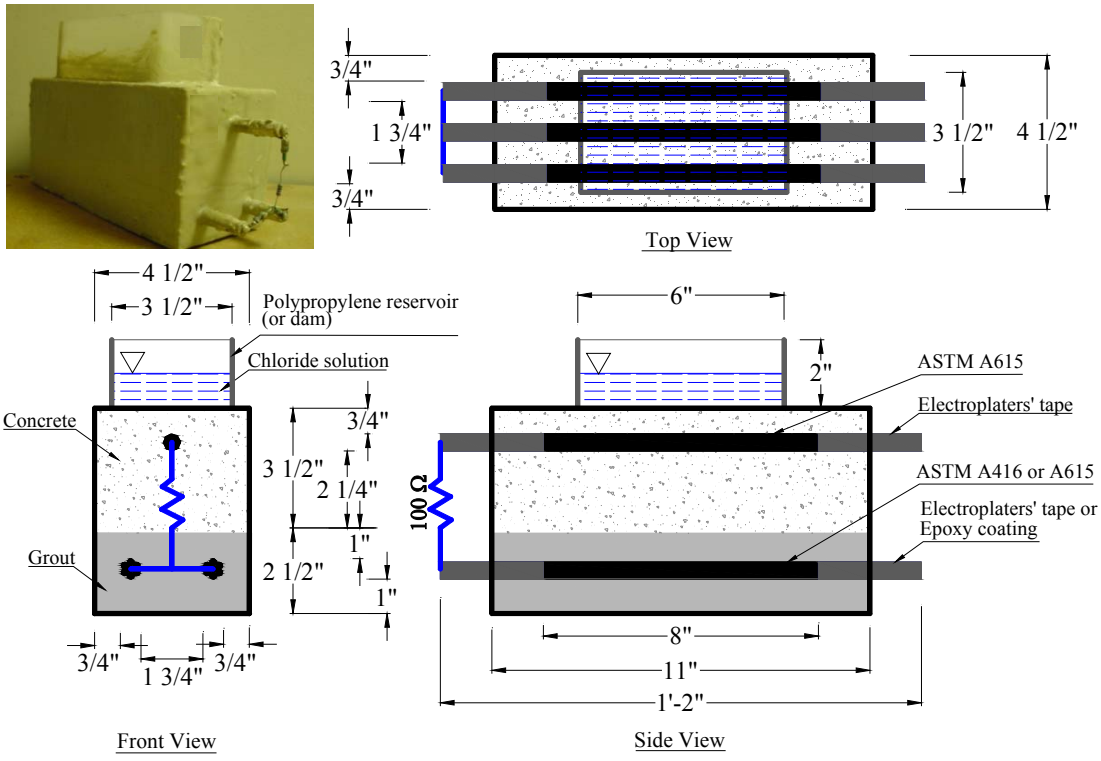


Notes

All dimensions are in inches [1 inch = 2.54 cm].

- ASTM A416 0.6 inch (15 mm) diameter seven-wire strand with epoxy coating at the ends.
- ASTM A615 0.625 inch (16 mm) diameter conventional reinforcement with electroplaters' tape at the ends

**Figure 5-6. Photograph and Schematic of a Modified ASTM G109 Test Specimen.**

### 5.4.3. Casting, curing, and exposure procedures - Modified ASTM G109 tests

The modified ASTM G109 test specimens were cast using 0.40 w/cm, Type III cement concrete and Class A and C grouts per the schematic shown in Figure 5-6 and the experimental design in Table 5-8. Both ASTM A615 and A416 steel reinforcements used to cast the specimen were 14-inch (360-mm) long. Prior to embedment, the reinforcement pieces were immersed in an ethyl alcohol bath and cleaned ultrasonically. Electroplaters' tape was then wrapped around the ends (i.e., 3 inches (76 mm) from each end) of the ASTM A615 reinforcement. In the case of ASTM A416 reinforcemnt, a thin layer of low-viscosity epoxy (Sikadur® 35 Hi-Mod LV) was applied around the ends (i.e., 3 inches (76 mm) from each end). These tape-wrappings or epoxy-coatings were to confine the corrosion to an 8-inch (200-mm) long exposed area near the center of the reinforcement and to avoid corrosion near the ends of the reinforcement pieces. This 8-inch (200-mm) long exposed area lies directly beneath the exposure solution reservoir and has nearly uniform chloride exposure.

When preparing the specimens, the inside surface of the wooden form was coated with a form-release agent. The anodic reinforcement piece was then placed inside the wooden form. The joints/edges were sealed using silicone caulk to prevent leakage of the fluid grout. Following the ASTM C192/C192M, *Standard Practice for making and Curing Concrete test specimens in the laboratory*, the concrete was prepared and placed into the wooden forms (up to a height of 3.5 inches (89 mm)) and allowed to cure for one day. The two cathodic reinforcement pieces were then placed inside the wooden forms and the Class A or C grout was prepared and placed in the remaining height (i.e., 2.5 inches (64 mm)) of the specimen. Following ASTM C192/C192M, the specimens were allowed to cure for an additional 28 days. The wooden forms were removed after 7 days of curing.

After the 28-day curing period, the specimens were allowed to dry at room conditions (approximately 73$^{o}$F (23$^{o}$C) and 50 %*RH*). A rectangular acrylic reservoir

(dam) was attached to the center of the top surface and a 100 Ω electrical resistor was fastened to the reinforcement pieces. A thick layer of high-viscosity epoxy (Sikadur® 32 Hi-Mod) was then applied to the concrete surfaces (four sides and the top surface area outside the reservoir) and the visible steel reinforcement surfaces. This is done to prevent moisture exchange through these concrete surfaces, allow one-dimensional diffusion of moisture and chlorides towards the embedded steel reinforcements during the WD exposure, and prevent corrosion at the ends of the reinforcement pieces.

After 14 days of curing, the specimens were moved to an environmental chamber with 100 ±5°F (37.7 ±3°C) temperature conditions. The WD exposure (14 days of ponding followed by 14 days of drying) was initiated on 15th day after the 28-day curing period. To prevent evaporation of exposure solution, the reservoir was covered using a polyethylene sheet. The test specimens were exposed to a total of 11 WD exposure cycles and corrosion measurements were made during the exposure. The corrosion measurement and evaluation procedures are provided in Subsection 5.4.6.

### 5.4.4. Experimental design and specimen layout - Bearing plate tests

In PT systems, the ASTM A536 cast-iron trumpets or bearing plates are surrounded by Type III concrete and filled with Class A or C grout. The concrete surrounding the bearing plates experience very large bursting forces. To sustain and distribute these large bursting forces, the spiral reinforcement (commonly known as bursting reinforcement) is provided around the bearing plates. These metallic and cementitious materials could be exposed to moisture and chloride conditions. To simulate these conditions and evaluate the magnitude of the galvanic corrosion, the bearing plate test specimen was designed. The experiment was designed to specifically assess the galvanic corrosion between the bearing plate and conventional spiral reinforcement in PT systems that experience WD exposure to ≈ 0 %$sCl^-$ and ≈ 9 %$sCl^-$ solutions. Table

5-9 provides the experimental design for the bearing plate test program. A total of 20 test specimens (with five specimens for each variable combination) were tested for an exposure period of 11 months.

Figure 5-6 shows the photographs of the partially and completely cast bearing plate specimen and its schematic drawings. As shown in Figure 5-7, each test specimen consists of an ASTM A536 bearing plate and ASTM A615 reinforcement. To simulate the field conditions, the ASTM A615 reinforcement was spiraled (at a nominal diameter equal to 10.6 inches (300 mm)) and placed around the ASTM A536 cast-iron bearing plate, the top surface of which is covered with a 0.5 w/cm mortar. The spiraled ASTM A615 reinforcement had 1.7 turns, providing a total surface area of approximately 87.5 inch$^2$ (565 cm$^2$). The total surface area of the ASTM A536 bearing plate (Model EC-6-7 manufactured by VSL International, Inc.) was 175 inch$^2$ (1129 cm$^2$). Therefore, the ratio between the surface areas of the bearing plate and spiral reinforcement was two, which is similar to that between the anodic and cathodic reinforcement pieces in the modified ASTM G109 test specimens. A 100 Ω resistor was connected across the bearing plate and the spiral reinforcement to measure electrical current.

**Table 5-9. Experimental Design for Bearing Plate Test Program.**

| Concrete type | Grout class | Chloride concentration in the exposure solution (%s$Cl^-$) | Anode | Cathode | Number of samples tested |
|---|---|---|---|---|---|
| Type III cement concrete with 0.40 w/cm | A (0.44 w/cm) | ≈ 0 | A615 | A536 (Cast iron) | 10 |
| | | ≈ 9 | A615 | A536 (Cast iron) | 10 |

Partially-cast specimen showing the bearing plate and spiral reinforcement

Completely-cast specimen showing the plastic dam and 100 Ω resistor (inside ellipse), and epoxy coated concrete surface

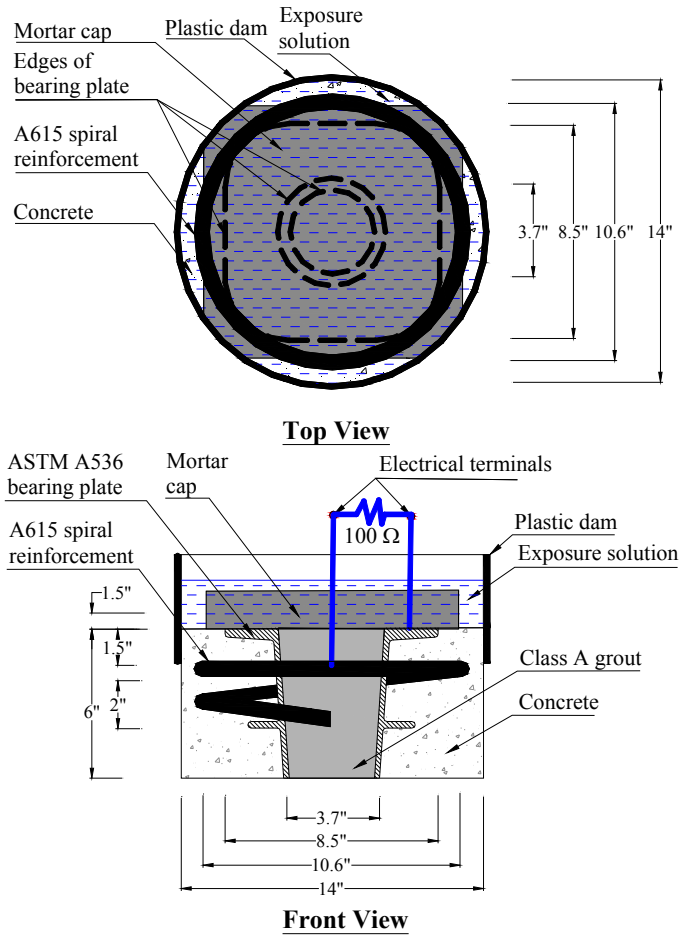


**Figure 5-7. Photographs and Schematics of a Bearing Plate Test Specimen.**

### 5.4.5. Casting, curing, and exposure procedures – Bearing plate tests

Figure 5-7 shows the schematic of the bearing plate test specimen. These specimens were cast using Type III cement concrete, Class A grout, and ASTM A536 and A615 reinforcement pieces. The experimental design was provided earlier in Table 5-8. The casting procedure is as follows. A 12-inch (300-mm) long electrical lead wire was fastened to one end of the spiral reinforcement. Another similar electrical lead wire was

fastened to a threaded hole on the flat surface of the bearing plate. A 14-inch (356-mm) diameter card board form was then placed on a flat and clean surface. The spiral reinforcement was then placed inside the circular card board form. Following this, the bearing plate was placed (the end with smaller diameter was facing downward) inside the form. Per ASTM C192/C192M, the Type III concrete was then prepared and placed in three layers into the card board form and allowed to cure for one day. On the second day, without removing the specimen from the curing room, the conical frustum inside the bearing plate was filled with Class A grout, the top surface of the specimen was covered with a 1.5-inch (38-mm) thick mortar layer, and the card-board form was removed. The specimens were then cured for additional 28 days.

After the 28-day curing period, the specimens were moved to a laboratory area with room conditions (approximately 73$^{o}$F (23$^{o}$C) and 50 %*RH*). The curved surface of the specimens was then coated with high-viscosity epoxy (Sikadur® 32 Hi-Mod). This was done to prevent moisture exchange through these concrete surfaces and allow one-dimensional diffusion of moisture and chlorides towards the embedded steel reinforcement during the WD exposure. A circular reservoir (dam) was prepared using a flexible and 0.08-inch (2-mm) thick plastic sheet. To prevent leakage of exposure solution, the gap between the concrete and the plastic sheet was sealed using water-proof silicone caulk. A 100 Ω electrical resistor was fastened to the free ends of the two lead wires.

After 14 days of curing, the specimens were moved to an environmental chamber with 100 ±5$^{o}$F (37.7 ±3$^{o}$C) temperature conditions; and as in the modified ASTM G109 test, the WD exposure (14 days of ponding followed by 14 days of drying) was initiated. To prevent evaporation of the exposure solution, the reservoir was covered using a polyethylene sheet. The WD exposure continued for a period of 11 months. Corrosion measurements were made during each WD cycle, per the procedures provided in Subsection 5.4.6.

### 5.4.6. Corrosion evaluation procedures

The corrosion evaluation procedures for both the modified ASTM G109 and bearing plate tests are identical and based on the ASTM G109 standard practice. On 7th day of ponding during each WD cycle (say, $i^{th}$ WD cycle), the voltage, $V_i$, across the 100 Ω resistor is measured. Using Ohm's law, the current, $I_i$, is determined as follows:

$$\text{Ohm's law: } I_i(\text{Amps}) = \frac{V_i(\text{volts})}{R(\text{ohms})} = \frac{V_i}{100\ \Omega} \tag{5.1}$$

The total electrical charge, $EC_i$, passed from the first WD cycle to the $i^{th}$ WD cycle can be determined using the following equation provided in the ASTM G109:

$$EC_j(\text{Coulombs}) = \underbrace{EC_{j-1}}_{\text{Coulombs}} + [\underbrace{(t_j - t_{j-1})}_{\text{Seconds}} \times \underbrace{(I_j - I_{j-1})}_{\text{Amps}} / 2] \tag{5.2}$$

This calculated total corrosion indicates the severity of ongoing corrosion in each test specimen. The results of these galvanic corrosion tests are provided in Subsection 6.3.

## 5.5. STRAND AND WIRE CORROSION TESTS

### 5.5.1. Introduction and objectives

In Subsection 2.2, various case histories on failure of strands in PT bridges were presented. In Subsection 2.7.1.1, it was noted that the tension capacity of strands is a critical parameter that directly influences the structural capacity of PT bridges. When exposed to various corrosive conditions, the tension capacity of strands can decrease as a function of time. However, no deterministic or probabilistic models currently exist to

predict the time-variant tension capacity of PT strands in tendons that are exposed to various void, material, environmental, stress, and other exposure conditions. The strand and wire corrosion tests were developed and performed to obtain the data necessary to develop probabilistic tension capacity models for PT strands. These tension capacity models are presented in section 7 and are used in the modeling and assessment of time-variant structural reliability of PT segmental bridges presented in section 10.

The main objectives of the strand and wire corrosion tests are to generate the data necessary to develop probabilistic models for the tension capacity ($C_T$) of strands that are exposed to both WD and CA conditions. These models are developed in Sections 7, 8, and 9. A total of 536 and 278 strand and wire specimens, respectively, were tested. Experimental designs and specimen layouts for the strand and wire corrosion tests are provided next.

### 5.5.2. Experimental design and specimen layout

The following four strand/wire corrosion test programs were performed:

a) Unstressed strand corrosion test - WD conditions (374 specimens)
b) Stressed strand corrosion test - WD conditions (162 specimens)
c) Unstressed wire corrosion test - WD conditions (64 specimens)
d) Unstressed wire corrosion test - CA conditions (61 specimens)

Figure 5-8 (a), (b), (c), and (d) show the experimental designs (in graphical format) for these four test programs, respectively.

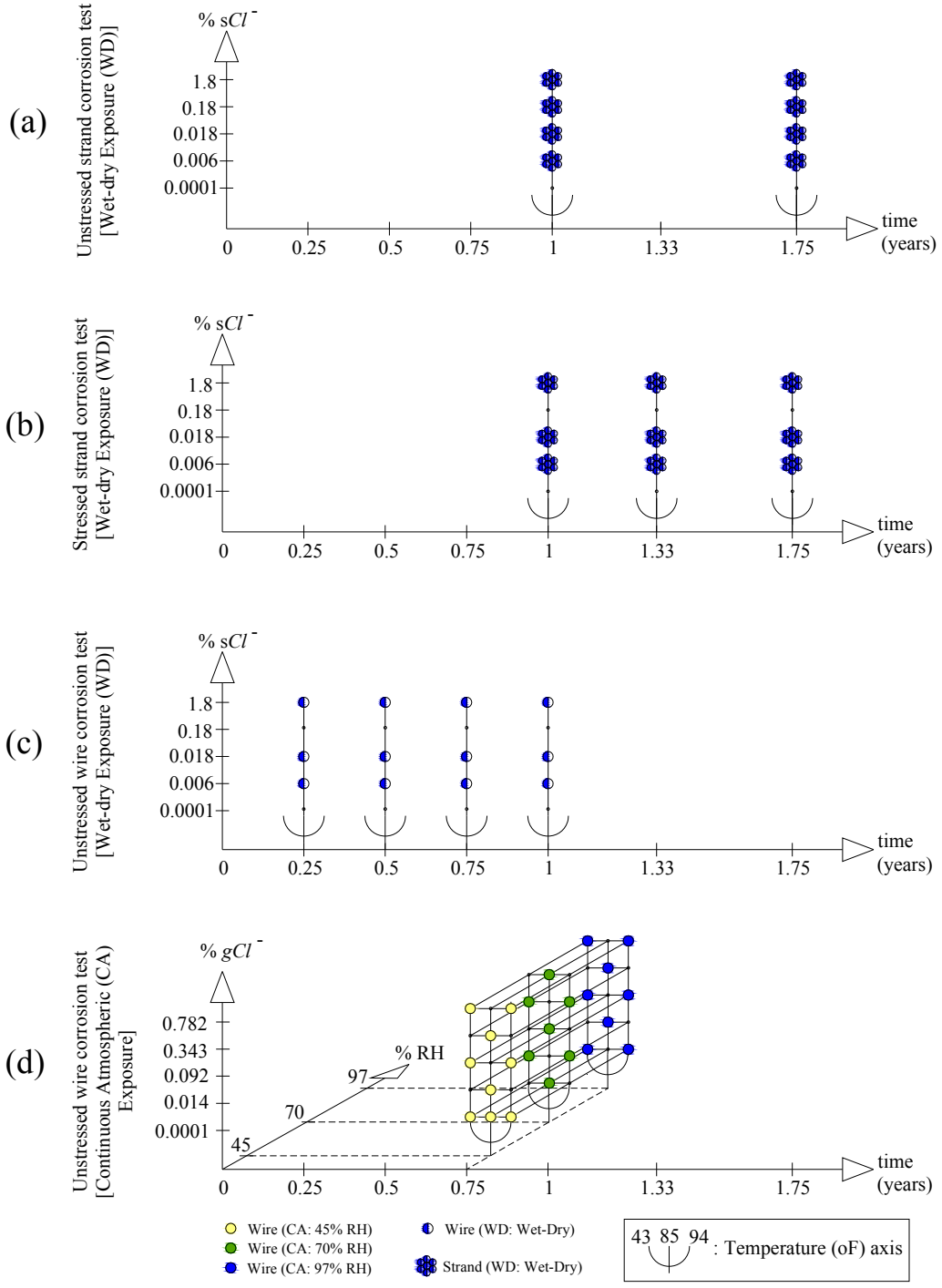


Note:
Tension capacities of "as-received" strands and wires with negligible corrosion were also determined.

**Figure 5-8 Experimental Designs for All the Strand and Wire Corrosion Tests.**

The first three test programs are under WD exposure conditions and the fourth test program is under CA exposure conditions. The half-filled, seven-circle markers and half-filled, single-circle markers indicate strand and wire specimens, respectively, under WD exposure conditions. The completely filled single-circle markers indicate wire specimens under CA exposure conditions. More detailed information of these four test programs is provided later. The factors and levels of test parameters have been designed such that a statistically valid and field relevant tension capacity results of strands and wires can be obtained. The Subsections 5.5.2.1 and 5.5.2.2 discuss the experimental designs and layouts of the strand and wire corrosion tests, respectively.

#### *5.5.2.1. Strand corrosion tests*

Figure 5-8 (a) and (b), Table 5-10, and Table 5-11 provide the experimental designs for the unstressed and stressed strand corrosion tests. A total of 374 and 162 unstressed and stressed strand corrosion specimens, respectively, were tested. The effects of the qualitative parameters void type (*VT*), grout class (*GC*), and $f_{axial}$ and quantitative parameters *MC*, $\%sCl^-$, and WD exposure time ($t_{WD}$) on strand corrosion and resulting loss in tension capacity were tested.

**Table 5-10. Experimental Design Showing the Number of Test Specimens in the Unstressed Strand Corrosion Test under WD Exposure Conditions[*].**

| Grout class, GC | Wet-dry exposure time, $t_{WD}$, months | Moisture content, *MC* | Chloride ion concentration in exposure solution, %sCl⁻ | Void type (*VT*) | | | | |
|---|---|---|---|---|---|---|---|---|
| | | | | No void (NV) | Parallel void (PV) | Orthogonal void (OV) | Inclined void (IV) | Bleed water void (BV) |
| A | 12 | Low | 0.0001** | 5 | 5 | 5 | 5 | 5 |
| | | High | 0.006 | 5 | 5 | 5 | 5 | 5 |
| | | | 0.018 | 5 | 5 | 5 | 5 | 5 |
| | | | 0.18 | 5 | 5 | 5 | 5 | – |
| | | | 1.8 | 5 | 3 | 3 | 5 | 5 |
| | 21 | Low | 0.0001** | 5 | 5 | 5 | 5 | 5 |
| | | High | 0.006 | 5 | 5 | 5 | 5 | 5 |
| | | | 0.018 | 5 | 5 | 5 | 5 | 5 |
| | | | 0.18 | 5 | 5 | 5 | 5 | – |
| | | | 1.8 | 5 | 4 | 4 | 5 | 5 |
| C | 12 | Low | 0.0001** | 5 | 5 | 5 | 5 | 5 |
| | | High | 0.006 | 5 | 5 | 5 | 5 | 5 |
| | | | 0.018 | 5 | 5 | 5 | 5 | 5 |
| | | | 0.18 | 5 | 5 | 5 | 5 | – |
| | | | 1.8 | 5 | 5 | 5 | 5 | 5 |
| | 21 | Low | 0.0001** | 5 | 5 | 5 | 5 | 5 |
| | | High | 0.006 | 5 | 5 | 5 | 5 | 5 |
| | | | 0.018 | 5 | 5 | 5 | 5 | 5 |
| | | | 0.18 | 5 | 5 | 5 | 5 | – |
| | | | 1.8 | 5 | 5 | 5 | 5 | 5 |
| Total number of unstressed strand specimens for each *VT* | | | | 80 | 77 | 77 | 80 | 60 |
| Total number of unstressed strand specimens | | | | 374 | | | | |

* 24 "as-received" strand specimens with negligible corrosion were also tested.

** Control specimens that are exposed to standard room conditions without WD cycles.

– Indicates no data available.

**Table 5-11. Experimental Design Showing the Number of Test Specimens in the Stressed Strand Corrosion Test under WD Exposure Conditions*.**

| Grout class, GC | Wet-dry exposure time, $t_{WD}$, months | Moisture content, MC | Chloride ion concentration in exposure solution, %sCl⁻ | Void type (*VT*) | | |
|---|---|---|---|---|---|---|
| | | | | No void (NV) | Parallel void (PV) | Orthogonal void (OV) |
| A | 12 | Low | 0.0001** | – | – | 2 |
| | | High | 0.006 | 3 | 3 | 3 |
| | | | 0.018 | 3 | 3 | 3 |
| | | | 1.8 | 3 | 3 | 3 |
| | 16 | Low | 0.0001** | – | – | 2 |
| | | High | 0.006 | – | 3 | 3 |
| | | | 0.018 | – | 3 | 3 |
| | | | 1.8 | – | 3 | 3 |
| | 21 | Low | 0.0001** | – | – | 2 |
| | | High | 0.006 | 3 | 4 | 4 |
| | | | 0.018 | 3 | 4 | 4 |
| | | | 1.8 | 3 | 4 | 4 |
| C | 12 | High | 0.006 | 3 | 3 | 3 |
| | | | 0.018 | 3 | 3 | 3 |
| | | | 1.8 | 3 | 3 | 3 |
| | 16 | High | 0.006 | – | 3 | 3 |
| | | | 0.018 | – | 3 | 3 |
| | | | 1.8 | – | 3 | 3 |
| | 21 | High | 0.006 | 3 | 4 | 4 |
| | | | 0.018 | 3 | 4 | 4 |
| | | | 1.8 | 3 | 4 | 4 |
| Total number of stressed strand test specimens | | | | 36 | 60 | 66 |
| Grand total number of stressed strand test specimens | | | | 162 | | |

* 24 "as-received" strand specimens with negligible corrosion were also tested.
** Control specimens that are exposed to standard room conditions without WD cycles.
– Indicates no data available.

Figure 5-9 shows the schematics of the strand corrosion test specimens. Each strand test specimen was made of a 41-inch (1040 mm) long strand piece meeting the ASTM A416 specifications. Five *VT*s that are intended to represent typical geometries of GAS interfaces found in PT bridges were identified. These *VT*s included

no void (NV), parallel void (PV), orthogonal void (OV), inclined void (IV), and bleed water void (BV) and are defined as follows:

- NV (see Figure 5-9(a)): No voids are present and the tendons are fully grouted. The 12-inch (300-mm) long strand surface beneath the reservoir (shown as "R" in Figure 5-9(a)) has a ¼-inch (6-mm) grout cover. (Although this indicates a condition without any voids, NV is considered as a level of the qualitative variable *VT* for convenience of presentation in this document, herein.)

- PV (see Figure 5-9(b)): The longitudinal axis of the partially embedded strand is parallel to the grout surface. The 12-inch (300-mm) long strand surface beneath the reservoir (shown as "R" in Figure 5-9(b)) is in direct contact with the exposure solution (i.e., no grout cover). This void condition may be found in the midspan region of PT girders with a horizontal tendon profile.

- OV (see Figure 5-9(c)): The longitudinal axis of the partially embedded strand is orthogonal to the grout surface. This void condition may occur in PT columns or piers or other elements with a vertical profile. In addition, depending on the flow characteristics of the fresh grout, the OV type may also be found in PT ducts with horizontal or inclined profiles.

- IV (see Figure 5-9(d)): The longitudinal axis of the partially embedded strand is at a $45^{o}$ angle to the grout surface. This represents a void condition that may be found near anchorage zones of PT girders with an inclined tendon profile.

- BV (see Figure 5-9(e)): This void condition can form due to the evaporation of bleed water. In the test specimens, this is represented by a 5-inch (127-mm) long thin grout layer on the strand surface near the GAS interface (shown as "GS" in Figure 5-9(e)). This thin grout covering is the only difference between the BV and IV samples. Note that in the field the length of such thin grout layers formed due to the formation and evaporation of bleed water could be much larger than 5 inches (127 mm).

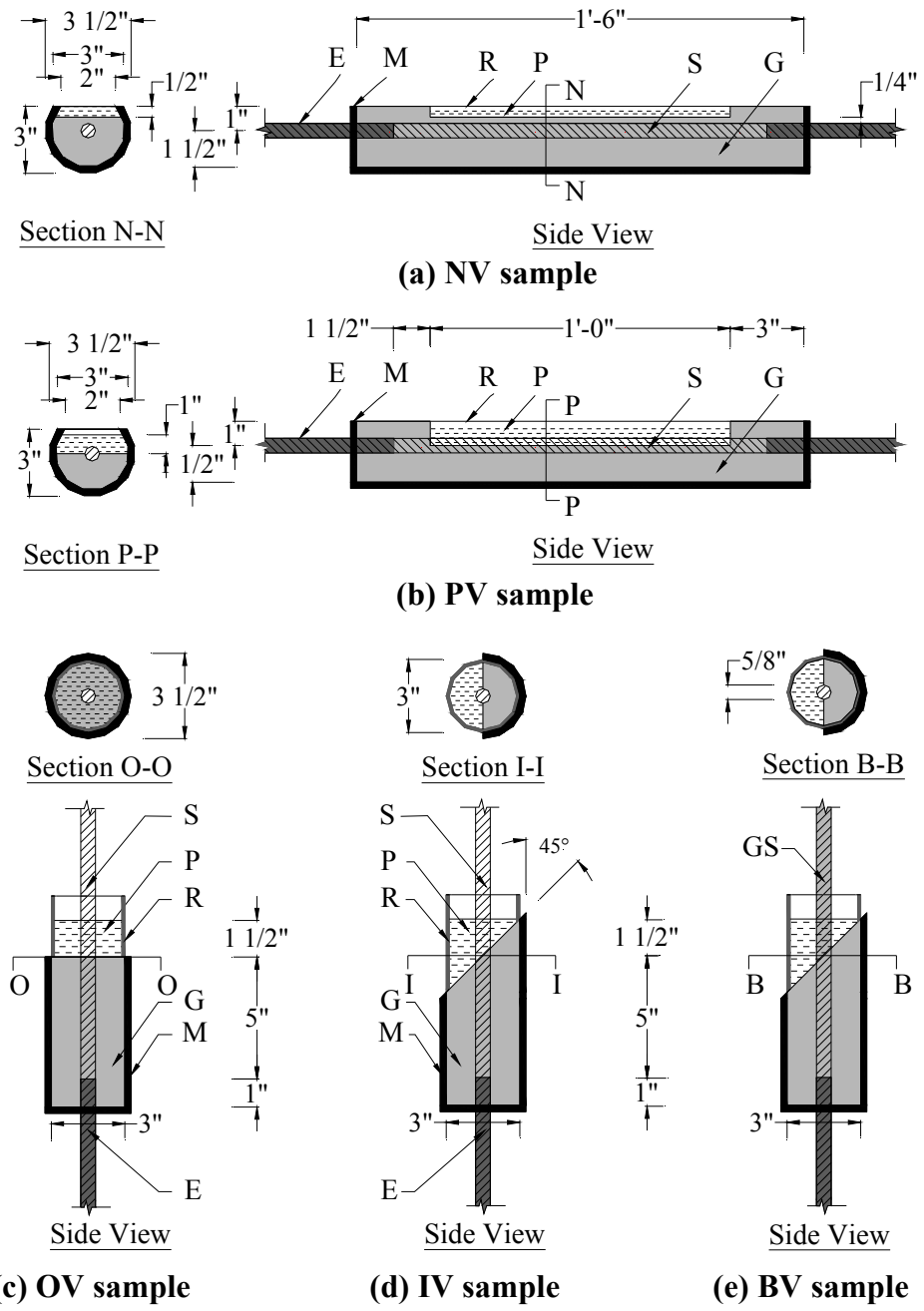


Notes: E - Epoxy; G - Grout; GS - Grout layered strand; M - HDPE mold; P - Ponding or exposure solution; R - Reservoir; S - Strand
All dimensions are in inches [1 inch = 2.54 mm].

**Figure 5-9. Schematics of Strand Corrosion Test Specimens.**

To test the effect of the qualitative parameter *GC* on tension capacity, an approximately equal number of test specimens were cast with Class A and C grouts.

An $f_{axial}$ level of 0 or approximately 150 ksi (0 or 1034 MPa) were applied to the test specimens and were denoted as unstressed and stressed strand specimens, respectively. IV and BV samples were not included in the stressed strand corrosion test program. Three stressed strand specimens were tested in each parameter combination as compared to five unstressed strand specimens.

Specimens *with* and *without* wet-dry (WD) exposure were considered to be under *high* and *low* MC (see third columns of Table 5-10 and Table 5-11). The chloride conditions tested include continuous-atmospheric (CA) environment with negligible chloride concentration and WD environments with 0.006, 0.018, 0.18, and 1.8 %$sCl^-$ solutions. For each test specimen, the strand surface area exposed to the grout and exposure solution can be considered as the cathode and anode regions, respectively (e.g., in the OV samples, the length of the portions of the strand exposed to grout and exposure solution are 5 and 1½ inches (127 and 38 mm), respectively; resulting in a cathode-to-anode ratio of 5:1½). Using this, the cathode-to-anode ratios on the OV, IV, BV, and PV samples were approximately 5:1½, 5:1½, 5:1½, and 2:1.

As shown in Table 5-10 and Table 5-11, the total duration of the strand corrosion test programs under WD exposure conditions was 21 months. In particular, the unstressed strand specimens were exposed for 0, 12, and 21 months and the stressed strand specimens were exposed for a period of 0, 12, 16, and 21 months.

#### *5.5.2.2. Wire corrosion tests*

Figure 5-8(c) and Table 5-12 show the experimental designs for the unstressed wire corrosion test program with under WD exposure conditions. Figure 5-8(d) and Table 5-13 show the experimental design of the unstressed wire corrosion test program under

CA exposure conditions. A total of 125 wire specimens were exposed to WD (64 specimens) and CA (61 specimens) exposure conditions for different test periods. At the end of each test period, the corroded wire specimens were tested for the residual tension capacity. The quantitative test parameters included in the WD test program were $t_{WD}$ and $\%sCl^-$. The quantitative parameters included in the CA test program were $t_{CA}$, $RH$, $T$, and $\%gCl^-$. Note that all the wire specimens were prepared using Class A grout and were not tested under stressed conditions. Also, only the effect of OV condition on wire capacity was tested in this program.

**Table 5-12. Experimental Design Showing the Number of Test Specimens in the Unstressed Wire Corrosion Test under WD Exposure Conditions*.**

| **Void type, *VT*** | **Grout class, GC** | **Wet-dry exposure time, $t_{WD}$, months** | **Chloride ion concentration of the exposure solution %sCl⁻** | | | | |
|---|---|---|---|---|---|---|---|
| | | | **0.0001** | **0.006** | **0.018** | **0.18** | **1.8** |
| OV | A | 3 | 3 | 3 | 3 | 3 | 3 |
| | | 6 | 3 | 3 | 3 | 4 | 4 |
| | | 9 | 3 | 3 | 3 | 4 | 4 |
| | | 12 | 3 | 3 | 3 | 3 | 3 |
| Total number of WD wire test specimens | | | 12 | 12 | 12 | 14 | 14 |
| Grand total number of WD wire test specimens | | | 64 | | | | |

* 6 "as-received" wire specimens with negligible corrosion were also tested.

**Table 5-13. Experimental Design Showing the Number of Test Specimens in the Unstressed Wire Corrosion Test under CA Exposure Conditions*.**

| Void type, *VT* | Grout class, GC | Continuous-atmospheric exposure time, $t_{CA}$, months | Ambient relative humidity *RH* (%) | Ambient temperature, *T*, °F (°C) | Chloride ion concentration in the grout at or near GAS interface, %$gCl^-$, %wt. cement (lb/yd$^3$) | | | | |
|---|---|---|---|---|---|---|---|---|---|
| | | | | | 0.00001 (0.0001) | 0.014 (0.13) | 0.092 (0.87) | 0.343 (3.25) | 0.782 (7.4) |
| OV | A | 9 | 45 | 43 (6.1) | 2 | – | 3 | – | 4 |
| | | | | 85 (29.4) | 2 | 3 | – | 4 | – |
| | | | | 94 (34.4) | 2 | – | 3 | – | 4 |
| | | | 70 | 43 (6.1) | – | 3 | – | 4 | – |
| | | | | 85 (29.4) | 3 | – | 4 | – | 4 |
| | | | | 94 (34.4) | – | 3 | – | 4 | – |
| | | | 97 | 43 (6.1) | 3 | – | 4 | – | 4 |
| | | | | 85 (29.4) | – | 3 | – | 4 | – |
| | | | | 94 (34.4) | 3 | – | 4 | – | 4 |
| Total number of CA wire test specimens | | | | | 15 | 12 | 18 | 16 | 20 |
| Grand total number of CA wire test specimens | | | | | 61 | | | | |

* 11 "as-received" wire specimens with negligible corrosion were also tested.
– indicates that no data is available.

Figure 5-10 shows the schematic and photograph of a wire corrosion test specimen with an OV condition. The wire corrosion test specimens were prepared using 7-inch (178 mm) long center king-wires removed from ASTM A416 strands.

As shown in Figure 5-8(c) and Table 5-12, the wire specimens under WD exposure conditions were exposed for a period of 3, 6, 9, and 12 months, respectively. As shown in Figure 5-8(d) and Table 5-13, the wire specimens under CA exposure conditions were tested only at 9 months.

For the WD test program, the five levels of %$sCl^-$ were 0.0001, 0.006, 0.018, 0.18, and 1.8 and match with those in the strand corrosion test program. For the CA test program, the five levels of %$gCl^-$ were 0.00001, 0.014, 0.092, 0.343, 0.782 % by weight of cement (0.0001, 0.13, 0.87, 3.25, and 7.4 lb/yd$^3$). In the probabilitistic models

developed in this document, the parameter $\%gCl^-$ will refer to the quantities in % by weight of cement.

Two additional quantitative parameters included in the experimental design for the CA test program were *RH* and *T*. Three levels of *RH* were considered and are 45, 70, and 97%. Three levels of temperature (*T*) considered were 43, 85, and 94 $^{o}$F (6.1, 29.4, and 34.4 $^{o}$C) representing cold, moderate, and hot climates.

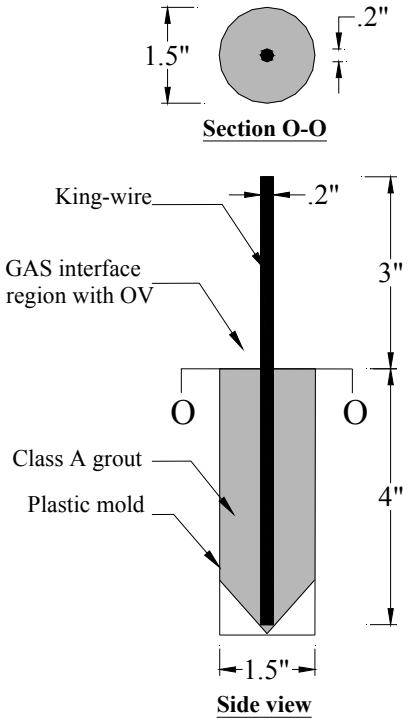


Note: All dimensions are in inches.
1 inch = 2.54 mm.

Photographs of a wire corrosion test specimen with an orthogonal void

**Figure 5-10. Schematic and Photograph of Wire Corrosion Test Specimen.**

### 5.5.3. Concrete reaction frames and stressing operations for stressed strand specimens

#### *5.5.3.1. Concrete reaction frames and layout*

In the case of stressed strand corrosion testing, $f_{axial}$ of approximately 150 ksi (1034 MPa) was applied and maintained by anchoring the strands to a specially designed concrete reaction frame (CRF). These CRFs were designed according to ACI 318-02/318R-02, *Building Code Requirements for Structural Concrete and Commentary*, to safely carry six stressed strand specimens. Structural detailing of the CRFs is provided in Appendix B. A total of 27 CRFs with 6×4×3 ft (1.8×1.2×0.9 m) overall dimensions were made to expose and test 162 stressed strand specimens. Six, 10, and 11 CRFs were used to expose and test 36 NV, 60 PV, and 66 OV samples, respectively. Figure 5-11 shows the schematic and photograph of a vertical CRF exposing six OV specimens (indicated by the numbers in the top view diagram). Figure 5-12 shows the schematic of a horizontal CRF exposing six NV specimens (indicated by the numbers in the side elevation view diagram). The CRF setup for PV specimens is similar to that for NV specimens. The photograph on the top right corner of Figure 5-12 shows two horizontal CRFs exposing six NV and six PV specimens (stacked one on top of the other). The stressing operations are discussed next.

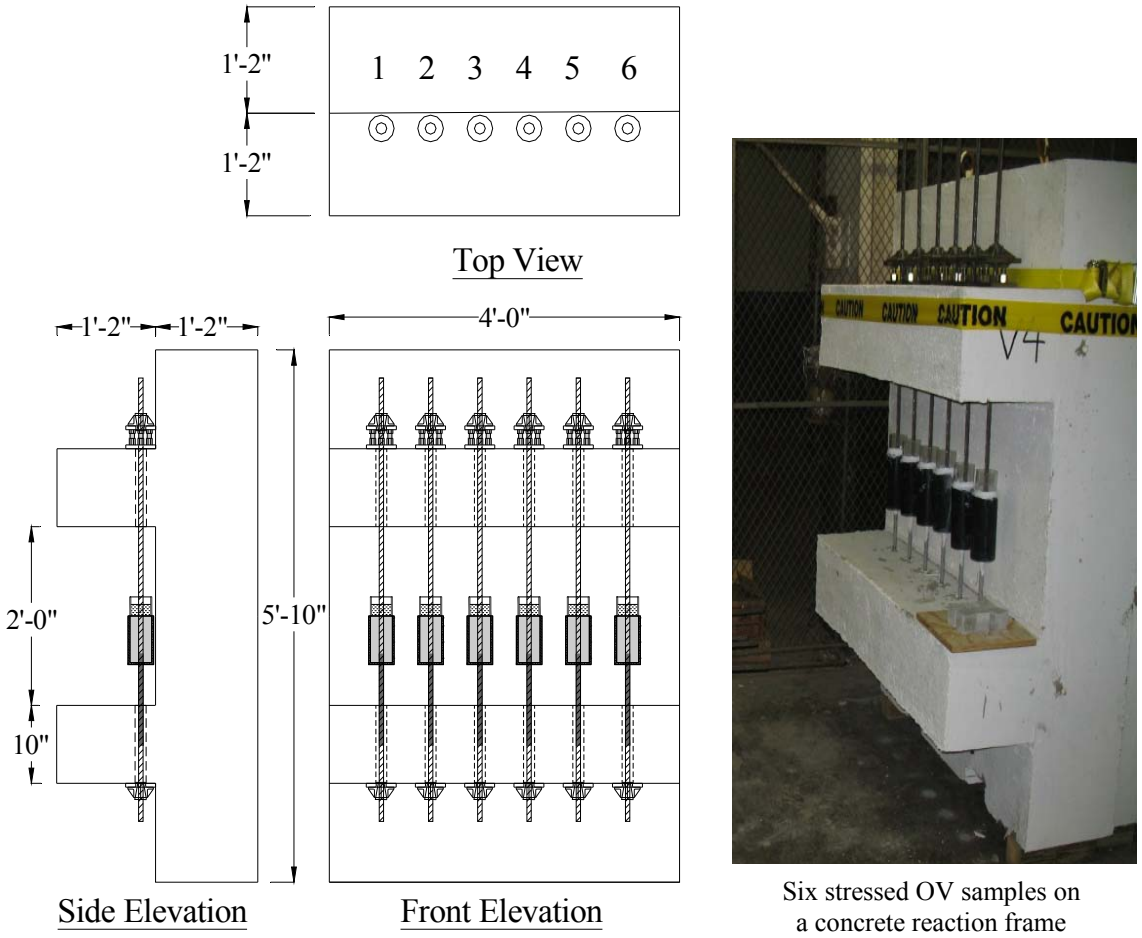


Six stressed OV samples on a concrete reaction frame

Note: All dimensions are in inches [1 inch = 2.54 mm].

**Figure 5-11. Schematic and Photograph of Vertical Concrete Reaction Frame with Stressed Strand Specimens.**

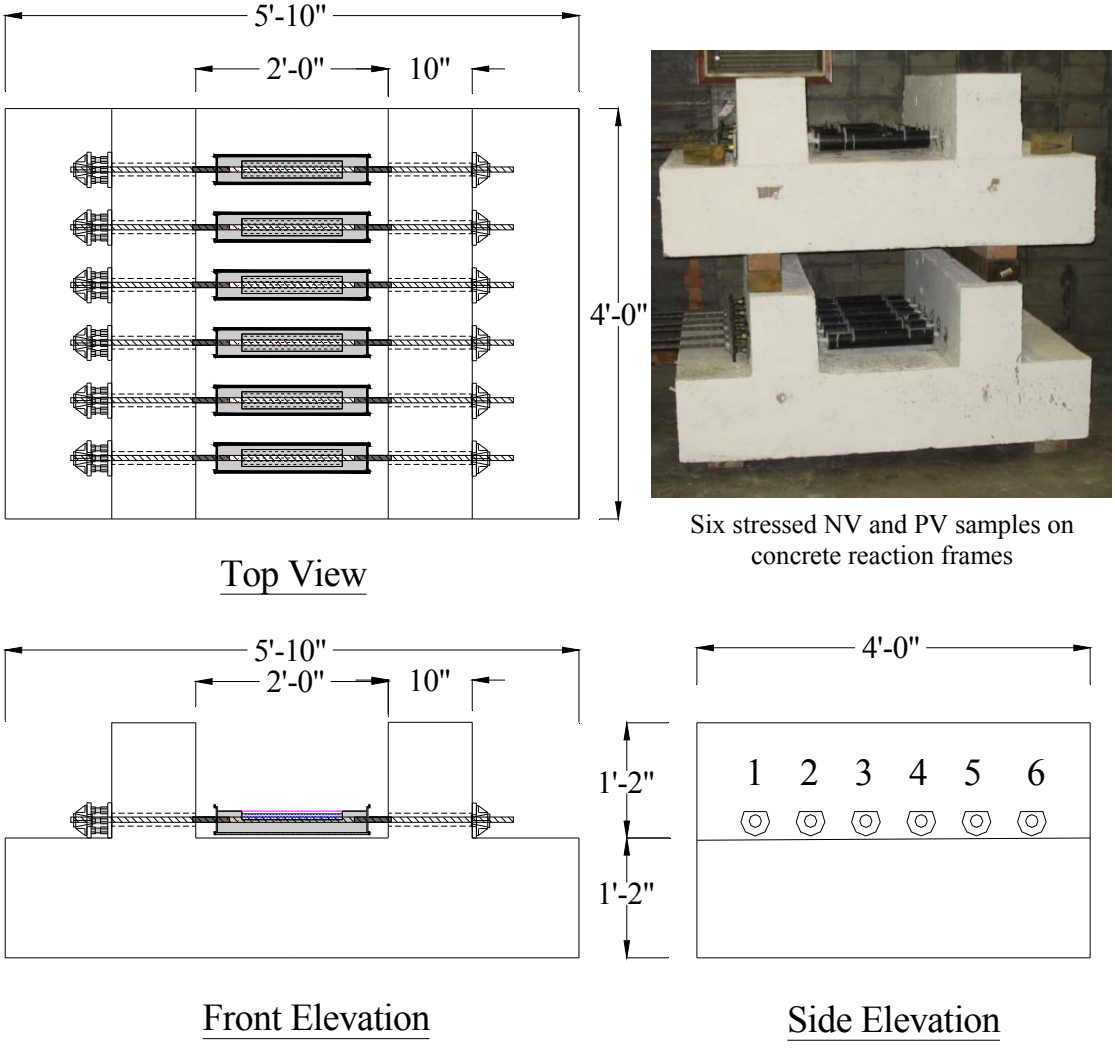


Note: All dimensions are in inches [1 inch = 2.54 mm].

**Figure 5-12. Schematic and Photograph of Horizontal Concrete Reaction Frames With Stressed Strand Specimens.**

*5.5.3.2. Stressing systems*

The stressing system consisted of a monoram with a calibrated pressure gauge, a stress-adjusting system (defined later), an LVDT (attached to the strand being stressed), a computerized data acquisition system (to dynamically read the LVDT data), and a spreadsheet program (to calculate the required jacking and remaining axial stresses). The strand end at which the monoram was attached during stressing was known as the live end and the other end is known as the dead end. In Figure 5-11, the live and dead ends of each stressed strand are shown at the top and bottom regions, respectively. In Figure 5-12, the live and dead ends of each stressed strand are shown at left and right sides, respectively. Figure 5-13 shows more detailed schematics and photographs of the live and dead ends.

The system at live end, as shown in Figure 5-13(a), is defined here as a "stress-adjusting system," which consists of three 0.75 inch (19 mm) diameter and 1.5 inch (38 mm) long bolts, corresponding hexnuts, and two face plates. The front face plate was 5×5×0.5 inch (127×127×13 mm) in size. The back face plate was 4×4×0.5 inch (102×102×13 mm) in size. Both face plates have a center hole through which the strand can pass. The head of the three bolts on the system is welded to the front face plate on which it is resting. The three hexnuts rest on the bottom face plate. The dead end consists of a standard system with one anchor plate and two wedges (see Figure 5-13(b)).

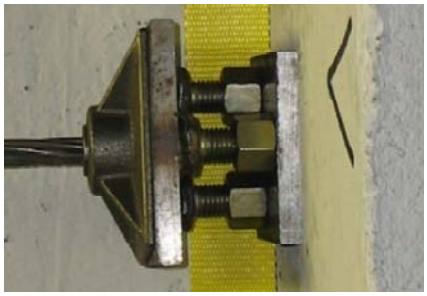

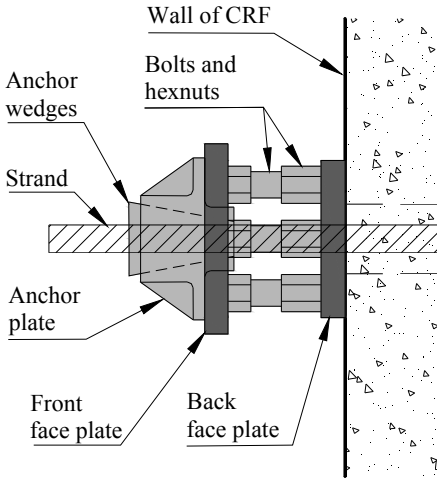


(a) Live end of stressing (shown at top and left side in Figure 5-11 and Figure 5-12, respectively)

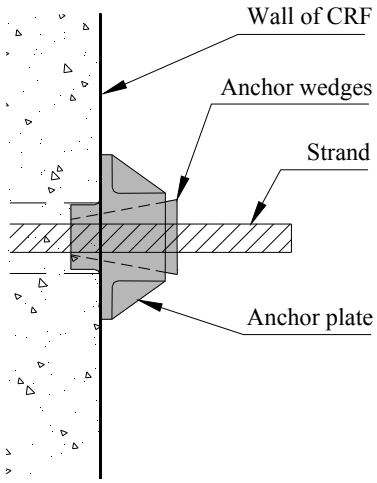


(b) Dead end of stressing (shown at bottom and right side in Figure 5-11 and Figure 5-12, respectively)

**Figure 5-13. Schematics and Photographs of (a) Live and (b) Dead End of the Stressed Strand on a Concrete Reaction Frame.**

During the stressing operations, the shortening of the strand was measured using the LVDT setup shown in Figure 5-14. A 10-inch (250-mm) long and 0.812-inch (21-mm) diameter LVDT (Schaevitz Model 2000 HR) with a nominal linear travel range

of ±2 inches (±51 mm) was used. The LVDT was connected to the strand using a special clamping system designed and fabricated in the laboratory. The clamping system consisted of two toggle clamps with neoprene pads and a knife edge (see right hand figure in Figure 5-14). The body of the LVDT was connected to the right toggle clamp. The core of the LVDT is connected to the left toggle clamp using a 10-inch (250-mm) long steel all-thread. The distance between the two knife edges was 22 inches (560 mm). This is because the inside-to-inside distance between the walls of the CRF was 24 inches (610 mm). The lead wire of the LVDT was connected to the laptop computer with a LabView® data acquisition program. The measured shortening was used to calculate the stress loss.

A spreadsheet program was prepared to calculate the stress loss using the AASHTO LRFD Specifications (2007) formulations. This was also used to calculate the required jacking stress for repeated stressing operations of each strand (as discussed later). The six strands were sequentially stressed in the CRF.

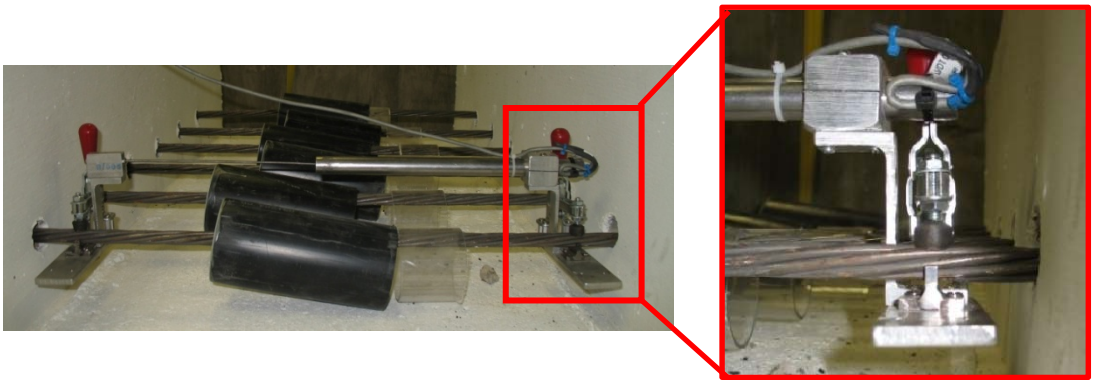

LVDT measurement setup with two toggle clamps  Clamping system

**Figure 5-14. LVDT Setup to Measure the Strand Shortening During Stressing Operation.**

*5.5.3.3. Stressing operations*

A sequential stressing operation was adopted to stress the six strands in each CRF. The sequence (or order) of stressing was selected in such a way that the possible unbalanced forces are minimized. The six strands on each CRF are indicated in the top and side elevation views in Figure 5-11 and Figure 5-12. On each CRF, the third strand was stressed first. The fourth, second, fifth, first, and sixth strands were then sequentially stressed. Each strand was repeatedly stressed until the required level of $f_{axial}$ was attained. Figure 5-15 shows the schematic and photograph of the live end of the stressing setup in detail.

The strand was initially kept in place with the CRF. Then the "stress-adjusting system" is kept on the strand and the steel chair is kept in between the monoram and the wall of the CRF, as shown in Figure 5-15. Then the V-grip on the monoram is manually tightened. The hydraulic pump is then switched on and the required jacking stress (calculated using the spreadsheet program) is applied. Then, as the monoram is resting on the steel chair, the three hexnuts are adjusted using an open-ended wrench. (To facilitate manual adjusting of the hexnuts, there should be no stress acting on them during the jacking operation. This is achieved by bypassing the jacking forces from the monoram to the strand though the steel chair. In other words, there will be no stress acting on the anchor plates or wedges at the time of jacking. The stress will be transferred to the anchor plates and wedges only after releasing the monoram.) The pump is then released and the strand will shorten because of the additional seating of the anchor wedges and compression of the stress-adjusting system, crushing of concrete, etc. The overall strand shortening is measured using an LVDT and the data acquisition system. The measured shortening is recorded and the stress loss is calculated using a spreadsheet program, which also calculates the additional required jacking stress. Then the same strand is stressed again using the same procedure discussed above. This process is repeated until sufficient stress is attained on the strand. Based on stress loss formulation in AASHTO LRFD Specifications (2007), the average stress on each strand

during the exposure periods of 12 and 21 months were estimated to be 150.4 ksi (1037 MPa) with a standard deviation of 2.6 ksi (17.9 MPa).

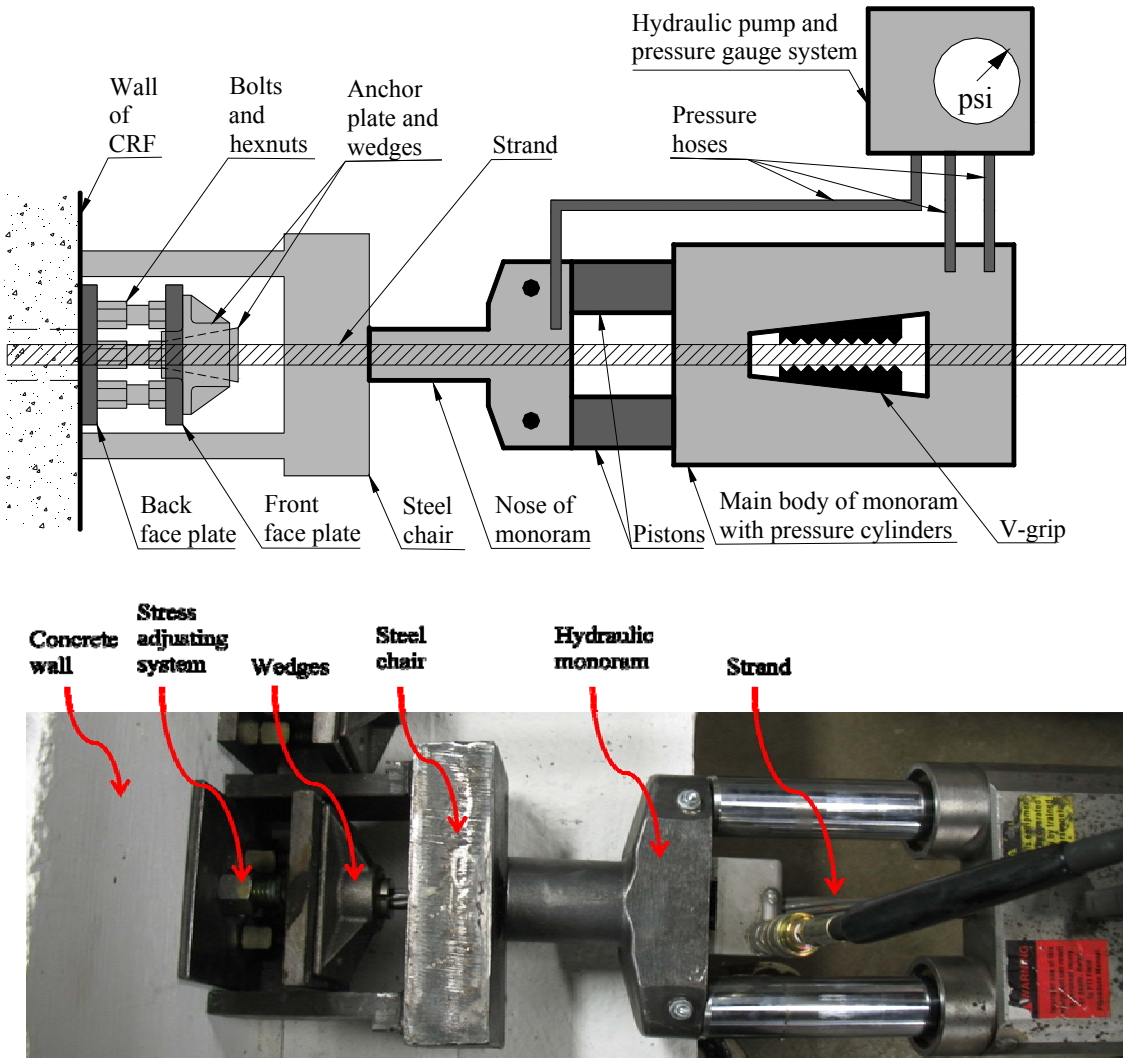


**Figure 5-15. Schematic and Photograph of Strand Stressing Setup.**

### 5.5.4. Casting, curing, and exposure procedures

#### *5.5.4.1. Strand specimens*

Figure 5-9, shown earlier, provides the schematic of the strand specimens. All the strand specimens were prepared using 41-inch (1041-mm) long ASTM A416 strand pieces obtained from the same spool, heat, and lot. The 3-inch (76-mm) diameter HDPE pipe molds were prepared to facilitate casting of the grout for the strand corrosion specimens as follows. Schematics of the NV and PV samples are shown in Figure 5-9(a) and (b). HDPE pipes that are 18 inches (457 mm) long and capped at both ends were used to cast these samples. The capped pipes were cut along the length such that a 2 × 18 inch (51 × 360 mm) opening is formed. A 0.75-inch (19-mm) diameter hole was then drilled through the end caps. The strands were then placed through these end holes. The joints on the mold were sealed using water-proof silicone. Schematic of an OV sample is shown in Figure 5-9(c). HDPE pipes that are 7 inches (178 mm) long and capped at one end were used to cast these samples. A 0.75 inch (19 mm) diameter hole was then drilled on caps at one end of the pipes. The strands were then inserted through this hole. All the joints were sealed using water-proof silicone. Schematics of the IV and BV samples are shown in Figure 5-9(d) and (e). To cast these samples, HDPE molds were prepared in the same way as was done for the OV samples, except that one end of the pipe was cut at $45^{o}$ angle. For all the specimens, the strands were placed and positioned inside the molds such that the NV, PV, OV, IV, and BV are formed after grouting. The strands were also fastened to the mold (using adhesive tape, as needed) to avoid movement while grouting. In the case of the unstressed strand specimens, temporary wooden frames were prepared to support the strands and molds while casting the specimen. In the case of stressed strand specimens, the strands and molds were self-supported by the CRFs. Freshly prepared grout was then placed in the space between the strand and HDPE molds (see Figure 5-9). Note that, in the case of the stressed strands, grouting was done after finishing the stressing operations.

These unstressed strand specimens were then cured (immediately after initial setting) at 73±3°F (23±1.5°C) and 95±5 % *RH* conditions for 28 days. The stressed strand specimens were cured at laboratory conditions at approximately 70-85 °F (21-29°C) and 50 to 70% *RH* for 28 days. After 28 days, each strand specimen was exposed to a pre-defined *MC* and %$sCl^-$ level (see Subsection 5.5.2) using WD exposure to solutions with various chloride concentrations. Each WD cycle consisted of a two-week wet (or ponding) period followed by a two-week dry period. In Figure 5-9, the reservoir and ponding solutions are indicated by letters "R" and "P." At the end of the exposure period, the stressed strand specimens were immediately removed from the CRFs using a cutting torch. The grout materials covering the unstressed and stressed strands were also immediately removed and the strands were visually assessed for corrosion characteristics and tested for tension capacity.

#### *5.5.4.2. Wire specimens*

Figure 5-10 shows the schematic and photograph of the wire corrosion test specimen (exposed to an OV condition). Each wire specimen was prepared using a 7-inch (178-mm) long king-wire that was obtained from the ASTM A416 strand. The standard plastic, self-standing, 1.5-inch (38-mm) diameter centrifuge tube with a conical bottom was used as the mold to cast the wire corrosion test specimen. The conical bottom facilitated the positioning of the wire at the center of the cylindrical grout covering. The cast specimens were then exposed to WD or CA conditions. The experimental designs were shown and discussed earlier in Table 5-12 and Table 5-13.

For the WD conditions, the %$sCl^-$ was attained by exposing the specimens to a WD environment using 0.0001, 0.006, 0.018, 0.18, and 1.8%$sCl^-$ solutions. A schematic of the test setup for the WD exposure is shown in Figure 5-16.

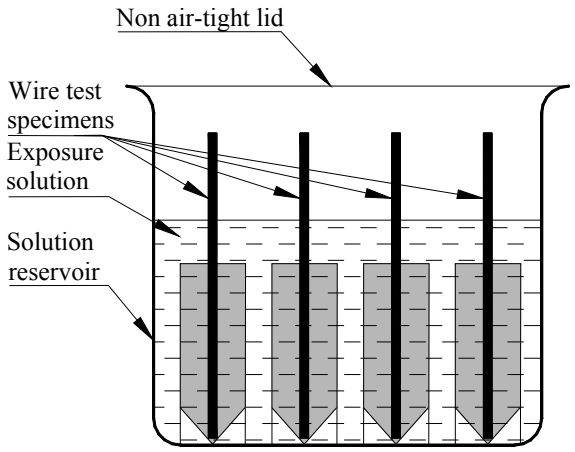


**Figure 5-16. Exposure of Wire Specimens to WD Conditions.**

For the wire specimens tested under CA exposure conditions, GAS interfaces with different chloride levels were obtained by immersing the specimens into 0.0001, 0.006, 0.018, 0.18, and 1.8 $\%sCl^-$ solutions. The specimens were immersed in the solutions after one day after casting and continued for three days. Using the SHRP (1992) test procedure, the representative $\%gCl^-$ at the GAS interface of these test specimens were determined to be 0.0001, 0.014, 0.092, 0.343, 0.782, respectively. The wire specimens with different $\%gCl^-$ levels were then placed in controlled environments with pre-defined levels of *RH* and *T*, as shown in Table 5-13. The *RH* and *T* were controlled as discussed in the following paragraphs.

To maintain a 100% *RH*, the ASTM D5032, *Standard practice for maintaining constant relative humidity by means of glycerine solutions*, was followed. According to this, distilled water inside an air-tight container will maintain 100% *RH* for an air-column of 10 $inch^3$ (16.4 $cm^3$) or less per $inch^2$ (per $cm^2$) of water surface. Following this approach, the wire specimens were kept inside a $6 \times 6 \times 10$ inch ($150 \times 150 \times 250$ mm) air-tight plastic containers, as shown in Figure 5-17. The plastic molds used to cast the wire specimens were not removed and the water level inside the

containers was kept below the GAS interface. This was done to keep the wire or the GAS interface region free from direct contact with water. Note that this arrangement does not prevent the potential formation of $H_2O$ molecules (due to condensation) at the GAS interface region or on the wire surface. Three such setups, as shown in Figure 5-17, were prepared and were kept in walk-in environmental rooms with *T* of 43, 85, and 94°F (6.1, 29.4, and 34.4°C), respectively.

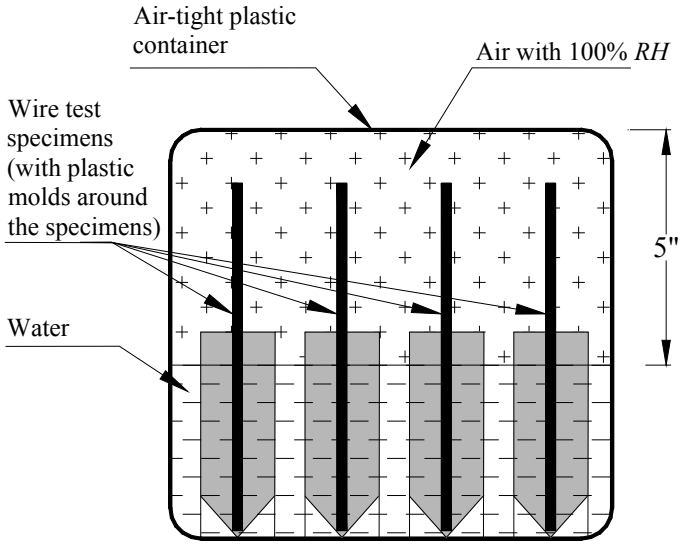


**Figure 5-17. Exposure of Wire Specimens to CA Conditions with 100% *RH*.**

To maintain a 45 or 70% *RH*, the test setups as shown in Figure 5-18 were developed. In this setup, the wire specimens were kept inside a 32 × 19 × 16 inch (8128 × 483 × 406 mm) air-tight plastic container. The volume of this container was 31 gallons (117 liters). This much air-volume was necessary to effectively control the *RH*, using the "*RH*-control system" discussed later. Three such air-tight containers were fabricated and were kept inside three walk-in environmental rooms with a *T* of 43, 85,

and 94$^{o}$F (6.1, 29.4, and 34.4$^{o}$C), respectively. The *RH* inside this container was controlled using an "*RH*-control system" consisting of two Drierite® columns, one container with a water-soaked sponge, four solenoid valves, two manual ball valves, and two mini-fans. These components were connected using clear, flexible nylon tubing (shown in light and dark grey colors in Figure 5-18) to carry air to and from the air-tight container. The solenoid valves and mini-fans were connected to a dual-channel electronic controller (shown in the photograph; not shown in the schematic). The first channel of the controller was set such that when the *RH* is two percent less than the pre-defined level, the solenoid valves #1 and #2 will open and the mini-fan #1 will switch on resulting in a flow of air through the "moist-air cell." The sponge inside the "moist-air cell" is soaked with water. Because of this, the water-body attains an effectively larger surface area and more $H_2O$ molecules can continuously diffuse into the atmosphere inside the "moist-air cell." Therefore, the dry-air flowing into the "moist-air cell" becomes moist. The moistened air then flows back into the air-tight container with the wire specimens resulting in an increase in *RH*. The second channel of the electronic controller was also set such that when *RH* was two percent greater than the pre-defined level, the solenoid valves #3 and #4 will open and the mini-fan #2 will switch on resulting in a flow of air through the drierite tube. The dried air flows back into the air-tight container resulting in a reduction in *RH*. Mini-fan #3 was run continuously to facilitate good air circulation in the container. During the preliminary development of the setup, it was found that Drierite® becomes saturated with moisture within a week. Because of this a second drierite tube (as a back-up) was installed on each setup. Only one drierite tube was used (selected using the manual ball valve) at a time, while the other was being de-saturated or dried.

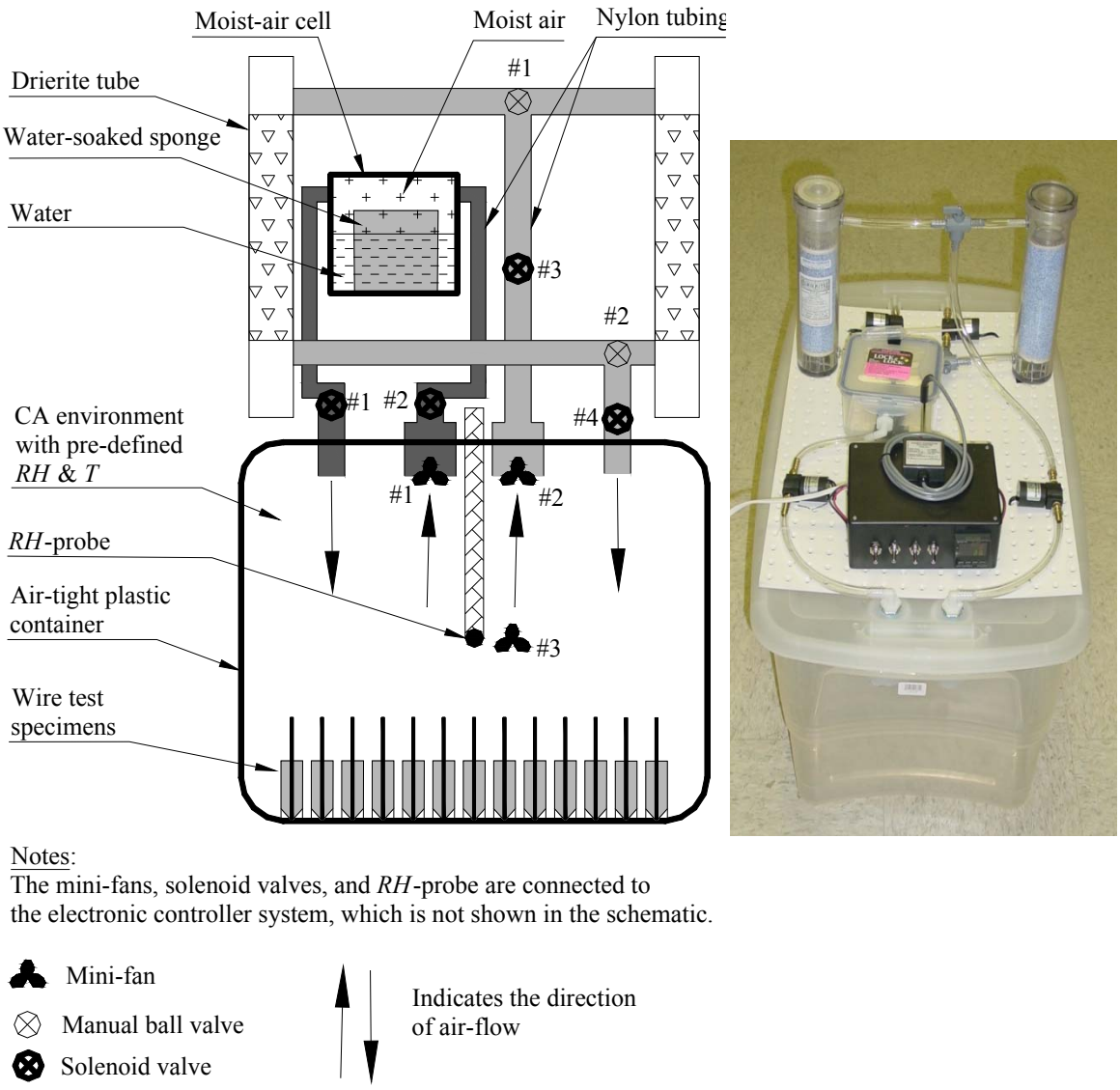


**Figure 5-18. Exposure of Wire Specimens to CA Conditions with 45 and 70% *RH*.**

As discussed, all the wire specimens were exposed to WD and CA exposure conditions. At the end of the pre-defined exposure period (see Table 5-12 and Table 5-13), the grout material on the wire specimens was removed. The exposed wire specimens were then inspected for corrosion characteristics, as discussed next.

### 5.5.5. Corrosion evaluation procedures

Subsection 2.4 provided a review of existing methods to clean and inspect strands in field. In the current research program, wires and strands were hand-rubbed with a synthetic cleaning pad until the loose corrosion products or rust were removed. In addition, small steel wire brushes were used to remove harder corrosion products that were difficult to remove with the synthetic cleaning pad. Photographs and micrographs of the GAS interfaces on strand and wire specimens were then collected. These photographs were then used to characterize surface corrosion, pitting corrosion, corrosion at or near GAS interfaces, or other unique patterns that could be found on corroding PT strands. These photographs of corroded PT strands (taken after cleaning) were compared with the corresponding tension capacity and can be used as a visual tool to estimate the tension capacity of strands in actual PT structures.

### 5.5.6. Tension capacity determination or estimation procedures

Tension capacities of the strand and wire specimens were determined using separate procedures. These procedures are discussed next.

#### *5.5.6.1. Strand specimens*

The remaining tension capacity of the corroded strands were determined using ASTM A 370-02, Standard test methods and definitions for mechanical testing of steel products, and ASTM E 111-02, Standard test method for Young's modulus, Tangent modulus, and Chord modulus. A 400-kip (1780-kN) universal testing machine was used for the testing and was equipped with steel hydraulic jaws and aluminum plates to grip the strand specimens at each end. Each aluminum plate (made of Alloy 2024 meeting ASTM B 211-03 and with a T351 temper) was 0.75-inch (19-mm) thick, 2-inch (50-mm) wide, and 7-inch (178-mm) long and had a 7-inch (178-mm) long semi-circular groove with a 0.25-inch (6-mm) radius. Prior to testing, a 7-inch (178-mm) long "as-received"

strand was placed along the groove and sandwiched between the two plates and then compressed to 250 kips (1112 kN) such that spiral indentations were formed. These grooved surfaces allowed for better seating of the strand specimen and reduced slip. Also, a thick paste made of aluminum oxide and glycerin was applied inside the grooves to improve the grip. This gripping setup also helped to minimize the stress concentration at the grips. The elongation over the 24-inch (610-mm) gage length between the two grips was measured using a LVDT (with ±2 inches (±51 mm) nominal travel range) fastened to the strand using a knife-edge holder.

#### *5.5.6.2. Wire specimens*

Tension capacities of 7-inch (178-mm) long wire specimens exposed to WD conditions were evaluated using a 100-kip (445-kN) tension testing machine and following ASTM A 370-02 and ASTM E 111-02 standard test procedures.

Among the 61 wire samples exposed to the various CA conditions for a period of 9 months, the tension capacity of 15 samples was determined using a 100-kip (445-kN) tension testing machine and ASTM A 370-02 and ASTM E 111-02 standard test procedures. Some of these wire capacity values were statistically similar to the pristine wire capacity. However, localized corrosion was visible at GAS interfaces of these specimens and they failed in tension or broke at the GAS interface region. This indicates that the weakest cross section was at or near the GAS interface region and there was very small reduction in tension capacity, which *was not sufficient or sensitive enough for the 100-kip (445-kN) tension testing equipment and standardized laboratory testing procedures to reliably determine.* However, it was necessary to estimate this small reduction in tension capacity to develop the probabilistic models in section 9.1. An *indirect* or *novel* approach is developed to calculate the tension capacity of unstressed wires, $C_{T,UW}$, using the corresponding cross-sectional area loss of unstressed wire samples, $A_{loss,\ UW}$.

$A_{loss,\ UW}$ was determined using a Dektak® 3 Stylus profilometer, which can measure vertical profiles ranging in height from $3.94 \times 10^{-7}$ to $2.56 \times 10^{-3}$ inches (10 to 65,000 nm) and has a stylus tracking force equal to $1.1 \times 10^{-4}$ lb ($4.9 \times 10^{-4}$ N). At first, the wire specimens were cleaned using the synthetic pad, as described in Subsection 5.5.5. Figure 5-19 depicts the procedure to calculate cross-sectional area using surface replicating media and a profilometer.

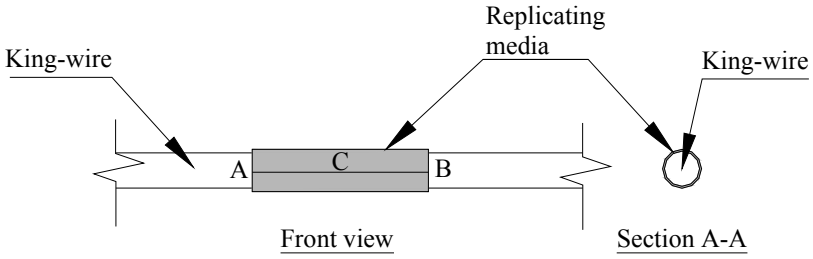


**a) Replicating media on GAS interface region on a wire specimen**

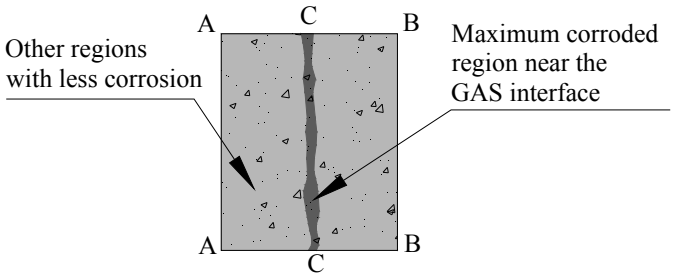


**b) Typical inside face of an cut-opened replicating media**

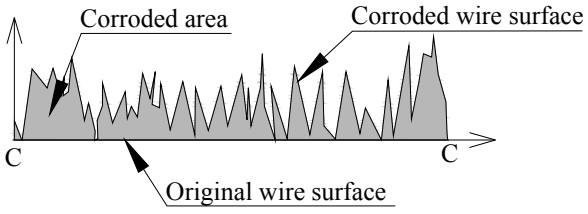


**c) Typical profile obtained using Dektak 3 Stylus profilometer**

**Note: All drawings are not on same scale.**

**Figure 5-19. Cross-sectional Area Measurement Using Surface Replicating Media and Profilometer.**

Figure 5-19(a), (b), and (c) are not drawn to same scale and, hence, the letters 'A', 'B', and 'C' are used as reference points. Then, as shown in Figure 5-19(a), the GAS interface region on the wire specimen was covered with a surface replicating media (Model No. 57-6002 manufactured by Beuhler Ltd.). The cured replicating media was cut through the line segment $\overline{AB}$ on Figure 5-19(a) and removed from the wire specimen. Figure 5-19(b) shows the inside face of the cured replicating media, which was in contact with the wire surface. The surface profile along the darker center-region in Figure 5-19(b) represents the profile of the GAS interface region and was then obtained using Dektak® 3 Stylus profilometer. Figure 5-19(c) shows a typical surface profile obtained using this technique. The shaded region in Figure 5-19(c) indicates $A_{loss,\ UW}$ and is calculated using the Dektak® 3 software.

A graphical representation of the analytical procedure to determine $C_{T,UW}$ at 9 months is provided in Figure 5-20. Note that the Figure 5-20 is not drawn to scale.

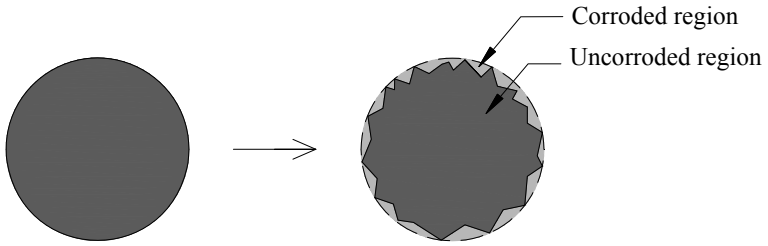


**Pristine wire** **Corroded wire**

Assumptions at $t_{CA}$ = 0 months:

$A_{ARW} = 0.0337 \text{ inch}^2 \ (21.71 \text{ mm}^2)$

$C_{T,ARW} = 9.30 \text{ kips } (41.37 \text{ kN})$

Estimations at $t_{CA}$ = 9 months:

$$A_{UW} = A_{ARW} - A_{loss,UW}$$

$$C_{T,UW} = \left( \frac{C_{T,ARW}}{A_{ARW}} \right) A_{UW}$$

**Figure 5-20. A Graphical Representation of the Analytical Determination of Tension Capacity of Wire Specimens Under 9-month CA Exposure.**

The detailed procedures for the analytical determination of $C_{T,UW}$ at 9 months using $A_{loss,UW}$ at 9 months are as follows:

1. The capacity of pristine wire, $C_{T,UW}$, is defined and assumed as follows:

$$C_{T,ARW}\big|_{max} = Max(C_{T,all\ ARW}) = 9.30 \text{ kips } (41.37 \text{ kN}) \tag{5.3}$$

   Due to material heterogeneity, measurement error, and other reasons, there exists a small scatter (ranging approximately 0.2 kips) among the pristine wire capacity values observed. Moreover, the cross-sectional area loss at $t_{CA}$ equal to 9 months, $A_{loss,\ UW}$ at 9 months was very small. In order to numerically express the corresponding small capacity loss at 9 months, a deterministic value for $C_{T,ARW}$ needs to be assumed. Also, in order to avoid the mathematical problems of obtaining a negative capacity loss, $C_{T,ARW}$ has to be set larger than or equal to all the experimentally observed wire capacities. In all the tension testing of wires, the largest capacity observed was 9.3 kips. Hence, $C_{T,ARW}$ is assumed to be 9.3 kips.

2. The cross-sectional area of pristine wire, $A_{ARW}$, , is assumed as follows:

$$A_{ARW} = \frac{\pi d_{ARW}^2}{4} = \frac{3.14 \times 0.207^2}{4} = 0.034 \text{ inch}^2 \ (21.7 \text{ mm}^2) \tag{5.4}$$

   where, $d_{ARW}$ = diameter of pristine wire.

3. Determine $A_{loss,UW}$ at $t_{CA}$ equal to 9 months using surface profilometry techniques given in Subsection 5.5.6.

4. Determine the available cross-sectional area of wires, $A_{UW}$ , at $t_{CA}$ equal to 9 months as follows:

$$A_{UW} = A_{ARW} - A_{loss,UW} \tag{5.5}$$

5. Estimate the corresponding wire capacity loss, $C_{T,UW}$, at $t_{CA}$ equal to 9 months as follows:

$$C_{T,UW} = \left( \frac{A_{ARW}}{C_{T,ARW}} \right) A_{UW} \tag{5.6}$$

Now, the superset of capacity data for wire specimens under CA exposure conditions can be developed by combining the capacity data obtained from both tension testing (15 wire specimens) and surface profilometry/analytical procedures (46 wire specimens). Although some of these data are analytically estimated or derived, this wire capacity will be referred to as "observed" or "measured" wire capacity herein. The full data set is provided in Appendix A.

## 5.6. SUMMARY

This section presented the details of the experimental program. First, the characteristics of the materials used in this experimental program were discussed. Then the objectives, design, layout, and procedures of various test programs were discussed. The test programs presented were cyclic polarization, galvanic corrosion, and strand/wire corrosion tests.

# 6. ELECTROCHEMICAL AND TENSION CAPACITY BEHAVIOR OF WIRES AND STRANDS - RESULTS

## 6.1. INTRODUCTION

This section presents the electrochemical and tension capacity results from the experimental program presented in Section 4. The electrochemical characteristics obtained from the cyclic polarization tests are presented first. The galvanic corrosion characteristics obtained form the modified ASTM G109 and bearing plate tests are then presented. Following this, the corrosion pattern observed on the tension capacity, $C_T$, of strand and wire corrosion test specimens are presented. The the critical parameters influencing $C_T$ of strands are then identified.

## 6.2. CYCLIC POLARIZATION TEST RESULTS

Subsection 5.3 presented the experimental program and procedures on cyclic polarization tests. Subsection 5.3.1 defined some electrochemical terms used in cyclic polarization curves. Figure 6-1(a), (b), and (c) show the cyclic polarization curves for ASTM A416 steel specimen when immersed in simulated concrete pore solutions with hydroxides and 0.0, 0.06, and 1.8 $\%sCl^-$. The solid-arrows along the curve indicate the direction of scan (i.e., forward and reverse scans). The horizontal dashed-arrows indicates the electrochemical parameters (i.e., $E_b$, $E_{rp}$, and $E_{pp}$) defined in Subsection 5.3. Note that all the potentials discussed in this subsection are measured with reference to that of Saturated Calomel Electrode ($E_{SCE}$).

Cyclic polarization curves in Figure 6-1(a) and (b) show negative hysteresis indicating that the passive films formed on the steel surface are either self-repaired or corrosion pits are not initiated when immersed in simulated pore solutions with 0.0 and

0.06 %$sCl^-$. However, the curve in Figure 6-1(c) shows a positive hysteresis. This indicates that either the passive films are not repaired or corrosion pits initiate when the ASTM A416 steel is immersed in simulated pore solution with 1.8 %$sCl^-$.

The Open Circuit Potential, OCP, of the ASTM A416 steel specimen when immersed for one hour in simulated pore solutions with 0.0, 0.06, and 1.8 %$sCl^-$ was determined to be approximately –0.370, –0.380, and –0.390 Volts, respectively. This indicates that the OCP remained approximately constant as the %$sCl^-$ increased from 0.0 to 0.06 and 1.8. When immersed in simulated pore solutions with 0.0, 0.06, and 1.8 %$sCl^-$, the electrical currents measured corresponding to the open circuit conditions were $3.7\times10^{-6}$, $4.7\times10^{-6}$, and $8.4\times10^{-6}$ Amps/inch$^2$ ($0.57\times10^{-6}$, $0.73\times10^{-6}$, and $1.30\times10^{-6}$ Amps/cm$^2$), respectively. This indicates 1.3 and 2.3 times increase in the open circuit current as %$sCl^-$ increases from 0.0 to 0.06 and 1.8, respectively.

The breakdown potential, $E_b$, in Figure 6-1(a) and (b) are 0.500 Volts and that in Figure 6-1(c) is approximately 0.400 Volts. This indicates that the passive film on ASTM A416 steel breaks down at a lower potential when immersed in 1.8 %$sCl^-$ solutions than when immersed in 0.0 or 0.06 %$sCl^-$ solutions, which would be expected.

When immersed in simulated pore solutions with 0.0 %$sCl^-$, the primary passivation potential, $E_{pp}$, was approximately –0.250 Volts. $E_{pp}$ was approximately –0.100 Volts, when immersed in simulated pore solutions with 0.06 and 1.8 %$sCl^-$. Although these values are approximate, they indicate that passive films on ASTM A416 steel immersed in simulated pore solutions with 0.06 and 1.8 %$sCl^-$ are stable when the potential is between –0.100 Volts and the corresponding $E_b$. These values show that the window of the passive region decreases as %$sCl^-$ increases. The variation in the environment in the field could induce a variation in the potential of PT strands; indicating more probability for active corrosion to occur with a narrower window of passive region.

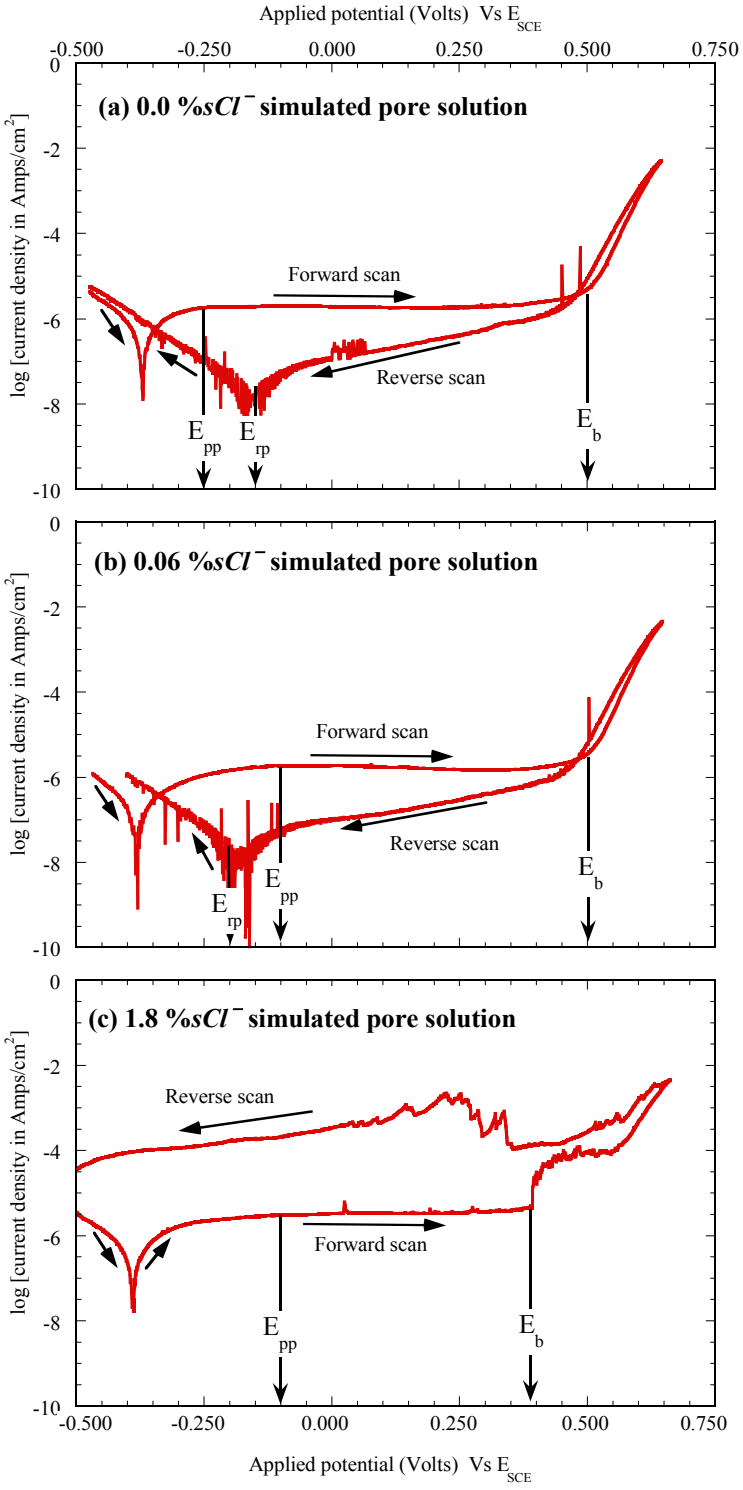


Negative hysteresis
$E_b$ = 0.500 Volts
$E_{pp}$ = – 0.250 Volts (approx.)
$E_{rp}$ = – 0.150 Volts (approx.)

Negative hysteresis
$E_b$ = 0.500 Volts
$E_{pp}$ = – 0.100 Volts (approx.)
$E_{rp}$ = – 0.200 Volts (approx.)

Positive hysteresis
$E_b$ = 0.400 Volts (approx.)
$E_{pp}$ = – 0.100 Volts (approx.)
$E_{rp}$ = not determined

**Figure 6-1. Cyclic Polarization Curves for ASTM A416 Steel.**

The repassivation potential, $E_{rp}$, was determined to be –0.150 and –0.200 Volts, when immersed in simulated pore solutions with 0.0 or 0.06 %$sCl^-$. When immersed in the simulated pore solution with 1.8 %$sCl^-$, a positive hysteresis was observed and repassivation did not occur during the cyclic polarization test. Because of this, $E_{rp}$ could not be determined. However, it can be concluded that $E_{rp}$ is more negative than –0.490 Volts, the potential at which the cyclic polarization test was started and ended.

Table 6-1 summarizes the approximate active, passive, and transpassive potential regions for the ASTM A416 steel. These potential regions are determined based on the forward scans in Figure 6-1(a), (b), and (c). In general, the passive region becomes narrower as %$sCl^-$ increases.

**Table 6-1. Approximate Active, Passive, and Transpassive Potential Regions for the ASTM A416 Steel.**

| Simulated pore solution with | Active region | Passive region | Transpassive region |
|---|---|---|---|
| 0.0 %$sCl^-$ | < –0.250 Volts | Between –0.250 and +0.500 Volts | > +0.500 Volts |
| 0.06 %$sCl^-$ | < –0.100 Volts | Between –0.100 and +0.500 Volts | > +0.500 Volts |
| 1.8 %$sCl^-$ | < –0.100 Volts | Between –0.100 and +0.400 Volts | > +0.400 Volts |

The broken passive films on the steel surface are self-healed and a negative hysteresis is observed when exposed to 0.00 and 0.06 %$sCl^-$ simulated concrete pore solution. The broken passive films are not repaired and a positive hysteresis is observed when exposed to 1.8 %$sCl^-$ solution. Based on this observation, it can be concluded that the critical chloride threshold level for the steel meeting the ASTM A416 specifications is in between 0.06 and 1.8 %$sCl^-$.

## 6.3. GALVANIC CORROSION TEST RESULTS

This subsection presents the results obtained from the Modified ASTM G109 and bearing plate tests presented in Subsection 5.4.

### 6.3.1. Modified ASTM G109 test results

Figure 6-2 and Figure 6-3 show the total corrosion observed on the modified ASTM G109 samples with WD exposure conditions to 0 and 9 %$sCl^-$ solutions, respectively. In Figure 6-2 and Figure 6-3, the hollow and solid data markers indicate the samples cast with Class A and C grouts, respectively. In both Figure 6-2 and Figure 6-3, the samples with Class A and C grouts show similar corrosion behavior. Figure 6-2(a) show the total corrosion on the samples with similar anode and cathode material (i.e., non-galvanic samples) and exposed to 0 %$sCl^-$ solution. Figure 6-2(b) show total corrosion on the samples with dissimilar anode and cathode material (i.e., galvanic samples) and exposed to 0 %$sCl^-$ solution. The total corrosion in both Figure 6-2(a) and (b) are negligible and similar in nature. This indicates that the presence of moisture only cannot initiate galvanic corrosion between the ASTM A416 and A615 steel at the anchorage zones in PT systems. The absence of galvanic corrosion also indicates that the corrosion potentials of ASTM A615 and A416 steels are similar when no-chloride conditions exist.

Figure 6-3(a) and (b) show the total corrosion on the non-galvanic and galvanic samples, respectively, exposed to 9 %$sCl^-$ solution. In general, the total corrosion was similar in both non-galvanic and galvanic samples. However, some samples in Figure 6-3 (b) show a slightly earlier onset of corrosion than that in Figure 6-3 (a). However, this difference is not sufficient to clearly state that galvanic corrosion occured in the latter case. Further experiments with more parameter combinations are needed; but not performed as part of this study.

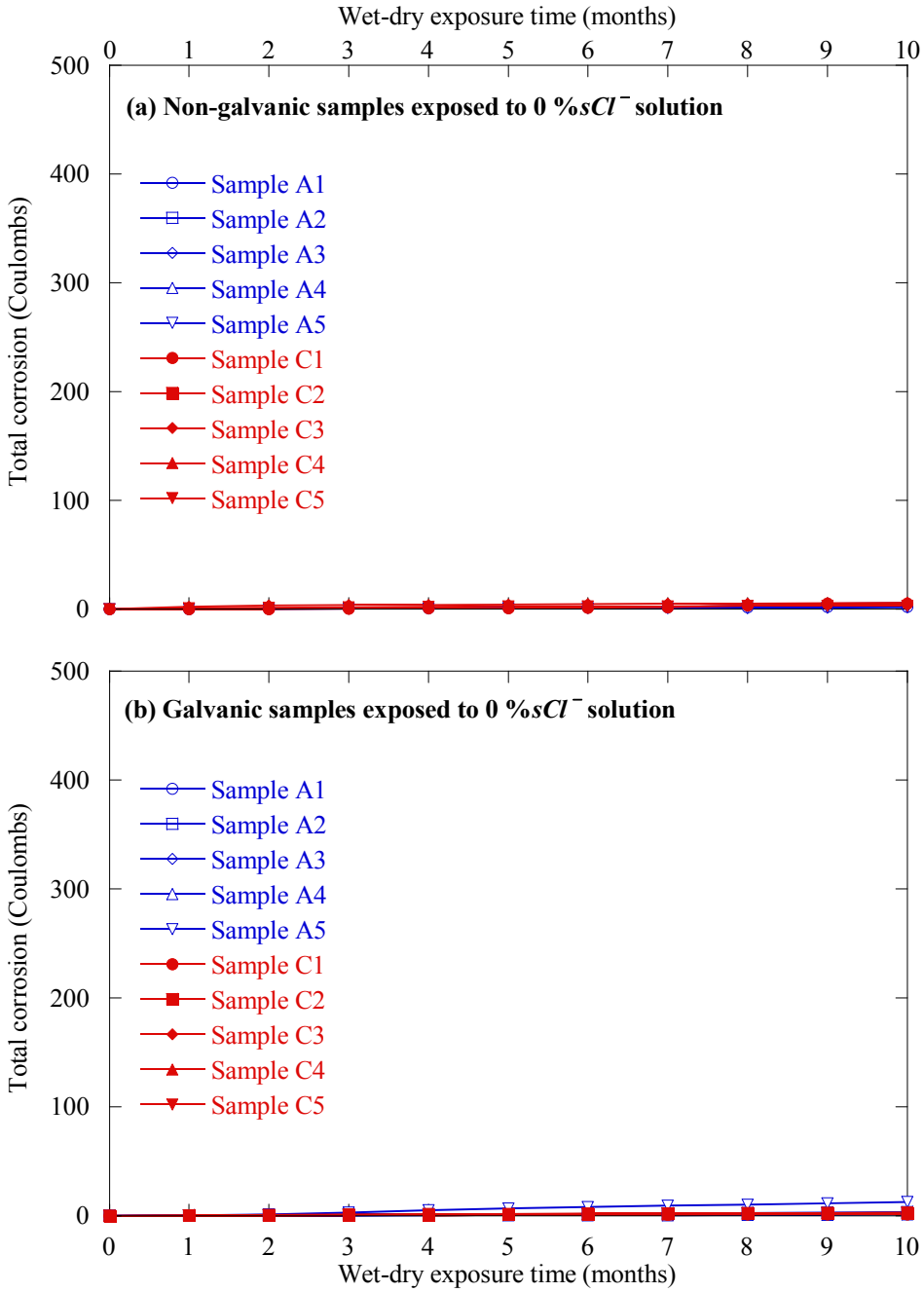


**Figure 6-2. Total Corrosion on the Modified ASTM G109 Samples With Wet-dry Exposure to 0 %$sCl^-$ Solution.**

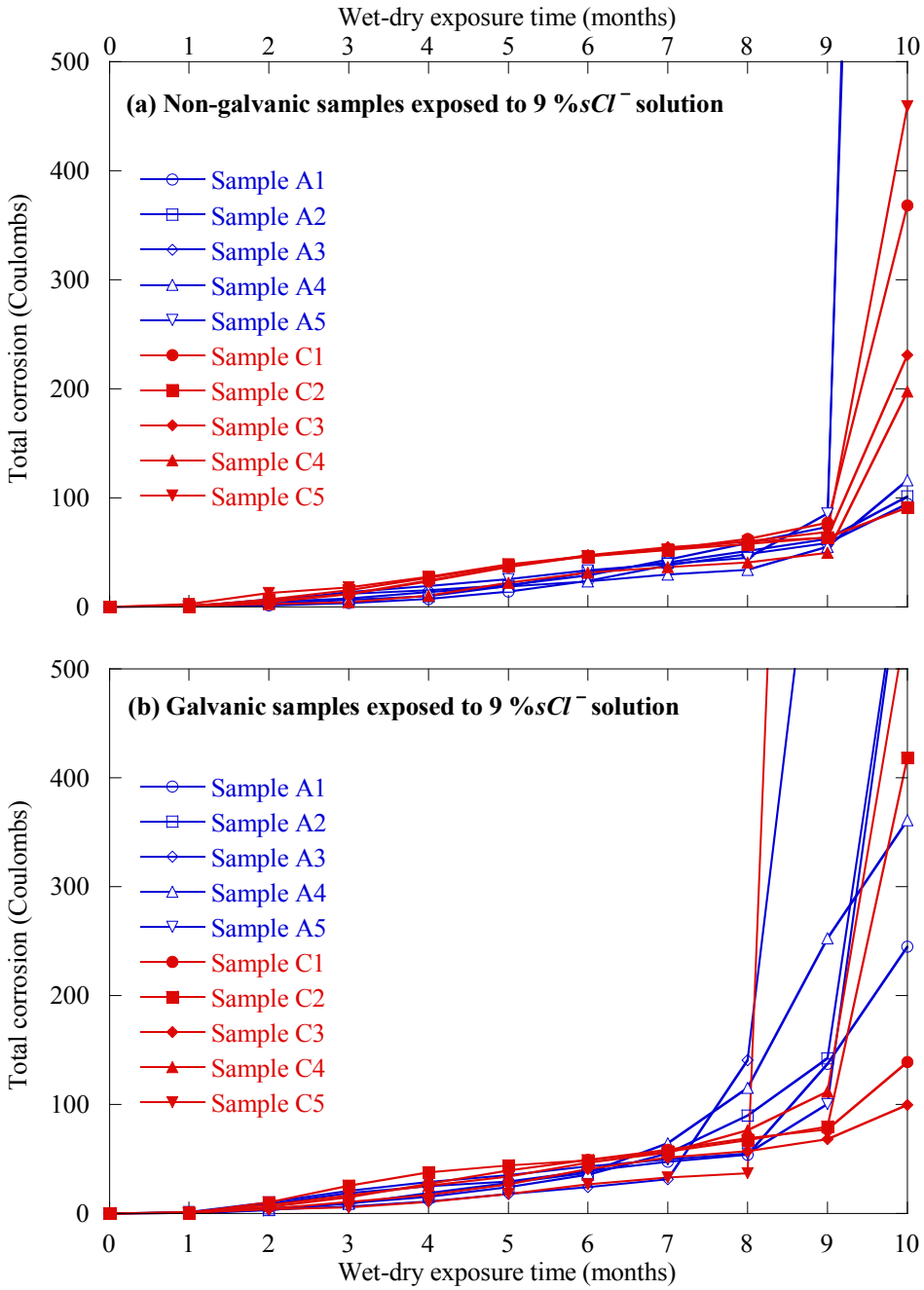


**Figure 6-3. Total Corrosion on the Modified ASTM G109 Samples With Wet-dry Exposure to 9 %*sCl*⁻ Solution.**

### 6.3.2. Bearing plate test results

Subsection 2.3.1 indicated that cast iron is more noble than steel when immersed in seawater. Figure 6-4 and Figure 6-5 show the total corrosion observed on the bearing plate samples with WD exposure to 0 and 9 %$sCl^-$ solutions, respectively. In both Figure 6-4 and Figure 6-5, active corrosion of the conventional spiral reinforcement initiated at approximately 9 months (or after 9 WD cycles). This indicates that the galvanic corrosion between ASTM A615 and A536 (cast iron) does occur and moisture alone is sufficient to initiate galvanic corrosion between ASTM A615 and A536 in PT systems.

The modified ASTM G109 tests indicated that the corrosion potentials of ASTM A615 and A416 steels are similar. Bearing plate tests indicate that galvanic corrosion can occur between ASTM A615 and A536 steels. Using these two results, it can be concluded that moisture alone is sufficient to initiate galvanic corrosion between ASTM A416 and A536 in PT systems. Also, the presence of high amounts of chlorides can accelerate corrosion between ASTM A416 and A536 in PT systems.

These test results indicate that the surface of the bearing plates may be coated with epoxy or other non-conductive material such that the galvanic corrosion between bearing plate and other metallic materials in the PT systems can be minimized.

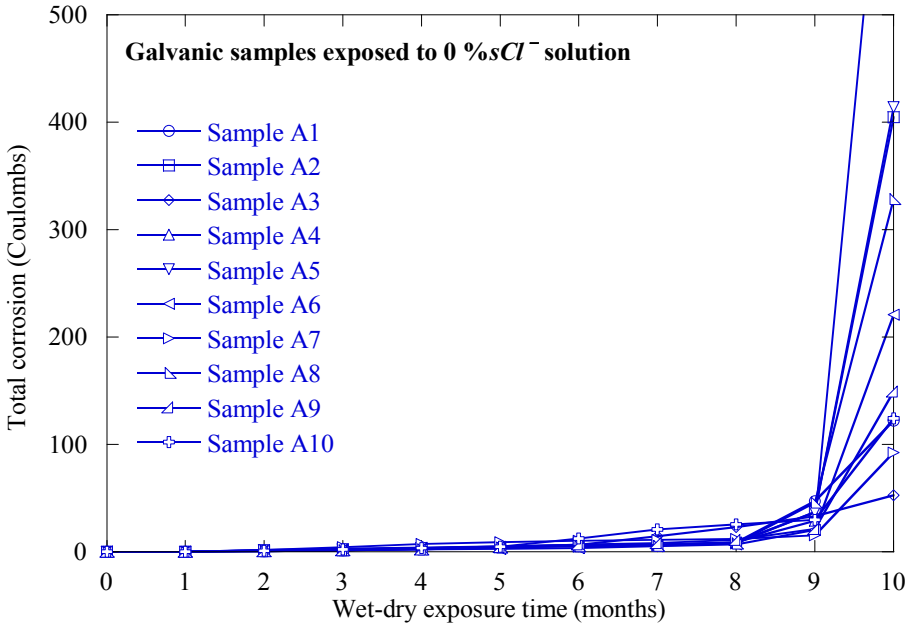


**Figure 6-4. Total Corrosion on the Bearing Plate Samples (0 %$sCl^-$ solution).**

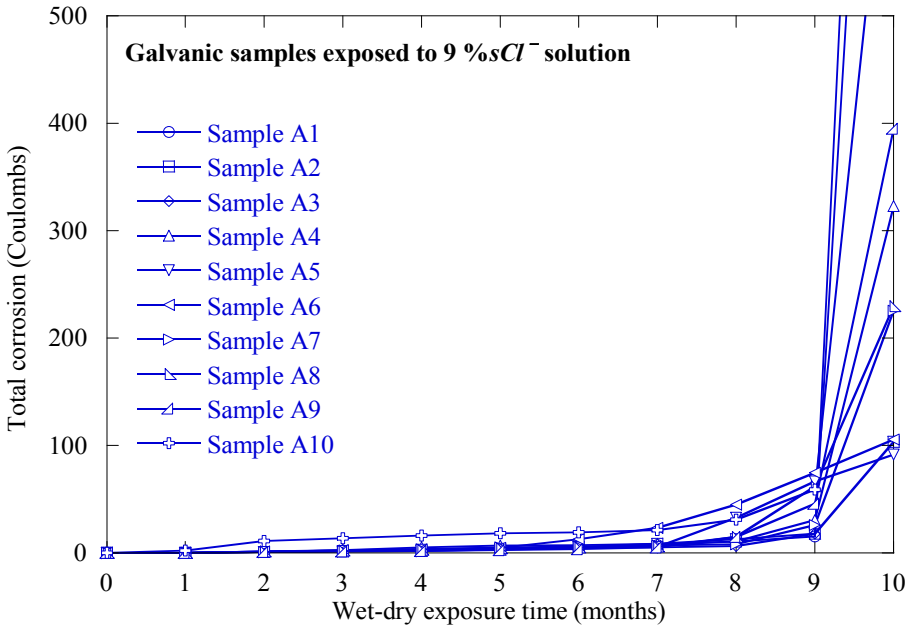


**Figure 6-5. Total Corrosion on the Bearing Plate Samples (9 %$sCl^-$ solution).**

## 6.4. STRAND AND WIRE CORROSION TEST RESULTS

This subsection presents experimental observations from the strand and wire corrosion test programs. The details of the experimental program were provided earlier in Subsection 5.5. A discussion on general observations of the cleaned strand and wire surfaces are provided first. Then a collection of photographs of corroded strands to estimate the $C_T$ of strands is provided. Following this, dot plots showing $C_T$ data generated from the strand and wire corrosion tests are provided.

### 6.4.1. General visual observations

PT strands are made of six outer wires spiraled around a straight center king wire resulting in a flower-like cross-sectional geometry. This geometry includes interstitial spaces between the king wire and outer wires. These small interstitial spaces may initiate and propagate crevice and other accelerated forms of corrosion. However, the gradual build-up of corrosion products in the interstitial spaces could result in reduced oxygen availability at these spaces, thus slowing the corrosion process. These conditions could lead to a more severe corrosion at the outer wire surface than on the center king wire. Figure 6-6 shows micrographs of a strand exposed to wet-dry conditions with high $\%sCl^-$, resulting in severe pitting corrosion. These pits are not clearly visible in Figure 6-6. However, they were visible using a microscope and were similar to the pits observed on reinforcement surfaces in chloride contaminated concrete systems. Most of this corrosion damage occurred near the GAS interface. In addition, the examination of the micrograph indicates linear patterns of corrosion along the longitudinal axis of the outer wires. This could be attributed to the surface treatment during the cold wire drawing or manufacturing process. The adverse effect of this maximum corrosion near the GAS interface was validated when the strands failed at the GAS interface during tension testing. Wire corrosion test specimens also exhibited similar type of corrosion behavior near the GAS interface.

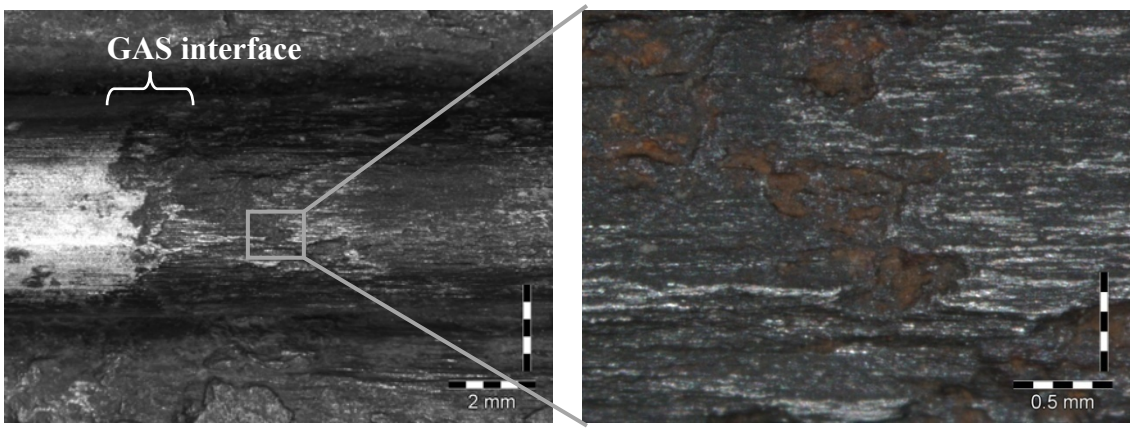


(a) (b)

**Figure 6-6. Micrographs Showing (a) Localized Corrosion Near Grout-air-strand (GAS) Interface; (b) Linear and Pitting Patterns of Corrosion.**

### 6.4.2. Estimating tension capacity from strand photographs

The first column in Figure 6-7 shows typical photographs of cleaned surfaces of corroded strands and their remaining $C_T$ generated from this test program. The second column in Figure 6-7 shows the definitions of the types of corrosion observed. Figure 6-7(a) shows the surface of an "as-received" strand, which showed a $C_T$ equal to 60.1 kips (267.4 kN). Figure 6-7(b) shows that minor pitting corrosion can cause the $C_T$ to fall below $MUTS_{ARS}$ (i.e., 58.6 to 57.7 kips (260.5 to 256.5 kN)). The observed $C_T$ decreases as more corrosion is observed (see Figure 6-7(c) through (e)). Figure 6-7(f) shows that more localized and pitting corrosion resulted in a greater loss of $C_T$.


Even surface
Low uniform surface corrosion
No pitting corrosion

(a)


Slightly uneven surface
Low localized or pitting corrosion

(b)


Moderately uneven surface
Moderate localized or pitting corrosion

(c)


Highly uneven surface
High localized or pitting corrosion

(d)


Highly uneven surface
High localized or pitting corrosion

(e)


Highly uneven surface
High localized or pitting corrosion

(f)

Note: 1 kip = 4.45 kN

**Figure 6-7. Cleaned Strand Surface, Corrosion Characteristics, and Residual Tension Capacity.**

### 6.4.3. Tension capacities of strand and wire specimens

The purpose of this subsection is to present all $C_T$ data generated from the strand and wire corrosion test programs outlined in Subsection 5.5. The data are graphically presented in Figure 6-8 through Figure 6-12. In addition, the same data in tabular format are presented in Appendix A. This subsection does not provide any statistical or quantitative analyses of the data. Such analyses are provided through the hypothesis testing in Subsection 6.5 and probabilistic modeling in section 7.

#### *6.4.3.1. Unstressed strand capacities under wet-dry exposure conditions*

The experimental design for the unstressed strand corrosion tests under WD conditions was provided in Figure 5-8(a) and Table 5-10 in Subsection 5.5.2.1. Figure 6-8 and Figure 6-9 show the $C_T$ of the unstressed strand specimens after exposure to various corrosive environments. There are thirteen columns in Figure 6-8 and Figure 6-9. The first columns in both Figure 6-8 and Figure 6-9 are identical to the first column in Figure 5-2 and shows the $C_T$ of "as-received" strands. The remaining twelve columns are separated into four groups (i,e., 0.006, 0.018, 0.18, and 1.8 $\%sCl^-$ levels) using vertical dashed lines. For each $\%sCl^-$ level, there are three data columns (with hollow, grey-shaded, and black-shaded data markers) corresponding to $t_{WD}$ equal to 12, 16, and 21 months, respectively. The vertical text "Not tested" indicates a parameter combination that was not tested in the program. For example, the unstressed strand specimens were not tested at 16 months and are indicated using the vertical text "Not tested." The solid-horizontal lines in each column indicate the mean values of $C_T$.

Figure 6-8(a) and (b) show the $C_T$ data corresponding to NV and PV conditions, respectively. Figure 6-9(a) through (d) show the $C_T$ data corresponding to OV, IV, BV, and BIOV conditions. The BIOV condition and the corresponding data were defined in Subsection 5.5.2.1 and represent all the data obtained from the samples exposed to OV,

IV, and BV conditions. This combination will be used to develop the probabilistic models for the BIOV conditions (see section 7).

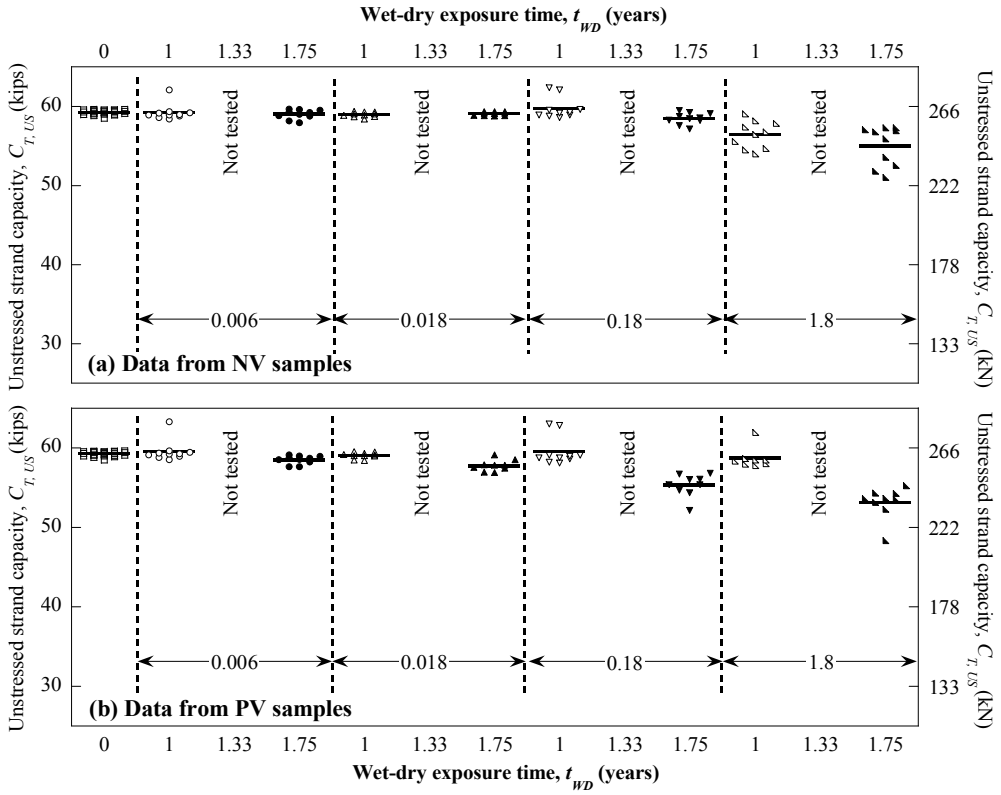


**Figure 6-8. Tension Capacities of Unstressed Strands Exposed to NV and PV Conditions.**

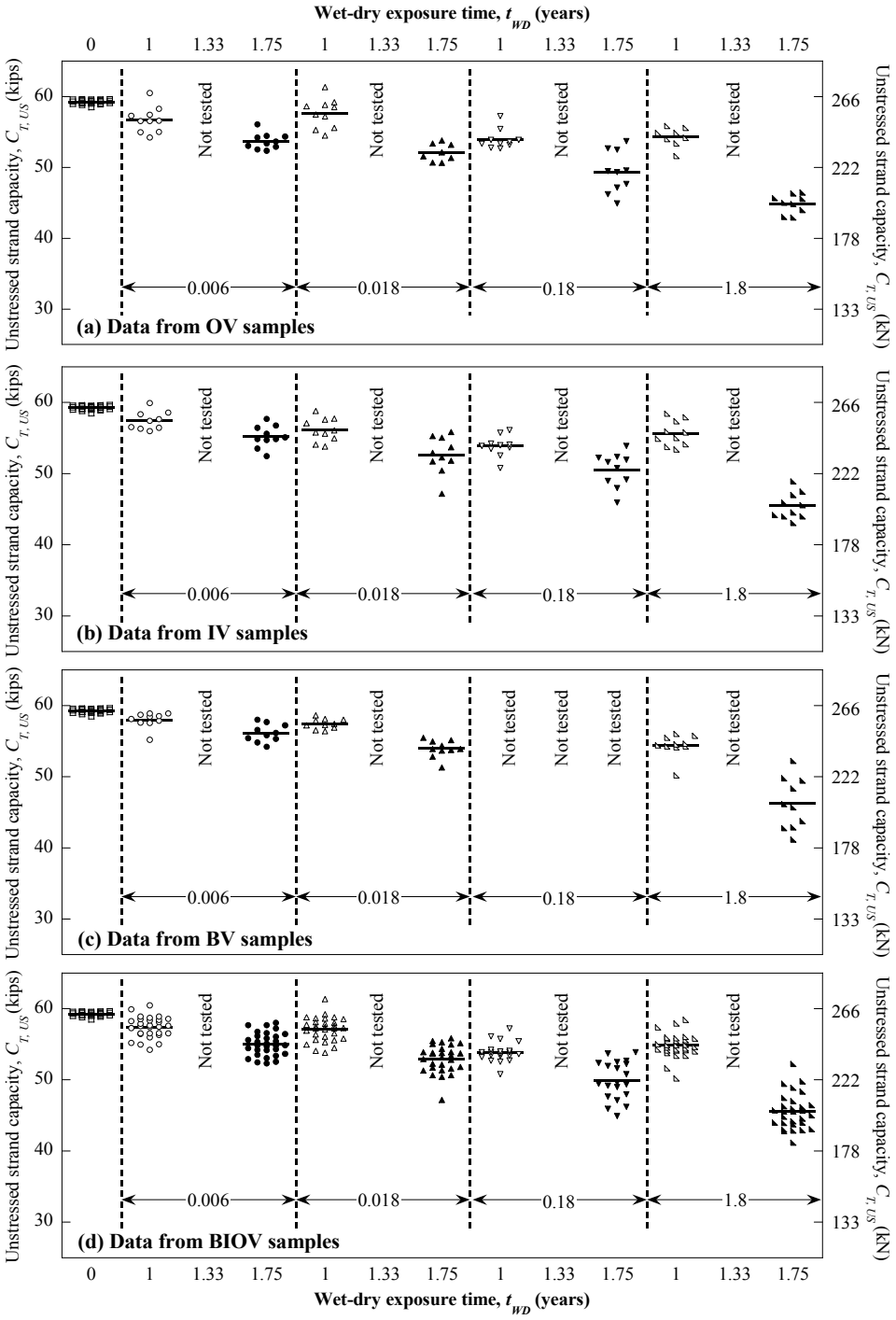


**Figure 6-9. Tension Capacities of Unstressed Strands Exposed to OV, IV, BV, and BIOV Conditions.**

### *6.4.3.2. Stressed strand capacities under wet-dry exposure conditions*

Figure 6-10 shows the $C_T$ obtained from the stressed strand corrosion tests under WD conditions. The experimental design for this test program was provided in Figure 5-8(b) and Table 5-11 in Subsection 5.5.2.1.

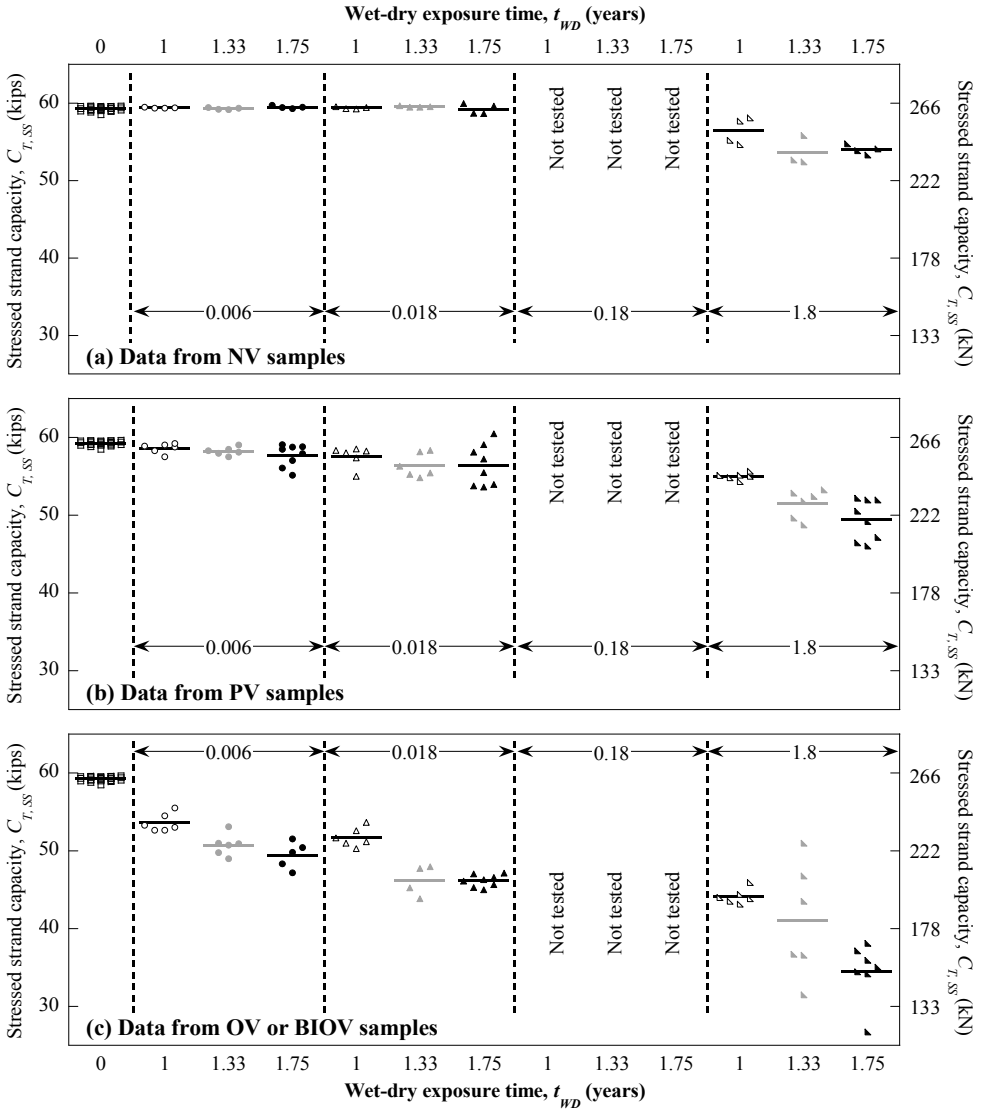


**Figure 6-10. Tension Capacities of Stressed Strands Exposed to NV, PV, and BIOV Conditions.**

Figure 6-10(a), (b), and (c) show the $C_T$ data obtained from the stressed strands exposed to NV, PV, and OV conditions. The stressed strand specimens were not tested at 0.18 %$sCl^-$ level. Also, the stressed strand specimens were not tested under the IV and BV conditions and, hence, only the data from the OV condition are used to develop the probabilistic models for BIOV conditions (see section 7).

#### *6.4.3.3. Unstressed wire capacities under wet-dry exposure conditions*

Figure 6-11 shows the $C_T$ data obtained from the unstressed wire corrosion tests exposed to WD and OV conditions. Figure 5-8(c) and Table 5-12 in Subsection 5.5.2.1 showed the experimental design for this test program. Figure 6-11(a) through (e) show the dot plots with the $C_T$ data obtained from wire specimens exposed to 0.0001, 0.006, 0.018, 0.18, and 1.8 %$sCl^-$, respectively, for 0, 3, 6, 9, and 12 months of exposure. In Figure 6-11(a) through (e), the first column is identical to the second column in Figure 5-2 and shows the $C_T$ of the "as-received" wires. This data from the wire samples with OV conditions will be used to develop the probabilistic models for wires under BIOV conditions (see section 7).

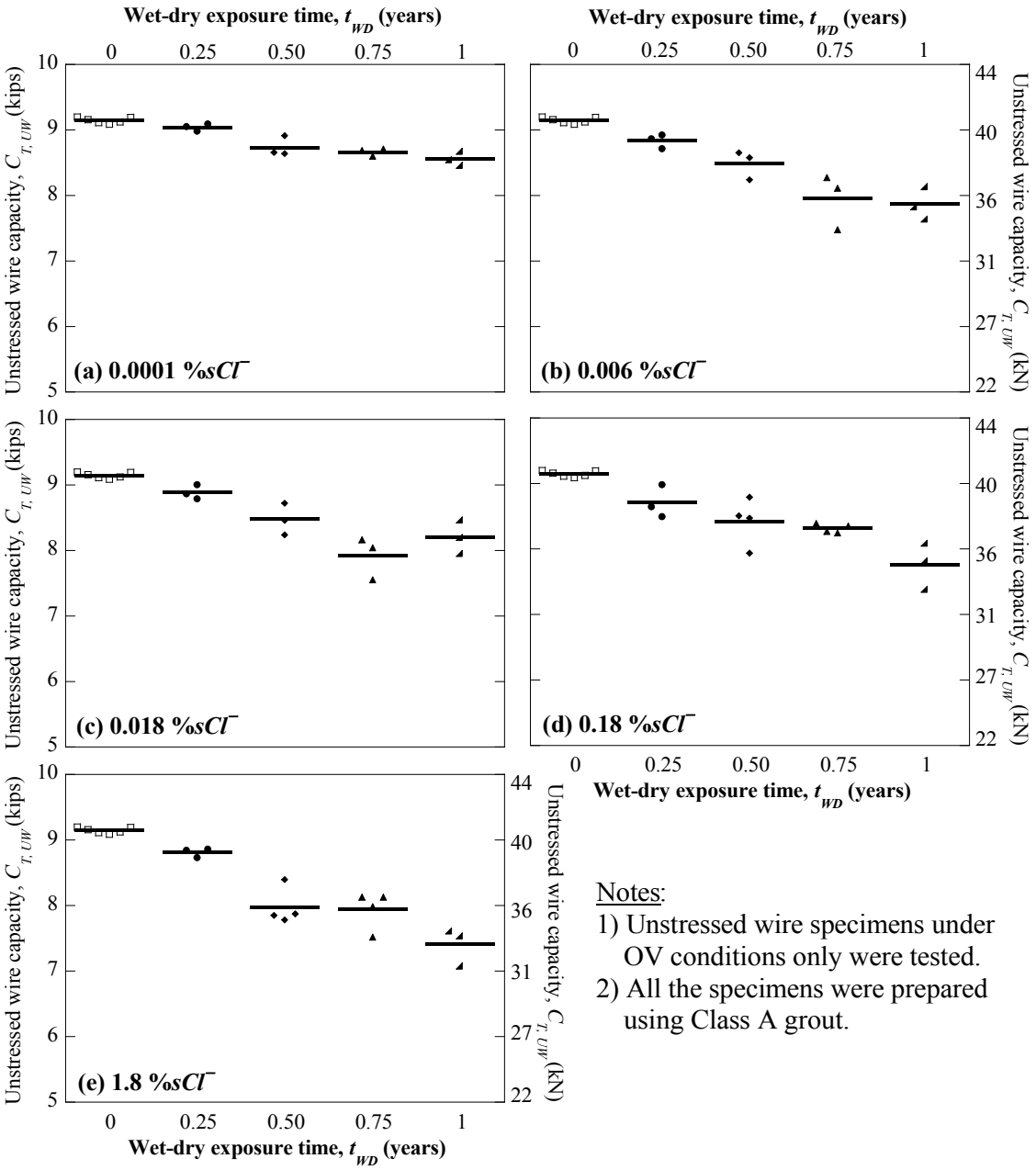


**Figure 6-11. Tension Capacities of Unstressed Wires Exposed to WD and OV Conditions.**

#### *6.4.3.4. Unstressed wire capacities under continuous-atmospheric exposure conditions*

Figure 6-12 shows the $C_T$ data obtained from the unstressed wire specimens exposed to the CA and OV conditions. Figure 5-8(c) and Table 5-13 in Subsection 5.5.2.1 showed the experimental design for this test program. The exposure conditions included three levels of *T*, three levels of *RH*, and five levels of $\%gCl^-$. However, the experimental design was not full-factorial and the data corresponding to some parameter combinations are not available. Figure 6-12(a) through (e) show the $C_T$ data obtained from the wire specimens exposed to 0.00001, 0.014, 0.092, 0.343, and 0.782 $\%gCl^-$, respectively, for 9 months of exposure. The abscissa indicates the level of *RH*. The data corresponding to the three observed levels of *T* (i.e., 43, 85, and 94°F (6.1, 29.4, and 34.4°C)) are shown using different data markers. For clarity in reading, these data are also aligned vertically with the three forks of the temperature-axis positioned at each observed level of *RH* (i.e., 45, 70, and 97%). Most data points except the four data points at 94°F (34.4°C), 97 %*RH*, and 0.782 $\%gCl^-$ in Figure 6-12(e) showed negligible loss in tension capacity. This data will be used to develop the probabilistic models for unstressed wires under CA and BIOV exposure conditions (see Section 7).

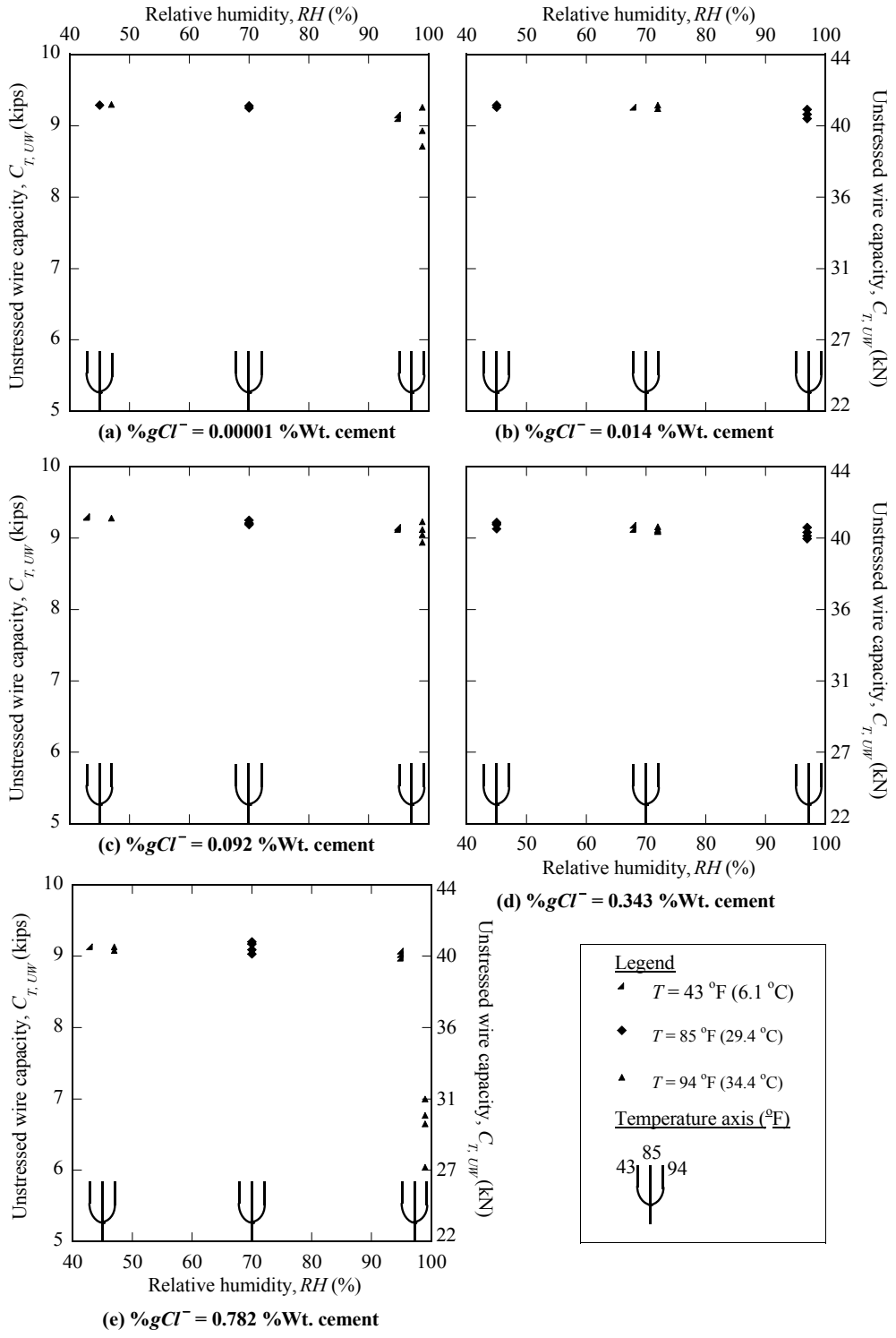


**Figure 6-12. Tension Capacities of Unstressed Wires Exposed to CA and OV Conditions.**

## 6.5. CRITICAL PARAMETERS INFLUENCING TENSION CAPACITY OF PT STRANDS

The unstressed and stressed strand corrosion tests were conducted at various factors/levels of test parameters such as *GC*, *MC*, %$sCl^-$, *VT*, and $f_{axial}$ (see Figure 5-8(a) and (b) and Table 5-10 and Table 5-11 for experimental designs). At the end of each exposure period, the remaining $C_T$ of unstressed and stressed strands was determined. In this subsection, the experimental data obtained at $t_{WD}$ equal to 12 months are used to identify the critical parameters (or statistically significant parameters) influencing $C_T$ of strands. This is done by performing statistical hypothesis tests on two sample data sets. The two sample data sets for each hypothesis test have one parameter at different levels/factors and all the other parameters at identical levels/factors. The procedure to select an appropriate hypothesis test is discussed next.

### 6.5.1. Statistical hypothesis tests

Two-independent sample hypothesis tests are used to check if a change in a test parameter causes a statistically significant change in $C_T$ of strands. At first, determine if the data sets follow normal distribution using the Kolmogorov-Smirnov normality test. If the sample data sets follow normal distributions, the Student's *t*-test can be used to check if a test parameter is significant. If the sample data set do not follow normal distributions, then the Mann-Whitney U (M-W U) test (also called Mann-Whitney-Wilcoxon or Wilcoxon rank sum test) can be used to determine if the test parameter is significant or the two data sets are statistically different. The M-W U hypothesis test is a nonparametric test equivalent to the two–sample Student's *t*–test. It does not make any assumptions about the data distribution and relies on the ranking of the observations. It can also deal with two independent data sets with small and unequal sample sizes, as is the case of tension capacity data sets from most parameter combinations in the current study. Five percent significance level is used for all the hypothesis tests in this study.

### 6.5.2. Effect of grout class

The corrosivity of the cementitious grout depends on the qualitative variable, *GC*, representing the combined effect of the chemical characteristics of the grout material and w/p. The M-W U hypothesis tests on the $C_T$ data sets with Class A and C grouts (all other variables being identical) resulted in large p-values (≈ 1) indicating no statistically significant difference in tension capacity with the change in *GC*. This indicates that, at a void location or GAS interface, both Class A and C grouts are associated with similar amounts of corrosion and $C_T$ loss (indicating similar probability of failure). However, in the field it is likely, based on other studies not reported here (ASBI 2000, FDOT 2001a and b), that Class A (non-thixotropic) grout results in more bleed water and therefore a greater number of voids and cracks than Class C (thixotropic and low-bleed) grouts. Hence, given that other variables and conditions remain the same, the tendons with Class A grout will likely have more void or crack locations with more corrosion than tendons with Class C grouts. This may result in a higher joint probability of failure of tendons with Class A grout than those with Class C grout. However, the current research focuses on conditions where a void or GAS interface exists. Because it is determined that *GC* is not a significant parameter for such conditions, it will not be discussed further.

### 6.5.3. Effect of moisture and chloride conditions

Figure 6-13 (a), (b), and (c) show the $C_T$ of unstressed and stressed strand specimens. Because IV and BV samples were not exposed to high $f_{axial}$ conditions, Figure 6-13 (d) and (e) show only the $C_T$ of only unstressed strand specimens. The data marker in each figure represents a specific combination of *VT*, *MC*, and $\%sCl^-$. The round markers indicate low *MC* level and diamond and triangular markers indicate high *MC* levels. Among these, the hollow and solid markers represent the unstressed and stressed conditions, respectively. Also, the letters U and S in the legend indicates unstressed and

stressed conditions, respectively. The statistical parameters of 12-month $C_T$ results are also summarized in Table 6-2.

Figure 6-13 and hypothesis tests indicate that the samples exposed to 0.0001 $\%sCl^-$ (i.e., standard room environment with *low MC* and no WD cycles) did not experience statistically significant reduction in tension capacity over the 12-month exposure period. Samples with WD exposures (i.e., *high MC*) experienced more corrosion. The samples exposed to 0.006 $\%sCl^-$ (standard water from laboratory sources) experienced severe localized corrosion near the GAS interface but did not experience pitting corrosion because of very small chloride availability. Samples exposed to 0.018, 0.18, and 1.8 $\%sCl^-$ solutions experienced pitting corrosion due to the presence of higher amount of chlorides. Based on the current experimental data, the critical chloride threshold for the strands (under direct exposure) is likely between 0.006 and 0.018 $\%sCl^-$. However, because it seems unnecessary, chloride threshold is not defined and used in this study.

For the NV samples, the M-W U hypothesis test exhibited no statistically significant difference in the $C_T$ as the $\%sCl^-$ level increased from 0.0001 to 0.018 (with levels/factors of all other variables being identical). The p-value of the hypothesis test was 0.0085 indicating a statistically significant difference in $C_T$ as the $\%sCl^-$ increased from 0.018 to 1.8 (with levels/factors of all other variables being identical). In the case of the NV samples with 1.8 $\%sCl^-$, large amount of chlorides precipitated inside the cracks formed in the ¼ inch (6 mm) grout cover and these chlorides were easily transported to the embedded strand surface causing pitting corrosion.

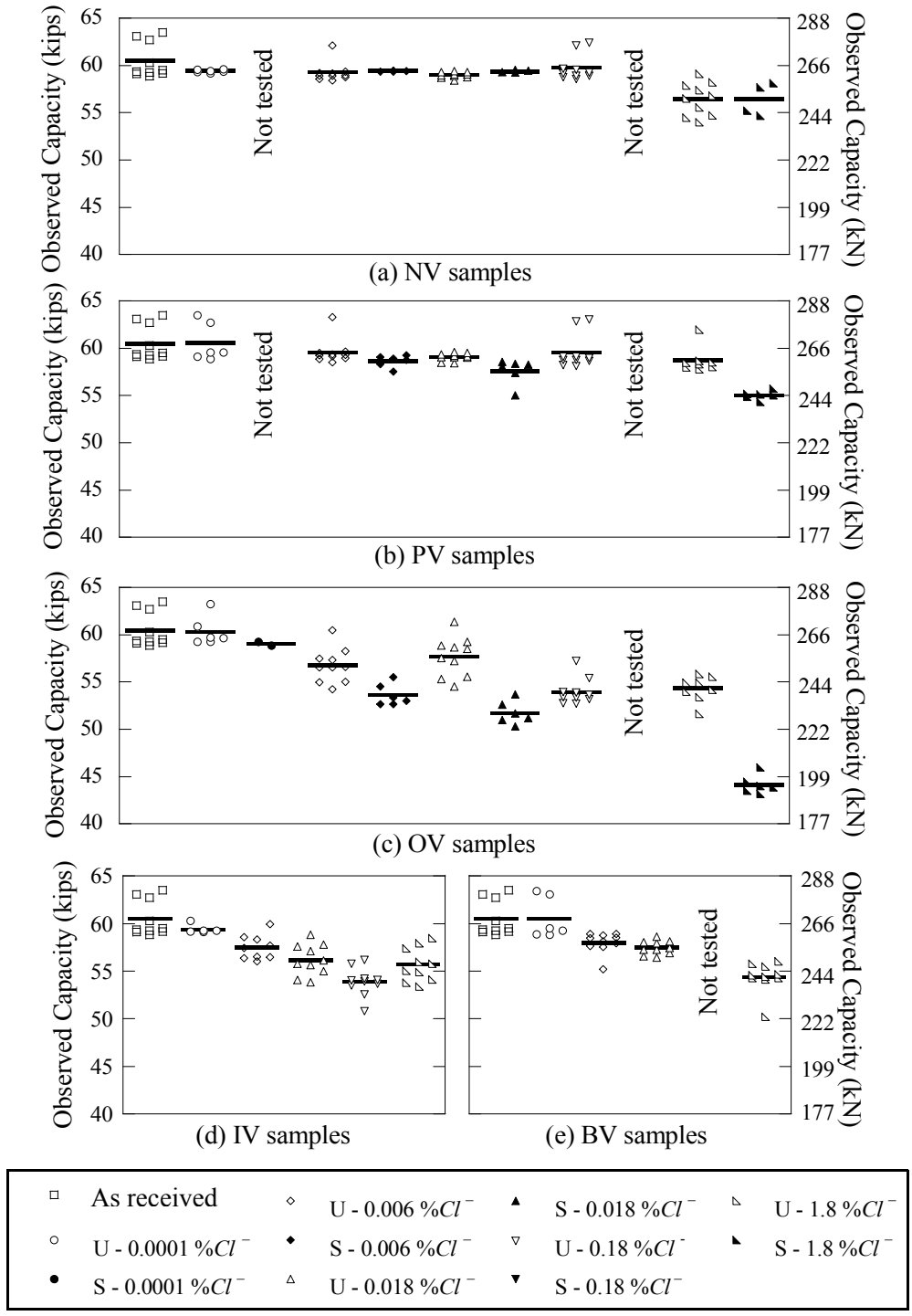


**Figure 6-13. Tension Capacity of Unstressed and Stressed Strand Specimens at the End of 12-months of WD Exposure.**

**Table 6-2. Mean‡, Coefficient of Variation (COV), and Mean Capacity Loss ($C_{T, loss}$)* of Tension Capacities Observed at the End of 12-month WD Exposure.**

| Axial stress level ($f_{axial}$) | Chloride concentration in exposure solution (%sCl⁻) | Statistical parameters | Void type (*VT*) | | | | |
|---|---|---|---|---|---|---|---|
| | | | No void (NV) | Parallel void (PV) | Orthogonal void (OV) | Inclined void (IV) | Bleed water void (BV) |
| ~ 0 ksi (~ 0 MPa) | 0.0001** | Mean (kips) | 59.4 | 60.5 | 60.33 | 59.4 | 60.5 |
| | | COV | 0.003 | 0.033 | 0.026 | 0.008 | 0.036 |
| | | $C_{T, loss}$ (%) | 1.8 | 0.0 | 0.2 | 1.8 | 0.0 |
| | 0.006 | Mean (kips) | 59.2 | 59.6 | 56.8 | 57.5 | 58 |
| | | COV | 0.018 | 0.023 | 0.032 | 0.022 | 0.019 |
| | | $C_{T, loss}$ (%) | 2.0 | 1.5 | 6.2 | 5.0 | 4.1 |
| | 0.018 | Mean (kips) | 59.0 | 59.1 | 57.7 | 56.2 | 57.5 |
| | | COV | 0.005 | 0.006 | 0.036 | 0.029 | 0.013 |
| | | $C_{T, loss}$ (%) | 2.5 | 2.3 | 4.6 | 7.1 | 5.0 |
| | 0.18 | Mean (kips) | 59.7 | 59.6 | 54.0 | 53.9 | - |
| | | COV | 0.023 | 0.030 | 0.026 | 0.028 | - |
| | | $C_{T, loss}$ (%) | 1.2 | 1.5 | 10.8 | 10.9 | - |
| | 1.8 | Mean (kips) | 56.5 | 58.7 | 54.3 | 55.7 | 54.4 |
| | | COV | 0.030 | 0.023 | 0.025 | 0.032 | 0.030 |
| | | $C_{T, loss}$ (%) | 6.6 | 2.9 | 10.2 | 7.9 | 10.1 |
| ~ 150 ksi (~ 1034 MPa) | 0.0001** | Mean (kips) | - | - | 59.1 | - | - |
| | | COV | - | - | 0.500 | - | - |
| | | $C_{T, loss}$ (%) | - | - | 2.3 | - | - |
| | 0.006 | Mean (kips) | 59.4 | 58.6 | 53.6 | - | - |
| | | COV | 0.001 | 0.011 | 0.022 | - | - |
| | | $C_{T, loss}$ (%) | 1.8 | 3.0 | 11.4 | - | - |
| | 0.018 | Mean (kips) | 59.4 | 57.6 | 51.7 | - | - |
| | | COV | 0.002 | 0.023 | 0.024 | - | - |
| | | $C_{T, loss}$ (%) | 1.8 | 4.8 | 14.4 | - | - |
| | 1.8 | Mean (kips) | 56.4 | 55.0 | 44.2 | - | - |
| | | COV | 0.031 | 0.008 | 0.022 | - | - |
| | | $C_{T, loss}$ (%) | 6.7 | 9.0 | 27.0 | - | - |
| Strands with negligible corrosion | | Mean (kips) | 59.27 | | | | |
| | | COV | 0.0049 | | | | |

‡ 1 kip = 4.45 kN

* $C_{T, loss}$ greater than 0.0049% indicates that the mean $C_T$ is less than the $MUTS_{ARS}$.

** Specimens were kept in standard room conditions and not exposed to wet-dry cycle.

\- Indicates that no samples were tested.

The average $C_T$ values (horizontal bar) in Figure 6-13 (d) shows an increase in remaining $C_T$ as the $\%sCl^-$ increased from 0.18 to 1.8. However, this is misleading because the p-value of the M-W U hypothesis test (at 5 percent significance level) between these two data sets was 0.0433, which is very close to the critical value of 0.05. Because $0.0433 \approx 0.05$, it can be concluded, on a rational basis, that the remaining $C_T$ of the IV samples exposed to 0.18 and 1.8 $\%sCl^-$ are statistically similar. Moreover, because of the variability in the corrosion-induced loss in the $C_T$, conclusions should not be made based only on average values, which do not represent the variability in the behavior even in controlled laboratory experiments. Figure 6-13 shows a general trend of increased corrosion activity for all void types with increased *MC* and $\%sCl^-$ levels. Also, the M-W U tests indicate that the *MC* and $\%sCl^-$ are significant parameters influencing $C_T$.

### 6.5.4. Effect of stress conditions

The NV, PV, and OV sample conditions were assessed for the effect of stress level. Both unstressed and stressed samples experienced similar reductions in $C_T$ when completely embedded in grout (i.e., the NV samples). Also, the p-values obtained in the corresponding M-W U tests were larger than 0.05; indicating no evidence to reject the null hypothesis that the $C_T$ of the NV samples with unstressed and stressed conditions are equal. This behavior is likely due to the passive protection by the uncontaminated and alkaline cementitious grout at the strand surface. When voids were present (i.e., PV and OV samples) the stressed samples exhibited significantly higher losses in the $C_T$ than that exhibited by the corresponding unstressed samples. For example, the M-W U test on the unstressed and stressed samples with PV and OV conditions at 1.8 $\%Cl^-$ resulted in a p-value of 0.002. The p-value from the M-W U test on the unstressed and stressed PV samples at 0.006 $\%Cl^-$ was 0.034 and that for M-W U test on unstressed and stressed OV samples at 0.006 $\%Cl^-$ was 0.005. A p-value less than 0.05 provides evidence to reject the null hypothesis that the stress level does not cause changes in tension capacity. Hence, the stress level is a statistically significant parameter affecting

the corrosion and $C_T$ of strands in void conditions. The general differences in the $C_T$ of the unstressed and stressed specimens were most significant with the OV samples exposed to 1.8 $\%Cl^-$; the condition representing a column or anchorage zones in girders with tendons exposed to chloride environments. The largest mean reduction in $C_T$ occurred on the stressed OV samples exposed to 0.006, 0.018 and 1.8 $\%Cl^-$; these reductions were 11.4, 14.4, and 27 percent, respectively. The $C_T$ reduction due to high levels of $f_{axial}$ can be attributed to the possible synergistic effects of small surface crack formation at high stress levels, infiltration of moisture and chlorides into these cracks, and resulting accelerated anodic dissolution at these sites.

### 6.5.5. Effect of void conditions

Of all the strand specimens, the maximum corrosion was observed at or near the GAS interfaces. The OV samples experienced more localized corrosion than the PV samples. For example, the p-values obtained with M-W U tests on the data sets from the OV and PV samples were less than 0.05, except for the room exposure conditions with 0.0001 $\%sCl^-$, where there was no significant change in the $C_T$. The p-values obtained from M-W U tests for IV and BV data sets with 0.0001, 0.006, 0.018, 0.18, and 1.8 $\%sCl^-$ were 1, 1, 0.063, 0.2475, and 1, respectively; indicating no statistically significant change in the $C_T$ as the void condition changed from IV to BV. Moreover, the differences between the mean values of $C_T$ from IV (or BV) samples and OV samples were less than 2.5%. As a result, the M-W U tests showed p-values larger than 0.1431 indicating no statistically significant differences in the $C_T$ as the type of void changed from IV (or BV) to OV. This can be explained by the differences in both the geometry and ratio of cathode-anode regions of these test samples. The cathode-to-anode ratio on the OV, IV, BV, and PV samples were 5:1, 5:1, 5:1, and 2:1; resulting in more localized corrosion on the OV, IV, and BV samples than on the PV samples. ASTM G109-07, longer-term corrosion test method, uses a cathode-to-anode ratio of 2:1. These results indicate that

the cathode-anode ratio likely influences the rate of localized corrosion of PT strands at or near the void locations.

Table 6-3 shows the three void groups (i.e., NV, PV, and BIOV), within which there are no statistically significant differences in $C_T$. Because the maximum corrosion activity and loss in $C_T$ was observed in the BIOV samples, this void group is defined as the governing void group. In summary, *VT* significantly influences the $C_T$ of strands and NV, PV, and BIOV conditions have statistically different effects on the loss of $C_T$.

**Table 6-3. Groups of Void Conditions with Similar Effects on Tension Capacity.**

| Name of void group (as denoted, herein) | Void conditions | Typical location on a PT bridge |
|---|---|---|
| NV | No void (NV) | At fully grouted regions on tendons |
| PV | Parallel void (PV) | At or near midspan of a girder |
| BIOV | Bleedwater void (BV)<br>Inclined void (IV)<br>Orthogonal void (OV) | At or near anchorage zones of girders<br>At or near high points in columns |

## 6.6. SUMMARY

This section presented the experimental program outlined in Section 4 and the critical parameters influencing tension capacity of strands. In Subsection 6.2, the electrochemical characteristics of ASTM A416 steel were determined using cyclic polarization tests. In Subsection 6.3, galvanic corrosion characteristics of PT systems were determined using the modified ASTM G109 and bearing plate tests. Following this, all $C_T$ data obtained from the strand and wire corrosion tests were presented in

Subsection 6.4. Finally, in Subsection 6.5, the critical parameters that affect the $C_T$ of strands were identified using statistical hypothesis tests.

# 7. MODELING TENSION CAPACITY OF STRANDS EXPOSED TO WET-DRY (WD) CONDITIONS

## 7.1. INTRODUCTION

This section first presents statistical procedures to develop probabilistic models. These procedures are used in this section and in Sections 8 and 9. The analytical program to develop the probabilistic models for $C_T$ of strands exposed to WD conditions is then developed. Following this, three sets of models for $C_T$ are formulated and assessed. Then the $C_T$ at future time is predicted using these developed probabilistic models and assumptions based on engineering judgments on potential field exposure conditions.

## 7.2. STATISTICAL PROCEDURES TO DEVELOP PROBABILISTIC MODELS

This subsection presents the statistical procedures that are used to develop the probabilistic models for $C_T$ of strands.

### 7.2.1. Statistical diagnosis of experimental data

In this step, possible forms of relationships (i.e., linear, logarithmic, exponential, power, etc.) between the response and predictor parameters are identified. This is done by first developing scatter plots between the basic or transformed response and predictor parameters. These scatter plots are then visually assessed to identify possible relationships and dependencies. This intuitive information is incorporated into the probabilistic model formulation, as discussed next.

### 7.2.2. Formulation of probabilistic capacity models

Linear or nonlinear probabilistic models are formulated considering the identified relationships or patterns from the diagnostic studies and underlying physical reasonings. The $C_T$ of strands and wires can be modeled using the following several probabilistic model forms developed by Gardoni et al. (2002a and b):

$$R_C\left(\mathbf{x}, \boldsymbol{\Theta}\right) = \gamma\left(\mathbf{x}, \boldsymbol{\theta}\right) + \sigma\varepsilon \tag{7.1}$$

where, $R_C(\mathbf{x}, \boldsymbol{\Theta})$ is the ratio between the actual $C_T$ of wires or strands, $C_T(\mathbf{x}, \boldsymbol{\Theta})$, and Minimum Absolute Tensile Strength of "as-received" strands ($MUTS_{ARS}$); $\gamma(\mathbf{x}, \boldsymbol{\theta})$ is a correction function; $\mathbf{x}$ is a vector of the predictor parameters or regressors; $\boldsymbol{\Theta} = (\boldsymbol{\theta}, \sigma)$ is a vector of unknown model parameters, where $\boldsymbol{\theta} = (\theta_1, ..., \theta_k)$ is a $1 \times k$ vector of model parameters and $k$ is the number of model parameters considered; $\sigma\varepsilon$ is the model error, where $\sigma$ represents the standard deviation of the model error and $\varepsilon$ is a random variable with zero mean and unit standard deviation. The term $\gamma(\mathbf{x}, \boldsymbol{\theta})$, captures two reasons why $C_T$ might be different from $MUTS_{ARS}$: (1) $C_{T, ARS}$ is typically greater than $MUTS_{ARS}$ (see Subsection 5.2.1) because of potential *liability concerns* with the manufacturer, and (2) corrosion might lead to a reduction in $C_T$.

To maximize the scope or range of applicability, probabilistic models with dimensionless terms (i.e., $R_C(\mathbf{x}, \boldsymbol{\Theta})$ and $\gamma(\mathbf{x}, \boldsymbol{\theta})$ are dimensionless) are developed. In the models developed in Section 7, the response and most predictor parameters are standardized to form corresponding dimensionless parameters. However, note that the time and temperature parameter have not been standardized due to the lack of an appropriate standardizing factor. Models with dimensionless response or predictor parameters have two benefits over those made of parameters with specific physical dimensions. First, $\boldsymbol{\theta}$ associated with dimensionless parameters are also dimensionless.

Second, a dimensionless model is applicable when the standardized predictor parameters fall within range of the standardized predictor parameters in the database used to assess the model. This typically expands the range of applicability of a probabilistic model, especially the parameters that are expressed in a dimensionless format.

### 7.2.3. Assessment or calibration of probabilistic capacity models

#### *7.2.3.1. Posterior statistics of model parameters*

The probabilistic models can be written in the following general form:

$$\mathbf{R}_C = \mathbf{G}\boldsymbol{\theta} + \sigma\boldsymbol{\varepsilon} \tag{7.2}$$

where $\mathbf{R}_C$ is a $n \times 1$ vector of standardized tension capacity observations, ($R_{C1}$, …, $R_{Cn}$); $n$ is the number of observations or sample size; $\mathbf{G}$ is a $n \times k$ matrix of known regressors; $k$ is the number of regression parameters (in this study, $k = 4$); and $\boldsymbol{\varepsilon}$ is a $n \times 1$ vector of normal random variables. The remaining quantities are as defined in Equation (7.1).

A closed-form solution for the posterior statistics of $\boldsymbol{\Theta}$ is available in the case of probabilistic models that are linear in $\boldsymbol{\Theta}$, for which no prior information is available and no upper or lower bound data are used (Box and Tiao 1992). Box and Tiao (1992) provides expressions for posterior statistics of $\boldsymbol{\Theta}$ as follows:

$$\begin{aligned} &p\left(\boldsymbol{\Theta}|\mathbf{R}_C\right) \propto p\left(\boldsymbol{\Theta}\right) p\left(s^2\left|\sigma^2\right.\right) p\left(\hat{\boldsymbol{\theta}}|\boldsymbol{\theta}, \sigma^2\right) \\ &\text{where, } \hat{\boldsymbol{\theta}} = \left(\mathbf{G}^{\mathrm{T}}\mathbf{G}\right)^{-1}\mathbf{G}^{\mathrm{T}}\mathbf{R}_C \\ &\qquad s^2 = \left(1/\nu\right)\left(\mathbf{R}_C - \hat{\mathbf{R}}_C\right)^{\mathrm{T}}\left(\mathbf{R}_C - \hat{\mathbf{R}}_C\right) \\ &\qquad \nu = n - k, \text{ and} \\ &\qquad \hat{\mathbf{R}}_C = \mathbf{G}\hat{\boldsymbol{\theta}} \end{aligned} \tag{7.3}$$

The marginal posterior distribution of $\boldsymbol{\theta}$ follows a multivariate student *t*-distribution, $t_k[\hat{\boldsymbol{\theta}}, s^2(\mathbf{G}^{\mathrm{T}}\mathbf{G})^{-1}, v]$, where $\hat{\boldsymbol{\theta}}$ is both the mode and the mean of $\boldsymbol{\theta}$, and the covariance matrix is $vs^2(\mathbf{G}^T\mathbf{G})^{-1}/(v-2)$. For a given $\mathbf{x}$, $\boldsymbol{\theta}$, and $\sigma$, the model variance, Var[$R_C(\mathbf{x}, \boldsymbol{\Theta})$], is equal to $\sigma^2$. Therefore $\sigma^2$ (or $\sigma$) can be used as a measure of the model accuracy. The marginal posterior distribution of $\sigma^2$ is $vs^2\chi_v^{-2}$, where $\chi_v^{-2}$ is the inverted chi-square distribution with $v$ degrees of freedom, mean $vs^2/(v-2)$ and variance $2v^2s^4/[(v-2)^2(v-4)]$. As an approximation, $\sigma$ can be calculated as $\sqrt{\sigma^2}$ and used to measure model accuracy.

In the case of nonlinear probabilistic models, the test parameters are nonlinear, no prior information is available about the distribution of $\boldsymbol{\Theta}$, and no upper or lower bound data are used. In this case, the parameters $\boldsymbol{\Theta}$ can be estimated using the updating rule as follows (Box and Tiao (1992)):

$$f(\boldsymbol{\Theta}) = \kappa L(\boldsymbol{\Theta})\, p(\boldsymbol{\Theta}) \tag{7.4}$$

where, $f(\boldsymbol{\Theta})$ = posterior distribution representing updated state of our knowledge about $\boldsymbol{\Theta}$; $L(\boldsymbol{\Theta})$ = likelihood function representing the objective information on $\boldsymbol{\Theta}$ contained in a set of observations; $p(\boldsymbol{\Theta})$ = prior distribution representing state of knowledge about $\boldsymbol{\Theta}$ prior to obtaining the observations; and $\kappa$ is the normalizing factor, which is defined as $\kappa = [\int L(\boldsymbol{\Theta})\, p(\boldsymbol{\Theta})\, d\boldsymbol{\Theta}]^{-1}$. The mathematical expression for the prior statistics of $\boldsymbol{\Theta}$ is as follows (Gardoni et al. 2002a):

$$p(\boldsymbol{\Theta}) \cong p(\Sigma) \propto |\boldsymbol{\rho}|^{-(q+1)/2} \prod_{i=1}^{q} \frac{1}{\sigma_i} \tag{7.5}$$

where, $\rho_{ij}$ is an element of the correlation matrix. If no upper or lower bound data are used and the observations are statistically independent, the likelihood function for the univariate model form is as follows:

$$L(\theta,\sigma) \propto \prod_{data}\left( p(\sigma)\varphi\left[\frac{r_i(\boldsymbol{\theta})}{\sigma}\right]\right);\ \text{where, } p(\sigma) \propto \frac{1}{\sigma};\ r_i = i^{th}\ \text{residual} \tag{7.6}$$

*7.2.3.2. Mean absolute percentage error*

In addition to $\sigma^2$ and $\sigma$, the Mean Absolute Percentage Error (MAPE) can also be used to provide an intuitive measure of model accuracy. The MAPE can be mathematically expressed as follows:

$$\text{MAPE} = \frac{1}{n}\left[\sum_{i=1}^{n}\left(\frac{\left| E\left[C_T\left(\mathbf{x}_i, \boldsymbol{\theta}\right)\right] - C_{T,i}\right|}{C_{T,i}}\right)\right]\times 100 \tag{7.7}$$

where $C_{T,i}$ is the observed tension capacity and $\mathrm{E}[C_T(\mathbf{x}_i,\boldsymbol{\theta})] = C_{Tn,\,ARS}\times\gamma(\mathbf{x}_i,\ \hat{\boldsymbol{\theta}})$ is the mean predicted capacity.

*7.2.3.3. Selection of the most parsimonious parameter set*

Although the diagnostic plots can assist in identifying the unimportant and important predictor parameters, their selection needs to be justified for being the most parsimonious parameter set (i.e., as few parameters, $\theta_i$, as possible). In other words, from a statistical standpoint, in order to avoid (1) the loss of precision on the estimates of the parameters and on the overall model (due to the inclusion of statistically redundant variables) and (2) overfitting the data, a model should have parsimonious

parameterization. To attain such a model, a stepwise variable deletion process can be carried out on the full model under consideration. Following the general procedure developed by Gardoni et al. (2002a and b), the coefficient of variation (COV) of the parameter estimates and $\sigma$ for the full and reduced models are compared to determine the most parsimonious model. Engineering judgment could, and should, play a role in final model selection.

#### *7.2.3.4. Possible high correlation coefficients between model parameters*

It should be noted that there exist practical difficulties in interpreting the numerical values of the correlation between the model parameters in the probabilistic models developed, especially in the cases of high positive and high negative correlations. "*When predictor variables are random variables, the multiple regression coefficients should not be simply interpreted as a relationship between the response and corresponding predictor variables…"* (Ryan 2007).

#### *7.2.3.5. Validation plot*

A validation plot is defined as the scatter plot between the observed and predicted values of the response parameter. A validation plot can be used to assess the overall model quality and investigate if the model agrees, at least approximately, with the homoskedasticity and normality assumptions. Definitions and use of some key elements of the validation plot are defined here.

- "1:1 line" is defined as the solid line (with unit slope) indicating the median predicted capacity values. There is a 50 percent probability for the true capacity to be above or below this line. If the data points fall along the 1:1 line, then the model can be assumed to be of good prediction quality. The pattern and width of the spread of data can be used to assess the bias or residual trend. If data points are spread with an approximately equal width and along the 1:1 line, then the homoskedasticity assumption for the model holds reasonably well. The homoskedasticity assumption means that the variance of the

model error is approximately constant and independent of the predictor variables. It should be noted that the greater the statistical sample size, the less the difficulty in visually observing the variance of the model error, if any, in the validation plot and thereby less difficulty in assessing the homoskedasticity characteristics.

- "±σ region" is defined as the region within one standard deviation from the median predicted capacity. This is indicated by the region within the two dashed lines (with unit slope) that are parallel to and located at one standard deviation away from the 1:1 line. Ideally, if 68.23 percent of data points lie inside this region, then the normality assumption holds good. Although this may not be the case with the capacity models presented in this document, reasonable assumptions on the validity of normality assumption can be made based on the spread of data in and out of the ±σ region. The normality assumption means that the model error follows a normal distribution. It should be noted that the greater the statistical sample size, the less the difficulty in visually observing a normally distributed data in the validation plot.

- In most of the validation plots provided in this document, the nominal and yield capacities of pristine strands are indicated using two vertical dashed lines. Also, for convenience, the abbreviated name of the model being assessed or validated is shown at the top left corner of every validation plot in this document.

- For a perfect prediction model, the predicted and observed capacities should line up along the 1:1 line. However, due to the inherent variability in the corrosion phenomena, measurement errors, and model errors due to missing variables in Equation (7.1) or an inaccurate model form, there is a scatter around the 1:1 line. In particular, significantly different capacities are observed for test samples that have identical combinations of test parameters. In the validation plots shown in the remaining sections in this document, this variability is evident from the long horizontal stretches of several observed data points corresponding to a particular or same predicted value. Conclusions on "the agreements of the probabilistic models with the homoskedasticity and normality assumptions" may be made based on the consideration that large variability is an inherent property of the electrochemical corrosion process and the resulting capacity loss. In other words, a probabilistic model for capacity of strands or wires may be considered to have good agreement with the homoskedasticity and normality assumptions even though there may be some scatter among the data points along the 1:1 line. This is

because the scatter in the data points may be due to the inherent scatter in the corrosion phenomenon and not due to poor model quality.

Statistical procedures to diagnose the experimental data and formulate the probabilistic capacity models have been presented. Also, procedures to estimate the MAPE, posterior statistics of the linear and nonlinear model parameters, and validation plots to assess the quality of the capacity models have been presented. These procedures are used to develop the probabilistic models for $C_T$ of strands. The developed probabilistic models are presented in section 7.

## 7.3. PROBABILISTIC MODELS FOR TENSION CAPACITY OF "AS-RECEIVED" STRANDS

The first column of Figure 5-2 in Subsection 5.2.1 shows the $C_T$ of 24 "as-received" strands. Based on this data and assuming a lognormal distribution, the $C_{T,ARS}$ can be statistically expressed as follows:

$$C_{T,ARS} \sim \text{LN}\left(\text{E}\left[C_{T,ARS}\right], \sqrt{\text{Var}\left[C_{T,ARS}\right]}\right) \sim \begin{array}{l} \text{LN}(59.27, 0.29)\ \text{kips} \\ \sim \text{LN}(263.7, 1.3)\ \text{kN} \end{array} \tag{7.8}$$

Herein, Equation (7.8) will be used to probabilistically predict $C_{T,ARS}$.

## 7.4. TENSION CAPACITY MODELS FOR STRANDS UNDER WD EXPOSURE CONDITIONS - ANALYTICAL PROGRAM

This subsection presents the program to develop probabilistic models for $C_T$ of strands exposed to WD conditions. Theoretical models for $C_T$ of strands under WD exposure conditions could not be developed or found in the literature. Historically, engineers have developed deterministic empirical models when model derived from scientific principles are not possible. In this document, probabilistic empirical models are

developed using the data obtained from the experimental program presented in Subsection 5.5 and statistical procedures discussed in Subsection 7.2.

Models for NV, PV, and BIOV conditions are developed using the experimental data from strand corrosion tests with WD exposure conditions. BIOV indicates the group of BV, IV, and OV. These are grouped because all these void types (*VT*s) have statistically similar effects on $C_T$.

The main objectives of this subsection are to:

1. Present the basic and standardized parameters used in the probabilistic models for tension capacity. See Subsection 7.4.1 for details.
2. Present analytical steps to develop probabilistic tension capacity models for strands under WD exposure conditions. See Subsection 7.4.2 for details.

To provide the reader with a sense of expected results, preliminary discussions of possible probabilistic model forms are also provided in this section. The developed probabilistic models are presented in section 7.5. The parameters used in these probabilistic models are presented next.

### 7.4.1. Parameters used in the models for wet-dry conditions

Subsection 7.2.2 suggested using dimensionless response parameters and their explanatory or predictor parameters to improve the the range of application of probabilistic models (Gardoni et al. 2002b). Based on this suggestion, the response and predictor parameters, except $t_{WD}$, $t_{CA}$, and $T$, are standardized. The following equations define these basic response and predictor parameters, which are used in probabilistic modeling of $C_T$.

$$R_{C_{T,US}} = \frac{\text{Tension capacity of unstressed strand}}{MUTS_{ARS}} = \frac{C_{T,US}}{MUTS_{ARS}} \tag{7.9}$$

$$R_{C_{T,SS}} = \frac{\text{Tension capacity of stressed strand}}{MUTS_{ARS}} = \frac{C_{T,SS}}{MUTS_{ARS}} \tag{7.10}$$

$$\begin{aligned} \gamma_{t_{WD}} &= \left( \frac{\text{Average wet-time in a year (months)}}{12 \text{ (months)}} \right) \times \text{Total wet-dry exposure time (years)} \\ &= \phi_{wet} \times t_{WD} \text{ (years)}; \ 0 \le \phi_{wet} \le 1 \end{aligned} \tag{7.11}$$

$$\gamma_{\%sCl^-} = \frac{\%Cl^- \text{ in the exposure solution}}{\%sCl^-_{\text{saturated chloride solution}}} = \frac{\%sCl^-}{35.7} \tag{7.12}$$

Using suitable transformations (such as exponential, logarithmic, etc.), if needed, of the basic response and predictor parameters defined and the procedures provided in Subsection 7.2, probabilistic models for $C_T$ of strands under WD and CA exposure conditions are developed. The next three subsections discuss the analytical steps involved in this process.

### 7.4.2. Analytical steps to develop capacity models for strands under wet-dry (WD) conditions (Steps WD-1 through WD-5)

Table 7-1 provides a list of nine probabilistic strand capacity models that are developed for WD exposure conditions. The subscripts in each model name indicate the exposure conditions. Model $US_{WD,\,NV}$, $US_{WD,\,PV}$, and $US_{WD,\,BIOV}$ are commonly referred to as Model $US_{WD}$. Similarly, Model $SS_{WD,\,NV}$, $SS_{WD,\,PV}$, and $SS_{WD,\,BIOV}$ are commonly referred to as Model $SS_{WD}$. Also, Model US-$SS_{WD,\,NV}$, US-$SS_{WD,\,PV}$, and US-$SS_{WD,\,BIOV}$ are commonly referred to as Model US-$SS_{WD}$.

**Table 7-1. List of Tension Capacity Models for Strands under WD Exposure Conditions.**

| Expanded model name | Abbreviations for specific models | Abbreviations for a group of models |
|---|---|---|
| Unstressed Strand$_{\text{Wet-Dry, No Void}}$ | US$_{\text{WD, NV}}$ | US$_{\text{WD}}$ |
| Unstressed Strand$_{\text{Wet-Dry, Parallel Void}}$ | US$_{\text{WD, PV}}$ | |
| Unstressed Strand$_{\text{Wet-Dry, Bleedwater, Inclined, and Orthogonal Void}}$ | US$_{\text{WD, BIOV}}$ | |
| Stressed Strand$_{\text{Wet-Dry, No Void}}$ | SS$_{\text{WD, NV}}$ | SS$_{\text{WD}}$ |
| Stressed Strand$_{\text{Wet-Dry, Parallel Void}}$ | SS$_{\text{WD, PV}}$ | |
| Stressed Strand$_{\text{Wet-Dry, Bleedwater, Inclined, and Orthogonal Void}}$ | SS$_{\text{WD, BIOV}}$ | |
| Unstressed Strand-Stressed Strand$_{\text{Wet-Dry, No Void}}$ | US-SS$_{\text{WD, NV}}$ (or $C_{T,\text{ WD, NV}}$) | US-SS$_{\text{WD}}$ (or $C_{T,\text{ WD}}$) |
| Unstressed Strand-Stressed Strand$_{\text{Wet-Dry, Parallel Void}}$ | US-SS$_{\text{WD, PV}}$ (or $C_{T,\text{ WD, PV}}$) | |
| Unstressed Strand-Stressed Strand$_{\text{Wet-Dry, Bleedwater, Inclined, and Orthogonal Void}}$ | US-SS$_{\text{WD, BIOV}}$ (or $C_{T,\text{ WD, BIOV}}$) | |

The flowchart in Figure 7-1 provides an overview of the steps used to develop the tension capacity models for PT strands under WD exposure conditions. The five boxes with thick border lines in Figure 7-1 indicate the five main steps. Each of these boxes also contains a smaller and inner box with rounded corners, which provide an indication of the result from the corresponding steps. These steps are numbered Step #WD-1 through #WD-5. Graphical representations provided in Figure 7-2 will also be used, as needed, in the following discussion.

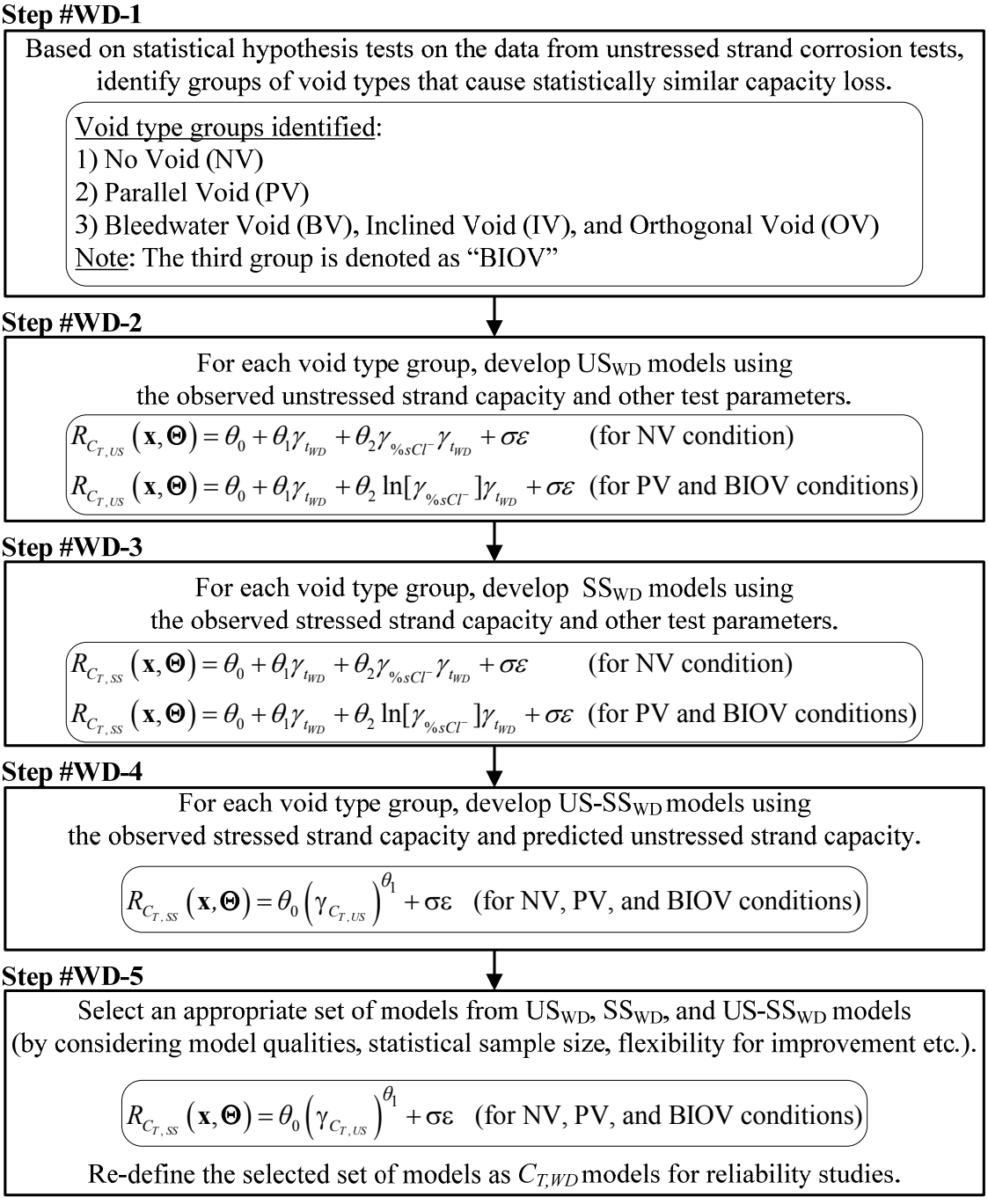


**Figure 7-1. Flowchart for Developing the Tension Capacity Models for Strands in WD Conditions.**

**Step WD-1**: Identify three groups of *VT*s (i.e., NV, PV, and BIOV) with statistically significant differences in their influence on $C_T$ (see first box in Figure 7-1). This is done by conducting statistical hypothesis tests on $C_T$ data obtained from strand samples exposed to different *VT*s and identical levels of other test parameters. Detailed results from this step are provided in Subsection 7.5.1.

**Step WD-2**: Develop probabilistic models for $C_{T,\,US}$ (i.e., $US_{WD}$ models) using the data from unstressed strand corrosion tests (see second box in Figure 7-1 and Figure 7-2(a)). The experimental design was shown in Figure 5-8(a) and Table 5-10). For convenience, this is reproduced in Figure 7-2 (a), where the unstressed strand samples inside the rectangular box and "as-received" samples tested at $t_{WD}$ equal to 0 month indicate the data used for Step WD-2. In particular, Models $US_{WD,\,NV}$ and $US_{WD,\,PV}$ are developed using the data from unstressed NV and PV samples, respectively. Model $US_{WD,\,BIOV}$ is developed by combining all the data from unstressed BV, IV, and OV samples. In Figure 7-1, the box with rounded corners indicates the possible linear model forms for Model $US_{WD}$. Results from this step are provided in Subsection 7.5.2.

**Step WD-3**: Develop probabilistic models for $C_{T,\,SS}$ (i.e., $SS_{WD}$ models) using the data from stressed strand corrosion tests (see third box in Figure 7-1 and Figure 7-2(b)). The experimental designs were shown in Figure 5-8(b). For convenience, this is reproduced in Figure 7-2(b), where the stressed strand samples inside the inner rectangular box and the data from "as-received" samples tested at $t_{WD}$ equal to 0 months indicate the data used for Step WD-3. In particular, Models $SS_{WD,\,NV}$, $SS_{WD,\,PV}$, and $SS_{WD,\,BIOV}$ will be developed using the data from stressed NV, PV, and OV samples, respectively. (IV and BV conditions have statistically similar influence on $C_T$ of strands. Because of this, the model based on the data from OV samples is applicable to IV and BV samples and, hence, referred to as Model $SS_{WD,\,BIOV}$.) In Figure 7-1, the inner box with rounded corners indicates two linear forms for Model $SS_{WD}$. Results from this step are provided in Subsection 7.5.3.

**Step WD-4**: Develop another set of probabilistic models for $C_{T,\,SS}$ (i.e., US-$SS_{WD,\,NV}$ models) using $C_{T,\,US}$ predicted using $US_{WD}$ models and $C_{T,\,SS}$ observed from stressed strand corrosion tests (see forth box in Figure 7-1 and Figure 7-2(b) and (c)). These predicted $C_{T,\,US}$ shown in Figure 7-2(c), observed $C_{T,\,SS}$ shown in Figure 7-2(b), and $C_{T,\,ARS}$ are used in Step WD-4. Probabilistic models are developed for NV, PV, and BIOV conditions and are denoted as Model US-$SS_{WD,\,NV}$, US-$SS_{WD,\,PV}$, and US-$SS_{WD,\,BIOV}$, respectively. In Figure 7-1, the inner box with rounded corners indicates a nonlinear power model form for US-$SS_{WD}$ models. Results from this step are provided in Subsection 7.5.4.

**Step WD-5**: Select a suitable set of models from $US_{WD}$, $SS_{WD}$, and US-$SS_{WD}$ models developed in steps #WD-2, #WD-3, and #WD-4, respectively (see fifth box in Figure 7-1). This selection will be based on the prediction quality of the models, sample size of the capacity data set used, and ease with which the model can be improved by future researchers. The inner box with rounded corners indicates that the US-$SS_{WD}$ models developed in Step WD-4 are selected and re-defined as $C_{T,\,WD}$ models. The $C_{T,\,WD,\,NV}$ and $C_{T,\,WD,\,BIOV}$ models are used in the modeling and analysis of structural reliability of PT bridges. Results from this step are provided in Subsection 7.5.5.

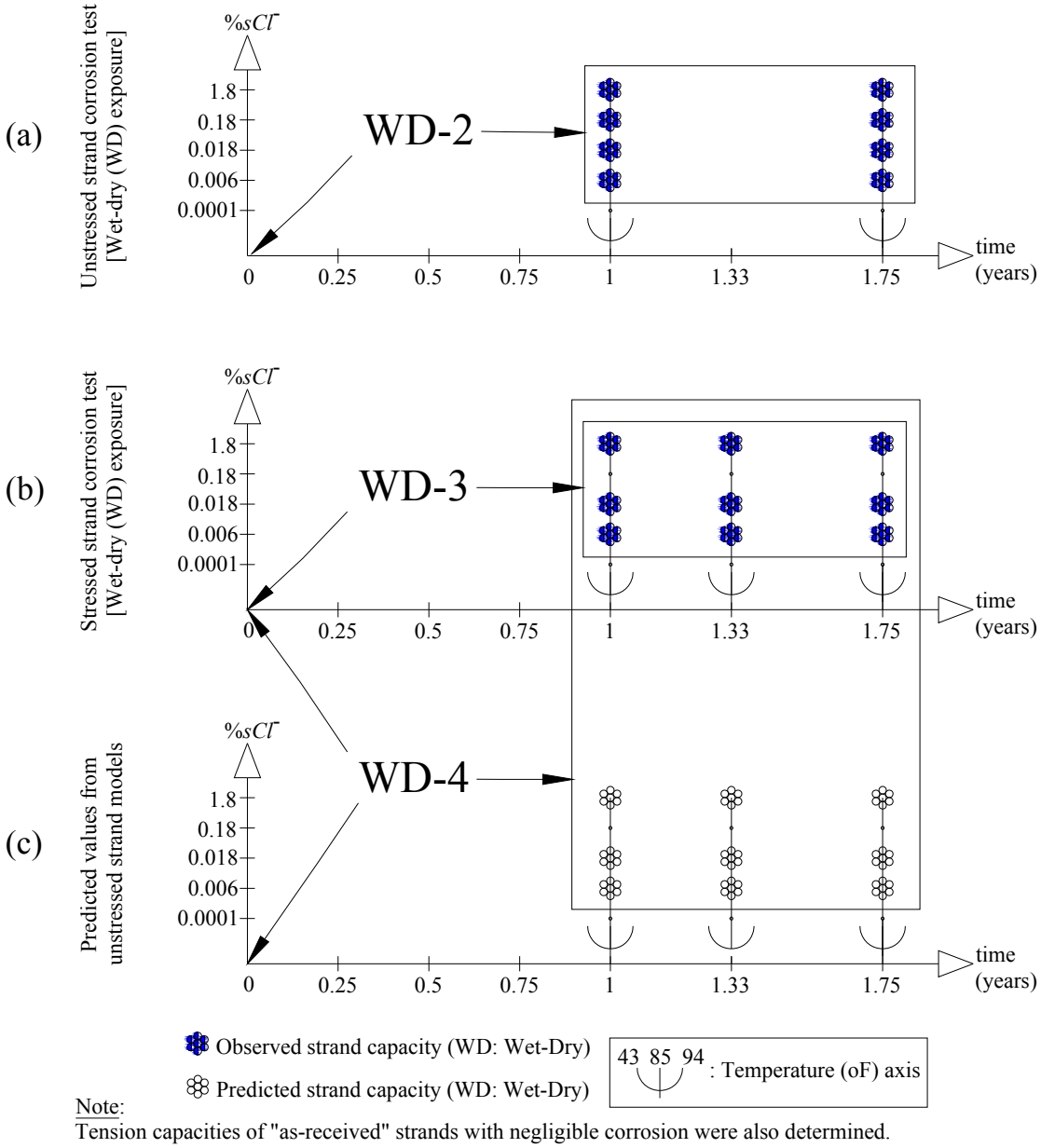


**Figure 7-2. Graphical Representations of Analytical Steps WD-2, WD-3, and WD-4.**

### 7.4.3. Assumptions for predicting strand capacity under wet-dry conditions

As a demonstration of the application of $US_{WD}$, $SS_{WD}$, and US-$SS_{WD}$ models, the $C_T$ of strands are predicted. One of the parameters in the $US_{WD}$ models is $\phi_{wet}$ (defined in Equation (7.11) in Subsection 7.4.1). As defined in Subsection 5.5.4, the laboratory WD exposure consisted of 14 wet days followed by 14 dry days and, hence, corresponds to $\phi_{wet}$ of 0.5. However, this may not be the case in the field. Moreover, $\phi_{wet}$ can vary from one tendon to another on the same bridge and is very complex to estimate. However, based on the literature review in Subsection 2.3.7, practical assumptions, and engineering judgment, an estimation ofn $\phi_{wet}$ is provided next.

In this analysis, a rain-day is defined as a day with non-zero precipitation. Note that each data marker in Figure 2-13 indicates a rain-day. The time required for the tendons to automatically dry is defined as $t_{drying}$. A wet-day (for the tendon) is defined as either a rain-day or a day with at least one rain-day for a period of $t_{drying}$ prior to the day under consideration. Figure 7-3 shows the number of wet-days, calculated based on the above mentioned definitions and the data shown in Figure 2-13.

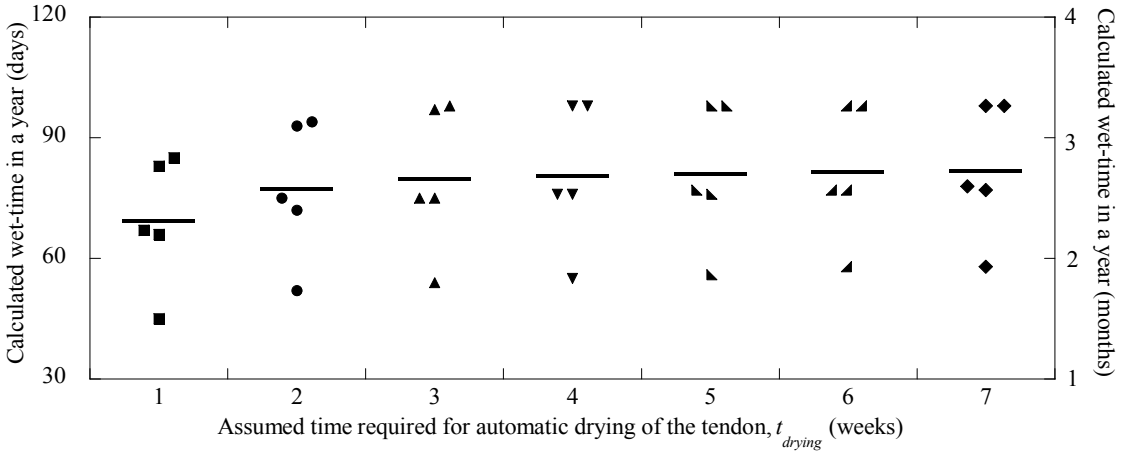


**Figure 7-3. Annual Wet-time for Tendons (Based on Assumed Values of Time Required to Dry the Tendons).**

In Figure 7-3, each column corresponds to an assumed value of $t_{drying}$ (i.e., 1, 2, 3, 4, 5, 6, and 7 weeks). The five data markers in each column indicate the number of wet-days in 2001, 2002, 2003, 2004, and 2005. The solid-horizontal line in each column indicates the mean number of wet-days for the corresponding $t_{drying}$. Based on this data for the downtown region in San Antonio, Texas, the average number of wet-days varies from 69 to 82. The corresponding values of $\phi_{wet}$ are 0.19 and 0.22.

For all the capacity predictions provided in the remainder of this section, $\phi_{wet}$ is assumed to be 0.17, which corresponds to an assumption of 2 months of wet-time in a period of $t_{WD}$ equal to 12 months (i.e., 2/12 = 0.17). Also, this value is very close to the above estimated range (i.e., between 0.19 and 0.22).

## 7.5. TENSION CAPACITY MODELS FOR STRANDS UNDER WD EXPOSURE CONDITIONS: RESULTS

The analytical steps (WD-1 through WD-5) to develop probabilistic models for $C_T$ of strands under WD exposure conditions were outlined in Subsection 7.4.2. These analytical steps are executed using the data presented in Subsection 6.4.3 and are presented next.

### 7.5.1. Step WD-1: Identifying groups of void types with statistically dissimilar effects on tension capacity

NV, PV, and BIOV were identified as three void groups with statistically dissimilar effects on $C_T$ of strands. Therefore, three probabilistic models (i.e., one each for NV, PV, and BIOV conditions) will be developed. Further details on this study were provided earlier in Subsection 6.5.5.

### 7.5.2. Step WD-2: Models for unstressed strands under WD exposure conditions (using unstressed strand data only)

This subsection presents probabilistic models for $C_{T,US}$ exposed to NV, PV, and BIOV conditions along with WD exposure conditions. These three models are named as $US_{WD, NV}$, $US_{WD, PV}$, and $US_{WD, BIOV}$ models, respectively. Experimental data from 100, 105, and 239 unstressed strand specimens have been used to develop the $US_{WD, NV}$, $US_{WD, PV}$, and $US_{WD, BIOV}$, respectively. This $C_T$ data was shown earlier in Figure 6-8 and Figure 6-9 in Subsection 6.4.3.1. Prior to discussing model formulation and assessments, statistical diagnosis on the effects of $t_{WD}$, $\%sCl^-$, and $\ln[\%sCl^-]$ on $C_{T,US}$ are presented.

#### *7.5.2.1. Diagnosis of the effect of wet-dry exposure time*

Figure 7-4 shows the scatter plot between $C_{T,US}$ and $t_{WD}$ for all the void conditions. The following observations are made based on Figure 7-4 (a), (b), and (c) for NV, PV, and BIOV conditions, respectively. A linear relationship seems to exist between $C_{T,US}$ and $t_{WD}$, when NV condition exists. However, note that this behavior is more predominant with the samples with higher chloride conditions. In the case of PV condition, the rate of loss of $C_{T,US}$ seems to be almost zero after 12 months, after which this rate increases. When BIOV condition exists, a linear relationship between $C_{T,US}$ and $t_{WD}$ seems to be appropriate. Also, a general trend of increasing scatter is observed in Figure 7-4. Because of this, a model with only linear time function might be heteroskedastic. This heteroskedasticity can be minimized by incorporating a two-way interaction term (later discussed in Subsection 7.5.2.3) between $t_{WD}$ and $\%sCl^-$ or $\ln[\%sCl^-]$. The main effects of $\%sCl^-$ and $\ln[\%sCl^-]$ terms on $C_{T,US}$ are discussed next.

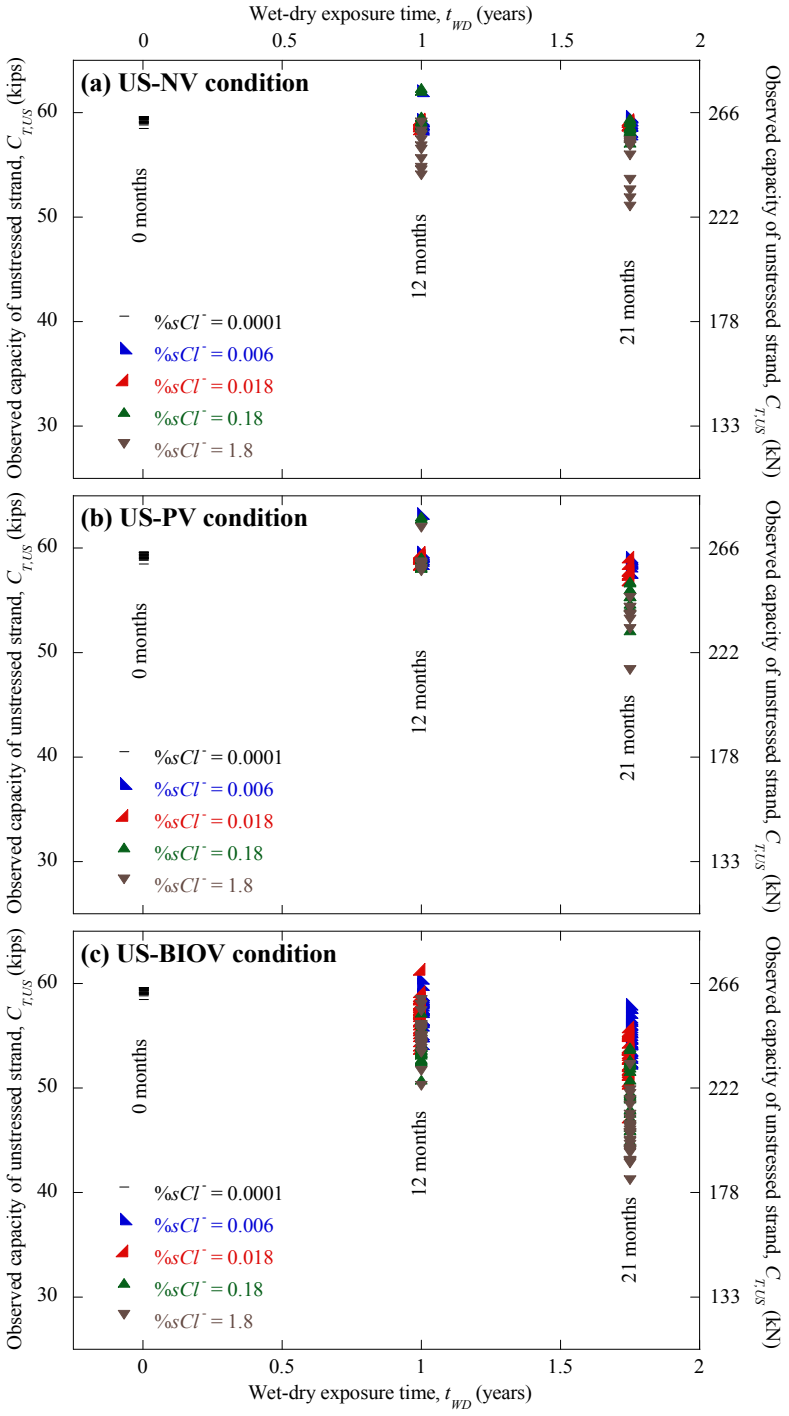


**Figure 7-4. Effect of Wet-dry Exposure Time on Capacity of Unstressed Strands (with $\phi_{wet}$ = 0.5).**

*7.5.2.2. Diagnosis of the effect of chloride concentration in exposure solution*

The scatter plots in Figure 7-5 and Figure 7-6 show the effect of $\%sCl^-$ and $\ln[\%sCl^-]$ on $C_{T,\,US}$. In Figure 7-5 and Figure 7-6, the vertical texts next to the data points indicate the actual $\%sCl^-$ values. In Figure 7-5, note that the data markers for samples corresponding to 0.0001, 0.006, and 0.018 $\%sCl^-$ are closely overlapping along the abscissa. However, this overlapping is avoided using a logarithmic transformation (see Figure 7-6).

A comparison between Figure 7-5 (a) and Figure 7-6 (a) indicates that, under NV conditions, a more appropriate linear relationship exists between $\%sCl^-$ and $C_{T,\,US}$ than between $\ln[\%sCl^-]$ and $C_{T,\,US}$. In addition, in Figure 7-6 (a), the slope is almost zero until 0.18 $\%sCl^-$, after which there is a slight increase in the slope. This is probably because a higher $\%sCl^-$ level than 0.18 was necessary to build sufficient amount of chlorides at the surface of strands (via diffusion through uncracked grout or transport through cracks in the grout cover) and then initiate/propagate corrosion within the test period. In Figure 7-5 (b) for PV conditions, the slope significantly reduces after 0.18 $\%sCl^-$, especially with the samples at $t_{WD}$ equal to 21 months. In Figure 7-6 (b), the slope seems to be same throughout the range of abscissa (i.e., $\ln[\%sCl^-]$) considered. This comparison between Figure 7-5 (b) and Figure 7-6 (b) indicates that $\ln[\%sCl^-]$ term is more appropriate than $\%sCl^-$ term to predict $C_{T,\,US}$ under PV conditions. Similarly, in Figure 7-5 (c) the slope seems to be flattening at or after 0.18 $\%sCl^-$ level. In Figure 7-6 (c), the slope seems to be constant throughout the considered range of $\ln[\%sCl^-]$. Hence, the $\ln[\%sCl^-]$ is a more appropriate term than $\%sCl^-$ to predict the $C_{T,\,US}$ under BIOV conditions. A general trend of increasing scatter as the $\%sCl^-$ increases is observed in Figure 7-5 and Figure 7-6. The model heteroskedasticity that can be induced because of this increasing scatter can be reduced by incorporating an interaction term between $t_{WD}$ and $\%sCl^-$ or $\ln[\%sCl^-]$.

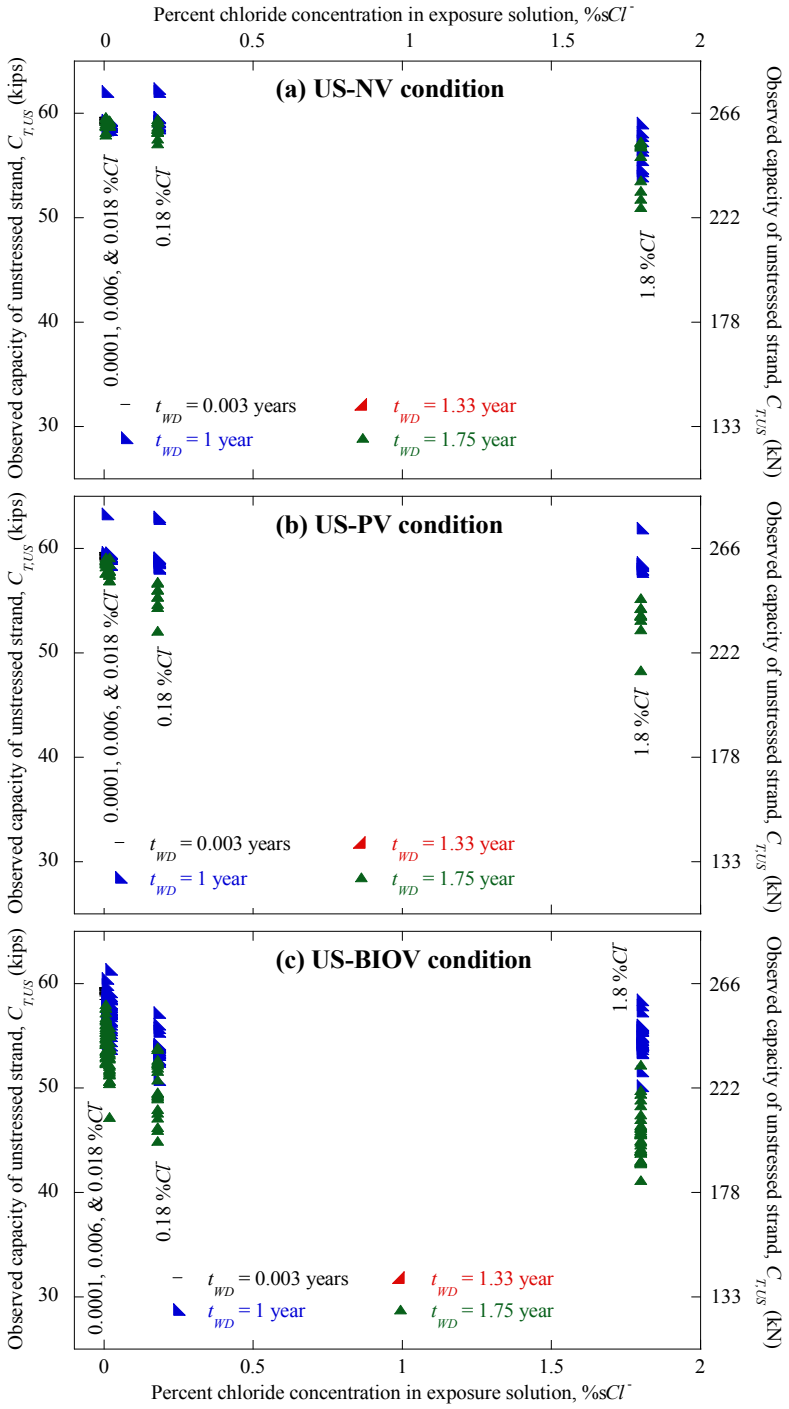


**Figure 7-5. Effect of %$sCl^-$ on Capacity of Unstressed Strands (with $\phi_{wet}$ = 0.5).**

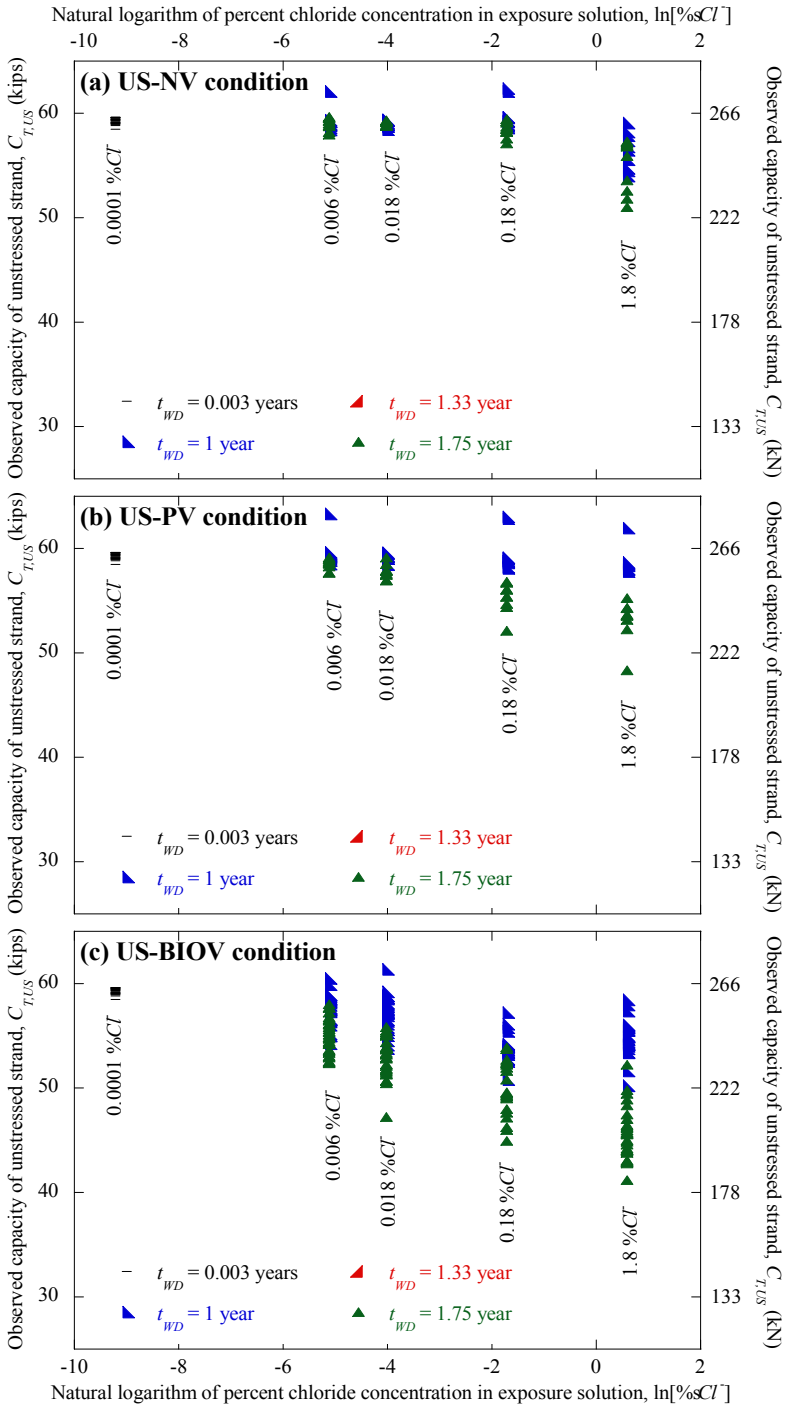


**Figure 7-6. Effect of ln[%$sCl^-$] on Capacity of Unstressed Strands (with $\phi_{wet}$ = 0.5).**

### *7.5.2.3. Diagnosis of the effect of interaction between chloride and time parameters*

From a statistical point of view, the main effects of $\%sCl^-$ or $\ln[\%sCl^-]$ terms seem to be good for incorporating into the probabilistic models for $C_{T,US}$. However, based on a corrosion point of view, these main effects are not useful to accurately predict the time-dependent corrosion process. For example, a high $t_{WD}$ value alone with very low $\%sCl^-$ and low moisture condition, or both (for instance, negligible amounts of chlorides or water for 100 years) or a high $\%sCl^-$, high moisture condition, or both with negligible $t_{WD}$ (for instance, seawater for 1 day) do not normally lead to significant corrosion and reduction in $C_{T,US}$. A two-way interaction term between chloride and time parameters is needed to improve the prediction accuracy, and homoskedasticity of the probabilistic models.

In Subsection 7.5.2.2, it was found that the appropriate main effect term for NV condition is $\%sCl^-$. Hence, the appropriate interaction term for the model for NV condition is $\%sCl^- \times t_{WD}$. It was also found that the appropriate main effect term for the models for PV and BIOV conditions is $\ln[\%sCl^-]$. Hence, the appropriate interaction term for the models for PV and BIOV conditions is $\ln[\%sCl^-] \times t_{WD}$.

### *7.5.2.4. Model formulation*

Based on the diagnostic studies, the probabilistic models for $C_{T,US}$ are formulated and parameters are assessed for each void type. These models are expressed as follows:

$$\begin{aligned} R_{C_{T,US}}(\mathbf{x},\boldsymbol{\Theta}) &= \theta_0 + \theta_1\gamma_{t_{WD}} + \theta_2\gamma_{\%sCl^-}\gamma_{t_{WD}} + \sigma\varepsilon \quad \text{(for NV condition)} \\ R_{C_{T,US}}(\mathbf{x},\boldsymbol{\Theta}) &= \theta_0 + \theta_1\gamma_{t_{WD}} + \theta_2 \ln[\gamma_{\%sCl^-}]\gamma_{t_{WD}} + \sigma\varepsilon \quad \text{(for PV and BIOV conditions)} \end{aligned} \tag{7.13}$$

where the terms are as defined in Equation (7.1) and Subsection 7.4.1. Note that the appropriate interation term for $US_{WD, NV}$ model is $\gamma_{\%sCl^-}\gamma_{t_{WD}}$ and that for $US_{WD, PV}$ or $US_{WD, BIOV}$ models is $\ln[\gamma_{\%sCl^-}]\gamma_{t_{WD}}$. When $t_{WD}$ is zero, the model should predict a capacity that is close to $MUTS_{ARS}$. The intercept term will help meet this criterion. As the corrosion process is a time-dependent phenomenon, each predictor parameter (except the intercept term) has to be a function of a time parameter (i.e., $\gamma_{t_{WD}}$). The two-way interaction term (i.e., $\gamma_{\%sCl^-}\gamma_{t_{WD}}$ or $\ln[\gamma_{\%sCl^-}]\gamma_{t_{WD}}$) will capture the effect of interaction between the chlorides and time parameters and thereby minimize the heteroskedasticity of the model. Following is a sequential and detailed discussion on the assessment of the three probabilistic models (i.e., Equation (7.13)) for $C_{T,US}$.

### *7.5.2.5. Model assessment - No Void (NV) conditions*

MAPE and posterior statistics of the model form for NV conditions (provided in Equation (7.13)) were assessed using the procedures provided in Subsection 7.2.3. It was found that the COV of $\theta_1$ (corresponding to $\gamma_{t_{WD}}$ term) was highly negative (i.e., –1.6785). Hence, the $\gamma_{t_{WD}}$ term was removed from the full model to form the reduced model. Table 7-2 provides the MAPE and posterior statistics of the reduced $US_{WD, NV}$ model. .

**Table 7-2. MAPE and Posterior Statistics of the $US_{WD, NV}$ Model.**

| Model Name | MAPE (%) | Parameters | Mean | Standard deviation | COV | Correlation coefficients between $\theta_i$ | |
|---|---|---|---|---|---|---|---|
| | | | | | | $\theta_0$ | $\theta_2$ |
| $US_{WD, NV}$ | 1.22 | $\theta_0$ | 1.0105 | 0.0022 | 0.002 | 1 | |
| | | $\theta_2$ | –1.6785 | 0.1362 | –0.08 | -0.47 | 1 |
| | | $\sigma$ | 0.0194 | 0.0073 | 0.38 | | |

Table 7-2 shows that the coefficients (i.e., $\theta_i$) of the predictor parameters have reasonably small COVs (i.e., 0.002 and −0.08). Also, the MAPE and σ are reasonably small (i.e., 1.22% and 0.0194, respectively). These observations indicate good prediction accuracies for the reduced model and that the reduced model is the most parsimonious model. Hence, **the reduced model in Table 7-2 is will be referred to as Model $US_{WD,\,NV}$ herein**.

The Model $US_{WD,\,NV}$ indicates that only the intercept and the two-way interaction terms are needed to predict the capacity, when the tendons are fully grouted. This can be physically supported by the fact that if the chloride exposure level is low, it takes long time for the available chloride ions to get transported through the ¼ inch grout cover, reach the strands in sufficient quantity, and initiate corrosion. So, the test durations (i.e., 12 and 21 months) were not long enough to cause chloride-induced corrosion, especially when the $\%sCl^-$ level of the test solution was 0.006 or 0.018. However, strands exposed to 0.18 and 1.8 $\%sCl^-$ exhibited relatively larger reduction in capacity.

A typical validation plot and its characteristics were provided in Subsection 7.2.3.5. Figure 7-7 shows the validation plot for the Model $US_{WD,\,NV}$. The spread (with an approximately equal width) of the most data points along the 1:1 line and within the ±σ region indicate an approximate agreement with both the homoskedasticity and normality assumptions, respectively.

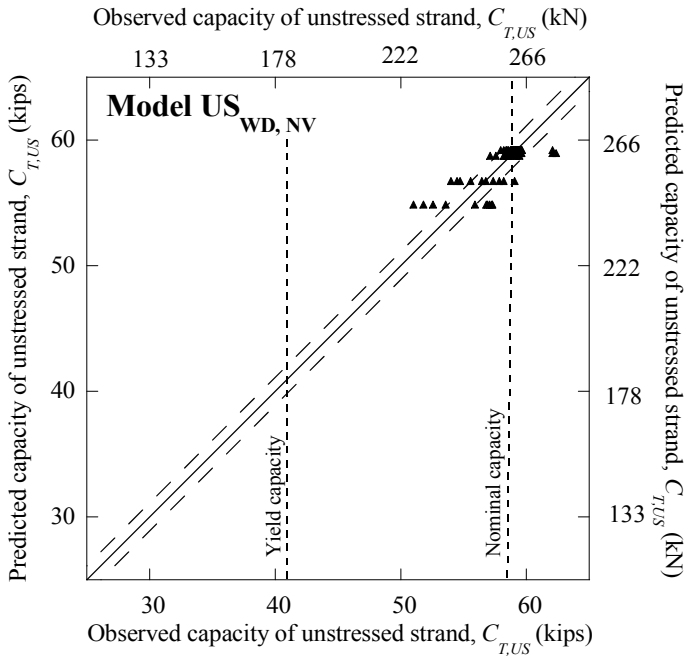


**Figure 7-7. Validation Plot for the Model US$_{WD, NV}$.**

### *7.5.2.6. Model assessment - Parallel Void (PV) conditions*

Table 7-3 summarizes the MAPE and posterior statistics of the model form for PV conditions (provided in Equation (7.13)). These were assessed using the procedures provided in Subsection 7.2.3 and the 100 experimental data points.

**Table 7-3. MAPE and Posterior Statistics of the US$_{WD, PV}$ Model.**

| Model Name | MAPE (%) | Parameters | Mean | Standard deviation | COV | Correlation coefficients between $\theta_i$ | | |
|---|---|---|---|---|---|---|---|---|
| | | | | | | $\theta_0$ | $\theta_1$ | $\theta_2$ |
| US$_{WD, PV}$ | 1.61 | $\theta_0$ | 1.0232 | 0.0047 | 0.005 | 1 | | |
| | | $\theta_1$ | –0.1553 | 0.0141 | –0.09 | –0.45 | 1 | |
| | | $\theta_2$ | –0.0153 | 0.0019 | –0.12 | 0.01 | 0.84 | 1 |
| | | $\sigma$ | 0.0256 | 0.0098 | 0.38 | | | |

Table 7-3 shows that the model parameters (i.e., $\theta_0$, $\theta_1$, and $\theta_2$) have smaller COVs (i.e., 0.005, –0.09, and –0.12, respectively) indicating good confidence in the mean parameter estimations. The mean estimates of these parameters indicate that $C_{T,US}$, when exposed to PV and WD conditions, is more sensitive to the $\gamma_{t_{WD}}$ term than the $\ln[\gamma_{\%Cl^-}]\gamma_{t_{WD}}$ term. Table 7-3 also shows that MAPE (i.e., 1.61%) and σ (i.e., 0.0256) of the Model $US_{WD, PV}$ are reasonably small. Because of these reasons, **the model in Table 7-3 is referred to as Model $US_{WD, PV}$ herein**.

A typical validation plot and its characteristics were provided in Subsection 7.2.3.5. The validation plot for the Model $US_{WD, PV}$ is shown in Figure 7-8. Among the 100 data points, the four data points near the top right region shows underestimation and two data points near the bottom left region show overestimation of $C_{T,US}$. Most of the remaining data points fall along the 1:1 line (spread with an approximately equal width) and exhibit no significant bias or residual trend; indicating a reasonably good agreement with the homoskedasticity assumption. The spread of the most data points along the 1:1 line indicates good prediction accuracy. In addition, 93 percent data fall within and 7 percent data fall outside the $\pm\sigma$ region; indicating reasonably good agreement with the normality assumptions.

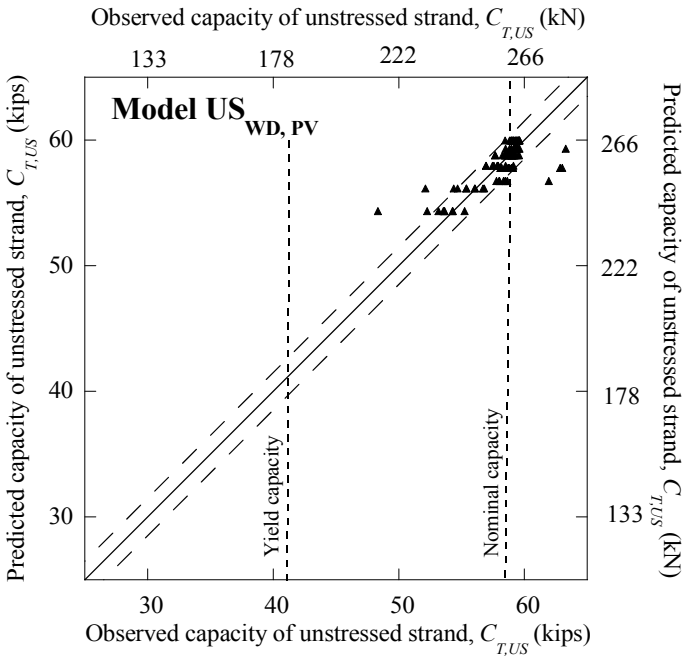


**Figure 7-8. Validation Plot for the Model US$_{WD, PV}$.**

### *7.5.2.7. Model assessment - Bleedwater, Inclined, and Orthogonal Void (BIOV) conditions*

Table 7-4 provides the MAPE and posterior statistics for the full model form for BIOV conditions (provided in Equation (7.13)). The model was assessed using the 239 data points.

**Table 7-4. MAPE and Posterior Statistics of the $US_{WD, BIOV}$ Model.**

| Model Name | MAPE (%) | Parameters | Mean | Standard deviation | COV | Correlation coefficients between $\theta_i$ | | |
|---|---|---|---|---|---|---|---|---|
| | | | | | | $\theta_0$ | $\theta_1$ | $\theta_2$ |
| $US_{WD, BIOV}$ | 3.15 | $\theta_0$ | 1.0333 | 0.0056 | 0.005 | 1 | | |
| | | $\theta_1$ | –0.3567 | 0.0124 | 0.03 | –0.61 | 1 | |
| | | $\theta_2$ | –0.0285 | 0.0015 | –0.05 | 0.01 | 0.74 | 1 |
| | | σ | 0.0350 | 0.0107 | 0.31 | | | |

Table 7-4 shows that the MAPE and σ for the full model are reasonably small (i.e., 3.15% and 0.0350, respectively) indicating good prediction accuracy. The mean estimates for $\theta_1$ and $\theta_2$ indicate that the capacity is more sensitive to $\gamma_{t_{WD}}$ than $\ln[\gamma_{\%sCl^-}]\gamma_{t_{WD}}$. The high confidence levels on the mean estimates of the model parameters $\theta_0$, $\theta_1$, and $\theta_2$ (i.e., 1.0333, –0.3567, and –0.0285, respectively) are evident from their reasonably small COVs (i.e., 0.005, –0.03, –0.05, respectively). Hence, **the reduced model in Table 7-4 is referred to as Model $US_{WD, BIOV}$ herein**.

A typical validation plot and its characteristics were provided in Subsection 7.2.3.5. In the validation plot in Figure 7-9, most data points lie within the ±σ region. This exhibits reasonably good prediction accuracy. As shown in Figure 7-9, although variability exists among the observed $C_{T,US}$ for identical exposure conditions, the mean of the observed values of $C_{T,US}$ corresponding to a particular predicted $C_{T,US}$ lies very close to the 1:1 line. This indicates good accuracy in model prediction, given the inherent variability (due to varying exposure conditions and strand characteristics) in the corrosion process.

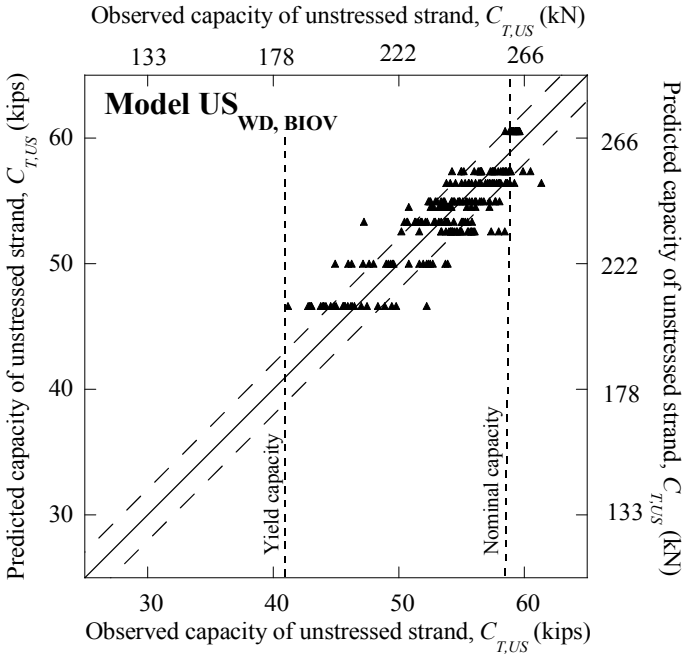


**Figure 7-9. Validation Plot for the Model $US_{WD, BIOV}$.**

*7.5.2.8. Prediction of tension capacity of unstressed strands*

In this subsection, the $US_{WD}$ models are used to predict or extrapolate $C_{T,US}$ when various void, moisture, and chloride conditions exist. Figure 7-10 (a), (b), (c), and (d) show the extrapolated $C_{T,US}$ under WD exposure conditions with 0.006, 0.018, 0.18, and 1.8 $\%sCl^-$ solutions, respectively. These predictions are based on the assumption that $\phi_{wet}$ is equal to 0.17 (see Equation (7.11) in Subsections 7.4.1 and 7.4.3 for details).

Comparison between, Figure 7-10 (a) and Figure 7-10 (b), (c), or (d) shows that when voids exist, $C_{T,US}$ can drop below $MUTS_{ARS}$ within approximately one year. However, the $C_{T,US}$ remained higher than yield capacity for up to approximately 18, 14, 10, and 7 years, respectively for the WD conditions with 0.006, 0.018, 0.18, and 1.8 $\%sCl^-$, respectively. These times are shown by the vertical-dashed arrows in Figure 7-10. The possibility of capacity to drop below $MUTS_{ARS}$ within a year, especially for conditions where WD cycles can be numerous, shows that the frequency of inspection

and structural assessment of PT bridges should be performed on a regular basis. The inspection frequency should depend on the likelihood of infiltration of water, chlorides, or both into the ducts. Such predictive models are not performed as part of this study; but could be the subject of future research.

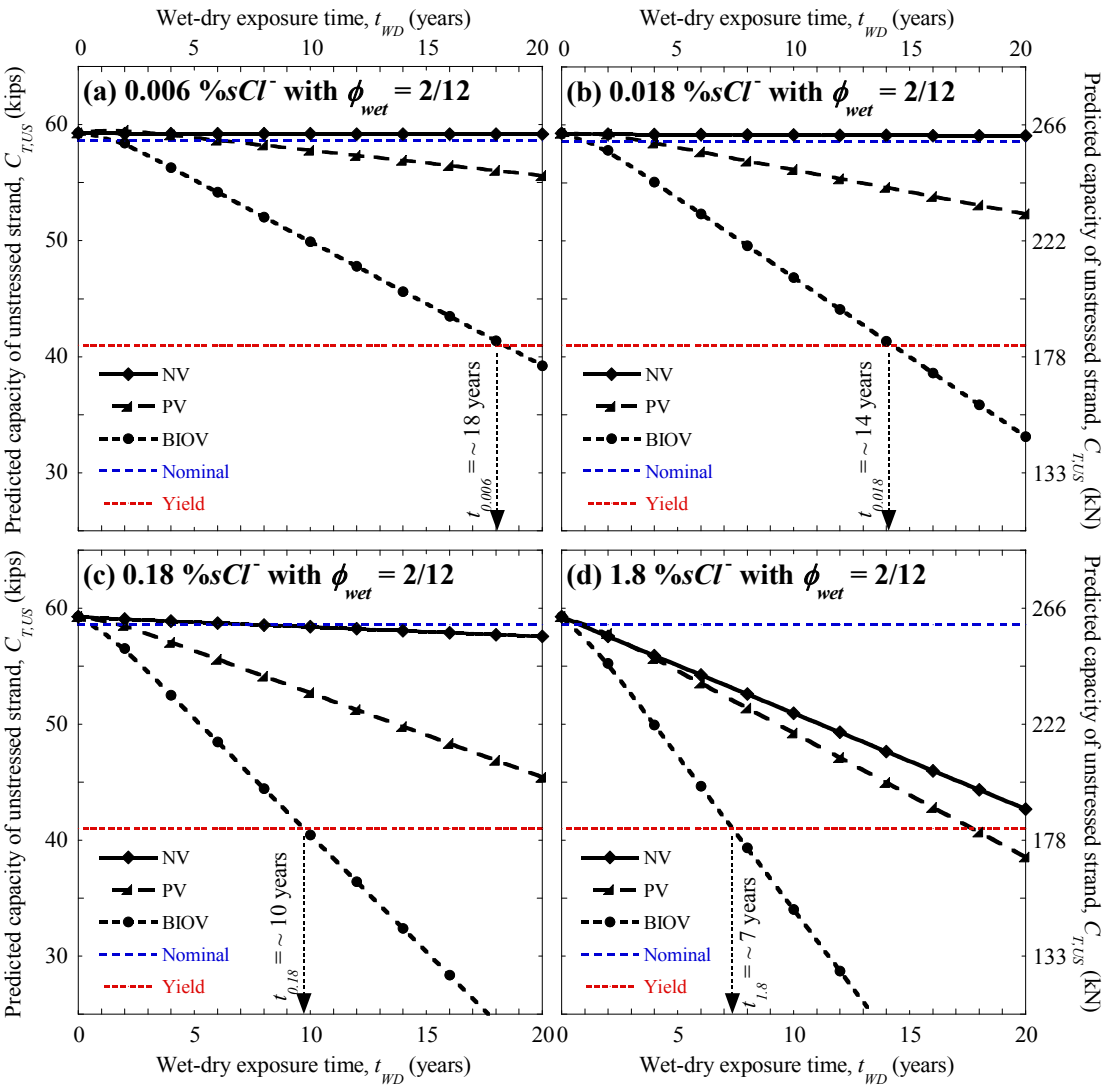


**Figure 7-10. Capacity of Unstressed Strands under WD Exposure to Various Chloride Solutions (Predicted Using $US_{WD}$ Models).**

### 7.5.3. STEP WD-3: Models for stressed strands under WD exposure conditions (using stressed strand data only)

In this subsection, three probabilistic models are developed to predict $C_T$ of stressed strands, exposed to WD conditions along with NV, PV, and BIOV conditions. These models are denoted as Model $SS_{WD,\,NV}$, Model $SS_{WD,\,PV}$, Model $SS_{WD,\,BIOV}$, respectively. Experimental data from 60, 85, and 79 stressed strand samples have been used to develop the $SS_{WD,\,NV}$, $SS_{WD,\,PV}$, and $SS_{WD,\,BIOV}$, respectively. Prior to formulating the models, the effects of various test parameters on $C_{T,SS}$ are diagnosed.

#### *7.5.3.1. Diagnosis of the effect of wet-dry exposure time*

The stressed strand samples were tested at 0, 12, 16, and 21 months. Figure 7-11 (a), (b), and (c) indicate that capacity of stressed strands under NV, PV, and BIOV conditions can also be modeled using a linear function of $t_{WD}$ as used in the case of unstressed strands. A comparison between Figure 7-11 (a), (b), and (c) shows that the slope of this linear fit increase as the void condition changes from NV, to PV, to BIOV. However, in general, the scatter in the capacity data increases as $t_{WD}$ increases. Hence, an interaction term, as presented in Subsection 7.5.3.3, can help in minimizing the heteroskedasticity and improving the model quality.

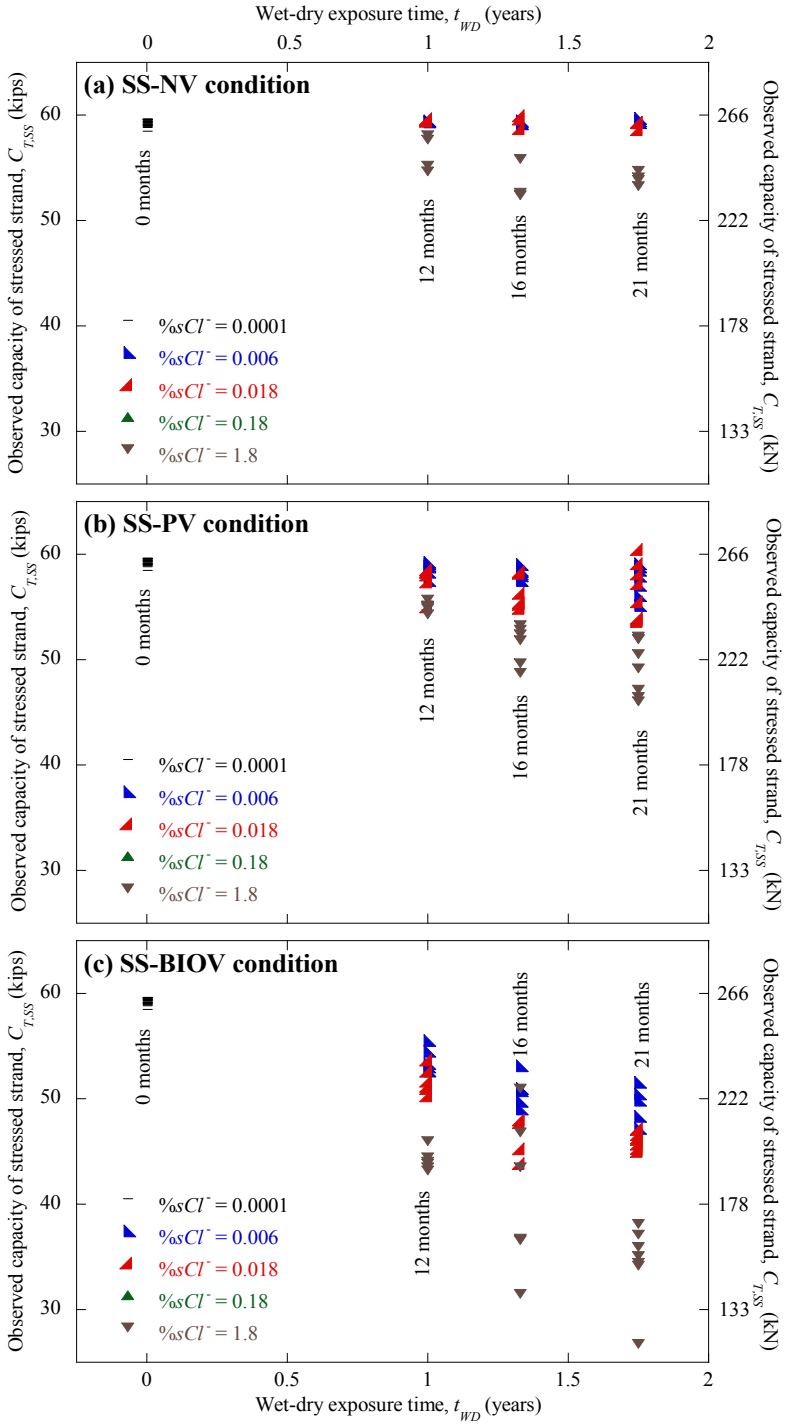


**Figure 7-11. Effect of Wet-dry Exposure Time on Capacity of Stressed Strands (with $\phi_{wet}$ = 0.5).**

*7.5.3.2. Diagnosis of the effect of chloride concentration in exposure solution*

Figure 7-12 (a) and Figure 7-13 (a) show the scatter plots between $C_{T,SS}$ (for NV conditions) and $\%sCl^-$ and ln[$\%sCl^-$], respectively. A comparison between the trends in these diagnostic plots indicates that $\%sCl^-$ is a more appropriate capacity predictor term than ln[$\%sCl^-$], when NV conditions exist. Similar to the observation made in the case of unstressed strands (see Figure 7-6 (a)), negligible $C_T$ loss is observed until 0.018 $\%sCl^-$, after which there is a slight increase in the slope. This is probably because longer time was needed to build up sufficient amount of chlorides at the surface of completely embedded strands and then initiate/propogate corrosion, when exposed to 0.006 and 0.018 $\%sCl^-$ solutions than when exposed to 1.8 $\%sCl^-$ solution. The comparison between the Figure 7-12 (b) and Figure 7-13 (b) for PV conditions, indicates that both $\%sCl^-$ and ln[$\%sCl^-$] term may be used as a linear term to predict $C_{T,SS}$. However, stressed strands were not tested at 0.18 $\%sCl^-$ condition or any other intermediate $\%sCl^-$ levels. Hence, the acceptance of $\%sCl^-$ term as a predictor can be questionable. In addition, Figure 7-13 (b) indicates an approximate linear relationship between capacity and ln[$\%sCl^-$]. Because of these reasons, and in order to keep the same model form as in the case of $US_{WD, PV}$ model, the ln[$\%sCl^-$] term seems to be more appropriate predictor term than $\%sCl^-$ term. Figure 7-12 (c) for BIOV conditions indicates a nonlinear relationship between $\%sCl^-$ level and capacity. In addition, Figure 7-13 (c) clearly shows a good linear relationship between ln[$\%sCl^-$] and $C_{T,SS}$, for the range of $\%sCl^-$ tested. Hence, for stressed strands under BIOV conditions, ln[$\%sCl^-$] is a more appropriate capacity predictor than $\%sCl^-$ . As observed with the case of unstressed strands in Subsection 7.5.2.2, Figure 7-12 and Figure 7-13 indicate a general trend of increasing scatter as the $\%sCl^-$ increases. This might induce some heteroskedasticity into the model. A two-way interaction term between $t_{WD}$ and $\%sCl^-$ or ln[$\%sCl^-$] might help in making the models more homoskedastic.

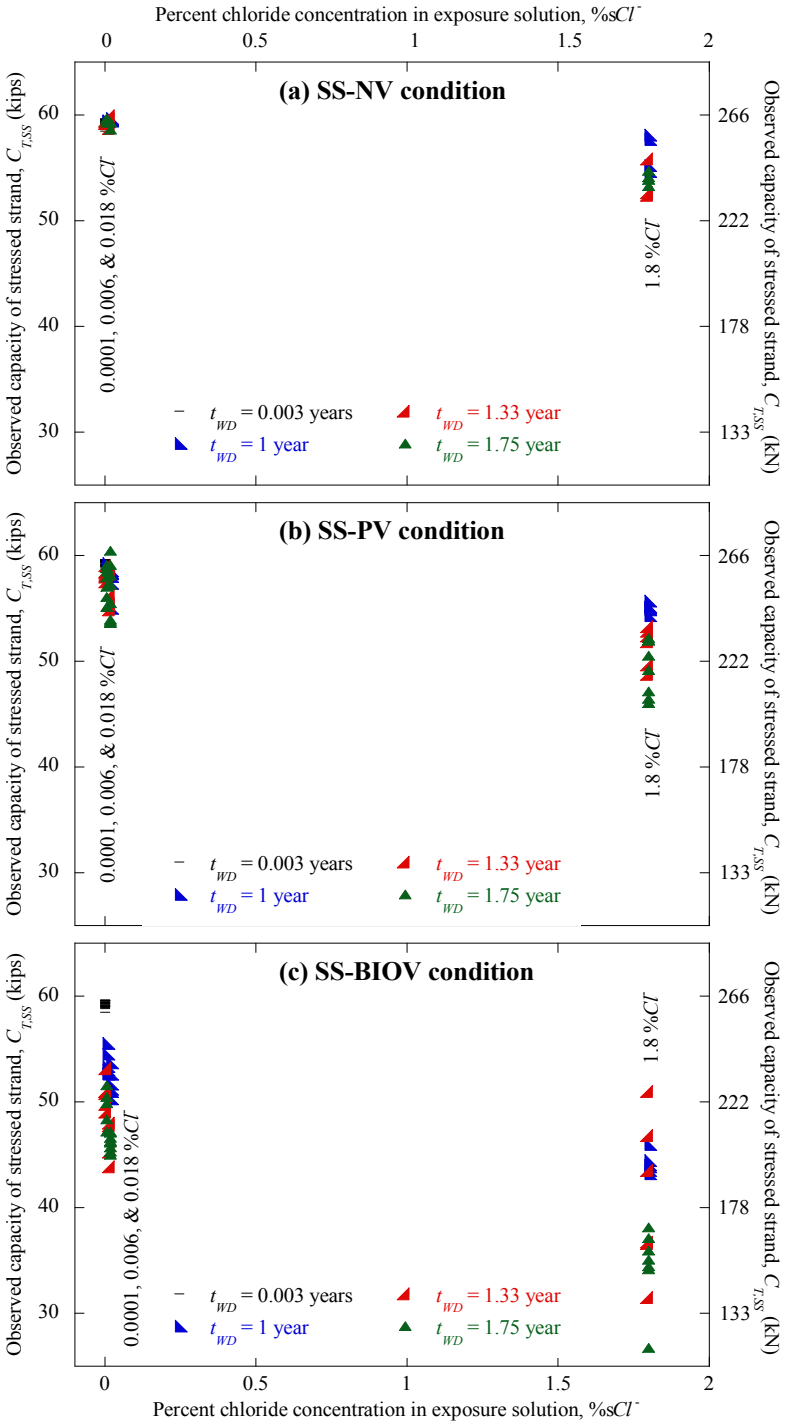


**Figure 7-12. Effect of %$sCl^-$ on Capacity of Stressed Strands (with $\phi_{wet}$ = 0.5).**

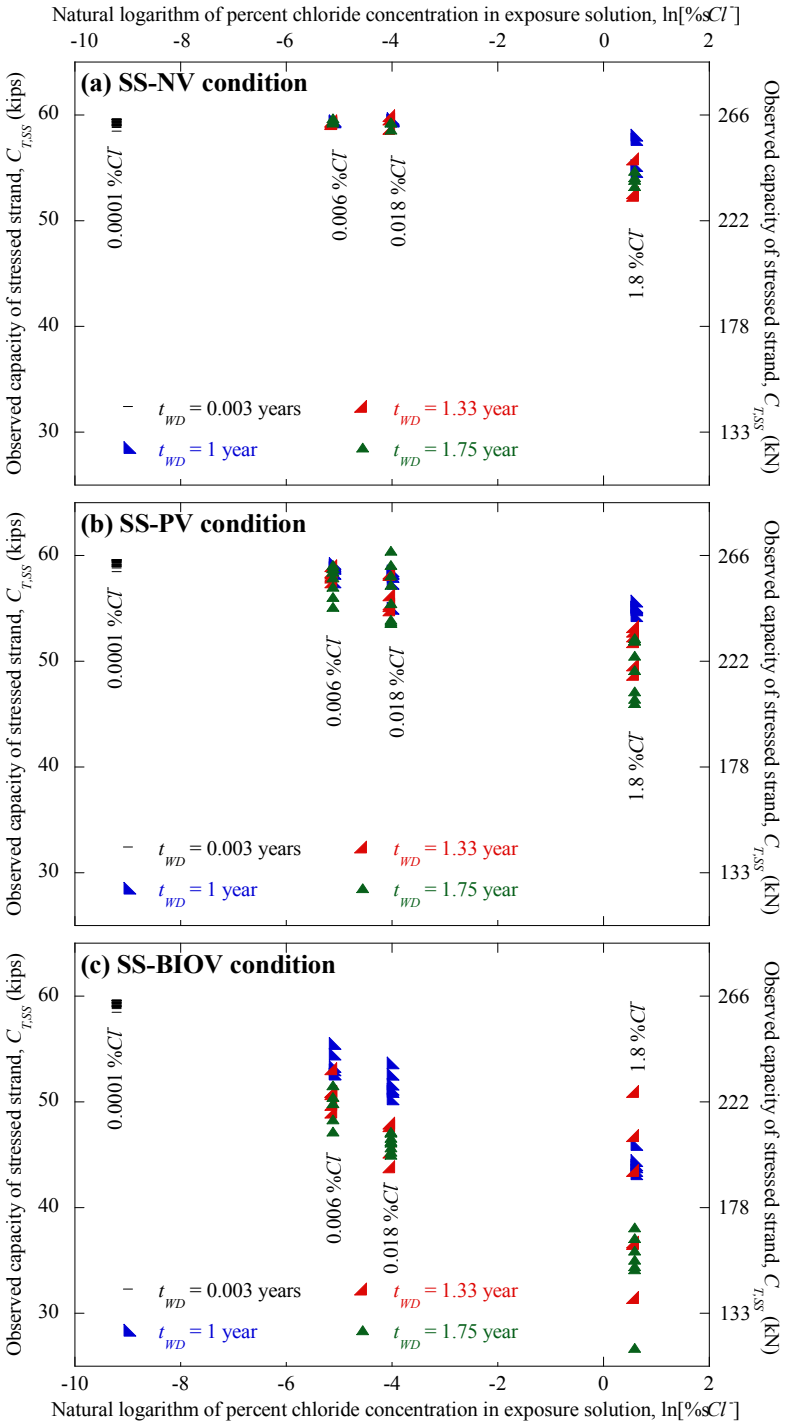


**Figure 7-13. Effect of ln[%$sCl^-$] on Capacity of Stressed Strands (with $\phi_{wet}$ = 0.5).**

### *7.5.3.3. Diagnosis of the effect of interaction between chloride and time parameters*

In the previous two subsections, a need for an interaction term to improve prediction accuracy, and agreements with homoskedasticity assumptions was cited. Detailed justification for incorporating a two-way interaction term was provided in Subsection 7.5.2.3 on modeling $C_{T,US}$. The same justifications are valid for modeling $C_{T,SS}$. In the previous subsection, it was found that $\%sCl^-$ is an appropriate capacity predictor term for NV condition. Hence, $\%sCl^- \times t_{WD}$ is an appropriate two-way interaction term to predict $C_{T,SS}$ under NV condition. In the previous subsection, it was also found that the $\ln[\%sCl^-]$ is an appropriate predictor for $C_{T,SS}$ under PV and BIOV conditions. Hence, $\ln[\%sCl^-]\ t_{WD}$ can be used as an appropriate two-way interaction term to predict $C_{T,SS}$ under PV and BIOV conditions.

### *7.5.3.4. Model formulation*

Based on the diagnostic study and physical principles behind the time-dependent corrosion process, three probabilistic model forms to predict $C_{T,SS}$ under NV, PV, and BIOV conditions are formulated as follows:

$$\begin{aligned} R_{C_{T,SS}}(\mathbf{x},\boldsymbol{\Theta}) &= \theta_0 + \theta_1\gamma_{t_{WD}} + \theta_2\gamma_{\%sCl^-}\gamma_{t_{WD}} + \sigma\varepsilon \quad \text{(for NV condition)} \\ R_{C_{T,SS}}(\mathbf{x},\boldsymbol{\Theta}) &= \theta_0 + \theta_1\gamma_{t_{WD}} + \theta_2 \ln[\gamma_{\%sCl^-}]\gamma_{t_{WD}} + \sigma\varepsilon \quad \text{(for PV and BIOV conditions)} \end{aligned} \tag{7.14}$$

where the terms are as defined in Equation (7.1) and Subsection 7.4.1. These $SS_{WD}$ model forms are similar to the $US_{WD}$ model forms (i.e., Equation (7.13)). When the $t_{WD}$ is zero, the intercept term will predict $C_{T,SS}$ that is practically very close to $MUTS_{ARS}$. The term $\gamma_{t_{WD}}$ in the predictor parameters will capture the effect of $t_{WD}$, where as the two-way interaction term (i.e., $\gamma_{\%sCl^-}\gamma_{t_{WD}}$ or $\ln[\gamma_{\%sCl^-}]\gamma_{t_{WD}}$) between the chloride and time parameters will minimize the model heteroskedasticity. The parameters in these model

forms are assessed using the procedures given in Subsection 7.2 and are provided in the next three subsections.

### *7.5.3.5. Model assessment - No Void (NV) conditions*

A total of 60 data points were used to develop this model. MAPE and posterior statistics of the full model form for NV conditions (see Equation (7.14)) were assessed using the procedures given in Subsection 7.2.3. However, because the COV of $\theta_1$ (i.e., the model parameter corresponding to $\gamma_{t_{WD}}$) is as large as 1.77, it seems that full model does not correspond to the most parsimonious parameter set. Because of this, the $\gamma_{t_{WD}}$ term was removed to formulate a reduced model for NV conditions. Table 7-5 summarizes the MAPE and posterior statistics of this reduced model. The reasonably small COVs of coefficients (i.e., $\theta_i$) in the reduced model indicates that the model can predict $C_{T,SS}$ with reasonable accuracy. The MAPE of the reduced model is 0.73%. In addition, the model error parameter, $\sigma$, of the reduced model is 0.0121. Further reduction of the model resulted in large MAPE and model errors. Based on these findings, **the reduced model in Table 7-5 is referred to as Model $SS_{WD, NV}$ herein**.

**Table 7-5. MAPE and Posterior Statistics of the $SS_{WD, NV}$ Model.**

| Model Name | MAPE (%) | Parameters | Mean | Standard deviation | COV | Correlation coefficients between $\theta_i$ | |
|---|---|---|---|---|---|---|---|
| | | | | | | $\theta_0$ | $\theta_2$ |
| $SS_{WD, NV}$ | 0.73 | $\theta_0$ | 1.0126 | 0.0017 | 0.002 | 1 | |
| | | $\theta_2$ | –2.2542 | 0.1141 | –0.05 | –0.43 | 1 |
| | | $\sigma$ | 0.0121 | 0.0053 | 0.44 | | |

Based on the discussions in Subsection 7.2.3.5 on validation plots, Figure 7-14 indicates reasonably good prediction model. The spread of the data in Figure 7-14 has an approximately equal width, lies along the 1:1 line, and does not show any significant residual trend or bias in prediction; indicating good agreement with the homoskedasticity assumption. Also, 88 percent data points lie inside the $\pm\sigma$ region indicating that normality assumption is reasonably agreeable. Because of the relatively small amount of corrosion and less scatter among the capacity data, the Model $SS_{WD,\ NV}$ has less MAPE than the models for PV and BIOV conditions discussed next.

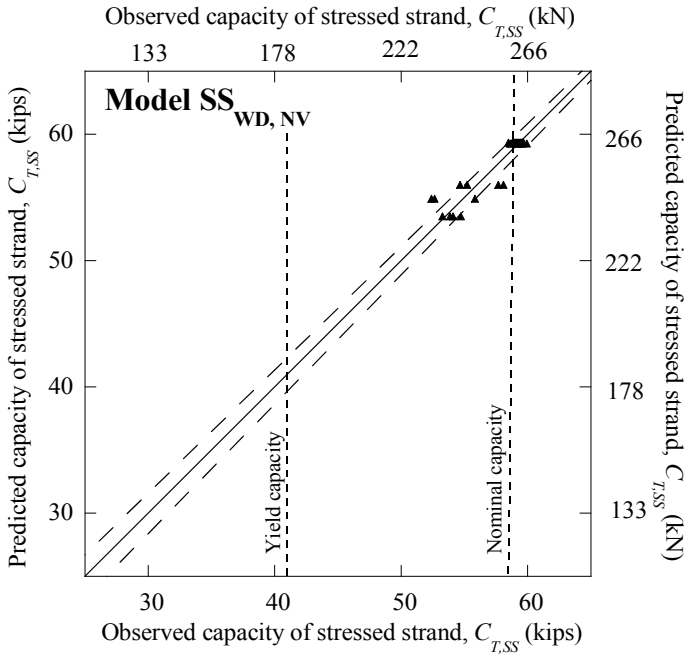


**Figure 7-14. Validation Plot for the Model $SS_{WD, NV}$.**

*7.5.3.6. Model assessment - Parallel Void (PV) conditions*

The model parameters for $SS_{WD, PV}$ model were assessed using the 85 data points. These statistical results are summarized in Table 7-6. The MAPE and σ (i.e., 1.89% and 0.0249, respectively) of the full model are reasonably small. In addition, the absolute COVs of the model parameters corresponding to the predictor parameters are less than 0.07; indicating good confidence in the mean estimates. In summary, the full model seems to be the most parsimonious model and has good prediction accuracy. **Hence, the full model in Table 7-6 is referred to as Model $SS_{WD, PV}$ herein**.

**Table 7-6. MAPE and Posterior Statistics of the $SS_{WD, PV}$ Model.**

| Model Name | MAPE (%) | Parameters | Mean | Standard deviation | COV | Correlation coefficients between $\theta_i$ | | |
|---|---|---|---|---|---|---|---|---|
| | | | | | | $\theta_0$ | $\theta_2$ | $\theta_3$ |
| $SS_{WD, PV}$ | 1.89 | $\theta_0$ | 1.0129 | 0.0048 | 0.005 | 1 | | |
| | | $\theta_1$ | –0.2719 | 0.0141 | –0.05 | –0.46 | 1 | |
| | | $\theta_2$ | –0.0277 | 0.0018 | –0.07 | 0.00 | 0.82 | 1 |
| | | σ | 0.0249 | 0.0100 | 0.40 | | | |

Based on the discussions in Subsection 7.2.3.5 on validation plots, the validation plot in Figure 7-15 suggests that the Model $SS_{WD, PV}$ provides good prediction. In Figure 7-15, the width of the spread of the data is approximately equal; indicating good agreement with the homoskedasticity assumption. Also, Figure 7-15 indicates no specific significant residual trend or bias. The means of the observed capacities corresponding to the predicted capacities seems to lie along the 1:1 line. This indicates reasonably good prediction of capacity, given the scatter in the data among the samples with identical exposure conditions. Also, the normality assumption is approximately satisfied because most data points lie inside and some lie outside the ±σ region.

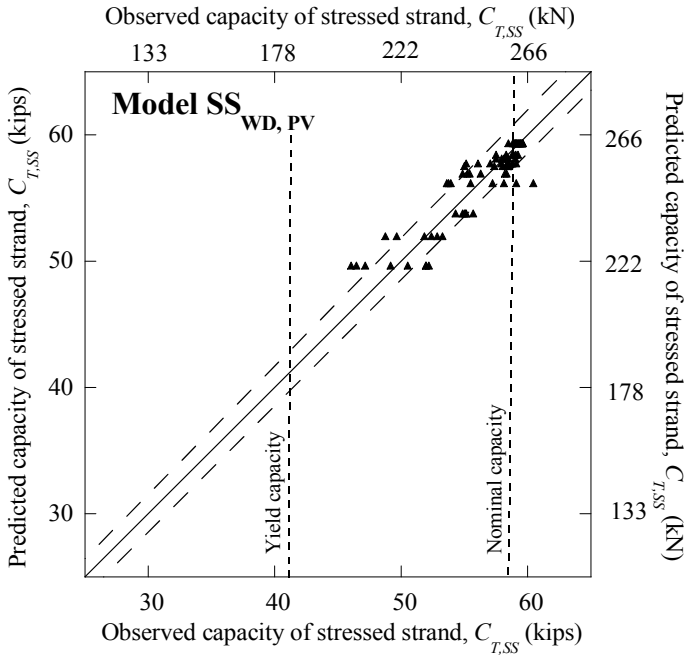


**Figure 7-15. Validation Plot for the Model SS$_{WD, PV}$.**

### *7.5.3.7. Model assessment - Bleedwater, Inclined, and Orthogonal Void (BIOV) conditions*

The model form for BIOV conditions in Equation (7.14) is assessed using the 79 data points from the stressed strands exposed to OV conditions only. However, this model can be used to predict $C_{T,SS}$ under BIOV conditions and is denoted as SS$_{WD, BIOV}$ model. This is justified because $C_{T,SS}$ under OV, IV and BV conditions are statistically similar (see Subsection 6.5.5 for details). Table 7-7 provides MAPE and posterior statistics for the SS$_{WD, BIOV}$ model. Table 7-7 shows that the MAPE of the full model form is 3.25%.

Although reasonable, this is slightly larger than that observed for $SS_{WD, PV}$ model; and is because of the larger scatter in the observed capacity data. Table 7-7 shows that the σ of the full model is 0.0175 (a reasonably small value). In addition, COVs of the model parameters (i.e., $\theta_0$, $\theta_1$, and $\theta_2$) corresponding to the intercept, $\gamma_{t_{WD}}$, and $\ln[\gamma_{\%Cl^-}]\gamma_{t_{WD}}$ terms are reasonably small (i.e., 0.01, –0.04, –0.07, respectively). Hence, **the full model in Table 7-7 is referred to as Model $SS_{WD, BIOV}$, herein**.

**Table 7-7. MAPE and Posterior Statistics of the $SS_{WD, BIOV}$ Model.**

| Model Name | MAPE (%) | Parameters | Mean | Standard deviation | COV | Correlation coefficients between $\theta_i$ | | |
|---|---|---|---|---|---|---|---|---|
| | | | | | | $\theta_0$ | $\theta_1$ | $\theta_2$ |
| $SS_{WD, BIOV}$ | 3.25 | $\theta_0$ | 1.0095 | 0.0083 | 0.01 | 1 | | |
| | | $\theta_1$ | –0.6274 | 0.0250 | –0.04 | –0.45 | 1 | |
| | | $\theta_2$ | –0.0485 | 0.0033 | –0.07 | 0.01 | 0.83 | 1 |
| | | σ | 0.0427 | 0.0175 | 0.41 | | | |

Discussions on reading the validation plots were provided earlier in Subsection 7.2.3.5. Figure 7-16 shows the validation plot for the Model $SS_{WD, BIOV}$. In this validation plot, the means of the observed values of $C_{T,SS}$ corresponding to a particular predicted $C_{T,SS}$ fall near the 1:1 line. In Figure 7-16, the large scatter among the data points corresponding to the predicted $C_{T,SS}$ of approximately 40 kips (178 kN) may seem to suggest that the homoskedasticity assumption is not satisfied. However, this is the scatter in $C_{T,SS}$ that is observed when exposed to 0.18 $\%sCl^-$ for a period of 16 months and not generated due to the model inadequacy. Moreover, $\sigma \times MUTS_{ARS}$ is equal to 3.02 kips (13 kN), which is less than the standard deviation of the observed $C_{T,SS}$ (i.e., 7.32 kips (32.6 kN)). Hence, the reduced model can be assumed to be practically homoskedastic. Also, because most data points lie within and some lie outside the ±σ region, the normality assumption seems to be reasonably validated.

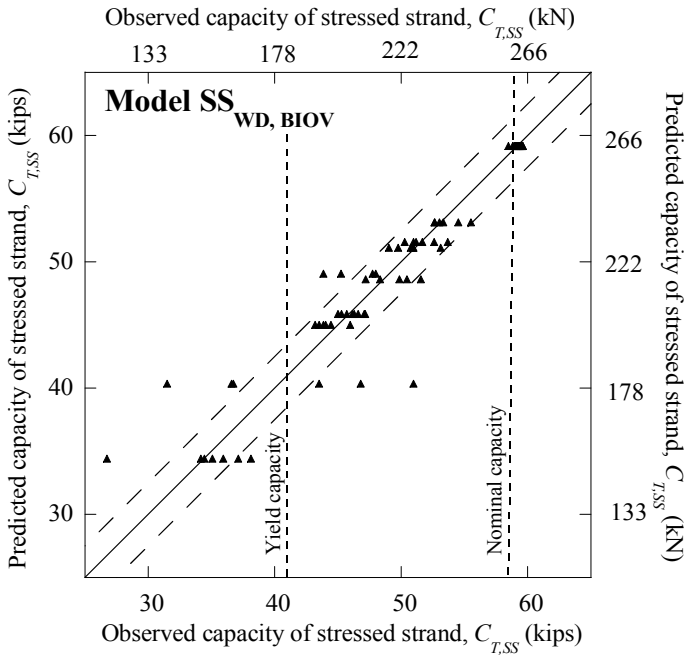


**Figure 7-16. Validation Plot for the Model SS$_{WD, BIOV}$.**

### *7.5.3.8. Prediction of tension capacity of stressed strands*

Subsection 7.4.3 presented $C_{T,US}$ extrapolated using the US$_{WD}$ models. This subsection presents $C_{T,SS}$ extrapolated or predicted using the SS$_{WD}$ models. Figure 7-17 (a), (b), (c), and (d) show the extrapolated $C_{T,SS}$ values when exposed to WD conditions with 0.006, 0.018, 0.18, and 1.8 $\%sCl^-$ solutions, respectively. These predictions are based on the assumption that $\phi_{wet}$ is equal to 0.17 (see Equation (7.11) in Subsection 7.4.1 and 7.4.3 for details). Note that $\phi_{wet}$ could be larger or smaller than this value; depending on varying field conditions. The larger the $\phi_{wet}$, the faster will be the rate of corrosion and capacity loss, and viceversa.

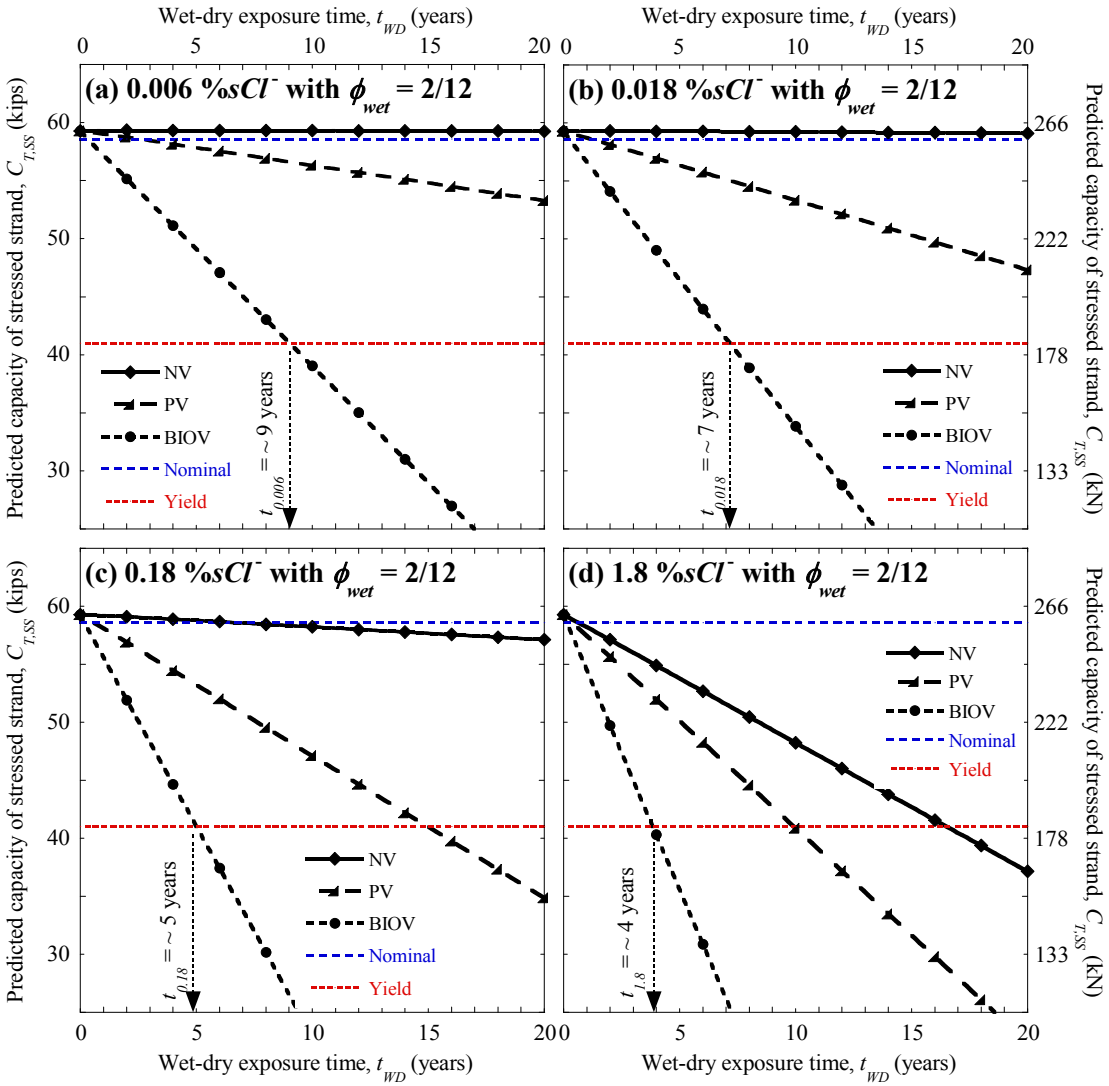


**Figure 7-17. Capacity of Stressed Strands under WD Exposure ($\phi_{wet}$ = 0.17) to Various Chloride Solutions (Predicted Using $SS_{WD}$ Models).**

Figure 7-17 (a) and (b) shows that negligible reduction in $C_{T,SS}$ is expected when exposed to NV and 0.006 or 0.18 $\%sCl^-$ conditions for $t_{WD}$ equal to 20 years. Figure 7-17 (c) and (d) show that, in the case of NV conditions, the exposure to 0.18 and 1.8 $\%sCl^-$ solutions (i.e., moderate and high chloride conditions) can cause $C_T$ to drop

below $MUTS_{ARS}$ (or nominal capacity) within seven and one year, respectively. From Figure 7-17 (a), (b), (c), and (d) it can be concluded that, for PV and BIOV conditions, the predicted $C_{T,SS}$ can, in general, fall below $MUTS_{ARS}$ (or nominal capacity)within approximately one year. For PV samples exposed to 0.006 $\%sCl^-$ condition, $C_{T,SS}$ dropped below $MUTS_{ARS}$ within approximately two years. Figure 7-17 (a), (b), (c), and (d) show that when BIOV and WD conditions exist, $C_{T,SS}$ can drop to a value below yield capacity within approximately 9, 7, 5, and 4 years (shown by vertical dashed arrows) when exposed to 0.006, 0.018, 0.18, and 1.8 $\%sCl^-$ solutions, respectively.

### 7.5.4. STEP WD-4: Models for stressed strands under WD exposure conditions (using unstressed strand model and stressed strand data)

This section presents three probabilistic capacity models to predict $C_{T,SS}$ under WD exposure conditions. These models are denoted as Model US-$SS_{WD,\,NV}$, Model US-$SS_{WD,\,PV}$, Model US-$SS_{WD,\,BIOV}$. Experimental data obtained from 60, 85, and 79 stressed strand samples and $C_{T,US}$ values predicted using $US_{WD,\,NV}$, $US_{WD,\,PV}$, and $US_{WD,\,BIOV}$ models are used to develop the US-$SS_{WD,\,NV}$, US-$SS_{WD,\,PV}$, and US-$SS_{WD,\,BIOV}$ models, respectively.

#### *7.5.4.1. Diagnosis of the relationship between the capacities of unstressed and stressed strands*

Figure 7-18 (a), (b), and (c) show the scatter plots between the predicted $C_{T,US}$ and observed $C_{T,SS}$ under similar exposure conditions. At first, it might seem that a linear relationship between $C_{T,US}$ and $C_{T,SS}$ is reasonable. However, preliminary model assessments indicated that a linear model will result in the overprediction of $C_{T,SS}$ near $MUTS_{ARS}$. This is because the slope of the relationship between $C_{T,US}$ and $C_{T,SS}$ reduces as $C_{T,SS}$ approaches $MUTS_{ARS}$. Hence, a power model seems to be more appropriate than a linear model.

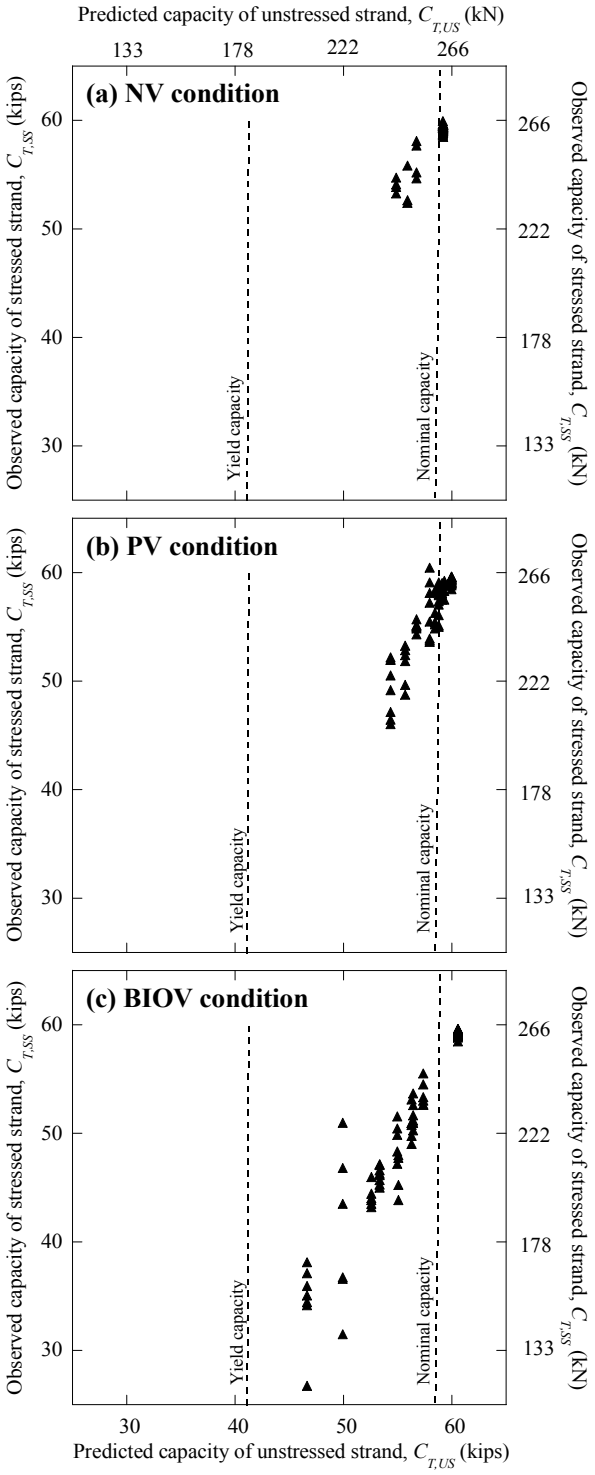


**Figure 7-18. Scatter Plots between the Capacities of Unstressed and Stressed Strands.**

### *7.5.4.2. Model formulation*

As determined in the previous subsection, a power model is formulated as follows:

$$R_{C_{T,SS}} = \theta_0 \left( \gamma_{C_{T,US}} \right)^{\theta_1} + \sigma\varepsilon \quad \text{(for NV, PV, and BIOV conditions)} \tag{7.15}$$

where the terms are as defined in Subsection 7.4.1 and $\gamma_{C_{T,US}}$ is equal to $R_{C_{T,US}}$ predicted using $C_{T,US}$, which is the median value predicted using an appropriate $US_{WD}$ model. In other words, $\gamma_{C_{T,US}}$ is the expression on the right side of the $US_{WD}$ models after excluding the model error term. $\sigma\varepsilon$. The power model form in Equation (7.15) does not have an intercept term and, hence, will ensure that $C_{T,SS}$ is zero when $C_{T,US}$ is zero. Also, the power model form helps in minimizing the overprediction of $C_{T,SS}$ as it approaches $MUTS_{ARS}$. The model parameters are assessed using the maximum likelihood approach for nonlinear models given in Subsection 7.2.3. Following is a discussion on the assessment of $US\text{-}SS_{WD,\,NV}$, $US\text{-}SS_{WD,\,PV}$, and $US\text{-}SS_{WD,\,BIOV}$ models.

### *7.5.4.3. Model assessment - No Void (NV) conditions*

This model can be used to predict $C_T$ of stressed strands inside fully grouted tendons. This model is assessed using the 60 observed data on $C_{T,SS}$ and the corresponding values of $C_{T,US}$ (predicted using $US_{WD,NV}$ model). Table 7-8 shows that the COVs (i.e., 0.001 and 0.05) of $\theta_0$ and $\theta_1$ are reasonably small indicating good confidence in their mean estimates. Also, the mean and COV of the model error term (i.e., $\sigma$) are 0.0117 and 0.09, respectively. These results indicate that the $US\text{-}SS_{WD,\,NV}$ model can predict $C_{T,SS}$ with reasonable accuracy. The MAPE of the $US\text{-}SS_{WD,\,NV}$ model is 0.73% (equivalent to that of $SS_{WD,\,NV}$ model). Based on these findings, **the model in Table 7-8 is referred to as Model $US\text{-}SS_{WD,\,NV}$ herein**. Figure 7-19 indicates that $US\text{-}SS_{WD,\,NV}$ can provide reasonably good prediction of capacity. The data in Figure 7-19 are spread along the

1:1 line, with an approximately equal width, and do not show any significant residual trend. These indicate reasonably good agreement with the homoskedasticity assumption. Also, most of the data points lie inside and some data points lie outside the ±σ region indicating that normality assumption is reasonably valid.

**Table 7-8. MAPE and Posterior Statistics of the US-SS$_{WD, NV}$ Model.**

| Model Name | MAPE (%) | Parameters | Mean | Standard deviation | COV | Correlation coefficients between $\theta_i$ | | |
|---|---|---|---|---|---|---|---|---|
| | | | | | | $\theta_0$ | $\theta_1$ | σ |
| SS$_{WD, NV}$ | 0.73 | $\theta_0$ | 0.9983 | 0.0014 | 0.001 | 1 | | |
| | | $\theta_1$ | 1.3576 | 0.0648 | 0.05 | 0.04 | 1 | |
| | | □ | 0.0117 | 0.0011 | 0.09 | 0.06 | −0.01 | 1 |

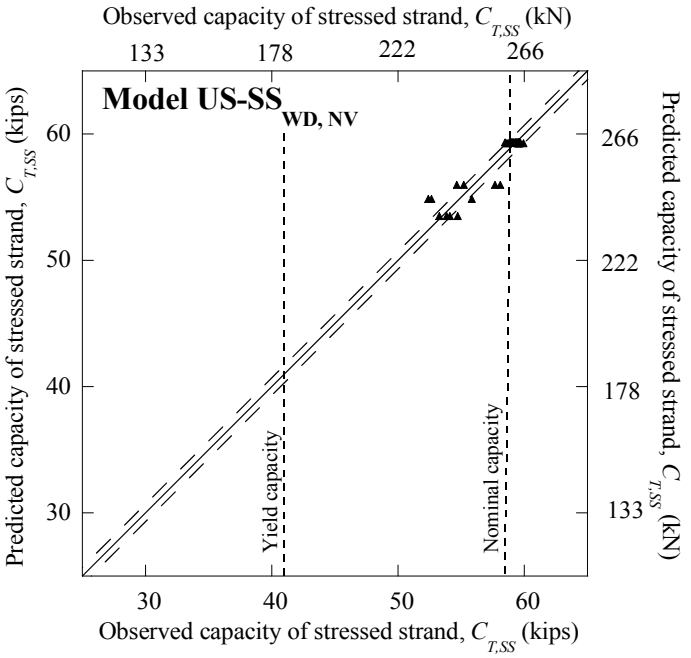


**Figure 7-19. Validation Plot for US-SS$_{WD, NV}$ Model.**

*7.5.4.4. Model assessment - Parallel Void (PV) conditions*

Model US-$SS_{WD,\ PV}$ can be used to predict $C_{T,SS}$ when voids exist at or near the midspan regions in tendons. The model parameters for the model form for PV conditions (provided in Equation (7.15)) were assessed using the 85 stressed strand data and corresponding $C_{T,US}$ values predicted using the $US_{WD,\ PV}$ model. The $US_{WD,\ PV}$ model was assessed based on 100 unstressed strand data points. Hence, a total of 185 data points are effectively used in developing US-$SS_{WD,\ PV}$ model. The statistical parameters of US-$SS_{WD,\ PV}$ model are summarized in Table 7-9.

**Table 7-9. MAPE and Posterior Statistics of the US-$SS_{WD,\ PV}$ Model.**

| Model Name | MAPE (%) | Parameters | Mean | Standard deviation | COV | Correlation coefficients between $\theta_i$ | | |
|---|---|---|---|---|---|---|---|---|
| | | | | | | $\theta_0$ | $\theta_1$ | $\theta_2$ |
| $SS_{WD,\ PV}$ | 1.93 | $\theta_0$ | 0.9748 | 0.0028 | 0.003 | 1 | | |
| | | $\theta_1$ | 1.8139 | 0.1009 | 0.06 | 0.14 | 1 | |
| | | □ | 0.0244 | 0.0020 | 0.08 | –0.04 | 0.002 | 1 |

Table 7-9 shows that the MAPE of the US-$SS_{WD,\ PV}$ model is 1.93%. This is almost identical to the MAPE of $SS_{WD,\ PV}$ model (i.e., 1.89%). Table 7-9 also shows that the model error term (i.e., σ) of the US-$SS_{WD,\ PV}$ model is 0.0244, which is a reasonably small value. In addition, COVs of the model parameters, $\theta_0$, and $\theta_1$ are 0.003 and 0.06, respectively. These are reasonably small and indicates good confidence in the corresponding mean estimates (i.e., 0.9748 and 1.8139, respectively). Because of these reasons, **the full model in Table 7-9 is referred to as Model US-$SS_{WD,\ PV}$ herein**.

Figure 7-20 shows the validation plot for the Model US-$SS_{WD,\ PV}$ and looks very similar to that in Figure 7-15 for $SS_{WD,\ PV}$ model. In Figure 7-20, the means of the observed capacities corresponding to a particular predicted capacity are falling near the 1:1 line. Also, the data points are spread in an approximately equi-width band along the

1:1 line. Also, no residual trend pattern is observed among the data points in Figure 7-20. These indicate that the model can be assumed to be practically homoskedastic. Also, the normality assumption seems to be reasonably aggreed because most data points lie within and some lie outside the ±σ region.

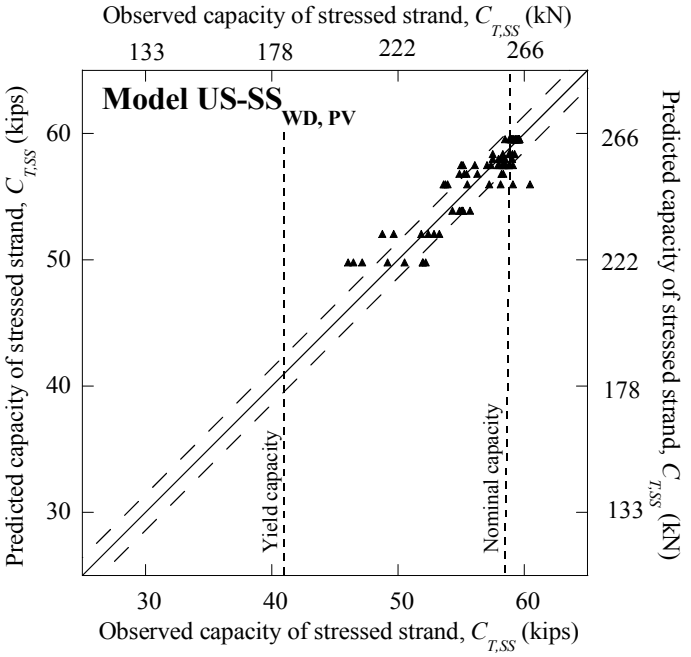


**Figure 7-20. Validation Plot for US-SS$_{WD, PV}$ Model.**

### *7.5.4.5. Model assessment - Bleedwater, Inclined, and Orthogonal Void (BIOV) conditions*

Model US-SS$_{WD, BIOV}$ can be used to predict $C_{T,SS}$ when voids exist at or near the anchorage regions of PT columns or girders. The power model model form for BIOV conditions (provided in Equation (7.15)) was assessed using the 79 stressed strand data

points and $C_{T,US}$ predicted using the $US_{WD,BIOV}$ model. The $US_{WD,BIOV}$ model was developed using 239 unstressed strand data points. Hence, a total of 318 data points are effectively used in developing the US-$SS_{WD, BIOV}$ model. The MAPE and posterior statistics of US-$SS_{WD, BIOV}$ model are provided in Table 7-10.

**Table 7-10. MAPE and Posterior Statistics of the US-$SS_{WD, BIOV}$ Model.**

| Model Name | MAPE (%) | Parameters | Mean | Standard deviation | COV | Correlation coefficients between $\theta_i$ | | |
|---|---|---|---|---|---|---|---|---|
| | | | | | | $\theta_0$ | $\theta_1$ | $\theta_2$ |
| US→$SS_{WD, BIOV}$ | 3.15 | $\theta_0$ | 0.9463 | 0.0064 | 0.007 | 1 | | |
| | | $\theta_1$ | 2.0301 | 0.0773 | 0.04 | 0.47 | 1 | |
| | | σ | 0.0411 | 0.0034 | 0.08 | 0.15 | 0.04 | 1 |

In Subsection 7.5.3.7, the MAPE of the $SS_{WD, BIOV}$ model was found to be 3.25%. Table 7-10 shows that the MAPE of the US-SS model is 3.15%. In addition to the reasonably small MAPE, the model error term (i.e., σ) of the US-SS model is 0.0411; indicating good model accuracy. The high confidence levels on the mean estimates of the model parameters (i.e., $\theta_0$ and $\theta_1$) are demonstrated by their small COVs (i.e., 0.007 and 0.04, respectively). Hence, **the model in Table 7-7 is referred to as Model US-$SS_{WD, BIOV}$, herein**.

The validation plot for the Model US-$SS_{WD, BIOV}$ is shown in Figure 7-21. As observed in Figure 7-16 for $SS_{WD, BIOV}$ model, in Figure 7-21 also shows the large scatter among the data points corresponding to the predicted capacity of approximately 40 kips (178 kN). This scatter in the validation plot is not due to the model inadequacy. This is due to the inherent scatter in $C_{T,SS}$ under identical exposure conditions. Because of these reasons, it can be concluded that the model is homoskedastic. It should also be noted that the 1:1 line passes through the mean value of $C_{T,SS}$ as it approaches $MUTS_{ARS}$. Also,

most data points lie within and some lie outside the ±σ region; agreeing to the normality assumption.

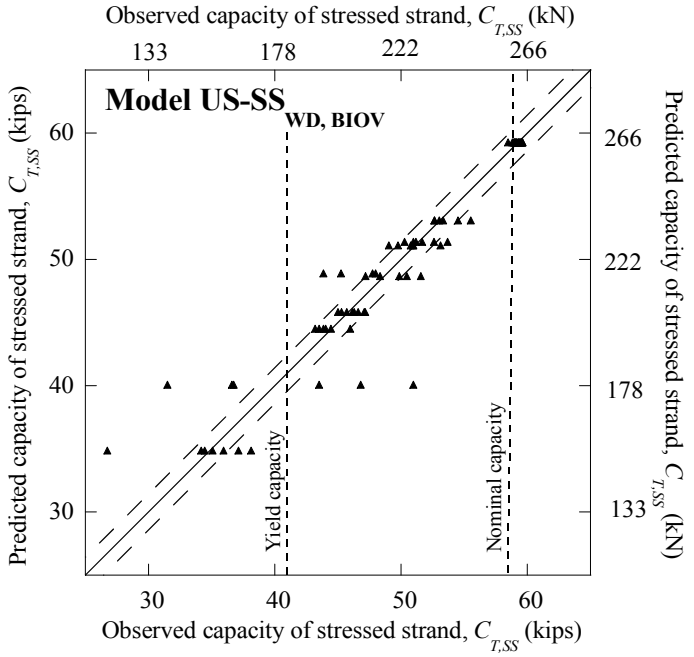


**Figure 7-21. Validation Plots for US-SS$_{WD, BIOV}$ Model.**

### *7.5.4.6. Prediction of tension capacity of stressed strands*

Figure 7-17 (a), (b), (c), and (d) in Subsection 7.4.3 provided $C_{T,SS}$ that were extrapolated or predicted using SS$_{WD}$ models. Figure 7-22 (a), (b), (c), and (d) show $C_{T,SS}$ for WD conditions with 0.006, 0.018, 0.18, and 1.8 $\%sCl^-$ solutions, respectively. These $C_{T,SS}$ values are extrapolated or predicted using US-SS$_{WD}$ models and are based on the assumption that $\phi_{wet}$ is equal to 0.17 (see Subsection 7.4.3 for details).

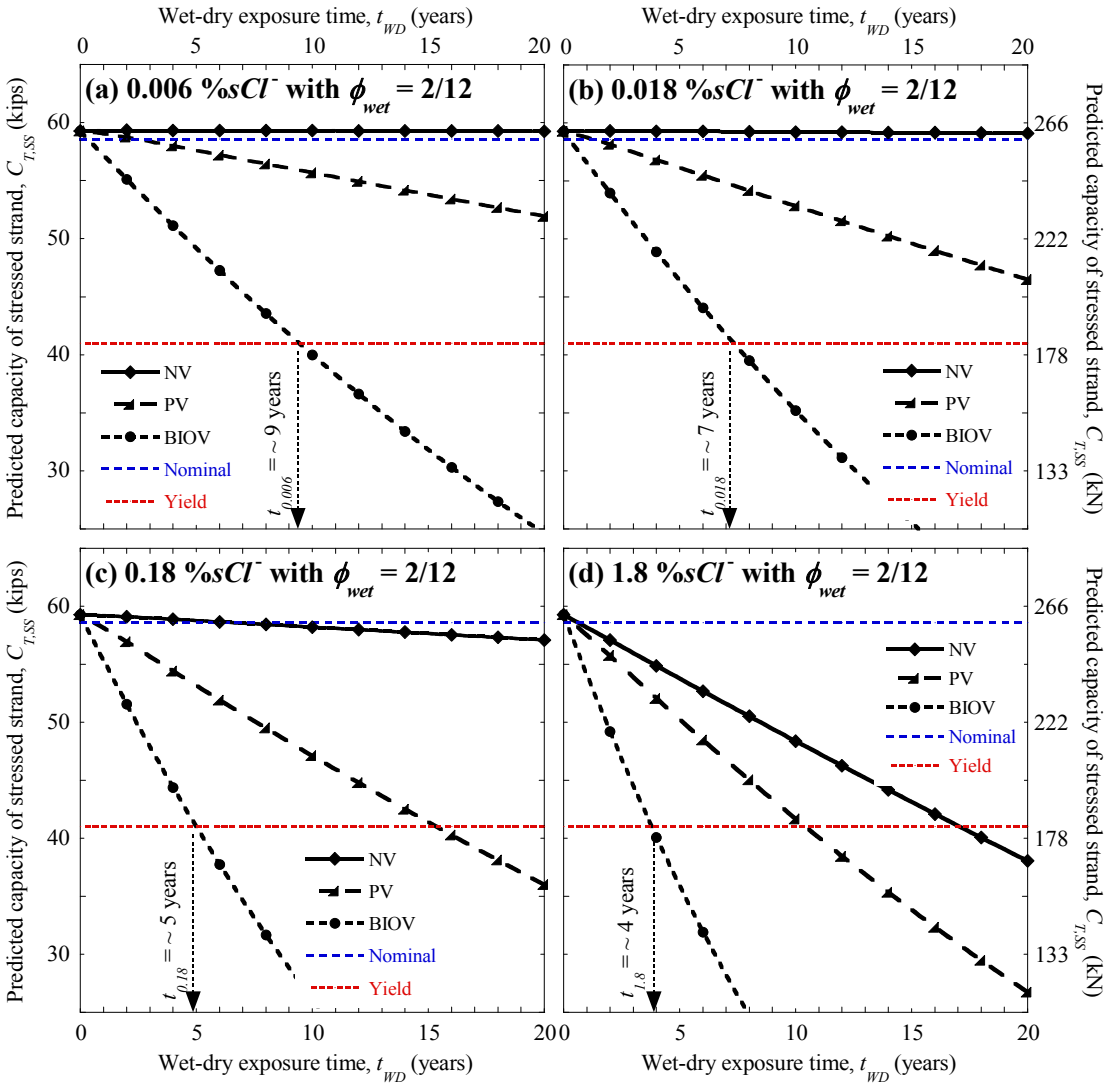


**Figure 7-22. Capacity of Stressed Strands under WD Exposure ($\phi_{wet}$ = 0.17) to Various Chloride Solutions (Predicted Using US-SS$_{WD}$ Models).**

Figure 7-22 (a) and (b) shows that negligible reduction in $C_{T,SS}$ may be expected when NV and 0.006 or 0.18 $\%sCl^-$ conditions exists for approximately 20 years. Figure 7-22 (c) and (d) show that, in the case of NV conditions, the exposure to 0.18 and 1.8 $\%sCl^-$ solutions (i.e., moderate and high chloride conditions) can cause $C_T$ to drop

below $MUTS_{ARS}$ (or nominal capacity) within seven and one year, respectively. From Figure 7-22 (a), (b), (c), and (d) it can be concluded that, for PV and BIOV conditions, the predicted $C_{T,SS}$ can, in general, fall below $MUTS_{ARS}$ within approximately one year. For PV samples exposed to 0.006 $\%sCl^-$ condition, $C_{T,SS}$ dropped below $MUTS_{ARS}$ within approximately two years. Figure 7-22 (a), (b), (c), and (d) show that when BIOV and WD conditions exist, $C_{T,SS}$ can drop to a value below yield capacity within approximately 9, 7, 5, and 4 years (shown by vertical dashed arrows) when exposed to 0.006, 0.018, 0.18, and 1.8 $\%sCl^-$ solutions, respectively.

### 7.5.5. STEP WD-5: Selection of the most appropriate set of models for WD conditions

Now we have three sets of models (i.e., $US_{WD,\,NV}$, $SS_{WD,\,NV}$, and US-$SS_{WD,\,NV}$ models) for predicting the capacity of strands under WD exposure conditions. Among these, the best set of models has to be selected. The MAPE and σ of all the models developed for WD exposure conditions are summarized in Table 7-11 and Table 7-12, respectively. Because of the significant influence of the $f_{axial}$, the $SS_{WD}$ models are better than $US_{WD}$ models to predict the $C_T$ of stressed strands in PT bridges. However, a scientific choice between the $SS_{WD}$ and US-$SS_{WD}$ models has to be made. Table 7-11 and Table 7-12 show that the MAPE and σ, respectively, of $SS_{WD}$ models are almost identical with that of the corresponding US-$SS_{WD}$ models.

**Table 7-11. MAPEs of $US_{WD}$, $SS_{WD}$, and US-$SS_{WD}$ Models.**

| Exposure condition | MAPE (%) of | | | Increase in MAPE [Δ = (US-SS) – SS] |
|---|---|---|---|---|
| | US model | SS model | US-SS model | |
| WD, NV | 1.22 | 0.73 | 0.73 | 0.00 |
| WD, PV | 1.61 | 1.89 | 1.93 | 0.04 |
| WD, BIOV | 3.15 | 3.25 | 3.15 | –0.10 |

**Table 7-12. Model Error Coefficients (σ) of $US_{WD}$, $SS_{WD}$, and US-$SS_{WD}$ Models.**

| Exposure condition | Model error coefficient (σ) of | | | Increase in MAPE [Δ = (US-SS) – SS] |
|---|---|---|---|---|
| | US model | SS model | US-SS model | |
| WD, NV | 0.0194 | 0.0121 | 0.0117 | –0.0004 |
| WD, PV | 0.0256 | 0.0249 | 0.0244 | –0.0005 |
| WD, BIOV | 0.0350 | 0.0427 | 0.0411 | –0.0016 |

Hence, the models may be selected based on the statistical sample size used and convenience for future research and devlopment. The $US_{WD, NV}$, $US_{WD, PV}$, and $US_{WD, BIOV}$ models were developed based on larger sample sizes (i.e., 105, 100, and 239 unstressed strand samples, respectively) than those used for developing $SS_{WD, NV}$, $SS_{WD, PV}$, and $SS_{WD, BIOV}$ models (i.e., 60, 85, and 79 stressed strand samples, respectively). Although the $SS_{WD}$ models exhibited reasonably good prediction accuracy, a set of three US-$SS_{WD}$ models were also developed based on $C_{T,SS}$ data and corresponding $C_{T,US}$ predicted using $US_{WD}$ models. Hence, effectively, all the experimental observations are used in developing the US-$SS_{WD}$ models. In future, the existing $US_{WD}$ models may be improved by performing less expensive unstressed strand tests with a wider spectrum of environmental conditions. Performing stressed strand tests is very expensive and cumbersome, hence, fewer stressed strand samples will be

made than unstressed strand samples. Fortunately, modified models for stressed strands may be developed by simply replacing the preditor parameter for the US-$SS_{WD}$ models with the modified $US_{WD}$ models (instead of performing expensive stressed strand tests). Based on these reasons, **the US-$SS_{WD}$ models are selected as the set of probabilistic models for strands under WD exposure conditions**.

### 7.5.6. Summary of strand capacity models for wet-dry conditions

Probabilistic models for $C_T$ of unstressed and stressed strands that are exposed to WD conditions were developed. A total of nine models (i.e., three $US_{WD}$, three $SS_{WD}$, and three US-$SS_{WD}$ models) are developed. These nine models are summarized as follows:

$$\begin{aligned}
&\textbf{Model US}_{\textbf{WD,NV}} &&: R_{C_{T,US}} = 1.0105 - 0.0000\gamma_{t_{WD}} - 1.6785\gamma_{\%sCl^-}\gamma_{t_{WD}} + 0.0194\varepsilon \\
&\textbf{Model US}_{\textbf{WD,PV}} &&: R_{C_{T,US}} = 1.0232 - 0.1553\gamma_{t_{WD}} - 0.0153\ln[\gamma_{\%sCl^-}]\gamma_{t_{WD}} + 0.0256\varepsilon \\
&\textbf{Model US}_{\textbf{WD,BIOV}} &&: R_{C_{T,US}} = 1.0333 - 0.3567\gamma_{t_{WD}} - 0.0285\ln[\gamma_{\%sCl^-}]\gamma_{t_{WD}} + 0.0350\varepsilon
\end{aligned} \tag{7.16}$$

$$\begin{aligned}
&\textbf{Model SS}_{\textbf{WD,NV}} &&: R_{C_{T,SS}} = 1.0126 - 0.0000\gamma_{t_{WD}} - 2.2542\gamma_{\%sCl^-}\gamma_{t_{WD}} + 0.0121\varepsilon \\
&\textbf{Model SS}_{\textbf{WD,PV}} &&: R_{C_{T,SS}} = 1.0129 - 0.2719\gamma_{t_{WD}} - 0.0277\ln[\gamma_{\%sCl^-}]\gamma_{t_{WD}} + 0.0249\varepsilon \\
&\textbf{Model SS}_{\textbf{WD,BIOV}} &&: R_{C_{T,SS}} = 1.0095 - 0.6274\gamma_{t_{WD}} - 0.0485\ln[\gamma_{\%sCl^-}]\gamma_{t_{WD}} + 0.0427\varepsilon
\end{aligned} \tag{7.17}$$

$$\begin{aligned}
&\textbf{Model US}-\textbf{SS}_{\textbf{WD,NV}} \textbf{ :-} \\
&R_{C_{T,SS}} = 0.9983\left[1.0105 - 0.0000\gamma_{t_{WD}} - 1.6785\gamma_{\%sCl^-}\gamma_{t_{WD}}\right]^{1.3576} + 0.0117\varepsilon \\
&\textbf{Model US}-\textbf{SS}_{\textbf{WD,PV}} \textbf{ :-} \\
&R_{C_{T,SS}} = 0.9748\left[1.0232 - 0.1553\gamma_{t_{WD}} - 0.0153\ln\left[\gamma_{\%sCl^-}\right]\gamma_{t_{WD}}\right]^{1.8139} + 0.0244\varepsilon \\
&\textbf{Model US}-\textbf{SS}_{\textbf{WD,BIOV}} \textbf{ :-} \\
&R_{C_{T,SS}} = 0.9463\left[1.0333 - 0.3567\gamma_{t_{WD}} - 0.0285\ln\left[\gamma_{\%sCl^-}\right]\gamma_{t_{WD}}\right]^{2.0301} + 0.0411\varepsilon
\end{aligned} \tag{7.18}$$

where the terms are as defined in Equation (7.1) and Subsection 7.4.1. These models were developed based on statistical procedures provided in Subsection 7.2 and the experimental data from strand corrosion tests. Then the developed $US_{WD}$, $SS_{WD}$, and US-$SS_{WD}$ models were used to predict $C_T$ of strands under WD exposure conditions. Finally, US-$SS_{WD}$ models were selected as the most appropriate set of models to predict $C_T$ under WD exposure conditions.

# 8. RELATIONSHIPS BETWEEN THE TENSION CAPACITIES OF UNSTRESSED WIRES AND STRESSED STRANDS

## 8.1. INTRODUCTION

This section first presents the analytical program to develop probabilistic relationships between the $C_T$ of unstressed wires and stressed strands exposed to WD conditions. Subsection 8.2 presents the analytical program, which uses the data obtained from the experimental program and the statistical procedures discussed in Subsection 7.2. Following this, two probabilistic models relating the $C_T$ of stressed strands and unstressed wires are formulated and assessed in Subsection 8.3. From the two models developed, the more suitable model is defined as the "unstressed wire-stressed strand" model for further use in Sections 9 and 10.

## 8.2. RELATIONSHIPS BETWEEN TENSION CAPACITIES OF STRESSED STRANDS AND UNSTRESSED WIRES – ANALYTICAL PROGRAM

### 8.2.1. Introduction and objectives

The objective of this subsection is to present an analytical program to develop a probabilistic model to predict $C_T$ of stressed strand from $C_T$ of unstressed wire. Note that this model is developed for BIOV conditions only. To provide the reader with a sense of expected results, preliminary discussions of possible probabilistic model forms are also provided in this section. The developed probabilistic models are presented in Subsection 8.3. The parameters used in these probabilistic models are presented next.

### 8.2.2. Parameters used in the probabilistic models for tension capacity

Subsection 7.2.2 suggested using dimensionless response and predictor parameters to improve the the range of application of probabilistic models. Based on this suggestion, the response and predictor parameters, except $t_{WD}$, are standardized. Because the strand manufacturer did not provide the nominal capacity of king-wires, $MUTS_{ARS}$ is used in modeling $C_T$ of wires (i.e., king-wires) instead of nominal tension capacity of "as-received" wires. The following equations define these basic response and predictor parameters, which are used in probabilistic modeling of $C_T$.

$$R_{C_{T,US}} = \frac{\text{Tension capacity of unstressed strand}}{MUTS_{ARS}} = \frac{C_{T,US}}{MUTS_{ARS}} \tag{8.1}$$

$$R_{C_{T,SS}} = \frac{\text{Tension capacity of stressed strand}}{MUTS_{ARS}} = \frac{C_{T,SS}}{MUTS_{ARS}} \tag{8.2}$$

$$R_{C_{T,UW}} = \frac{\text{Tension capacity of unstressed wire}}{MUTS_{ARS}} = \frac{C_{T,UW}}{MUTS_{ARS}} \tag{8.3}$$

$$\begin{aligned} \gamma_{t_{WD}} &= \left( \frac{\text{Wet-time in a year (months)}}{12} \right) \times \text{Total wet-dry exposure time (years)} \\ &= \phi_{wet} \times t_{WD} \text{ (years)};\ 0 \le \phi_{wet} \le 1 \end{aligned} \tag{8.4}$$

$$\gamma_{\%sCl^-} = \frac{\%Cl^- \text{in the exposure solution}}{\%sCl^-_{\text{saturated chloride solution}}} = \frac{\%sCl^-}{35.7} \tag{8.5}$$

Probabilistic models for $C_T$ of strands under WD and CA exposure conditions are developed using suitable transformations (such as exponential, logarithmic, etc.) of the basic response and predictor parameters defined and the procedures provided in Subsection 7.2. The next three subsections discuss the analytical steps involved in this process.

### 8.2.3. Analytical steps to develop "unstressed wire-stressed strand" capacity model (Steps WS-1 through WS-4)

In the previous subsection, the analytical steps to develop probabilistic models for $C_T$ of strands under WD exposure conditions were discussed. In this subsection, the analytical steps to develop probabilistic models to predict $C_{T,\,SS}$ from $C_{T,\,UW}$ for BIOV exposure conditions are provided. Table 8-1 shows the list of probabilistic models discussed in this subsection.

**Table 8-1. List of Wire and "Wire-strand" Capacity Models for BIOV Conditions.**

| Expanded model name | Abbreviated model name |
|---|---|
| Unstressed $\text{Wire}_{\text{Wet-Dry, Bleedwater, Inclined, and Orthogonal Void}}$ (for below and above $\%sCl^-$ threshold) | $\text{UW}_{\text{WD, BIOV}}$ ($\text{UW}_{\text{WD, below}}$ and $\text{UW}_{\text{WD, above}}$) |
| Unstressed Wire-Unstressed $\text{Strand}_{\text{Wet-Dry, Bleedwater, Inclined, and Orthogonal Void}}$ | $\text{UW-US}_{\text{WD, BIOV}}$ |
| Unstressed Wire-Unstressed Strand-Stressed $\text{Strand}_{\text{Wet-Dry, Bleedwater, Inclined, and Orthogonal Void}}$ | $\text{UW-US-SS}_{\text{WD, BIOV}}$ |
| Unstressed Wire-Stressed $\text{Strand}_{\text{Wet-Dry, Bleedwater, Inclined, and Orthogonal Void}}$ | $\text{UW-SS}_{\text{WD, BIOV}}$ |
| Unstressed Wire-Stressed $\text{Strand}_{\text{Bleedwater, Inclined, and Orthogonal Void}}$ | $\text{UW-SS}_{\text{BIOV}}$ |

Based on the fact that the cross-sectional area of wires and strands are linearly related, one would imagine that their capacities could be linearly related, if exposed to identical conditions. However, $C_T$ of strands might not be directly proportional to $C_T$ of wires because of the flower-like cross section of strands instead of a solid circular cross section and the ongoing complex corrosion mechanisms (for example, crevice corrosion due to flower-like cross section of strands, pitting corrosion due to chlorides, localized corrosion due to GAS interfaces, etc.). Therefore, the data from both strand and wire corrosion tests under WD exposure conditions are used in developing these models. Figure 8-1 shows the flowchart with four steps (i.e., WS-1 through WS-4 (WS indicating "wire-strand")) for developing UW-$SS_{BIOV}$ model. In Figure 8-1, the boxes with thick border lines indicate these four steps. The inner boxes with rounded corners provide preliminary information on the results from each step. These four analytical steps are also graphically represented in Figure 8-2 and Figure 8-3(b) and are discussed next.

**Step WS-1:** Develop $UW_{WD,\ BIOV}$ models for $C_T$ of wires under WD and BIOV conditions (see first box in Figure 8-1 and Figure 8-2). The experimental design was shown in Figure 5-8(c) and Table 5-12. For convenience, Figure 5-8 (c) is reproduced in Figure 8-2(a). To minimize the error in prediction, two individual models for below and above $\%sCl^-$ threshold levels are developed with only $t_{WD}$ as predictor parameter, instead of, a general $UW_{WD,\ BIOV}$ model with both $t_{WD}$ and $\%sCl^-$ as predictor parameters. The top two rectangles in Figure 8-2(a) indicate the experimental data used to develop the Model $UW_{WD,\ below}$. The bottom most rectangle in Figure 8-2(a) indicates the experimental data used to develop the Model $UW_{WD,\ above}$. These two models are then used to predict the $C_T$ of wires at 12, 16, and 21 months of exposure, as shown by the hollow circles within the rectangles in Figure 8-2(b). These are the times at which stressed strands were tested.

**Step WS-2**: Develop the UW-US-$SS_{WD, BIOV}$ model to predict $C_{T, SS}$ using the observed $C_{T,US}$ and $C_{T,SS}$ and the predicted $C_{T,UW}$ (see second box in Figure 8-1 and Figure 8-3(a) and (b)). This model is developed using the following substeps:

> **Substep WS-2a**: Develop the UW-$US_{WD, BIOV}$ model using the predicted $C_{T, UW}$ (from $UW_{WD, BIOV}$ models) and observed $C_{T,US}$. These predicted and observed $C_T$ values are depicted through the two vertical rectangles combining Figure 8-3(a) and (b). Note that Figure 8-3(b) is identical to Figure 8-2(b).
>
> **Substep WS-2b**: Develop the UW-US-$SS_{WD, BIOV}$ model by nesting the UW-$US_{WD, BIOV}$ model (from substep #WS-2a) into the US-$SS_{WD, BIOV}$ model (see step #WD-4).

**Step WS-3**: Develop the UW-$SS_{WD, BIOV}$ model using the observed $C_{T, SS}$ and corresponding $C_{T,UW}$ predicted using $UW_{WD, BIOV}$ models. This is depicted through the three ellipses connecting Figure 8-3(b) and (c).

**Step WS-4**: Select the more suitable model from steps #WS-2 and #WS-3 and define it as UW-$SS_{BIOV}$ model, which can be used for both WD and CA exposure conditions.

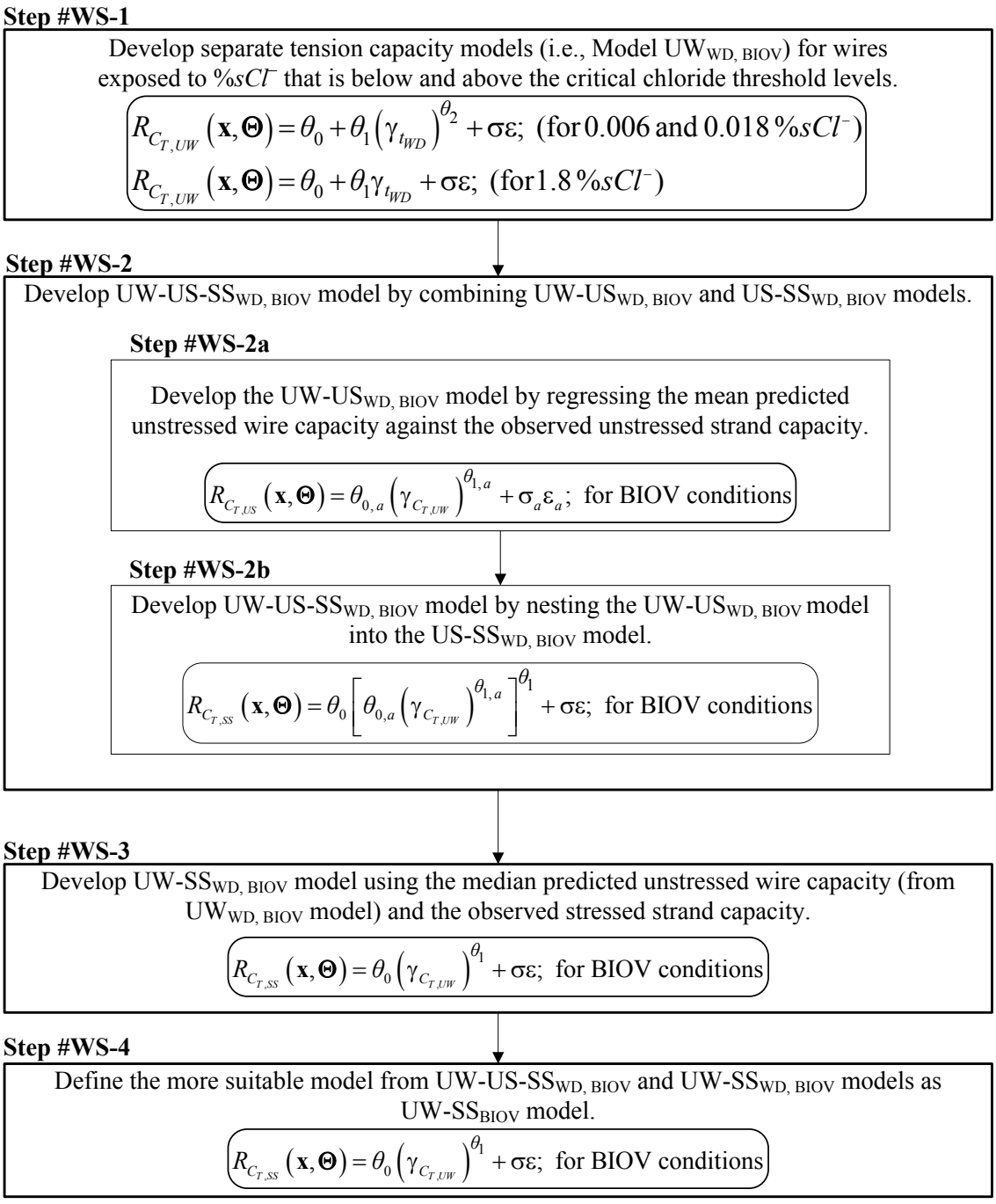


**Figure 8-1. Flowchart for Developing the "Wire-strand" Capacity Relationships.**

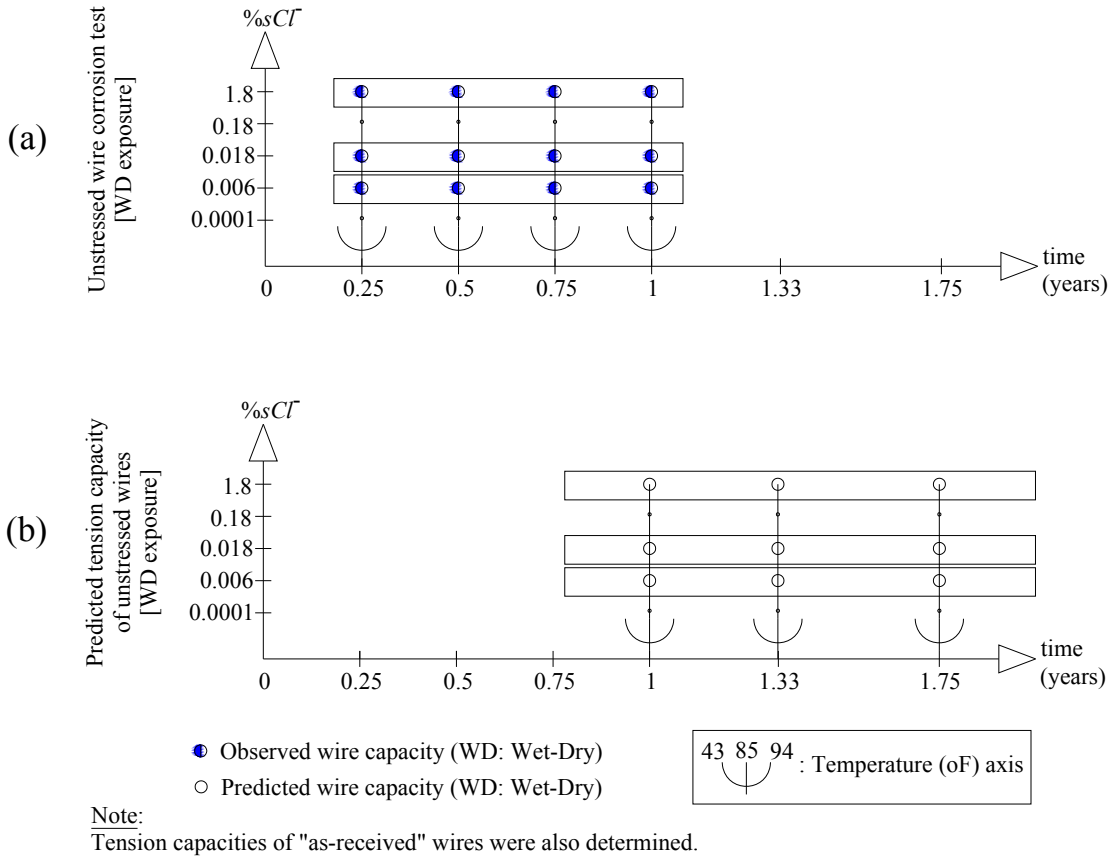


Note:
Tension capacities of "as-received" wires were also determined.

**Figure 8-2. Graphical Representation of Step WS-1.**

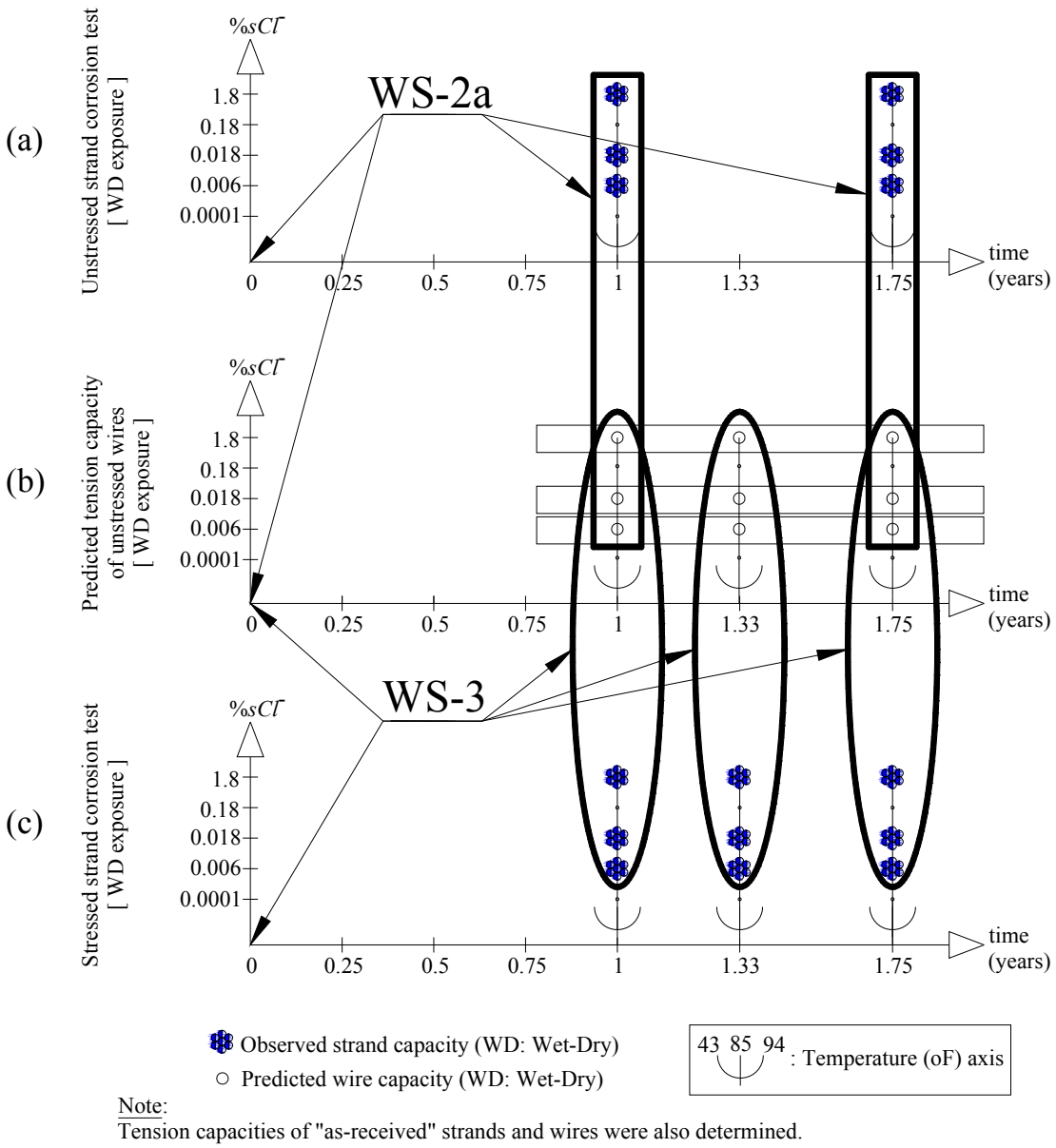


**Figure 8-3. Graphical Representations of Steps WS-2a and WS-3.**

## 8.3. RELATIONSHIPS BETWEEN TENSION CAPACITIES OF STRESSED STRANDS AND UNSTRESSED WIRES - RESULTS

The analytical steps (WS-1 through WS-4) to develop probabilistic relationships between $C_T$ of strands and wires under WD exposure conditions were outlined in Subsection 8.2. These analytical steps are executed using the data presented in Subsection 6.4.3 and are presented next.

### 8.3.1. STEP WS-1: Develop models for wires exposed to solutions with %$sCl^-$ levels below and above critical chloride threshold

#### *8.3.1.1. Diagnosis of the effect of wet-dry exposure time*

As a first step in the modeling process, diagnostic plots are developed to study the effect of $\gamma_{t_{WD}}$ on $C_{T,UW}$. As shown in Figure 8-4 (a) and (b), the rate of capacity loss has reduced after 9 months, when exposed to 0.006 and 0.018 %$sCl^-$, respectively. Therefore, $C_{T,UW}$ can be modeled as a power function of $\gamma_{t_{WD}}$ ,when exposed to 0.006 and 0.018 %$sCl^-$ conditions. This reduction in the rate of capacity loss could be attributed to the presence less soluble corrosion products around the steel surface. This condition reduces the oxygen availability resulting in a smaller corrosion rate. In addition, the negative hysteresis in Figure 6-1 (b) indicates that the chloride threshold level for the steel meeting ASTM A416 specifications is greater than 0.06 %$sCl^-$. Because 0.006 and 0.018 %$sCl^-$ are less than the critical chloride threshold level, the wire samples exposed to these two solutions could exhibit similar corrosion behavior. This is observed in Figure 8-4 (a) and (b).

The positive hysteresis in Figure 6-1 (c) indicates that the critical chloride threshold level for the steel meeting ASTM A416 specifications is less than 1.8 %$sCl^-$. As shown in Figure 8-4 (c), when the %$sCl^-$ was 1.8 %$sCl^-$ (i.e., above the critical

chloride threshold level), the rate of capacity loss did not change significantly even after 9 months of exposure. This is attributed to the fact that the solubility of corrosion products increases as $\%sCl^-$ increases or exceeds the critical chloride ethreshold level, resulting in the similar oxygen availability and corrosion rate over time. Therefore, $C_{T,UW}$ can be modeled as a linear function of $\gamma_{t_{WD}}$, when exposed to 1.8 $\%sCl^-$ condition. Considering these behavior, $\gamma_{t_{WD}}$ is incorporated into the models formulated in the next subsection.

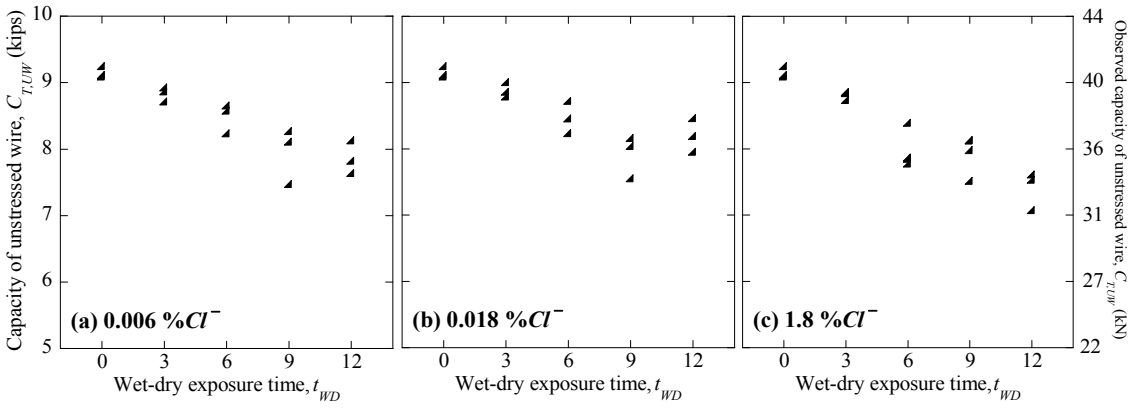


**Figure 8-4. Scatter Plot between Capacity of Unstressed Wires, $C_{T,UW}$, and Wet-dry Exposure Time, $t_{WD}$.**

### *8.3.1.2. Formulation and assessment*

Following the general model form (Equation (7.1)), the two probabilistic models for $C_{T,UW}$ under WD exposure conditions (with $\%sCl^-$ level below and above the critical chloride threshold level) can be expressed as follows:

$$R_{C_{T,UW}}(\mathbf{x},\boldsymbol{\Theta}) = \theta_0 + \theta_1\left(\gamma_{t_{WD}}\right)^{\theta_2} + \sigma\varepsilon;\ (\text{for } 0.006 \text{ and } 0.018\ \%\, sCl^-)$$
$$R_{C_{T,UW}}(\mathbf{x},\boldsymbol{\Theta}) = \theta_0 + \theta_1\gamma_{t_{WD}} + \sigma\varepsilon;\ (\text{for } 1.8\ \%\, sCl^-) \quad (8.6)$$

where the terms are as defined in Equation (7.1) and Subsection 7.4.1. The unknown model parameters in Equation (8.6) were assessed using the statistical procedures provided in Subsection 7.2. Table 8-2 summarizes the MAPE and posterior statistics of these two models (i.e., for below and above $\%sCl^-$ threshold conditions) with only $\gamma_{t_{WD}}$ as the predictor variable. The MAPE values of $UW_{WD,\ below}$ and $UW_{WD,\ above}$ models are 2.58, and 2.77%, respectively; indicating reasonably good prediction for practical engineering purposes. Also, the MAPE values increase as the $\%sCl^-$ increases. This is because of the inherent increase in the scatter induced by the presence of increasing amount of chlorides on the steel surface. The COVs of the σ for these two models are 0.12 and 0.66, respectively. These values are very high because of the inherent scatter among the observed capacities exhibited by the samples exposed identical conditions and the small statistical sample size. However, the small MAPE values suggest that the model can provides sufficiently accurate prediction for practical engineering purposes.

**Table 8-2. MAPE and Posterior Statistics of $UW_{WD}$ Models.**

| Model Name | MAPE (%) | Parameters | Mean | Standard deviation | COV | Correlation | |
|---|---|---|---|---|---|---|---|
| | | | | | | $\theta_0$ | $\theta_1$ |
| $UW_{WD,\ below}$ | 2.58 | $\theta_0$ | 0.1565 | 0.0014 | 0.01 | 1 | |
| | | $\theta_1$ | –0.0026 | 0.0011 | 0.41 | –0.59 | 1 |
| | | $\theta_2$ | –0.8289 | 0.1612 | 0.19 | –0.45 | 0.98 |
| | | σ | 0.0041 | 0.0005 | 0.12 | | |
| $UW_{WD,\ above}$ | 2.77 | $\theta_0$ | 0.1555 | 0.0022 | 0.01 | 1 | |
| | | $\theta_1$ | –0.0023 | 0.0003 | –0.13 | –0.84 | 1 |
| | | σ | 0.0050 | 0.0033 | 0.66 | | |

Figure 8-5 and Figure 8-6 show the validation plots for $UW_{WD,\ below}$ and $UW_{WD,\ above}$ models. The details on analyzing validation plots are provided in Subsection 7.2.3.5. In general, the data in Figure 8-5 and Figure 8-6 are spread in an approximately uniform width along the 1:1 line and shows no signs of significant residual trend or bias in the overall prediction. Following the procedures in Subsection 7.2.3.5, these indicate that homoskedasticity assumptions are approximately satisfied. Also, some data points are lying outside the ±σ region indicating approximately normal distribution of data.

The $UW_{WD,\ below}$ and $UW_{WD,\ above}$ models can be used to predict $C_{T,UW}$ at 12, 16, and 21 months of WD exposure and can then be compared with $C_{T,US}$ and $C_{T,SS}$ at 12, 16, and 21 months of WD exposure to develop the UW-US-$SS_{WD,\ BIOV}$ and UW-$SS_{WD,\ BIOV}$ models in the following subsections.

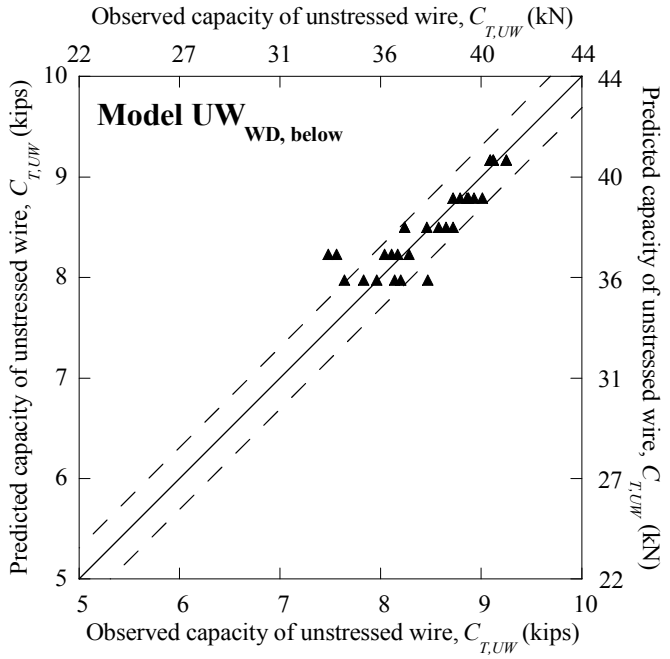


**Figure 8-5. Validation Plot for the $UW_{WD,\ below}$ Model.**

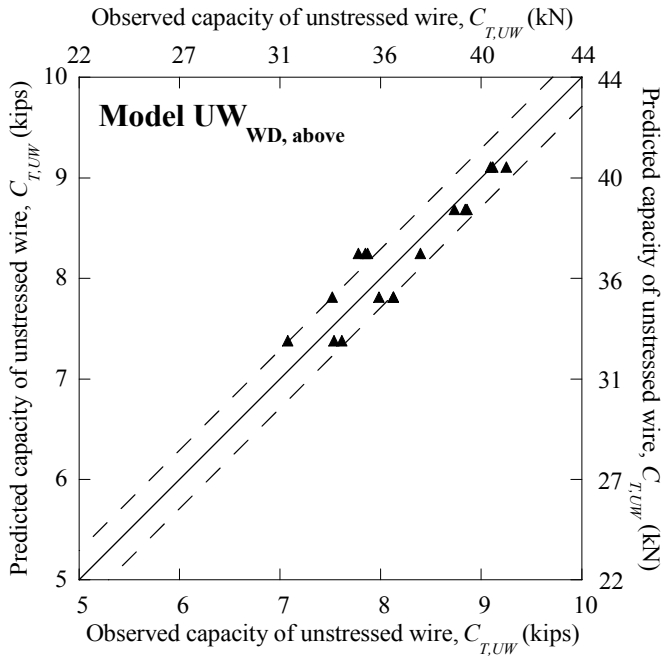


**Figure 8-6. Validation Plot for the $UW_{WD, above}$ Model.**

### 8.3.2. STEP WS-2: Develop UW-US-$SS_{WD, BIOV}$ model

As shown in Figure 8-1, the UW-US-$SS_{WD}$ model is developed in two substeps as discussed next.

#### *8.3.2.1. Step WS-2a: Develop Model UW-$US_{WD, BIOV}$*

Figure 8-7 shows the diagnostic plot between $C_{T,US}$ and $C_{T,UW}$. $C_{T,UW}$ plotted in Figure 8-7 is predicted using $UW_{WD}$ models (Equation (8.6)). Figure 8-7 shows that a power function of $C_{T,UW}$ is a good approximation and is incorporated into the probabilistic model form provided next.

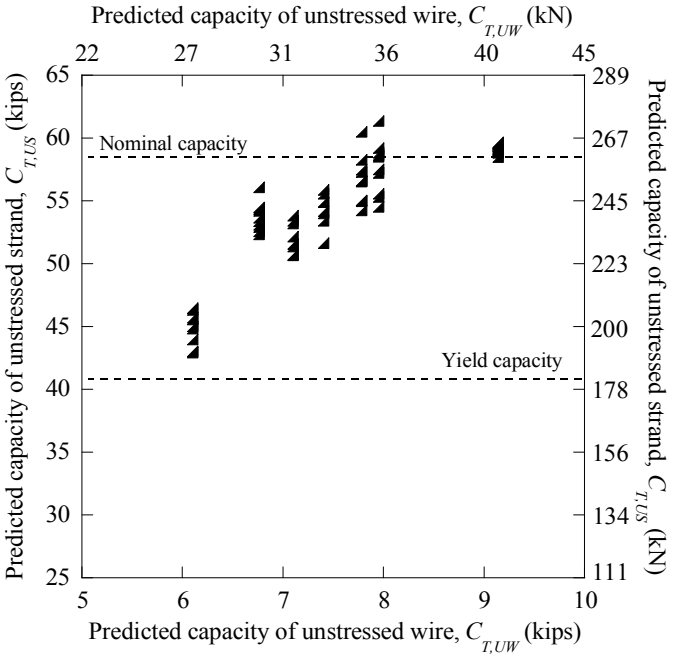


**Figure 8-7. Scatter Plot between Predicted Capacity of Unstressed Wires, $C_{T,UW}$, and Observed Capacity of Unstressed Strands, $C_{T,US}$.**

The following model form was developed to predict $C_{T,US}$ from $C_{T,UW}$:

$$\text{Model UW-US}_{\text{WD}}: \; R_{C_{T,US}} = \theta_{0,a}\left(\gamma_{C_{T,UW}}\right)^{\theta_{1,a}} + \sigma_a \varepsilon_a \tag{8.7}$$

where, the terms are as defined in Equation (7.1) and Subsection 7.4.1. In order to improve clarity in Step WS-2-c, the subscript '*a*' has been added to all the model parameters in Equation (8.7). Table 8-3 shows the posterior statistics of the UW-US$_{\text{WD, BIOV}}$ model. The MAPE of the full model form is 3.29 percent, which is a reasonable value. In addition, the COVs of all the parameters estimates are reasonably small. The model error, σ, is also reasonable (i.e., 0.0374 with a standard deviation of 0.30); considering the amount of data available and the inherent scatter observed among

the data points with identical exposure conditions. Because of these reasons, **the model is referred to as UW-US$_{WD, BIOV}$ model herein**.

**Table 8-3. MAPE and Posterior Statistics of UW-US$_{WD, BIOV}$ Full Model.**

| Model Name | MAPE (%) | Parameters | Mean | Standard deviation | COV | Correlation coefficients between $\theta_i$ | |
|---|---|---|---|---|---|---|---|
| | | | | | | $\theta_0$ | $\theta_1$ |
| Model US-US$_{WD, BIOV}$ | 3.29 | $\theta_{0, a}$ | 2.8020 | 0.1904 | 0.07 | 1 | |
| | | $\theta_{1, a}$ | 0.5399 | 0.0337 | 0.06 | –0.99 | 1 |
| | | $\sigma_a$ | 0.0374 | 0.0030 | 0.08 | | |

Figure 8-8 shows the validation plot for the reduced UW-US$_{WD, BIOV}$ model. The details on analyzing validation plots are provided in Subsection 7.2.3.5. The plot indicates that, in general, the Model UW-US$_{WD}$ provides reasonably good estimation of $C_{T,US}$. However, in Figure 8-8, as corrosion is severe (for example, when $C_{T,US}$ is approximately 47 kips (209 kN)) there is a slight leftward deviation from the 1:1 line. In some other instances (for example, at $C_{T,US}$ equal to approximately 50 and 57 kips (222 and 254 kN)) the deviation is slightly rightward. However, these deviations do not seem to be more serious than the inherent scatter among the observed data. Hence, it is concluded that the model approximately satisfies the homoskedasticity assumption. Although not perfect, the nature of data points falling both inside and outside the ±σ region exhibits an approximate agreement with the normality assumption.

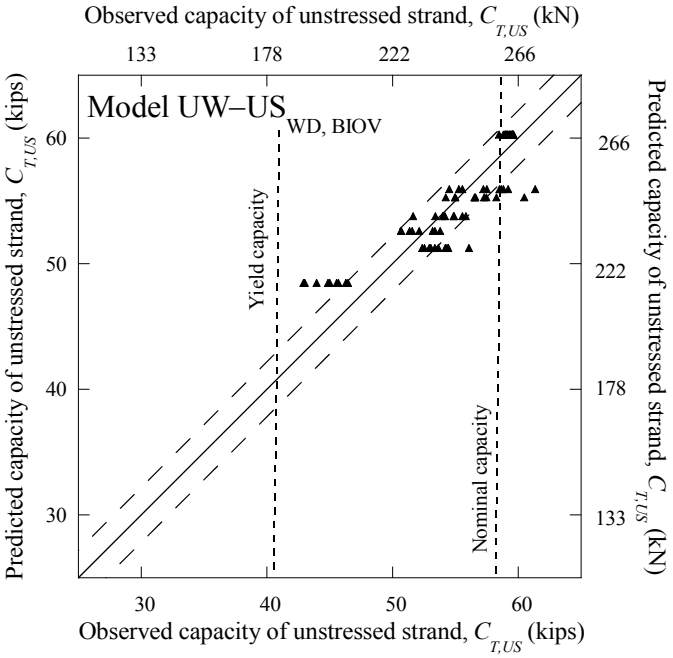


**Figure 8-8. Validation Plots for UW-US$_{WD}$ Model.**

A model to predict $C_{T,US}$ from $C_{T,UW}$ is now developed. However, in order to use this model to predict $C_{T,SS}$, a model relating the $C_{T,US}$ and $C_{T,SS}$ is needed and is developed next.

### *8.3.2.2. Step WS-2b: Develop Model UW-US-SS$_{WD, BIOV}$*

The UW-US-SS$_{WD, BIOV}$ model has been developed by nesting the UW-US$_{WD, BIOV}$ model (developed in Step WS-2a) into the US-SS$_{WD, BIOV}$ model (developed in Step WD-4 in Subsection 7.4.1). For clarity, the US-SS$_{WD, BIOV}$ model is modified with a subscript '*b*' as follows:

$$R_{C_{T,SS}} = \theta_{0,b}\left(\gamma_{C_{T,US}}\right)^{\theta_{1,b}} + \sigma_b \varepsilon_b \tag{8.8}$$

By substituting the term $\gamma_{C_{T,US}}$ in Equation (8.8) with the UW-US$_{WD,\ BIOV}$ we get,

$$R_{C_{T,SS}} = \theta_{1,b} \underbrace{\left[\theta_{0,a}\left(\gamma_{C_{T,UW}}\right)^{\theta_{1,a}}\right]}_{\substack{\text{median function of} \\ \text{Model UW-US}_{WD,\ BIOV}}}^{\theta_{2,b}} + \sigma_b \varepsilon_b \tag{8.9}$$

Note that the the error term, $\sigma_a \varepsilon_a$ was removed from the UW-US$_{WD,BIOV}$ model to avoid the issues associated with correlated random variables. By substituting the mean estimates in Table 8-3, the Equation (8.9) becomes,

$$R_{C_{T,SS}} = 0.9463 \underbrace{\left[2.8020\left(\gamma_{C_{T,UW}}\right)^{0.5399}\right]}_{\substack{\text{median function of} \\ \text{Model UW-US}_{WD,\ BIOV}}}^{2.0301} + 0.0411\varepsilon_b \tag{8.10}$$

**Equation (8.10) is referred to as Model UW-US-SS$_{WD,\ BIOV}$ herein**. The MAPE of this model is determined to be 7.19%. Figure 8-9 is the validation plot for the UW-US-SS$_{WD,\ BIOV}$ model. The details on analyzing validation plots are provided in Subsection 7.2.3.5. The data points near $MUTS_{ARS}$ are very close to the 1:1 line. However, there is a leftward deviation when capacity is below the yield capacity and a rightward deviation when the capacity is between $MUTS_{ARS}$ and yield strength. Although the ±σ region is drawn, it should be noted that this is an approximation after removing $\sigma_a \varepsilon_a$.

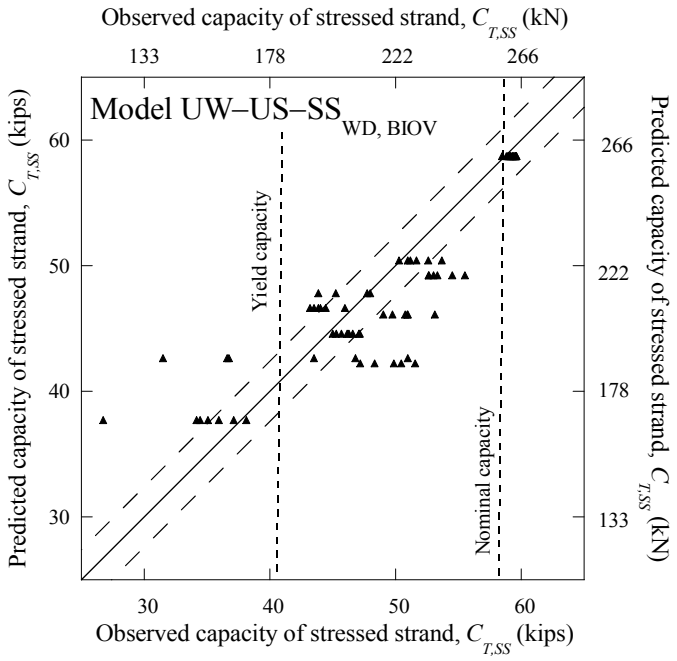


**Figure 8-9. Validation Plot for UW-US-SS$_{WD, BIOV}$ Model.**

### 8.3.3. STEP WS-3: Develop UW-SS$_{WD, BIOV}$ Model

This subsection presents the statistical diagnosis of possible predictor parameters for the UW-SS$_{WD, BIOV}$ model. The UW-SS$_{WD, BIOV}$ model is developed directly (i.e., without any intermediate models or substeps as in UW-US-SS$_{WD, BIOV}$ model development) using the observed capacities of unstressed wires, stressed strands, and %$sCl^-$ concentrations.

Figure 8-10 shows the scatter plot between $C_{T,SS}$ and the $C_{T,UW}$. Each $C_{T,UW}$ value was predicted using the appropriate UW$_{WD}$ model based on the %$sCl^-$ concentrations of each observed value of $C_{T,SS}$. Figure 8-10 indicates that $C_{T,SS}$ can be expressed as a power function of $C_{T,UW}$. This power model form will help the fitted model to pass closely through the $MUTS_{ARS}$.

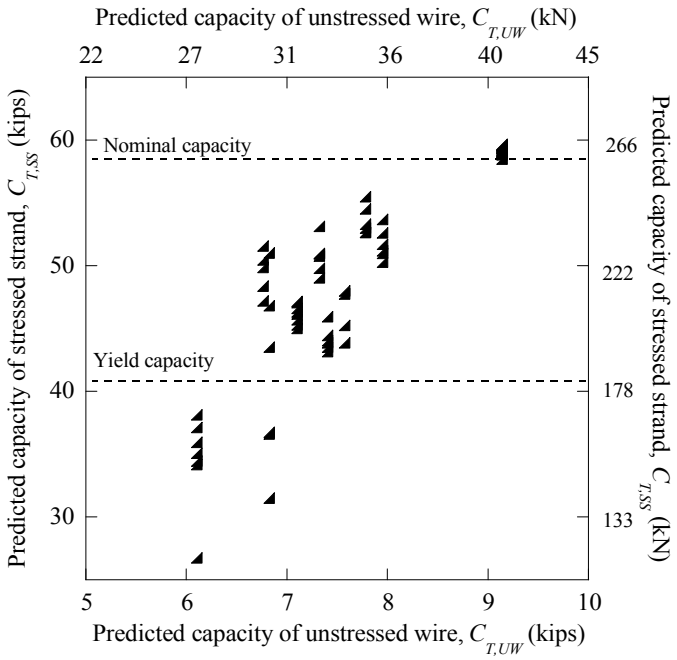


**Figure 8-10. Scatter Plot between Predicted Capacity of Unstressed Wires, $C_{T,UW}$, and Observed Capocity of Stressed Strands, $C_{T,SS}$.**

Following the general model form (Equation (7.1)) and using the findings in the diagnostic study, the probabilistic models for $C_{T,SS}$ is formulated as follows:

$$R_{C_{T,SS}}(\mathbf{x},\boldsymbol{\Theta}) = \theta_0 \left(\gamma_{C_{T,UW}}\right)^{\theta_1} + \sigma\varepsilon \tag{8.11}$$

where the terms are as defined in Equation (7.1) and Subsection 7.2. This power model form is similar to that of UW-US-$SS_{WD,\,BIOV}$ model form (i.e., Equation (8.10)) and supports the fact that $C_{T,SS}$ should be zero when $C_{T,UW}$ reaches zero. Table 8-4 summarizes the MAPE and posterior statistics of the UW-$SS_{WD,\,BIOV}$ model, assessed using the procedures provided in Subsection 6.5.

**Table 8-4. MAPE and Posterior Statistics of Full UW-SS$_{WD, BIOV}$ Model.**

| Model Name | MAPE (%) | Parameters | Mean | Standard deviation | COV | Correlation coefficients between $\theta_i$ | |
|---|---|---|---|---|---|---|---|
| | | | | | | $\theta_0$ | $\theta_1$ |
| UW-SS$_{WD, BIOV}$ | 6.73 | $\theta_0$ | 7.7492 | 0.9532 | 0.12 | 1 | |
| | | $\theta_1$ | 1.0924 | 0.0617 | 0.06 | 0.99 | 1 |
| | | σ | 0.0619 | 0.0047 | 0.08 | | |

The small COVs, as shown in Table 8-4, indicate that all the model parameters have been estimated with good confidence. Also, the MAPE and σ are reasonably small, considering the scatter in the observed data from the samples with identical exposure conditions. Moreover, the σ of model is 0.0619; a reasonably small value. Because of these reasons, **this model is referred to as UW-SS$_{WD}$ herein**.

Figure 8-11 is the validation plot showing a comparison between predicted (using Model UW-SS$_{WD}$) and observed values of $C_{T,SS}$ at $t_{WD}$ equal to 0, 12, 16, and 21 months. The details on analyzing validation plots are provided in Subsection 7.2.3.5. Approximately 85% data points fall along the 1:1 line and within ±σ region. This shows a reasonably good model prediction. Also, the data points corresponding to $MUTS_{ARS}$ or nominal capacity (i.e., 58.6 kips (258 kN)) lie very close to the 1:1 line; indicating good prediction in this region. However, as with UW-US-SS$_{WD, BIOV}$ model, a slight leftward deviation exists near the yield capacity region. As an improvement from UW-US-SS$_{WD, BIOV}$ model, the UW-SS$_{WD, BIOV}$ model exhibits less rightward shift between the nominal and yield capacity values. Considering the inherent scatter in the corrosion phenomenon, the model seems to exhibit no 'serious' systematic bias or residual trend, except when $C_{T,SS}$ is below yield strength. Also, only approximately 17% percentage of data points falls outside the ±σ region indicating a reasonably good agreement with the normality assumption.

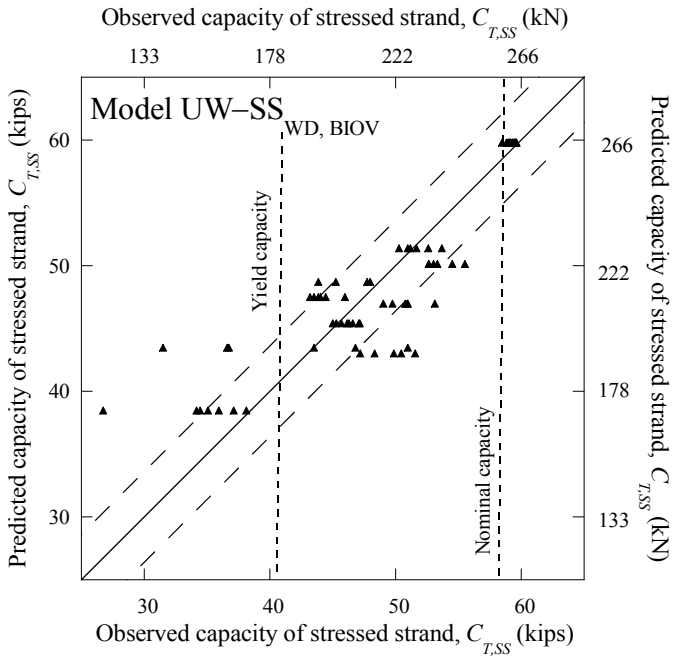


**Figure 8-11. Validation Plot for the UW-SS$_{WD, BIOV}$ Model.**

### 8.3.4. Step WS-4: Select the more suitable "wire-strand" relationship for both WD and CA exposure conditions

Comparing Figure 8-9 and Figure 8-11, it is observed that both the UW-US-SS$_{WD, BIOV}$ and UW-SS$_{WD, BIOV}$ models show similar predictions. The MAPE of UW-SS$_{WD, BIOV}$ model (i.e., 6.73%) is slightly less than that of UW-US-SS$_{WD}$ model (i.e., 7.19%). Moreover, the UW-SS$_{WD, BIOV}$ model provides better prediction near the $MUTS_{ARS}$ region than that predicted by the UW-US-SS$_{WD, BIOV}$ model. In addition, the UW-SS$_{WD, BIOV}$ model was developed in single step whereas the UW-US-SS$_{WD, BIOV}$ model was developed in multiple steps and involve the approximations such as removal of the inner error terms (i.e., $\sigma_a\varepsilon_a$). Because of these reasons, the UW-SS$_{WD, BIOV}$ model is better than UW-US-SS$_{WD, BIOV}$ model. Because this model can be used for both WD and CA exposure conditions, it will be **denoted as UW-SS$_{BIOV}$ model herein**, and is used in Step CA-3 presented later.

### 8.3.5. Summary of wire-strand relationships

In Subsection 8.3.1, the $UW_{WD,\ below}$ and $UW_{WD,\ above}$ models were developed to predict $C_{T,UW}$. Then using the predicted $C_{T,UW}$ and the observed values of $C_{T,US}$ and $C_{T,SS}$, the UW-US-$SS_{WD,\ BIOV}$ and UW-$SS_{WD,\ BIOV}$ models were developed in Subsections 8.3.2 and 8.3.3, respectively, and are summarized as follows:

**UW - US - $SS_{WD,BIOV}$ : -**

$$R_{C_{T,SS}}(\mathbf{x},\boldsymbol{\Theta}) = 0.9463\underbrace{\left[2.8020\left(\gamma_{C_{T,UW}}\right)^{0.5399}\right]^{2.0301}}_{\substack{\text{median function of} \\ \text{Model UW-US}_{WD,\ BIOV}}} + 0.0411\varepsilon_b \tag{8.12}$$

**UW - $SS_{WD,BIOV}$ : -**

$$R_{C_{T,SS}} = 7.7492\left(\gamma_{C_{T,UW}}\right)^{1.0924} + 0.0619\varepsilon$$

Then in Subsection 8.3.4, the UW-$SS_{BIOV}$ model was defined to be used in the next subsection to develop the model for $C_{T,SS}$ under CA and BIOV conditions.

# 9. MODELING TENSION CAPACITY OF STRANDS EXPOSED TO CONTINUOUS-ATMOSPHERIC (CA) CONDITIONS

## 9.1. INTRODUCTION

This subsection develops probabilistic models for tension capacity ($C_T$) of strands under continuous-atmospheric (CA) conditions. Theoretical models for $C_T$ of strands under CA exposure conditions could not be developed or found in typical literature. Historically, engineers have developed deterministic empirical models, when theoretical modeling is not possible. Based on this convention, probabilistic empirical models for $C_T$ of wires and strands under CA conditions are developed using the data obtained from the experimental program and statistical procedures discussed in Subsection 7.2.

## 9.2. DISCLAIMER

During the preliminary stages of research, the author attempted to develop models with simple predictor parameters. However, the prediction errors of these simple models were large and resulted in non-conservtaive predictions, especially when the loss in $C_T$ is larger. The results from these failed attempts are provided in Appendix C. The models presented in this section have complex (e.g., double exponential) predictor parameters. There are limitations in the use of these models and the following disclaimer is valid:

> ***This section presents the probabilistic models to predict the $C_T$ of wires and strands exposed to CA conditions. The developed model for the $C_T$ of unstressed wires (i.e., $C_{T,\,UW}$) fits the scarce data available. However, these models may not be the best models and should not be used to predict the $C_T$ of wires or strands when the predictor parameters in the models are far away from their observed values that were used in calibrating the models.***

## 9.3. PROBABILISTIC MODELS FOR TENSION CAPACITY OF STRANDS – ANALYTICAL PROGRAM

### 9.3.1. Introduction and objectives

In this case of CA exposure conditions, it is assumed that NV condition does not have significant influence on $C_T$. As observed in Subsection 6.5.5, PV condition has less severe effects on $C_T$ than BIOV condition. Hence, no strand and wire samples were tested under PV and CA exposure conditions and no models were developed for these conditions.

BIOV samples experienced most severe corrosion and capacity loss under WD conditions. However, no strand specimens were tested under BIOV and CA exposure conditions. Because of this an indirect analytical approach was designed to develop probabilistic models for $C_T$ of strands under BIOV and CA exposure conditions. This indirect approach included two steps as follows: 1) develop a model (denoted as UW-$SS_{BIOV}$ model) to predict $C_T$ of stressed strands from $C_T$ of unstressed wires and 2) develop $C_T$ model for unstressed wires exposed to CA conditions and nest it into the UW-$SS_{BIOV}$ model.

The main objective of this subsection is to present analytical steps to develop probabilistic tension capacity models for strands under BIOV and CA exposure conditions. See Subsection 9.3.3 for details. To provide the reader with a sense of expected results, preliminary discussions of possible probabilistic model forms are also provided in this section. The developed probabilistic models are presented in section 7. The parameters used in these probabilistic models are presented next.

### 9.3.2. Parameters used in the probabilistic models for tension capacity

Subsection 7.2.2 suggested using dimensionless response and predictor parameters to improve the the range of application of probabilistic models. Based on this aproach, the response and predictor parameters, except $t_{CA}$, and $T$, are standardized. The following equations define these basic response and predictor parameters, which are used in probabilistic modeling of $C_T$.

$$R_{C_{T,SS}} = \frac{\text{Tension capacity of stressed strand}}{MUTS_{ARS}} = \frac{C_{T,SS}}{MUTS_{ARS}} \tag{9.1}$$

$$R_{C_{T,UW}} = \frac{\text{Tension capacity of unstressed wire}}{MUTS_{ARS}} = \frac{C_{T,UW}}{MUTS_{ARS}} \tag{9.2}$$

$$\gamma_{t_{CA}} = \text{Total continuous-atmospheric exposure time (years)} \tag{9.3}$$

$$\gamma_T = \text{Ambient exposure temperature } (^{o}\text{F}) = T(^{o}\text{F}) \tag{9.4}$$

$$\gamma_{RH} = \frac{RH\ (\%)}{\text{Maximum relative humidity (\%)}} = \frac{RH\ (\%)}{100\%} \tag{9.5}$$

$$\gamma_{\%sCl^-} = \frac{\%Cl^- \text{in the exposure solution}}{\%sCl^-_{\text{saturated chloride solution}}} = \frac{\%sCl^-}{35.7} \tag{9.6}$$

$$\gamma_{\%gCl^-} = \frac{\%Cl^- \text{ in the grout at or near GAS interface}}{\%sCl^-_{\text{saturated chloride solution}}} = \frac{\%gCl^-}{35.7} \tag{9.7}$$

Using suitable transformations (such as exponential, logarithmic, etc.) of the basic response and predictor parameters defined and the procedures provided in Subsection 7.2, probabilistic models for $C_T$ of strands under WD and CA exposure conditions are developed. The next three subsections discuss the analytical steps involved in this process.

### 9.3.3. Steps to develop tension capacity models for strands under CA conditions (Steps CA-1 through CA-4)

In this subsection, analytical steps to develop $C_T$ of strands under CA exposure conditions will be presented. Most CA exposure conditions found in the field are typically not as aggressive as WD exposure conditions. For example, in the case of strands under NV and CA conditions, corrosion rate is assumed to be negligible. Hence, $C_{T,\,SS}$ when NV and CA conditions exist can be assumed to be equal to $C_{T,\,\mathrm{ARS}}$. This is shown in the Step CA-1 discussed later in this subsection.

BIOV and CA exposure conditions might result in aggressive corrosion. As discussed in Subsection 6.5.5, BIOV condition causes statistically dissimilar and more severe loss in $C_T$ than the PV condition. Moreover, Table 2-1 showed that the probabilities of finding a tendon with PV and BIOV conditions are approximately 6 and 78%, respectively. These numbers indicate a much higher importance or need for assessing corrosion of strands with BIOV conditions. In addition, it is highly unlikely that there will be a PV and not a BIOV condition inside a tendon. Based on these field scenarios and experimental convenience it is concluded that BIOV is the most critical *VT* influencing $C_T$ of strands exposed to CA conditions. Hence, probabilistic model for $C_T$ of strands under BIOV and CA conditions only is developed and that for $C_T$ of strands under PV and CA conditions is not developed.

A *direct approach* of developing probabilistic models for $C_{T,SS}$ under BIOV and CA conditions would be by conducting a long term stressed strand corrosion test under

BIOV and CA conditions. However, under most BIOV and CA exposure conditions, the strands will possibly have to be exposed for several decades in order to cause a capacity reduction that could be reliably determined using conventional tension testing equipment in laboratory. Hence, this *direct approach* is time consuming and expensive, and therefore relatively impractical. An *indirect approach* has been designed to develop probabilistic models for $C_{T,\,SS}$ when CA and BIOV conditions exist. This approach uses the UW-$SS_{BIOV}$ model developed in Step WS-4, data from the wire corrosion tests performed under CA exposure conditions, and extrapolation procedures. Three steps (i.e., Steps CA-2, CA-3, and CA-4) are defined in this approach. Following is a discussion of Steps CA-1 through CA-4.

**Step CA-1**: Develop the $C_{T,\,CA,\,NV}$ model to predict $C_{T,\,SS}$ when CA and NV conditions exist. This model is a logarithmic distribution based on the mean and standard deviation of $C_T$ of "as-received" strands obtained in Subsection 5.2.1.

**Step CA-2**: Develop the $UW_{CA,\,BIOV}$ model to predict $C_{T,\,UW}$ at 9 months of CA exposure (see first box in Figure 9-1 and Figure 9-2(a)). The $UW_{CA,\,BIOV}$ model is developed using the data from unstressed wire corrosion tests under CA exposure conditions. The experimental design for this was shown earlier in Figure 5-8(d) and Table 5-13. For convenience, Figure 5-8(d) is reproduced in Figure 9-2(a).

**Step CA-3**: Nest the $UW_{CA,\,BIOV}$ model (developed in Step CA-2) into the UW-$SS_{BIOV}$ model (developed in Step WS-4). Use this nested model to predict $C_{T,\,SS}$ at 9 months of CA exposure (see second box in Figure 9-1 and the strand marker in Figure 9-2(b)). Note that the wire samples were tested only at $t_{CA}$ equal to 9 months and, hence, $UW_{CA,\,BIOV}$ model does not contain the time parameter, $t_{CA}$. To be used in the time-variant reliability models, this predicted $C_{T,\,SS}$ need to be extrapolated for future time instants.

**Step CA-4**: Develop the $C_{T,\,CA,\,BIOV}$ model to predict $C_{T,\,SS}$ when CA and BIOV conditions exist. This is done by modifying the formulation developed in Step CA-3

into a power model form discussed in Subsections 2.6.2 and 2.6.3 (see third box in Figure 9-1 and the solid curve in Figure 9-2(b)). The power term is denoted as $n_{CA}$.

Results from Steps CA-1 through CA-4 are provided in Subsection 9.4.

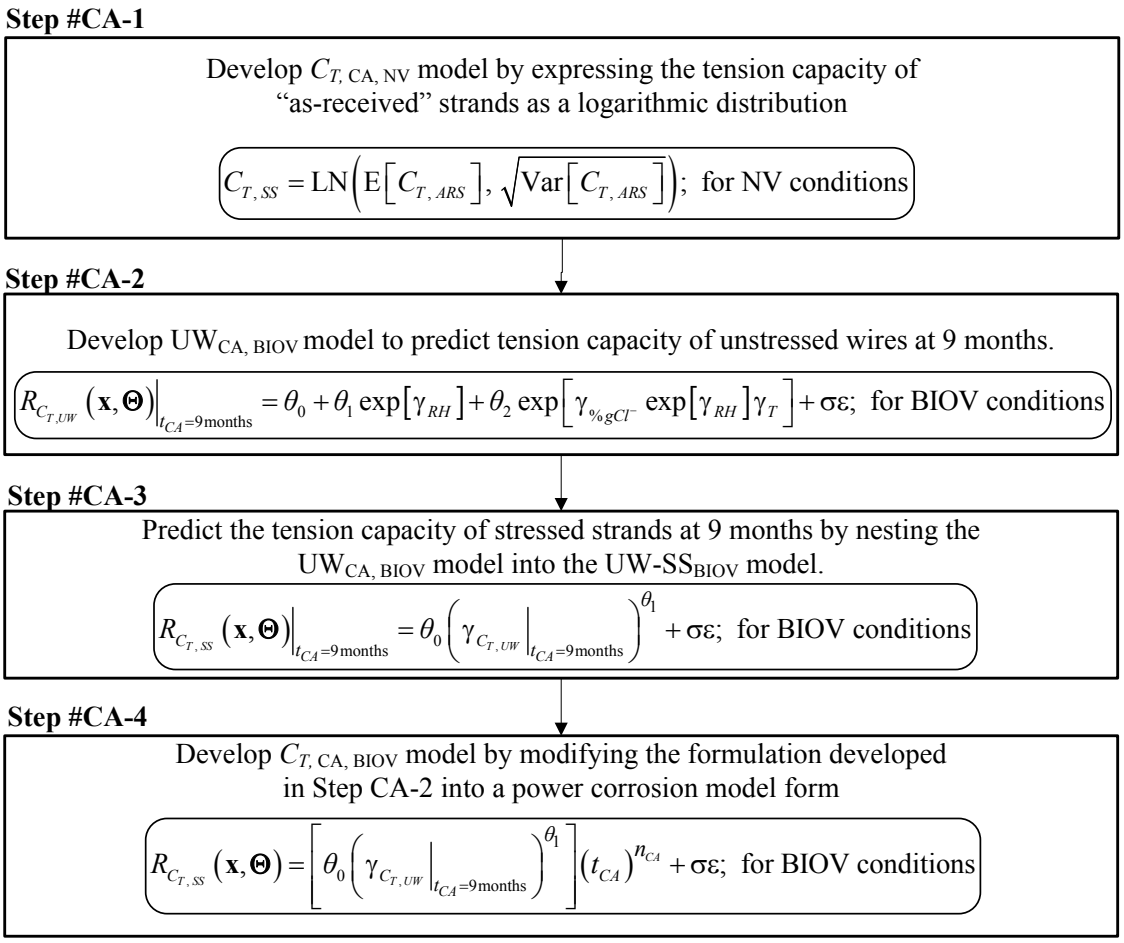


**Figure 9-1. Flowchart for Developing the Tension Capacity Models for Strands Under CA and BIOV Exposure Conditions.**

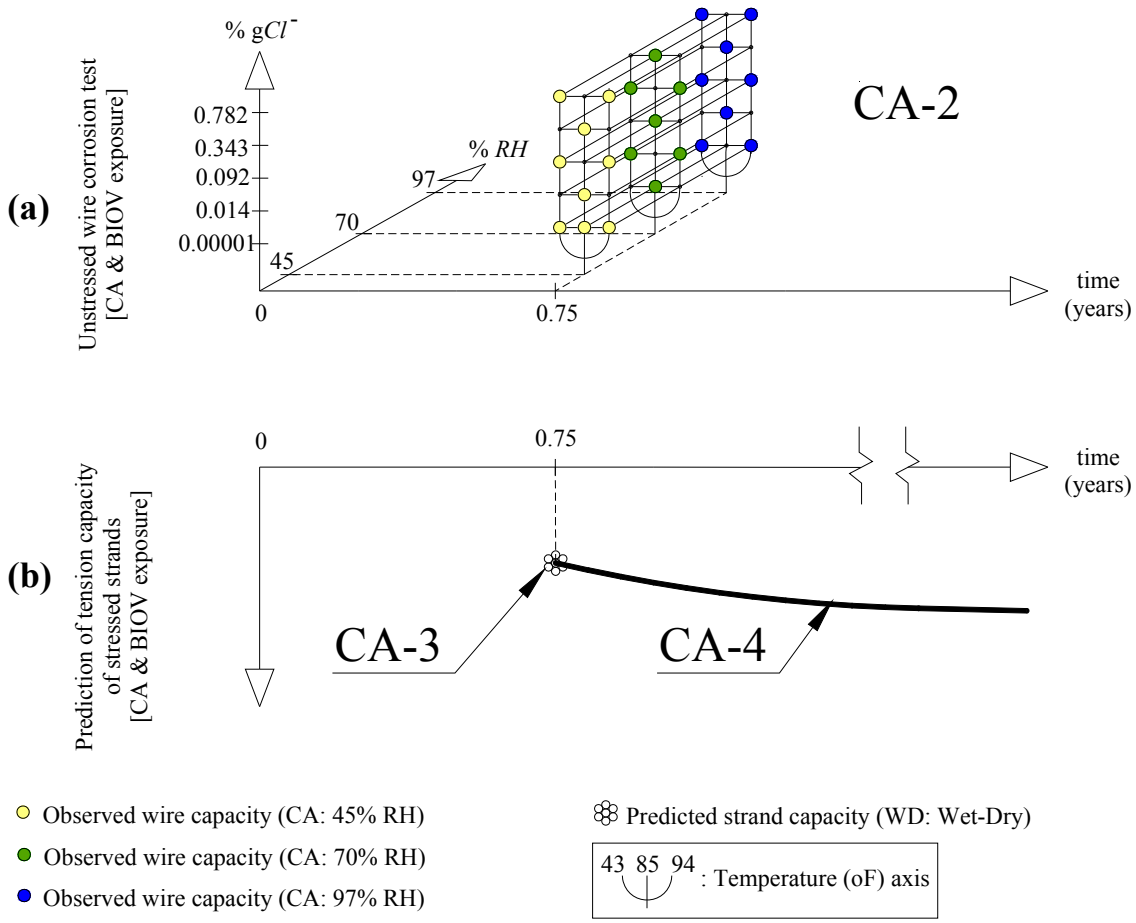


**Figure 9-2. Graphical Representations of Steps CA-2, CA-3, and CA-4.**

### 9.3.4. Assumptions for predicting strand capacity under CA conditions

Accurate estimation of the value of the power term, $n_{CA}$, is very critical to improve the accuracy of the predicted or extrapolated $C_{T,SS}$ at a future time instant. However, no long-term information could be obtained from long-term laboratory or field tests conducted as part of this study. Based on an engineering judgement, $n_{CA}$ is assumed to be equal to –0.005, herein.

## 9.4. TENSION CAPACITY MODELS FOR STRANDS UNDER CA EXPOSURE CONDITIONS-RESULTS

This subsection develops the probabilistic model for the $C_{T,SS}$ under CA and BIOV exposure conditions based on the analytical steps that were outlined in Subsection 9.3.3.

### 9.4.1. Step CA-1: Develop probabilistic model for tension capacity of strands under CA and NV conditions

Negligible corrosion is expected when CA and NV exposure conditions exist. This indicates that $C_{T,SS}$ can be assumed to be equal to $C_{T,ARS}$. Hence, Equation (7.8) provided in Subsection 7.3 will be used to probabilistically predict $C_{T,SS}$ under CA and NV conditions.

### 9.4.2. Step CA-2: Develop probabilistic models for unstressed wires under CA and BIOV conditions

This subsection presents the diagnostic study on the data from wire samples exposed to *CA* conditions. Figure 9-3 shows the diagnostic plot showing the effect of $\%gCl^-$ on $C_{T,UW}$ at 9 months of CA exposure. Except the four data points inside the ellipse, no significant reduction in $C_{T,UW}$ has been observed. These four data points correspond to the extreme corrosive condition with 0.782 $\%gCl^-$, 97 $\%RH$, and 94$^o$F (34.4$^o$C). Figure 9-4 shows the diagnostic plot of the effect of $\%RH$ on $C_{T,UW}$ at 9-month CA exposure. As observed in Figure 9-3, Figure 9-4 also shows the four data points (inside the ellipse) with significant reduction in $C_{T,UW}$. In addition to this, a few data points near top right corner (inside the small ellipse) indicates some reduction in $C_{T,UW}$ due to high $\%RH$. Other than these four observations, all the data points show no significant reduction $C_{T,UW}$.

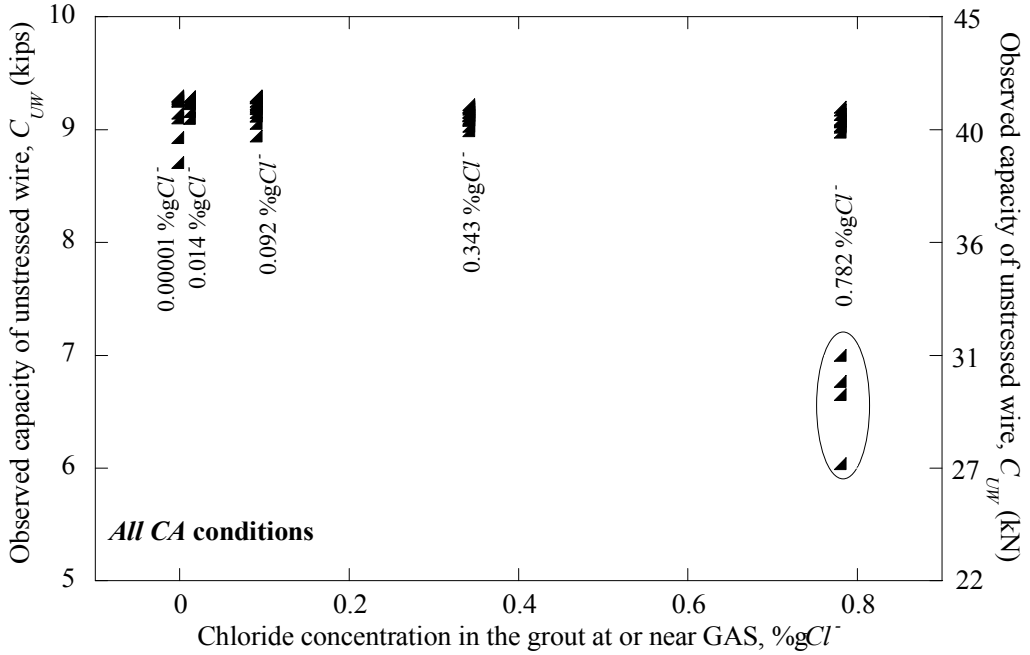


**Figure 9-3. Scatter Plot between %$gCl^-$ and Wire Capacity at 9-month CA Exposure.**

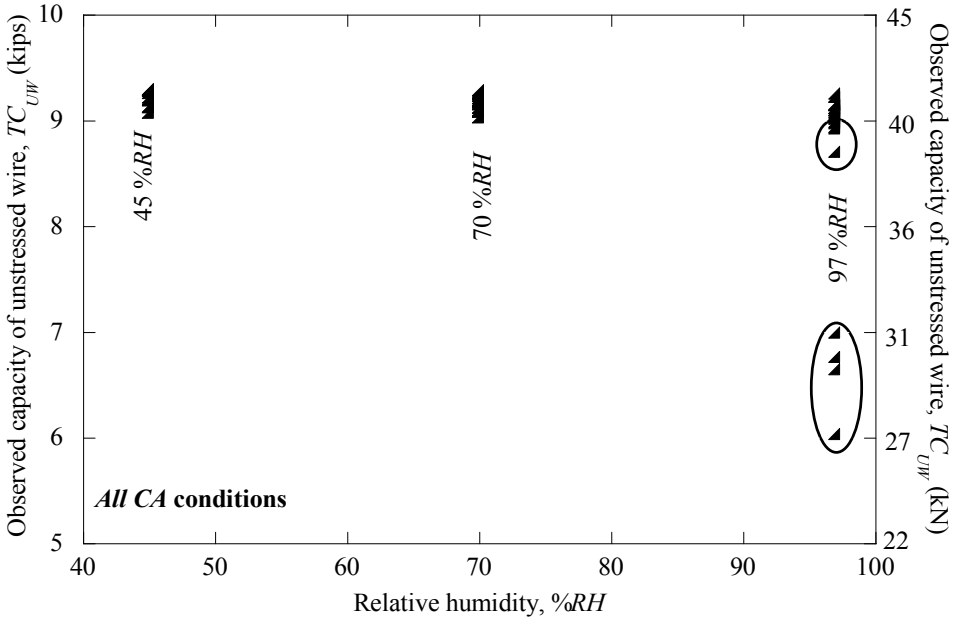


**Figure 9-4. Scatter Plot between %*RH* and Wire Capacity at 9-month CA Exposure.**

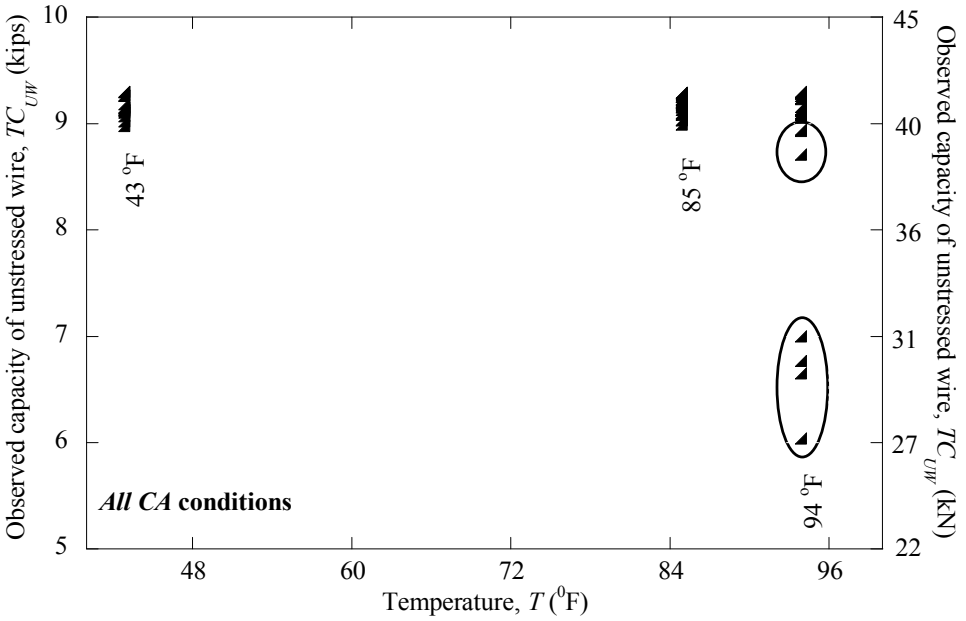


**Figure 9-5. Scatter Plot between *T* and Wire Capacity at 9-month CA Exposure.**

Figure 9-5 shows the scatter plot showing the effect of *T* on the capacity of wires at 9-month CA exposure. The four data points corresponding to the extreme exposure condition with 0.782 %$gCl^-$, 97 %*RH*, and 94°F shows significant reduction in capacity and are shown inside the ellipse near bottom right corner. As observed in Figure 9-4, the data point inside the small ellipse near top right corner show some reduction in $C_T$ and correspond to the condition with high *T* and high *RH*.

These diagnostic plots indicate that an appropriate 3-way interaction term (between functions of %$gCl^-$, %*RH*, and 94°F) needs to be incorporated into the probabilistic model form. Figure 9-6 shows that the $\gamma_{\%gCl^-} \exp[\gamma_{RH}]\gamma_T$ term has an exponential effect on $C_{T,UW}$. Hence, this term could be incorporated into the model form. However, this 3-way interaction term cannot effectively capture the smaller reduction in $C_{T,UW}$ as exhibited by the data points inside the smaller ellipse on the top left corner in Figure 9-6. These data points correspond to 97 %*RH,* 94$^o$*F,* and 0.0001 %$gCl^-$. Literature (see Subsection 2.3.9) suggests that %*RH* has an exponential effect on

atmospheric corrosion process. Hence, the $\exp[\gamma_{RH}]$ term is also incorporated into the probabilistic model form. Based on the diagnostic study and information from literature, the $UW_{CA,\,BIOV}$ model has been formulated as follows:

$$R_{C_{T,UW}}(\mathbf{x},\boldsymbol{\Theta})\Big|_{t_{CA}=9\text{ months}} = \theta_0 + \theta_1 \exp[\gamma_{RH}] + \theta_2 \exp\left[\gamma_{\%gCl^-} \exp[\gamma_{RH}]\gamma_T\right] + \sigma\varepsilon \tag{9.8}$$

where the terms are as defined in Equation (7.1) and Subsection 7.4.1. Note that the model form in Equation (9.8) model form does not have a time function. A suitable form of time function will be discussed later. The full model form was assessed using the statistical procedures provided in section 7.2.3. Table 9-1 provides the posterior statistics of the model.

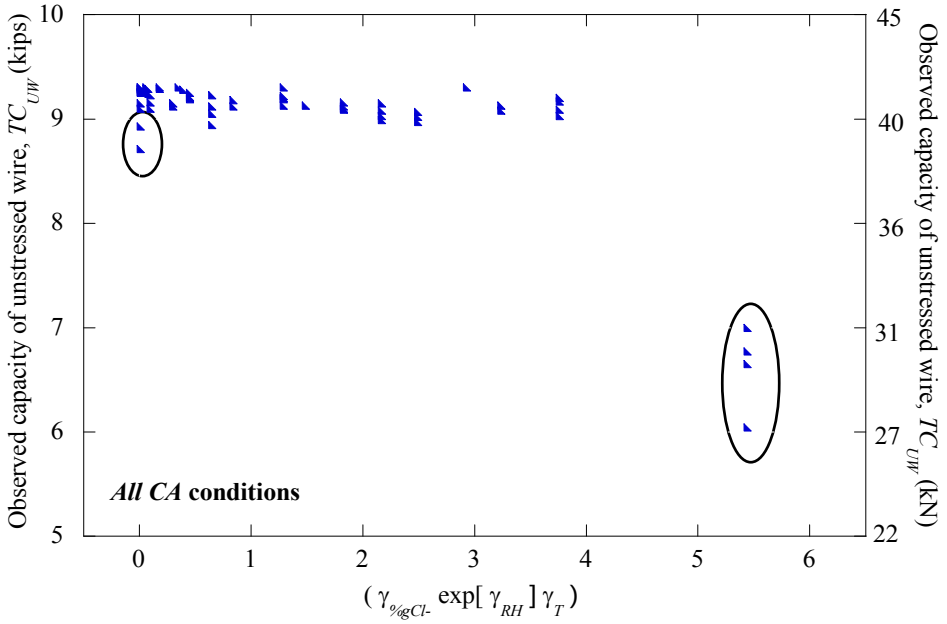


**Figure 9-6. Scatter Plot between the 3-way Interaction Term and Wire Capacity at 9-month CA Exposure.**

**Table 9-1. MAPE and Posterior Statistics of $UW_{CA, BIOV}$ Model.**

| Model Name | MAPE (%) | Parameters | Mean | Standard deviation | COV | Correlation coefficients between $\theta_i$ | |
|---|---|---|---|---|---|---|---|
| | | | | | | $\theta_0$ | $\theta_2$ |
| $UW_{CA, BIOV}$ | 1.11 | $\theta_0$ | 0.1637 | 0.0018 | 0.01 | 1 | |
| | | $\theta_1$ | –0.0030 | 0.0008 | –0.28 | –0.98 | 1 |
| | | $\theta_2$ | –0.0002 | 0.0000 | –0.04 | 0.20 | –0.27 |
| | | σ | 0.0027 | 0.0012 | | | |

The MAPE of the developed model is 1.11%. This very small MAPE does not necessarily mean that the model is extremely good. The MAPE is very small because very small amount of corrosion was observed with most data points and the observed wire capacity exhibited very small scatter. Moreover, the COV of the $\exp[\gamma_{RH}]$ term is –0.28, which is relatively moderate. Given the fact that most atmospheric corrosion models in literature accepts variables with COVs as high as approximately 60%, the mean estimate of the coefficient of $\exp[\gamma_{RH}]$ term is acceptable. In addition, the COV of the coefficient corresponding to the $\gamma_{\%gCl^-}\exp[\gamma_{RH}]\gamma_T$ term is very small (i.e., –0.04) indicating good confidence in its mean estimate. Considering these values, the model form in Equation (9.8) with the statistical estimates in Table 9-1 provides reasonably good prediction, on the grounds of available experimental data. Because of these reasons, this **model is referred to as Model $UW_{CA, BIOV}$ herein** and can be expressed as follows:

$$R_{C_{T,UW}}(\mathbf{x},\Theta)\Big|_{t_{CA}=9\text{ months}} = 0.1637 - 0.0030\exp[\gamma_{RH}] - 0.0002\exp\left[\gamma_{\%gCl^-}\exp[\gamma_{RH}]\gamma_T\right] + 0.0027\varepsilon \tag{9.9}$$

Figure 9-7 shows the validation plot for the $UW_{CA, BIOV}$ model. The details on analyzing validation plots are provided in Subsection 7.2.3.5. As it will be expected from a good

capacity model, most data points are spread along the 1:1 line. Although a few data points near the top right corner lie outside the ±σ region, most other data points including the four data points near the lower left corner (i.e, those corresponding to the extreme exposure conditions) are adequately predicted. In general, the $UW_{CA, BIOV}$ model seems to provide good prediction of $C_{T,UW}$ under *CA* exposure conditions.

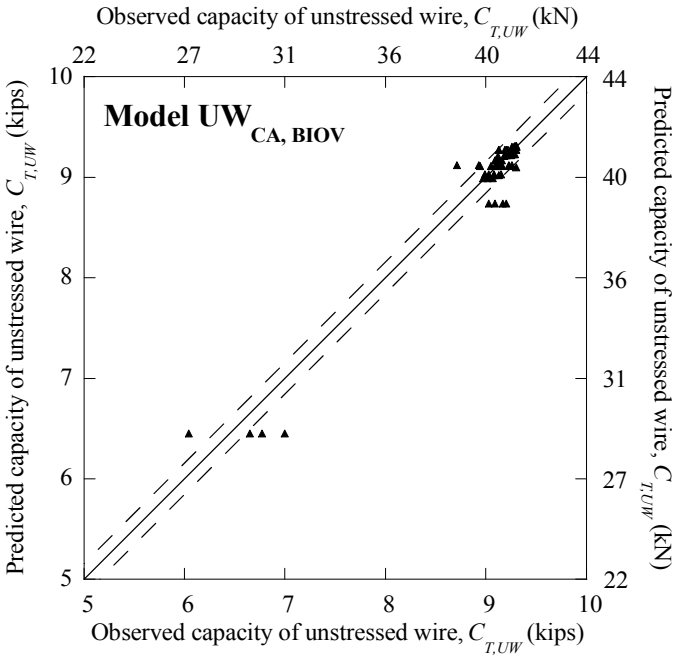


**Figure 9-7. Validation Plot for the $UW_{CA, BIOV}$ Model.**

### 9.4.3. Step CA-3: Predict the capacity of stressed strands at 9 months

$C_{T,SS}$ at 9-month exposure to CA and BIOV conditions can be predicted by nesting the $UW_{CA, BIOV}$ model (developed in Subsection 9.4.2) into the UW-$SS_{BIOV}$ model

(developed in Subsection 8.3.4). Based on the definition in Subsection 8.3.4, the UW-$SS_{BIOV}$ model is:

$$R_{C_{T,SS}}\Big|_{t_{CA}=9\text{ months}} = \theta_0\left(\gamma_{C_{T,UW}}\Big|_{t_{CA}=9\text{ months}}\right)^{\theta_1} + \sigma\varepsilon = 7.7492\left(\gamma_{C_{T,UW}}\Big|_{t_{CA}=9\text{ months}}\right)^{1.0924} + 0.0619\varepsilon \tag{9.10}$$

By substituting the term $\gamma_{C_{T,UW}}\Big|_{t_{CA}=9\text{ months}}$ in Equation (9.10) with the right-hand side of Equation (9.9), and we get:

$$R_{C_{T,SS}}\Big|_{t_{CA}=9\text{ months}} = 7.7492\left(0.1637 - 0.0030\exp\left[\gamma_{RH}\right] - 0.0002\exp\left[\gamma_{\%gCl^-}\exp\left[\gamma_{RH}\right]\gamma_T\right] + 0.0027\varepsilon\right)^{1.0924} + 0.0619\varepsilon \tag{9.11}$$

In Equation (9.11) the standard normal variables (i.e., ε) appear in two places. Because these two terms are correlated, Equation (9.11) is simplified by removing the the inner error term (i.e., 0.0027ε). This will avoid the complexities associated with correlated random variables. The reduced expression is as follows:

$$R_{C_{T,SS}}\Big|_{t_{CA}=9\text{ months}} = 7.7492\left(0.1637 - 0.0030\exp\left[\gamma_{RH}\right] - 0.0002\exp\left[\gamma_{\%gCl^-}\exp\left[\gamma_{RH}\right]\gamma_T\right]\right)^{1.0924} + 0.0619\varepsilon \tag{9.12}$$

Equation (9.12) can be used to predict $C_{T,SS}$ at $t_{CA}$ equal to 9 months.

### 9.4.4. Step CA-4: Develop the model for stressed strands under CA and BIOV exposure conditions

The value of $C_{T,SS}$ at any time, $t_{CA}$, can be predicted by incorporating Equation (9.12) into a power model form as follows:

$$R_{C_{T,SS}} = R_{C_{T,SS}}\Big|_{t_{CA}=9\text{ months}} \times \left(\frac{t_{CA}}{0.75}\right)^{n_{CA}} + \sigma\varepsilon;\ 9\text{ months} = 0.75\text{ years} \tag{9.13}$$

where $t_{CA}$ is the total time of CA exposure (in years); $n_{CA}$ is a constant; and $R_{C_{T,SS}}\Big|_{t_{CA}=9\text{ months}}$ is as defined in Equation (9.12). Note that the model error term (i.e., $\sigma\varepsilon$) is added after extrapolation process using the power model form. **Equation (9.13) is defined as Model $SS_{CA,\,BIOV}$ herein,** and can be used to predict $C_{T,SS}$ under *CA* and BIOV conditions.

### 9.4.5. Prediction of tension capacity of stressed strands under CA and BIOV conditions

The prediction of $C_T$ using the developed models is heavily dependent on the value of $n_{CA}$. Ideally, the value of $n_{CA}$ should be obtained based on the calibration of the developed models with the field data. Such field data can be obtained from an investigation of corrosion on PT strands exposed to CA conditions for long exposure periods (say, decades).

In this subsection, $n_{CA}$ is assumed to be equal to –0.005 and $C_{T,SS}$ values are predicted using the $SS_{CA,\,BIOV}$ model.

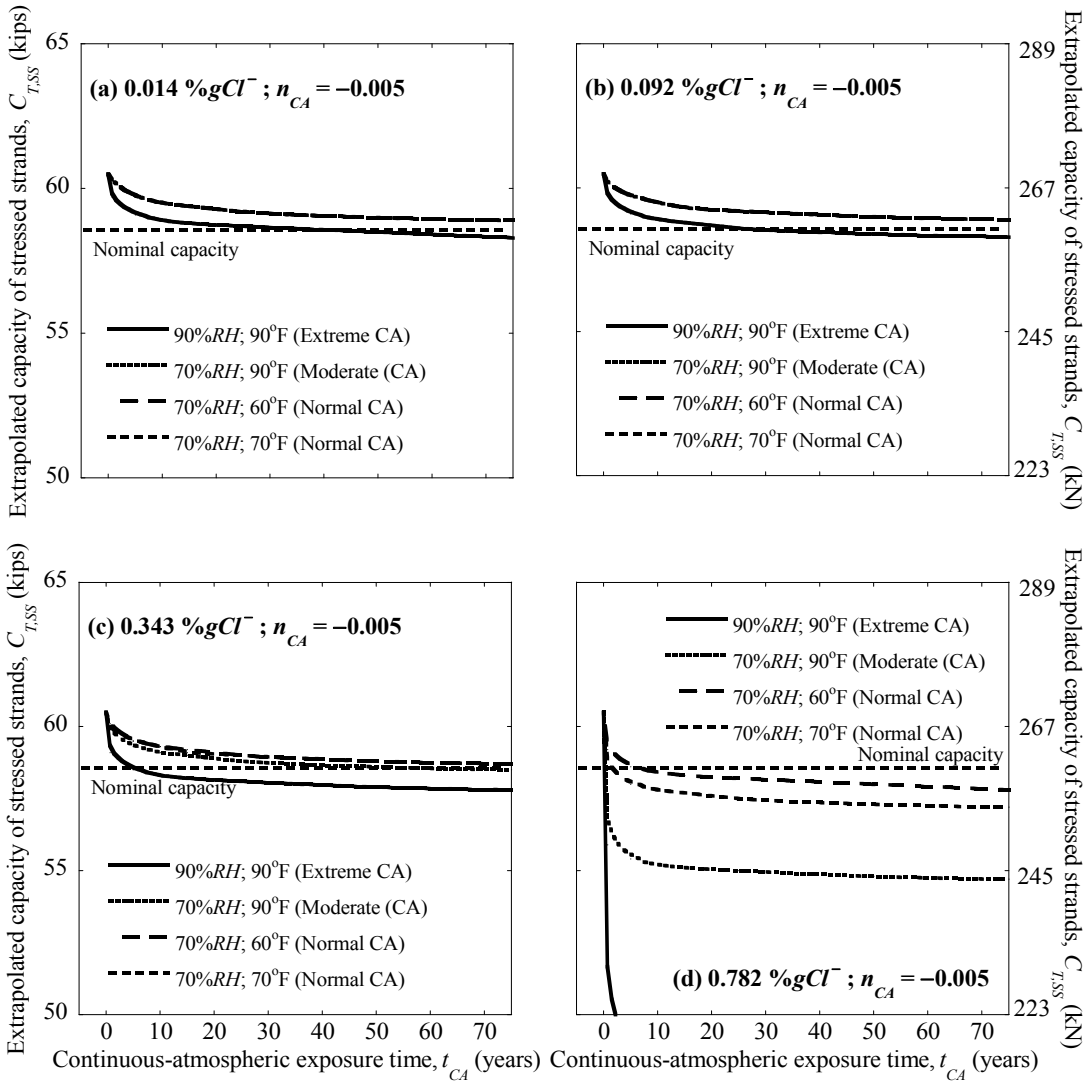


**Figure 9-8. Capacity of Stressed Strands under CA Conditions with $n_{CA}$ = –0.005.**

Figure 9-8 (a), (b), (c), and (d) show the predicted $C_{T,SS}$ values corresponding to %$gCl^-$ values of 0.014, 0.092, 0.343, and 0.782 %$gCl^-$, respectively. The horizontal-dashed lines in Figure 9-8 indicate the nominal capacity of strands

(i..e, $MUTS_{ARS}$) that is 58.6 kips (261 kN). Extrapolated values of $C_{T,SS}$ corresponding to the following four combinations of *RH* and *T* are shown.

1. An extreme CA condition with 90% *RH* and 90°F (32.2°C),
2. A moderate CA condition with 70% *RH* and 90°F (32.2°C),
3. A normal CA condition with 70% *RH* and 60°F (15.6°C), and
4. A normal CA condition with 70% *RH* and 70°F (21.1°C).

A general conclusion that synergistic occurances of high *RH-T* or high *RH-T-%gCl*$^-$ levels can cause severe localized atmospheric corrosion and capacity loss in a very short period of time as compared to the design life of the bridge.

## 9.5. SUMMARY

In this section, probabilistic model for $C_T$ of stressed strands under CA exposure were developed using the stressed strand-unstressed wire relationships (from Section 8) and experimental data on unstressed wires (from 6.4.3.4). The probabilistic models developed in Sections 7 and 9 will appropriately be used in the next section on modeling and assessment of structural reliability of segmental concrete bridges with voided PT systems.

# 10. MODELING AND ASSESSMENT OF STRUCTURAL RELIABILITY OF SEGMENTAL BRIDGES

## 10.1. INTRODUCTION AND OBJECTIVE

This section presents the modeling and assessment of the structural reliability of PT bridges. First, a framework to determine the generalized reliability index, $\beta$, is presented. Following this, the strength reliability index, $\beta_{strength}$, is formulated as a function of moment capacity ($C_M$) and moment demand ($D_M$). The algorithms for determining $C_M$ and $D_M$ are then developed. The service reliability index, $\beta_{service}$, is then formulated as a function of stress capacity ($C_f$) and stress demand ($D_f$). The algorithms for determining $C_f$ and $D_f$ are then developed using the existing formulations for allowable and applied flexural stresses at girder midspan. Following this, the statistical models of all the random variables are provided. A typical PT bridge is then defined on the basis of geometrical and structural characteristics. As an application of the developed reliability models, time-variant values of $\beta_{strength}$ and $\beta_{service}$ (up to 75 years) for this typical PT bridge are determined based on a pre-defined set of constant and random parameters.

The objective of this section is to model and assess the time-variant strength and service reliabilities (i.e., $\beta_{strength}$ and $\beta_{service}$) of a typical PT bridge experiencing HS20 and HL93 loading conditions.

## 10.2. FRAMEWORK TO DETERMINE STRUCTURAL RELIABILITY

Figure 10-1 shows a simplified flowchart of the process used in this research to determine the generalized reliability index, $\beta$, of PT bridges. In Figure 10-1, the box with a thick border indicates the Monte Carlo simulation process used to determine $P_f$. The simulation process is continued until the coefficient of variation of $P_f$ (i.e., COV($P_f$))

reaches a value less than or equal to a target value (i.e., $COV(P_f)_{target}$). Once this condition is achieved the value of $\beta$ is determined. The two shaded boxes in Figure 10-1 indicate the definition of the random parameters and the $COV(P_f)_{target}$ and the evaluation of the limit state function, $g$.

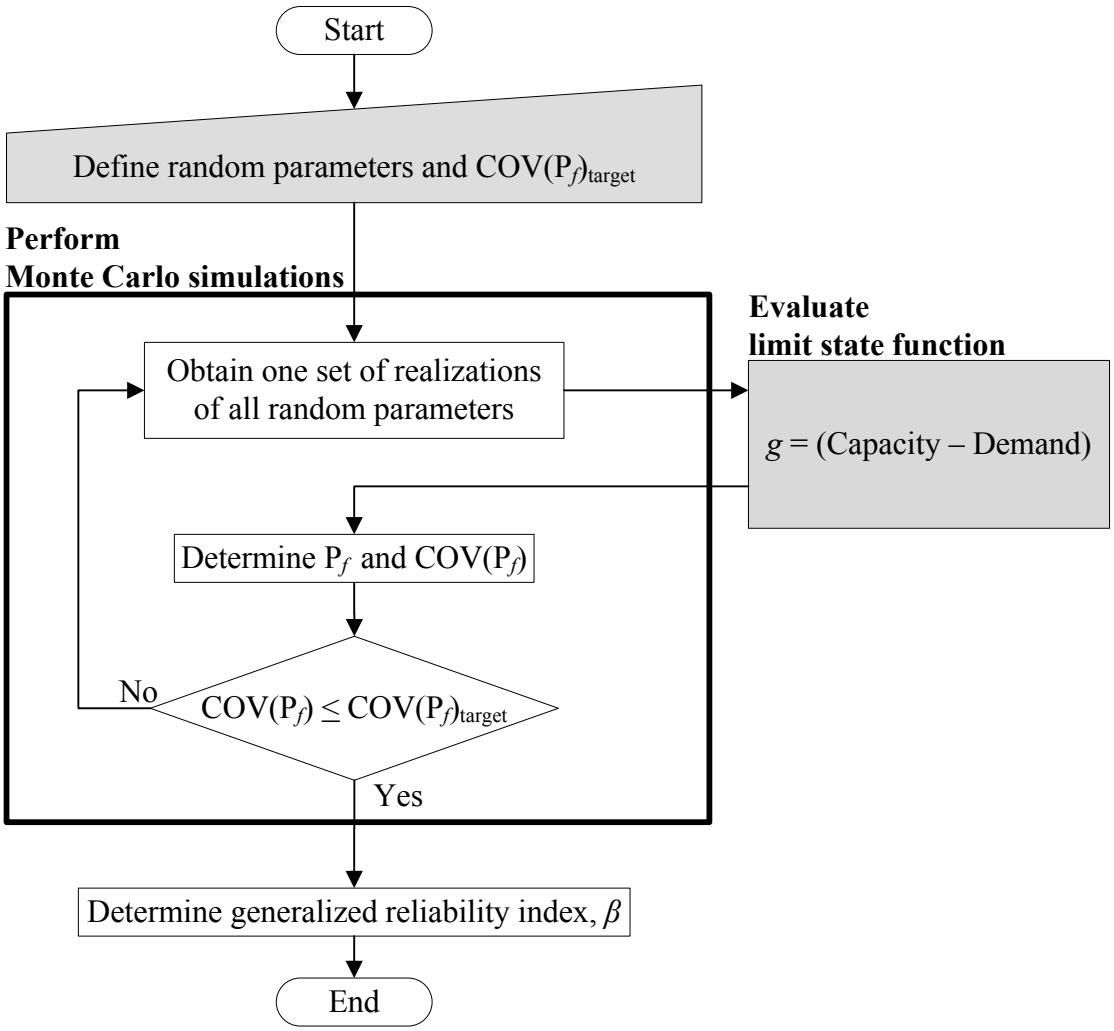


**Figure 10-1. Framework to Determine the Generalized Reliability Index, $\beta$.**

Formulations to evaluate $g$, $P_f$, $COV(P_f)$, and $\beta$ are available in the literature and were reviewed in Subsection 2.9.1. The literature provides analytical formulations to estimate $g$ for strength and service limit states (i.e., $g_{strength}$ and $g_{service}$) for pre-tensioned structural systems with "as-received" strands. However, these models do not capture the potential reduction in $\beta_{strength}$ and $\beta_{service}$ due to corrosion and the resulting reduction in the $C_T$ of strands as a function of time.

In the following subsections, $g_{strength}$ and $g_{service}$ are formulated based on capacity and demand functions. Various parameter uncertainties are taken into account while formulating these capacity and demand functions. The uncertainties associated with the tension capacity ($C_T$) and prestress loss ($P_{loss}$) of individual strands, compressive strength of concrete ($f_c$), void condition ($VC$) in individual external ducts, damage conditions ($DC$) of individual external ducts, and elements of applied dead load ($DL$) and live load ($LL$) are considered. The analytical formulations for the capacity and demand functions for $g_{strength}$ and $g_{service}$ are then programmed using MATLAB® and incorporated into FERUM (discussed in Subsection 2.9.1.3) to determine $\beta_{strength}$ and $\beta_{service}$.

## 10.3. MODELING STRENGTH RELIABILITY

### 10.3.1. Strength limit state function, probability of strength failure, and strength reliability index

A review on limit state functions, probability of failure, and reliability indices was provided in Subsection 2.9.1.1. Following the conventional structural reliability theory (Ditlevsen and Madsen 1996), the strength limit state function, $g_{strength}$, is defined as follows:

$$g_{strength} = C_M - D_M \tag{10.1}$$

such that the events with $g_{strength} < 0$ represent strength failure. Based on Monte Carlo simulations of $g_{strength}$, the probability of strength failure, $P_{f,\,strength}$ can be determined as follows:

$$P_{f,\,strength} = \frac{N_{f,\,strength}}{N_{sim,\,strength}} \tag{10.2}$$

where $N_{f,\,strength}$ and $N_{sim,\,strength}$ indicate the number of instances with strength failure and number of simulations, respectively. The value of $COV(P_{f,\,strength})$ is determined as follows (Haldar and Mahadevan 2000):

$$COV\left(P_{f,\,strength}\right) \approx \frac{1}{P_{f,\,strength}} \cdot \sqrt{\frac{\left(1 - P_{f,\,strength}\right) P_{f,\,strength}}{N_{sim,strength}}} \tag{10.3}$$

Based on the estimated $P_{f,\,strength}$ the generalized strength reliability index, $\beta_{strength}$, can be determined as follows (Ditlevsen and Madsen 1996):

$$\beta_{strength} = -\Phi^{-1}\left(P_{f,\,strength}\right) \tag{10.4}$$

where $\Phi$ is the cumulative distribution function (CDF) of the standard normal distribution. To determine $\beta_{strength}$, $C_M$ and $D_M$ need to be modeled.

### 10.3.2. Probabilistic modeling of moment capacity of the girder at midspan

Ting and Nowak (1991) developed a computer algorithm to study the effect of a decrease in the $C_T$ of strands on $C_M$ of pre-tensioned beams. Ting and Nowak (1991)

assumed constant values for the initial prestress force, $P_i$, loss in prestress force, $P_{loss}$, and loss in $C_T$, for all the strands at the same depth in a beam. Depending on the uncertainties associated with the stress-strain and corrosion mechanisms, this might not be the case in segmental, PT bridges.

AASHTO (1999) and AASHTO LRFD Specifications (2007) provide guidance for flexural design of segmental bridges. These specifications are calibrated to design new bridges with a target strength reliability index, $\beta_{strength,\ \text{target}}$, value of 3.5 (Nowak and Collins 2000). Not all formulations in these design documents can be used for assessing $C_M$ of existing segmental bridges. This is because of the existing uncertainties in the capacity and demand parameters and the associated difficulties in estimating $C_M$ when the amount of corrosion and resulting capacity loss and the prestress loss vary from one strand to another. A probabilistic approach is needed to determine $C_M$ of segmental, PT bridges.

The present research developed an algorithm to determine the probabilistic $C_M$ of PT bridges. This algorithm uses the probabilistic models for $C_T$ of strands developed in Sections 7 and 9, the formulations for stress and strain in concrete from Todeschini et al. (1964), and the formulations for nominal tensile stress of unbonded strands from the AASHTO LRFD specifications (2007). The nonlinear stresss-strain model for concrete by Todeschini et al. (1964) was selected because it is a single closed-form solution, and hence, suitable for efficient numerical simulation. The formulation for nominal tensile stress of unbonded strands from the AASHTO LRFD specifications (2007) was used based on the fact that the external tendons are unbonded and the assumption that the internal tendons are unbonded.

Figure 10-2 shows a general schematic of sectional analysis of a typical T-girder at nominal conditions including the strain, stress, and force distributions on the cross section.

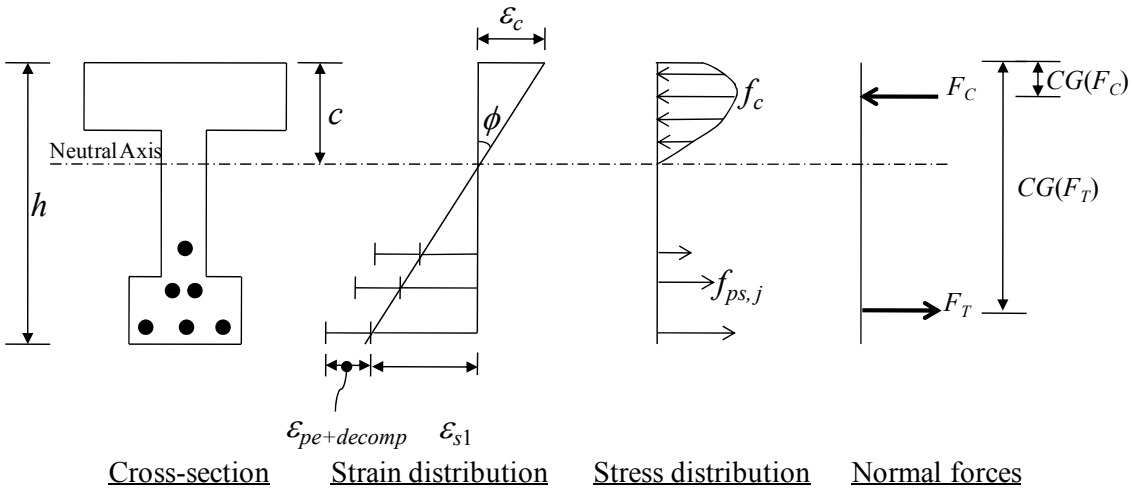


**Figure 10-2. Sectional Analysis of a Typical T-girder at Nominal Conditions.**

In the strain diagram, the compressive strain in concrete, $\varepsilon_c$, is assumed linear and can be calculated using the values of the curvature, $\phi$, and neutral axis depth, $c$, that are determined using an iterative algorithm as discussed later. The compressive stress in the concrete, $f_c$, is calculated using the nonlinear stress-strain model from Todeschini (1964). The term $\varepsilon_{pe+decomp}$ is defined as the the total tensile strain in the strands when concrete decompression begins; and this could vary from one strand to another. In this research, $\varepsilon_{pe+decomp}$ is assumed to be the sum of the strains induced by the total effective prestress and the additional stress in strands due to the decompression moment. This sum of these two stresses is denoted as $f_{pe}$, herein. Note that in this research, $f_{pe}$ is calculated by subtracting prestress losses at a given time due to long-term effects, $\Delta f_{pLT}$, from the initial prestress after anchoring, $f_{pi}$ (see Subsection 2.7.1.2 for further details). In this research, $f_{pi}$ is assumed to be $0.70 \times MUTS_{ARS}$ (per TxDOT bridge drawings) and short-term losses are assumed to be negligible. [In post-tensioning applications, because of the advanced jacking and monitoring techniques, the desired level of $f_{pi}$ can be achieved without significant short-term stress losses.] The additional tensile strain in strand induced by the additional moment above decompression and the resulting $\phi$ and $c$ is denoted as $\varepsilon_{s1}$. The total stress (i.e., $\varepsilon_{pe+decomp} + \varepsilon_{s1}$) in each strand is

denoted as $f_{ps,j}$ ($j$ indicating $j^{th}$ strand) and calculated using the formulation in the AASHTO LRFD Specifications (2007). In the force diagram, the total compressive force in concrete ($F_C$) and tensile force in the strands ($F_T$) and corresponding centers of gravity are shown.

The value of $C_M$ is determined by considering the tension failure of individual strands and compression failure of concrete. The algorithm to determine $C_M$ is structured using a main function to compute $C_M$ and three subfunctions as follows:

- Subfunction "*M"* to determine the bending moment, $M_\phi$, when curvature, $\phi$, is known.
- Subfunction "$F_T$" to determine total normal tensile force, $F_T$.
- Subfunction "$F_C$" to determine the total normal compressive force, $F_C$.

*10.3.2.1. The main function to determine moment capacity*

The main function algorithm (see Figure 10-3 for flowchart) to determine the probabilistic $C_M$ is as follows:

1. **Input parameters:** Obtain input parameters including effective concrete cross-sectional geometry, material characteristics of strand and concrete; area and location of "as-received" strands; environmental, void, and damage conditions inside tendons; exposure time; etc. Note that the dimensions of the effective cross section are obtained using the AASHTO LRFD Specifications (2007) for the effective flange width used to compute nominal moment.
2. **Define the range and increment of curvature:** Set the minimum curvature, $\phi_{min} = 0$ and maximum curvature, $\phi_{max} = 0.01$ radians/inch. Also, set the incremental curvature, $\delta_\phi = 1 \times 10^{-6}$ radians/inch.
3. **Determine curvature, $\phi$, for the current iteration:** Set the curvature, $\phi = (\phi_{min} + \phi_{max})/2$. Also set $\phi+ = (\phi + \delta_\phi)$ and $\phi- = (\phi - \delta_\phi)$ to assist in calculating the slope of moment-curvature curve. These points are moved to either leftward or rightward based on a decision process as

described later in Step 8. The positions of $\phi$, $\phi+$, and $\phi-$ during the first iteration are shown in Figure 10-4.

4. **Calculate moment, *M*, at, before, and after $\phi$:** Call Subfunction "*M*" to calculate bending moment. (This subfunction is presented in Subsection 10.3.2.2). Calculate bending moment corresponding to $\phi$, $\phi+$, and $\phi-$ (i.e, $M_{\phi}$, $M_{\phi+}$, and $M_{\phi-}$, respectively).

5. **Calculate slope of *M*-$\phi$ curve before and after $\phi$:** Using $\phi$, $M_{\phi}$, $\phi-$, and $M_{\phi-}$, determine the slope of the moment-curvature curve between $\phi-$ and $\phi$ and (i.e., $S_{\phi-}$). Using $\phi$, $M_{\phi}$, $\phi+$, and $M_{\phi+}$, determine the slope of moment-curvature curve between $\phi$ and $\phi+$ and (i.e., $S_{\phi+}$). $S_{\phi-}$ and $S_{\phi+}$ during the first iteration are shown in Figure 10-4. Go to Step 6.

6. **Decision on next iteration of $\phi$:** If $S_{\phi+} > 0$, then set $\phi_{\min} = \phi$ to move the $\phi$ rightward and repeat Steps 3 through 5. If $S_{\phi-} \leq 0$ and $S_{\phi+} \leq 0$, then set $\phi_{\max} = \phi$ to move the $\phi$ leftward and repeat Steps 3 through 5. [Note: Possible positions of $\phi$, $\phi+$, and $\phi-$ in the second iteration (i.e., after moving either leftward or rightward) are shown in Figure 10-4. For simplicity, Figure 10-4 does not show these positions in further iterative processes or until a solution is obtained.] If $S_{\phi-} > 0$ and $S_{\phi+} < 0$, then define $C_M$ equal to $M_{\phi}$ [Note: The "peak point" in Figure 10-4, corresponds to $C_M$.]

In each iteration, Step 4 of the main function determines $\phi$, $\phi+$, and $\phi-$ and calls the subfunction *M* to calculate $M_{\phi}$, $M_{\phi+}$, and $M_{\phi-}$. The details of the subfunction *M* are discussed next.

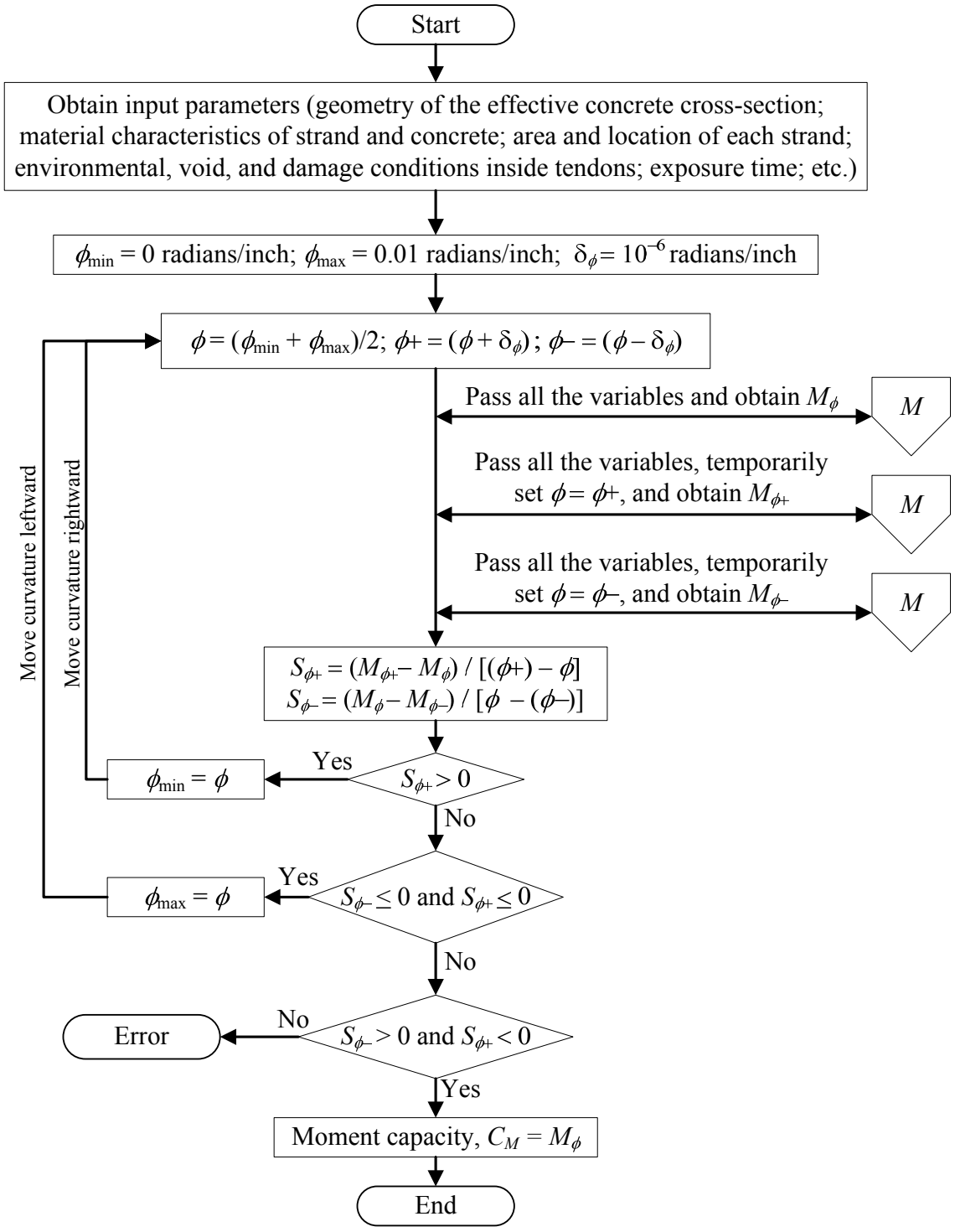


**Figure 10-3. Simplified Flowchart of the Main Function to Determine Moment Capacity of a PT Girder.**

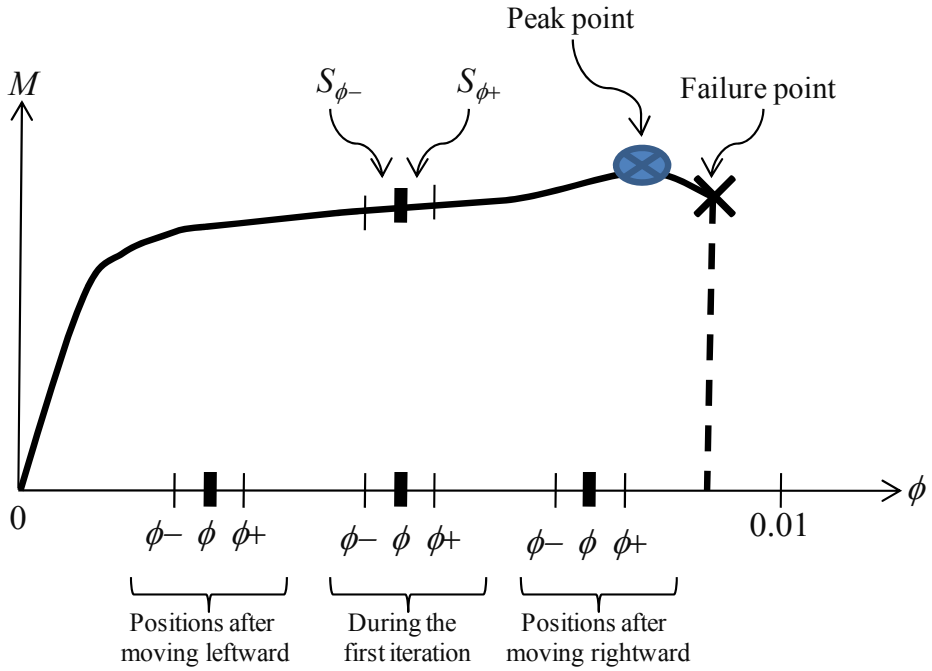


**Figure 10-4. Schematic Showing the Movement of Curvature, $\phi$.**

*10.3.2.2. The subfunction to determine bending moment corresponding to a curvature*

Within a given iteration, Step 4 of the main function for calculating $C_M$ calls the subfunction to calculate $M_{\phi}$, $M_{\phi+}$, and $M_{\phi-}$. The algorithm to calculate $M$ at any value of $\phi$ is as follows (see Figure 10-5 for flowchart):

1. **Input parameters:** Obtain the value of curvature, $\phi$, and other parameters from the calling function. Overall height of the girder = $h$.

2. **Define the range of neutral axis depth, $c$:** Set $c_{min} = 0$ and $c_{max} = h$. (Note that all the distances are measured from the top face of the girder).

3. **Determine $c$ for the current iteration:** Set the neutral axis depth, $c = (c_{min} + c_{max})/2$.

4. **Check for compression failure:** If the strain at the extreme compression fiber ($c\phi$) is greater than 0.003, the maximum usable concrete compressive strain defined by AASHTO LRFD Specifications (2007), then set $c_{max} = c$ to move the neutral axis upward. Go to Step 3.

5. **Calculate normal tensile force:** Call the subfunction to calculate the total normal tensile force, $F_T$, and its center of gravity, CG($F_T$). [This subfunction is presented in Subsection 10.3.2.3].

6. **Calculate normal compressive force:** Call the subfunction to calculate the total normal compressive force, $F_C$, and its center of gravity, CG($F_C$). [This subfunction is presented in Subsection 10.3.2.4].

7. **Determine the direction for moving *c* for next iteration:** If $(|F_T| - |F_C|) > 0.001 \times |F_C|$, then force equilibrium does not exist. If $|F_C| > |F_T|$, then set $c_{max} = c$ to move the neutral axis upward. Go to Step 3. If $|F_C| < |F_T|$, then set $c_{min} = c$ to move the neutral axis downward. Go to Step 3.

8. **Checking force equilibrium conditions and calculate moment:** If $(|F_T| - |F_C|) \leq 0.001 \times |F_C|$, then force equilibrium exists. Calculate average normal force, $F = [(|F_T| + |F_C|)/2]$. Calculate the moment arm, $k = \text{CG}(F_T) - \text{CG}(F_C)$. Calculate bending moment, $M$, by multiplying $F$ and $k$. Return the value of $M$ to the calling function.

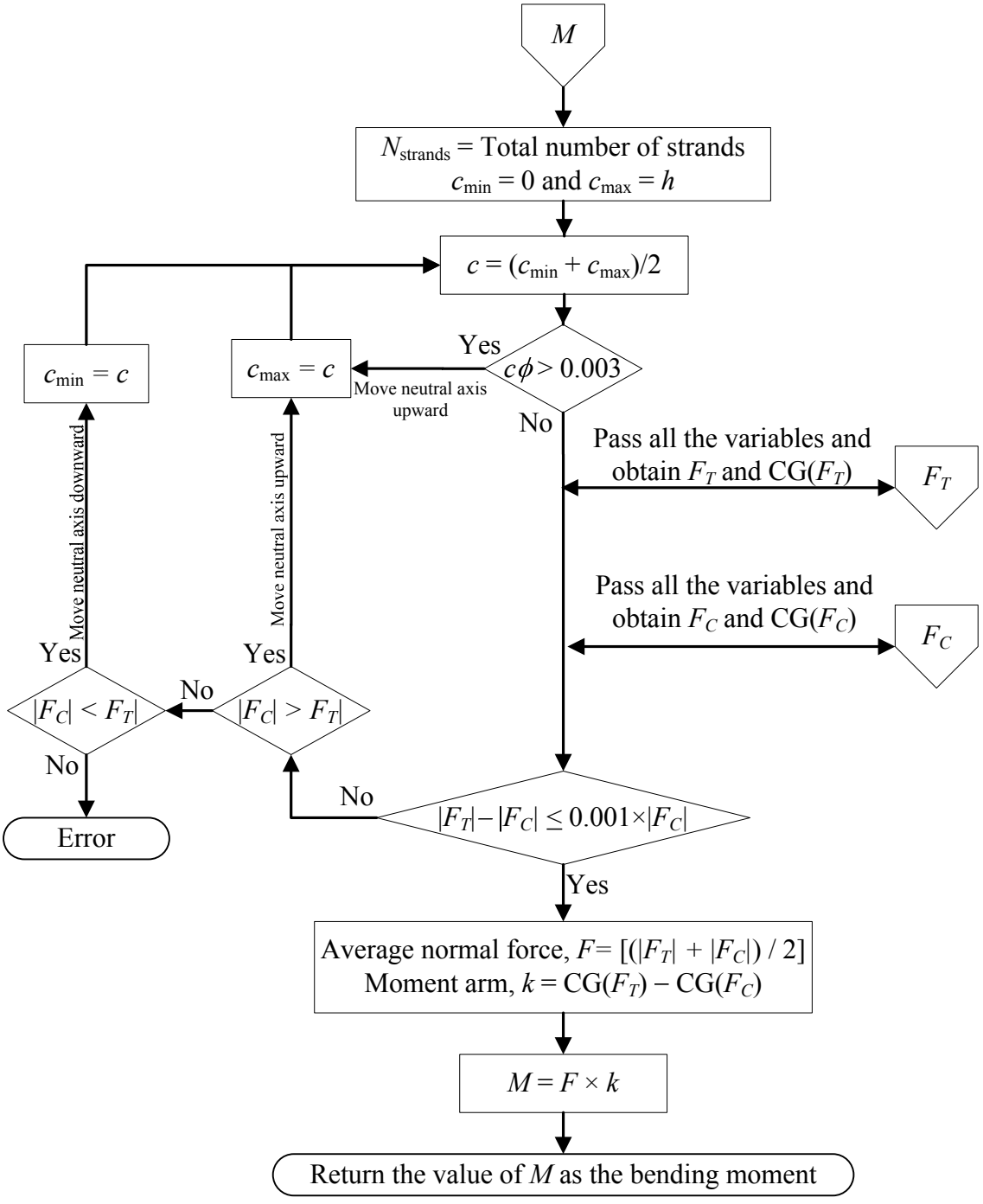


**Figure 10-5. Simplified Flowchart of the Subfunction to Determine the Bending Moment Corresponding to a Curvature.**

*10.3.2.3. The subfunction to determine the total normal tensile forces*

Step 5 in the subfunction "*M*" to calculate bending moment calls the subfunction "$F_T$" to calculate tensile forces, $F_T$. The algorithm (see Figure 10-6 for flowchart) for this subfunction to calculate $F_T$ is provided here.

1. **Obtain input parameters:** Obtain all the parameters from the calling subfunction, *M*.

2. **Initialize:** Set the count for each strand, $j = 1$.

3. **Determine effective prestress on strands:** Obtain the configuration and location of each strand. Then, calculate the effective prestress on each strand, $f_{pe,\,j}$, as follows:

$$f_{pe,\,j} = f_{pi,\,j} - \Delta f_{pLT,\,j} = \left( \frac{\left(0.70 \times MUTS_{ARS}\right)}{A_{ARS}} - \frac{P_{loss,\,j}}{A_{ARS}} \right) \tag{10.5}$$

   where the subscript $j$ indicates the $j^{\text{th}}$ strand; $f_{pi,\,j}$ is the average prestress after anchoring; $\Delta f_{pLT,\,j}$ is the total prestress loss due to time-dependent effects; $P_{loss,\,j}$ is the loss in prestress force; and $MUTS_{ARS}$ and $A_{ARS}$ are minimum ultimate tensile strength and cross-sectional area of "as-received" strand with negligible corrosion.

4. **Determine $C_T$ and area of strands:** Obtain the environmental, void, and damage conditions. Following the strategy provided later in Subsection 10.5.2, select the probabilistic model for $C_T$ of each strand. Calculate the $C_{T,j}$ for each strand. Calculate the remaining area of each strand, $A_{ps,\,j}$, as follows:

$$A_{ps,\,j} = C_{T,\,j} \left( \frac{A_{ARS}}{C_{T,\,ARS}} \right) \tag{10.6}$$

where the subscript $j$ indicates the $j^{th}$ strand, and $A_{ARS}$ and $C_{T,\,ARS}$ are the cross-sectional area and average tension capacity of "as-received" strands with negligible corrosion.

5. **Remove completely corroded strands:** If $A_{ps,\,j}$ is zero, then set $f_{ps,\,j}$ and $f_{pe,\,j}$ to zero. Go to Step 7.

6. **Calculate total stress on partially corroded or uncorroded strands:** If $A_{ps,\,j}$ is greater than zero, calculate the average stress, $f_{ps,j}$ (ksi), in each strand at nominal conditions using Equation (10.7) for unbonded prestressing strands, provided in AASHTO LRFD Specifications (2007).

$$f_{ps,j} = \underbrace{\left[ f_{pe,j} + 900\left( \frac{d_{p,j} - c}{l_e} \right) \right]}_{f_{ps,j,calculated}} \le f_{py};\; l_e = \left( \frac{2l_i}{2 + N_s} \right) \tag{10.7}$$

where $f_{pe,\,j}$ (ksi) is the effective prestress in the $j^{th}$ strand, $d_{p,\,j}$ is the distance between the extreme compression fiber and centroid of the $j^{th}$ strand (inches), $l_e$ is the effective tendon length (inches), $l_i$ is the length of the strand between anchorages (inches), $N_s$ is the number of support hinges crossed by the strand between the anchorages, and $f_{py}$ is the yield strength of strand (ksi). The value of $f_{ps,\,j,\,calculated}$ varies due to the variation in $c$. If $f_{ps,\,j,\,calculated}$ is greater than the ultimate tensile stress capacity of strand, $f_{pu}$, then the strand fails in tension and is removed from further calculations by setting the corresponding $f_{ps,\,j}$, $f_{pe,\,j}$ $P_{e,j}$, and $A_{ps,\,j}$ to zero. If $f_{ps,\,j,\,calculated}$ is greater than zero and less than $f_{py}$, then $f_{ps,\,j}$ is set equal to $f_{ps,\,j,\,calculated}$.

7. **Calculate normal tensile forces on each strand:** Calculate $F_{T,\,j}$ for the strands by multiplying $A_{ps,\,j}$ with $f_{ps,\,j}$. Go to Step 5 until $F_{T,\,j}$ for all the strands are determined (i.e., $j$ reaches $N_{strands}$).

8. **Determine the total tensile force and its center of gravity:** Determine the total tensile force, $F_T$, by adding the tensile forces acting on each strand, $F_{T,\,j}$. Determine the center of gravity of $F_T$, CG($F_T$). Note that this is measured from the top face of the girder. See Figure 10-2 for graphical representation of $F_T$ and CG($F_T$). Return the value of $F_T$ and CG($F_T$) to the calling function.

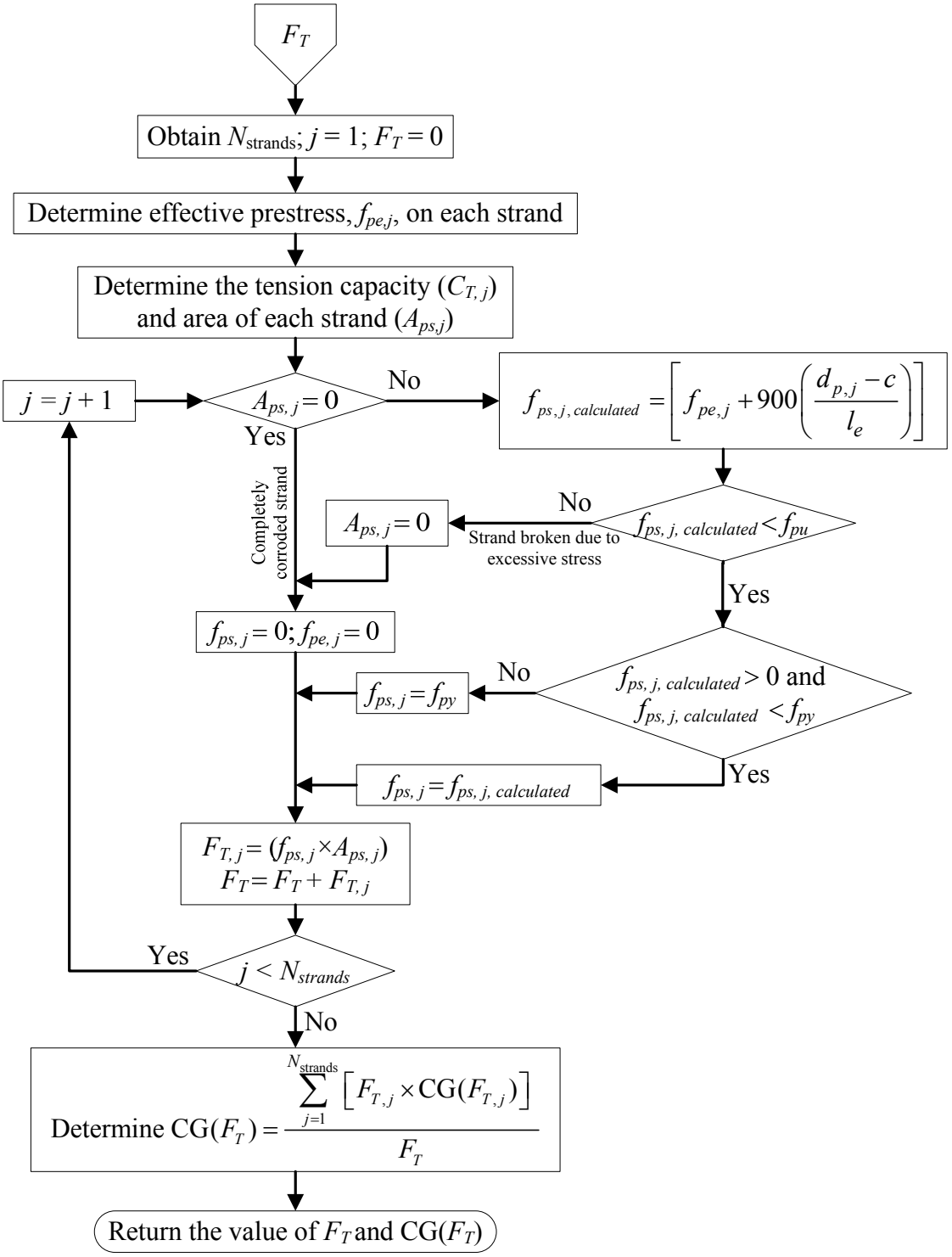


**Figure 10-6. Simplified Flowchart of the Subfucntion to Determine the Total Tensile Force, $F_T$.**

*10.3.2.4. The subfunction to determine the total normal compressive forces*

Step 6 in the subfunction to calculate bending moment, $M$, calls the subfunction to calculate $F_C$. The algorithm (see Figure 10-7 for flowchart) for this subfunction to calculate $F_C$ is provided here.

1. **Obtain input parameters:** Obtain all the parameters from the calling subfunction, $M$.

2. **Initialization:** Set the count for each subsection, $k = 1$.

3. **Determine section properties:** Divide the effective cross section into convenient rectangular or triangular subsections. Also, assume that the two web sections are vertical. Now, determine sectional properties (area, moment of inertia, position of top and bottom fiber, etc.) of each concrete subsection. Set the total number of subsections equal to $N_{\text{subsections}}$.

4. **Determine compressive strain in concrete:** Determine the total compressive strain at the top and bottom ($\varepsilon_{\text{top}}$ and $\varepsilon_{\text{bottom}}$) of the $k^{\text{th}}$ subsection using the current value of $c$ and $\phi$.

5. **Determine the compressive force in concrete:** Using Todeschini (1964) model, determine the total compressive force in the $k^{\text{th}}$ subsection, $F_{C,k}$. This is done by determining concrete compressive stress, $f_c$, using $\varepsilon_{\text{top}}$ and $\varepsilon_{\text{bottom}}$ and then integrating the estimated $f_c$ over the area of each of these subsections. Also, determine the center of gravity of $F_{C,k}$ (i.e., CG($F_{C,k}$). Go to Step 4 until $F_{C,k}$ for all the subsections are determined (i.e., $k$ reaches $N_{\text{subsections}}$). [Note: Further details on Todeschini's model are provided in Subsection 2.7.5].

6. **Determine the total compressive force and its center of gravity:** Calculate the total compressive force, $F_C$, by adding all the forces in each subsection. Also, calculate the center of gravity of $F_C$, denoted as CG($F_C$), using the $F_C$, $F_{C,k}$ and CG($F_{C,k}$). Note that CG($F_C$) is measured from the top face of the girder. See Figure 10-2 for a graphical representation of $F_C$ and CG($F_C$). Return the value of $F_C$ and CG($F_C$) to the calling function.

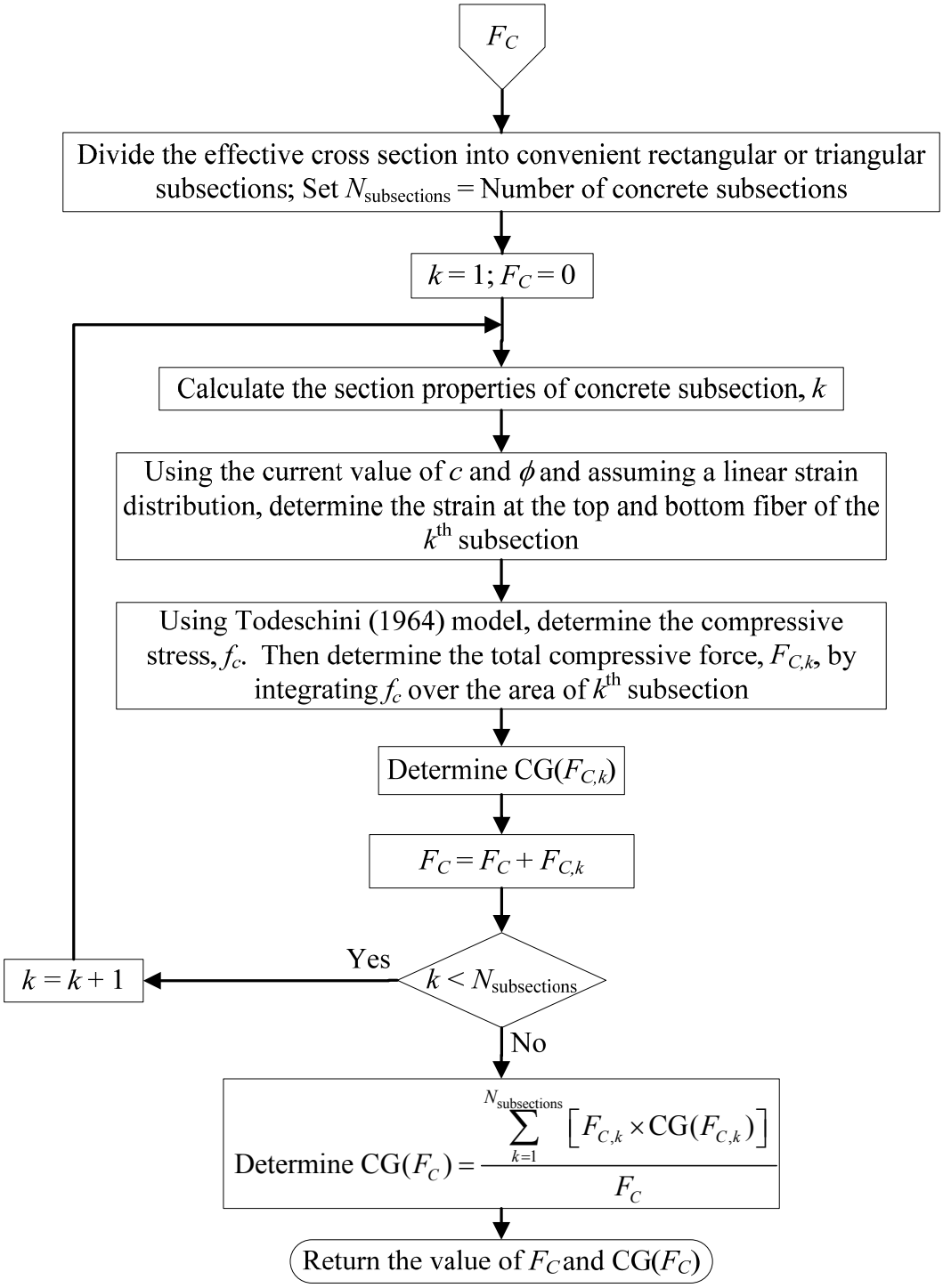


**Figure 10-7. Simplified Flowchart of the Subfunction to Determine the Total Compressive Force, $F_C$.**

An algorithm to determine $C_M$ of a segmental, PT bridge with unbonded tendons that are exposed to various corrosive conditions is now developed.

### 10.3.3. Probabilistic modeling of moment demand on the girder at midspan

Dead, live, and impact loads are used in modeling $D_M$. Uniformly distributed dead load can be calculated using the unit weight and volume of the reinforced concrete (or other materials) used in the box section, overlay and future wearing surface, and side barriers. The permanent dead load due to the weight of box section is denoted as $DL_1$. The total weight of the overlay and future wearing surface, and side barriers is denoted as $DL_2$. Following the procedures in AASHTO (1996) and AASHTO LRFD Specifications (2007), the design lane ($LL_{lane}$), truck ($LL_{truck}$), and tandem ($LL_{tandem}$) loads are used to calculate the total live load for HS20 and HL93 loading conditions. Per AASHTO (1996), an impact load equal to (50 / [125 + span in ft])% of live load is included for HS20 loading. Per AASHTO LRFD Specifications (2007), an impact load equal to 33% of live load is included for HL93 loading. Herein, these summations of live and impact loads are denoted or represented by "*LL*". Using structural mechanics principles and influence line theory, the critical section with the maximum moment is determined for the simply-supported segmental girder. $D_M$ is defined to be equal to this maximum moment. The uncertainty in $D_M$ is captured using random parameters, $DL_1$, $DL_2$, $LL_{lane}$, $LL_{truck}$, and $LL_{tandem}$.

## 10.4. MODELING SERVICE RELIABILITY

### 10.4.1. Service limit state function, probability of service failure, and service reliability index

A review of $g$, $P_f$, and $\beta$ was provided in Subsection 2.9.1.1. Following conventional structural reliability theory (Ditlevsen and Madsen 1996), the service limit state function, $g_{service}$, is defined as follows:

$$g_{service} < 0 \begin{cases} g_{f,top,1} < 0; \quad g_{f,top,1} = C_{f,top,1} - D_{f,top,1} \\ \text{or} \\ g_{f,top,2} < 0; \quad g_{f,top,2} = C_{f,top,2} - D_{f,top,2} \\ \text{or} \\ g_{f,bottom} < 0; \; g_{f,bottom} = C_{f,bottom} - D_{f,bottom} \end{cases} \tag{10.8}$$

where $g_{f,\,top,\,1}$, $g_{f,\,top,\,2}$, and $g_{f,\,bottom}$ are defined as the limit state functions for *compressive* stresses at the extreme top and bottom fibers; $C_{f,\,top,\,1}$ and $D_{f,\,top,\,1}$ represent the allowable and applied compressive stresses, respectively, at extreme top fiber when subjected to dead load only; $C_{f,\,top,\,2}$ and $D_{f,\,top,\,2}$ represent the allowable and applied compressive stresses, respectively, at extreme top fiber when subjected to dead and live loads; $C_{f,\,bottom}$ and $D_{f,\,bottom}$ represent the allowable and applied stresses at extreme bottom fiber when subjected to dead and live loads. The events $g_{service} < 0$ represent the service failure. As for $P_{f,\,strength}$, based on Monte Carlo simulations of $g_{service}$, the probability of service failure, $P_{f,\,\text{service}}$ can be determined as follows:

$$P_{f,service} = \frac{N_{f,service}}{N_{sim,service}} \tag{10.9}$$

where $N_{f,\,service}$ and $N_{sim,\,service}$ indicate the number of instances with service failure and number of Monte Carlo simulations, respectively. The COV($P_{f,\,service}$) is determined as follows (Haldar and Mahadevan 2000):

$$\mathrm{COV}\left(\mathrm{P}_{f,service}\right) \approx \frac{1}{\mathrm{P}_{f,service}} \cdot \sqrt{\frac{\left(1-\mathrm{P}_{f,service}\right)\mathrm{P}_{f,service}}{N_{sim,service}}} \tag{10.10}$$

Based on the estimated $P_{f,\,service}$, the generalized strength reliability index, $\beta_{service}$, can be determined as follows (Ditlevsen and Madsen 1996):

$$\beta_{service} = -\Phi^{-1}\left(\mathrm{P}_{f,service}\right) \tag{10.11}$$

where $\Phi$ is the CDF of the standard normal distribution. The models for $C_{f,\,top,\,1}$, $C_{f,\,top,\,2}$, $C_{f,\,bottom}$, $D_{f,\,top,\,1}$, $D_{f,\,top,\,2}$, and $D_{f,\,bottom}$ need to be developed such that the value of $g_{service}$ and then $\beta_{service}$ can be determined.

### 10.4.2. Probabilistic modeling of stress capacity of extreme fibers at midspan

Table 2-6 provides the limiting compressive and tensile stress criteria per the AASHTO LRFD Specifications (2007). In this research, these limiting values are considered as the flexural stress capacity ($C_f$) at extreme fibers. The compressive and tensile stress limits at extreme top and bottom fibers are prescribed in AASHTO LRFD Specifications (2007) and are based on the the stress limit reduction factor, $\phi_w$, and specified compressive strength of concrete, $f'_c$. However, because the actual compressive strength of concrete, $f_c$, is a random parameter, the $f'_c$ needs to be replaced with $f_c$. A probabilistic expression for $f_c$ is provided in Subsection 10.5.4. Based on these

above-mentioned AASHTO stress limits, the expressions for $C_{f,\,top,\,1}$, $C_{f,\,top,\,2}$, and $C_{f,\,bottom}$ in this study are defined as follows:

$$\begin{aligned} C_{f,top,1}(\text{ksi}) &= 0.45 f_c (\text{in ksi}) \\ C_{f,top,2}(\text{ksi}) &= 0.60 \phi_w f_c (\text{in ksi}) \\ C_{f,bottom}(\text{ksi}) &= 0 \end{aligned} \tag{10.12}$$

### 10.4.3. Probabilistic modeling of stress demand on extreme fibers at midspan

Subsection 2.7.6 reviewed the formulations to determine the applied compressive and tensile stresses (i.e., stress demands) at service at the extreme fibers. Estimating the stresses at extreme fibers is straight forward, when the strands are in "as-received" condition. However, the $C_T$ of strands reduces as a function of time and exposure conditions, resulting in changes in the effective prestress in strands, which in turn induces changes in flexural stresses on the cross section. Typically, $D_M$ under service load conditions is in the linear region of the moment-curvature diagram. However, because $D_M$ is a random parameter, some realizations might be large enough that some strands can break, especially if they are in a deteriorated condition. The effective stress, $f_{pe}$, earlier imposed by these broken strands should be removed from further calculations. Considering these factors, an iterative algorithm to determine the probabilistic values for $D_{f,\,top,\,1}$, $D_{f,\,top,\,2}$, and $D_{f,\,bottom}$ has been developed. This algorithm is as follows:

1. **Determine the moment demand under service load conditions and moment capacity:** Determine $D_M$ using the procedures in Subsection 10.3.3. Determine $C_M$ using the procedures in Subsection 10.3.2. If $D_M$ is greater than $C_M$, the girder will fail in flexure. Therefore, go to Step 8. If $D_M$ is less than or equal to $C_M$, the girder will not fail in flexure. Therefore, go to Step 2.

2. **Initialize:** Set $\phi_{\min} = 0$, $\phi_{\max} = 0.01$, and $\delta_\phi = 1 \times 10^{-6}$ radians/inch.

3. **Calculate the curvature, $\phi$, for current iteration:** $\phi = (\phi_{min} + \phi_{max})/2$. [Note: These points are moved to either leftward or rightward based on a decision process as described later in Step 6.]

4. **Calculate bending moment for current iteration:** Call the Subfunction "*M*" to calculate bending moment (this subfunction is presented in 10.3.2.2). Calculate bending moment corresponding to $\phi$ (i.e, $M_\phi$). Also, obtain the updated values of effective prestress force for each strand, $P_{e,j}$, which will be equal to zero for completely corroded or broken strands and equal to $A_{ps,j} \times f_{pe,j}$ for uncorroded, partially corroded, and unbroken strands.

5. **Determine the difference between calculated bending moment and demand moment:** Determine the value of $\delta_M = ||D_M| - |M_\phi||$. Also, set the maximum limit for $\delta_M$, $\delta_{M,\,max} = 0.001 \times |D_M|$. [Note: For the typical PT bridge section defined in Subsection 10.6.1, the moment of inertia, I, is equal to $5.86 \times 10^8$ inch$^4$. When $D_M$ is $3 \times 10^8$ or $6 \times 10^8$ lb-in, $\delta_{M,\,max}$ can cause negligible tensile stresses of 3.4 or 6.5 psi, respectively, at the extreme bottom fiber. Therefore, the potential error in the reliability estimates due to $\delta_{M,\,max}$ is expected to be negligible.]

6. **Decide the direction of movement for $\phi$:** If $M_\phi > 0$ and $\delta_M > \delta_{M,\,max}$ and $M_\phi < D_M$, then set $\phi_{min} = \phi$ to move the $\phi$ rightward and repeat Steps 2 through 5. If $M_\phi > 0$ and $\delta_M > \delta_{M,\,max}$ and $M_\phi > D_M$, then set $\phi_{max} = \phi$ to move the $\phi$ leftward and repeat Steps 2 through 5. [Note: Possible positions of $\phi$ in the second iteration (i.e., after moving either leftward or rightward) are shown in Figure 10-8. Also note that Figure 10-8 does not show these positions in further iterative processes or until a solution is obtained.] If $\delta_M \leq \delta_{M,\,max}$, then go to Step 7.

7. **Determine stress demands when moment demand is less than moment capacity:** Determine $D_{f,\,top,\,1}$, $D_{f,\,top,\,2}$, and $D_{f,\,bottom}$ using Equation (10.13) [PCI 1999, Nawy 2003, and Naaman 2004]:

$$D_{f,top,1} = (-1)\left[\sum_{j=1}^{N_{strands}}\left\{-\frac{P_{e,j}}{A_c}\left(1-\frac{e_j c_t}{r^2}\right)\right\}-\left(\frac{D_{M,DL}}{S^t}\right)\right]$$

$$D_{f,top,2} = (-1)\left[\sum_{j=1}^{N_{strands}}\left\{-\frac{P_{e,j}}{A_c}\left(1-\frac{e_j c_t}{r^2}\right)\right\}-\left(\frac{D_{M,DL}+D_{M,LL}}{S^t}\right)\right] \qquad (10.13)$$

$$D_{f,bottom} = (+1)\left[\sum_{j=1}^{N_{strands}}\left\{-\frac{P_{e,j}}{A_c}\left(1+\frac{e_j c_b}{r^2}\right)\right\}+\left(\frac{D_{M,DL}+\gamma_{load}D_{M,LL}}{S_b}\right)\right]$$

where, $P_{e,j}$ is the effective prestress force in the $j^{th}$ strand after losses; $e$ is the eccentricity of each strand from the center of gravity of the concrete cross section; $r$ is the radius of gyration; $A_c$ is the area of the concrete cross section; $D_{M,DL}$ is the moment demand due to dead load only; and $D_{M,LL}$ is the moment demand due to live and impact loads; the term $\gamma_{load}$ is 1.0 and 0.8, when HS20 and HL93 loadings, respectively, are considered; $S^t$ and $S_b$ are section modulii of concrete section with reference to the extreme top and bottom fibers, respectively; and $c_t$ and $c_b$ are the distance to the extreme top and bottom fibers, respectively, from the centroid of the concrete cross section. [Notes: (1) The value of $\gamma_{load}$ for HL93 loading is defined based on the live load factor for SERVICE III limit state given in Table 3.4.1-1 of AASHTO LRFD Specifications (2007). (2) Because of the multiplicative term "–1", the equations for $D_{f,top,1}$ and $D_{f,top,2}$ provides a positive value when compressive stress exists and a negative value when tensile stress exists. Therefore, the corresponding limit state function attains a negative value when compressive stress exceeds the limiting stress. (3) The equation for $D_{f,bottom}$ provides a positive value when tensile stress exists and a negative value when compressive stress exists. Therefore, the corresponding limit state function attains a negative value when tensile stress exceeds the limiting value of zero; indicating crack formation.] Go to Step 9.

8. **Determine stress demands when girder fails in flexure:** Set the value of $D_{f,bottom} = 1$. This will result in $g_{f,bottom}$ equal to –1 (because $C_{f,bottom}$ is equal to 0), which in turn will result in $g_f$ less than 0 (indicating service failure).

9. Stop.

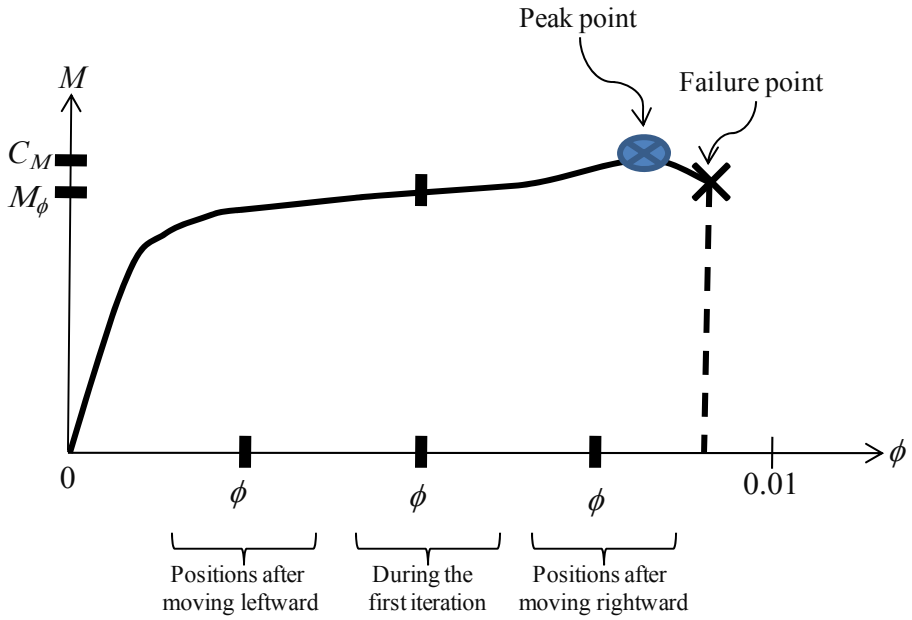


**Figure 10-8. Schematic Showing the Movement of Curvature, $\phi$.**

A model to determine $D_{f,\,top,1}$, $D_{f,\,top,2}$, and $D_{f,\,bottom}$ of a PT bridge with unbonded tendons that are exposed to various corrosive conditions is now developed.

## 10.5. RANDOM PARAMETERS IN THE PROBABILISTIC MODELS

Subsections 10.3 and 10.4 developed the strength and service reliability models, respectively. This subsection presents the random parameters used in the probabilistic models in the strength and service reliability analysis.

### 10.5.1. Void and damage/opening conditions on post-tensioning systems

In this study, the void condition (*VC*) and the damage condition (*DC*) are defined on the basis of the probability of finding a voided tendon ($P_{VT}$) and the probability of finding a damaged tendon ($P_{DT}$). In this study, a tendon with at least one void is considered as a

voided tendon. A damaged tendon is defined as a tendon with at least one unsealed hole or vent at the anchorage region or an unsealed vent or crack on HDPE ducts. As Woodward (1981) and Woodward et al. (2001) determined, $P_{VT}$ can be determined based on inspection of sample bridges or tendons or assumed based on sound engineering judgment. Similarly, $P_{DT}$ can be determined or assumed. Based on $P_{VT}$ and $P_{DT}$, $VC$ and $DC$ are modeled as binomial distributions. A binomial distribution is suitable to randomly identify the tendons with and without voids and with and without damages. Based on the data from TxDOT (2004), $P_{VT}$ and $P_{DT}$ are assumed to be 78.6 and 12 percent, respectively, in this study. These can be statistically expressed as follows:

$$\begin{aligned} VC &\sim \mathrm{B}(1, 0.786) \\ VD &\sim \mathrm{B}(1, 0.12) \end{aligned} \tag{10.14}$$

### 10.5.2. Tension capacity of strands

Sections 7 and 9 developed probabilistic models for the $C_T$ of strands under various exposure conditions. Four of these models are used to assess the structural reliability based on a model selection strategy provided in Figure 10-9. These models are summarized here. Table 10-1 and Table 10-2 show definitions of the terms and the median estimates of the unknown model parameters, $\Theta$, as defined in Subsection 7.2.2 and 7.2.3. The standard deviations and correlation coefficients of these parameters are shown in Sections 7 and 9.

$$\begin{aligned} \textbf{Model 1}: C_T &\sim \mathrm{LN}(59.27,\ 0.29) \text{ kips} \\ &\sim \mathrm{LN}(263.7, 1.3) \text{ kN} \end{aligned} \tag{10.15}$$

$$\textbf{Model 2}: C_T = C_{T,n}\left[ A\left(\gamma_{t_{CA}}\right)^{n_{CA}} + \sigma\varepsilon \right] \qquad (10.16)$$

$$\text{where, } A = \theta_1 \left\{ \theta_2 - \theta_3 \exp\left(\gamma_{RH}\right) - \theta_4 \exp\left[ \gamma_{\%gCl^-} \exp\left(\gamma_{RH}\right)\gamma_T \right] \right\}^{\theta_1}$$

$$\textbf{Model 3}: C_T = C_{T,n}\left[ \theta_1 \left[ \theta_2 - \theta_3 \gamma_{\%sCl^-} \gamma_{t_{WD}} \right]^{\theta_4} + \sigma\varepsilon \right] \qquad (10.17)$$

$$\textbf{Model 4}: C_T = C_{T,n}\left[ \theta_1 \left[ \theta_2 - \theta_3 \gamma_{t_{WD}} - \theta_4 \ln[\gamma_{\%sCl^-}]\gamma_{t_{WD}} \right]^{\theta_5} + \sigma\varepsilon \right] \qquad (10.18)$$

**Table 10-1. Definitions of the Terms in the Strand Capacity Models.**

| Terms | Definitions |
|---|---|
| $C_{T,n}$ | Nominal tension capacity of "as-received" strand |
| $\theta_i$ | Unknown model parameter |
| $\sigma$ | Standard deviation of model error |
| $\varepsilon$ | Standard normal variable ~N(0,1) |
| $\gamma_{t_{CA}}$ | $\dfrac{\text{Total atmospheric exposure time (years)}}{\text{standardizing factor}} = \dfrac{t_{CA}}{0.75}$ |
| $n_{CA}$ | Constant term based on field information |
| $\gamma_T$ | Ambient exposure temperature $(^{\circ}\text{F}) = T(^{\circ}\text{F})$ |
| $\gamma_{RH}$ | $\dfrac{\text{Ambient relative humidity (\%)}}{\text{Maximum Relative humidity (\%)}} = \dfrac{RH\ (\%)}{100}$ |
| $\gamma_{\%gCl^-}$ | $\dfrac{\%Cl^-\text{ in the grout (by weight)}}{\%sCl^-_{\text{saturated chloride solution}}} = \dfrac{\%gCl^-}{35.7}$ |
| $\gamma_{\%sCl^-}$ | $\dfrac{\%Cl^-\text{in the water inside the tendon}}{\%sCl^-_{\text{saturated chloride solution}}} = \dfrac{\%sCl^-}{35.7}$ |
| $\phi_{wet}$ | $\left(\dfrac{\text{Wet-time in a year (months)}}{\text{12 (months)}}\right);\ 0 \le \phi_{wet} \le 1$ |
| $\gamma_{t_{WD}}$ | $\phi_{wet} \times$ Total exposure time (years) $= \phi_{wet} \times t_{WD}$ |

**Table 10-2. Mean estimates of Model Parameters in the Strand Capacity Models.**

| | Model 2 | Model 3 | Model 4 |
|---|---|---|---|
| $\theta_1$ | 7.7492 | 0.9983 | 0.9463 |
| $\theta_2$ | 0.1637 | 1.0105 | 1.0333 |
| $\theta_3$ | 0.0030 | 1.6785 | 0.3567 |
| $\theta_4$ | 0.0002 | 1.3576 | 0.0285 |
| $\theta_5$ | 1.0924 | - | 2.0301 |
| σ | - | 0.0117 | 0.0350 |

For each Monte Carlo simulation, an appropriate probabilistic model for $C_T$ of each strand is selected based on the tendon type, environmental condition (*EC*), and randomly selected *VC* and *DC*. Figure 10-9 shows the strategy used to select the strand capacity models, where the circles indicate the model numbers for each exposure category (i.e., combinations of tendon type, *EC*, *VC*, and *DC*). The *EC* is manually selected per Figure 10-11 and *VC* and *DC* are randomly selected per Equation (10.14). The two *VC*s considered are "No void" and "Void" conditions. The two *DC*s considered are "No damage" and "Damage" conditions. Because the "Wet-Dry" condition occurs only if there are damages on the tendon system, the "No damage" condition corresponding to the "Wet-Dry" conditions is not shown in Figure 10-9.

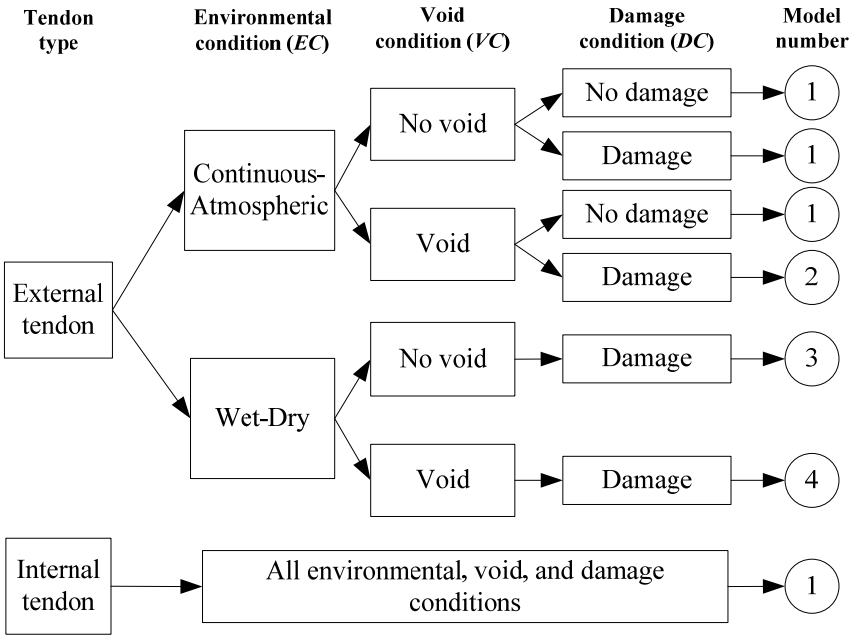


**Figure 10-9. Strategy to Select the Strand Capacity Models Based on Exposure Conditions.**

### 10.5.3. Prestress loss of strands

The literature review provided in Subsection 2.7.1.2 did not identify sufficient existing information to develop a probabilistic expression for $P_{loss}$ for PT bridge tendons. AASHTO LRFD Specifications (2007) provides a lump sum estimate of 19 ksi (131 MPa) for prestress losses in box girders. There exist some cautions (see Subsection 2.7.1.2) in using this lump sum loss estimate for deterministic structural assessment of segmental bridges. $P_{loss}$ corresponding to 19 ksi (131 MPa) is 4123 lbs (18 kN) for a 0.6-inch (15 mm) diameter strand. In this study, $P_{loss}$ is assumed to follow a lognormal distribution with a mean value equal to this lump sum estimate. Because the COV of $P_{loss}$ could not be estimated from field data, in this study it is assumed to be 0.15. $P_{loss}$ can be statistically expressed as follows:

$$P_{loss} \sim \text{LN}(4123, 618) \text{ lbs} \\ \sim \text{LN}(18, 2.8) \text{ kN} \quad (10.19)$$

### 10.5.4. Compressive strength of concrete

According to TxDOT (2004), Class H concrete with $f'_c$ equal to 6 ksi (41.3 MPa) was used in the construction of precast segments in Texas bridges constructed in the 1980s, and 1990s. Because of liability reasons, in general, contractors provide concrete with an actual compressive strength, $f_c$, higher than the specified compressive strength, $f'_c$. Hence, a mean compressive strength, $\overline{f_c}$, of 6 ksi (41.3 MPa) is reasonable for this study. Based on the information in Table 2-5, assuming a COV of 0.15 for concrete with $f'_c$ equal to 6 ksi is reasonable. This will result in a calculated standard deviation of 0.7 ksi. Because $f_c$ is always a positive number, it is expressed as a lognormal distribution as follows:

$$f_c \sim \text{LN}(6.0, 0.9) \text{ ksi} \\ \sim \text{LN}(41.3, 6.2) \text{ MPa} \quad (10.20)$$

### 10.5.5. Dead and live load parameters

The values of $DL_1$ and $DL_2$, are always positive, and therefore are assumed to follow lognormal distributions. The mean value of these parameters can be obtained using the cross-sectional geometry (see Subsection 10.6.1) and unit weight of the materials (see Table 2-7) of the selected PT girder. The standard deviation can be obtained by assuming a COV equal to 0.10 (see Subsections 2.8.1 and 2.8.2).

The live load parameters, $LL_{lane}$, $LL_{truck}$, and $LL_{tandem}$, are assumed to follow normal distributions (Nowak and Collins 2000). The mean values are obtained using the standard procedures provided in AASHTO (1996) for HS20 loading and AASHTO

LRFD Specifications (2007) for HL93 loading conditions. Based on the discussions in Subsection 2.8.2, a COV of 0.18 is assumed after the impact load is appropriately added to the live load combinations.

## 10.6. TIME-VARIANT STRUCTURAL RELIABILITY ASSESSMENT OF TYPICAL POST-TENSIONED BRIDGE

### 10.6.1. Geometrical and structural characteristics of typical post-tensioned bridge

Based on the prevalence of Type III girders for segmental bridges in Texas, a typical Type III girder has been selected for the structural reliability assessment. Figure 10-10 shows the cross section of a typical Type-III girder. Table 2-11 provides the depths of the tendons in this cross section at midspan. The shaded region in Figure 10-10 indicates the effective cross section used to estimate $g_{strength}$ and $g_{service}$. The effective flange widths, $b_e$, on each side of the web is calculated using the formulations and empirical curves provided in Article 4.6.2.6.2 of AASHTO LRFD Specifications (2007) and are summarized in Table 10-3.

The girder in this study is assumed to be simply supported. The $D_M$ calculations are performed based on this assumption. It is important to note that the selected cross section is similar to the Type-III girders used in the San Antonio "Y" bridge. However, because of the sequence of the post-tensioning and the falsework removal process, the behavior of San Antonio "Y" bridge is somewhere in between that of a simply supported and a continuous beam. Hence, the obtained reliability results do not represent those of the San Antonio "Y" bridge. Further modifications to the developed models and MATLAB programs are needed to conduct an analysis of a specific bridge.

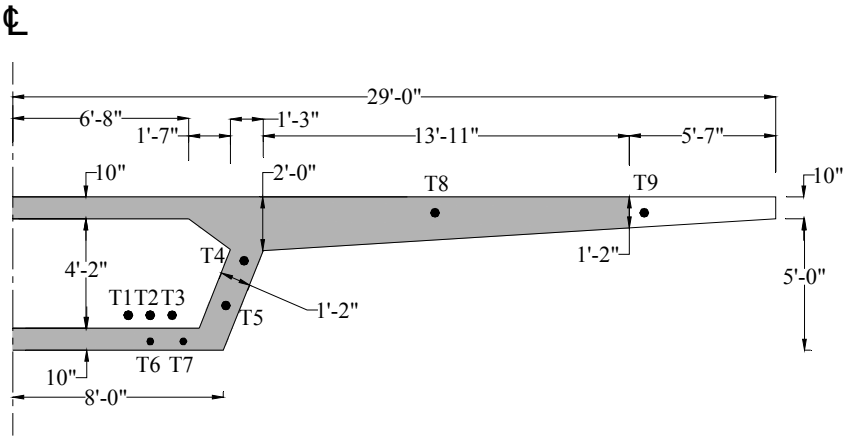


Notes:
1) The cross-section is symmetrical about the center-line.
2) Nominal diameter of all the strands is 0.6 inch (15 mm).
3) One half of the cross-section contains 9 tendons.
4) Tendons T1, T2, T3, T4, T5, T8, and T9 contain 19 strands each.
5) Tendons T6 and T7 contains 12 strands each.
6) Tendons T8 and T9 are not used in flexural capacity calculations.
7) Shaded region indicates effective cross-section, per AASHTO LRFD (2007).

**Figure 10-10. Cross Section at Midspan of the Typical PT Girder Used in This Study.**

**Table 10-3. Effective Flange Widths for Each Side of the Web.**

| | $b$ inch (m) | $l_i$ feet (m) | $b/l_i$ | $b_e/b$ | $b_e$ inch (m) |
|---|---|---|---|---|---|
| **b1** | 234 (5.94) | 10 (30.48) | 0.195 | 0.74 | 173 (4.40) |
| **b3 + b4** | 99 (2.51) | 10 (30.48) | 0.083 | 0.95 | 94 (2.39) |
| **b5** | 82 (2.08) | 10 (30.48) | 0.068 | 0.97 | 80 (2.02) |

b1, b3, and b4 are defined in Figure 2-23 and Table 2-12. $b$, $b_e$, and $l_i$ are physical width, effective width, and notional span, specified in Article 4.6.2.6.2 of AASHTO LRFD Specifications (2007).

In the service reliability model, the compressive stress limit reduction factor, $\phi_w$, is determined following the Article 5.7.4.7.1 in AASHTO LRFD Specifications (2007). For a simply supported box girder, the webs, interior top slab, and the exterior top

flanges experience maximum compressive stresses under service loads. The slenderness ratios (based on the clear dimensions and thicknesses) for the webs, interior top slab, and the exterior top flanges for the box girder in considered are 2.3, 11.6, and 13.8, respectively. As these ratios are less than 15, the value of $\phi_w$ is assumed to be 1.

### 10.6.2. Definitions of parameters for the reliability assessment

In this study, $\beta_{strength}$ and $\beta_{service}$ of the typical PT bridge experiencing HS20 and HL93 loading conditions will be assessed. $\beta_{strength}$ and $\beta_{service}$ of the typical PT bridge with six external tendons for various combinations of loading and exposure conditions is assessed using the developed strength and service reliability models. These parameter combinations are shown in Figure 10-11. The exposure times in Figure 10-11 are selected based on the expected time for complete corrosion of strands under certain exposure conditions. For example, when exposed to 0.006, 0.018, and 1.8 %$sCl^-$ conditions (with ratio of wet-time to dry-time in a year, $\phi_{wet}$, equal to 0.17), the times required for the strands to completely corrode are 57, 45, and 23 years, respectively. The time intervals for each %$sCl^-$ condition were selected such that maximum information is obtained to effectively capture the change in $\beta$. Table 10-4 shows that the average annual relative humidity and temperature of most cities in the United States are approximately 70 percent and 70°F, respectively. Based on this, the values of $T$, and $RH$ are assumed to be 70°F (21.1°C) and 70 percent, respectively, for the reliability analysis. Also, the values of $\phi_{wet}$, $n_{CA}$, are assumed to be 0.17 and –0.005, respectively. The effects of WD conditions with 0.006, 0.018, and 1.8 %$sCl^-$ levels in 0, 1, 2, 3, 4, 5, and 6 external tendons on $\beta_{strength}$ and $\beta_{service}$ are assessed. The tendons without WD conditions will be assumed to have a CA condition with 0.014, 0.092, or 0.782 %$gCl^-$ level. The exposure periods at which $\beta_{strength}$ and $\beta_{service}$ will be determined are provided in the fifth column in Figure 10-11.

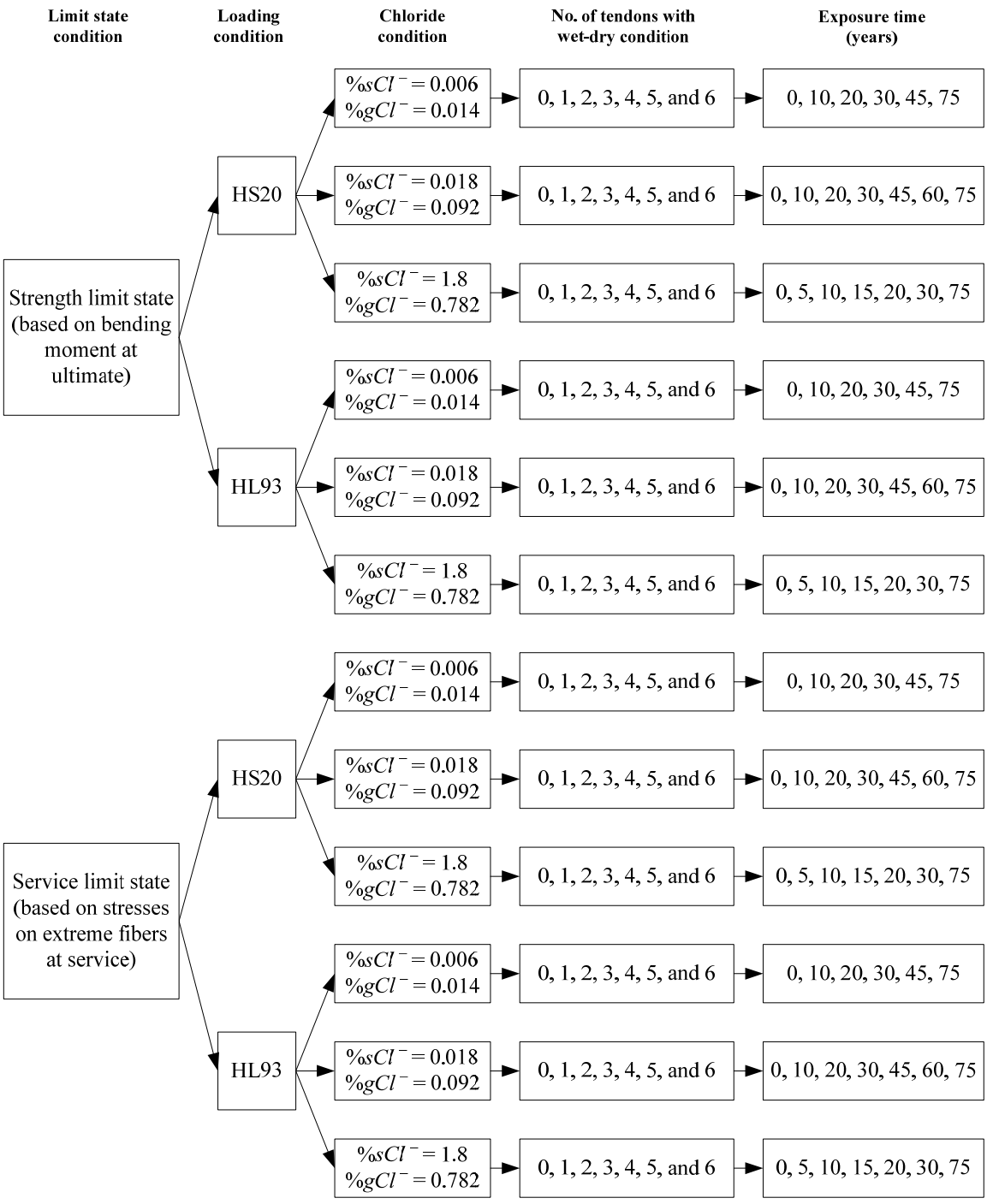


Other parameters:
Ambient $RH = 70\%$; $RH$ inside undamaged tendons = 50%;
$T = 70^{o}$F (24.4 $^{o}$C); $\phi_{wet} = 2/12 = 0.17$; $n_{CA} = -0.005$

**Figure 10-11. Parameter Combinations for the Reliability Assessment Program.**

**Table 10-4. Average Annual Temperature and Relative Humidity Conditions in Some Major Cities in the US (Source: www.cityrating.com).**

| Name of the US city | Average annual ambient temperature, $T$ ($^{o}$F) | Average annual ambient relative humidity, $RH$ (%) |
|---|---|---|
| Atlanta | 61 | 69 |
| Austin | 69 | 71 |
| Chicago | 49 | 71 |
| Dallas-Fort Worth | 65 | 70 |
| Houston | 68 | 77 |
| Los Angeles | 63 | 72 |
| Miami | 76 | 72 |
| New York | 55 | 64 |
| Orlando | 72 | 73 |
| San Antonio | 69 | 70 |
| Seattle | 53 | 73 |
| Tampa | 72 | 74 |
| Washington D.C. | 54 | 69 |

Table 10-5 summarizes all the random parameters used in this study. Note that the dead and live load parameters (i.e., *DL* and *LL*) in Table 10-5 are calculated based on the geometry of the typical PT bridge being studied.

**Table 10-5. Random Parameters for Reliability Assessment.**

| Parameter | Distribution type | Statistics |
|---|---|---|
| Void condition, *VC* | Binomial | ~ B (1, 0.79) |
| Damage condition, *DC* | Binomial | ~ B (1, 0.12) |
| Error term in the strand capacity model, ε | Normal | ~ N (0, 1) |
| Prestress loss, $P_{loss}$ | Lognormal | ~ LN (4123, 618) kips |
| Compressive strength of concrete, $f_c$ | Lognormal | ~ LN (6, 0.9) ksi |
| Dead load due to concrete overlay, $DL_1$ | Lognormal | ~ LN (2.7, 0.27) kip/ft |
| Dead load due to box girder, $DL_2$ | Lognormal | ~ LN (14.3, 1.43) kip/ft |
| Live load due to multiple lane load, $LL_{lane}$ | Normal | ~ N (0.5, 0.1) kip/ft |
| Live load due to design truck load, $LL_{truck}$ | Normal | ~ N (25.6, 4.6) kips |
| Live load due to design tandem load, $LL_{tandem}$ | Normal | ~ N (20.0, 3.6) kips |

Note: 1 kip = 4.45 kN; 1 ksi = 6.89 kN/mm$^2$; 1 kip/ft = 14.6 kN/m.

### 10.6.3. Time-variant strength reliability index

The time-variant $\beta_{strength}$ and $P_{f,\ strength}$ of the selected PT bridge was assessed using the strength reliability model developed in Subsection 10.3. The $COV(P_f)_{target}$ was set to be 0.05 for strength reliability assessment. The parameter combinations for this parametric study were presented in Figure 10-11. Note that, in this analysis, all the internal tendons were assumed to be intact and protected from corrosion, which might not be the actual case in the field. Also note that the $\phi_{wet}$ was equal to 0.17, which corresponds to 2 months of wet time in every year, in this analysis.

The ISO 13822 (2001) standard suggests $\beta_{target}$ values of 2.3, 3.1, 3.8, and 4.3 (corresponding to $P_{f,\ strength}$ of $1.0\times10^{-2}$, $9.7\times10^{-4}$, $7.2\times10^{-5}$, and $8.5\times10^{-6}$) for structures with very low, low, medium, and high consequences of failure, respectively (see Table 2-9). The consequence of failure of massive amounts of structures in a city due to an earthquake could be considered medium or high (depending on the magnitude of damage). The consequence of failure of a nuclear power plant could also be considered medium or high (depending on the toxicity of radiation and the proximity to a human populated area). In comparison to these cases, the consequence of failure of a typical

segmental bridge may be considered as low or medium, especially for segmental, PT bridges on major urban highways. The following discussions include comparisons of the estimated reliability with $\beta_{target}$ used in AASHTO LRFD Specifications (2007) code calibration (i.e., 3.5) and recommended by ISO 13822 (2001) for strength failure with low consequences of failure (i.e., 3.1). See Table C-1 in Appendix D for complete results.

### *10.6.3.1. Strength reliability when strands are in "as-received" condition*

For the selected PT bridge, it seems that the $\beta_{strength}$ remained above 3.5 (corresponding to a probability of strength failure, $P_{f,\ strength}$, equal to $2.3\times10^{-4}$) when all the strands are in "as-received" condition. However, the actual value of $\beta_{strength}$ for this case could not be determined because the number of failure cases after 50 million Monte Carlo simulations was 0 and the simulation process was ended due to limited computing resources and time required to attain a $COV(P_f)_{target}$ of 0.05. In addition, no failure was observed among 50 million simulations when only one tendon (i.e., 19 strands), which constitutes about 8 percent of total tendons, was completely corroded or failed and the HL93 loading was applied. The similar was the case when HS20 loading was applied.

### *10.6.3.2. Strength reliability when exposed to 0.006 %s$Cl^-$ condition*

Figure 10-12 shows the variation of $\beta_{strength}$ with time when exposed to 0.006 %s$Cl^-$ solution. In Figure 10-12, the horizontal lines with long dashes indicate the basis for the calibration of AASHTO LRFD Specifications (2007) document for ultimate conditions. The horizontal lines with short dashes in these figures indicate the $\beta_{target}$ (i.e., 3.1) for a failure case with low consequences of failure (per ISO13822 [2001]). Note that a $\beta_{strength}$ of 3.1 corresponds to a $P_{f,\ strength}$ of $9.7\times10^{-4}$. The dashed and solid curves indicate the cases with HS20 and HL93 loading conditions, respectively. The hollow and solid data markers also indicate the cases with HS20 and HL93 loading conditions, respectively.

Different data markers are used to represent the number of tendons subjected to WD exposure cycles, defined as "WDT". The figures in the Subsections 10.6.4.3 and 10.6.4.4 are also formatted in this manner.

Most of the $\beta_{strength}$ values that are above 3.5 could not be obtained due to the limited computing resources and time; the corresponding curves or data markers are not shown in Figure 10-12. When only two tendons are subjected to HS20 loading and exposed to 0.006 %s$Cl^-$ solution (hollow square markers), the value of $\beta_{strength}$ at 75 years is above 3.5. For this case, when subjected to HL93 loading instead of HS20 loading (solid square markers), the $\beta_{strength}$ drops below 3.5 in about 30 years and stays above 3.1 up to 75 years. When more than two tendons are exposed to WD cycles (all triangular markers), the maximum time needed for $\beta_{strength}$ to drop below 3.5 is 25 years and to drop below 3.1 is 35 years. In the most severe case with HL93 loading and 6 WDTs, it takes only about 12 years for $\beta_{strength}$ to drop below 3.1.

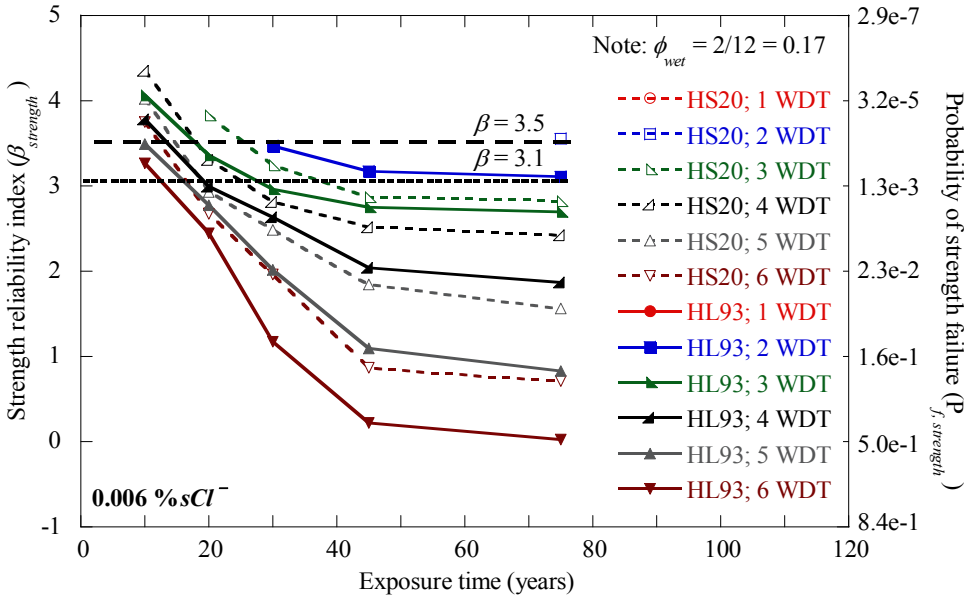


**Figure 10-12. Strength Reliability of the Typical PT Bridge with Tendons Exposed to Wet-dry Cycles (0.006 %s$Cl^-$).**

### *10.6.3.3. Strength reliability when exposed to 0.018 %s$C^-$ condition*

Figure 10-13 shows the variation of $\beta_{strength}$ with time when exposed to 0.018 %s$Cl^-$ solution. The format of Figure 10-13 is same as that of Figure 10-12. If only two tendons are subjected to HS20 loading and exposed to 0.018 %s$Cl^-$ solution (hollow square markers), then the value of $\beta_{strength}$ stays above 3.5. For this case, when subjected to HL93 loading instead of HS20 loading (solid square markers), the $\beta_{strength}$ drops below 3.5 in about 22 years and stays above 3.1 up to 75 years. When three or more tendons are exposed to WD cycles (all triangular markers), the maximum time needed for $\beta_{strength}$ to drop below 3.1 is approximately 28 years, as opposed to 35 years in the case with exposure to 0.006 %s$Cl^-$ solution. In the most severe case with HL93 loading and 6 WDTs, it is estimated to take only about 8 years for $\beta_{strength}$ to drop below 3.1, as opposed to 12 years in the case with exposure to 0.006 %s$Cl^-$ solution.

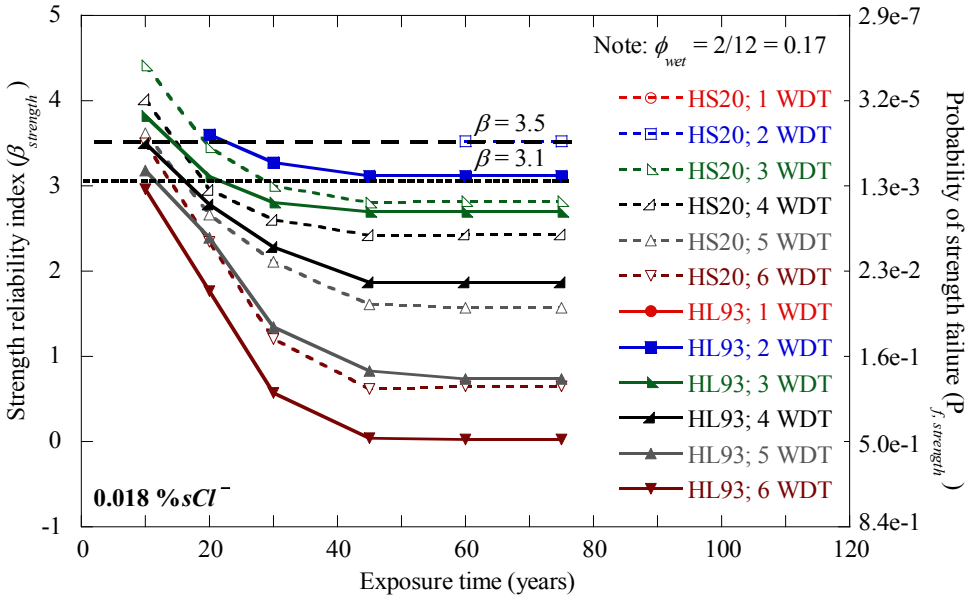


**Figure 10-13. Strength Reliability of the Typical PT Bridge with Tendons Exposed to Wet-dry Cycles (0.018 %s$Cl^-$).**

### *10.6.3.4. Strength reliability when exposed to 1.8 %s$Cl^-$ condition*

Figure 10-14 shows the variation of $\beta_{strength}$ with time when exposed to 1.8 %s$Cl^-$ solution. The format of Figure 10-14 is same as that of Figure 10-12. When the bridge is subjected to HS20 or HL93 loading and there is only one WDT (round markers), $\beta_{strength}$ stays above 3.5. However, because exact $\beta_{strength}$ values for these cases could not be obtained, they are not shown in Figure 10-14. When the bridge is subjected to HS20 or HL93 loading and there are two WDTs (square markers), $\beta_{strength}$ drops below 3.5 and stays above 3.1. When three or more tendons are exposed to WD cycles (all triangular markers), the maximum time needed for $\beta_{strength}$ to drop below 3.1 is approximately 13 years, as opposed to 35 and 28 years in the cases with exposure to 0.006 and 0.018 %s$Cl^-$ solutions, respectively.

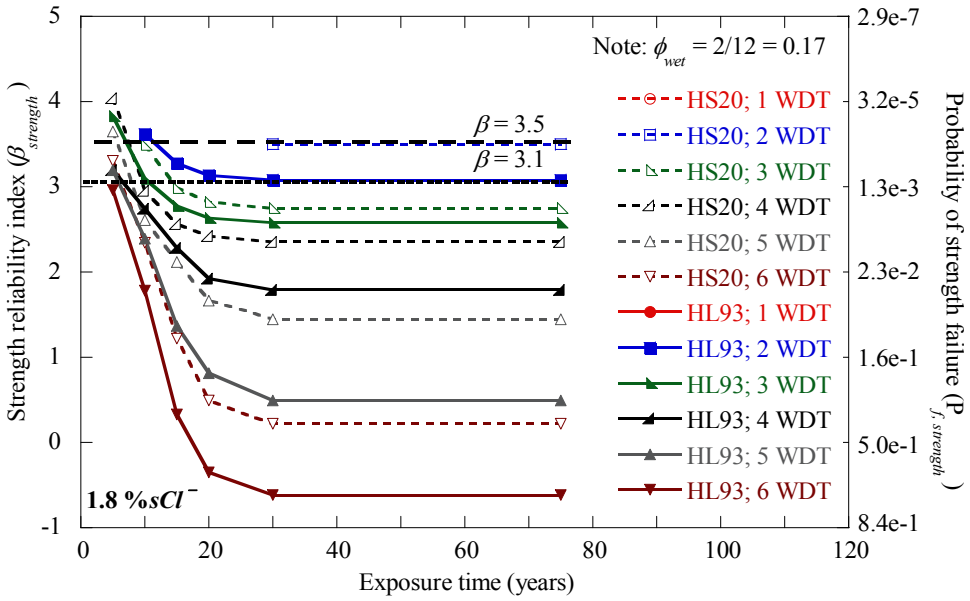


**Figure 10-14. Strength Reliability of the Typical PT Bridge with Tendons Exposed to Wet-dry Cycles (1.8 %s$Cl^-$).**

In the most severe case with HL93 loading and 6 WDTs, it is estimated to take less than 5 years for $\beta_{strength}$ to drop below 3.1, as opposed to 12 and 8 years, respectively, in the cases with exposure to 0.006 and 0.018 %s$Cl^-$ solutions.

### 10.6.4. Time-variant service reliability index

The time-variant $\beta_{service}$ and $P_{f,\ service}$ of the selected PT bridge was assessed using the service reliability model developed in Subsection 10.4. Because the typical values of $P_{f,\ service}$ are much larger than the typical values of $P_{f,\ strength}$, the $COV(P_f)_{target}$ was set to be 0.01 for service reliability assessment as opposed to 0.05 in the case of strength reliability assessment. The parameter combinations for this study were the same as those used for the strength reliability assessment (see Figure 10-11). The $\phi_{wet}$ used in this analysis is equal to 0.17, which corresponds to 2 months of wet time in every year.

The ISO 13822 (2001) standard suggests $\beta_{target}$ values of 0 and 1.5 (corresponding to probabilities of service failure, $P_{f,\ service}$, equal to 0.50 and 0.07) for reversible and irreversible consequences of failure, respectively (see Table 2-9). There are concrete materials that are capable of self-healing microcracks. When the tensile stresses exceed the limit state, cracks may form and may not self-heal, depending on the type of concrete material used. Such cases could be defined to have an irreversible consequence of failure. In addition, exceeding the compressive stress limits (i.e., stress beyond the elastic range) results in inelastic stresses and could be considered to have an irreversible consequence of failure. However, although not typical, there may also be cases with reversible consequences of failure (such as in the case of concrete with good self-healing of tensile cracks and elastic behavior in compression). The following discussions include comparisons of the estimated $\beta_{service}$ with $\beta_{target}$ recommended by ISO 13822 (2001) for service failures with reversible and irreversible consequences of failure (i.e., 0 and 1.5). See Table C-2 in Appendix D for complete results.

#### *10.6.4.1. Service reliability when strands are in "as-received" condition*

The recommended target values for $\beta_{service}$ when the consequences of failure are irreversible and reversible are 1.5 and 0, respectively. For the selected PT bridge, $\beta_{service}$ is below 1.5 and above 0 when the strands are in "as-received" condition. In particular, the values of $\beta_{service}$ are 1.22 and 0.63, when the bridge is subjected to HS20 and HL93 loadings, respectively. Note that these vaues are specific to the typical PT bridge defined in Subsection 10.6.1. The corresponding values of $\beta_{service}$ for an actual PT bridge could be different from these values and the values presented in the following discussions.

#### *10.6.4.2. Service reliability when exposed to 0.006 %s$Cl^-$ condition*

Figure 10-15 shows the variation of $\beta_{service}$ with time when exposed to 0.006 %s$Cl^-$ solution. The horizontal lines with short and long dashes in Figure 10-15 indicate the $\beta_{\text{target}}$ values for reversible and irreversible consequences of service failure (per ISO13822 [2001]). The dashed and solid curves indicate the cases with HS20 and HL93 loading conditions, respectively. The hollow and solid data markers also indicate the cases with HS20 and HL93 loading conditions, respectively. Different data markers are used to represent the number of tendons subjected to WD exposure cycles, defined as "WDT." The figures in the Subsections 10.6.4.3 and 10.6.4.4 are also formatted in this manner.

When there is only one WDT and the bridge is subjected to HS20 loading (hollow round markers), the value of $\beta_{service}$ is below 1.5 and above 0 for more than 75 years. For this case, when the bridge is subjected to HL93 loading (solid round markers), the value of $\beta_{service}$ stays above 0 for up to ~25 years. When there are two WDTs (square markers), these two time estimates (i.e., > 75 and ~25 years) reduce to about 25 and 10 years, respectively. If the bridge is subjected to HS20 loading and there are three or more WDTs (all hollow triangular markers), then the time needed for $\beta_{service}$ to drop below 0 is between 7 and 15 years. If the bridge is subjected to HL93 loading and there are three or more WDTs (all solid triangular markers), then the time needed for $\beta_{service}$ to drop below 0 is between 3 and 5 years. The quick drop in the curves corresponding to 4, 5 and 6 WDTs and HS20 or HL93 loading is because $\beta_{service}$ quickly reached –8.21 (i.e., $P_{f,\,service}$ reached 1). Similar occurrences in the figures in the following subsections are not discussed herein.

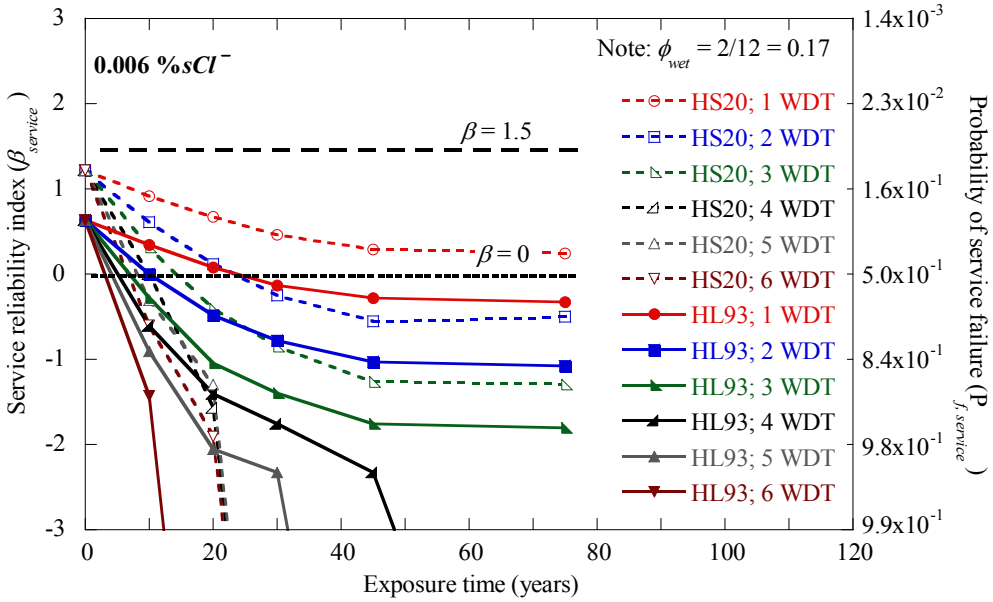


**Figure 10-15. Service Reliability of the Typical PT Bridge with Tendons Exposed to Wet-dry Cycles (0.006 %$sCl^-$).**

### *10.6.4.3. Service reliability when exposed to 0.018 %s$Cl^-$ condition*

Figure 10-16 shows the variation of $\beta_{service}$ with time when exposed to 0.018 %s$Cl^-$ solution. The format of Figure 10-16 is same as that of Figure 10-15. When there is only one WDT and the defined PT bridge is subjected to HS20 loading (hollow round markers), the value of $\beta_{service}$ stays above 0 for more than 75 years, as in the case of exposure to 0.006 %s$Cl^-$ solution. For this case, when the bridge is subjected to HL93 loading (solid round markers), the value of $\beta_{service}$ stays above 0 for up to about 20 years, as opposed to about 25 years in the case of exposure to 0.006 %s$Cl^-$ solution. When there are only two WDTs (square markers), these two time estimates (i.e., > 75 and 20 years) significantly reduce to about 18 and 9 years, respectively. If the bridge is subjected to HS20 loading and there are three or more WDTs (all hollow triangular markers), then the time needed for $\beta_{service}$ to drop below 0 is between about 6 and 13 years. For similar cases with HL93 loading (all solid triangular markers), the time needed for $\beta_{service}$ to drop below 0 is between about 3 and 7 years.

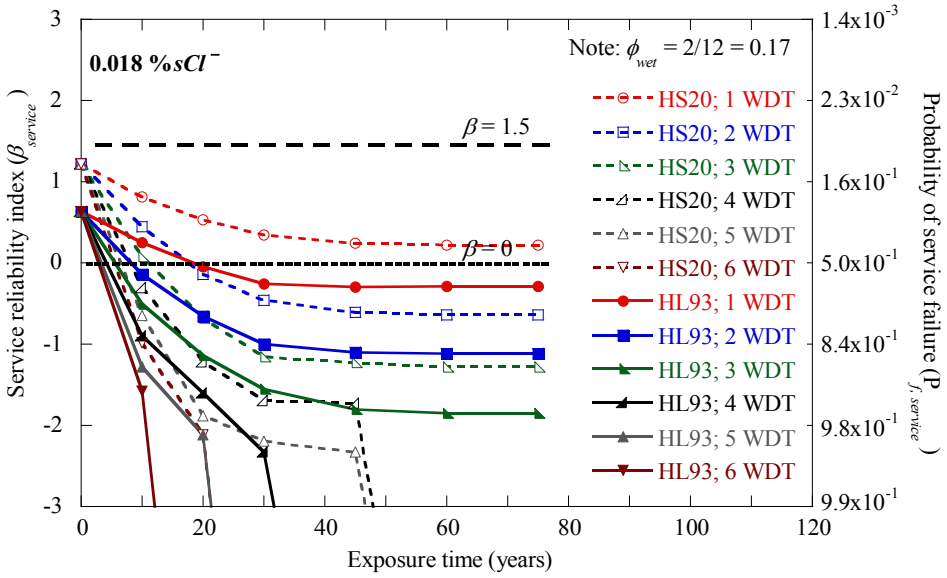


**Figure 10-16. Service Reliability of the typical PT Bridge with Tendons Exposed to Wet-dry Cycles (0.018 %s$Cl^-$).**

*10.6.4.4. Strength reliability when exposed to 1.8 %s$Cl^-$ condition*

Figure 10-17 (with the same format as that of Figure 10-15) shows the variation of $\beta_{service}$ with time when exposed to 1.8 %s$Cl^-$ solution. When there is only one WDT and the bridge is subjected to HS20 loading (hollow round markers), the value of $\beta_{service}$ stays below 1.5 and above 0 for more than 75 years, as in the cases of exposures to 0.006 and 0.018 %s$Cl^-$ solutions. For this case, when HL93 loading exists (solid round markers), the value of $\beta_{service}$ stays above 0 for up to about 9 years, as opposed to about 25 and 20 years in the cases of exposures to 0.006 and 0.018 %s$Cl^-$ solutions. When there are two WDTs (square markers), these two time estimates (i.e., > 75 and ~9 years) significantly reduce to about 9 and 4 years, respectively. If the bridge is subjected to HS20 loading and there are three or more WDTs (all hollow triangular markers), then the time needed for $\beta_{service}$ to drop below 0 is between about 5 and 2 years.

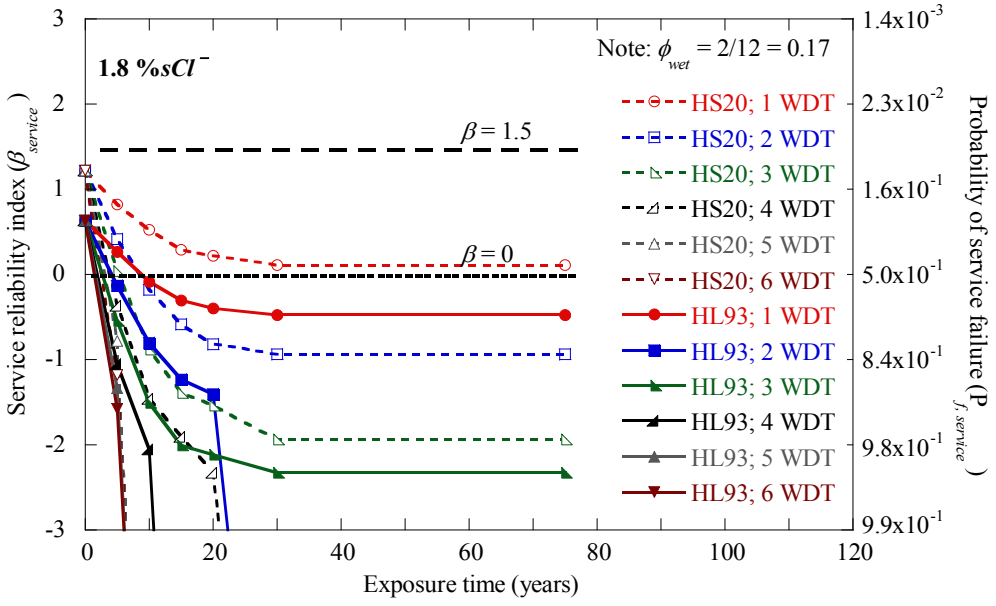


**Figure 10-17. Service Reliability of the Typical PT Bridge with Tendons Exposed to Wet-dry Cycles (1.8 %s$Cl^-$).**

If the bridge is subjected to HL93 loading and there are three or more WDTs (all solid triangular markers), then the time needed for $\beta_{service}$ to drop below 0 is between about 1 and 3 years.

## 10.7. SUMMARY

This section assessed the strength and service reliability of a typical PT bridge. At first, the strength and service reliability models along with the required capacity and demand models were presented. The $\beta_{strength}$ and $\beta_{service}$ of a typical simply supported PT bridge were then assessed using these models. The uncertainty was captured using the probabilistic models for $C_T$ of strands (developed in Sections 7 and 9), and other random parameters defining the material characteristics of concrete, prestress losses, voids and damage conditions in PT systems, and structural loading conditions. The values of $\beta_{strength}$ and $\beta_{service}$ were determined for up to 75 years for a range of specified environmental conditions, and randomly selected void and damage conditions.

In general, it was found that the strength and service reliabilities of PT bridges can reduce significantly when the tendons are exposed to severe moisture conditions. The presence of chlorides in these tendons can increase the rate of reduction of the reliability index. Service reliability is more adversely and quickly affected than strength reliability. For the typical PT bridge considered, $\beta_{\text{strength}}$ does not fall below the desired target value of 3.5 (corresponding to a $P_{f,\text{ strength}}$ equal to $2.3\times10^{-4}$) until 2 of 14 tendons are completely corroded or broken. For the typical PT bridge considered, $\beta_{\text{service}}$ is in between the ISO 13822 recommended $\beta_{\text{target}}$ values of 0 and 1.5 (for reversible and irreversible service failures, respectively) when the tendons are in "as-received" condition. These $\beta_{\text{target}}$ values of 0 and 1.5 correspond to $P_{f,\text{ service}}$ equal to 0.50 and 0.07, respectively. The value of $\beta_{\text{service}}$ can fall below 0 in about 10 years, if one tendon experiences severe wet-dry conditions. In addition, $\beta_{\text{service}}$ can fall below 0 in about a year, if three or more tendons experience severe wet-dry conditions.

# 11. CONCLUSIONS AND RECOMMENDATIONS

## 11.1. INTRODUCTION

This section provides conclusions drawn from a research project on the effects of void, environmental, and other exposure conditions on the long-term performance of post-tensioned (PT) bridges. Initially, environmental characterization maps of Texas were developed. The electrochemical and tension capacity ($C_T$) behavior of PT systems were then experimentally investigated. Based on these experimental results and engineering judgment and assumptions, probabilistic models to determine $C_T$ of strands were then developed. Following this, time-variant structural reliability models were developed. Using these reliability models, the strength and service reliabilities of a typical PT bridge for a period of 75 years were assessed.

## 11.2. LIMITATIONS AND ASSUMPTIONS

Limitations and assumptions associated with the results obtained from this research include:

- Sufficient field data on wet-dry (WD) conditions inside the tendons were not obtained to more accurately calibrate the probabilistic models for $C_T$ of strands exposed to WD exposure conditions.
- Sufficient field data on the amount of strand corrosion under continuous-atmospheric (CA) conditions could not be obtained to more accurately calibrate the probabilistic models for $C_T$ of strands exposed to CA exposure conditions.
- Engineering judgment and assumptions were made to calibrate the probabilistic models to potential field conditions.
- Probabilistic models for the $C_T$ of strands were used in the structural reliability analysis. Hence, the limitations of the probabilistic models for the $C_T$ of strands are also applicable to the structural reliability assessment.

- All internal tendons were assumed to be intact and free from corrosion.
- Structural reliability models developed in this research consider only a simply supported condition.
- Structural reliability models developed here consider only uniaxial bending mechanisms. These models do not consider biaxial bending, shear, torsion, or other structural mechanisms, which can influence the system reliability of PT bridges.

Although limitations exist, some valuable conclusions are drawn from this research and are presented next.

## 11.3. CONCLUSIONS

### 11.3.1. Corrosion risks at different geographic locations in Texas

Section 4 presented maps showing freeze-days, temperature, relative humidity, and rain-days in Texas. These maps were developed using Geographic Information Systems (GIS) technology and the data collected from the internet and Texas Department of Transportation district engineers. The conclusions drawn from these maps are:

- The majority of Texas has a moderate level of corrosion risk and some areas have a high level of corrosion risk.
- Coastal regions have the most critical conditions due to consistent exposure to chloride-contaminated environments.
- These general maps should be used only for initial screening purposes. Corrosion risk of a specific PT bridge should be assessed based on additional relevant information (such as the presence of voids, damage, moisture, chlorides, etc. inside the tendons).

### 11.3.2. Cyclic polarization curves of prestressing steel

Subsections 5.3 and 6.2 presented the cyclic polarization testing of the steel meeting ASTM A416 specifications and the corresponding results, respectively. The conclusions include the following:

- The broken passive films on the steel surface are self-healed and a negative hysteresis is observed when exposed to 0.00 and 0.06 %$sCl^-$ simulated concrete pore solution. The broken passive films are not repaired and a positive hysteresis is observed when exposed to 1.8 %$sCl^-$ solution. Based on these observations, it can be concluded that the critical chloride threshold level for the steel meeting the ASTM A416 specifications is in between 0.06 and 1.8 %$sCl^-$.

### 11.3.3. Galvanic corrosion testing of post-tensioned systems

The galvanic corrosion test program and results are provided in Subsections 5.4 and 6.3, respectively. The conclusions include the following:

- The corrosion potentials of conventional reinforcement and prestressing strands are similar. It was determined from this testing that there was limited galvanic corrosion between conventional reinforcement and prestressing strands.

- The presence of moisture can initiate galvanic corrosion between bearing plates and conventional reinforcement and bearing plates and strands in PT systems. Also, the presence of high amounts of chlorides can accelerate corrosion.

### 11.3.4. Probabilistic tension capacity of strands and wires

Section 5 presented the experimental program and results on strand and wire corrosion tests. Sections 7, 8, and 9 presented the probabilistic models for tension capacity ($C_T$) of strands and wires. Subsection 5.5.2 presented the definitions and schematics of different void conditions (i.e., NV, PV, OV, IV, BV, and BIOV). The conclusions derived from these results are as follows:

- The corrosion mechanisms for a PT system containing voids and one containing no voids are different and the presence of the voids has a more significant effect on the corrosion rate than the grout material characteristics, such as chemical composition and water-cementitious materials ratio.

- The moisture level has a statistically significant influence on the corrosion and $C_T$ of PT strands. The $C_T$ of strands exposed to high moisture levels can be up to 17 percent less than the $C_T$ of strands exposed to low moisture levels, provided other exposure conditions remain the same.

- The chloride level has a statistically significant influence on the corrosion rate and $C_T$ of PT strands. The $C_T$ of strands exposed to high chloride levels can be up to 25 percent less than the $C_T$ of strands exposed to negligible chloride levels, provided other exposure conditions remain the same.

- The in-service stress level has a statistically significant influence on the corrosion and $C_T$ of PT strands. The $C_T$ of stressed strands can be 1.6 to 17 percent less than the $C_T$ of unstressed strands, provided other exposure conditions remain same.

- The type of void, especially the orientation of grout-air-strand (GAS) interface, has a statistically significant influence on the corrosion rate and resulting reduction in the tension capacity of strands. Typically, more localized corrosion will occur at strands in PT columns and anchorage zones on PT girders than at strands near the midspan region of PT girders.

- In fully grouted tendons (i.e., NV conditions), moisture and chlorides are the most influential factors in accelerating corrosion and reducing the $C_T$ of the exposed strands. Hence, as long as the fully grouted

tendons are protected from chloride and moisture ingress, the corrosion rate and capacity loss should be negligible. However, this protection is very difficult to accomplish as cracks were found in both Class A and Class C grouts prepared in the laboratory. This is likely to be the case in the field also. In addition, cracks or openings were found on PT ducts and anchorages in the field.

- BV, IV, and OV conditions have statistically similar effect on the $C_T$ of strands. Because of the larger cathode-to-anode ratio and a smaller cathode-anode contact region, PV conditions facilitate a less corrosive environment than the BIOV condition, provided other exposure conditions remain similar.

- In general, the corrosivity of NV conditions is less than that of PV conditions and the corrosivity of PV conditions is less than that of BIOV conditions.

- In voided tendons, the presence of moisture or standing water is a critical factor in accelerating corrosion and reducing the $C_T$ of the exposed strands. Hence, moisture should be prevented from infiltrating the ducts.

- When continuous-atmospheric (CA) and BIOV conditions exist, combinations of high relative humidity and temperature or the combinations of high relative humidity, temperature, and chlorides can cause severe corrosion in relatively short periods of time. When relative humidity and temperature are both low, the corrosion rates were found to be lower.

- When exposed to similar conditions, a seven-wire strand can lose more $C_T$ than the sum of $C_T$ lost by seven individual wires or a solid wire with seven times more area. A power relationship between the $C_T$ of strands and wires exhibits better accuracy than a linear relationship.

### 11.3.5. Structural reliability of post-tensioned bridges

Section 10 developed the structural reliability models for PT bridges. The time-variant strength and service reliabilities of a typical PT bridge were then assessed using the developed reliability models. The WD condition that is assumed for the analysis consisted of 2 months of wet time and 10 months of dry time in every year.

The conclusions derived from the study on strength reliability are:

- Strength reliability models can be developed and can be used to predict the flexural strength reliability index, $\beta_{strength}$, of PT bridges at future times.
- For the typical PT bridge (defined in Subsection 10.6.1) the $\beta_{strength}$ based on the parameters defined in Subsection 10.6.2 is as follows:
  - When all the strands are in "as-received" conditions, $\beta_{strength}$ is above the $\beta_{target}$ used for calibrating the AASHTO LRFD Specifications (2007) (i.e., 3.5) and recommended by ISO 13822 (2001) for the cases with low consequences of failure (i.e., 3.1).
  - If one tendon is exposed to WD cycles and completely corrodes or fails in tension due to high stress levels, the strength reliability model shows that the value of $\beta_{strength}$ stays above 3.5.
  - If two tendons are exposed to WD cycles and compeletely corrode or fail in tension due to high stress levels, the value of $\beta_{strength}$ drops below 3.5 but stays above 3.1.
  - When the bridge is subjected to HS20 loading and three or more external tendons are exposed to WD cycles with 0.006 percent chloride solution, the value of $\beta_{strength}$ drops below 3.5 within 25 years and below 3.1 within 35 years. These time estimates reduce to about 10 and 13 years when exposed to WD cycles with 1.8 percent chloride solution.

The conclusions derived from the study on service reliability are:

- Service reliability models can be developed and can be used to estimate the reliability index for maintaining the flexural stress limits for service load conditions, $\beta_{service}$, of PT bridges at future times.

- For the typical PT bridge (defined in Subsection 10.6.1) the $\beta_{service}$ based on the parameters defined in Subsection 10.6.2 is as follows:

  - When the defined PT bridge is subjected to HS20 loading and all the strands are in "as-received" condition, the reliability model shows that value of $\beta_{service}$ is above 1.5 (i.e., the $\beta_{target}$ value recommended by ISO 13822 [2001] for the cases with irreversible consequence of failure).

  - When the defined PT bridge is subjected to HS20 or HL93 loading and all the strands are in "as-received" condition, the reliability models show that the $\beta_{service}$ is between 0 and 1.5 (i.e., the $\beta_{target}$ values recommended by ISO 13822 (2001) for the cases with irreversible and reversible consequences of failure).

  - When the bridge is subjected to HS20 loading and only one tendon is exposed to WD cycles with 0.006, 0.018, or 1.8 percent chloride solutions, the reliability models show that $\beta_{service}$ stays above 0 for more than 75 years.

  - When the bridge is subjected to HL93 loading and only one tendon is exposed to WD cycles with 0.006 percent chloride solution, $\beta_{service}$ can drop to a value below 0 within about 25 years. This time estimate reduces to about 9 years when exposed to 1.8 percent chloride solution.

  - Serviceability reduces significantly if more than one tendon is exposed to WD cycles.

## 11.4. RECOMMENDATIONS FOR FUTURE RESEARCH

Recommendations for future research include the following:

- Testing and evaluation of long-term performance of construction materials and systems under field conditions should be conducted.

- Information should be gathered from the field to better understand the exposure conditions and corrosion levels on strands in PT systems.

- Additional information on chloride exposure and chloride usage factors (such as the application rate of de-icing or anti-icing salts on bridges) in Texas should be collected and incorporated into the developed maps.

- A larger number of specimens should be tested to increase the statistical significance of the test results obtained. Also, experiments should be performed using more combinations of test parameters.

- Additional modified ASTM G109 and bearing plate tests should be performed with more parameter combinations to better evaluate this potential issue.

- Additional experiments should be conducted on unstressed strands with more combinations of test variables. The models for stressed strands developed in this research may then be re-calibrated using this new information on the $C_T$ behavior of unstressed strands.

- The effect of the interface between the existing and repair grouts on corrosion and resulting loss in the $C_T$ of strands should be investigated. The test specimens used in this research program could be modified to perform these tests.

- Strand surfaces inside the voided anchorages are inaccessible. This makes it difficult to estimate the level of corrosion at these void locations and sufficient data on corrosion of strands in the field are not available. Special remote-controlled tools that can clean and collect the corrosion products at these strand surfaces need to be developed. Such tools can then be used to collect data on corrosion of strands in the field, especially under CA exposure conditions. These data could then be used in estimating the long-term performance of PT bridges.

- The following modifications should be incorporated into the structural reliability models developed in this research:
    - Develop probabilistic models to evaluate the moment demand due to continuous support conditions;
    - Develop probabilistic models to predict $C_T$ of corroding strands in internal tendons;
    - Develop a model to more accurately assess the time-dependent prestress losses;
    - Develop models to assess reliability of girders with both bonded and unbonded tendons.
    - Develop a model to accommodate the effect of construction practices on structural behavior. These practices include sequential pre-stressing, type of construction technique (such as span-by-span, cantilever construction etc.), sequence in which the falsework is removed, and other influential factors.
- Collect field information on actual loading conditions and develop corresponding structural demand models.
- Develop structural reliability models based on shear, torsion, and other structural limit states.
- Develop a system reliability model for PT bridges based on the above recommended models for additional limit states.
- Assess the time-variant structural reliability of specific PT bridges in Texas.
- Assess the time-variant structural reliability of different standard AASHTO pre-tensioned bridges.

## 11.5. RECOMMENDATIONS FOR FIELD IMPLEMENTATIONS

Recommendations for implementations in the field include the following:

- Consider coating the inside and outside surfaces of bearing plates with epoxy or other dielectric material such that the galvanic corrosion between the bearing plate and other metallic materials in the PT systems can be minimized.

- Inspect the PT strands and girders at regular intervals, especially when the importance measures of the bridge and the likelihood of the occurrence of WD conditions inside the tendons are high.

- Prevent the infiltration of water and chlorides into PT systems and the formation of voids in PT systems during construction. Maintain dry conditions in the voids in tendons until the effects of grout repairs on strand corrosion can be assessed.

# REFERENCES

AASHTO., (1982). “AASHTO bridge design specifications.” American Association of State Highway and Transportation Officials (AASHTO), Washington, D.C.

AASHTO., (1992). “Standard specifications for highway bridges.” American Association of State Highway and Transportation Officials (AASHTO), Washington, D.C.

AASHTO., (1994). “Standard specifications for highway bridges.” American Association of State Highway and Transportation Officials (AASHTO), Washington, D.C.

AASHTO., (1996). “AASHTO LRFD bridge design specifications.” American Association of State Highway and Transportation Officials (AASHTO), Washington, D.C.

AASHTO., (1998). “AASHTO LRFD bridge design specifications.” American Association of State Highway and Transportation Officials (AASHTO), Washington, D.C.

AASHTO., (1999). “Guide Specifications for design and construction of segmental concrete bridges.” American Association of State Highway and Transportation Officials (AASHTO), Washington D.C.

AASHTO., (2006). “Standard specifications for highway bridges.” 17th Edition, American Association of State Highway and Transportation Officials (AASHTO), Washington, D.C.

AASHTO., (2004). “AASHTO LRFD bridge design specifications.” American Association of State Highway and Transportation Officials (AASHTO), Washington, D.C.

AASHTO., (2007). “AASHTO LRFD bridge design specifications.” Association of State Highway and Transportation Officials (AASHTO), Washington, D.C.

ACI., (2003). "ACI 222R-03 – Protection of metals in concrete against corrosion." ACI Committee 222, Document No. 22203, American Concrete Institute (ACI), Farmington Hills, Michigan.

Akgul, F. and Frangopol, D.M., (2004). "Lifetime performance analysis of existing prestressed concrete bridge superstructures." *ASCE Journal of Structural Engineering*, 130(12), 1889-1903.

Albrecht, P. and Hall, T.T., (2003). "Atmospheric corrosion resistance of structural steels." *Journal of Materials in Civil Engineering*, 150th Anniversary Paper, 15(1), 2-24.

ArcView, (2009). "ArcView – Desktop GIS for mapping, data integration, and analysis." http://www.esri.com/software/arcview/, Last Accessed on March 15, 2009.

ASBI., (2000). "American segmental bridge institute grouting committee: Interim statement on grouting practices." American Segmental Bridge Institute (ASBI), Phoenix, Arizona.

Barton, K., (1980)., "Schutz gegan atmospherische Korrosion - Theorie und Technik, Verlag Chemie." *Protection of Metals*, Z. Metallov. Translator, 16, 387.

Box, G.E.P. and Tiao, G.C., (1992). *Bayesian inference in statistical analysis,* 113-122. Addison-Wesley, Reading, Massachusetts.

Brooks, C.E.P., (1946), "Climate and the deterioration of materials," *Quarterly Journal of Royal Meteorological Society*, 72(311), 87-97.

Cavell, D.G. and Waldron, P., (2001). "Parametric study of the residual strength of deteriorating simply-supported post-tensioned concrete bridges." *Proceedings of the Institution of Civil Engineers*, 1, 341-352.

CDCHB., (1991). "Chinese design code for highway bridges." People's Communication Press, Beijing, China.

Chung, S.C., Lin, A.S., Chang, J.R., and Shih, H.C., "EXAPS study of atmospheric corrosion products on zinc at the initial stage." *Corrosion Science*, 42, 1599-1610.

Corvo, F., Minotas, J., Delgado, J., and Arroyave, C., (2005). "Changes in atmospheric corrosion rate caused by chloride ions depending on rain regime." *Corrosion Science*, 47, 883-892.

Corvo, F., Perez, T., Martin, Y. Reyes, J., Dzib, L.R., Gonzalez-Sanchez, J., and Castaneda, A., (2008). "Time of wetness in tropical climate: Considerations on the estimation of TOW according to ISO 9223 standard." *Corrosion Science*, 50, 206-219.

Cui, F., and Sagues, A., (2003). "Corrosion performance of stainless steel clad rebar in simulated pore water and concrete." *Corrosion 2003*, NACE International, Houston, Paper No. 03310.

Dean S.W. and Reiser D.B., (2002). "Analysis of long-term atmospheric corrosion results from ISO CORRAG program," *Outdoor Atmospheric Corrosion*, ASTM STP 1421, Townsend, H.E., (Ed.). American Society of Testing and Materials (ASTM), West Conshohoken, Pennsylvania, 3-18.

Decker, J.B., Rollins, K.M., and Ellsworth, J.C., (2008). "Corrosion rate evaluation and prediction for piles based on long-term field performance." *Journal of Geotechnical and Geoenvironmental Engineering*, 134(3), 341-351.

Der Kiureghian, A., Haukaas, T., and Fujimura, A., (2006). Structural reliability software at the University of California, Berkeley. *Structural Safety*, 28(1-2), 44-67.

Diamond, S., (1981). "Effects of two Danish flyshes on alkali contents of pore solutions of cement-lyash pastes." *Cement and Concrete Research*, 11, 383-394.

Ditlevsen, O. and Madsen, O.H., (1996). *Structural reliability methods,* Monograph, John Wiley & Sons Ltd, Chichester, UK.

Drazic, D.M. and Vascic, V., (1989). "The correlation between accelerated laboratory corrosion tests and atmospheric corrosion station tests on steels." *Corrosion Science*, 29(10), 1197-1204.

Du, J.S. and Au, F.T.K., (2005). "Deterministic and reliability analysis of prestressed concrete bridge girders: Comparison of the Chinese, Hong Kong, and AASHTO LRFD Codes." *Structural Safety*, (27), 230-245.

Duncan, J.R., and Balance, J.A., (1988). "Marine salts contribution to atmospheric corrosion." *Degradation of Metals in the Atmosphere*, ASTM STP 965, Dean, S.W., and Lee, T.S., (Eds.). American Society of Testing and Materials (ASTM), West Conshohoken, PA, 317-326.

Ellingwood, B., (1994). "Probability-based codified design for earthquakes." *Engineering Structures,* 16(7), 498-506.

Emmanuel, M., (1980). *Contemporary architects*, St. Martin's Press, New York.

FDOT. (1999). "Corrosion evaluation of post-tensioned tendons on the Niles Channel bridge." *FDOT* Report, Florida Department of Transportation, Tallahassee, Florida.

FDOT., (2001a). "Mid-Bay bridge post-tensioning evaluation – Final Report." Corven Engineering, Inc., Florida Department of Transportation (FDOT), Tallahassee, Florida.

FDOT., (2001b). "Sunshine skyway bridge post-tensioned tendons investigation." Parsons Brinckerhoff Quade and Douglas, Inc., Florida Department of Transportation (FDOT), Tallahassee, Florida.

FDOT., (2002). "Galvanic testing of stressed strands inside carbon steel pipe – Final report." State Materials Office, Corrosion Research Laboratory, Florida Department of Transportation, Tallahassee, Florida.

Feliu, S., Morcillo, M., and Feliu, S. Jr., (1993). "The prediction of atmospheric corrosion from meteorological and pollution parameters – 1. Annual corrosion." *Corrosion Science*, 34(3), 403-414.

FIB., (2001). "Durability of Post-tensioning tendons." *Technical Report*, Féd. Int. du Béton (FIB), ISBN: 2883940738, November 2001, Ghent, Belgium.

Gardoni, P.G., Der Kiureghian, A., and Mosalam, K.M., (2002a). "Probabilistic capacity models and fragility estimates for bridge components and systems." *PEER Report No. 2002/13*, Pacific Earthquake Engineering Research Center, Department of Civil Engineering, University of California, Berkeley, California.

Gardoni, P.G., Der Kiureghian, A., and Mosalam, K.M., (2002b). "Probabilistic capacity models and fragility estimates for reinforced concrete columns based on experimental observations." *Journal of Engineering Mechanics,* 128(10), 1024-1038.

Ghosn, M., and Moses, F., (1985). 'Markov renewal model for maximum bridge loading', *ASCE Journal of Engineering Mechanics*, 111(9), 1093-1104.

Guttman, H. and Serada, P.J., (1968). "Metal corrosion in the atmosphere." STP 435, American Society for Testing and Materials, West Conshohoken, Pennsylvania.

Hakkarainen, T., and Ylasaari, S., (1982). "Atmospheric corrosion testing in Finland." *Atmospheric Corrosion*, Ailor, W.H., (Ed.), John Wiley and Sons, NewYork, NY.

Haldar, A. and Mahadevan, S., (1999). *Probability, reliability and statistical methods in engineering design,* John Wiley and Sons, Inc., New York.

Hansen, B., (2007). "Forensic engineering: Tendon failure raises questions about grout in post-tensioned bridges." *Civil Engineering News*, November, 17-18.

Haynie, F.H., and Upham, J.B., (1974). "Correlation between corrosion behavior of steel and atmospheric pollution data." *Corrosion in Natural Environments*, *ASTM STP 558*, American Society of Testing and Materials, 33-51.

Hognestad, E. A., (1951). "A study of combined bending and axial load in reinforced concrete members." *Bulletin Series No. 399*, University of Illinois Engineering Experiment Station, Urbana, Illinois.

Iribarren Laco, J.I., Leisa Mestres, F., Cadena Villota, F., and Bilurnina Alter, L., (2004). "Urban and marine corrosion: Comparative behavior between field and laboratory conditions." *Materials and Corrosion*, 55(9), 689-694.

ISO 13822 (2001). "Bases for design of structures - Assessment of existing structures." International Standards Organization, Switzerland.

Jones, D. A., (1996). *Principles and prevention of corrosion*, Prentice Hall, Inc., New Jersey.

Klinesmith, D.E., McCuen, R.H., and Albrecht, P., (2007). "Effect of environmental conditions on corrosion rates." *Journal of Materials in Civil Engineering*, 19(2), 121-129.

Knotkova, D., Gullman, J., Holler, P., Kucera, V., (1984). "Assessment of corrosivity by short-term atmospheric field tests of technically important materials." *Proceedings of the 9th International Congress on Metallic Corrosion*", National Research Council of Canada, Toronto, 198-205.

Kobus, J., (2000)."Long-term atmospheric corrosion monitoring." *Materials and Corrosion*, 51, 104-108.

Kovač, J., Leban, M., and Legat, A., (2007). "Detection of SCC on prestressing steel wire by the simultaneous use of electrochemical noise and acoustic emission measurements." *Electrochemica Acta*, 52, 7607-7616.

Kovac, J., Leban, M., and Legat, A., (2007). "Detection of SCC on prestressing steel wire by the simultaneoususe of electrochemical noise and acoustic emission measurements." *Electrochemica Acta*, 52, 7607-7616.

Krauss, P.D., and Nmai, C.K., (1997). "Preliminary corrosion investigation of prestressed concrete piles in a marine environment: Deerfield beach fishing pier." *Techniques to Assess Corrosion Activity of Steel Reinforced Concrete Structures*, ASTM STP 1276, (Eds. Berke, N.S., Escalante, E., Nmai, C.K., and Whiting, D.,). American Society of Testing and Materials (ASTM), West Conshohoken, Pennsylvania, 161-172.

Kucera, V., and Mattsson, E., (1987). "Atmospheric corrosion." *Corrosion mechanisms*, Mansfeld, F., (Ed.), Marcel Dekker, Inc., NewYork, NY. 211-284.

Laco, J.I.I., Mesters, F.L., Villota, F.C., and Alter, L.B., (2004). "Urban and marine corrosion: Comparative behavior between field and laboratory conditions." *Materials and Corrosion,* 55(9), 689-694.

Li, X-Y., Xie, Z-K., and Yan, X-K., (2004). "Runoff characteristics of artificial catchment materials for rainwater harvesting in the semiarid regions of China." *Agricultural Water Management*, 65, 211-224.

Liu P.-L., Lin H.-Z., and Der Kiureghian, A., (1989). "*CalREL user manual*." Report No. UCB/SEMM-89/18, Structural Engineering, Mechanics, and Materials, Department of Civil Engineering, University of California, Berkeley, California.

Mammoliti, L.T., Brown, L.C., Hasson, C.M., and Hope, B.B., (1996). "The influence of surface finish of reinforcing steel and pH of the test solution on the chloride threshold concentration for corrosion initiation in synthetic pore solutions." *Cement and Concrete Research*, 26(4), 545-550.

Mander, J. B., Priestley, M. J. N. and Park, R., (1988a). "Theoretical stress-strain model for confined concrete." *ASCE Journal of Structural Engineering*, 114(8), 1804-1826.

Mander, J. B., Priestley, M. J. N. and Park, R., (1988b). "Observed stress-strain behavior of confined concrete." *ASCE Journal of Structural Engineering*, 114(8), 1827-1849.

Mander, J. B. and Basoz, N., (1999). "Seismic fragility curve theory for highway bridges." *Proc., 5th US Conference on Lifeline Earthquake Engineering*, ASCE, Seattle, Washington.

Mansfield, F., (1979). "Atmospheric corrosion rates, time-of-wetness, and relative humidity." *Werkstoffe und Korrosion*, 30, 38-42.

McCuen, R.H., Albrecht, P, and Cheng, J., (1992). "A new approach to power-model regression of corrosion penetration data." *Corrosion and Control for Infrastructure*, ASTM STP 1137, American Society of Testing and Materials, West Conshohoken, Pennsylvania.

McCuen, R.H. and Albrecht, P., (2004). "Reanalysis of thickness loss data for weathering steel." *Journal of Materials in Civil Engineering*, 16(3), 237-246.

McGray, J.P., (1998). "North American free trade agreement truck highway corridors: US-Mexico truck rivers of trade." *Transportation Research Record-1613*, Paper No. 98-0757, 71-78.

McKenna, F., Fenves, G. L., and Scott. M. H., (2000). "Open system for earthquake engineering simulation (OpenSEES)." http://opensees.berkeley.edu, Last Accessed on November 1, 2009.

Melchers, R.E., (1998). "Probabilistic modeling of immersion marine corrosion." *Structural Safety and Reliability*, 3, 1143-1149.

Melchers, R.E., (1999). "Corrosion uncertainty modeling for steel structures." *Journal of Constructional Steel Research*, 52, 3-19.

Naaman, A.E., (2004). *Prestressed concrete analysis and design,* Techno Press, Ann Arbor, Michigan.

Naaman, A.E. and Alkhahiri, F.M., (1992). "Stress at ultimate in unbonded post-tensioning tendons: Part 2 - Proposed methodology." *ACI Structural Journal*, 88(6), 683-692.

Natesan, M., Venkatachari, G., and Palaniswamy, N., (2006). "Kinetics of atmospheric corrosion of mild steel, zinc, galvanized iron and aluminum at 10 exposure stations in India." *Corrosion Science*, 48, 3584-3608.

Nawy, E.G., (2003). *Prestressed concrete – A fundamental approach*, Prentice Hall, Saddle River, New Jersey.

NCDC., (2009). National Climatic Data Center (NCDC), www.ncdc.noaa.gov, last accessed on November 1, 2009.

NCHRP., (1998). "Durability of precast segmental bridges." NCHRP Web Document No.15, Project 20-7/Task 92, National Cooperative Highway Research Program (NCHRP), Transportation Research Board, National Research Council, Washington, D.C.

NCHRP., (2003). "Prestress losses in pretensioned high-strength concrete bridge girders." National Cooperative Highway Research Program (NCHRP), Transportation Research Board, National Research Council, Washington, D.C.

Neville, A. M., (1998). *Properties of concrete*, 4th Ed., John Wiley & Sons, Inc., NewYork.

Nowak, A. S., and Collins, K. R., (2000). *Reliability of structures*, McGraw-Hill Companies, Inc., Boston, Massachussets.

Nowak, A.S., (1993). "Live load model for highway bridges", *Structural Safety*, 13(1), 53-66.

Nowak, A.S., and Hong, Y-K., (1991). "Bridge live load models," *ASCE Journal of Structural Engineering*, 117(9), 2757-2767.

PCI., (1985). “Manual for quality control for plants and production of precast and prestressed concrete products.” Precast/Prestressed Concrete Institute (PCI), Chicago, Illinois.

PCI., (1999). *PCI design handbook,* Precast/Prestressed Concrete Institute (PCI), Chicago, Illinois.

Perret, S., Khayat, K.H., Gagnon, E., and Rhazi, J., (2002). “Repair of 130-year old masonry bridge using high-performance cement grout.” *Journal of Bridge Engineering*, 7(1), 31-38.

Pillai, R.G., (2003). “Accelerated quantification of critical parameters for predicting the service life and life cycle costs of chloride-laden reinforced concrete structures.” M.S. Thesis, Zachry Department of Civil Engineering, Texas A&M University, College Station, Texas, USA.

Pillai, R.G. and Trejo, D., (2005). “Surface reinforcement effects on critical chloride threshold of steel reinforcement.” *ACI Materials Journal*, 102(2), 103-109.

Pillai, R.G., Gardoni, P., Hueste, M.D., Reinschmidt, K., and Trejo, D., (2007). “Probabilistic capacity models for corroding strands in post-tensioned bridges with voided tendons.” *Proc., 10th International Conference on Applications of Statistics and Probability in Civil Engineering*, July 31−August 3, Tokyo, Japan.

Poston, W.R., Frank, K.H., and West, J.S., (2003). “Enduring strength.” *Civil Engineering*, American Society of Civil Engineering, 73(9), pp.58-63.

Proverbio, E., and Longo, P., (2003). “Failure mechanisms of high strength steels in bicarbonate solutions under anodic polarization.” *Corrosion Science*, 45, 2017-2030.

PTI., (1998). “Acceptance standards for post-tensioning applications.” Post-tensioning Institute, Pheonix, Arizona.

PTI., (2003). “Specification for grouting of post-tensioned structures.” Post-Tensioning Institute, Phoenix, Arizona.

Roadstothefuture, (2009). http://www.roadstothefuture.com/I295_VA_JRB.jpg, Last accessed on January 28, 2009.

Roberge, P.R., (1999). *Handbook of corrosion engineering*, McGraw-Hill Book Company, New York.

Roberge, P.R., Klassen, R.D., and Haberecht, P.W., (2002). "Atmospheric corrosivity modeling – a review." *Materials and Design*, 23, 32-330.

Roberts-Wollmann, C.L., Breen, J.E., and Kreger, M.E., (2001). *"*Live load tests on the San Antonio "Y". *Journal of Bridge Engineering*, 6(6), 556-563.

Romanoff, M., (1962). "Corrosion of steel pilings in soils." NBS Monograph No. 58, National Bureau of Standards, U.S. Dept. of Commerce, Washington, D.C.

Ryals, K., Wollmann, G.P., Breen, J.E., and Kreger, M.E., (1993). "Fretting fatigue of external tendons in segmental bridge deviators." *Proceedings of the Workshop on Behavior of External Prestressing in Structures*., Association Francaise Pour la Construction, Saint-Remy-les-Chevreuse, France, 131-140.

Ryan, T.P., (2007). *Modern engineering statistics,* Wiley Interscience, Hoboken, New Jersey.

Sagüés, A., (2003). "Durability research." http://www.dot.state.fl.us/statematerialsoffice/administration/meetings/dme/presentation/corrosiondurability.pdf, last accessed on February 4, 2008.

Sagüés, A., Powers, R. G., and Wang, H., (2003). "Mechanism of corrosion of steel strands in post tensioned grouted assemblies." Paper No. 03312, Corrosion/2003, NACE International, Houston, Texas.

Sanchez, J., Fullea, J., Andrade, C., and Alonso, C., (2007). "Stress corrosion cracking mechanism of prestressing steels in bicarbonate solutions." *Corrosion Science*, 49, 4069-4080.

Sanchez, J., Trejo, D., and Hueste, M.D., (2003) "Personal communication on possible corrosion mechanisms in PT bridges in Texas,"Austin, Texas.

Sason, A. S., (1992). "Evaluation of degree of rusting on prestressed concrete strand." *PCI Journal*, May−June, 25-30.

Schlosser, F., and Bastick, M., (1991). "Reinforced earth." *Foundation engineering handbook*, Fang, H-Y., (Ed.) Chapman and Hall, NewYork, NY. 778-795.

Schupack, M., (2004). “PT grout: Bleedwater voids.” *Concrete International*, 26(8), 69-77.

SDMHR., (1997). *structures design manual for highways and railways*, Highways Department, Government of the Hong Kong Special Administrative Region, 2nd ed., with Amendment No. 1/2002, Hong Kong.

SHRP-S/FR-92-110., (1992). “Standard test method for chloride content in concrete using the specific ion probe.” *Condition evaluation of concrete bridges relative to reinforcement corrosion - Volume 8: Procedure manual*, Strategic Highway Research Program, Washington, D.C., 85-105.

Southwell, C.R., Bultman, J.D., and Hummer, C.W. Jr., (1979). “Estimation of service life of steel in seawater.” *Seawater corrosion handbook*, Noyes Data Corporation, Park Ridge, New Jersey, 374-387.

Stewart, M.G., (1996).” Optimization of serviceability load combinations for structural steel beam design.” *Structural Safety*, 18(2), 225-238.

Structurae, (2009). http://en.structurae.de/photos/index.cfm?JS=15986, last accessed on January 28, 2009.

Tabsh, S.W., (1995). “Structural safety of post-tensioned concrete slab bridges with unbonded tendons.” *ACI Structural Journal*, 92(4), 1-7.

Tang, L., Li, X., Si, Y., Mu, G., and Liu, G., (2006). “The synergistic inhibition between 8-hydroxyquinoline and chloride ion for the corrosion of cold rolled steel in 0.5 M sulfuric acid.” *Materials Chemistry and Physics*, 95, 29-38.

Ting, S-C. and Nowak, A.S., (1991). “Effect of tendon-area loss on flexural behavior of P/C beams.” *Journal of Structural Engineering*, 117(4), 1127-1143.

Todeschini, C. E., Bianchini, A. C., and Kesler, C. E., (1964). “Behaviour of concrete columns reinforced with high strength steels.” *ACI Journal*, 61~67, 701-716.

Trejo, D. and Pillai, R.G., (2003). “Accelerated chloride threshold testing: Part 1 – ASTM A 615 and A 706 Reinforcement.” *ACI Materials Journal*, 100(6), 519-527.

TRRL., (1987). “Seventh report of the committee for the two years ending July 1987.” EA/88/4, Standing Committee on Structural Safety, Transport and Road Research Laboratory (TRRL), Crowthorne, United Kingdom.

TxDOT., (2004). “Critical evaluation and condition assessment of post-tensioned bridges in Texas − Final Report.” Texas Department of Transportation, Austin, Texas.

Wikipedia, (2009). http://en.wikipedia.org/wiki/Image:Sunsky.jpg, last accessed on January 28, 2009.

Wollmann, C.L.R., Breen, J.E., and Kreger, M.E., (2001). “Live load tests on San Antonio Y,” *ASCE Journal of Journal of Bridge Engineering*, 6(6), 556-563.

Woodward, R. J., (1981). “Conditions within ducts in post-tensioned prestressed concrete bridges.” LR 980, Transport and Road Research Laboratory, Department of Transport, Crowthorne, Berkshire, United Kingdom.

Woodward, R., Cullington, D., and Lane, J., (2001). “Strategies for the management of post-tensioned concrete bridges.” *Current and future trends in bridge design, construction, and maintenance 2: Safety, economy, sustainability, and aesthetics*, Thomas Telford, Hong Kong, 23-32.

Worldbreak, (2009). http://watertowers.worldbreak.com/ChoctawhatcheeMidBay.jpg, last accessed on January 28, 2009.

YouTube, (2009). http://www.youtube.com/watch?v=PUg_EqQN6Gg&feature=related, Last accessed on January 28, 2009.

Zor, S., Yazici, B., and Erbit, M., (2005). “Inhibition effects of LAB and LABS on iron corrosion in chlorine solutions at different temperatures.” *Corrosion Science*, 47, 2700-2710.

# APPENDIX A
# ALL TENSION CAPACITY DATA

**Table A.1. Tension capacity of unstressed strands exposed to WD conditions.**

| Sample ID | Tensile strength (kips) | Chloride (%Cl-) | Void type | Exposure time (months) |
|---|---|---|---|---|
| 531 | 59.62 | 0.0001 | No corrosion | 0.03 |
| 532 | 59.36 | 0.0001 | No corrosion | 0.03 |
| 533 | 59.01 | 0.0001 | No corrosion | 0.03 |
| 601 | 59.29 | 0.0001 | No corrosion | 0.03 |
| 602 | 59.16 | 0.0001 | No corrosion | 0.03 |
| 603 | 58.83 | 0.0001 | No corrosion | 0.03 |
| 521 | 59.16 | 0.0001 | No corrosion | 0.03 |
| 522 | 59.54 | 0.0001 | No corrosion | 0.03 |
| 523 | 59.41 | 0.0001 | No corrosion | 0.03 |
| 591 | 59.33 | 0.0001 | No corrosion | 0.03 |
| 592 | 59.32 | 0.0001 | No corrosion | 0.03 |
| 593 | 59.58 | 0.0001 | No corrosion | 0.03 |
| 524 | 58.49 | 0.0001 | No corrosion | 0.03 |
| 525 | 58.99 | 0.0001 | No corrosion | 0.03 |
| 526 | 59.09 | 0.0001 | No corrosion | 0.03 |
| 594 | 59.03 | 0.0001 | No corrosion | 0.03 |
| 595 | 58.93 | 0.0001 | No corrosion | 0.03 |
| 596 | 59.12 | 0.0001 | No corrosion | 0.03 |
| 534 | 59.64 | 0.0001 | No corrosion | 0.03 |
| 535 | 59.59 | 0.0001 | No corrosion | 0.03 |
| 536 | 59.45 | 0.0001 | No corrosion | 0.03 |
| 604 | 59.54 | 0.0001 | No corrosion | 0.03 |
| 605 | 59.40 | 0.0001 | No corrosion | 0.03 |
| 606 | 59.56 | 0.0001 | No corrosion | 0.03 |
| 541 | 58.59 | 0.0060 | No Void | 12 |
| 542 | 58.93 | 0.0060 | No Void | 12 |
| 543 | 58.92 | 0.0060 | No Void | 12 |
| 544 | 62.11 | 0.0060 | No Void | 12 |
| 545 | 59.17 | 0.0060 | No Void | 12 |
| 611 | 58.79 | 0.0060 | No Void | 12 |
| 612 | 59.34 | 0.0060 | No Void | 12 |
| 613 | 58.98 | 0.0060 | No Void | 12 |
| 614 | 58.41 | 0.0060 | No Void | 12 |

**Table A.1. Continued.**

| Sample ID | Tensile strength (kips) | Chloride (%Cl-) | Void type | Exposure time (months) |
|---|---|---|---|---|
| 615 | 59.20 | 0.0060 | No Void | 12 |
| 561 | 59.39 | 0.0180 | No Void | 12 |
| 562 | 58.76 | 0.0180 | No Void | 12 |
| 563 | 58.43 | 0.0180 | No Void | 12 |
| 564 | 58.89 | 0.0180 | No Void | 12 |
| 565 | 59.07 | 0.0180 | No Void | 12 |
| 631 | 59.29 | 0.0180 | No Void | 12 |
| 632 | 58.71 | 0.0180 | No Void | 12 |
| 633 | 59.29 | 0.0180 | No Void | 12 |
| 634 | 58.94 | 0.0180 | No Void | 12 |
| 635 | 59.05 | 0.0180 | No Void | 12 |
| 571 | 59.55 | 0.1800 | No Void | 12 |
| 572 | 59.64 | 0.1800 | No Void | 12 |
| 573 | 62.39 | 0.1800 | No Void | 12 |
| 574 | 58.78 | 0.1800 | No Void | 12 |
| 575 | 59.26 | 0.1800 | No Void | 12 |
| 641 | 58.59 | 0.1800 | No Void | 12 |
| 642 | 58.93 | 0.1800 | No Void | 12 |
| 643 | 58.92 | 0.1800 | No Void | 12 |
| 644 | 62.11 | 0.1800 | No Void | 12 |
| 645 | 59.17 | 0.1800 | No Void | 12 |
| 581 | 53.99 | 1.8000 | No Void | 12 |
| 582 | 57.86 | 1.8000 | No Void | 12 |
| 583 | 58.20 | 1.8000 | No Void | 12 |
| 584 | 59.08 | 1.8000 | No Void | 12 |
| 585 | 54.49 | 1.8000 | No Void | 12 |
| 651 | 57.39 | 1.8000 | No Void | 12 |
| 652 | 55.56 | 1.8000 | No Void | 12 |
| 653 | 56.48 | 1.8000 | No Void | 12 |
| 654 | 56.77 | 1.8000 | No Void | 12 |
| 655 | 54.71 | 1.8000 | No Void | 12 |
| 546 | 59.55 | 0.0060 | No Void | 21 |
| 547 | 59.61 | 0.0060 | No Void | 21 |
| 548 | 58.78 | 0.0060 | No Void | 21 |
| 549 | 59.67 | 0.0060 | No Void | 21 |
| 550 | 59.31 | 0.0060 | No Void | 21 |
| 616 | 59.27 | 0.0060 | No Void | 21 |
| 617 | 58.19 | 0.0060 | No Void | 21 |

**Table A.1. Continued.**

| Sample ID | Tensile strength (kips) | Chloride (%Cl-) | Void type | Exposure time (months) |
|---|---|---|---|---|
| 618 | 57.95 | 0.0060 | No Void | 21 |
| 619 | 59.03 | 0.0060 | No Void | 21 |
| 620 | 58.85 | 0.0060 | No Void | 21 |
| 566 | 58.90 | 0.0180 | No Void | 21 |
| 567 | 59.33 | 0.0180 | No Void | 21 |
| 568 | 59.33 | 0.0180 | No Void | 21 |
| 569 | 58.84 | 0.0180 | No Void | 21 |
| 570 | 59.18 | 0.0180 | No Void | 21 |
| 636 | 58.80 | 0.0180 | No Void | 21 |
| 637 | 59.13 | 0.0180 | No Void | 21 |
| 638 | 59.33 | 0.0180 | No Void | 21 |
| 639 | 58.83 | 0.0180 | No Void | 21 |
| 640 | 59.18 | 0.0180 | No Void | 21 |
| 576 | 58.21 | 0.1800 | No Void | 21 |
| 577 | 57.14 | 0.1800 | No Void | 21 |
| 578 | 57.58 | 0.1800 | No Void | 21 |
| 579 | 58.48 | 0.1800 | No Void | 21 |
| 580 | 59.25 | 0.1800 | No Void | 21 |
| 646 | 59.47 | 0.1800 | No Void | 21 |
| 647 | 58.56 | 0.1800 | No Void | 21 |
| 648 | 59.12 | 0.1800 | No Void | 21 |
| 649 | 58.73 | 0.1800 | No Void | 21 |
| 650 | 58.27 | 0.1800 | No Void | 21 |
| 586 | 52.58 | 1.8000 | No Void | 21 |
| 587 | 57.28 | 1.8000 | No Void | 21 |
| 588 | 51.01 | 1.8000 | No Void | 21 |
| 589 | 56.81 | 1.8000 | No Void | 21 |
| 590 | 53.59 | 1.8000 | No Void | 21 |
| 656 | 56.92 | 1.8000 | No Void | 21 |
| 657 | 55.92 | 1.8000 | No Void | 21 |
| 658 | 51.82 | 1.8000 | No Void | 21 |
| 659 | 57.08 | 1.8000 | No Void | 21 |
| 660 | 57.30 | 1.8000 | No Void | 21 |
| 431 | 57.91 | 0.0060 | Bleedwater | 12 |
| 432 | 58.13 | 0.0060 | Bleedwater | 12 |
| 433 | 58.74 | 0.0060 | Bleedwater | 12 |
| 434 | 58.47 | 0.0060 | Bleedwater | 12 |
| 435 | 57.62 | 0.0060 | Bleedwater | 12 |

**Table A.1. Continued.**

| Sample ID | Tensile strength (kips) | Chloride (%Cl-) | Void type | Exposure time (months) |
|---|---|---|---|---|
| 481 | 58.90 | 0.0060 | Bleedwater | 12 |
| 482 | 57.56 | 0.0060 | Bleedwater | 12 |
| 483 | 55.20 | 0.0060 | Bleedwater | 12 |
| 484 | 58.53 | 0.0060 | Bleedwater | 12 |
| 485 | 58.92 | 0.0060 | Bleedwater | 12 |
| 451 | 56.40 | 0.0180 | Bleedwater | 12 |
| 452 | 56.55 | 0.0180 | Bleedwater | 12 |
| 453 | 57.27 | 0.0180 | Bleedwater | 12 |
| 454 | 56.90 | 0.0180 | Bleedwater | 12 |
| 455 | 58.12 | 0.0180 | Bleedwater | 12 |
| 501 | 57.45 | 0.0180 | Bleedwater | 12 |
| 502 | 57.91 | 0.0180 | Bleedwater | 12 |
| 503 | 58.03 | 0.0180 | Bleedwater | 12 |
| 504 | 58.63 | 0.0180 | Bleedwater | 12 |
| 505 | 57.25 | 0.0180 | Bleedwater | 12 |
| 461 | 54.67 | 1.8000 | Bleedwater | 12 |
| 462 | 54.42 | 1.8000 | Bleedwater | 12 |
| 463 | 55.48 | 1.8000 | Bleedwater | 12 |
| 464 | 54.57 | 1.8000 | Bleedwater | 12 |
| 465 | 54.27 | 1.8000 | Bleedwater | 12 |
| 511 | 56.04 | 1.8000 | Bleedwater | 12 |
| 512 | 54.14 | 1.8000 | Bleedwater | 12 |
| 513 | 55.75 | 1.8000 | Bleedwater | 12 |
| 514 | 54.28 | 1.8000 | Bleedwater | 12 |
| 515 | 50.21 | 1.8000 | Bleedwater | 12 |
| 436 | 54.83 | 0.0060 | Bleedwater | 21 |
| 437 | 55.43 | 0.0060 | Bleedwater | 21 |
| 438 | 54.24 | 0.0060 | Bleedwater | 21 |
| 439 | 57.69 | 0.0060 | Bleedwater | 21 |
| 440 | 56.61 | 0.0060 | Bleedwater | 21 |
| 486 | 55.34 | 0.0060 | Bleedwater | 21 |
| 487 | 57.23 | 0.0060 | Bleedwater | 21 |
| 488 | 56.16 | 0.0060 | Bleedwater | 21 |
| 489 | 55.84 | 0.0060 | Bleedwater | 21 |
| 490 | 58.02 | 0.0060 | Bleedwater | 21 |
| 456 | 55.49 | 0.0180 | Bleedwater | 21 |
| 457 | 51.30 | 0.0180 | Bleedwater | 21 |
| 458 | 53.89 | 0.0180 | Bleedwater | 21 |

**Table A.1. Continued.**

| Sample ID | Tensile strength (kips) | Chloride (%Cl-) | Void type | Exposure time (months) |
|---|---|---|---|---|
| 459 | 53.75 | 0.0180 | Bleedwater | 21 |
| 460 | 52.83 | 0.0180 | Bleedwater | 21 |
| 506 | 53.92 | 0.0180 | Bleedwater | 21 |
| 507 | 55.17 | 0.0180 | Bleedwater | 21 |
| 508 | 54.99 | 0.0180 | Bleedwater | 21 |
| 509 | 53.68 | 0.0180 | Bleedwater | 21 |
| 510 | 54.38 | 0.0180 | Bleedwater | 21 |
| 466 | 48.35 | 1.8000 | Bleedwater | 21 |
| 467 | 49.79 | 1.8000 | Bleedwater | 21 |
| 468 | 45.74 | 1.8000 | Bleedwater | 21 |
| 469 | 49.46 | 1.8000 | Bleedwater | 21 |
| 470 | 43.79 | 1.8000 | Bleedwater | 21 |
| 516 | 42.78 | 1.8000 | Bleedwater | 21 |
| 517 | 52.25 | 1.8000 | Bleedwater | 21 |
| 518 | 41.20 | 1.8000 | Bleedwater | 21 |
| 519 | 46.18 | 1.8000 | Bleedwater | 21 |
| 520 | 42.91 | 1.8000 | Bleedwater | 21 |
| 301 | 59.92 | 0.0060 | Inclined | 12 |
| 302 | 58.59 | 0.0060 | Inclined | 12 |
| 303 | 58.34 | 0.0060 | Inclined | 12 |
| 304 | 56.01 | 0.0060 | Inclined | 12 |
| 305 | 56.53 | 0.0060 | Inclined | 12 |
| 371 | 56.34 | 0.0060 | Inclined | 12 |
| 373 | 57.43 | 0.0060 | Inclined | 12 |
| 374 | 57.67 | 0.0060 | Inclined | 12 |
| 375 | 56.47 | 0.0060 | Inclined | 12 |
| 321 | 54.09 | 0.0180 | Inclined | 12 |
| 322 | 57.77 | 0.0180 | Inclined | 12 |
| 323 | 58.82 | 0.0180 | Inclined | 12 |
| 324 | 55.80 | 0.0180 | Inclined | 12 |
| 325 | 57.11 | 0.0180 | Inclined | 12 |
| 391 | 53.80 | 0.0180 | Inclined | 12 |
| 392 | 54.99 | 0.0180 | Inclined | 12 |
| 393 | 57.61 | 0.0180 | Inclined | 12 |
| 394 | 56.11 | 0.0180 | Inclined | 12 |
| 395 | 55.61 | 0.0180 | Inclined | 12 |
| 331 | 54.22 | 0.1800 | Inclined | 12 |
| 332 | 53.50 | 0.1800 | Inclined | 12 |

**Table A.1. Continued.**

| Sample ID | Tensile strength (kips) | Chloride (%Cl-) | Void type | Exposure time (months) |
|---|---|---|---|---|
| 333 | 53.92 | 0.1800 | Inclined | 12 |
| 334 | 50.81 | 0.1800 | Inclined | 12 |
| 335 | 56.14 | 0.1800 | Inclined | 12 |
| 401 | 54.00 | 0.1800 | Inclined | 12 |
| 402 | 54.09 | 0.1800 | Inclined | 12 |
| 403 | 53.69 | 0.1800 | Inclined | 12 |
| 404 | 55.76 | 0.1800 | Inclined | 12 |
| 405 | 52.56 | 0.1800 | Inclined | 12 |
| 341 | 55.80 | 1.8000 | Inclined | 12 |
| 342 | 55.96 | 1.8000 | Inclined | 12 |
| 343 | 57.95 | 1.8000 | Inclined | 12 |
| 344 | 54.91 | 1.8000 | Inclined | 12 |
| 345 | 54.15 | 1.8000 | Inclined | 12 |
| 411 | 57.37 | 1.8000 | Inclined | 12 |
| 412 | 58.45 | 1.8000 | Inclined | 12 |
| 413 | 53.78 | 1.8000 | Inclined | 12 |
| 414 | 53.38 | 1.8000 | Inclined | 12 |
| 415 | 55.03 | 1.8000 | Inclined | 12 |
| 306 | 57.72 | 0.0060 | Inclined | 21 |
| 307 | 56.78 | 0.0060 | Inclined | 21 |
| 308 | 55.11 | 0.0060 | Inclined | 21 |
| 309 | 56.48 | 0.0060 | Inclined | 21 |
| 310 | 55.63 | 0.0060 | Inclined | 21 |
| 376 | 54.88 | 0.0060 | Inclined | 21 |
| 377 | 54.89 | 0.0060 | Inclined | 21 |
| 378 | 54.75 | 0.0060 | Inclined | 21 |
| 379 | 52.47 | 0.0060 | Inclined | 21 |
| 380 | 53.54 | 0.0060 | Inclined | 21 |
| 326 | 55.32 | 0.0180 | Inclined | 21 |
| 327 | 52.27 | 0.0180 | Inclined | 21 |
| 328 | 47.21 | 0.0180 | Inclined | 21 |
| 329 | 53.71 | 0.0180 | Inclined | 21 |
| 330 | 51.75 | 0.0180 | Inclined | 21 |
| 396 | 51.85 | 0.0180 | Inclined | 21 |
| 397 | 50.45 | 0.0180 | Inclined | 21 |
| 398 | 52.92 | 0.0180 | Inclined | 21 |
| 399 | 55.86 | 0.0180 | Inclined | 21 |
| 400 | 55.09 | 0.0180 | Inclined | 21 |

**Table A.1. Continued.**

| Sample ID | Tensile strength (kips) | Chloride (%Cl-) | Void type | Exposure time (months) |
|---|---|---|---|---|
| 336 | 50.81 | 0.1800 | Inclined | 21 |
| 337 | 51.64 | 0.1800 | Inclined | 21 |
| 338 | 49.01 | 0.1800 | Inclined | 21 |
| 339 | 53.89 | 0.1800 | Inclined | 21 |
| 340 | 51.97 | 0.1800 | Inclined | 21 |
| 406 | 49.17 | 0.1800 | Inclined | 21 |
| 407 | 52.23 | 0.1800 | Inclined | 21 |
| 408 | 45.97 | 0.1800 | Inclined | 21 |
| 409 | 47.98 | 0.1800 | Inclined | 21 |
| 410 | 52.39 | 0.1800 | Inclined | 21 |
| 346 | 48.90 | 1.8000 | Inclined | 21 |
| 347 | 43.06 | 1.8000 | Inclined | 21 |
| 348 | 45.94 | 1.8000 | Inclined | 21 |
| 349 | 47.48 | 1.8000 | Inclined | 21 |
| 350 | 44.02 | 1.8000 | Inclined | 21 |
| 416 | 47.01 | 1.8000 | Inclined | 21 |
| 417 | 44.02 | 1.8000 | Inclined | 21 |
| 418 | 45.60 | 1.8000 | Inclined | 21 |
| 419 | 44.57 | 1.8000 | Inclined | 21 |
| 420 | 44.20 | 1.8000 | Inclined | 21 |
| 21 | 60.49 | 0.0060 | Orthogonal | 12 |
| 22 | 58.26 | 0.0060 | Orthogonal | 12 |
| 23 | 56.56 | 0.0060 | Orthogonal | 12 |
| 24 | 57.31 | 0.0060 | Orthogonal | 12 |
| 25 | 54.23 | 0.0060 | Orthogonal | 12 |
| 91 | 56.61 | 0.0060 | Orthogonal | 12 |
| 92 | 57.46 | 0.0060 | Orthogonal | 12 |
| 93 | 54.98 | 0.0060 | Orthogonal | 12 |
| 94 | 55.03 | 0.0060 | Orthogonal | 12 |
| 95 | 56.54 | 0.0060 | Orthogonal | 12 |
| 41 | 58.66 | 0.0180 | Orthogonal | 12 |
| 42 | 57.51 | 0.0180 | Orthogonal | 12 |
| 43 | 57.23 | 0.0180 | Orthogonal | 12 |
| 44 | 58.84 | 0.0180 | Orthogonal | 12 |
| 45 | 59.22 | 0.0180 | Orthogonal | 12 |
| 111 | 55.30 | 0.0180 | Orthogonal | 12 |
| 112 | 55.57 | 0.0180 | Orthogonal | 12 |
| 113 | 61.37 | 0.0180 | Orthogonal | 12 |

**Table A.1. Continued.**

| Sample ID | Tensile strength (kips) | Chloride (%Cl-) | Void type | Exposure time (months) |
|---|---|---|---|---|
| 114 | 58.52 | 0.0180 | Orthogonal | 12 |
| 115 | 54.52 | 0.0180 | Orthogonal | 12 |
| 51 | 53.21 | 0.1800 | Orthogonal | 12 |
| 52 | 52.70 | 0.1800 | Orthogonal | 12 |
| 53 | 52.77 | 0.1800 | Orthogonal | 12 |
| 54 | 55.44 | 0.1800 | Orthogonal | 12 |
| 55 | 57.25 | 0.1800 | Orthogonal | 12 |
| 121 | 53.34 | 0.1800 | Orthogonal | 12 |
| 122 | 53.39 | 0.1800 | Orthogonal | 12 |
| 123 | 53.63 | 0.1800 | Orthogonal | 12 |
| 124 | 53.91 | 0.1800 | Orthogonal | 12 |
| 125 | 53.90 | 0.1800 | Orthogonal | 12 |
| 64 | 53.99 | 1.8000 | Orthogonal | 12 |
| 65 | 55.86 | 1.8000 | Orthogonal | 12 |
| 66 | 54.90 | 1.8000 | Orthogonal | 12 |
| 131 | 55.57 | 1.8000 | Orthogonal | 12 |
| 132 | 51.64 | 1.8000 | Orthogonal | 12 |
| 133 | 54.89 | 1.8000 | Orthogonal | 12 |
| 134 | 54.18 | 1.8000 | Orthogonal | 12 |
| 135 | 53.41 | 1.8000 | Orthogonal | 12 |
| 26 | 53.66 | 0.0060 | Orthogonal | 21 |
| 27 | 54.47 | 0.0060 | Orthogonal | 21 |
| 28 | 52.92 | 0.0060 | Orthogonal | 21 |
| 29 | 54.21 | 0.0060 | Orthogonal | 21 |
| 30 | 53.08 | 0.0060 | Orthogonal | 21 |
| 96 | 52.35 | 0.0060 | Orthogonal | 21 |
| 97 | 53.38 | 0.0060 | Orthogonal | 21 |
| 98 | 52.56 | 0.0060 | Orthogonal | 21 |
| 99 | 56.09 | 0.0060 | Orthogonal | 21 |
| 100 | 54.35 | 0.0060 | Orthogonal | 21 |
| 46 | 52.14 | 0.0180 | Orthogonal | 21 |
| 47 | 50.69 | 0.0180 | Orthogonal | 21 |
| 48 | 53.19 | 0.0180 | Orthogonal | 21 |
| 49 | 53.81 | 0.0180 | Orthogonal | 21 |
| 50 | 53.39 | 0.0180 | Orthogonal | 21 |
| 116 | 50.67 | 0.0180 | Orthogonal | 21 |
| 117 | 51.58 | 0.0180 | Orthogonal | 21 |
| 119 | 51.37 | 0.0180 | Orthogonal | 21 |

**Table A.1. Continued.**

| Sample ID | Tensile strength (kips) | Chloride (%Cl-) | Void type | Exposure time (months) |
|---|---|---|---|---|
| 56 | 49.36 | 0.1800 | Orthogonal | 21 |
| 57 | 52.52 | 0.1800 | Orthogonal | 21 |
| 58 | 52.72 | 0.1800 | Orthogonal | 21 |
| 59 | 49.60 | 0.1800 | Orthogonal | 21 |
| 60 | 47.66 | 0.1800 | Orthogonal | 21 |
| 126 | 44.95 | 0.1800 | Orthogonal | 21 |
| 127 | 49.49 | 0.1800 | Orthogonal | 21 |
| 128 | 47.17 | 0.1800 | Orthogonal | 21 |
| 129 | 53.72 | 0.1800 | Orthogonal | 21 |
| 130 | 46.24 | 0.1800 | Orthogonal | 21 |
| 67 | 46.31 | 1.8000 | Orthogonal | 21 |
| 68 | 43.03 | 1.8000 | Orthogonal | 21 |
| 69 | 42.93 | 1.8000 | Orthogonal | 21 |
| 70 | 43.98 | 1.8000 | Orthogonal | 21 |
| 136 | 44.85 | 1.8000 | Orthogonal | 21 |
| 137 | 45.69 | 1.8000 | Orthogonal | 21 |
| 138 | 45.00 | 1.8000 | Orthogonal | 21 |
| 139 | 46.48 | 1.8000 | Orthogonal | 21 |
| 140 | 45.57 | 1.8000 | Orthogonal | 21 |
| 161 | 59.63 | 0.0060 | Parallel | 12 |
| 162 | 58.84 | 0.0060 | Parallel | 12 |
| 163 | 59.14 | 0.0060 | Parallel | 12 |
| 164 | 58.96 | 0.0060 | Parallel | 12 |
| 165 | 59.37 | 0.0060 | Parallel | 12 |
| 231 | 59.48 | 0.0060 | Parallel | 12 |
| 232 | 58.52 | 0.0060 | Parallel | 12 |
| 233 | 59.29 | 0.0060 | Parallel | 12 |
| 234 | 59.24 | 0.0060 | Parallel | 12 |
| 235 | 63.29 | 0.0060 | Parallel | 12 |
| 181 | 59.02 | 0.0180 | Parallel | 12 |
| 182 | 59.20 | 0.0180 | Parallel | 12 |
| 183 | 59.04 | 0.0180 | Parallel | 12 |
| 184 | 59.33 | 0.0180 | Parallel | 12 |
| 185 | 59.04 | 0.0180 | Parallel | 12 |
| 251 | 59.58 | 0.0180 | Parallel | 12 |
| 252 | 58.48 | 0.0180 | Parallel | 12 |
| 253 | 59.16 | 0.0180 | Parallel | 12 |
| 254 | 58.43 | 0.0180 | Parallel | 12 |

**Table A.1. Continued.**

| Sample ID | Tensile strength (kips) | Chloride (%Cl-) | Void type | Exposure time (months) |
|---|---|---|---|---|
| 255 | 59.50 | 0.0180 | Parallel | 12 |
| 191 | 63.04 | 0.1800 | Parallel | 12 |
| 192 | 59.09 | 0.1800 | Parallel | 12 |
| 193 | 58.79 | 0.1800 | Parallel | 12 |
| 194 | 62.85 | 0.1800 | Parallel | 12 |
| 195 | 58.76 | 0.1800 | Parallel | 12 |
| 261 | 58.96 | 0.1800 | Parallel | 12 |
| 262 | 58.22 | 0.1800 | Parallel | 12 |
| 263 | 59.12 | 0.1800 | Parallel | 12 |
| 264 | 58.11 | 0.1800 | Parallel | 12 |
| 265 | 58.63 | 0.1800 | Parallel | 12 |
| 204 | 61.95 | 1.8000 | Parallel | 12 |
| 205 | 58.48 | 1.8000 | Parallel | 12 |
| 210 | 58.34 | 1.8000 | Parallel | 12 |
| 271 | 57.98 | 1.8000 | Parallel | 12 |
| 272 | 58.67 | 1.8000 | Parallel | 12 |
| 273 | 57.79 | 1.8000 | Parallel | 12 |
| 274 | 58.03 | 1.8000 | Parallel | 12 |
| 275 | 58.51 | 1.8000 | Parallel | 12 |
| 166 | 58.27 | 0.0060 | Parallel | 21 |
| 167 | 58.95 | 0.0060 | Parallel | 21 |
| 168 | 57.68 | 0.0060 | Parallel | 21 |
| 169 | 58.54 | 0.0060 | Parallel | 21 |
| 170 | 57.68 | 0.0060 | Parallel | 21 |
| 236 | 59.00 | 0.0060 | Parallel | 21 |
| 237 | 58.59 | 0.0060 | Parallel | 21 |
| 238 | 58.78 | 0.0060 | Parallel | 21 |
| 239 | 59.13 | 0.0060 | Parallel | 21 |
| 240 | 58.72 | 0.0060 | Parallel | 21 |
| 186 | 58.52 | 0.0180 | Parallel | 21 |
| 187 | 57.86 | 0.0180 | Parallel | 21 |
| 188 | 56.94 | 0.0180 | Parallel | 21 |
| 189 | 57.87 | 0.0180 | Parallel | 21 |
| 190 | 57.47 | 0.0180 | Parallel | 21 |
| 256 | 59.13 | 0.0180 | Parallel | 21 |
| 257 | 56.97 | 0.0180 | Parallel | 21 |
| 259 | 57.91 | 0.0180 | Parallel | 21 |
| 260 | 57.59 | 0.0180 | Parallel | 21 |

**Table A.1. Continued.**

| Sample ID | Tensile strength (kips) | Chloride (%Cl-) | Void type | Exposure time (months) |
|---|---|---|---|---|
| 196 | 56.81 | 0.1800 | Parallel | 21 |
| 197 | 54.69 | 0.1800 | Parallel | 21 |
| 198 | 56.08 | 0.1800 | Parallel | 21 |
| 199 | 56.72 | 0.1800 | Parallel | 21 |
| 200 | 56.06 | 0.1800 | Parallel | 21 |
| 266 | 54.37 | 0.1800 | Parallel | 21 |
| 267 | 55.40 | 0.1800 | Parallel | 21 |
| 268 | 52.14 | 0.1800 | Parallel | 21 |
| 270 | 55.38 | 0.1800 | Parallel | 21 |
| 206 | 53.62 | 1.8000 | Parallel | 21 |
| 207 | 52.27 | 1.8000 | Parallel | 21 |
| 208 | 54.31 | 1.8000 | Parallel | 21 |
| 209 | 55.25 | 1.8000 | Parallel | 21 |
| 276 | 48.36 | 1.8000 | Parallel | 21 |
| 277 | 53.67 | 1.8000 | Parallel | 21 |
| 278 | 53.17 | 1.8000 | Parallel | 21 |
| 279 | 53.55 | 1.8000 | Parallel | 21 |
| 280 | 54.28 | 1.8000 | Parallel | 21 |

**Table A.2. Tension capacity data from stressed strand samples exposed to WD conditions.**

| Sample ID | Tensile strength (kips) | Chloride (%Cl-) | Void type | Exposure time (months) |
|---|---|---|---|---|
| 531 | 59.62 | 0.0001 | No corrosion | 0.03 |
| 532 | 59.36 | 0.0001 | No corrosion | 0.03 |
| 533 | 59.01 | 0.0001 | No corrosion | 0.03 |
| 601 | 59.29 | 0.0001 | No corrosion | 0.03 |
| 602 | 59.16 | 0.0001 | No corrosion | 0.03 |
| 603 | 58.83 | 0.0001 | No corrosion | 0.03 |
| 521 | 59.16 | 0.0001 | No corrosion | 0.03 |
| 522 | 59.54 | 0.0001 | No corrosion | 0.03 |
| 523 | 59.41 | 0.0001 | No corrosion | 0.03 |
| 591 | 59.33 | 0.0001 | No corrosion | 0.03 |
| 592 | 59.32 | 0.0001 | No corrosion | 0.03 |
| 593 | 59.58 | 0.0001 | No corrosion | 0.03 |
| 524 | 58.49 | 0.0001 | No corrosion | 0.03 |
| 525 | 58.99 | 0.0001 | No corrosion | 0.03 |
| 526 | 59.09 | 0.0001 | No corrosion | 0.03 |
| 594 | 59.03 | 0.0001 | No corrosion | 0.03 |
| 595 | 58.93 | 0.0001 | No corrosion | 0.03 |
| 596 | 59.12 | 0.0001 | No corrosion | 0.03 |
| 534 | 59.64 | 0.0001 | No corrosion | 0.03 |
| 535 | 59.59 | 0.0001 | No corrosion | 0.03 |
| 536 | 59.45 | 0.0001 | No corrosion | 0.03 |
| 604 | 59.54 | 0.0001 | No corrosion | 0.03 |
| 605 | 59.40 | 0.0001 | No corrosion | 0.03 |
| 606 | 59.56 | 0.0001 | No corrosion | 0.03 |
| S-541 | 59.40 | 0.0060 | No Void | 12 |
| S-542 | 59.47 | 0.0060 | No Void | 12 |
| S-543 | 59.22 | 0.0060 | No Void | 16 |
| S-546 | 59.44 | 0.0060 | No Void | 16 |
| S-547 | 59.47 | 0.0060 | No Void | 21 |
| S-548 | 59.43 | 0.0060 | No Void | 21 |
| S-611 | 59.36 | 0.0060 | No Void | 12 |
| S-612 | 59.35 | 0.0060 | No Void | 12 |
| S-613 | 59.17 | 0.0060 | No Void | 16 |
| S-616 | 59.34 | 0.0060 | No Void | 16 |

**Table A.2. Continued.**

| Sample ID | Tensile strength (kips) | Chloride (%Cl-) | Void type | Exposure time (months) |
|---|---|---|---|---|
| S-617 | 59.70 | 0.0060 | No Void | 21 |
| S-618 | 59.29 | 0.0060 | No Void | 21 |
| S-561 | 59.53 | 0.0180 | No Void | 12 |
| S-562 | 59.42 | 0.0180 | No Void | 12 |
| S-563 | 59.49 | 0.0180 | No Void | 16 |
| S-566 | 59.55 | 0.0180 | No Void | 16 |
| S-567 | 59.63 | 0.0180 | No Void | 21 |
| S-568 | 59.95 | 0.0180 | No Void | 21 |
| S-631 | 59.26 | 0.0180 | No Void | 12 |
| S-632 | 59.31 | 0.0180 | No Void | 12 |
| S-633 | 59.67 | 0.0180 | No Void | 16 |
| S-636 | 59.49 | 0.0180 | No Void | 16 |
| S-637 | 58.72 | 0.0180 | No Void | 21 |
| S-638 | 58.63 | 0.0180 | No Void | 21 |
| S-581 | 55.22 | 1.8000 | No Void | 12 |
| S-582 | 54.66 | 1.8000 | No Void | 12 |
| S-583 | 52.42 | 1.8000 | No Void | 16 |
| S-586 | 52.66 | 1.8000 | No Void | 16 |
| S-587 | 54.73 | 1.8000 | No Void | 21 |
| S-588 | 53.28 | 1.8000 | No Void | 21 |
| S-651 | 57.69 | 1.8000 | No Void | 12 |
| S-652 | 58.10 | 1.8000 | No Void | 12 |
| S-653 | 55.83 | 1.8000 | No Void | 16 |
| S-657 | 54.10 | 1.8000 | No Void | 21 |
| S-658 | 53.86 | 1.8000 | No Void | 21 |
| S-021 | 55.51 | 0.0060 | Orthogonal | 12 |
| S-022 | 50.98 | 0.0060 | Orthogonal | 16 |
| S-023 | 54.53 | 0.0060 | Orthogonal | 12 |
| S-024 | 53.32 | 0.0060 | Orthogonal | 12 |
| S-025 | 50.93 | 0.0060 | Orthogonal | 16 |
| S-026 | 53.12 | 0.0060 | Orthogonal | 16 |
| S-028 | 51.56 | 0.0060 | Orthogonal | 21 |
| S-029 | 49.86 | 0.0060 | Orthogonal | 21 |
| S-030 | 50.46 | 0.0060 | Orthogonal | 21 |
| S-091 | 52.65 | 0.0060 | Orthogonal | 12 |
| S-092 | 50.78 | 0.0060 | Orthogonal | 16 |
| S-093 | 53.01 | 0.0060 | Orthogonal | 12 |

**Table A.2. Continued.**

| Sample ID | Tensile strength (kips) | Chloride (%Cl-) | Void type | Exposure time (months) |
|---|---|---|---|---|
| S-094 | 52.65 | 0.0060 | Orthogonal | 12 |
| S-095 | 49.02 | 0.0060 | Orthogonal | 16 |
| S-096 | 49.78 | 0.0060 | Orthogonal | 16 |
| S-097 | 47.20 | 0.0060 | Orthogonal | 21 |
| S-099 | 48.36 | 0.0060 | Orthogonal | 21 |
| S-041 | 53.68 | 0.0180 | Orthogonal | 12 |
| S-042 | 45.25 | 0.0180 | Orthogonal | 16 |
| S-043 | 51.69 | 0.0180 | Orthogonal | 12 |
| S-044 | 52.60 | 0.0180 | Orthogonal | 12 |
| S-047 | 46.31 | 0.0180 | Orthogonal | 21 |
| S-048 | 46.15 | 0.0180 | Orthogonal | 21 |
| S-049 | 47.17 | 0.0180 | Orthogonal | 21 |
| S-050 | 46.59 | 0.0180 | Orthogonal | 21 |
| S-111 | 50.29 | 0.0180 | Orthogonal | 12 |
| S-112 | 47.76 | 0.0180 | Orthogonal | 16 |
| S-113 | 51.18 | 0.0180 | Orthogonal | 12 |
| S-114 | 50.99 | 0.0180 | Orthogonal | 12 |
| S-115 | 43.87 | 0.0180 | Orthogonal | 16 |
| S-116 | 47.98 | 0.0180 | Orthogonal | 16 |
| S-117 | 45.69 | 0.0180 | Orthogonal | 21 |
| S-118 | 45.00 | 0.0180 | Orthogonal | 21 |
| S-119 | 45.29 | 0.0180 | Orthogonal | 21 |
| S-120 | 47.07 | 0.0180 | Orthogonal | 21 |
| S-061 | 43.18 | 1.8000 | Orthogonal | 12 |
| S-062 | 44.02 | 1.8000 | Orthogonal | 12 |
| S-063 | 43.52 | 1.8000 | Orthogonal | 12 |
| S-064 | 43.52 | 1.8000 | Orthogonal | 16 |
| S-065 | 46.80 | 1.8000 | Orthogonal | 16 |
| S-066 | 51.00 | 1.8000 | Orthogonal | 16 |
| S-067 | 35.94 | 1.8000 | Orthogonal | 21 |
| S-068 | 38.12 | 1.8000 | Orthogonal | 21 |
| S-069 | 37.13 | 1.8000 | Orthogonal | 21 |
| S-131 | 45.96 | 1.8000 | Orthogonal | 12 |
| S-132 | 31.49 | 1.8000 | Orthogonal | 16 |
| S-133 | 44.44 | 1.8000 | Orthogonal | 12 |
| S-134 | 43.85 | 1.8000 | Orthogonal | 12 |
| S-135 | 36.59 | 1.8000 | Orthogonal | 16 |
| S-136 | 36.73 | 1.8000 | Orthogonal | 16 |

**Table A.2. Continued.**

| Sample ID | Tensile strength (kips) | Chloride (%Cl-) | Void type | Exposure time (months) |
|---|---|---|---|---|
| S-137 | 26.75 | 1.8000 | Orthogonal | 21 |
| S-138 | 35.08 | 1.8000 | Orthogonal | 21 |
| S-139 | 34.45 | 1.8000 | Orthogonal | 21 |
| S-140 | 34.18 | 1.8000 | Orthogonal | 21 |
| S-161 | 58.79 | 0.0060 | Parallel | 12 |
| S-162 | 58.49 | 0.0060 | Parallel | 16 |
| S-163 | 59.24 | 0.0060 | Parallel | 12 |
| S-164 | 58.90 | 0.0060 | Parallel | 12 |
| S-165 | 58.12 | 0.0060 | Parallel | 16 |
| S-166 | 57.97 | 0.0060 | Parallel | 16 |
| S-167 | 59.10 | 0.0060 | Parallel | 21 |
| S-168 | 58.48 | 0.0060 | Parallel | 21 |
| S-169 | 58.79 | 0.0060 | Parallel | 21 |
| S-170 | 58.83 | 0.0060 | Parallel | 21 |
| S-231 | 58.30 | 0.0060 | Parallel | 12 |
| S-232 | 57.51 | 0.0060 | Parallel | 16 |
| S-233 | 57.51 | 0.0060 | Parallel | 12 |
| S-234 | 59.06 | 0.0060 | Parallel | 12 |
| S-235 | 59.05 | 0.0060 | Parallel | 16 |
| S-236 | 58.33 | 0.0060 | Parallel | 16 |
| S-237 | 57.92 | 0.0060 | Parallel | 21 |
| S-238 | 55.14 | 0.0060 | Parallel | 21 |
| S-239 | 57.05 | 0.0060 | Parallel | 21 |
| S-240 | 56.07 | 0.0060 | Parallel | 21 |
| S-181 | 58.55 | 0.0180 | Parallel | 12 |
| S-182 | 55.42 | 0.0180 | Parallel | 16 |
| S-183 | 58.37 | 0.0180 | Parallel | 12 |
| S-184 | 58.27 | 0.0180 | Parallel | 12 |
| S-185 | 58.34 | 0.0180 | Parallel | 16 |
| S-186 | 58.18 | 0.0180 | Parallel | 16 |
| S-187 | 59.09 | 0.0180 | Parallel | 21 |
| S-188 | 60.47 | 0.0180 | Parallel | 21 |
| S-189 | 57.23 | 0.0180 | Parallel | 21 |
| S-190 | 58.14 | 0.0180 | Parallel | 21 |
| S-251 | 57.37 | 0.0180 | Parallel | 12 |
| S-252 | 54.85 | 0.0180 | Parallel | 16 |
| S-253 | 58.04 | 0.0180 | Parallel | 12 |
| S-254 | 55.00 | 0.0180 | Parallel | 12 |

**Table A.2. Continued.**

| Sample ID | Tensile strength (kips) | Chloride (%Cl-) | Void type | Exposure time (months) |
|---|---|---|---|---|
| S-255 | 55.26 | 0.0180 | Parallel | 16 |
| S-256 | 56.31 | 0.0180 | Parallel | 16 |
| S-257 | 53.94 | 0.0180 | Parallel | 21 |
| S-258 | 53.64 | 0.0180 | Parallel | 21 |
| S-259 | 55.49 | 0.0180 | Parallel | 21 |
| S-260 | 53.78 | 0.0180 | Parallel | 21 |
| S-201 | 55.01 | 1.8000 | Parallel | 12 |
| S-202 | 54.86 | 1.8000 | Parallel | 12 |
| S-203 | 55.11 | 1.8000 | Parallel | 12 |
| S-204 | 51.84 | 1.8000 | Parallel | 16 |
| S-205 | 52.41 | 1.8000 | Parallel | 16 |
| S-206 | 49.66 | 1.8000 | Parallel | 16 |
| S-207 | 47.15 | 1.8000 | Parallel | 21 |
| S-208 | 46.48 | 1.8000 | Parallel | 21 |
| S-209 | 51.96 | 1.8000 | Parallel | 21 |
| S-210 | 51.99 | 1.8000 | Parallel | 21 |
| S-271 | 54.33 | 1.8000 | Parallel | 12 |
| S-272 | 52.84 | 1.8000 | Parallel | 16 |
| S-273 | 55.16 | 1.8000 | Parallel | 12 |
| S-274 | 55.69 | 1.8000 | Parallel | 12 |
| S-275 | 53.26 | 1.8000 | Parallel | 16 |
| S-276 | 48.78 | 1.8000 | Parallel | 16 |
| S-277 | 52.19 | 1.8000 | Parallel | 21 |
| S-278 | 49.17 | 1.8000 | Parallel | 21 |
| S-279 | 50.54 | 1.8000 | Parallel | 21 |
| S-280 | 46.04 | 1.8000 | Parallel | 21 |

**Table A.3. Tension capacity data from unstressed wire samples exposed to WD conditions.**

| Sample Number | Tension Capacity (kips) | Test Times, t (months) | Observed Temperature, T (oF) | Chloride concentration, (%Cl-) |
|---|---|---|---|---|
| 195 | 9.06 | 3 | 85 | 0.0001 |
| 196 | 8.98 | 3 | 85 | 0.0001 |
| 197 | 9.09 | 3 | 85 | 0.0001 |
| 210 | 8.64 | 6 | 85 | 0.0001 |
| 211 | 8.92 | 6 | 85 | 0.0001 |
| 212 | 8.66 | 6 | 85 | 0.0001 |
| 227 | 8.60 | 9 | 85 | 0.0001 |
| 228 | 8.69 | 9 | 85 | 0.0001 |
| 229 | 8.71 | 9 | 85 | 0.0001 |
| 244 | 8.68 | 12 | 85 | 0.0001 |
| 245 | 8.46 | 12 | 85 | 0.0001 |
| 246 | 8.54 | 12 | 85 | 0.0001 |
| 198 | 8.87 | 3 | 85 | 0.006 |
| 199 | 8.93 | 3 | 85 | 0.006 |
| 200 | 8.72 | 3 | 85 | 0.006 |
| 213 | 8.24 | 6 | 85 | 0.006 |
| 214 | 8.65 | 6 | 85 | 0.006 |
| 215 | 8.58 | 6 | 85 | 0.006 |
| 230 | 8.28 | 9 | 85 | 0.006 |
| 231 | 8.11 | 9 | 85 | 0.006 |
| 232 | 7.48 | 9 | 85 | 0.006 |
| 247 | 8.14 | 12 | 85 | 0.006 |
| 248 | 7.83 | 12 | 85 | 0.006 |
| 249 | 7.64 | 12 | 85 | 0.006 |
| 201 | 9.01 | 3 | 85 | 0.018 |
| 202 | 8.79 | 3 | 85 | 0.018 |
| 203 | 8.86 | 3 | 85 | 0.018 |
| 216 | 8.72 | 6 | 85 | 0.018 |
| 217 | 8.46 | 6 | 85 | 0.018 |
| 218 | 8.24 | 6 | 85 | 0.018 |
| 233 | 8.17 | 9 | 85 | 0.018 |
| 234 | 8.04 | 9 | 85 | 0.018 |
| 235 | 7.56 | 9 | 85 | 0.018 |

**Table A.3. Continued.**

| Sample Number | Tension Capacity (kips) | Test Times, t (months) | Observed Temperature, T (oF) | Chloride concentration, (%Cl-) |
|---|---|---|---|---|
| 250 | 8.20 | 12 | 85 | 0.018 |
| 251 | 7.96 | 12 | 85 | 0.018 |
| 252 | 8.47 | 12 | 85 | 0.018 |
| 204 | 8.65 | 3 | 85 | 0.18 |
| 205 | 8.98 | 3 | 85 | 0.18 |
| 206 | 8.49 | 3 | 85 | 0.18 |
| 219 | 8.47 | 6 | 85 | 0.18 |
| 220 | 8.79 | 6 | 85 | 0.18 |
| 221 | 8.51 | 6 | 85 | 0.18 |
| 222 | 7.93 | 6 | 85 | 0.18 |
| 236 | 8.35 | 9 | 85 | 0.18 |
| 237 | 8.27 | 9 | 85 | 0.18 |
| 238 | 8.25 | 9 | 85 | 0.18 |
| 239 | 8.39 | 9 | 85 | 0.18 |
| 253 | 7.38 | 12 | 85 | 0.18 |
| 254 | 8.09 | 12 | 85 | 0.18 |
| 255 | 7.82 | 12 | 85 | 0.18 |
| 207 | 8.86 | 3 | 85 | 1.8 |
| 208 | 8.84 | 3 | 85 | 1.8 |
| 209 | 8.74 | 3 | 85 | 1.8 |
| 223 | 7.85 | 6 | 85 | 1.8 |
| 224 | 7.78 | 6 | 85 | 1.8 |
| 225 | 8.40 | 6 | 85 | 1.8 |
| 226 | 7.87 | 6 | 85 | 1.8 |
| 240 | 7.98 | 9 | 85 | 1.8 |
| 241 | 8.13 | 9 | 85 | 1.8 |
| 242 | 7.52 | 9 | 85 | 1.8 |
| 243 | 8.13 | 9 | 85 | 1.8 |
| 256 | 7.54 | 12 | 85 | 1.8 |
| 257 | 7.61 | 12 | 85 | 1.8 |
| 258 | 7.07 | 12 | 85 | 1.8 |

**Table A.4. Tension capacity data from unstressed wire samples exposed to CA conditions.**

| Tension Capacity (kips) | Test Times, t (months) | Relative humidity, RH % | Observed Temperature, T (oF) | Chloride concentration in surface grout at GAS interface, (%gCl-), Wt % cement |
|---|---|---|---|---|
| 9.15 | 9 | 97 | 43 | 1.05683E-05 |
| 9.10 | 9 | 97 | 43 | 1.05683E-05 |
| 9.29 | 9 | 45 | 85 | 1.05683E-05 |
| 9.28 | 9 | 70 | 85 | 1.05683E-05 |
| 9.25 | 9 | 70 | 85 | 1.05683E-05 |
| 9.30 | 9 | 45 | 94 | 1.05683E-05 |
| 9.26 | 9 | 97 | 94 | 1.05683E-05 |
| 8.71 | 9 | 97 | 94 | 1.05683E-05 |
| 8.93 | 9 | 97 | 94 | 1.05683E-05 |
| 9.26 | 9 | 70 | 43 | 0.013738816 |
| 9.26 | 9 | 70 | 43 | 0.013738816 |
| 9.29 | 9 | 45 | 85 | 0.013738816 |
| 9.26 | 9 | 45 | 85 | 0.013738816 |
| 9.16 | 9 | 97 | 85 | 0.013738816 |
| 9.10 | 9 | 97 | 85 | 0.013738816 |
| 9.23 | 9 | 97 | 85 | 0.013738816 |
| 9.24 | 9 | 70 | 94 | 0.013738816 |
| 9.29 | 9 | 70 | 94 | 0.013738816 |
| 9.29 | 9 | 45 | 43 | 0.091944384 |
| 9.30 | 9 | 45 | 43 | 0.091944384 |
| 9.12 | 9 | 97 | 43 | 0.091944384 |
| 9.15 | 9 | 97 | 43 | 0.091944384 |
| 9.20 | 9 | 70 | 85 | 0.091944384 |
| 9.21 | 9 | 70 | 85 | 0.091944384 |
| 9.25 | 9 | 70 | 85 | 0.091944384 |
| 9.19 | 9 | 70 | 85 | 0.091944384 |
| 9.28 | 9 | 45 | 94 | 0.091944384 |
| 9.28 | 9 | 45 | 94 | 0.091944384 |
| 8.94 | 9 | 97 | 94 | 0.091944384 |
| 9.23 | 9 | 97 | 94 | 0.091944384 |
| 9.05 | 9 | 97 | 94 | 0.091944384 |
| 9.12 | 9 | 97 | 94 | 0.091944384 |

**Table A.4. Continued.**

| Tension Capacity (kips) | Test Times, t (months) | Relative humidity, RH % | Observed Temperature, T (oF) | Chloride concentration in surface grout at GAS interface, (%gCl-), Wt % cement |
|---|---|---|---|---|
| 9.18 | 9 | 70 | 43 | 0.3434704 |
| 9.12 | 9 | 70 | 43 | 0.3434704 |
| 9.20 | 9 | 45 | 85 | 0.3434704 |
| 9.22 | 9 | 45 | 85 | 0.3434704 |
| 9.19 | 9 | 45 | 85 | 0.3434704 |
| 9.13 | 9 | 45 | 85 | 0.3434704 |
| 9.08 | 9 | 97 | 85 | 0.3434704 |
| 9.15 | 9 | 97 | 85 | 0.3434704 |
| 8.99 | 9 | 97 | 85 | 0.3434704 |
| 9.03 | 9 | 97 | 85 | 0.3434704 |
| 9.10 | 9 | 70 | 94 | 0.3434704 |
| 9.16 | 9 | 70 | 94 | 0.3434704 |
| 9.12 | 9 | 70 | 94 | 0.3434704 |
| 9.09 | 9 | 70 | 94 | 0.3434704 |
| 9.13 | 9 | 45 | 43 | 0.78205568 |
| 9.13 | 9 | 45 | 43 | 0.78205568 |
| 9.07 | 9 | 97 | 43 | 0.78205568 |
| 9.02 | 9 | 97 | 43 | 0.78205568 |
| 8.97 | 9 | 97 | 43 | 0.78205568 |
| 9.20 | 9 | 70 | 85 | 0.78205568 |
| 9.03 | 9 | 70 | 85 | 0.78205568 |
| 9.17 | 9 | 70 | 85 | 0.78205568 |
| 9.09 | 9 | 70 | 85 | 0.78205568 |
| 9.13 | 9 | 45 | 94 | 0.78205568 |
| 9.08 | 9 | 45 | 94 | 0.78205568 |
| 6.77 | 9 | 97 | 94 | 0.78205568 |
| 6.04 | 9 | 97 | 94 | 0.78205568 |
| 6.65 | 9 | 97 | 94 | 0.78205568 |
| 7.00 | 9 | 97 | 94 | 0.78205568 |

# APPENDIX B

# STRUCTURAL DETAILING OF CONCRETE REACTION FRAMES

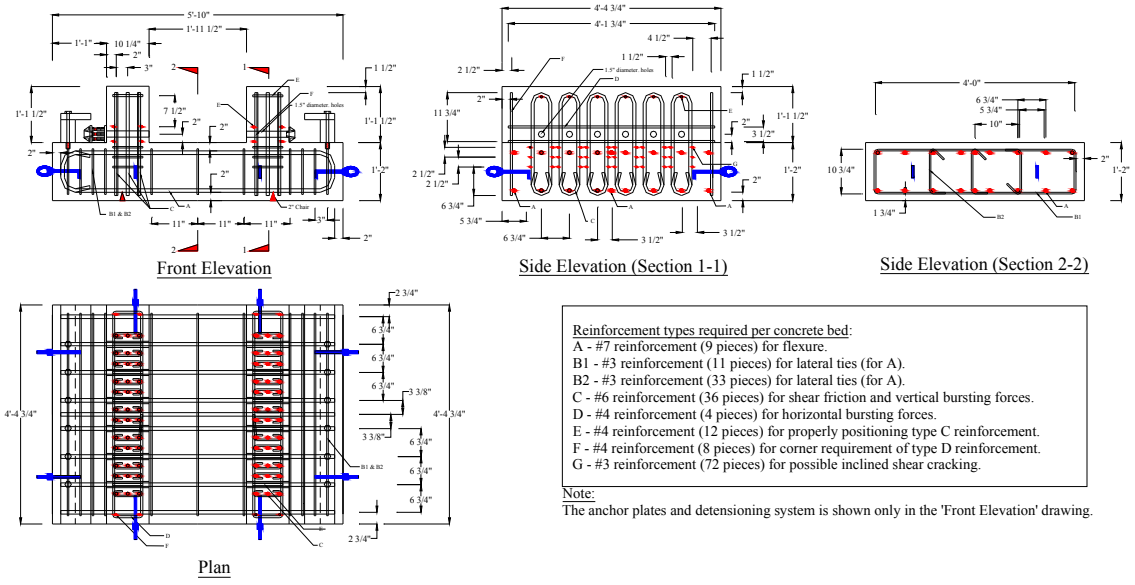


**Figure B.1. Structural Detailing of Concrete Reaction Frames - All Views.**

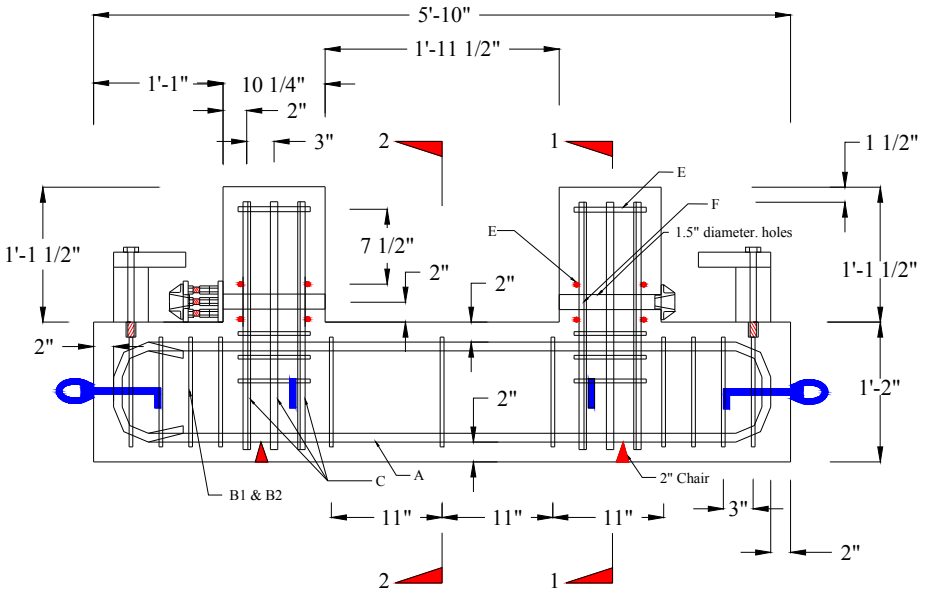


**Figure B.2. Structural Detailing of Concrete Reaction Frame – Front Elevation.**

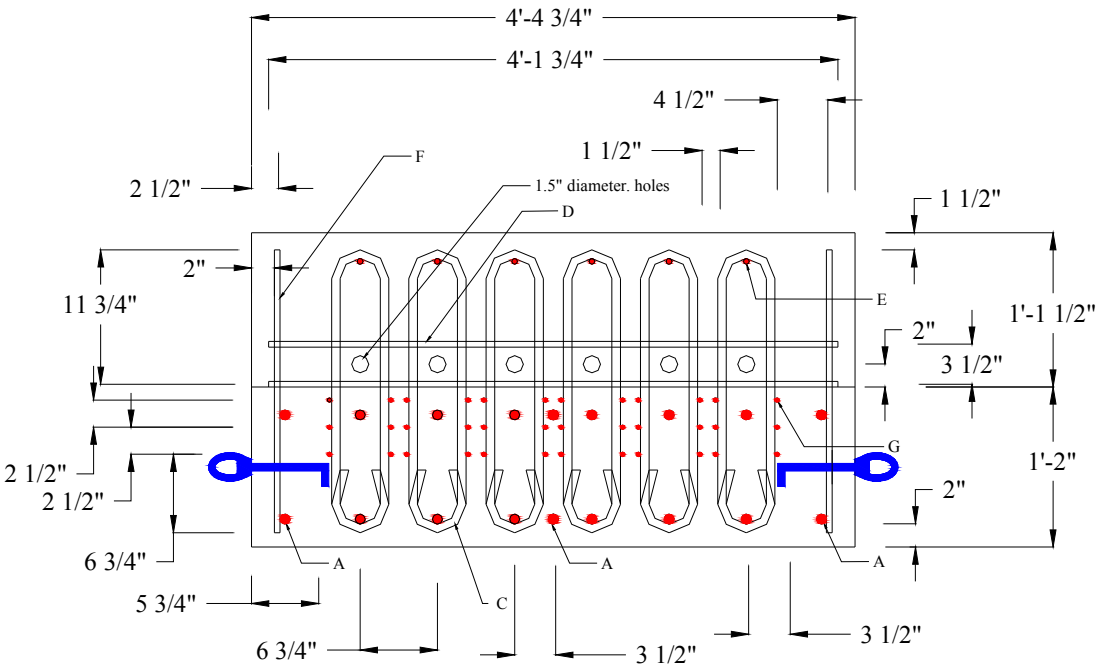


**Figure B.3. Structural Detailing of Concrete Reaction Frame – Section 1-1.**

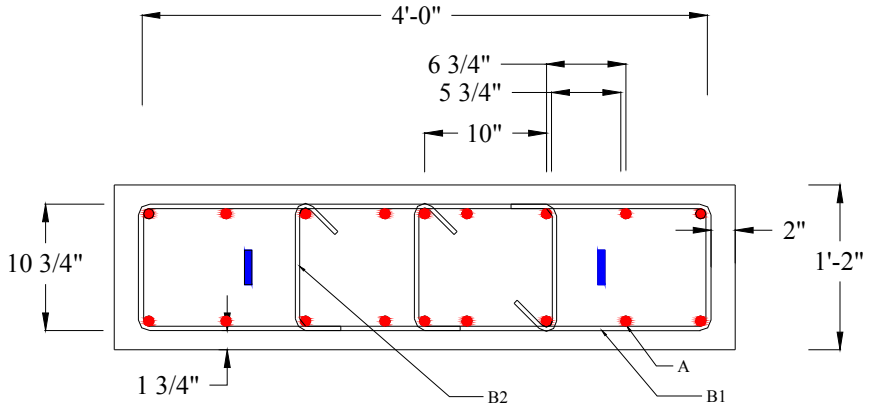


**Figure B.4. Structural Detailing of Concrete Reaction Frame – Section 2-2.**

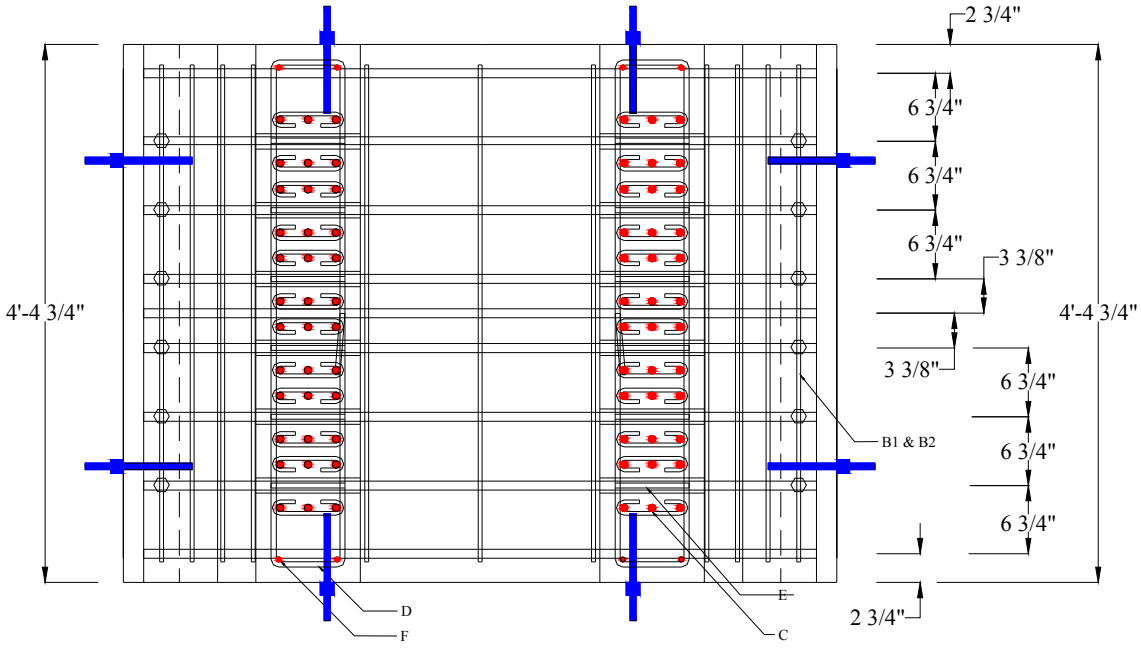


**Figure B.5. Structural Detailing of Concrete Reaction Frame – Plan View.**

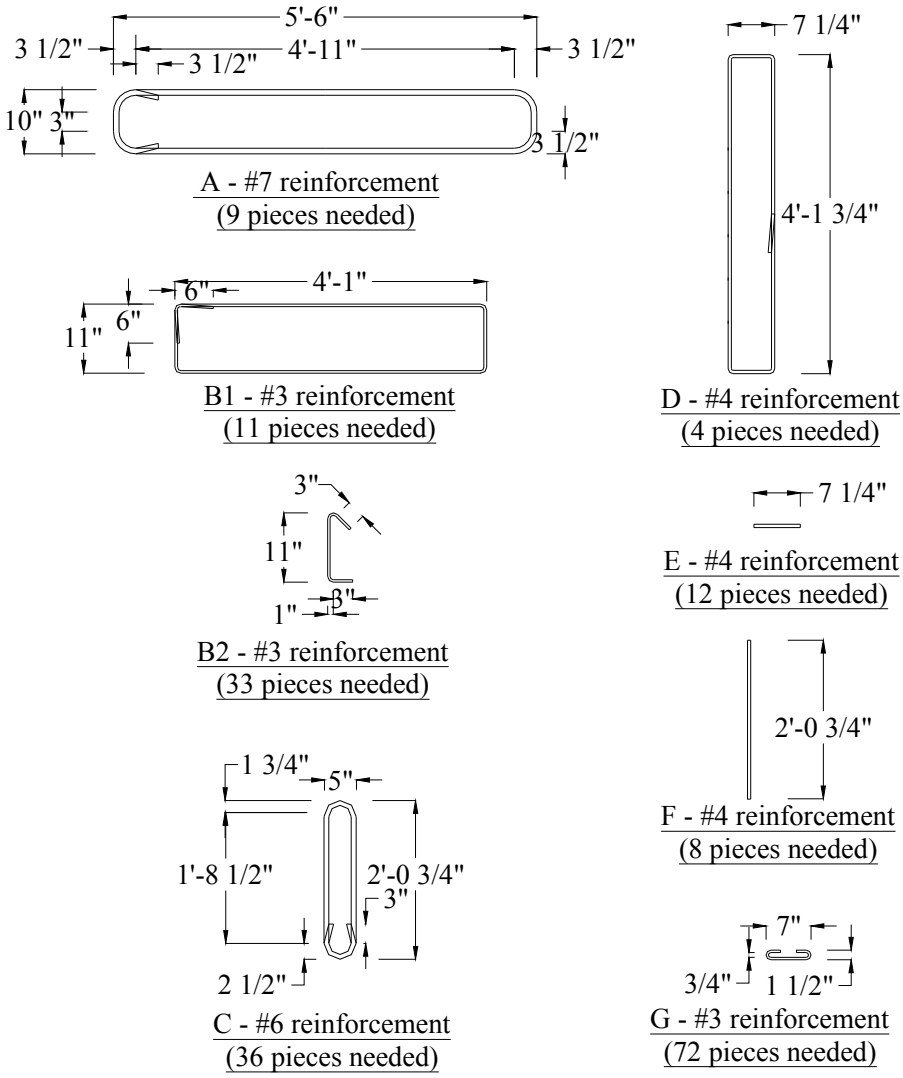


Reinforcement types required per concrete bed:
A - #7 reinforcement (9 pieces) for flexure.
B1 - #3 reinforcement (11 pieces) for lateral ties (for A).
B2 - #3 reinforcement (33 pieces) for lateral ties (for A).
C - #6 reinforcement (36 pieces) for shear friction and vertical bursting forces.
D - #4 reinforcement (4 pieces) for horizontal bursting forces.
E - #4 reinforcement (12 pieces) for properly positioning type C reinforcement.
F - #4 reinforcement (8 pieces) for corner requirement of type D reinforcement.
G - #3 reinforcement (72 pieces) for possible inclined shear cracking.

**Figure B.6. Detailing of Reinforcement Required for one Concrete Reaction Frame.**

# APPENDIX C

# TRIAL MODELS FOR THE TENSION CAPACITY OF WIRES UNDER CONTINUOUS-ATMOSPHERIC CONDITIONS

## Table C-1. List of Trial Models

| Model Name | Model form $\left( R_{C_{T,UW}}(\mathbf{x},\boldsymbol{\Theta})\Big\|_{t_{CA}=9\text{ months}} = R_{C_{T,UW}} \right)$ |
|---|---|
| UW-CA-2 | $R_{C_{T,UW}} = \theta_0 + \theta_1 \exp\left[\theta_2 \gamma_{RH}\right] + \theta_3 \gamma_{\%gCl^-} + \theta_4 \gamma_T + \theta_5 \gamma_{\%gCl^-} \exp\left[\theta_6 \gamma_{RH}\right] + \theta_7 \gamma_T \exp\left[\theta_8 \gamma_{RH}\right] + \theta_9 \gamma_{\%gCl^-} \gamma_T + \theta_{10} \gamma_{\%gCl^-} \exp\left[\theta_{11} \gamma_{RH}\right] \gamma_T + \sigma\varepsilon$ |
| UW-CA-3 | $R_{C_{T,UW}} = \theta_0 + \theta_1 \exp\left[\theta_2 \gamma_{RH}\right] + \theta_3 \gamma_{\%gCl^-} + \theta_4 \gamma_{\%gCl^-} \exp\left[\theta_5 \gamma_{RH}\right] + \theta_6 \gamma_T \exp\left[\theta_7 \gamma_{RH}\right] + \theta_8 \gamma_{\%gCl^-} \gamma_T + \theta_9 \gamma_{\%gCl^-} \exp\left[\theta_{10} \gamma_{RH}\right] \gamma_T + \sigma\varepsilon$ |
| UW-CA-4 | $R_{C_{T,UW}} = \theta_0 + \theta_1 \exp\left[\theta_2 \gamma_{RH}\right] + \theta_3 \gamma_{\%gCl^-} \exp\left[\theta_4 \gamma_{RH}\right] + \theta_5 \gamma_T \exp\left[\theta_6 \gamma_{RH}\right] + \theta_7 \gamma_{\%gCl^-} \gamma_T + \theta_8 \gamma_{\%gCl^-} \exp\left[\theta_9 \gamma_{RH}\right] \gamma_T + \sigma\varepsilon$ |
| UW-CA-5 | $R_{C_{T,UW}} = \theta_0 + \theta_1 \exp\left[\theta_2 \gamma_{RH}\right] + \theta_3 \gamma_{\%gCl^-} \exp\left[\theta_4 \gamma_{RH}\right] + \theta_5 \gamma_T \exp\left[\theta_6 \gamma_{RH}\right] + \theta_7 \gamma_{\%gCl^-} \exp\left[\theta_8 \gamma_{RH}\right] \gamma_T + \sigma\varepsilon$ |
| UW-CA-6 | $R_{C_{T,UW}} = \theta_0 + \theta_1 \exp\left[\theta_2 \gamma_{RH}\right] + \theta_3 \gamma_{\%gCl^-} \exp\left[\theta_4 \gamma_{RH}\right] + \theta_5 \gamma_{\%gCl^-} \exp\left[\theta_6 \gamma_{RH}\right] \gamma_T + \sigma\varepsilon$ |
| UW-CA-7 | $R_{C_{T,UW}} = \theta_0 + \theta_1 \gamma_{\%gCl^-} \exp\left[\theta_2 \gamma_{RH}\right] + \theta_3 \gamma_{\%gCl^-} \exp\left[\theta_4 \gamma_{RH}\right] \gamma_T + \sigma\varepsilon$ |
| UW-CA-8 | $R_{C_{T,UW}} = \theta_0 + \theta_1 \exp\left[\theta_2 \gamma_{RH}\right] + \theta_3 \gamma_{\%gCl^-} \exp\left[\theta_4 \gamma_{RH}\right] \gamma_T + \sigma\varepsilon$ |

**Model UW-CA-2**

$$R_{C_{T,UW}} = \theta_0 + \theta_1 \exp\left[\theta_2 \gamma_{RH}\right] + \theta_3 \gamma_{\%gCl^-} + \theta_4 \gamma_T + \theta_5 \gamma_{\%gCl^-} \exp\left[\theta_6 \gamma_{RH}\right] + \theta_7 \gamma_T \exp\left[\theta_8 \gamma_{RH}\right] + \theta_9 \gamma_{\%gCl^-} \gamma_T + \theta_{10} \gamma_{\%gCl^-} \exp\left[\theta_{11} \gamma_{RH}\right] \gamma_T + \sigma\varepsilon$$

**Table C-2. Summary Statistics and Validation Plot for UW-CA-2 Model.**

| Parameter | Mean | COV | Validation plot |
|---|---|---|---|
| $\theta_0$ | 0.158019 | 0.019700 | 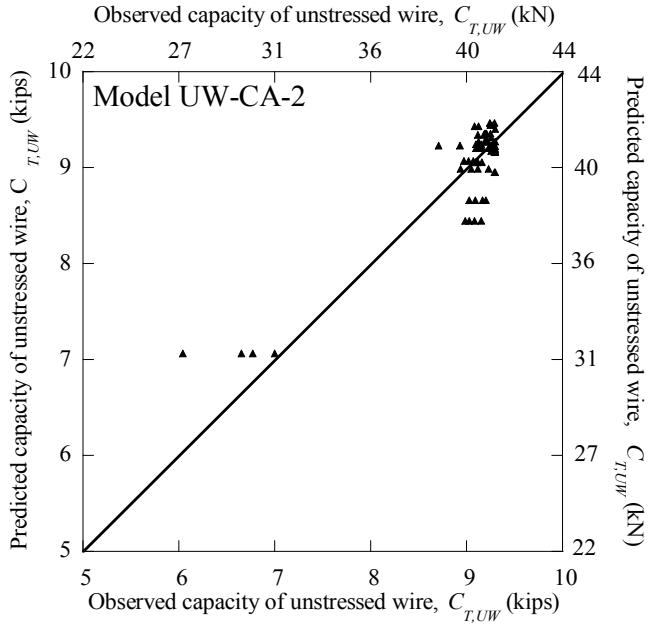 |
| $\theta_1$ | -0.341983 | 0.037000 | |
| $\theta_2$ | -7.795676 | 0.001900 | |
| $\theta_3$ | -17.940950 | 0.000900 | |
| $\theta_4$ | 0.000507 | 0.248200 | |
| $\theta_5$ | 17.574070 | 0.000800 | |
| $\theta_6$ | 0.086942 | 0.185200 | |
| $\theta_7$ | -0.000333 | 0.268300 | |
| $\theta_8$ | 0.439560 | 0.008700 | |
| $\theta_9$ | -0.426721 | 0.002000 | |
| $\theta_{10}$ | 0.451462 | 0.007200 | |
| $\theta_{11}$ | -0.134635 | 0.112300 | |
| σ | 0.004977 | 0.000002 | |

**Model UW-CA-3**

$$R_{C_{T,UW}} = \theta_0 + \theta_1 \exp\left[\theta_2 \gamma_{RH}\right] + \theta_3 \gamma_{\%gCl^-} + \theta_4 \gamma_{\%gCl^-} \exp\left[\theta_5 \gamma_{RH}\right] + \theta_6 \gamma_T \exp\left[\theta_7 \gamma_{RH}\right] + \theta_8 \gamma_{\%gCl^-} \gamma_T + \theta_9 \gamma_{\%gCl^-} \exp\left[\theta_{10} \gamma_{RH}\right] \gamma_T + \sigma\varepsilon$$

**Table C-3. Summary Statistics and Validation Plot for UW-CA-3 Model.**

| Parameter | Mean | COV | Validation plot |
|---|---|---|---|
| $\theta_0$ | 0.1588543 | 0.0079 | |
| $\theta_1$ | -6.470238 | 0.0166 | |
| $\theta_2$ | -17.57031 | 0.1189 | |
| $\theta_3$ | -139.4134 | 0.0048 | |
| $\theta_4$ | 142.3089 | 0.0061 | |
| $\theta_5$ | -0.0209625 | 0.1513 | |
| $\theta_6$ | 48.85621 | 0.0205 | |
| $\theta_7$ | -2701.301 | 0.0004 | |
| $\theta_8$ | -0.0156514 | 0.2159 | |
| $\theta_9$ | -176.6118 | 0.0023 | |
| $\theta_{10}$ | -23.63623 | 0.0781 | |
| σ | 0.00661583 | 1.86E-06 | |

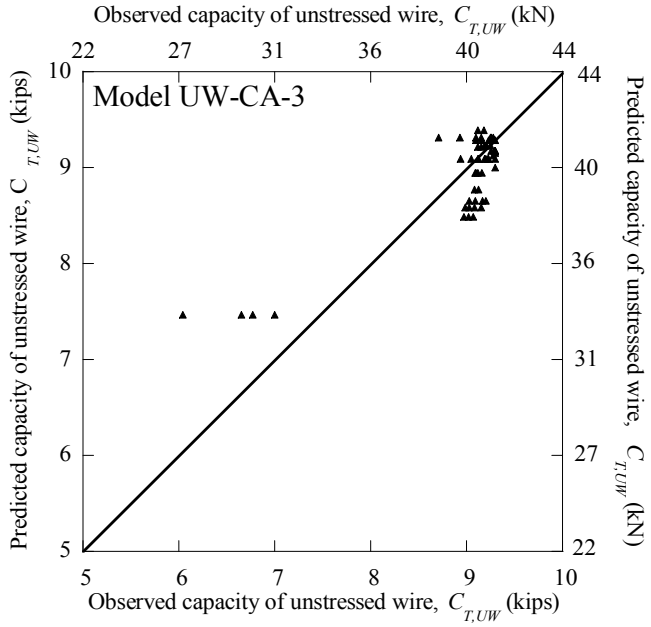

**Model UW-CA-4**

$$R_{C_{T,UW}} = \theta_0 + \theta_1 \exp\left[\theta_2 \gamma_{RH}\right] + \theta_3 \gamma_{\%gCl^-} \exp\left[\theta_4 \gamma_{RH}\right] + \theta_5 \gamma_T \exp\left[\theta_6 \gamma_{RH}\right] + \theta_7 \gamma_{\%gCl^-} \gamma_T + \theta_8 \gamma_{\%gCl^-} \exp\left[\theta_9 \gamma_{RH}\right] \gamma_T + \sigma\varepsilon$$

**Table C-4. Summary Statistics and Validation Plot for UW-CA-4 Model.**

| Parameter | Mean | COV |
|---|---|---|
| $\theta_0$ | 0.1580805 | 0.0078 |
| $\theta_1$ | -3305.029 | 0.0003 |
| $\theta_2$ | -16527.72 | 0.0001 |
| $\theta_3$ | 3.404923 | 0.2422 |
| $\theta_4$ | -1.935418 | 0.3044 |
| $\theta_5$ | 24.11192 | 0.0415 |
| $\theta_6$ | -1381.957 | 0.0007 |
| $\theta_7$ | -0.0189404 | 0.1673 |
| $\theta_8$ | 4.530774 | 0.2207 |
| $\theta_9$ | -281.7407 | 0.0035 |
| σ | 0.0072819 | 0.0850 |

**Validation plot**

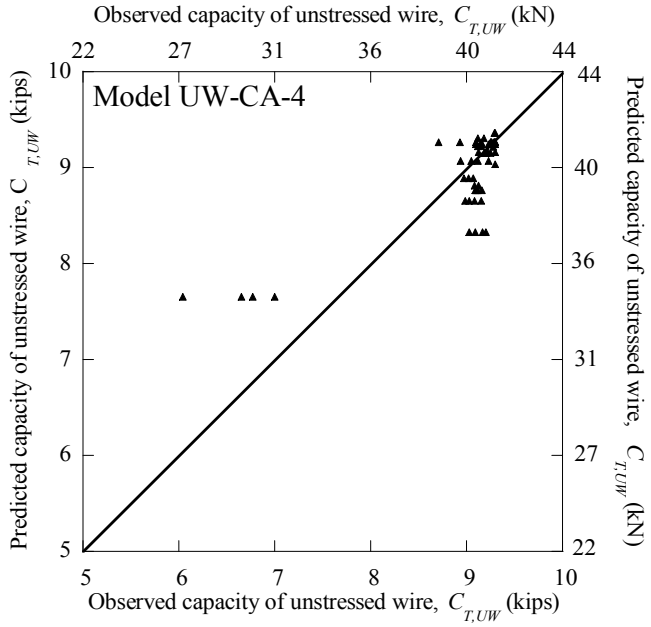

**Model UW-CA-5**

$$R_{C_{T,UW}} = \theta_0 + \theta_1 \exp\left[\theta_2 \gamma_{RH}\right] + \theta_3 \gamma_{\%gCl^-} \exp\left[\theta_4 \gamma_{RH}\right] + \theta_5 \gamma_T \exp\left[\theta_6 \gamma_{RH}\right] + \theta_7 \gamma_{\%gCl^-} \exp\left[\theta_8 \gamma_{RH}\right] \gamma_T + \sigma\varepsilon$$

**Table C-5. Summary Statistics and Validation Plot for UW-CA-5 Model.**

| Parameter | Mean | COV |
|---|---|---|
| $\theta_0$ | 0.1579481 | 0.0038 |
| $\theta_1$ | 7.95969 | 0.0253 |
| $\theta_2$ | -28.25957 | 0.0034 |
| $\theta_3$ | 0.00655044 | 0.2537 |
| $\theta_4$ | 5.452533 | 0.0351 |
| $\theta_5$ | 49.30347 | 0.0203 |
| $\theta_6$ | -2661.687 | 0.0004 |
| $\theta_7$ | -5.997E-05 | 0.0767 |
| $\theta_8$ | 6.519461 | 0.0003 |
| $\sigma$ | 0.00406109 | 0.0908 |

**Validation plot**

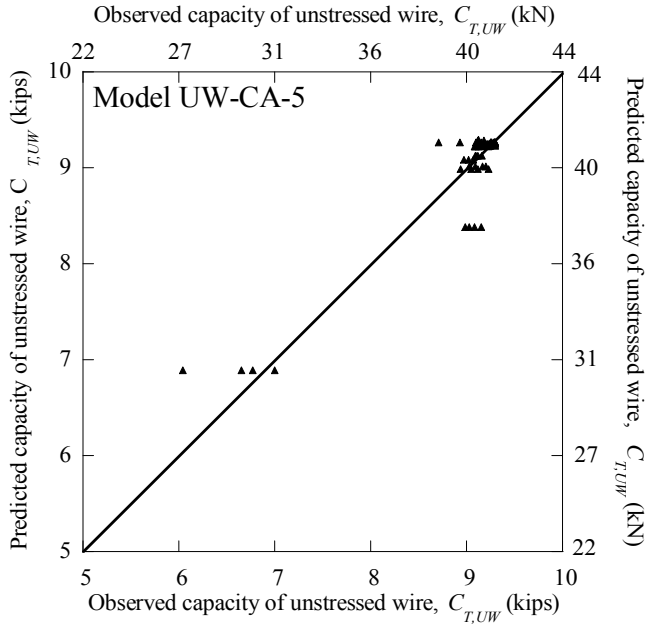

**Model UW-CA-6**

$$R_{C_{T,UW}} = \theta_0 + \theta_1 \exp\left[\theta_2 \gamma_{RH}\right] + \theta_3 \gamma_{\%gCl^-} \exp\left[\theta_4 \gamma_{RH}\right] + \theta_5 \gamma_{\%gCl^-} \exp\left[\theta_6 \gamma_{RH}\right] \gamma_T + \sigma\varepsilon$$

**Table C-6. Summary Statistics and Validation Plot for UW-CA-6 Model.**

| Parameter | Mean | COV |
|---|---|---|
| $\theta_0$ | 0.2165476 | 0.0093 |
| $\theta_1$ | -0.0597658 | 0.0648 |
| $\theta_2$ | -0.0309949 | 0.0672 |
| $\theta_3$ | 0.00020876 | 2.1778 |
| $\theta_4$ | 8.977964 | 0.0002 |
| $\theta_5$ | -1.17E-05 | 1.0891 |
| $\theta_6$ | 8.204005 | 0.0003 |
| $\sigma$ | 0.05 | 20.2926 |

**Validation plot**

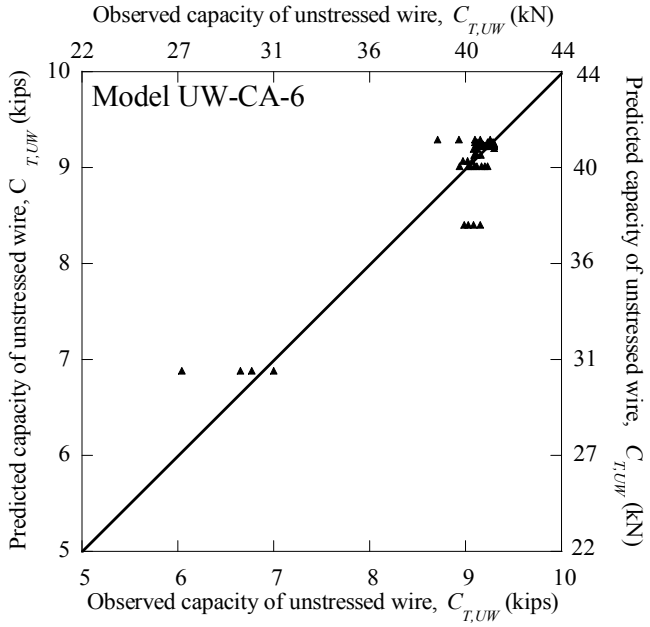

**Model UW-CA-7**

$$R_{C_{T,UW}} = \theta_0 + \theta_1 \gamma_{\%gCl^-} \exp\left[\theta_2 \gamma_{RH}\right] + \theta_3 \gamma_{\%gCl^-} \exp\left[\theta_4 \gamma_{RH}\right] \gamma_T + \sigma\varepsilon$$

**Table C-7. Summary Statistics and Validation Plot for UW-CA-7 Model.**

| Parameter | Mean | COV |
|---|---|---|
| $\theta_0$ | 0.1578797 | 0.016 |
| $\theta_1$ | 0.00011212 | 3.0487 |
| $\theta_2$ | 9.631754 | 0.0004 |
| $\theta_3$ | -5.303E-06 | 1.3589 |
| $\theta_4$ | 9.011664 | 0.0005 |
| σ | 0.04 | 64.6101 |

**Validation plot**

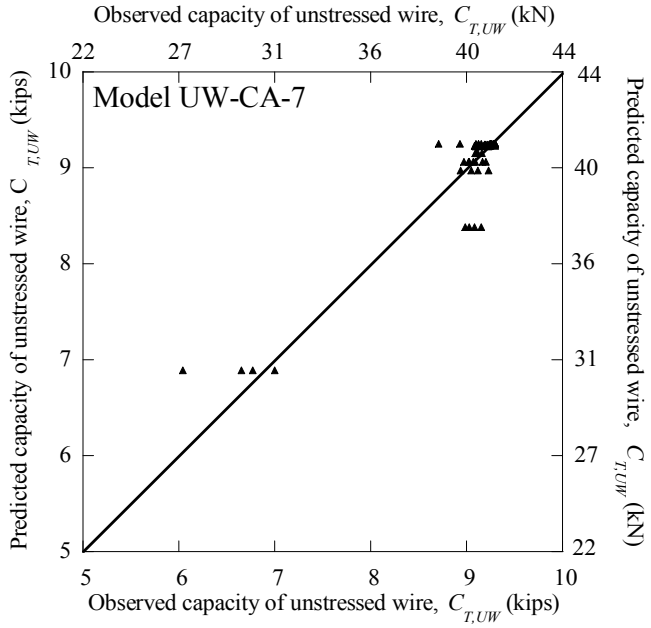

**Model UW-CA-8**

$$R_{C_{T,UW}} = \theta_0 + \theta_1 \exp\left[\theta_2 \gamma_{RH}\right] + \theta_3 \gamma_{\%gCl^-} \exp\left[\theta_4 \gamma_{RH}\right] \gamma_T + \sigma\varepsilon$$

**Table C-8. Summary Statistics and Validation Plot for UW-CA-8 Model.**

| Parameter | Mean | COV |
|---|---|---|
| $\theta_0$ | -0.6305386 | 0.8151 |
| $\theta_1$ | 0.798094 | 0.6441 |
| $\theta_2$ | -0.0241001 | 0.695 |
| $\theta_3$ | 5.43627 | 0.6946 |
| $\theta_4$ | -4962.669 | 0.6937 |
| σ | 0.01024392 | 0.0035 |

**Validation plot**

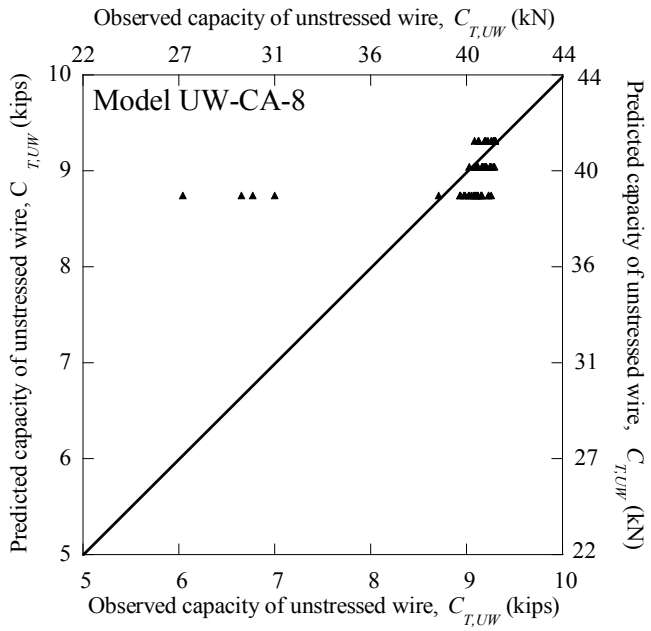

# APPENDIX D

# STRENGTH AND SERVICE RELIABILITY INDICES

**Table D.1. Strength Reliability Indices of the Defined Typical PT Bridge.**

| Chloride condition | Time (years) | Structural loading condition | | | | | | | | | | | |
|---|---|---|---|---|---|---|---|---|---|---|---|---|---|
| | | HS20 | | | | | | HL93 | | | | | |
| | | Number of tendons undergoing wet-dry conditions | | | | | | | | | | | |
| | | 1 | 2 | 3 | 4 | 5 | 6 | 1 | 2 | 3 | 4 | 5 | 6 |
| 0.006 %$sCl^-$ and 0.014 %$sCl^-$ | 0 | | | | | | | | | | | | |
| | 10 | | | | 4.35 | 4.02 | 3.75 | | | 4.06 | 3.78 | 3.49 | 3.26 |
| | 20 | | | 3.83 | 3.30 | 2.93 | 2.67 | | | 3.36 | 2.99 | 2.77 | 2.44 |
| | 30 | | | 3.24 | 2.81 | 2.48 | 1.96 | | 3.47 | 2.96 | 2.63 | 2.01 | 1.17 |
| | 45 | | | 2.87 | 2.51 | 1.84 | 0.87 | | 3.17 | 2.75 | 2.04 | 1.09 | 0.22 |
| | 75 | | 3.55 | 2.82 | 2.42 | 1.56 | 0.71 | | 3.11 | 2.69 | 1.87 | 0.83 | 0.02 |
| 0.018 %$sCl^-$ and 0.092 %$sCl^-$ | 0 | | | | | | | | | | | | |
| | 10 | | | 4.41 | 4.01 | 3.62 | 3.50 | | | 3.82 | 3.50 | 3.18 | 2.96 |
| | 20 | | | 3.45 | 2.95 | 2.66 | 2.34 | | 3.60 | 3.11 | 2.78 | 2.39 | 1.76 |
| | 30 | | | 3.00 | 2.60 | 2.11 | 1.20 | | 3.27 | 2.80 | 2.28 | 1.34 | 0.57 |
| | 45 | | | 2.80 | 2.42 | 1.61 | 0.62 | | 3.12 | 2.69 | 1.87 | 0.83 | 0.04 |
| | 60 | | 3.52 | 2.82 | 2.43 | 1.57 | 0.65 | | 3.12 | 2.69 | 1.87 | 0.73 | 0.02 |
| | 75 | | 3.52 | 2.82 | 2.43 | 1.57 | 0.65 | | 3.12 | 2.69 | 1.87 | 0.73 | 0.02 |
| 1.8 %$sCl^-$ and 0.782 %$sCl^-$ | 0 | | | | | | | | | | | | |
| | 5 | | | | 4.04 | 3.65 | 3.30 | | | 3.83 | 3.19 | 3.19 | 2.96 |
| | 10 | | | 3.49 | 2.95 | 2.61 | 2.34 | | 3.62 | 3.09 | 2.74 | 2.39 | 1.78 |
| | 15 | | | 2.98 | 2.56 | 2.12 | 1.22 | | 3.27 | 2.77 | 2.28 | 1.37 | 0.33 |
| | 20 | | | 2.82 | 2.42 | 1.66 | 0.49 | | 3.13 | 2.63 | 1.92 | 0.81 | -0.35 |
| | 30 | | 3.50 | 2.75 | 2.35 | 1.44 | 0.22 | | 3.08 | 2.58 | 1.79 | 0.49 | -0.62 |
| | 75 | | 3.50 | 2.75 | 2.35 | 1.44 | 0.22 | | 3.08 | 2.58 | 1.79 | 0.49 | -0.62 |

Note: Empty cells indicate that the values are greater than 3.5 and could not be determined.

**Table D.2. Service Reliability Indices of the Defined Typical PT Bridge.**

| Chloride condition | Time (years) | Structural loading condition | | | | | | | | | | | |
|---|---|---|---|---|---|---|---|---|---|---|---|---|---|
| | | HS20 | | | | | | HL93 | | | | | |
| | | Number of tendons undergoing wet-dry conditions | | | | | | | | | | | |
| | | 1 | 2 | 3 | 4 | 5 | 6 | 1 | 2 | 3 | 4 | 5 | 6 |
| 0.006 %$sCl^-$ and 0.014 %$sCl^-$ | 0 | 1.2 | 1.2 | 1.2 | 1.2 | 1.2 | 1.2 | 0.6 | 0.6 | 0.6 | 0.6 | 0.6 | 0.6 |
| | 10 | 0.9 | 0.6 | 0.3 | 0.0 | -0.3 | -0.6 | 0.3 | 0.0 | -0.3 | -0.6 | -0.9 | -1.4 |
| | 20 | 0.7 | 0.1 | -0.4 | -1.6 | -1.3 | -1.9 | 0.1 | -0.5 | -1.1 | -1.4 | -2.1 | -8.2 |
| | 30 | 0.5 | -0.3 | -0.9 | -8.2 | -8.2 | -8.2 | -0.1 | -0.8 | -1.4 | -1.8 | -2.3 | -8.2 |
| | 45 | 0.3 | -0.6 | -1.3 | -8.2 | -8.2 | -8.2 | -0.3 | -1.0 | -1.8 | -2.3 | -8.2 | -8.2 |
| | 75 | 0.2 | -0.5 | -1.3 | -8.2 | -8.2 | -8.2 | -0.3 | -1.1 | -1.8 | -8.2 | -8.2 | -8.2 |
| 0.018 %$sCl^-$ and 0.092 %$sCl^-$ | 0 | 1.2 | 1.2 | 1.2 | 1.2 | 1.2 | 1.2 | 0.6 | 0.6 | 0.6 | 0.6 | 0.6 | 0.6 |
| | 10 | 0.8 | 0.4 | 0.1 | -0.3 | -0.7 | -1.0 | 0.2 | -0.1 | -0.5 | -0.9 | -1.3 | -1.6 |
| | 20 | 0.5 | -0.1 | -0.7 | -1.2 | -1.9 | -2.1 | -0.1 | -0.7 | -1.1 | -1.6 | -2.1 | -8.2 |
| | 30 | 0.3 | -0.5 | -1.2 | -1.7 | -2.2 | -8.2 | -0.3 | -1.0 | -1.6 | -2.3 | -8.2 | -8.2 |
| | 45 | 0.2 | -0.6 | -1.2 | -1.7 | -2.3 | -8.2 | -0.3 | -1.1 | -1.8 | -8.2 | -8.2 | -8.2 |
| | 60 | 0.2 | -0.6 | -1.3 | -8.2 | -8.2 | -8.2 | -0.3 | -1.1 | -1.9 | -8.2 | -8.2 | -8.2 |
| | 75 | 0.2 | -0.6 | -1.3 | -8.2 | -8.2 | -8.2 | -0.3 | -1.1 | -1.9 | -8.2 | -8.2 | -8.2 |
| 1.8 %$sCl^-$ and 0.782 %$sCl^-$ | 0 | 1.2 | 1.2 | 1.2 | 1.2 | 1.2 | 1.2 | 0.6 | 0.6 | 0.6 | 0.6 | 0.6 | 0.6 |
| | 5 | 0.8 | 0.4 | 0.0 | -0.4 | -0.8 | -1.2 | 0.3 | -0.1 | -0.5 | -1.1 | -1.3 | -1.6 |
| | 10 | 0.5 | -0.2 | -0.9 | -1.5 | -8.2 | -8.2 | -0.1 | -0.8 | -1.5 | -2.1 | -8.2 | -8.2 |
| | 15 | 0.3 | -0.6 | -1.4 | -1.9 | -8.2 | -8.2 | -0.3 | -1.2 | -2.0 | -8.2 | -8.2 | -8.2 |
| | 20 | 0.2 | -0.8 | -1.5 | -2.3 | -8.2 | -8.2 | -0.4 | -1.4 | -2.1 | -8.2 | -8.2 | -8.2 |
| | 30 | 0.1 | -0.9 | -1.9 | -8.2 | -8.2 | -8.2 | -0.5 | -8.2 | -2.3 | -8.2 | -8.2 | -8.2 |
| | 75 | 0.1 | -0.9 | -1.9 | -8.2 | -8.2 | -8.2 | -0.5 | -8.2 | -2.3 | -8.2 | -8.2 | -8.2 |

# VITA

Radhakrishna Pillai Gopalakrishnan was born in Jaipur, India and was brought up in Kerala, India. In August 1999, he received his Bachelor of Engineering degree in civil engineering from Motilal Nehru Regional Engineering College, University of Allahabad, Allahabad, India. In Fall 2000 he started his Master of Science (M.S.) studies in civil engineering (with specialization in structural engineering) at Texas A&M University in College Station, Texas. During his M.S. studies, he worked as a graduate research assistant with the Texas Engineering Experiment Station in College Station, Texas. After graduating with M.S. degree he remained in College Station and worked as a research associate at Texas Transportation Institute. In January 2004, Dr. Pillai started his doctoral studies in civil engineering (with specialization in structural and materials performance) at Texas A&M University, College Station, Texas. During his doctoral studies, he worked as a graduate research assistant with the Texas Transportation Institute and a graduate teaching assistant with Zachry Department of Civil Engineering, Texas A&M Univeristy.

Dr. Pillai can be contacted at:

c/o Shri Gopalakrishna Pillai P.A.
Carnic House, Milma Road,
Kalleppully, P.O.
Palakkad District, Kerala State – 678-005
India
Ph: +1 (979) 575-9524 (mobile)
E-mail: radhakpg@yahoo.com